JOURNAL
OF
APPLIED PHYSICS

Vol. 31, No. 8 August, 1960

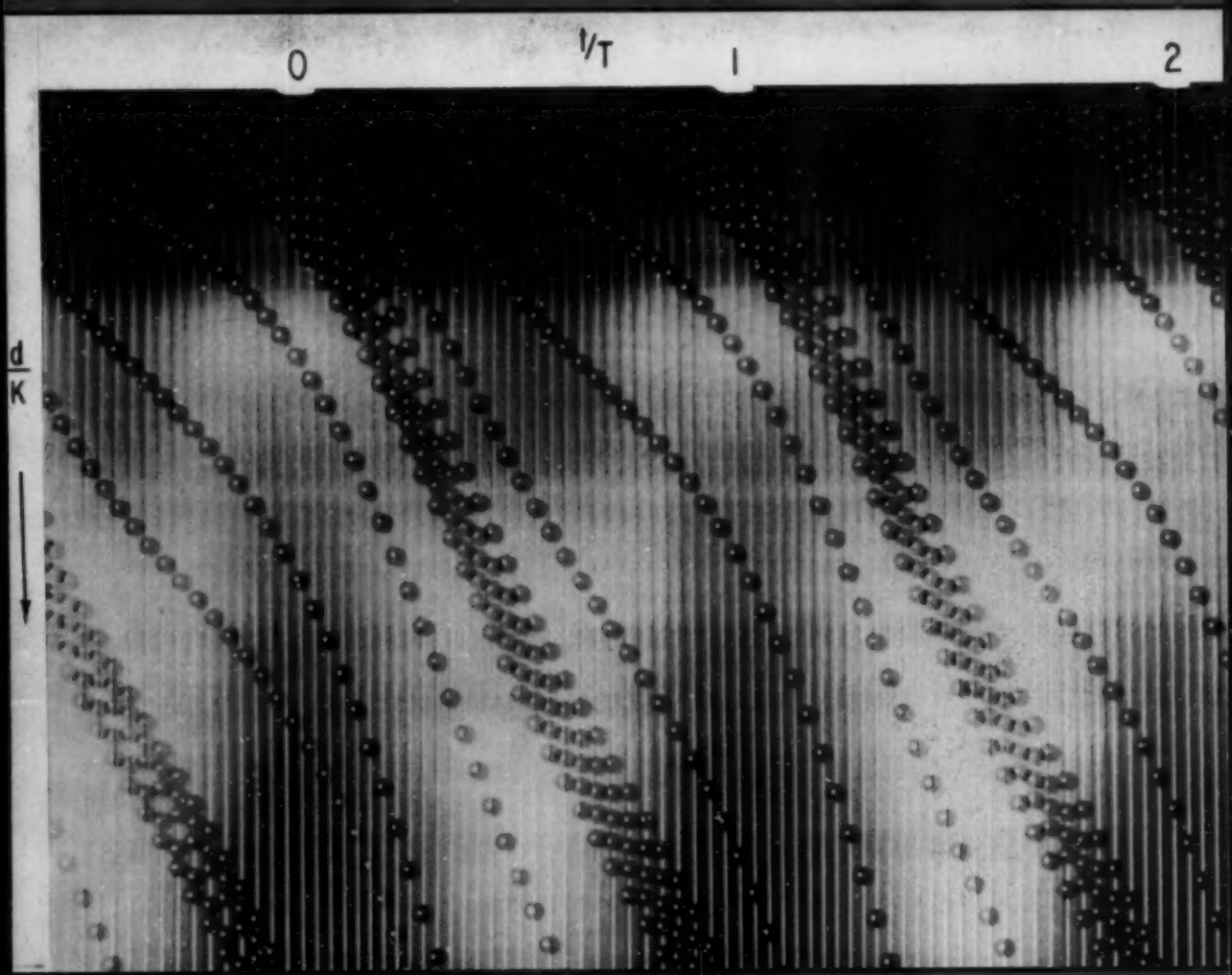

Analog Study of Large-Signal High-Frequency Diodes.
See Page 1431.

Shock from a first stick of explosive (below) causes sympathetic initiation of a second stick (above) in this series of frames photographed in the time sequence noted. The Model 189 Framing Camera used is a complete system with automatic controls for simple, reproducible operation. At rates up to 4.3 million frames per second.

explosive autograph

made with Model 189 Framing Camera

Photos, courtesy Ballistics Research Laboratory, Aberdeen Proving Ground

Beckman & Whitley Research Cameras of other types including sweeping-image models are solving analytical problems for many organizations. Send for details.

Beckman & Whitley INC.

SAN CARLOS 8 CALIFORNIA

instruments for 4-dimensional documentation

JOURNAL OF APPLIED PHYSICS

Vol. 31, No. 8 AUGUST, 1960

In This Issue

Transitory Electrical Properties of *n*-Type Germanium After a Neutron Pulse . . . . . H. J. Stein 1309

Performance of a Thermoelectric Converter under Constant Heat Flux Operation . . . . . P. S. Castro and W. W. Happ 1314

Some Elastic Properties of a Screw Dislocation Wall . . . . . James C. M. Li and Charles D. Needham 1318

X-Ray Reflection Studies of the Anneal and Oxidation of Some Thin Solid Films . . . . . N. Wainfan and L. G. Parratt 1331

Phase Oscillations in High Current Synchrotrons . . . . . Irvin G. Henry 1338

Current Noise due to Ohmic Contacts on Cadmium Sulfide . . James J. Brophy and Robert J. Robinson 1343

Growth from the Melt. I. Influence of Surface Intersections in Pure Metals . . . . . G. F. Bolling and W. A. Tiller 1345

Partition Noise in Electron Beams at Microwave Frequencies . . . . . A. Ashkin and L. D. White 1351

Thermal Expansion Coefficients of Bismuth . . . . . E. F. Cave and L. V. Holroyd 1357

Dislocations in Silicon Carbide . . . . . S. Amelinckx, G. Strumane, and W. W. Webb 1359

Three-Dimensional Space Charge Flow . . . . . Jorge Rosenblatt 1371

Stress Waves in Solids . . . . . C. R. Cassity 1377

Spectral Emissivity, Total Emissivity, and Thermal Conductivity of Molybdenum, Tantalum, and Tungsten above 2300°K . . . . . Robert D. Allen, Louis F. Glasier, Jr., and Paul L. Jordan 1382

Exchange Anisotropy Memory Effect . . . . . I. S. Jacobs and P. E. Lawrence 1388

Forces on Ion-Bombarded Electrodes in a Low-Pressure Plasma . . . . . G. K. Wehner 1392

Contribution of Anode Emission to Space Charge in Thermionic Power Converters . . Anthony F. Dugan 1397

Electromagnetic Theory of dc Effects in Ferromagnetic Resonance . . . . . H. J. Juretschke 1401

Temperature Dependence of Young's Modulus of Vitreous Germania and Silica . . . . . S. Spinner and G. W. Cleek 1407

Thermal Conductivity of Eight Halide Crystals in the Temperature Range 220° K to 390°K . . . . . Kathryn A. McCarthy and Stanley S. Ballard 1410

Dislocations in Metal Crystals Grown from the Melt . . . . . C. Elbaum 1413

Spiral Dislocations on Glass Fracture Surfaces . . . . . W. C. Levengood and T. S. Vong 1416

Characteristic Energy Losses of Electrons in Carbon . . . . . Lewis B. Leder and J. A. Suddeth 1422

Elastic Constants of Single-Crystal Aluminum Antimonide . . . . . D. I. Bolef and M. Menes 1426

Heat Treatment of Gallium Arsenide . . . . . J. T. Edmond 1428

Analog Study of Large-Signal High-Frequency Diodes . . . . . C. L. Andrews 1431

Plasma Propulsion by a Rapidly Varying Magnetic Field . . . Milton M. Klein and Keith A. Brueckner 1437

Parametric Amplifier Theory for Plasmas and Electron Beams . . . . . G. S. Kino 1449

Determination of Surface Structure using Ultra-High Vacuum Replication . . . . . L. Bachmann, W. H. Orr, T. N. Rhodin, and B. M. Siegel 1458

Negative Glow Plasma as a Cathode for Electron Tubes . . . . . J. M. Anderson and L. A. Harris 1463

Permanent Magnets Obtained by Drawing Compacts of Parallel Iron Wires . . . . . F. P. Levi 1469

Effect of Cu Precipitation on Dislocation Etch Pits in Ge . . . . . Howard Savage 1472

Diffusion of Deuterium in Deuteron-Irradiated Copper . . . . . Mark T. Robinson, A. L. Southern, and William R. Willis 1474

Simple Theory Concerning the Reflection of Electrons from Solids . . . . . T. E. Everhart 1483

Spreading Resistance in Cylindrical Semiconductor Devices . . . . . David P. Kennedy 1490

Letters to the Editor:

Inversions by Fast Passage in a Multilevel Spin System . . . P. E. Wagner, J. G. Castle, Jr., and P. F. Chester 1498

Detection of Growth Striations in Germanium Crystals . . . . . Albert C. English 1498

Metastable Solid Solutions in the Gallium Antimonide-Germanium Pseudobinary System . . . . . Pol Duwez, R. H. Willens, and W. Klement, Jr. 1500

Anomalous Thermionic Emission from UC and $(ZrC)_{0.2}(UC)_{0.2}$ . . . . . G. C. Kuczynski 1500

Dislocation Networks in a Low-Alloy Steel . . . . . A. S. Keh 1501

Probes at High Pressure . . . . . John E. White 1502

Cleavage Whiskers . . . . . John D. Venables 1503

Device for Measurement of the Electrical Properties of Bi_2Se_3 at Elevated Temperatures . . . . . Mac J. Smith, E. S. Kirk, and C. W. Spencer 1504

Field Induced Photoemission and Hot-Electron Emission from Germanium . . . R. E. Simon and W. E. Spicer 1505

Charred Dextrose as a Paramagnetic Resonance Standard . . . . . R. H. Hoskins and R. C. Pastor 1506

Precipitation of Copper in Gallium Arsenide . . . . . J. M. Whelan and C. S. Fuller 1507

Preparation of Large Calcium-Tungstate Crystals Containing Paramagnetic Ions for Maser Applications . . . . . K. Nassau and L. G. Van Uitert 1508

Generation of Alternating Current in the Cesium Cell . . . . . H. L. Garvin, W. B. Teutsch, and R. W. Pidd 1508

Books Reviewed 1509

Books Received 1510

Announcements 1510

JOURNAL OF APPLIED PHYSICS

A journal of general physics and its applications to other sciences and to industry

Published by the

American Institute of Physics

GOVERNING BOARD

Members

Ralph A. Sawyer, *Chairman*
James G. Baker
R. H. Bolt
W. R. Brode
Harvey Brooks
Dirk Brouwer
J. W. Buchta
Vernet E. Eaton
J. H. Elliott
Herbert A. Erf
S. A. Goudsmit
W. W. Havens, Jr.
Winston E. Kock
R. Bruce Lindsay
H. V. Neher
C. J. Overbeck
G. E. Pake
Ray Pepinsky
F. W. Sears
Frederick Seitz
John Strong
George E. Uhlenbeck
M. E. Warga
Victor F. Weisskopf
W. R. Willets

ADMINISTRATION

Elmer Hutchisson
Director

Wallace Waterfall
Secretary and Treasurer

Henry A. Barton
Administrative Consultant

W. C. Kelly
Director of Education

Eugene H. Kone
Director of Public Relations

Hugh C. Wolfe
Director of Publications

Kathryn Setze
Assistant Treasurer

Norma Frankel
Publications Editor

Sistina Greco
Circulation Manager

Edward Tober
Manager, Production and Distribution

Theodore Vorburger
Advertising Manager

Emily Wolf
Manager, Special Services

Editor James A. Krumhansl

Assistant Editor Ethel McMillan

Editorial Board

J. H. Crawford, J. E. Goldman, Herman A. Haus
Arthur Kantrowitz, J. L. Tuck, C. Lester Hogan
A. F. Kip, C. A. Wert, R. S. Rivlin

THE JOURNAL OF APPLIED PHYSICS is devoted to general physics and its applications to other sciences, to engineering, and to industry. Previous to 1937, this journal was called PHYSICS.

The JOURNAL OF APPLIED PHYSICS welcomes articles of two distinct kinds: (1) Descriptions of new results in experimental or theoretical physics which are of general interest to physicists. The author should explain his contribution in such a way that a physicist or engineer in another field of specialization can appreciate its objectives and essential features. (2) Critical reviews of particular areas of physics or surveys of extensive investigations at a single laboratory. Authors contemplating writing such should correspond with the Editor before they begin writing.

The JOURNAL OF APPLIED PHYSICS welcomes Letters to the Editor which are short [approximately four (4) typewritten pages] communications without abstracts. Timeliness, briefness, and degree of current importance of the subject matter will be of primary concern in the publication of Letters. Letters should not be looked upon as partial publication or announcement of more comprehensive work, but rather self-contained presentations in themselves.

Manuscripts should be submitted to the Editor, James A. Krumhansl, Rockefeller Hall, Cornell University, Ithaca, New York. Authors should read the "Information for Contributors," facing page 1 of the January issue, before writing articles or letters. The *Style Manual* of the American Institute of Physics is also helpful to writers preparing manuscripts for journals published by the American Institute of Physics. It can be obtained for $1.00 from the American Institute of Physics, 335 East 45 Street, New York 17, New York.

Corrected proofs and all correspondence concerning papers in the process of publication should be addressed to the Publication Manager, American Institute of Physics, 335 East 45 Street, New York 17, New York.

Subscriptions, renewals, and orders for back numbers should be addressed to the American Institute of Physics, 335 East 45 Street, New York 17, New York.

Subscription Price	**U.S. and Canada**	**Elsewhere**
To members of member organizations of the American Institute of Physics and Affiliated Societies ..	$12.00	$13.00
To all others	14.00	16.00

Back Number Prices

Yearly back number rate when complete year is available: $17.00.
Single copies: $1.75 each (exception: March, 1958—$3.00 each).

Changes of address should be sent to the American Institute of Physics.

Advertising rates supplied on request. Orders, advertising copy, and cuts should be sent to the American Institute of Physics.

The Journal of Applied Physics is published monthly at Prince and Lemon Streets, Lancaster, Pennsylvania.
Second-class postage paid at Lancaster, Pa.

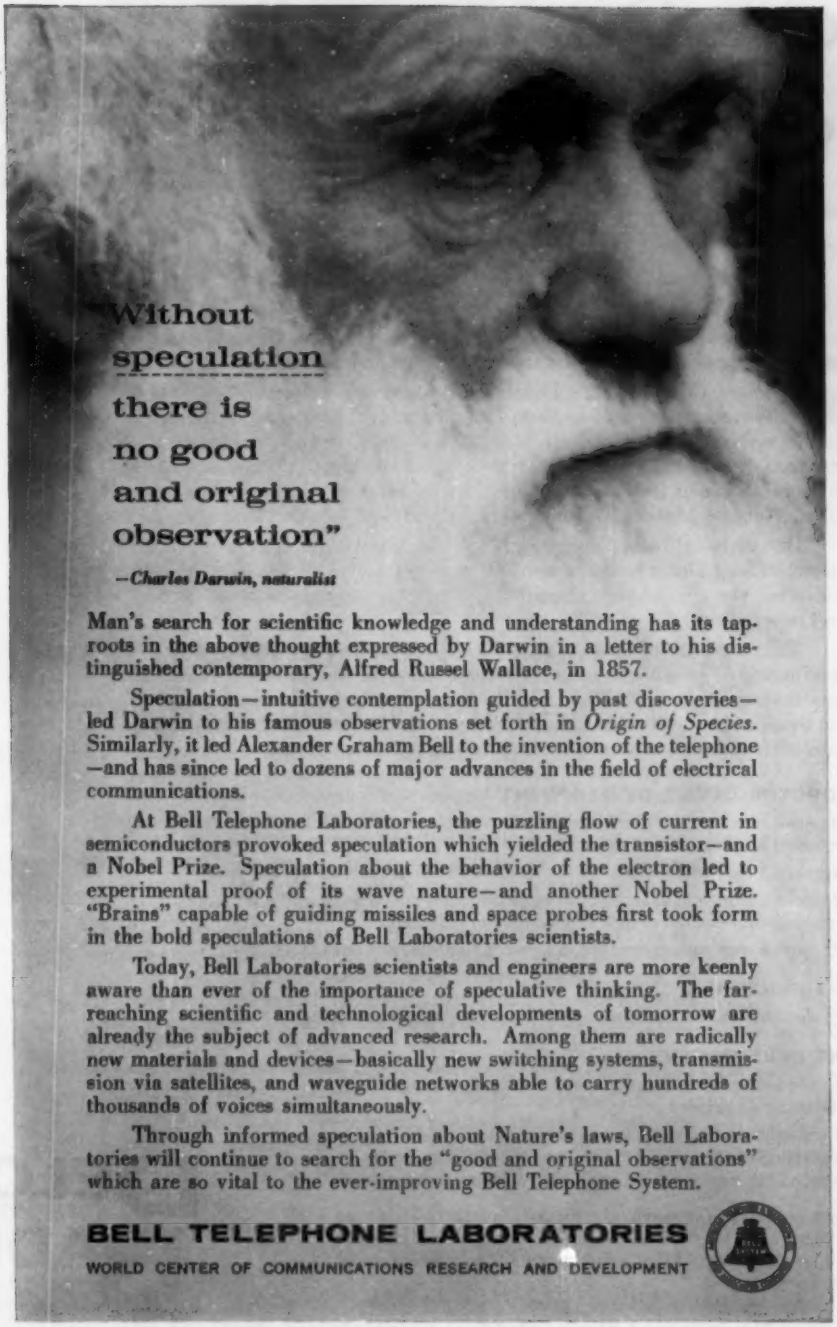

Man's search for scientific knowledge and understanding has its tap-roots in the above thought expressed by Darwin in a letter to his distinguished contemporary, Alfred Russel Wallace, in 1857.

Speculation—intuitive contemplation guided by past discoveries—led Darwin to his famous observations set forth in *Origin of Species*. Similarly, it led Alexander Graham Bell to the invention of the telephone—and has since led to dozens of major advances in the field of electrical communications.

At Bell Telephone Laboratories, the puzzling flow of current in semiconductors provoked speculation which yielded the transistor—and a Nobel Prize. Speculation about the behavior of the electron led to experimental proof of its wave nature—and another Nobel Prize. "Brains" capable of guiding missiles and space probes first took form in the bold speculations of Bell Laboratories scientists.

Today, Bell Laboratories scientists and engineers are more keenly aware than ever of the importance of speculative thinking. The far-reaching scientific and technological developments of tomorrow are already the subject of advanced research. Among them are radically new materials and devices—basically new switching systems, transmission via satellites, and waveguide networks able to carry hundreds of thousands of voices simultaneously.

Through informed speculation about Nature's laws, Bell Laboratories will continue to search for the "good and original observations" which are so vital to the ever-improving Bell Telephone System.

BELL TELEPHONE LABORATORIES

WORLD CENTER OF COMMUNICATIONS RESEARCH AND DEVELOPMENT

How Do You Meet a Challenge?

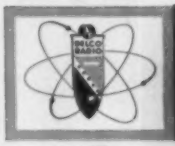

Delco Radio is doing it with TALENT and RESOURCES

We feel the challenge of new concepts in electronics and Solid State Physics can only be met by an intelligent application of outstanding abilities and resources.

To meet this challenge, Delco—over the years—has built up over one million square feet of modern manufacturing, laboratory and office facilities. Newest in the Delco complex is a 125,000 sq. ft. engineering and research facility now under construction in Kokomo, Ind., and scheduled for completion in 1961. In addition, Delco has available the extensive services of the General Motors Technical Center and field test facilities.

But physical resources are only half the answer. It took bold, imaginative talent to lead Delco to its present respected position in the electronics industry. Likewise, the challenge of the future requires a constant infusion of new ideas and new talent.

To maintain and further expand leadership in these areas, we are conducting aggressive programs in semiconductor device development and new materials research. This activity has created unusual opportunities for those who qualify. Specifically, we are vitally interested in ambitious men with experience and TALENT in the following areas:

SEMICONDUCTOR DEVICE DEVELOPMENT

We need men with experience in the techniques of semiconductor device development including alloying and diffusion.

We need a man with experience in the chemistry of semiconductor devices.

We need a man with experience in semiconductor materials to lead a program on metallurgical research of new semiconductor materials.

We need a man with experience in semiconductor device encapsulation.

PROCESS ENGINEERING

We need several men for production set-up and trouble shooting.

EQUIPMENT DEVELOPMENT

We need men to develop automatic and semi-automatic fabrication equipment.

We're eager to find experienced personnel with a desire for a stimulating challenge and the abilities to fulfill this challenge. Responsible positions are available for those who qualify.

If you're interested in becoming a member of our Delco—GM team of outstanding scientists and engineers, send your resume today to the attention of Mr. Carl Longshore, Supervisor Salaried Employment.

DELCO RADIO
DEPENDABILITY
RELIABILITY

Division of General Motors · Kokomo, Indiana

Varian fills a growing research need...

with a **completely matched** four-inch electromagnet system...

This outstanding matched magnet system features the Varian V-4004 Four-inch Laboratory Electromagnet . . . a versatile instrument designed to meet a variety of general purpose applications, particularly where the exceptional field homogeneity and stability of Varian's larger magnets is not required. The V-4004 magnet with its matching power supply and optional current regulator is ideal for studies of susceptibility, Zeeman or Hall Effects . . . for testing magnetic materials . . . for lecture demonstrations . . . for many other applications requiring a magnetic field. Priced within the limits of a modest laboratory equipment budget, it can be purchased complete with matched power supply, current regulator and accessories . . . or in any combination your needs warrant.

These Components Comprise the Complete V-4004 Magnet System:

- V-4004 Four-inch Magnet
- V-2300A Power Supply (unregulated)
- V-2301A Current Regulator (for V-2300A Power Supply)
- V-4084 Tapered Pole Caps
- V-4084-1 Cylindrical Pole Caps
- V-4055 Rolling Cabinet (houses complete magnet system)

For Complete Information on the completely matched V-4004 Magnet System, write to the Instrument Division for data sheets and specifications.

VARIAN associates
PALO ALTO 36, CALIFORNIA

Engineers • Scientists

SYLVANIA

ARL
Applied Research Laboratory

Invites inquiries from men of established professional competence

The principal task of Sylvania's Applied Research Laboratory is to define and solve complex systems problems by the use of modern analytical methods. Whenever possible, verification of these analyses is established through fabrication of experimental models. Utilizing these models we are able to extrapolate what operational characteristics and parameters will be and thus prove the feasibility of the system. The continuing goal of the Applied Research Laboratory is, therefore, the formulation of advanced systems and techniques whose design criteria have been substantiated through detailed laboratory experiments.

The highly creative mission of this laboratory has given it a flexible organizational structure that affords individuals ample opportunity to pursue basic and applied research in diverse technological areas. At the present time a number of openings are available for highly qualified engineers and scientists who possess an advanced degree and broad experience in one of these areas:

INFORMATION & COMMUNICATION THEORY
ELECTROMAGNETIC PROPAGATION • HYPERSONIC GASDYNAMICS
NEW TECHNIQUE INSTRUMENTATION • MICRO-ELECTRONICS
MATHEMATICAL ANALYSIS & OPERATIONS RESEARCH

We invite your inquiries. Please write in confidence to:
Dr. Leonard Sheingold
Director, Applied Research Laboratory

Waltham Laboratories / **SYLVANIA ELECTRONIC SYSTEMS**
A Division of

SYLVANIA

Subsidiary of GENERAL TELEPHONE & ELECTRONICS

100 First Avenue – Room 8-B – Waltham 54, Massachusetts

3 *good ways to make dc measurements*

KEITHLEY ELECTROMETERS have up to 64 voltage, resistance and current ranges

1 Model 610A, 64 ranges

The line-operated 610A is a refinement of the popular 610, covering virtually every dc laboratory test. It measures nine voltage ranges from 0.01 to 100 volts full scale with 2% accuracy, current from three amperes to 1 x 10^{-13} ampere full scale, and resistance from 10 ohms to 10^{14} ohms full scale. The 610A also serves as a useful dc pre-amplifier with precise gains to 1000 and outputs for driving scopes and recorders. Input resistance is variable from one ohm to over 10^{14} ohms. The instrument checks its own resistance standards. Zero drift is within two millivolts per hour. **$480.00**

2 Model 600A, 54 ranges

This portable instrument is a battery-operated counterpart of the 610A. Its ranges cover 10 mv to 10 volts, 3 amperes to 10^{-13} ampere, and 10^{4} to 10^{13} ohms full scale. Like the 610A, it has selectable input resistance, a dc to 100 cps bandwidth, and output sufficient to drive recorders directly. Battery life is 500 hours; condition may be checked on the panel meter. **$380.00**

Three accessory probes and test shield are available to facilitate measurements and extend voltage ranges to 30 kv (Model 610A) or 10 kv (Model 600A).

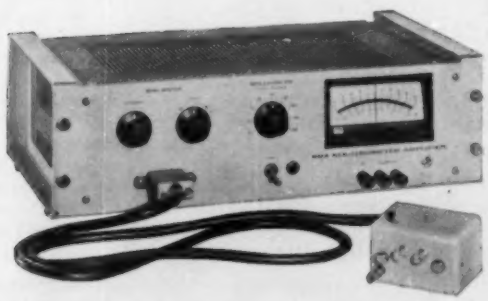

3 Model 603, differential input

This instrument is a wide-band dc amplifier, with an extremely high input impedance, high voltage and current sensitivity, and a remote differential input. Its separate input head permits measurements up to 24 feet from the amplifier. The 603 has nine ranges from 2.5 to 1000 mv, with precise gains up to 4000, and a 10-volt output at 10 ma. Bandwidth is dc to 10 kc on the 2.5 mv range, rising to 30 kc on the 1000 mv range. **$650.00**

KEITHLEY INSTRUMENTS, INC.
12415 EUCLID AVENUE CLEVELAND 6, OHIO

some men see only gulls...

but a man of imagination named Otto Lilienthal saw more, and conceived an idea of consequence to the future of the world. The sources of world-shaping ideas are myriad; the men capable of conceiving these ideas, few.

In this age, more than ever before, there is a need for men of ideas. Now, at the new Autonetics Research Center in Whittier, California, a group of men are working to apply advanced physical concepts to the electromechanical technology of tomorrow. More men with advanced degrees are needed for this important work. Men to do research in moletronics, micromagnetics, advanced materials, and cryogenics.

Perhaps you are a man with new ideas... a man of imagination... one who requires the stimulation of new challenges. If you are, we invite you to share in the work at the new Autonetics Research Center.

Write: A. P. Knutson, Autonetics Research Center, 12000 E. Washington Boulevard, Whittier, California.

Current Openings for Experienced Ph.D's:

Solid State Physicists • Physical Chemists • Electrochemists • Physical Metallurgists • High Vacuum Technologists.

Autonetics

A DIVISION OF NORTH AMERICAN AVIATION, INC.

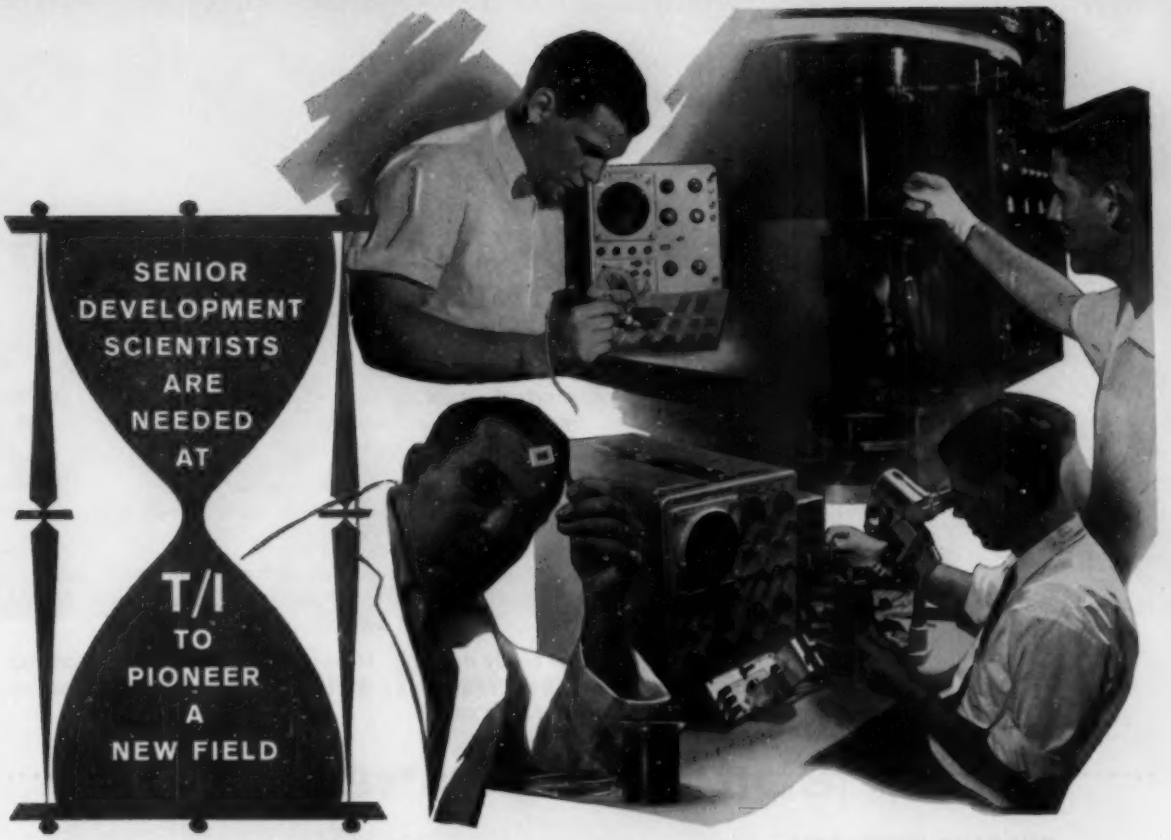

THE GOAL is microelectronics. **THE PROBLEM** is to provide microminiature circuits which are more reliable...smaller in size...lighter in weight...lower in cost...than conventional components. **THE SOLUTION** is *Solid Circuit** semiconductor networks–a new and rapidly expanding field at Texas Instruments.

This wide-ranging project — the opening of a true frontier — requires continuing and new investigations. Explorations involve such techniques as solid state diffusion, alloying of metals and semiconductors, vacuum deposition of metals, semiconductor surface chemistry, solid state physical measurements. Immediate creative application of skills in various sciences is required: solid state physics, physical chemistry, inorganic chemistry, metallurgy, electronics, and mechanical engineering.

The need is for the scientist or engineer sufficiently experienced that he can explore this project from his own viewpoint and make immediate, significant contribution. Depending entirely on his own qualifications, he may either join a semiconductor network team — or he may take charge of such a group. The opportunity for leadership — whether immediate or in the future — is here.

The desire to see the full semiconductor technology... curiosity concerning both circuits and devices... the ability to direct and inspire... these drives will advance the scientist at TI.

*Trademark of Texas Instruments Incorporated.

This — in actual size — is an interconnected stack of 11 semiconductor networks. *Solid Circuit* semiconductor networks are complete electronic circuits synthesized within a semiconductor material. By selectively diffusing and shaping conductance paths in this material, semiconductor networks have been designed to perform such circuit functions as amplification, switching, counting, pulse generation, etc. In addition to effecting a significant advance in microelectronics, semiconductor networks provide improved reliability and performance. This TI development is now producing devices which are being evaluated for satellite, missile and airborne applications.

INTERVIEWS are scheduled for your area. If the challenge and opportunity of the semiconductor network field at TI intrigues you, please send a confidential resume immediately to C. A. BESIO, Dept. 125.

TEXAS INSTRUMENTS INCORPORATED
SEMICONDUCTOR - COMPONENTS DIVISION
POST OFFICE BOX 312 • DALLAS, TEXAS

ti ti ti tips ti ti ti ti

TEXAS INSTRUMENTS INCORPORATED
Semiconductor-Components Division
Box 312, Dept. 125, Dallas, Texas

Please send me the booklet *TIPS* containing details on career openings in my field at TI S-C and information on living in Dallas.

NAME_____

ADDRESS_____

CITY_____ STATE_____

My professional field is_____

My specialty is_____

Physicists...

S

I

RESEARCH AND DEVELOPMENT IN SEMICONDUCTORS

Pacific Semiconductors, Inc. recently has made a number of notable accomplishments in the field of semiconductors, including a range of high frequency power transistors, micro miniaturized diodes and transistors. For example, the PSI high frequency transistor line ranges from the largest (100 watts at 5 mc) to the smallest silicon mesa transistors available.

These accomplishments have created important new opportunities at PSI. In addition, PSI is broadening its range of activities to include such new fields as solid state circuits.

The nature of the semiconductor field has created an unusual need and opportunity for physicists at PSI. We are seeking highly competent scientists who have an interest in solid state research and development.

Experience in the field is highly desirable. However, if you lack such experience but believe you have unusual ability and a desire for stimulating and challenging work, we would like to hear from you.

SURFACE RESEARCH Basic research on semiconductor surfaces with the ultimate objective of increasing the state of understanding of semiconductor surface phenomena. Whatever theoretical and experimental approaches are required in order to accomplish this goal will be employed. An important part of this objective will be the correlation of surface film composition and structure with the physical model of the surface. A surface design theory of fundamental value might reasonably be expected to be an important outgrowth of this endeavor.

SOLID STATE DIFFUSION Investigation and improvement of solid state diffusion processes. This includes fundamental work on diffusion mechanisms and the growth and control of oxide layers at the surface. Some or all of the following experience is highly desirable: High furnace temperature operation, gaseous purge systems, light interference measurement techniques.

DEVICE PHYSICS Balanced experimental and theoretical research on new processes and new devices of advanced types. Read and understand semiconductor literature. Work with chemists, metallurgists and electronic engineers. Supervise experiments involving advanced laboratory measurement techniques, including infrared, X-ray and electrical. Diffusion, surfaces, crystal imperfections, device theory, process theory.

SEMICONDUCTOR MATERIALS — INTERMETALLIC COMPOUNDS Physical chemists or physicists to work in preparation and purification of semiconductor elements and intermetallic compounds. The work also may include the study of decomposition reactions of silanes and halides of silicon to form single crystal deposits of pure silicon. Interest in infrared absorption studies desirable.

These are only a few of the many fine opportunities available at PSI. If you have an M.S. or Ph.D. degree in physics or a B.S. degree and equivalent experience in semiconductor physics, write today in confidence to:

DR. J. W. PETERSON, *Director, Research and Development*

or MR. LARRY LONG, *Head, Technical Staff Placement*

PSI®

Pacific Semiconductors, Inc.

10451 WEST JEFFERSON BOULEVARD • CULVER CITY, CALIFORNIA

Expanding the Frontiers of Space Technology in

SPACE PHYSICS

Lockheed Missiles and Space Division is broadening its studies in space physics to keep pace with this rapidly growing field of fundamental research.

Positions are available for physicists with advanced degrees, at our Palo Alto facilities in the Stanford Industrial Park, for work in basic research on the physics of the earth's upper atmosphere and beyond.

Typical research projects include: measurement of atmospheric composition and density at satellite altitudes; laboratory experiments on upper atmospheric atomic and molecular reactions; hydromagnetic interactions with the earth's magnetic field; simulation and study of meteor impacts; and particle radiation.

The successful solution to problems such as these calls for advancement of the state of the art to unknown environments and the maximum of scientific effort.

Engineers and Scientists—We invite you to join us in this challenging effort and to share in the future of a company that has an outstanding record of achievement. Write: Research and Development Staff, Dept. H-32, 962 W. El Camino Real, Sunnyvale, California. U.S. citizenship or existing Department of Defense industrial security clearance required.

Lockheed / **MISSILES AND SPACE DIVISION**

Systems Manager for the Navy POLARIS FBM; the Air Force AGENA Satellite in the DISCOVERER, MIDAS and SAMOS Programs; Air Force X-7; and Army KINGFISHER

SUNNYVALE, PALO ALTO, VAN NUYS, SANTA CRUZ, SANTA MARIA, CALIFORNIA
CAPE CANAVERAL, FLORIDA • ALAMOGORDO, NEW MEXICO • HAWAII

Timely McGRAW-HILL Books

Bharucha-Reid—ELEMENTS OF THE THEORY OF MARKOV PROCESSES AND THEIR APPLICATIONS, 469 pages, $11.50

Clement and Johnson—ELECTRICAL ENGINEERING SCIENCE, 588 pages, $9.50

Chernov—WAVE PROPAGATION IN A RANDOM MEDIUM, 176 pages, $7.50

Collin—FIELD THEORY OF GUIDED WAVES, *Ready in October.*

Ledley—DIGITAL COMPUTER AND CONTROL ENGINEERING, 835 pages, $14.50

Lindsay—MECHANICAL RADIATION, 415 pages, $10.00

Moore—TRAVELING WAVE ENGINEERING, *Ready in September.*

Overman and Clark—RADIOISOTOPE TECHNIQUES, 496 pages, $10.00

Slater—QUANTUM THEORY OF ATOMIC STRUCTURE, Volume I, 502 pages, $11.00

Yeh and Abrams—PRINCIPLES OF MECHANICS OF SOLIDS AND FLUIDS, Volume I, *Ready in August.*

Send for copies on approval

McGraw-Hill
BOOK COMPANY, INC.
330 West 42nd Street New York 36, N.Y.

Science, non fiction at Los Alamos

Is this the shape of things to come in Sherwood?

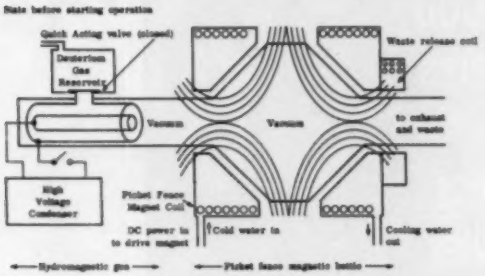

The cusped geometry or picket fence was proposed back in 1954 independently by Grad at N.Y.U. and Tuck at Los Alamos, to get around hydromagnetic instability of plasma-magnetic field interfaces. Nobody did much about it at the time. The pinch effect seemed to hold more promise, so why bother about a leaky picket fence? A large magnet to produce a DC picket fence geometry was built but laid aside. For several years the stabilized toroidal pinch (called Perhapsatron at Los Alamos) held the stage. But as our measuring techniques got better, the pinches began to show a most sinister behavior. An apparently stabilized pinch which should have been radiating energy at the rate of several kilowatts, turned out to be losing it at a rate of hundreds of megawatts. As we got the impurities out of the system, the losses seemed to go down. One pinch (Perhapsatron S-5) has seemed so clean we are trying to raise its temperature to thermonuclear levels by pouring in more power.

Then there appeared the spectre of plasma oscillations and their evil effects on magnetic confinement. In principle, plasma oscillations can thrive on the interaction of a fast wind of plasma electrons moving through a slower cloud of plasma ions. This makes things look bad for the pinch effect, because the plasma has to have a large electric current in it, and therefore an electron wind.

The Russians delivered the next blow. Trubnikov and Kondryatsev predicted an enormous cyclotron radiation flux from a plasma containing a magnetic field. This would ruin the chances for DD reactors, and make things tough even for DT reactors. Among other complications, a nearly perfect mirror would have to be placed around the inner wall of the plasma container to reflect the radiation back.

Then Rosenbluth and Drummond argued that when the angular distribution is considered, the radiation isn't really so bad—say 1/50th of what T and K say. Now Trubnikov has come right back with another paper that says it is five times worse than R and D said it was. The above theories are pretty simple—the real problem is exceedingly difficult theoretically. It may be quite a while before there is anything new in this direction.

Anyhow, the point is that DD reactors with magnetized plasmas now seem to be out. But some people, like Tuck, claim that DD reactors are the only ones that make sense, since a DT reactor which must carry on its back a monstrosity of a tritium recovery plant could never compete with fission power anyhow.

This brings us to the point that if we want to have a DD reactor, it has to have no magnetic field in its plasma. So all right, don't put a magnetic field in the plasma. Unfortunately, there aren't any magnetic confinement systems stable enough to hold a pure plasma, except one. You've guessed it—it's the picket fence.

So we went back to the warehouse and dusted off the magnet we built long ago. Already it is going full blast, a second one has been built and a third one is on its way. Of course, we aren't alone any more in this field. Small cusped geometries are being studied at General Atomic, Livermore, Stevens, Harwell, Utrecht and Kharkov. Pretty soon we will have only picket fences and plasma guns at Los Alamos, aside from a few Scyllas to study plasma at thermonuclear temperatures, unless old Perhapsatron S-5 does something pretty spectacular. The diagram of Picket Fence I (above), run by D. Hagerman and J. Osher, shows how plasma is injected as a slug, strong enough to push through the magnetic field and spread out inside. (This is called entropy trapping, but that's another story). Does it work? Well, that depends. It's a lot more complicated than we thought. At first, we nearly died of joy when the plasma was shot in and seemed to stay around for ages in our time scale (1000 microseconds), emitting light in the process. But when a magnetic probe was inserted, the harsh truth was revealed—the containment lasted only a few microseconds. In other words, the long time period we thought we had observed was merely cold plasma emitting light by recombination.

Just lately, however, Messrs. Hagerman and Osher have cleaned things up to the point that hot plasmas are pushing the field aside strongly and are keeping the inside field pushed aside for very satisfying periods, like 50 microseconds. Also, if we keep the magnetic probe out of the way of the plasma, it stays around longer, which is what it should do. This particular picket fence is a horror to keep a vacuum in, as it is completely overrun with O rings. The next one will be baked. Fun, eh?

What about the leaks in the fence? It is pretty leaky, but we think we have an answer to that too, so watch for the story on the TLC picket fence one of these days.

For employment information write:
Personnel Director, Division 60-78

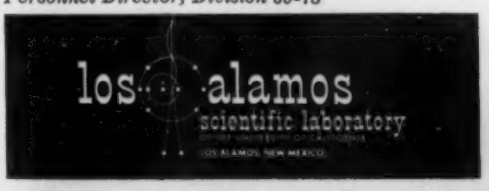

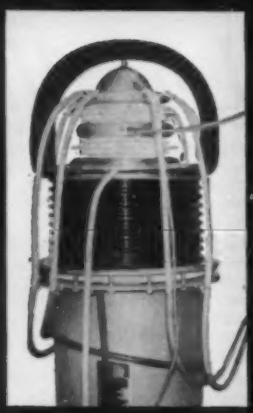

600,000 amperes help harness H-power

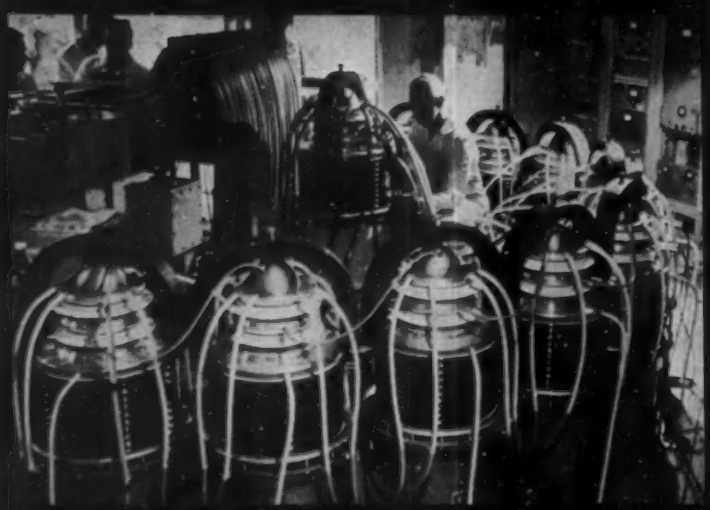

At the historic Geneva Atoms-For-Peace Conference, Los Alamos scientists unveiled **Scylla**—a fusion device used to heat a plasma of ionized heavy hydrogen particles millions of degrees by blasting it with a 600,000-ampere thunderbolt.

Surrounding the heart of this thermonuclear machine is a bank of low-inductance, energy-storage capacitors...each rated at 100,000 volts, each capable of a 20,000 megawatt peak surge.

This unique installation, like others of its type, is the result of long experience in capacitor specialization. If adherence to rigid specifications is a 'must' on your project—call us in to help with creative engineering. We invite inquiries for a single energy-storage capacitor or a complete energy-storage system including capacitors, racks, interconnecting lines, protective devices and charging power supply.

For further technical information, write for Bulletin No. 191 to Cornell-Dubilier Electric Corporation, New Bedford, Mass.

CDE

CORNELL-DUBILIER ELECTRONICS DIVISION
FEDERAL PACIFIC ELECTRIC COMPANY

information processing new research programs at Hughes Research Laboratories

High speed digital systems, thin magnetic film phenomena, logical elements utilizing complex memory circuits, methods for communicating with very fast computers, analog to digital conversion—these are representative of the broad areas of Information Processing now under study at the Hughes Research Laboratories.

Because of the increasing importance of Information Processing, Hughes is continuing to expand its research activities in this area. Openings exist for engineers and scientists who have a keen desire to advance the state-of-the-art. If your interests are related to this field, your inquiry is encouraged.

The new facilities of the Hughes Research Laboratories are located in Malibu, California—overlooking the Pacific Ocean. Here scientists and engineers are offered the academic atmosphere which is essential for effective research effort.

Your inquiry regarding staff openings may be directed in confidence to: Mr. D. A. Bowdoin, **HUGHES RESEARCH LABORATORIES,** *Malibu 7, California.*

Creating a new world with ELECTRONICS

HUGHES

RESEARCH LABORATORIES

HUGHES AIRCRAFT COMPANY

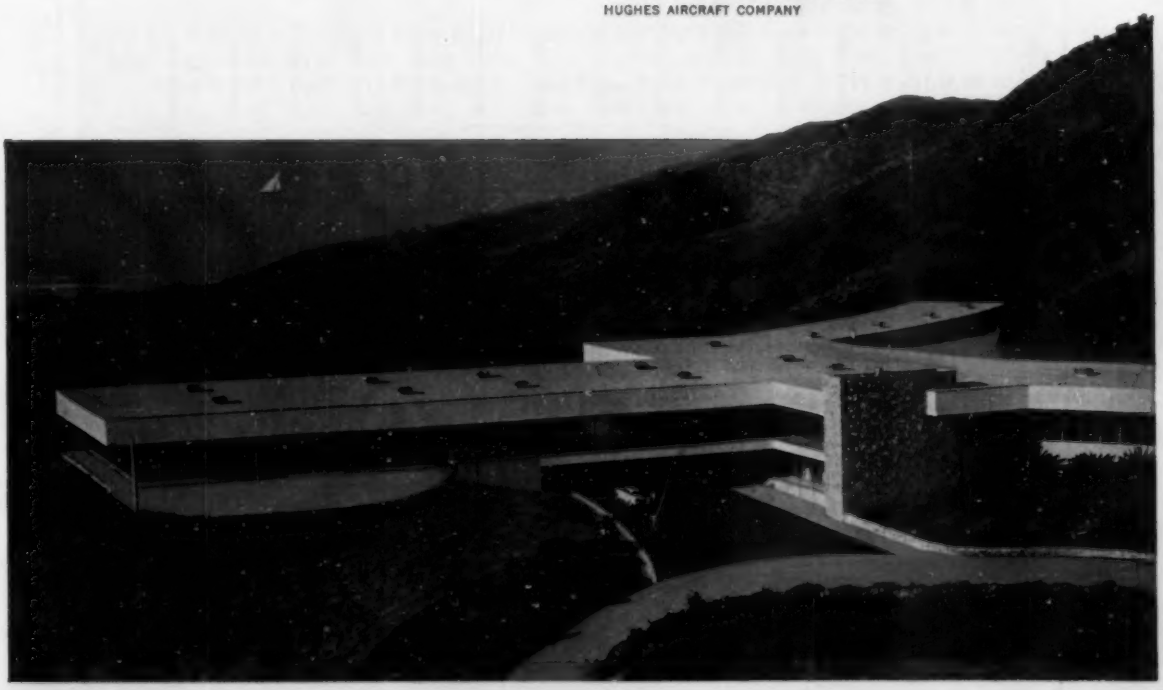

1959 Edition Shows All The Latest Discoveries

WELCH CHART OF THE ATOMS

Chart and 48-page Key Booklet both completely revised

by Dr. William F. Meggers, National Bureau of Standards

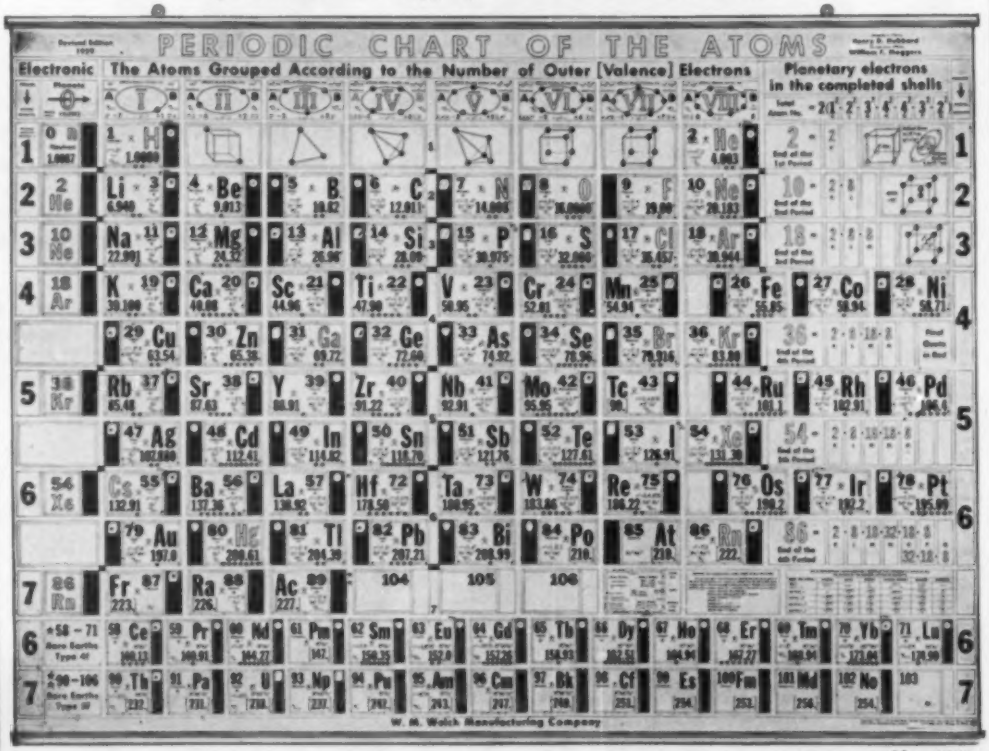
PERIODIC CHART OF THE ATOMS
Electronic
The Atoms Grouped According to the Number of Outer [Valence] Electrons
Planetary electrons in the completed shells
W. M. Welch Manufacturing Company

No. 4854.

All specific information including a tabulation of principal isotopes now arranged for greater clarity • Nobelium 102 (most recent discovery) included

Improved readability • Large size—42 X 58 inches • Lithographed in 6 colors

Lists latest atomic weights compiled by International Union for Pure & Applied Chemistry

No. 4854. CHART OF THE ATOMS—1959 Edition. Lithographed in six colors on heavy chart paper, coated with a plastic film especially treated to prevent glare, with formed-metal chart molding at top and bottom with eyelets for hanging and a 48-page key booklet ..... Each $7.50

Write for Complete Circular

W. M. WELCH SCIENTIFIC COMPANY

DIVISION OF W. M. WELCH MANUFACTURING COMPANY

ESTABLISHED 1880

1515 Sedgwick Street, Dept. C-1 Chicago 10, Illinois U. S. A.

Manufacturers of Scientific Instruments and Laboratory Apparatus

Journal
of
Applied Physics

Volume 31, Number 8 August, 1960

Transitory Electrical Properties of *n*-Type Germanium After a Neutron Pulse

H. J. Stein
Sandia Corporation, Albuquerque, New Mexico
(Received March 21, 1960)

The stability of neutron bombardment damage in Sb-doped Ge has been investigated by making continuous measurements of the electrical conductivity and Hall mobility following a neutron pulse. Measurements were made in the temperature range from 77° to 308°K with a time resolution of 1 sec. At temperatures near 195°K an initial decrease in conductivity and mobility was followed by an additional decrease which exhibited nearly second-order kinetics. At 273°K and above, an initial decrease in conductivity and mobility was observed, but was followed by a recovery consistent with an activation energy of 0.68 ev. The void region model of Gossick and Crawford has been employed to explain the initial decrease in mobility and a major portion of the initial decrease in conductivity. The transitory changes in mobility and conductivity after the neutron pulse are considered as changes in the void volumes.

INTRODUCTION

THE stabilized effects of neutron produced damage in *n*-type Ge have been summarized by Crawford and Cleland.[1,2] We have investigated the neutron pulse produced damage in *n*-type Ge that is unstable at and below 300°K.

The James-Lark-Horovitz model for Frenkel defects was used extensively in the interpretations of the earlier work. Gossick[3] has proposed a model which suggests that the mobility and conductivity behavior of neutron irradiated *n*-type Ge is influenced by disordered regions in the *n*-type matrix. The disordered region of Gossick's model is considered to be *p*-type since the asymptotic behavior of irradiated *n*-type Ge is *p*-type. A potential gradient about the *p*-type disordered region will extend an appreciable distance into the *n*-type matrix when the electron concentrations are small. The volume affected by the potential gradient will be stripped of its conduction electrons and is assumed to act as an insulator. In *n*-type Ge near 10 ohm-cm, the radius of the insulating region is nearly ten times the disordered region itself. Crawford[2] found the mobility behavior of neutron irradiated *n*-type Ge supported the model.

Observations on recovery behavior of neutron irradiated Ge are rather sketchy. Cleland, *et al.*,[4] have reported two nonreversible maxima in the conductivity of *n*-type Ge at 134° and 165°K upon warming from the irradiation temperature of 114°K. The behavior was interpreted as a release of minority carriers from discrete trapping levels. Warming to 260°K resulted in an increase in conductivity above 173°K, but no details of the recovery were resolved.

The present investigation deals with the production, enlargement and recovery of the neutron-induced decrease of the electrical conductivity and the Hall mobility in *n*-type Ge. The irradiation and measurements were made at discrete temperatures in a range from 77° to 308°K. A neutron pulse irradiation was used making possible the investigation of the stability of defects created by neutrons in Ge at temperatures near room ambient. Since the sample was stabilized at the measurement temperature during irradiation, time resolution in the measurements was not limited by a thermal stabilization time.

The material investigated to the greatest extent was 5 ohm-cm antimony-doped Ge. The experimentally

[1] J. H. Crawford and J. W. Cleland, Progr. in Semiconductors **2**, 67 (1957).
[2] J. H. Crawford and J. W. Cleland, J. Appl. Phys. **30**, 1204 (1959).
[3] B. R. Gossick, J. Appl. Phys. **30**, 1214 (1959).
[4] J. W. Cleland, J. H. Crawford, and J. C. Pigg, Phys. Rev. **98**, 1742 (1955).

Copyright © 1960 by the American Institute of Physics.

observed initial decrease in mobility has been interpreted by the disordered region model of Gossick while the initial decrease in conductivity has been considered as resulting from a combination of void regions and point defects. Activation energies have been determined that are consistent with the observed reordering. By using the Gossick model the reordering was restricted to processes which change the effective void volume.

EXPERIMENTAL DETAILS

Irradiation Source

The neutron pulses were obtained from the Los Alamos prompt critical Godiva II assembly which was discussed by T. F. Wimett at the 1958 Geneva Conference.[5] The prompt fission burst is limited by thermal expansion to give an average pulse width of 100 μsec at half-maximum fission rate. A delayed critical activity continues until the system is scrammed at 50 msec. From source considerations, the time resolution of our experiments is limited by the scram time. The neutron energy spectrum is a slightly degraded fission spectrum with the most probable neutron energy being approximately 0.5 Mev.

Samples and Temperature Control

The samples were cut from single-crystal Sb-doped Ge into a shape which provided arms for the attachment of resistivity and Hall voltage probes. Each sample was enclosed in an aluminum container and held between, but electrically insulated from, two steel posts that extended through the bottom of the aluminum container. A meter magnet was brought into contact with the steel post extensions to supply the magnetic field for Hall mobility measurements.

A temperature measuring thermocouple was attached to one of the steel posts and near the sample. Sample temperatures were controlled within ± 0.025°C with a recording sensitivity of 0.002°C. At 77°, 195°, and 273°K, the sample containers were placed directly into liquid nitrogen, a dry ice and alcohol mixture, and an ice-water slush, respectively. At 303° and 308°K, the sample containers were placed in an insulating chamber which was equipped with a circulating fan and heater coil. A control thermocouple sensed the air temperature and the output was amplified to give on-off control to the heater. At 207.5° and 218°K, a similar system was used without the circulating fan but with a conducting outer container surrounded by a dry ice and alcohol bath; and at 282.5°K, the conducting outer container was surrounded by an ice bath. Irradiation heating from the burst caused average temperature increases of 0.025°C.

TABLE I. Initial conductivity and mobility changes.

Temp (°K)	Φ(n/cm²) >1 Kev	Resistivity (ohm-cm)	Conductivity decrease (%)	Mobility decrease (%)	f (Void fraction)
308	4.4×10^{12}	6.0	...	1.7	0.035
308	3.8×10^{12}	6.0	5.25	...	...
303	2.2×10^{12}	10.0	9.0	...	...
282.5	2.7×10^{12}	5.0	3.5	...	...
273	6.6×10^{12}	4.5	8.15	...	...
218	3.1×10^{12}	5.0	7.0	...	...
207.5	3.2×10^{12}	5.0	7.0	...	...
195	2.6×10^{12}	5.0	6.0	...	...
195	2.8×10^{12}	6.0	...	1.15	0.023
77	2.8×10^{12}	4.5	5.0[a]	...	...

[a] Reaches a 7% conductivity decrease after 30 min.

Instrumentation

The resistance measurements at 77°, 195°, and 303°K were made with a dc system. The remainder of the resistance measurements and the Hall mobility measurements were made with a 400 cps ac system which eliminated a power supply drift problem. A block diagram of the ac system is shown in Fig. 1. The ac system reads out in ohms when used for a resistance measurement, but reads out as a fractional change when used for a mobility measurement.

The common practice of reversing the magnetic field direction, to correct for possible probe offset voltages in Hall voltage measurements, could not be applied in our measurements. We selected samples for minimum offset voltage and used a constant voltage across the sample. If the damage is uniform in the sample, the offset voltage will not change with resistivity. No

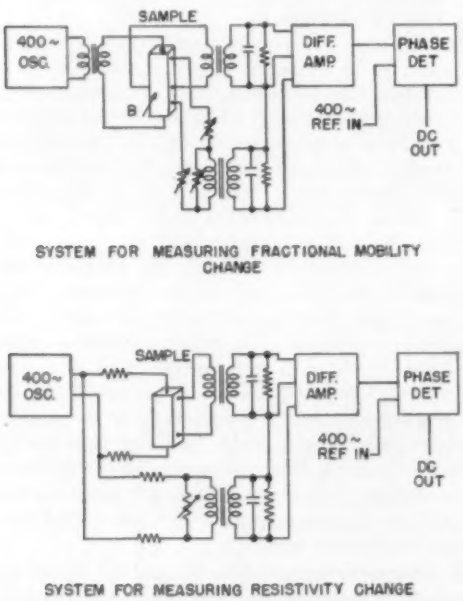

FIG. 1. 400 cps ac system for Hall voltage and resistivity measurements.

[5] T. F. Wimett and J. D. Orndoff, Proc. Second Intern. Conf. Peaceful Uses Atomic Energy **10**, 449 (1958).

change in offset voltage was observed at 195°K, but a 3% change was observed at 308°K where the ratio of Hall voltage to offset voltage was 15 to 1.

EXPERIMENTAL RESULTS

Initial Changes

The initial changes of conductivity and Hall mobility for Sb-doped Ge are listed in Table I.

The initial conductivity decrease $(-d\sigma/d\Phi)$ for a 10 ohm-cm Ge sample at 303°K is -4.1×10^{-15} ohm^{-1}-cm/n and -2.3×10^{-15} ohm^{-1}-cm/n for a 6 ohm-cm Ge sample at 308°K. The ratio

$$\frac{(-d\sigma/d\Phi)_{10\Omega\text{cm}}}{(-d\sigma/d\Phi)_{6\Omega\text{cm}}}=1.78,$$

while the ratio

$$\frac{(\sigma_0)_{10\Omega\text{cm}}}{(\sigma_0)_{6\Omega\text{cm}}}=\frac{1}{1.67}.$$

Since the carrier mobility in 6 and 10 ohm-cm Ge is essentially the same near 300°K, the carrier concentration determines the conductivity ratio and thus the magnitude of the initial $-d\sigma/d\Phi$ such that the greater the carrier concentration the smaller $-d\sigma/d\Phi$. For a given carrier concentration the ratio

$$\frac{(-d\sigma/d\Phi)_{200^\circ\text{K}}}{(-d\sigma/d\Phi)_{300^\circ\text{K}}}\approx2.$$

This is the direction but a smaller magnitude than expected for acceptor introduction by the well-known defect level near 0.2 ev. However, Brown[6] found the acceptor introduction rate to increase with temperature in electron irradiated n-type Ge.

Crawford[2] has applied the insulating void region model to explain the mobility decrease in reactor irradiated n-type Ge. His expression for conductivity σ is

$$\sigma=\sigma_0\frac{1-f}{1+f/2}, \tag{1}$$

where f is the fraction of the total volume which acts like a void. Since

$$\sigma=ne\mu \tag{2}$$

and n, the carrier concentration, should be

$$n=n_0(1-f), \tag{3}$$

then μ, the mobility, would be given by

$$\mu=\frac{\mu_0}{1+f/2}. \tag{4}$$

The ratio of incremental conductivity changes to incremental mobility changes is given by

$$\frac{d\sigma/\sigma_0}{d\mu/\mu_0}=3 \tag{5}$$

for void regions.

Using the observed mobility change and Eq. (5), a conductivity decrease of 5% would be expected for 4.4×10^{12} n/cm² at 308°K. The observed value is 6% as extrapolated from an exposure to 3.8×10^{12} n/cm². The difference may represent a carrier removal due to point defects. At 195°K and 2.8×10^{12} n/cm², a conductivity decrease of 3.5% would be expected from the voids for 6 ohm-cm Ge. The observed change is 6% for 5 ohm-cm Ge and if the difference is from carrier removal by isolated defects, the ratio of carriers removed at 195°K to those removed at 308°K is about 4 to 1.

The average individual volume size (V) is given by[2]

$$V=f/\Sigma_v\Phi=\tfrac{4}{3}\pi r_2^3=4\pi\psi_p\epsilon r_1/qN_D, \tag{6}$$

where Σ_v is the probability per centimeter that a neutron will produce an insulating void, r_1 is the radius of the disordered region, r_2 is the radius of the void, ψ_p is the difference in the electrostatic potential between the matrix and the disordered region, ϵ is the dielectric constant, and N_D is the donor density in the matrix. For $\Sigma_v=0.13$ cm^{-1}, $N_D=3.4\times10^{14}$ cm^{-3}, $\psi_p=0.3$ v, $\Phi=4.4\times10^{12}$ n/cm, and $f=0.035$ (obtained from mobility measurement at 308°K), values of 62 A and 2450 A are obtained for r_1 and r_2, respectively.

Changes after Burst

At temperatures near 200°K the resistivity continues to increase after the neutron pulse by a nearly second order process. A recovery from the initial increase in resistivity is observed for temperatures of 273°K and above. The data are presented as fractional alterations of the initial changes in resistivity and Hall mobility. Figure 2 shows a plot of $(\rho_t-\rho_0)/(\rho_\infty-\rho_0)$ vs log time for temperatures near 300°K. ρ_0 is the original resistivity, ρ_t is the resistivity at time t, and ρ_∞ is the

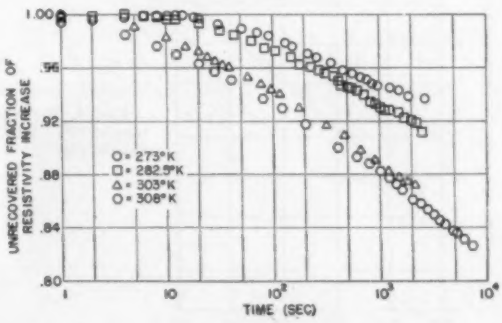

FIG. 2. Recovery from initial resistivity increase at different temperatures near 300°K.

[6] W. L. Brown and W. M. Augustyniak, J. Appl. Phys. **30**, 1300 (1959).

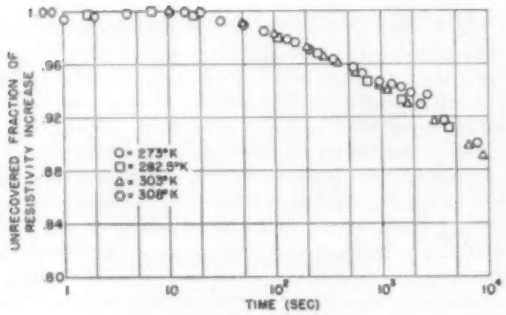

FIG. 3. A superposition of the plots in Fig. 2 by shifting the time scale.

maximum resistivity observed. By shifting the time scale, a superposition of the recoveries on the recovery at 273°K is obtained and shown in Fig. 3. The superposition indicates that the same process or processes are being observed at all temperatures. None of the recoveries go to completion during the observation period. Figure 4 is a plot of the log time required for a 6% recovery vs $1/T$, where T is the absolute temperature. The behavior is consistent with an activation energy of 0.68 ev.

Figure 5 shows the results from a plot of $(\rho_t-\rho_0)/(\rho_\infty-\rho_0)$ vs log time for 195°, 207.5° and 218°K. The resistivity is not a maximum immediately after the burst, but reaches a maximum after some reordering process or processes. The reordering is near completion at the end of the observation period and is consistent with an activation energy near 0.45 ev. A calculated bimolecular process has been included in Fig. 5 for comparison with observed behavior. The increasing resistivity during the first 10 sec at 273°K which can be seen in Fig. 2 is thought to be the tail of the processes observed at the lower temperatures. A sample irradiated at 195°K was later warmed to 273°K and recooled to 195°K. The resistivity was unchanged by the temperature cycle.

The time dependence of μ and σ at 308°K is plotted in Fig. 6. The mobility data have been plotted as $(\mu_t-\mu_{t_1})/\mu_0$ where μ_0 is the original mobility, μ_{t_1} is the mobility at 1 sec, and μ_t is the mobility at any time t greater than 1 sec. A plot of $3(\mu_t-\mu_{t_1})/\mu_0$ is shown for comparison with the conductivity data since Eq. (5) shows the ratio of conductivity to mobility change to be 3. The observed changes of σ are somewhat smaller than predicted but are in general agreement with the void size changes. The same information is plotted for 195°K in Fig. 7 where the calculated and observed values coincide very well except near the origin.

A sample irradiated at 77°K was cycled at 30-sec intervals, beginning at burst time, from a position at 10 cm to a position 100 cm from the source. At this temperature, gamma rays from the decaying source had definite ionization effects on the sample conductivity; therefore, no data were taken that could be related to defect reordering. The same procedure was used at 195°K but no effects were observed.

DISCUSSION AND CONCLUSIONS

Crawford[2] concluded the Hall mobility in neutron irradiated n-type Ge supports the void region model and gives a lower limit of 21 A for the disordered region radius in 10 ohm-cm Ge. Fujita and Gonser[7] reported low angle x-ray scattering from deuteron irradiated Ge near 90°K which indicated the presence of defect regions with radii near 30 A. The scattered x-ray intensity decreased by about a factor of 5 when the irradiated Ge was warmed to room temperature. Truell[8] has reported strain regions in neutron irradiated

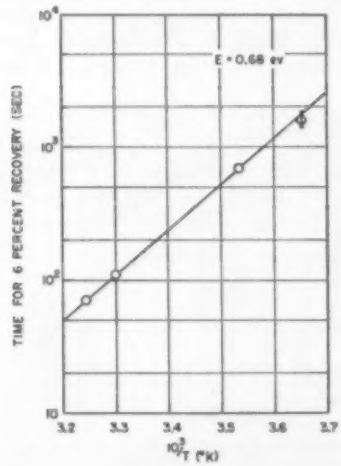

FIG. 4. Recovery time vs $10^3/T$ for the data of Fig. 2.

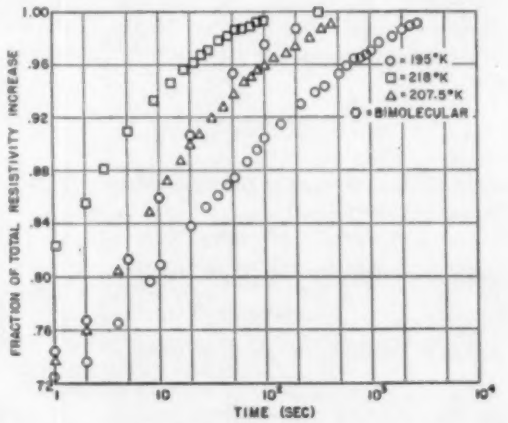

FIG. 5. Additional increase in the resistivity of n-type Ge following neutron irradiation at different temperatures near 200°K.

[7] F. E. Fujita and U. Gonser, J. Phys. Soc. Japan **13**, 1068 (1958).
[8] R. Truell, Phys. Rev. **116**, 890 (1959).

Si which have a lower limit of 100 A as determined by ultrasonic velocity attenuation measurements.

The results in this paper give a value of 62 A for the initial radius of the disordered region at 308°K. The disordered region is unstable and causes an increase in void volume size near 200°K following irradiation and a decrease in void volume size near 300°K following irradiation.

According to Eq. (6) the void volume (V) is dependent upon the variables ψ_p, r_1, and N_D. Either ψ_p, r_1, or N_D may change, or they may all change simultaneously with time following the irradiation. N_D enters the conductivity expression both through the void volume and as the carrier concentration in the matrix. For a given change of N_D the associated change of σ should be greater than predicted by a void volume change as determined from the Hall mobility. Since the observed conductivity changes are not greater than predicted from the void volume changes (Figs. 6 and 7), ψ_p and r_1 must determine the void volume alterations.

It is suggested that the time dependence of the mobility and conductivity following irradiation near 200°K is determined by a reordering in the disordered regions. Reordering near 200°K has also been observed by Vook and Balluffi[9] in their expansion measurements on deuteron irradiated high purity Ge and by Brown[10] in his electrical measurements on electron irradiated p-type Ge. The recovery from the mobility and conductivity decrease following irradiation at temperatures near 300°K could result from a flow out of vacancies from the disordered regions which would reduce ψ_p and r_1. Once in the n-type matrix these vacancies, acting as acceptors, would cause some decrease in conductivity. Preliminary transistory resistivity measurements on near intrinsic n-type Ge and p-type Ge near 300°K show a recovery which implies that acceptors are lost or donors are added in the matrix following irradiation. It is therefore suggested that vacancies move from the disordered regions and isolated sites in the crystal to sinks where they no longer behave as acceptors. The effect of acceptor loss from the matrix may not have been apparent in the 5 and 10 ohm-cm n-type Ge since the void volumes are responsible for the major changes in the conductivity.

Work is in progress to determine the transitory electrical properties of p-type Ge following a neutron pulse.

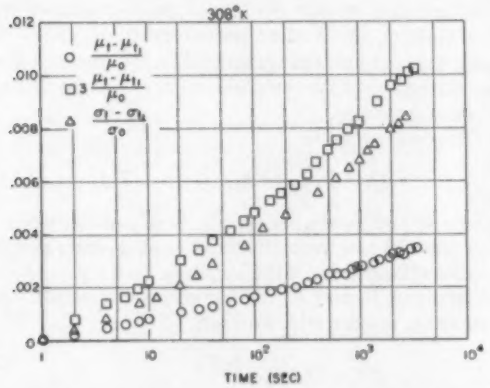

FIG. 6. A comparison of the conductivity behavior at 308°K with predicted values using observed mobility behavior and the void region model. (Subscripts 0, t_1, and t denote initial values, values at 1 sec, and values for $t>1$ sec, respectively.)

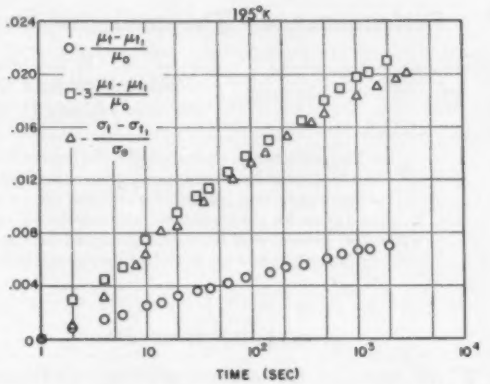

FIG. 7. A comparison of the conductivity behavior at 195°K with predicted values using observed mobility behavior and the void region model. (Subscripts 0, t_1, and t denote initial values, values at 1 sec, and values for $t>1$ sec, respectively.)

ACKNOWLEDGMENTS

The author wishes to express his appreciation to Dr. G. K. Wertheim and Professor B. R. Gossick for helpful discussions, and also to F. M. McIver and J. H. Smalley for the development of the instrumentation.

[9] F. L. Vook and R. W. Balluffi, Phys. Rev. **113**, 72 (1959).
[10] W. L. Brown, W. M. Augustyniak, and T. R. Waite, J. Appl. Phys. **30**, 1258 (1959).

Performance of a Thermoelectric Converter under Constant Heat Flux Operation

P. S. Castro and W. W. Happ
Lockheed Missiles and Space Division, Palo Alto, California
(Received February 17, 1960; and in final form May 2, 1960)

The performance characteristics of a conventional thermoelectric generator operating under constant heat flux conditions have been computed. Expressions for power output, optimum efficiency, and optimum ratio of internal-to-load resistance show that optimization requires operating conditions appreciably different from those for the operation of thermoelectric generators having constant hot and cold junction temperatures. Performance curves are presented for the optimum ratio of internal-to-load resistance when either the internal resistance or the load resistance is under the control of the designer.

INTRODUCTION

THE conditions for optimum efficiency of a thermoelectric generator for constant temperature operation are given by Ioffe[1] and Jaumot[2] and are summarized in Table I. All symbols used will be defined below. Constant temperature operation assumes that the hot and cold junction temperatures do not change as m (the ratio of load resistance R to generator resistance r) is varied; this corresponds to an infinite heat source and an infinite heat sink, conditions only approximated in practice. Heat sources and heat sinks having nonzero thermal resistances have been considered by Gray,[3] who derives first-order correction terms when these resistances are small.

The method of operation of the thermoelectric generator to be considered here differs from the conventional one considered in the foregoing in a manner analogous to the way the constant current operation of an electric network differs from its constant voltage operation. The hot junction is assumed to be receiving a constant heat flux from an external source; thus, the heat power absorbed by the hot junction is constant. An operation of this type occurs, for example, when the hot junction of the thermoelectric generator is fueled by a nuclear power source or in the case of power generation for space vehicles, when the hot junction absorbs heat power directly from the sun (see Fig. 1). It is understood that the total heat power passed on to the thermoelectric generator can be controlled by controlling the area the hot junction presents to the heat source either by an actual change in the dimensions of the area or by an effective change by means of a focusing device.[4] Radiation losses from the hot junction have been neglected in this analysis.

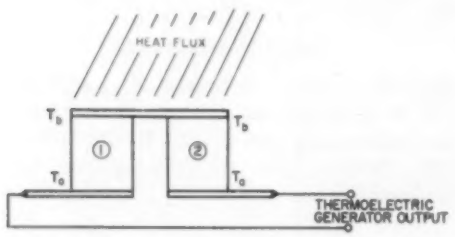

FIG. 1. Thermoelectric generator operating under constant heat flux.

HEAT BALANCE EQUATION

A heat balance at the hot junction leads to

$$Q_i = Q_c + Q_p - Q_j/2, \tag{1}$$

where Q_i is the heat input to the hot junction per unit time, Q_c the heat conducted from the hot junction to the cold junction through the legs of the thermocouple per unit time, Q_p the Peltier heat per unit time, and Q_j the joule heat per unit time generated by the current I flowing through the total internal resistance r of the thermoelectric generator.

Thus we can write

$$Q_c = (k_1A_1/l + k_2A_2/l)(T_b - T_a), \tag{2}$$

where k_1 and k_2 are the specific heat conductivities of legs one and two, respectively, A_1 and A_2 their average cross-sectional areas, l the length of each leg (assumed equal), and T_b and T_a the hot and cold junction temperatures, respectively. Further,

$$Q_p = I\sigma T_b, \tag{3}$$

where σ is the average Seebeck coefficient of materials one and two over the temperature range from T_a to T_b, and

$$Q_j = I^2r. \tag{4}$$

The electrical power output is given by

$$P_0 = I^2R, \tag{5}$$

where R is the load resistance of the thermoelectric generator, and the current I is given by

$$I = \sigma(T_b - T_a)/R + r. \tag{6}$$

[1] A. F. Ioffe, *Semiconductor Thermoelements and Thermoelectric Cooling* (Infosearch Ltd., London, 1957).
[2] F. E. Jaumot, Proc. Inst. Radio Engrs. **46**, 538–554 (1958).
[3] P. E. Gray, "The effect of source and sink thermal resistance on thermoelectric generator performance," Trans. A.I.E.E. (to be published).
[4] N. F. Schuh and R. J. Tallent, Electronic Eng. **78**, 1172–1176 (1959).

TABLE I. Comparison of constant heat-flux operation with constant temperature operation.

Known quantities	Mode of operation	Conditions for optimum value of m	Optimum efficiency	Normalized temperature difference
		Constant temperature operation		
Z, σ, T_a, T_b, r or R	Maximum electrical Power transfer	$m=1$	$\eta_m=\dfrac{2(\zeta_b-\zeta_a)}{8+3\zeta_b+\zeta_a}$	$Z\Delta T=\zeta_b-\zeta_a$
Z, σ, T_a, T_b, r or R	Maximum efficiency	$M=\left(1+\dfrac{\zeta_a+\zeta_b}{2}\right)^{\frac{1}{2}}$	$\eta_{max}=\dfrac{(\zeta_b-\zeta_a)(M-1)}{\zeta_b M+\zeta_a}$	$Z\Delta T=\zeta_b-\zeta_a$
		Constant heat flux operation		
Z, σ, T_a, Q_i, r_a	Maximum efficiency	$[2M_R^2+(1-2\zeta_a)M_R+\zeta_a+1]\times[M_R-\zeta_a-1]-\dfrac{2Z^2}{\sigma^2}(Q_i r)=0$	$\eta_R=\dfrac{2M_R(M_R-\zeta_a-1)}{2M_R^2+(1-2\zeta_a)M_R+\zeta_a+1}$	$Z\Delta T=(M_R+1)(M_R-\zeta_a-1)$
Z, σ, T_a, Q_i, R	Maximum efficiency	$M_r^3(2M_r^3+2M_r+\zeta_a+1)-\dfrac{Z^2}{2\sigma^2}(Q_i R)=0$	$\eta_r=\dfrac{2M_r^3}{2M_r^3+2M_r+\zeta_a+1}$	$Z\Delta T=2M_r(M_r+1)$

In terms of electrical power output, Eq. (1) becomes

$$Q_i=P_0\left(\frac{2m+1}{2m}\right)+(P_0/R)^{\frac{1}{2}}\left[\frac{\sigma(1+m)}{z}+\sigma T_a\right], \quad (7)$$

where

$$m=R/r \quad (8)$$

and

$$1/z=(k_1A_1/l+k_2A_2/l)r/\sigma^2. \quad (9)$$

To minimize the necessary heat input for given values of the other parameters of Eq. (7), the quantity z should be maximized. If ρ_1 and ρ_2 are the specific resistivities of materials one and two, respectively, substituting

$$r=\rho_1\frac{l}{A_1}+\rho_2\frac{l}{A_2} \quad (10)$$

into Eq. (9) and setting

$$dz/d(A_1/A_2)=0, \quad (11)$$

yields

$$z_{max}=Z=\frac{\sigma^2}{[(k_1\rho_1)^{\frac{1}{2}}+(k_2\rho_2)^{\frac{1}{2}}]^2} \quad (12)$$

for

$$A_1/A_2=(k_2\rho_1/k_1\rho_2)^{\frac{1}{2}}$$

In terms of Z, Eq. (7) becomes

$$Q_i=P_0\left(\frac{2m+1}{2m}\right)+\frac{\sigma}{Z}(P_0/R)^{\frac{1}{2}}(m+\zeta_a+1), \quad (13)$$

where

$$\zeta_a=ZT_a \quad (14)$$

is the normalized cold junction temperature.

Similarly,

$$\zeta_b=ZT_b \quad (15)$$

may be defined as the normalized hot junction temperature.

OPTIMUM LOAD RESISTANCE

Considering the internal resistance of the thermoelectric generator r as fixed, an optimum load resistance yielding maximum power output can be found by differentiating Eq. (13) with respect to R and setting $dP_0/dR=0$, noting that only m and P_0 depend on R. The optimum load resistance must then satisfy

$$M_R^{\frac{1}{2}}-(\zeta_a+1)M_R^{\frac{1}{2}}-\frac{Z}{\sigma}(P_0 r)^{\frac{1}{2}}=0, \quad (16)$$

in which M_R is the optimum value of R/r (and thus yields R since r is considered as known). Figure 2 is a plot of this expression as a function of ζ_a. We see that the optimum value of M_R always exceeds $1+\zeta_a$. This expression is only useful if P_0 is known beforehand, which in practice seldom occurs. A more useful expression for the determination of M_R can be obtained by combining Eqs. (13) and (16) to give

$$[M_R-\zeta_a-1][2M_R^2+(1-2\zeta_a)M_R+\zeta_a+1]-\frac{2Z^2}{\sigma^2}(Q_i r)=0, \quad (17)$$

in which M_R is given in terms of the presumed known Q_i. Combining Eqs. (16) and (17) yields the optimum efficiency

$$\eta_R=\frac{P_0}{Q_i}=\frac{2M_R(M_R-\zeta_a-1)}{2M_R^2+(1-2\zeta_a)M_R+\zeta_a+1}. \quad (18)$$

It should be noted that this expression gives maximum efficiency since maximizing power output also maximizes efficiency when power input is constant.

It is advantageous to know the temperature difference between the hot and cold junctions. In terms of nor-

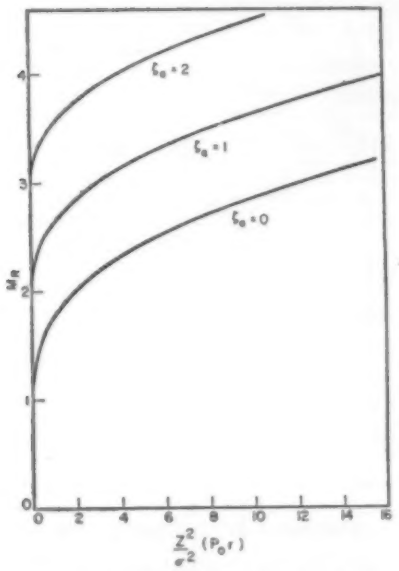

FIG. 2. Constant heat flux operation. Optimum value of m for fixed internal resistance.

malized temperature, this temperature difference is

$$\zeta_b-\zeta_a=Z\Delta T=(M_R+1)(M_R-\zeta_a-1). \quad (19)$$

Equations (17)–(19) as plotted in the composite graph, Fig. 3, are useful for design purposes. Inspection of the graph shows that it is desirable to maximize the quantity $Z\Delta T$. Perhaps this is done most easily by plotting empirical measurements of Z versus temperature and finding the greatest range ΔT over which the product of the average value of Z and ΔT is a maximum.

OPTIMUM INTERNAL RESISTANCE

In some cases the value of the load resistance to be used with the thermoelectric generator cannot be chosen at the discretion of the designer. For these cases it is possible to optimize the internal resistance of the thermoelectric generator for maximum power output. We proceed by rewriting Eq. (13) as

$$Q_i=P_0\left(\frac{2m+1}{2m}\right)+\frac{\sigma}{Z}(P_0/r)^{\frac{1}{2}}\left[\frac{m+\zeta_a+1}{(m)^{\frac{1}{2}}}\right], \quad (20)$$

and taking the derivative of this equation with respect to r (note again that only P_0 and m depend on r). Setting $dP_0/dr=0$ gives the condition

$$M_r^2=\frac{Z}{2\sigma}(P_0R)^{\frac{1}{2}}, \quad (21)$$

where M_r is the optimum value of R/r considering R as fixed. This equation is plotted in Fig. 4.

In terms of Q_i, the optimum value M_r is given by the equation

$$M_r^2(2M_r^2+2M_r+\zeta_a+1)-\frac{Z^2}{2\sigma^2}(Q_iR)=0, \quad (22)$$

and the optimum efficiency for this mode of operation is given by

$$\eta_r=\frac{P_0}{Q_i}=\frac{2M_r^2}{2M_r^2+2M_r+\zeta_a+1}. \quad (23)$$

The normalized temperature difference between the hot and cold junction is bound to be

$$\zeta_b-\zeta_a=Z\Delta T=2M_r(M_r+1), \quad (24)$$

which depends on the cold junction temperature through the dependency of M_r on the cold junction temperature.

Equations (22)–(24) are plotted in Fig. 5 in correspondence to those plotted in Fig. 3. The same general conclusions made in connection with Fig. 3 also hold, except that now the optimum value of R/r extends to zero and, in fact, for existing materials is generally less than unity. In addition, it is seen that the value of the cold junction temperature has a smaller effect upon the optimum values of M_r and η_r than for the case discussed previously.

DESIGN CALCULATION

To illustrate the use of graphs in the design of a thermoelectric generator, consider a numerical example. Assume a thermoelectric material with a Seebeck coefficient σ equal to 4×10^{-4} $v/°K$ and a figure of merit Z equal to $2\times10^{-3}/°K$ and that it is desired to operate the thermoelectric generator at a cold junction temperature of 300°K so that ζ_a is 0.6. The generator is constructed with an internal resistance r of 0.07 ohm and a cross-sectional area of 2 cm² so that when placed in sunlight with a thermal constant of 100 mw/cm², the heat received by the hot junction Q_i is 0.2 w. To find the load resistance, the efficiency, and the temperature rise of the generator when operating under optimum condi-

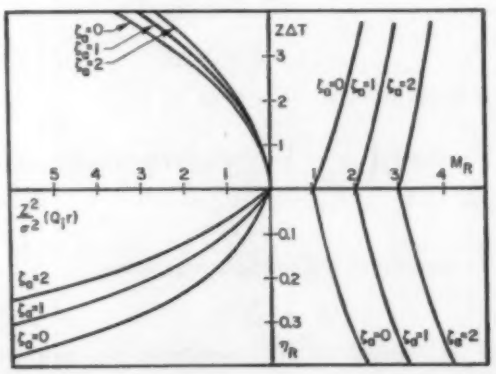

FIG. 3. Optimum operating conditions. Fixed internal resistance.

tions, calculate first

$$Z^2/\sigma^2(Q_i r) = 0.35.$$

Figure 3 shows that $M_R = 1.7$; thus, the load resistance R is 0.12 ohm. Also from the same figure, $Z\Delta T = 0.27$ and the temperature difference between the hot and cold junction is thus 185°K. The efficiency is found from this figure to be 3.86% and the electrical power output is then 7.7 mw.

CASCADING THERMOCOUPLES

In the preceding discussion, the objective was the optimum design of a single thermocouple. To extend the results to the important case in practice of n identical thermocouples electrically in series and thermally in parallel, simply calculate the parameters for one couple,

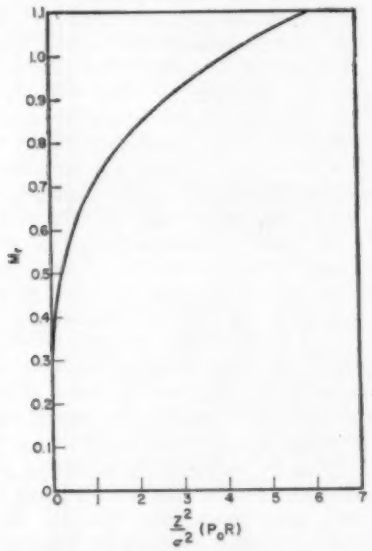

FIG. 4. Constant heat flux operation. Optimum value of m for fixed load resistance.

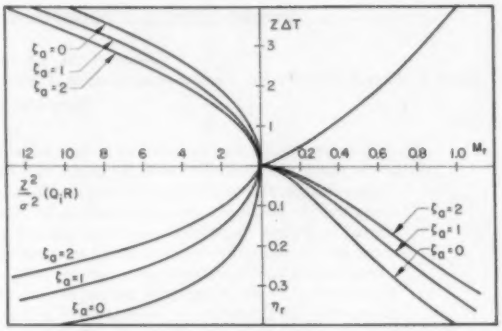

FIG. 5. Optimum operating conditions. Fixed load resistance.

but take the heat input to the single couple as Q_i/n, the load resistance as R/n, and the required power output as P_0/n.

CONCLUSIONS

The optimum conditions for constant heat flux of a thermoelectric generator are appreciably different from those of constant temperature operation. Table I summarizes and compares optimum conditions for both modes of operation.

For the constant heat flux mode of operation, two optimum conditions exist, depending on whether one fixes the load resistance or the internal resistance of the thermoelectric generator.

That two optimum conditions occur is the result of the nonlinearity appearing in the square root term of Eq. (13). Because of this nonlinearity, no optimum conditions exist if both R and r are allowed to vary independently; indeed, one cannot first adjust the resistance r for a maximum power output and then attempt to adjust R for an even greater power output. In doing so, both R and r get larger, the hot junction temperature T_h rises, the efficiency goes up, and the power output increases. In the limit, R, r, and T_h approach infinity, the efficiency approaches unity, and the power output approaches the heat input.

Some Elastic Properties of a Screw Dislocation Wall*

JAMES C. M. LI AND CHARLES D. NEEDHAM
Edgar C. Bain Laboratory For Fundamental Research, United States Steel Corporation Research Center, Monroeville, Pennsylvania

(Received February 25, 1960)

The stress fields of an infinite and a finite screw dislocation wall are given and from them the interactions of the screw dislocation walls with parallel and nonparallel dislocations have been studied. The nature of the penetration through a screw dislocation wall of a number of parallel screw dislocations driven by external stress and the possible stress concentration for a pileup against the wall are discussed in detail. The forces exerted by a screw dislocation wall on nonparallel edge and screw dislocations are calculated. The significance of the local torques due to these forces as a possible mechanism for the screw dislocation wall to become a source for generating dislocations is pointed out. The metastability of the screw dislocation walls is demonstrated and their strain energy is estimated and compared with that of the edge dislocation walls. It is concluded that the resistance to penetration of a dislocation wall increases in the following order: infinite edge dislocation wall, finite edge dislocation wall, finite screw dislocation wall, and infinite screw dislocation wall. It is also found that the strength of a dislocation wall increases with its surface strain energy.

INTRODUCTION

SUBSTRUCTURE boundaries as well as grain boundaries have long been regarded as barriers for plastic deformation in crystals.[1,2] The detailed nature of the strengthening effect is, however, not very well understood. This is due, at least partly, to the unknown structure of these boundaries. At the present time, although the structure of the grain boundary is still mysterious, the understanding of the structure of a subboundary is greatly simplified by the use of a dislocation model.[3]. This model enables study of the properties of substructure boundaries in terms of the elastic field of dislocations. For example, a low angle simple tilt boundary can be regarded as a wall of edge dislocations. Webb[4] has studied the interaction of solute atoms with such a boundary and the hindering effect to its motion. Vreeland[5] has studied the motion of a partially pinned tilt boundary and found that it can move at stress levels which do not produce general slip. Li[6,7] has studied the interaction of parallel edge dislocations with such a boundary, as well as some properties of an edge dislocation wall which terminates in the middle of a grain. The results of both Vreeland and Li indicate that a tilt boundary is not a very effective barrier for plastic deformation.

The fact that the mechanical behavior of a grain boundary does depend on the type of boundary has been demonstrated by Gilman in zinc.[8] The same must hold true for a subboundary. The results of Washburn,[9] also in zinc, seem to indicate that a twist boundary is stronger than a tilt boundary. The strength of the latter develops only after annealing near the melting point. This leads one to suspect that the strengthening effect arises from vacancy condensation onto the edge dislocations in the wall to form jogs on them. On the other hand, the strength of a twist boundary develops without annealing. Holt[10] has recently studied the effects of torsion on the tensile strength of aluminum. All these seem to indicate that screw dislocations play an important role in the strength of the crystal. Since a twist boundary is a wall or a crossed grid of screw dislocations, it is probably a stronger barrier than a tilt boundary. It seems desirable therefore to study first some properties of a wall of screw dislocations. This constitutes the purpose of the present communication. Although a screw dislocation wall is unstable by itself, it can be stabilized by extending into edge dislocations such as in the case of a slip band, by introducing some edge components into the screw dislocations, or by pinning with jogs or point defects. It is hoped that the results of this study, together with the results for edge dislocation walls,[6,7] will form a basis for the study of all other dislocation substructure boundaries.

THE STRESS FIELD OF AN INFINITE SCREW DISLOCATION WALL

The stress field[11] of a right-handed screw dislocation situated along the z axis is given by

$$\sigma_{zz} = -(\mu b/2\pi)y/(x^2+y^2), \tag{1}$$

and

$$\sigma_{yz} = (\mu b/2\pi)x/(x^2+y^2), \tag{2}$$

* Presented in part by Li at the annual meeting of the Metallurgical Society of AIME, February 14–19, 1960, in New York; J. of Metals 12, 72 (1960).

[1] A. H. Cottrell, "The yield point in single crystal and polycrystalline metals," *Symposium on Plastic Deformation of Crystalline Solids* at Mellon Institute, Pittsburgh, May, 1950, p. 60–76.

[2] E. R. Parker and T. Hazlett, chapter in *Relation of Properties to Microstructure* "Principles of solution hardening," Cleveland ASM, 1954.

[3] W. T. Read, Jr., and W. Shockley, Phys. Rev. 78, 275 (1950).

[4] W. W. Webb, Acta Met. 5, 89 (1957).

[5] T. Vreeland, Jr., Acta Met. 7, 240 (1959).

[6] J. C. M. Li, "The interaction of parallel edge dislocations with a Simple Tilt Boundary," (to be published).

[7] J. C. M. Li, "Some elastic properties of an edge dislocation wall," (to be published).

[8] J. J. Gilman, Trans. A.I.M.E. 212, 783 (1958).

[9] J. Washburn, Trans. A.I.M.E. 203, 675, 1262 (1955).

[10] D. B. Holt, Acta Met. 7, 446 (1959).

[11] A. H. Cottrell, *Dislocations and Plastic Flow in Crystals* (Clarendon Press, Oxford, England, 1953), p. 36.

for a right-handed rectangular-coordinate system such as the one shown by Cottrell.[12] The same equations apply for a left-handed screw dislocation in a left-handed coordinate system. For a right-handed screw dislocation in a left-handed coordinate system or vice versa, both Eqs. (1) and (2) have to change sign. In a cylindrical coordinate system, Eqs. (1) and (2) can be transformed simply into

$$\sigma_{\theta z}=\mu b/2\pi r. \tag{3}$$

It is seen that the constant stress curves are circles in the xy plane with the center at the origin. The direction of the shear stress can be represented by a vector tangent to the circle pointing in the counterclockwise direction. For this reason, a right-handed screw dislocation can also be regarded as a positive screw dislocation, since it is obvious that a left-handed screw dislocation, with the shear stress vector pointing to the clockwise direction along the circle, can be regarded as a negative screw dislocation. A simple way of finding out whether a screw dislocation is right or left-handed is to compare the threading planes with those of a right or left-handed screw. Walking clockwise on the threading planes around a screw dislocation[13] (as you would if you try to turn a right-handed screw), if one finds that he is going down, it is a right-handed screw dislocation. Otherwise, it is a left-handed one. Bilby[14] has a simple rule for deciding the type of a screw dislocation when it has an edge segment. It is noted here that the sign of a screw dislocation, unlike that of an edge dislocation, does not depend on the way one looks at it. A right-handed screw dislocation remains right-handed even if the crystal is turned around or over. Therefore we can use a symbol for each kind of screw dislocation. Following Amelinckx and Dekeyser,[15] we shall use "S" for the right-handed or positive screw and "$-S$" for the left-handed or negative screw dislocation.

The stress field of an infinite wall of right-handed screw dislocations uniformly spaced in the yz plane can be obtained[16] by adding up the stresses of individual dislocations to give

$$\sigma_{xz}=-\frac{\mu b}{4h}\frac{\sin(2\pi y/h)}{\sin^2(\pi y/h)+\sinh^2(\pi x/h)}, \tag{4}$$

$$\sigma_{yz}=\frac{\mu b}{4h}\frac{\sinh(2\pi x/h)}{\sin^2(\pi y/h)+\sinh^2(\pi x/h)}. \tag{5}$$

It is readily seen that when x and y are both very small (near one of the dislocations in the wall), Eqs. (4) and (5) reduce to Eqs. (1) and (2), respectively. At large distances from the wall (large x), σ_{xz} approaches zero but σ_{yz} approaches $\mu b/2h$. Such long-range stresses indicate that a wall of screw dislocations is not stable. The equivalue contours of σ_{xz} are the same as those of the dilatational strain field of an infinite wall of edge dislocations.[17] Figure 1 of Webb's paper[17] can be used for the contours of σ_{xz} if the unit of stress is taken as $-\mu b/2h$. The equivalue contours of σ_{yz} are shown in Fig. 1 of this paper. It is seen that the curves which represent contours for $\sigma_{yz}=\mu b/2h$ are

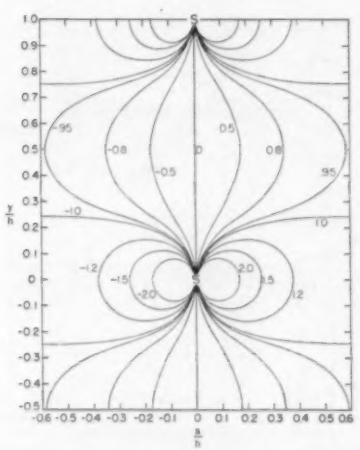

FIG. 1. Shear stress field of an infinite screw dislocation wall, σ_{yz}. Unit of stress: $\mu b/2h$.

$$y=(h/2\pi)\cos^{-1}\exp(-2\pi x/h), \tag{6}$$

which separate the regions where σ_{yz} is greater than $\mu b/2h$ from the regions where σ_{yz} is smaller than $\mu b/2h$. It is seen also that only at distances from the wall smaller than $h/2$, does the σ_{yz} differ substantially from $\mu b/2h$. For the same x, the stress σ_{yz} at $y=0$ is just the reciprocal of that at $y=h/2$ when the unit is $\mu b/2h$, since they are, respectively,

$$\sigma_{yz}=(\mu b/2h)\coth(\pi x/h) \quad \text{at} \quad y=0, \tag{7}$$

and

$$\sigma_{yz}=(\mu b/2h)\tanh(\pi x/h) \quad \text{at} \quad y=h/2. \tag{8}$$

To give another way of looking at the shear stress field of an infinite wall of positive screw dislocations, a combined shear stress in the xy plane is given by

$$\sigma=(\sigma_{xz}^2+\sigma_{yz}^2)^{\frac{1}{2}}=\frac{\mu b}{2h}\left[\frac{\cosh(2\pi x/h)+\cos(2\pi y/h)}{\cosh(2\pi x/h)-\cos(2\pi y/h)}\right]^{\frac{1}{2}}. \tag{9}$$

The equivalue contours of Eq. (9) are shown in Fig. 2,

$$\cos(2\pi y/h)=\frac{(2\sigma h/\mu b)^2-1}{(2\sigma h/\mu b)^2+1}\cosh(2\pi x/h). \tag{10}$$

[12] Footnote 11, p. 32.
[13] W. T. Read, Jr., *Dislocations in Crystals* (McGraw-Hill Book Company, Inc., New York, 1953), p. 16.
[14] B. A. Bilby, J. Inst. Metals **76**, 613 (1950) or see work cited in footnote 11, p. 27.
[15] S. Amelinckx and W. Dekeyser, Solid State Physics **8**, 409 (1959).
[16] Footnote 15, p. 410, note the misprinting and the sign in σ_{xz}.
[17] Footnote 4, p. 90.

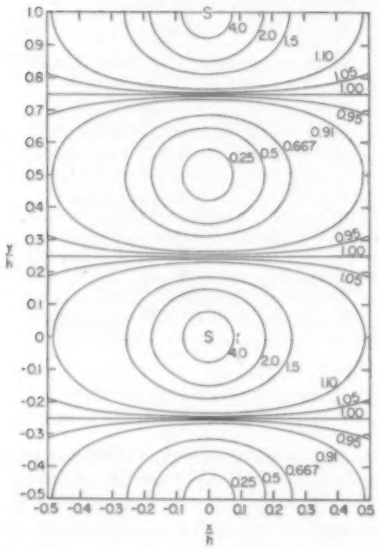

FIG. 2. Shear stress field of an infinite screw dislocation wall, $\sigma=(\sigma_{xz}^2+\sigma_{yz}^2)^{\frac{1}{2}}$. Unit of stress: $\mu b/2h$.

Here again, it is seen for the same x, every $h/2$ change in y changes the stress to the reciprocal of its original value if the unit of the stress is $\mu b/2h$. The lines $\cos(2\pi y/h)=0$, or $y=(2n+1)h/4$, where n is any integer, separate the crystal into bands with stresses alternately greater (if the band contains a screw dislocation) and smaller (if the band does not contain a dislocation) than $\mu b/2h$. Near one of the dislocations in the wall, the stress contours reduce to those of a single screw dislocation [circles as shown by Eq. (3)] as expected. The direction of the combined stress σ can be best represented by a family of curves satisfying the direction field

$$\frac{dy}{dx}=\frac{\sigma_{yz}}{\sigma_{xz}}=-\frac{\sinh(2\pi x/h)}{\sin(2\pi y/h)}. \tag{11}$$

Equation (11) can be easily integrated to give the following family of curves:

$$\cosh(2\pi x/h)-\cos(2\pi y/h)=\text{const.} \tag{12}$$

These curves have a family of trajectories

$$\tanh(\pi x/h)/\tan(\pi y/h)=\text{const.} \tag{13}$$

Both Eqs. (12) and (13) are plotted in Fig. 3. The trajectories are also the flow lines of parallel screw dislocations attracted toward or repelled from the wall. We shall discuss this later. It is seen that σ_{yz} predominates at distances farther than $h/2$ from the wall. The direction field near one of the dislocations in the wall reduces to that of the single positive screw dislocation (counterclockwise circles) as expected.

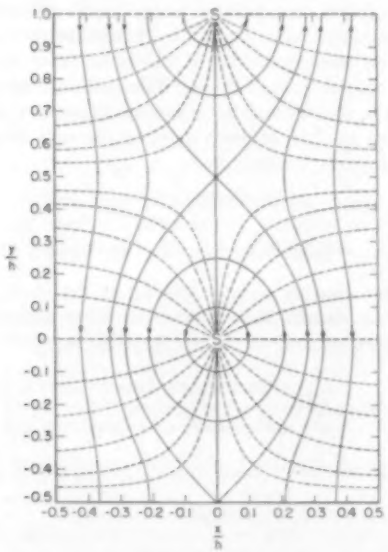

FIG. 3. Stress field of an infinite screw dislocation wall, direction of shear stress in the x-y plane.

METASTABILITY OF A SCREW DISLOCATION WALL

We have indicated earlier that due to the long-range stress field, a screw dislocation wall cannot be stable. We shall see here that each screw dislocation in a wall is indeed sitting on a saddle point of potential energy. The forces exerted on a screw dislocation when displaced from the wall are

$$f_x=b\sigma_{yz}=\frac{\mu b^2}{4h}\left[\frac{\sinh(2\pi x/h)}{\sin^2(\pi y/h)+\sinh^2(\pi x/h)}-\frac{2h}{\pi}\frac{x}{x^2+y^2}\right]\text{ per unit length,} \tag{14}$$

$$f_y=-b\sigma_{xz}=\frac{\mu b^2}{4h}\left[\frac{\sin(2\pi y/h)}{\sin^2(\pi y/h)+\sinh^2(\pi x/h)}-\frac{2h}{\pi}\frac{y}{x^2+y^2}\right]\text{ per unit length.} \tag{15}$$

When the dislocation is displaced in the x direction, it is seen that $f_y=0$ and,

$$f_x=(\mu b^2/2h)[\coth(\pi x/h)-(h/\pi x)]\text{ per unit length.} \tag{16}$$

The change in potential energy of the system is therefore,

$$\Delta F=-\frac{\mu b^2}{2\pi}\ln\frac{\sinh(\pi x/h)}{\pi x/h}\text{ per unit length.} \tag{17}$$

Both Eqs. (16) and (17) are plotted in Fig. 4. It is seen that the force increases from zero to $\mu b^2/2h$ per unit length at large distances from the wall. The system is metastable with respect to the displacement of screw dislocations in the x direction. On the other hand, when the dislocation is displaced in the y direction, it is seen that $f_x=0$ and

$$f_y=(\mu b^2/2h)[\cot(\pi y/h)-(h/\pi y)] \text{ per unit length.} \quad (18)$$

The change in potential energy of the system is

$$\Delta F=\frac{\mu b^2}{2\pi}\ln\frac{\pi y/h}{\sin(\pi y/h)} \text{ per unit length.} \quad (19)$$

Both Eqs. (18) and (19) are plotted in Fig. 5. It is seen that the force is restoring and increases from zero to infinity at $y=h$. The system is stable with respect to the displacement of screw dislocations in the y direction. It is metastable with respect to the displacement in any other direction. The potential energy of a displaced

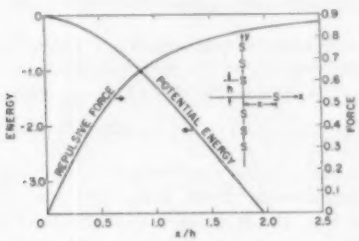

FIG. 4. Repulsive force and potential energy of a screw dislocation displaced from the wall in the x direction. Unit of force: $\mu b^2/2h$ per unit length; unit of energy: $\mu b^2/2\pi$ per unit length.

screw dislocation in any direction is

$$\Delta F=\frac{\mu b^2}{4\pi}\ln\frac{\pi^2(x^2+y^2)/h^2}{\sin^2(\pi y/h)+\sinh^2(\pi x/h)}. \quad (20)$$

The equivalue contours of potential energy are plotted in Fig. 6. The nature of the saddle point is demonstrated very clearly, and the motion of the screw dislocation may be visualized.

THE INTERACTION OF A SCREW DISLOCATION WALL WITH PARALLEL DISLOCATIONS

The forces exerted on a foreign screw dislocation of the same b as that of the dislocations in the wall are given by the first terms of Eqs. (14) and (15). The equivalue contours of these forces can be seen, respectively, from Fig. 1 of this paper and Fig. 1 of Webb's paper[17] if the unit of force is taken as $\mu b^2/2h$ per unit length. Without the influence of the external stress, the natural paths of parallel dislocations are shown in Fig. 3 by the dotted lines. The forces along the natural

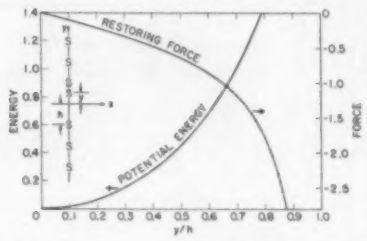

FIG. 5. Restoring force and potential energy of a screw dislocation displaced from the wall in the y direction. Unit of force: $\mu b^2/2h$ per unit length; unit of energy: $\mu b^2/2\pi$ per unit length.

paths are plotted in Fig. 7. They are

$$f=\frac{\mu b^2}{2h}\left(\cos^2\frac{\pi y_\infty}{h}\coth^2\frac{\pi x}{h}+\sin^2\frac{\pi y_\infty}{h}\tanh^2\frac{\pi x}{h}\right)^{\frac{1}{2}}$$

per unit length (21)

where y_∞ is the limiting y coordinate of the foreign screw dislocation at large distances from the wall. It is seen that the force lies between the limits

$$f=(\mu b^2/2h)\coth(\pi x/h) \quad \text{when} \quad y_\infty=0, \quad (22)$$

and

$$f=(\mu b^2/2h)\tanh(\pi x/h) \quad \text{when} \quad y_\infty=h/2. \quad (23)$$

The force has a minimum at

$$\tanh(\pi x/h)=[\cot(\pi y_\infty/h)]^{\frac{1}{2}}, \quad (24)$$

when $\cot(\pi y_\infty/h)<1$, with the value

$$f_{\min}=(\mu b^2/2h)[\sin(2\pi y_\infty/h)]^{\frac{1}{2}}. \quad (25)$$

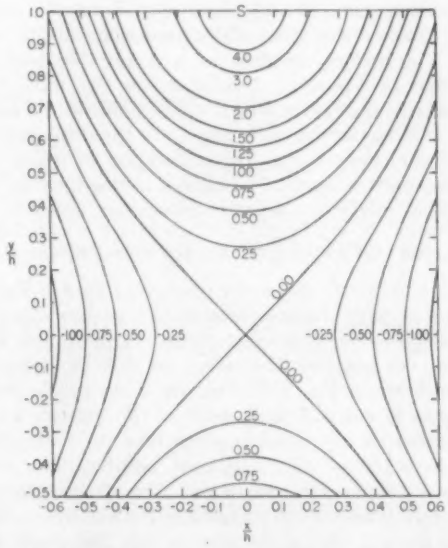

FIG. 6. Potential energy surface of a screw dislocation displaced from a screw dislocation wall. Unit of energy: $\mu b^2/4\pi$ per unit length.

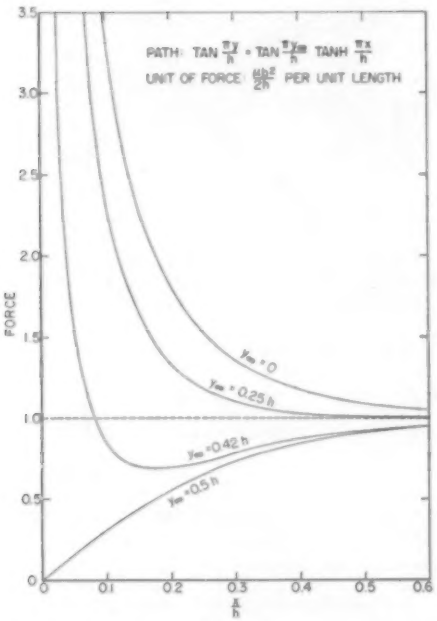
PATH: TAN $\frac{\pi y}{h}$ = TAN $\frac{\pi y_\infty}{h}$ TANH $\frac{\pi x}{h}$
UNIT OF FORCE: $\frac{\mu b^2}{2h}$ PER UNIT LENGTH
FORCE
y_∞ = 0
y_∞ = 0.25 h
y_∞ = 0.42 h
y_∞ = 0.5 h
$\frac{x}{h}$

FIG. 7. Force along the path of a single screw dislocation approaching or leaving a wall. Path: $\tan(\pi y/h)=\tan(\pi y_\infty/h)\times\tanh(\pi x/h)$; unit of force: $\mu b^2/2h$ per unit length.

These forces are repulsive for screw dislocations of the same sign as that of the dislocations in the wall, and are attractive otherwise. The attraction of a screw dislocation of opposite sign into a wall will eliminate one of the dislocations in the wall unless the foreign screw dislocation glides in the plane $y=h/2$. In the latter case, the negative screw dislocation will join the wall and will become situated in a metastable position between two positive dislocations in the wall. The metastable position is also a saddle point in the sense that it is metastable with respect to the displacement in all directions except the x direction in which the displacement is stable. To obtain a feeling for this, the potential energy of a negative dislocation, which is

$$\Delta F=(\mu b^2/4\pi)\ \ln[\sin^2(\pi y/h)+\sinh^2(\pi x/h)], \quad (26)$$

relative to that at the saddle point, is plotted in Fig. 8. This is actually the same kind of plot as shown in Fig. 3, though having a different physical significance. The paths of a negative dislocation are still the same as those shown in Fig. 3. The nature of the saddle point is shown in Fig. 8. Displacement of the negative screw dislocation in any other direction than the x direction will be attracted to the nearest positive dislocation along one of paths just mentioned. The potential energy of a positive dislocation pushed into the wall by external stress along $y=h/2$ is the same as Eq. (26) except for the sign. If a positive screw dislocation is pushed into the wall on any other plane by external stress, it can easily displace one of the dislocations in the wall. We shall discuss later the case where the wall is pinned.

A metastable negative dislocation in a wall can be pushed away by another negative screw dislocation gliding on $y=h/2$. Let the equilibrium distance of the first negative dislocation be x when the second dislocation is at x_0. The condition of equilibrium is

$$\tanh(\pi x/h)=h/\pi(x-x_0). \quad (27)$$

Eq. (27) is plotted in Fig. 9. It is seen that the first dislocation moves very little until the second one is within the dislocation spacing in the wall. At $x=-x_0=0.246h$, the two dislocations are equivalent and form another metastable configuration. From there on, the separation between the two dislocations approaches h/π. The force exerted on the second dislocation is

$$f=-(\mu b^2/2h)[\tanh(\pi x_0/h)+\tanh(\pi x/h)]$$
per unit length. (28)

The potential energy of the system relative to the above-mentioned symmetric metastable configuration can be calculated using a reversible path to be

$$\Delta F=\frac{\mu b^2}{2\pi}\ln\frac{\sinh(\pi x/h)\cosh(\pi x_0/h)}{\sinh(\pi x'/h)\cosh(\pi x_0'/h)}$$
per unit length (29)

where x' and x'_0 are the equilibrium values at the metastable configuration. Both Eqs. (28) and (29) are plotted in Fig. 10. It is seen that the force changes

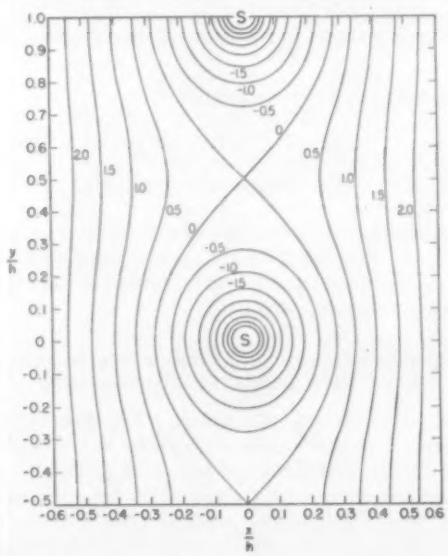

FIG. 8. Potential energy of a negative screw dislocation at a positive screw dislocation wall. Unit of energy: $\mu b^2/4\pi$ per unit length.

from $\mu b^2/2h$ to $-\mu b^2/h$ per unit length. The minimum in potential energy indicates stability with respect to displacement in the x direction. It is also a saddle point because it is metastable with respect to displacement in any other direction than the x direction. From the calculation of Eshelby, Frank, and Nabarro,[18] it can be easily shown that the maximum resistive force exerted on a third negative dislocation which must be overcome before the first two can be pushed through a wall is $-3\mu b^2/2h$; similarly, the maximum resistive force on the Nth dislocation which must be overcome before the $N-1$ dislocations can be pushed through the wall is $-N\mu b^2/2h$ per unit length. However, the external stress required to push any number of dislocations through the wall is still $\mu b/2h$. This can be seen from the following calculation.

The external stress required to push two negative screw dislocations through a wall is $\sigma_{yz}{}^0$

$$-(\mu b^2/2h)\tanh(\pi x_0/h)+\sigma_{yz}{}^0 b -[\mu b^2/2\pi(x-x_0)]=0 \quad (30$$

$$-(\mu b^2/2h)\tanh(\pi x/h)+\sigma_{yz}{}^0 b +[\mu b^2/2\pi(x-x_0)]=0. \quad (31)$$

The equilibrium distances can be obtained by subtracting one from the other of the above two equations and the stress can be calculated subsequently

$$\sigma_{yz}{}^0=(\mu b/4h)[\tanh(\pi x_0/h)+\tanh(\pi x/h)]. \quad (32)$$

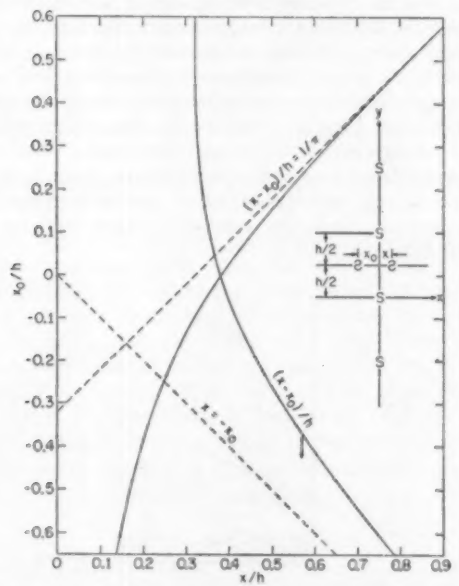

FIG. 9. Equilibrium distances of a negative screw dislocation caught between two positive screw dislocations in a wall when another negative dislocation is approaching the wall.

[18] J. D. Eshelby, F. C. Frank, and F. R. N. Nabarro, Phil. Mag. 42, 351 (1954).

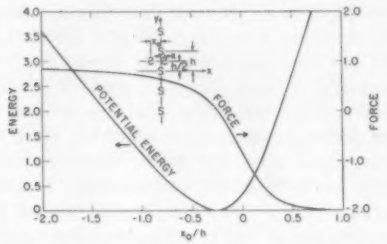

FIG. 10. Force and potential energy of the second negative screw dislocation when the first one assumes equilibrium position at a positive screw dislocation wall. Unit of force: $\mu b^2/2h$ per unit length; unit of energy: $\mu b^2/2\pi$ per unit length.

Both the equilibrium distances and the external stress are plotted in Fig. 11. The two screw dislocations are now equivalent to each other. The curve for the equilibrium positions is symmetric to the line $x=-x_0$. The motion is something like a displacement, because when x_0 is negatively large,

$$\pi x/h=\tanh^{-1}[(2h/\pi x_0)-1], \quad (33)$$

and when x is positively large,

$$\pi x_0/h=\tanh^{-1}[1-(2h/\pi x)]. \quad (34)$$

Thus, when the second one is far away, the first one is at the wall and when the second one is at the wall, the first one is then far away. The reversible stress for this displacement as given by Eq. (32) varies from $-\mu b/2h$ to $\mu b/2h$, as expected. The reversible stress for pushing N negative screw dislocations through the wall can be obtained from the following N equations $[(i,j)=1,2,\cdots N]$

$$-\frac{\mu b^2}{2h}\tanh\frac{\pi x_i}{h}+\sigma_{yz}{}^0 b-\frac{\mu b^2}{2\pi}\sum_{i\neq i}\frac{1}{x_j-x_i}=0. \quad (35)$$

The sum of these equations gives

$$\sigma_{yz}{}^0=\frac{\mu b}{2Nh}\sum_i \tanh\frac{\pi x_i}{h}, \quad (36)$$

which varies also from $-\mu b/2h$ to $\mu b/2h$. Therefore, the same stress is required to push any number of

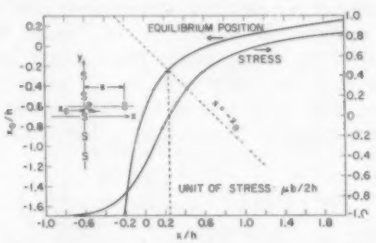

FIG. 11. Equilibrium positions and stresses required to push two negative screw dislocations through a positive screw dislocation wall.

negative dislocations through the wall. It is noted here that the situation is entirely different from the case of a simple tilt boundary[6] where it is possible to reduce the necessary external stress by pushing a number of dislocations at the same time. The details of the motion of these dislocations are also different. Here the dislocations will be attracted one by one to approach the wall until an equilibrium configuration is formed at zero external stress (for example, in the case of three dislocations, one at the middle and other two each at $0.516h$ from the wall). Then the process is reversed; that is, the dislocations are pushed away one by one to leave the wall. In the case of a simple tilt boundary[6] where the foreign edge dislocations are gliding in the slip plane of one of the free dislocations in the wall, or between two dislocations in the wall, the processes of penetration are such that no more than two dislocations can be near the boundary.

This characteristic of the barrier presented by the screw dislocation wall, such that a number of dislocations cannot pile up to create a stress concentration at the wall in the usual manner, can also be demonstrated by calculating the stress or force exerted on a pinned screw dislocation in a wall by a pileup of N screw dislocations of the same sign. The equilibrium positions of the N dislocations can be calculated from the following N equations ($i, j=1, 2, \cdots N$):

$$-\frac{\mu b^2}{2h}\coth\frac{\pi x_i}{h}+\sigma_{yz}{}^0 b-\frac{\mu b^2}{2\pi}\sum_{j\neq i}\frac{1}{x_j-x_i}=0. \tag{37}$$

The sum of these equations gives the required external stress

$$\sigma_{yz}{}^0=\frac{\mu b}{2Nh}\sum_i \coth\frac{\pi x_i}{h}. \tag{38}$$

Since the value of a hyperbolic cotangent function is always greater than unity, it is seen that the external stress has to be greater than $\mu b/2h$ before any pileup of screw dislocations is possible. Now for a screw dislocation wall of 0.1 degree or more, $\mu b/2h \geq$ about $10^{-3}\mu$, a high stress. The problem is therefore to see whether a stress concentration is possible by piling up a large number of dislocations under a stress not much greater than $\mu b/2h$. To simplify the calculation, we take advantage of the fact that the value of $\coth(\pi x_i/h)$ is nearly unity except when x_i is very small. Since the external stress is not much greater than $\mu b/2h$, we assume that the only $\coth(\pi x_i/h)$ which is much different from unity is that for $i=1$, namely, the one nearest to the wall. This enables us to estimate x_1

$$x_1=\frac{h}{2\pi}\ln\left\{1+\frac{\mu b/2h}{(N/2)[\sigma^0-(\mu b/2h)]}\right\}, \tag{39}$$

where σ^0 represents $\sigma_{yz}{}^0$. When $N\gg 1$ such that $N[\sigma^0-(\mu b/2h)]$ is much greater than $\mu b/h$, x_1 can be approximated to be

$$x_1=\mu b/2\pi N[\sigma^0-(\mu b/2h)]. \tag{40}$$

The rest of the dislocations ($i=2, 3, \cdots N$) now form a simple pileup under the uniform stress of $\sigma^0-\mu b/2h$. The results of Eshelby, Frank, and Nabarro[18] can be utilized here to calculate the stress concentration at the wall. The distance x_2-x_1 is given by

$$x_2-x_1=1.84\mu b/2\pi N[\sigma^0-(\mu b/2h)], \tag{41}$$

and the length of the pileup x_N-x_1 is

$$x_N-x_1=N\mu b/\pi[\sigma^0-(\mu b/2h)]. \tag{42}$$

Therefore

$$x_1:(x_2-x_1):(x_N-x_1)=1:1.84:2N^2. \tag{43}$$

This enables us to use an approximation developed by Stroh[19] for the calculation of a stress concentration at the wall. It gives, including the external stress:

$$\sigma=\sqrt{2}N[\sigma^0-(\mu b/2h)]+(\mu b/2h), \quad (N\gg 1). \tag{44}$$

It is interesting to compare this with that due to the nearest screw dislocation and the external stress, which is

$$\sigma=(N+1)[\sigma^0-(\mu b/2h)]+(\mu b/2h). \tag{45}$$

In any case, the stress concentration is now entirely different from the usual value of $(N+1)\sigma^0$ exerted by a pileup of N dislocations against a barrier. In fact, when the angle of the wall is sufficiently high, no such pileup is even possible under ordinary stress. It seems therefore that a pinned screw dislocation wall is a stronger barrier for the penetration of parallel screw dislocations than is a pinned edge dislocation wall for the penetration of parallel edge dislocations.[6] Although a screw dislocation wall is thermally metastable, it has been pointed out earlier that it can be stabilized by pinning or introducing some edge component into the wall dislocations.

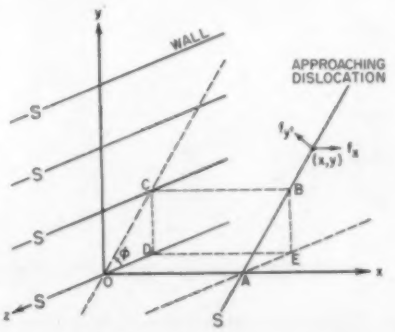

FIG. 12. Coordinate system for the interaction of a nonparallel dislocation with a screw dislocation wall.

[19] A. N. Stroh, Proc. Roy. Soc. (London) **A223**, 404 (1954).

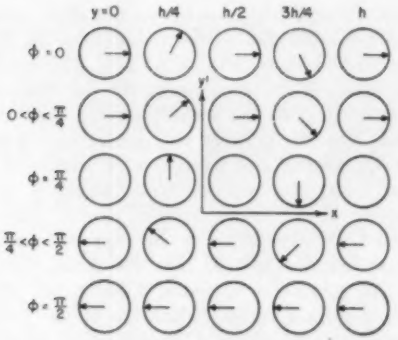

FIG. 13. Direction of forces exerted by a screw dislocation wall on a nonparallel foreign screw dislocation.

There is no interaction between a screw dislocation wall and parallel edge dislocations. The edge dislocations can penetrate a screw dislocation wall as if the wall were not there. When the edge dislocation meets a screw dislocation in the wall, they can combine into a mixed dislocation without any change in elastic energy (unless there is some change in core energy). In case that there is a decrease in free energy after the combination, the screw dislocation wall becomes a barrier for the penetration of parallel edge dislocations only if the combined dislocation is difficult to move and subsequent decomposition is necessary to continue the plastic flow. Otherwise, the edge dislocations can pass through a screw dislocation wall without any combination with the screw dislocations in the wall, except that perhaps there may be some change in the Peierls-Nabarro energy in crossing the screw dislocation core which can change the speed of the edge dislocation.

THE INTERACTION OF A SCREW DISLOCATION WALL WITH NONPARALLEL DISLOCATIONS

The forces that a screw dislocation wall exerts on a screw dislocation which is parallel to the plane of the wall but not parallel to the screw dislocations in the wall are very interesting. The coordinate system is shown in Fig. 12. The approaching screw dislocation is assumed to have the same sign and $|b|$ as that of the dislocations in the wall. It makes an angle ϕ with each of the wall dislocations. At any point (x,y) on the approaching dislocation, there exists a force in the x direction to produce a motion perpendicular to the plane of the wall (in the plane $OABC$)

$$f_x = b\sigma_{yz}\cos 2\phi = \frac{\mu b^2}{4h}\,\frac{\cos 2\phi \sinh(2\pi x/h)}{\sin^2(\pi y/h)+\sinh^2(\pi x/h)}$$

per unit length, (46)

and a force in the direction perpendicular to both f_x and the dislocation line to produce a motion parallel to the plane of the wall (in the plane ABE)

$$f_{y'} = -b\sigma_{xz}\cos\phi = \frac{\mu b^2}{4h}\,\frac{\cos\phi \sin(2\pi y/h)}{\sin^2(\pi y/h)+\sinh^2(\pi x/h)}$$

per unit length. (47)

The combined force is therefore of the magnitude

$$f = (f_x^2 + f_{y'}^2)^{\frac{1}{2}}, \tag{48}$$

and the direction is

$$\tan\theta = \frac{\cos\phi \sin(2\pi y/h)}{\cos 2\phi \sinh(2\pi x/h)}, \tag{49}$$

where θ is the angle between the resultant force and the f_x. This resultant force can be easily shown to be the maximum force among the forces acting in all directions at the same point. The direction of the resultant force changes along the dislocation line in a manner as summarized in Fig. 13. It is seen from inspection of the figure or integration of $f_{y'}$ along the dislocation line that the overall force to move the dislocation parallel to the plane of the wall vanishes except when $\phi=0$. When $\phi=0$, the force is constant (both in magnitude and direction) along the dislocation line but changes only with the position of the line. This has been discussed in detail in the foregoing section. The other force that moves the dislocation perpendicular to the plane of the wall is repulsive when $0\leq\phi<\pi/4$ or when $3\pi/4<\phi\leq\pi$, attractive when $\pi/4<\phi<3\pi/4$, and zero when $\phi=\pi/4$ or $3\pi/4$. The average perpendicular force can be calculated by integration of f_x along the dislocation line with the following simple result

$$\bar{f}_x = (\mu b^2/2h)\cos 2\phi \text{ per unit length.} \tag{50}$$

Equation (50) cannot, of course, apply to the case when $\phi=0$ since then the integration over y becomes meaningless. The interesting result that the average perpendicular force does not depend on the distance of the foreign dislocation from the wall is illustrated in Fig. 14. The large attractive force exerted by the wall on the perpendicular dislocations ($\phi=\pi/2$) of the same sign causes the formation of a twist boundary con-

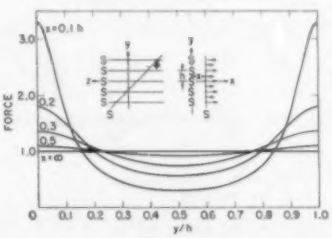

FIG. 14. Perpendicular forces exerted by a screw dislocation wall on a nonparallel screw dislocation. Unit of force: $\mu b^2\cos 2\phi/2h$ per unit length.

sisting of a crossed grid of screw dislocations. We shall discuss this later.

The forces that are parallel to the plane of the wall average to zero as mentioned earlier. However, they may produce local torques that increase in magnitude when the foreign screw dislocation approaches the wall. To obtain a feeling for such torques, the parallel forces are plotted in Fig. 15. The maximum local torque around a point where $y=0$ can be calculated to be

$$Q_0=(\mu b^2 h\cos\phi/2\pi)[\ln\cosh(\pi x/h)-(\pi x/h)+\ln 2], \quad (51)$$

pointing to the x direction. Another torque which points to the opposite direction around a point where $y=h/2$ is

$$Q_{\frac{1}{2}}=\frac{\mu b^2 h\cos\phi}{2\pi}\left(\frac{\pi x}{h}-\ln 2-\ln\sinh\frac{\pi x}{h}\right). \quad (52)$$

Here again, Eqs. (51) and (52) cannot apply to the case when $\phi=0$. These torques are plotted in Fig. 16. It is seen that $Q_{\frac{1}{2}}$ is always larger than Q_0. They approach each other at large distances from the wall while they both approach zero. The torque $Q_{\frac{1}{2}}$, unlike Q_0 which has a limit at $x=0$, becomes very large when x is small. This large torque should produce wiggles on the screw dislocation line. Such wiggles are believed to contribute to the ability of a substructure boundary to act as a source of dislocations. Were the wiggles not there, a straight screw dislocation would have to cut through the wall forming a jog at each interesection which can move only with difficulty, or would have to bypass each screw dislocation with a stress of the order of $\mu/2\pi$ to continue the plastic flow. The latter stress arises from the fact that at the other side of the wall, dislocations of different sign have to pass through each other at a distance of one Burgers vector. With the wiggles formed by the large torque, the approaching dislocation becomes a number of sources and can bypass the dislocations in the wall with less difficulty than can a straight dislocation. This is due to the fact that now at the other side of the wall, dislocations have to pass each other only at a larger distance. This behavior enables continuation of plastic flow through a subboundary. However, in order for this mechanism to operate, certain geometric conditions have to be fulfilled. First, the approaching screw dislocation shall not be perpendicular to the dislocations in the wall. The torque becomes zero at $\phi=\pi/2$. The smaller the ϕ, the better is the opportunity for the dislocation to penetrate. Second, the wiggles formed shall be such that the segments between two dislocations in the wall lie on slip planes and have enough length to act as sources under the applied stress. Third, if the edge component in the source segment cannot glide on the slip plane, the separation of the edge and screw components shall be easy so that the screw component alone can operate as a source. Finally, the stress required to push a screw dislocation of the same sign near the wall is $\mu b\cos 2\phi/2h$ and that required to generate the sources is roughly $\mu b(2\sin\phi-\cos 2\phi)/2h$. Therefore if the former stress is sufficient for the latter purpose the angle ϕ shall be less than $\pi/6$ or 30°. This indicates also that a screw dislocation wall is a better barrier against screw dislocations of a different sign than against those of the same sign since in the former case the stress required to generate the sources is now roughly $\mu b(2\sin\phi+\cos 2\phi)/2h$ which is at least $\mu b/2h$ and has a maximum at $\phi=\pi/6$ equal to $1.87\,\mu b/2h$.

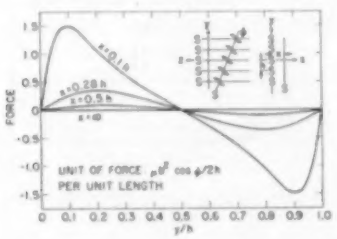

FIG. 15. Parallel forces exerted by a screw dislocation wall on a nonparallel screw dislocation.

The interaction of a screw dislocation wall with nonparallel edge dislocations can be analyzed in a similar way. We can still refer to Fig. 12 for the coordinate system. The forces are now

$$f_x=b_x\sigma_{xz}\sin\phi+b_{y'}\sigma_{yz}\sin 2\phi \text{ per unit length}, \quad (53)$$

$$f_{y'}=-b_{y'}\sigma_{xz}\sin\phi=\frac{\mu b b_{y'}}{4h}\cdot\frac{\sin\phi\sin(2\pi y/h)}{\sin^2(\pi y/h)+\sinh^2(\pi x/h)}$$

$$\text{per unit length}, \quad (54)$$

where b_x and $b_{y'}$ are the components of the Burgers vector of the edge dislocation along the x and the y' direction, respectively. The maximum force

$$f=(f_x^2+f_{y'}^2)^{\frac{1}{2}} \quad (55)$$

is not, however, exerted in the slip plane of the edge dislocation. The force that is exerted in the slip direction is

$$f_{\text{slip}}=-\frac{\mu(b_x^2-b_{y'}^2)\sin\phi\sin(2\pi y/h)-b_x b_{y'}\sin 2\phi\sinh(2\pi x/h)}{4h[\sin^2(\pi y/h)+\sinh^2(\pi x/h)]}$$

$$\text{per unit length}. \quad (56)$$

This force varies periodically along the edge dislocation line with a period h. The average force is zero if either b_x or $b_{y'}$ is zero. The local forces form torques that can also produce wiggles in the slip plane of the edge dislocation. These wiggles are not likely to become sources for generating dislocations in other slip planes. The interaction of a screw dislocation wall with edge dislocations is such that the average force along the y' direction

is zero and that along the x direction is the second term in Eq. (53) with σ_{yz} replaced by $\mu b/2h$. The maximum force in the slip direction of an edge dislocation is one-half of that exerting on a screw dislocation of the same $|b|$. An edge dislocation, after cutting a screw dislocation, possesses a jog which is also an edge dislocation. This jog can glide in the slip direction of the edge dislocation. Therefore, a screw dislocation wall is a less effective barrier for the penetration of edge dislocations than that for the penetration of screw dislocations.

The interaction of a screw dislocation wall with nonparallel dislocations of a mixed type can be calculated by summing up the interactions with the edge

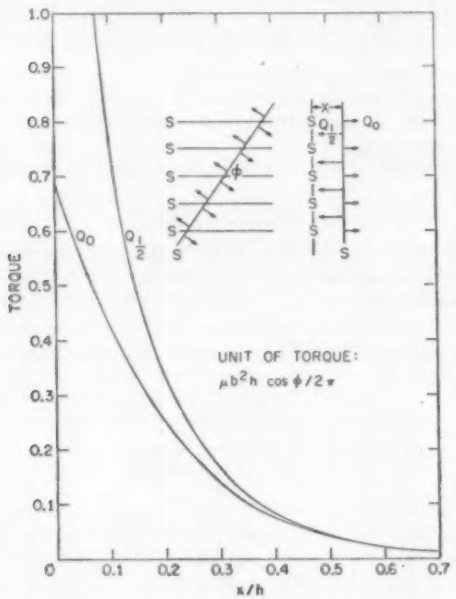

FIG. 16. Torques due to parallel forces exerted by a screw dislocation wall on a nonparallel screw dislocation. Unit of torque: $\mu b^2 h \cos\phi/2\pi$.

and screw components. A particular case of interest is the interaction of a screw dislocation wall with a dislocation of the same slip vector as that of the dislocations in the wall. This kind of dislocation can be "absorbed" into the wall and disappears. The mechanism is shown in Fig. 17. The kink formed in the wall is due to the line tension of the dislocations and will, for the same reason, straighten out eventually. Thus, a screw dislocation wall is a sink for dislocations of the same slip vector (care should be taken as to the sign of the slip vectors; for example, a positive screw dislocation wall is a sink for negative parallel screw dislocations, but not for positive ones). However, nonparallel dislocations of the same slip vector have slip planes parallel to the plane of the screw dislocation wall

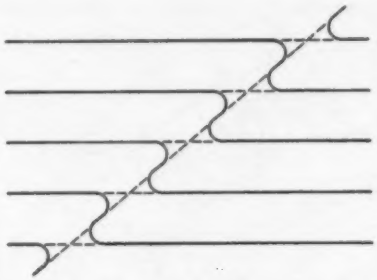

FIG. 17. Interaction of a screw dislocation wall with a nonparallel dislocation of the same slip vector.

and therefore do not easily disappear into the wall. On the other hand, an edge dislocation wall is a much better sink for nonparallel dislocations of the same slip vector. This is another factor which supports the conclusion that a screw dislocation wall is a stronger deterrent of plastic deformation than is an edge dislocation wall.

THE STRESS FIELD OF A FINITE SCREW DISLOCATION WALL

The foregoing calculations are based on the stress field of an infinite array of parallel screw dislocations. The results will be true for a finite array, if the distance between the wall and the approaching dislocation is sufficiently small. In order to have a feeling for this, it seems desirable to calculate the stress field of a finite screw dislocation wall. As a first-order approximation, the stress of the wall can be calculated by integrating the stresses of individual dislocations [Eqs. (1) and (2)]

$$\sigma_{xz}=-\frac{\mu b}{4\pi h}\ln\frac{x^2+(y+L)^2}{x^2+(y-L)^2} \tag{57}$$

$$\sigma_{yz}=\frac{\mu b}{2\pi h}\left(\tan^{-1}\frac{y+L}{x}-\tan^{-1}\frac{y-L}{x}\right) \tag{58}$$

where L is the half length of the wall and is equal to $Nh/2$ with N being the total number of dislocations in the wall. The combined shear stress in the xy plane is

$$\sigma=(\sigma_{xz}^2+\sigma_{yz}^2)^{\frac{1}{2}}, \tag{59}$$

whose contours are plotted in Fig. 18 together with the direction field

$$dy/dx=\sigma_{yz}/\sigma_{xz}, \tag{60}$$

which can be integrated to give the following family of curves:

$$2x\left[\tan^{-1}\frac{y+L}{x}-\tan^{-1}\frac{y-L}{x}\right]+(y+L)\ln\frac{x^2+(y+L)^2}{L^2}$$
$$-(y-L)\ln\frac{x^2+(y-L)^2}{L^2}=CL, \tag{61}$$

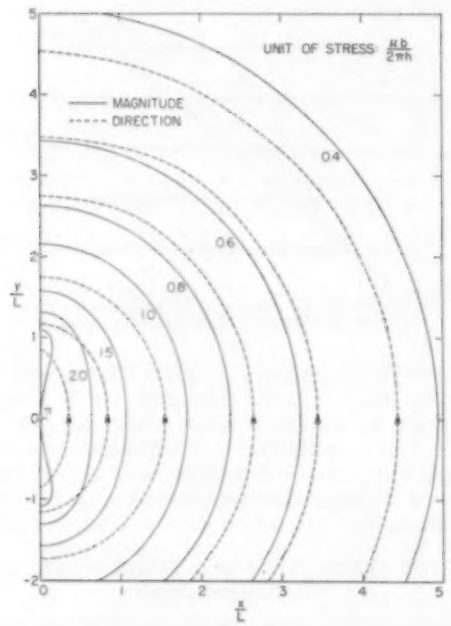

FIG. 18. Shear stress field of a finite screw dislocation wall. Unit of stress: $\mu b/2\pi h$.

where C is an integration constant. Equation (61) is plotted also in Fig. 18 to give the direction of the shear stresses in the xy plane. In terms of polar coordinates (r,θ), Eqs. (59) and (61) become, respectively

$$\sigma=\left(\frac{\mu b}{2\pi h}\right)\left[\frac{1}{4}\left(\ln\frac{r^2+L^2+2rL\sin\theta}{r^2+L^2-2rL\sin\theta}\right)^2+\left(\tan^{-1}\frac{2rL\cos\theta}{r^2-L^2}\right)^2\right]^{\frac{1}{2}},$$

and

$$2r\cos\theta\tan^{-1}\frac{2rL\cos\theta}{r^2-L^2}+(r\sin\theta+L)\ln\frac{r^2+L^2+2rL\sin\theta}{L^2}-(r\sin\theta-L)\ln\frac{r^2+L^2-2rL\sin\theta}{L^2}=CL, \quad (63)$$

which at large r reduce to, respectively,

$$\sigma=N\mu b/2\pi r, \quad (64)$$

and

$$\ln(r/L)=(C-4)/4. \quad (65)$$

Therefore, the stress field at large distances from the wall approaches that of a single screw dislocation of strength Nb as expected.

To compare the approximate results obtained by integration with the exact ones, the shear stress σ_{yz} at the middle of a finite screw dislocation wall calculated from Eq. (58) is plotted in Fig. 19 together with those of walls of 1, 2, $\cdots$, 9 and 10 dislocations calculated exactly by direct summation of the stresses of individual dislocations. It is seen how the stress field approaches that of the integration approximation when the number of dislocations in the wall increases. From the plot it can be concluded that the approximation is good at or farther away than $\pm h$ from the wall. It becomes better the larger the distance from the wall.

It seems desirable here to include the stress field of a wall of only two screw dislocations so that one can imagine the stress field between any two dislocations in a finite wall. The stress in the xy plane for a two-dislocation wall can be best represented by a family of curves of constant magnitude in the polar coordinates

$$\sigma=\frac{\mu b}{2\pi h}\cdot\frac{8rh}{(16r^4+8r^2h^2\cos2\theta+h^4)^{\frac{1}{2}}}, \quad (66)$$

and another family of curves describing the direction field

$$C=(2r^4+r^2h^2\cos2\theta)/h^4. \quad (67)$$

They are shown in Fig. 20. It is seen that the stress field between two screw dislocations in a finite wall approaches that of the infinite wall (Figs. 2 and 3), and that outside (more than about $\pm h$) the finite wall it approaches that of the integration approximation, Fig. 18.

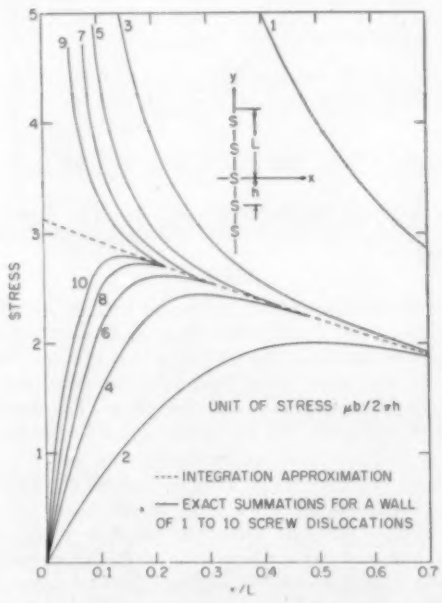

FIG. 19. Shear stress at the middle of a finite screw dislocation wall, σ_{yz}. Dotted line, integration approximation. Solid line, exact summations for a wall of 1 to 10 screw dislocations.

In summary, the stress field of a finite screw dislocation wall is entirely different from that of an infinite wall. It approaches the latter only at points closer than $\pm h$ from the wall. As a result, the finite wall will not be as strong a barrier against the penetration of screw dislocations as an infinite wall, since now a long pile-up can create a higher stress concentration against the wall than is possible in the case of an infinite wall. However, a finite screw dislocation wall is still a stronger barrier than a finite edge dislocation wall for the following reasons: (1) The stress is large in the vicinity of a screw dislocation wall but is small in the vicinity of an edge dislocation wall.[7] Since the internal stress at the tip of a pile-up is very important for the stress concentration which can be created by external stress, it would be easier for a pile-up to penetrate an edge dislocation wall than for it to penetrate a screw dislocation wall. (2) Nonparallel dislocations can cut through edge dislocation walls without forming slowly moving jogs, while for the same to cut through a screw dislocation wall, jogs must be formed when there is screw component in the moving dislocation, and these jogs will slow down or prohibit motion when the angle of the wall is high. The only way to continue plastic flow in the latter case is to generate dislocations from the wall under the conditions discussed in the last section. (3) Dislocations with the same slip vector as that of those in the wall can disappear into an edge dislocation wall more easily than into a screw dislocation wall to decrease the angle of the wall. This has been discussed earlier.

THE STRAIN ENERGY OF A SCREW DISLOCATION WALL

The strain energy of an infinite screw dislocation wall can be calculated by relaxing the stress of each dislocation on a slip plane perpendicular to the plane of the wall. This can be done simply by the use of Eq. (7). The result is

$$\Delta F=\frac{\mu b^2}{4\pi h}\ln\frac{\sinh(\pi R/h)}{\sinh(\pi r_0/h)}\text{ per unit area,}\qquad(68)$$

where R is the radius of the specimen and r_0 that of the core of the screw dislocation. Under the condition where $R\gg h\gg r_0$, we have

$$\Delta F=\frac{\mu b}{2\pi}\theta\left(\frac{2\pi R\theta}{b}-\ln\frac{4\pi r_0}{b}-\ln\theta\right)\text{ per unit area,}\qquad(69)$$

where $\theta=b/2h$. It is seen that the surface energy of an infinite screw dislocation wall, unlike that of an infinite edge dislocation wall, increases without limit with the size of the specimen. It is also different from that given by the general formula of the surface energy of a grain boundary.

The strain energy of a finite screw dislocation wall

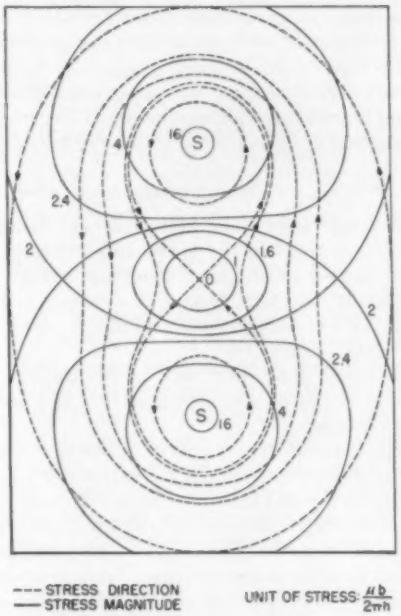

FIG. 20. Stress field of two positive screw dislocations. Dotted line, stress direction. Solid line, stress magnitude.

can be calculated by viewing the wall as the slip plane. The strain energy is equal to the self energy of all the N dislocations and the interaction energy of bringing them together from a large distance R. After using the Sterling approximation and replacing one of the summations by an integration, we obtain the strain energy of a wall of N screw dislocations

$$\Delta F=(\mu b^2/4\pi)[N^2\ln(Re/2L)+N\ln(h/er_0)]$$
per unit length of wall. (70)

In terms of surface energy, this is equivalent to

$$\Delta F=(\mu b/2\pi)\theta[(4L\theta/b)\ln(Re/2L)-\ln(2er_0/b)-\ln\theta]$$
per unit area. (71)

It is seen that, although this equation is quite similar to Eq. (69), the surface energy of an infinite screw dislocation wall is always larger, for the same θ, than that of a finite screw dislocation wall. This, again, is just opposite to the case of an edge dislocation wall where the surface energy of a finite wall is always larger than that of an infinite wall. The latter fact can be understood easily by realizing that the average energy per dislocation in an infinite edge dislocation wall is equal to that of a single edge dislocation situated in a specimen of radius $he^2/2\pi$ and that the average energy per dislocation in a finite edge dislocation wall[7] is larger than that of a single edge dislocation in a specimen of a radius of the order of the height of the wall.

Since for the same angle of misfit, a screw dislocation

wall has twice as many dislocations per unit height as an edge dislocation wall, the surface energy of dislocation walls increases in the order: infinite edge dislocation wall, finite edge dislocation wall, finite screw dislocation wall, and infinite screw dislocation wall. The resistance to penetration of dislocation walls also increases in this order.

CONCLUSIONS

(1) A screw dislocation wall in the yz plane with dislocations parallel to the z axis and spaced h apart has a stress field which can be described essentially by $\sigma_{yz}=\mu b/2h$ at distances greater than about $h/2$ from the wall. This stress extends to a large distance if the wall is infinitely high.

(2) A screw dislocation wall is metastable. Each dislocation in the wall is sitting on a saddle point of potential energy.

(3) The external stress required to push any number of parallel negative screw dislocations through a positive screw dislocation wall is $\mu b/2h$. The motion is such that the negative dislocations will be attracted, one by one, to approach the wall until an equilibrium configuration is formed at zero external stress. Then the negative dislocations will be pushed, one by one, to leave the wall. The nature of the motion is entirely different from the case where a number of parallel edge dislocations is pushed through an edge dislocation wall. In the latter case, no more than two dislocations can be near the boundary.

(4) The stress concentration at a pinned screw dislocation wall due to a pileup of a large number of parallel screw dislocations of the same sign by an external stress σ_0 is approximately equal to that due to the same pileup against a stress-free boundary by an external stress $\sqrt{2}[\sigma^0-(\mu b/2h)]$. Thus the stress concentration is greatly reduced due to the stress field of the wall and under certain conditions, a pileup is not even possible at ordinary stress.

(5) The interaction of a screw dislocation wall with a nonparallel screw dislocation of the same sign is such that the force is repulsive if the angle between the approaching dislocation and the wall dislocations is less than 45° and is attractive if it is larger than 45°. The attractive force causes the formation of a stable twist boundary consisting of a crossed grid of screw dislocations. The average force per unit length is simply $\mu b^2 \cos 2\phi/2h$ and is not a function of the distance between the approaching dislocation and the wall.

(6) When a nonparallel screw dislocation is close enough to a screw dislocation wall, the latter exerts local torques perpendicular to the plane of the wall on the approaching dislocation. These torques may increase without limit when the distance between the wall and the nonparallel dislocation is very small and may produce wiggles on the latter. Under certain geometric conditions, these wiggles may become sources for generating dislocations on the other side of the boundary. This will reduce the effectiveness of a screw dislocation wall as a barrier for plastic deformation.

(7) There is no interaction between a parallel edge dislocation and a screw dislocation wall. The interaction between a nonparallel edge dislocation and a screw dislocation wall is such that the maximum average force exerted by the wall on the slip plane of the edge dislocation is one-half of that exerting on a screw dislocation of the same magnitude of Burgers vector as that of the edge dislocation. A screw dislocation wall is therefore a less effective barrier against the penetration by edge dislocations than by screw dislocations.

(8) A finite screw dislocation wall has a stress field at large distances approaching that of a single screw dislocation of strength Nb where N is the number of dislocations in the wall. The stress field approaches that of an infinite wall only at distances closer than $\pm h$ from the wall. As a result, a finite wall will not be as strong a penetration barrier as an infinite wall. But for reasons given in the text, a finite screw dislocation wall is a still stronger barrier than a finite edge dislocation wall.

(9) Dislocation walls can be arranged in the following order of increasing resistance to penetration: infinite edge dislocation wall, finite edge dislocation wall, finite screw dislocation wall, and infinite screw dislocation wall. The surface energy of dislocation walls increases also in this order. It can be said that the strength of a dislocation wall increases with the strain energy per unit surface area.

ACKNOWLEDGMENTS

The authors wish to thank Dr. L. S. Darken, Dr. R. A. Oriani, and Dr. Y. T. Chou of this Laboratory for discussion and comment. The numerical calculation of Fig. 18 was carried out with an electronic computer by R. W. Whitmore and his group. Some suggestions are due to Prof. E. R. Parker of the University of California.

X-Ray Reflection Studies of the Anneal and Oxidation of Some Thin Solid Films

N. WAINFAN AND L. G. PARRATT*
Cornell University
(Received November 5, 1959)

The technique of the total reflection of x rays has been applied to the study of thin films of Cu, Ni, Ge, and Se vacuum-deposited onto polished glass substrates. Starting with fresh films, "smooth" enough to exhibit pronounced x-ray interference fringes in the region just beyond the critical angle, the effects of vacuum anneal and oxidation were studied. Changes in the reflection curves are interpreted in terms of possible structural changes in the films. Reflection from layers of particles of carbon or polystyrene latex deposited onto "smooth" substrates was also studied for comparison.

I. INTRODUCTION

FROM among the various techniques that have been used to obtain information about the structure of thin films, the method of the total reflection of x rays has recently been revived and extended.[1] The reflection coefficient for x rays is measured as a function of the glancing angle in the vicinity of the critical angle. From an analysis of the reflection curves information about the density, thickness, and "smoothness" of the films can, under some circumstances, be obtained.[2–4]

In the work here described, the effects of the anneal in vacuum and, in some cases, the effects of oxidation in air were studied. The films, vacuum-deposited onto optically flat Pyrex or soft glass substrates, were sufficiently uniform to exhibit strong x-ray interference fringes in the region just beyond the critical angle. A range of film thicknesses was chosen so that thickness measurements and "smoothness" determinations could be made from the interference fringes. Films of copper were examined with some thoroughness, and nickel, selenium, and germanium films were each considered briefly.

II. THEORY

The complex index of refraction for x rays has been calculated, and the x-ray reflection coefficients for the region of total reflection from mulitple-layer systems have been computed.[5–7] For single-layered films of uniform thickness and density, having plane parallel interfaces, the relation

$$N=R+\frac{2t}{\lambda}(\theta_m^2-\theta_c^2)^{\frac{1}{2}}$$

can be used to obtain the thickness t.[7,8] Here, N is the order number of the x-ray fringe, R is a constant related to the phase changes on reflection, θ_c is the critical angle and θ_m is the angular position of the fringe maximum. For the work reported here, θ_c was approximated by the angular position at which the reflection coefficient fell to a value of $\frac{1}{2}$.[9] Use of this approximate value of the critical angle in the relation presented in the foregoing introduces only small errors in the thickness determination for films whose thickness is greater than 200 A.[6]

If the roughness of the film can be represented by a random undulation of the continuous film's vacuum interface within the area illuminated by the x-ray beam, then the presence of strong interference maxima consistent with the relation given above may be used as a criterion of the film "smoothness." If the range of variation of the thickness of the film is such as to shift, locally, the order number of a fringe over a range of $\frac{1}{2}$ order, that fringe and all higher-order fringes would be essentially destroyed. The variation in the thickness, Δt, which would smear out the first-order fringe would be

$$\Delta t=\frac{\lambda}{4(\theta_{m_1}^2-\theta_c^2)^{\frac{1}{2}}}.$$

For a copper film of a nominal thickness of 800 A with 1.54 A radiation incident upon it, Δt would be of the order of 300 A. This analysis can be extended to account for the disappearance of individual higher-order fringes.[10]

The details of the interaction of a beam of x rays with a very rough (badly broken up) surface at small glancing angles is apparently not amenable to a simple analysis. However, if some assumptions are made it is possible to make qualitative predictions about the behavior of the film as an x-ray mirror. The assumptions are: (1) The reflection coefficient is high for any rough surface at sufficiently small glancing angles. (2) As the surface becomes rough, the x-ray penetration increases and reflection falls off first at the larger glancing angles.

* This research was supported by the U. S. Air Force through the Air Force Office of Scientific Research of the Air Research and Development Command, under contract.

[1] L. G. Parratt, Phys. Rev. **95**, 359 (1954).
[2] N. Wainfan, N. J. Scott, and L. G. Parratt, J. Appl. Phys. **30**, 1604 (1959).
[3] R. Riedmiller, Ann. phys. **20**, 377 (1934).
[4] W. Hink and W. Petzold, Z. angew. Phys. **10**, 553 (1958).
[5] L. G. Parratt and C. F. Hempstead, Phys. Rev. **94**, 1593 (1954).
[6] L. G. Parratt, J. chim. phys. **53**, 597 (1956).
[7] N. J. Scott, "Study of thin vacuum-deposited copper films by x-ray total reflection," Technical Rept. No. 11, December 30, 1957, Document Nos. AFOSR TN-57-779 and ASTIA AD 148010.
[8] H. Kiessig, Ann. phys. **10**, 715, 769 (1931).
[9] See Table III of work cited in footnote 1.
[10] A somewhat related criterion of film smoothness for x-ray reflection has been given by F. Jentzsch, Physik. Z. **30**, 268 (1929).

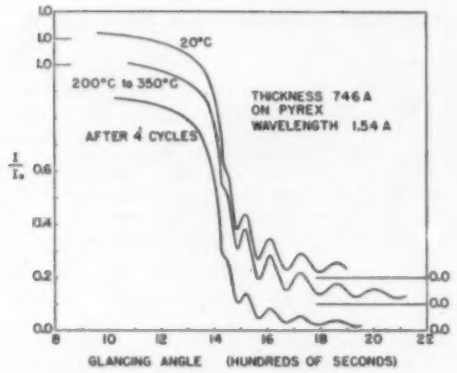

FIG. 1. Copper on Pyrex, vacuum-annealed.

Accordingly, for a very rough film deposited on a "smooth" substrate the reflection coefficient at very small angles would be large, and as the glancing angle of incidence is increased the reflection coefficient should fall. As the incident angle is further increased on the rough film, the reflection from the film itself continues to decrease; but, note also that the absorption path in the film itself becomes shorter, and, therefore, a larger fraction of the x-ray beam reaches and is reflected from the smooth substrate. Thus, for angles beyond some intermediate value, the *net* reflection coefficient may actually increase. Finally, as the angle is still further increased, beyond the critical angle of the substrate, the reflection coefficient will again fall to small values. In addition, it might be expected that, in the region where there is appreciable x-ray penetration through the rough film and reflection back from the smooth substrate, the reflected beam might be spread by small-angle scattering on the double passage through the rough film.

III. EXPERIMENTAL PROCEDURE

The films that were used in this work were in the thickness range between 240 and 1200 A. The film

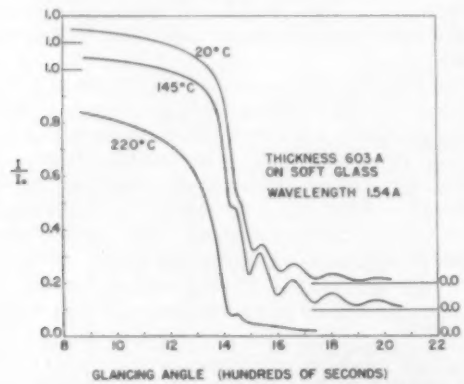

FIG. 2. Copper on soft glass, vacuum-annealed.

materials were vacuum-deposited onto optically flat soft glass or Pyrex substrates at an ambient pressure of 10^{-5} to 10^{-6} mm Hg. Most of the substrates were $1\frac{1}{2}\times 2$-in. plates made to fit a new vacuum reflectometer which is discussed briefly in the following. Some copper films, made for the oxidation study, were deposited on $11.8\times 5.4\times 1.6$-cm Pyrex blocks which were used in an older reflectometer. All the substrates were flat to within either $\frac{1}{10}$ or $\frac{1}{4}\lambda$ of the mercury green line. No differences in the results were noticed between the $\frac{1}{4}$ and the $\frac{1}{10}\lambda$ substrates of a given material for films in the thickness range described here, but significant differences were found for soft glass as contrasted with Pyrex substrates.

Copper, nickel, and germanium were evaporated from tungsten helices or tungsten spiral baskets. Selenium was evaporated from a tantalum boat. In all cases the evaporations were completed in times of the order of 30 sec. This fast evaporation minimized film contamination and produced films smooth enough to exhibit pronounced x-ray interference structure. All the films

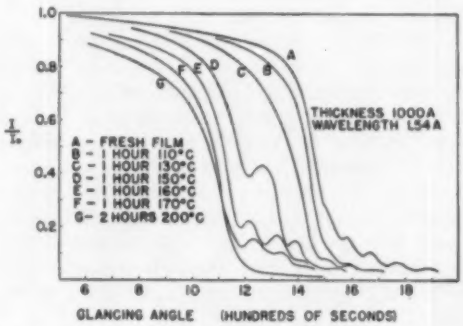

FIG. 3. Copper on Pyrex, oxidized in air in successive steps.

were exposed to the laboratory atmosphere during substrate transfer from the evaporator to the reflectometer, and some of the reflection curves were measured in air. The substrates used for the deposit of the copper and nickel films were cleaned by dissolving any previous metal film off in HNO_3, after which the flats were repeatedly rinsed in distilled water, acetone, and finally in isopropyl alcohol. Selenium residue yielded to concentrated H_2SO_4 and some scrubbing with a soft cloth under solvent. All the germanium films were put onto unused substrates or ones that had previously been coated with metal films and cleaned as described. Some changes were observed in the reflection curves of bare soft glass flats after the copper or selenium had been removed,[11] but the details of the interference patterns for films in the present thickness range are not sensitive to such a change in the substrate's reflectivity.

A new x-ray reflectometer was used to obtain most

[11] This aberration is also reported in the case of copper by Nancy J. Scott, footnote 7.

of the data presented here. A detailed description of this instrument will be presented in another paper. In this reflectometer the film subsrtate was held stationary in a temperature-controlled vacuum chamber, and the x-ray monochromator with its x-ray tube was pivoted about an axis in the face of the "mirror" to the required angle of incidence. The x-ray intensity was measured with a proportional counter system. Counting precision was $\pm 2\%$ at the full counting rate. An angular resolution of about ± 6 seconds of arc could be achieved with this instrument. The precision of the glancing angle was such that the standard derivation was less than 5 seconds of arc at any fixed temperature and the accuracy was within 10 seconds at a glancing angle of 2000 seconds. The angular displacement of the substrate holder, as the temperature of the vacuum chamber was raised from 20° to 420°C, was of the order of 10 seconds of arc after thermal equilibrium was reached. The width of the x-ray beam and the length of the substrates

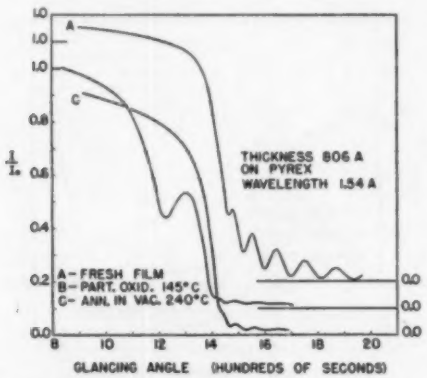

FIG. 4. Copper on Pyrex, partially oxidized in air and reduced in vacuum.

limited reliable measurements to glancing angles larger than 100 seconds of arc for the small substrates and about 60 seconds of arc for the large ones. The working pressure in the reflectometer vacuum chamber was about 10^{-6} mm Hg at 400°C and less than 2×10^{-7} mm at room temperature after bakeout. The x-ray monochromator was set to yield the 1.54 A Cu $K\alpha$ line for all the work discussed here.

All the vacuum annealing was done in the reflectometer vacuum chamber. The films to be oxidized were heated in air in a Fisher "Isotemp" laboratory oven or in a Hevi Duty type G-05-Pt furnace. No attempt was made to control the chemical composition of the atmosphere around the film during the oxidation. In an attempt to avoid the long thermal time lags which occurred in the vacuum reflectometer, some of the selenium films were annealed in an argon-filled Pyrex bottle heated in the laboratory oven.

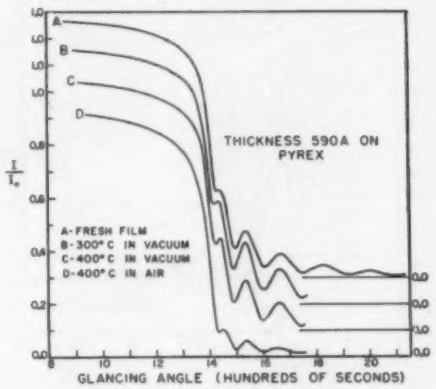

FIG. 5. Nickel on Pyrex, vacuum-annealed and then heated in air.

IV. RESULTS

Copper

The x-ray reflection study of the copper films can be separated into three phases. First, the effect of vacuum anneal is examined. Next, the effect of oxidation in air is considered. Finally, the vacuum anneal of partially oxidized copper films is investigated.

Reflection curves for a 746 A copper film deposited on Pyrex and vacuum-annealed are presented in Fig. 1, and the results for a 603 A film on soft glass are shown in Fig. 2. These curves are separated vertically to avoid confusion. In each case the initial increase in temperature resulted in an *increase* in the contrast in the x-ray interference pattern. As the temperature was increased beyond 200°C the x-ray fringe system was destroyed for the film on the soft glass substrate. The copper film deposited onto the Pyrex continued to support a strong x-ray interference pattern beyond a temperature of 350°C. No appreciable dimunition in the fringe contrast in this latter case was observed until several heating and cooling cycles were completed. The rapidity of these cycles was limited, by the thermal time lag in the

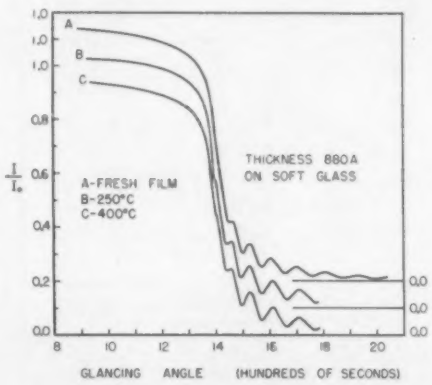

FIG. 6. Nickel on soft glass, vacuum-annealed.

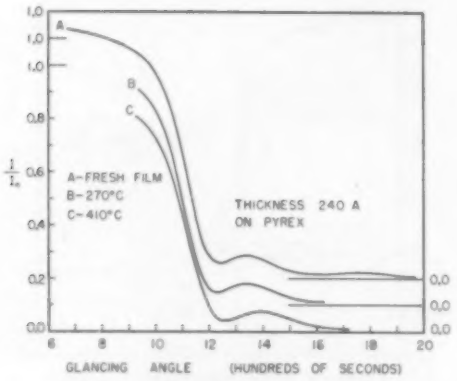

FIG. 7. Germanium on Pyrex, vacuum-annealed.

vacuum chamber, to between 6 and 8 hr/cycle. Ordinarily the condition of the film remained such that the reflection curves made at high temperature and after slow cooling were the same.

Figure 3 illustrates the effect of oxidation in air on the x-ray reflection from a 1000-A copper film deposited on a large Pyrex substrate. It can be seen that, as the oxidation proceeds, the nature of the x-ray interference pattern changes. The interference fringes were observable as long as the film, as viewed through the back of the substrate, was copper colored. When the oxidation proceeded to a point where the oxide reached or came very close to the substrate, as judged by the loss of the copper color, the x-ray interference pattern vanished. At this stage of oxidation the critical angle had diminished to approximately that expected for Cu_2O.

The last phase of the study of the copper films was the consideration of the effects of anneal in vacuum on partially oxidized films. Figure 4 presents the reflection coefficients of 806-A film of copper on Pyrex (a) for the fresh film, (b) for the partially oxidized film, and (c) for the film after vacuum anneal. It might be remarked that, although the partially oxidized film was a uniform

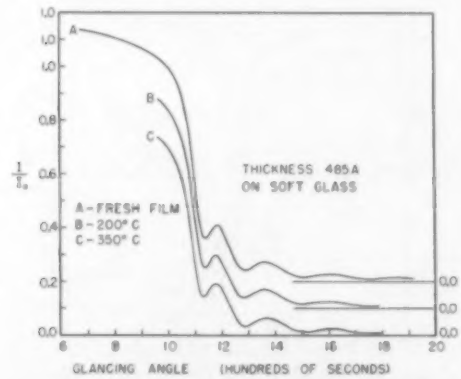

FIG. 8. Germanium on soft glass, vacuum-annealed.

blue color in reflected light, the fresh film before it was oxidized and the oxidized film after anneal showed the same bright copper mirror appearance. Even though the vacuum anneal restored the optical appearance of the film to its pre-oxidized state, the x-ray investigation showed an almost complete destruction of the x-ray fringes after anneal. It should be noted also that the anneal does not restore completely the position of the x-ray critical angle to its original value. Similar experiments with soft glass substrates yielded substantially the same results.

Nickel

The effects of vacuum anneal on nickel films are presented in Figs. 5 and 6. Figure 5 contains the reflection curve for 590 A of nickel on a Pyrex substrate, and Fig. 6 the results for a soft glass substrate with an 880-A film on it. In each case the initial temperature rise was accompanied by a modest increase in the contrast of the

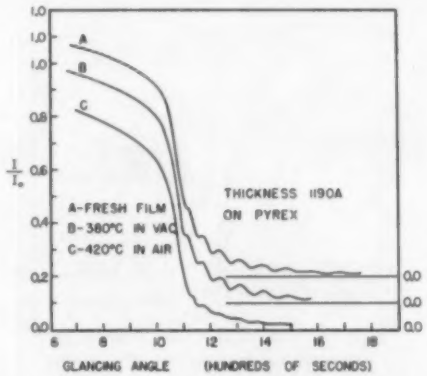

FIG. 9. Germanium on Pyrex, vacuum-annealed and then heated in air.

x-ray interference pattern. In each case the films continued to support a strong x-ray interference system to a temperature of about 400°C. The film on the Pyrex substrate showed a small decrease in fringe contrast at the higher temperatures. An attempt was made to oxidize the nickel film on the Pyrex substrate by heating in air. This procedure diminished but did not extinguish nor otherwise greatly change the structure of the interference pattern, although it must be noted that the interference fringes appear to be somewhat closer together.

Germanium

The reflection data for the germanium films are represented in Figs. 7, 8, and 9. Results for a 240-A film on Pyrex and 485-A film on soft glass appear in Figs. 7 and 8. In an attempt to find a thickness effect due to the annealing process, a 1190-A film on Pyrex was also examined; the reflection curve is shown in Fig. 9. For each of these films the reflection curve was not altered

very much by vacuum anneal up to a temperature of 400°C. The 240-A germanium film, when annealed to about 400°C, exhibited a small shift of the critical angle towards larger glancing angles. The 1190-A film was heated in air to a temperature of 200°C with no apparent effect on the reflection curve. The temperature of the air anneal was then brought up to 420°C, and the resulting partial suppression of the x-ray interference pattern is shown as a part of Fig. 9.

Selenium

It is known that selenium, vacuum-deposited onto a substrate held at room temperature, forms an amorphous film.[12] If the substrate is then heated to a temperature above about 60°C the selenium undergoes a phase transition from the amorphous to a crystalline form. Figure 10 presents the x-ray reflection data for a 500 A selenium film on a Pyrex substrate. A curve was taken first with the fresh film in its amorphous state and then after transition to the crystalline form by annealing in

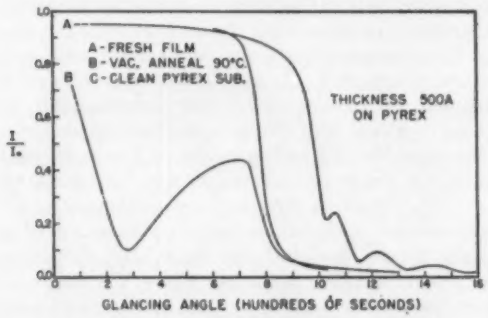

FIG. 10. Selenium on Pyrex, vacuum-annealed.

vacuum. The fresh selenium film (orange in color) exhibits the x-ray interference fringes characteristic of the fresh films of the other evaporated materials. The film, after vacuum anneal (slightly foggy looking and colorless), showed no x-ray interference fringes beyond the critical angle and exhibited a pronounced small-angle dip in the reflection curve. Essentially the same results were obtained for selenium deposited onto soft glass.

An attempt was made to examine the effects of the phase transition in its early stages; the change in phase took place, however, in less time than the 20 min that was required to measure the x-ray reflection characteristics. A separate anneal in an argon-filled bottle was done in an effort to "freeze in" intermediate changes. The crude techniques employed were not very successful, and refinement of the method was not undertaken. The only intermediate reflection curve obtained is presented in Fig. 11; however, the reflection coefficients had changed as much as 14% in the 20-min time it took to make these measurements.

[12] H. Friedmann, Z. Naturforsch. **11a**, 373 (1956).

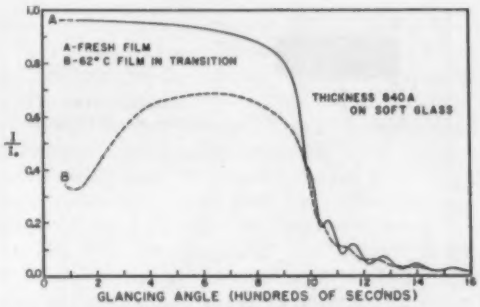

FIG. 11. Selenium on Pyrex, vacuum-annealed.

Synthetic Rough Films

X-ray reflection curves of the sort obtained for the annealed selenium films have been observed before for films of heat treated aluminum and for certain aged copper films.[13] To investigate the notion that such a reflection curve, having a pronounced small-angle minimum, might be characteristic of a grossly broken film on a smooth substrate, a few very rough films and surfaces were examined. Figure 12 contains the reflection curves for (a) a thick evaporated copper film, (b) a block of polycrystalline copper polished to a fair mirror finish, (c) a polished Pyrex glass surface, then (d) for the same Pyrex surface after grinding (but not polishing) with an abrasive. The rough surfaces show monotonically decreasing reflection coefficients with increasing glancing angles.

A thin layer formed by depositing candle soot and monodisperse polystyrene latex spheres onto smooth Pyrex substrates gave the reflection curves shown in Fig. 13.[14] The curves have a small-angle minimum. Also contained in Fig. 13 are reproductions of photographs made of the incident x-ray beam and of the beam reflected from the film of latex spheres on the Pyrex sub-

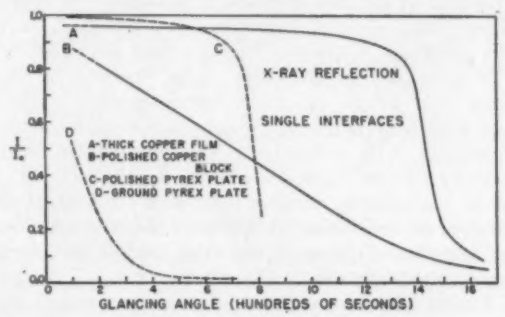

FIG. 12. Reflection curves for rough single surface of copper and of Pyrex.

[13] R. C. Duncan and L. G. Parratt, "A study of evaporated aluminum films by x-ray total reflection," Technical Rept. No. 13, August 21, 1958, Document Nos. AFOSR TN 58-680, ASTIA AD 162 212.

[14] The polystyrene latex was kindly furnished by Dr. J. W. Vanderhoff of the Dow Chemical Company.

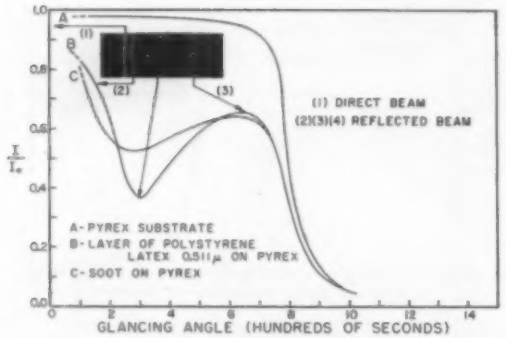

FIG. 13. Reflection curves for rough latex and soot films on smooth Pyrex. A photograph of the x-ray beams reflected from the latex-coated substrate.

strate at each of three different glancing angles. The reflected beam, at a small glancing angle, shows very little if any spread when compared to the incident beam, but the reflected beam does exhibit considerable spread at an angle corresponding to the reflection minimum and again at the larger-angle maximum. The beams reflected at any angle from a film exhibiting an x-ray interference pattern are not spread by the reflection.

V. DISCUSSION

All the vacuum-deposited films considered in this work showed several orders of x-ray interference fringes before the films were annealed or oxidized. Some of the films in the thickness range around 800 A showed well defined interference in orders as high as the 7th and 8th.[15] Use of the simple criterion for smoothness discussed in Sec. II would indicate that the random undulation of such films is of the order of 40 A. It is unsafe to push such an analysis too far since the details of the way in which the x-ray beam samples the rough surface are not unambiguously understood, and the areal distribution of the film thickness is not known in detail. There exist electron microscope studies which show the surfaces of evaporated films of copper and nickel.[16,17] For films of the thickness range explored in this work the nature of the vacuum-deposited surface is a sensitive function of the substrate surface and the conditions of the evaporation. The film surfaces examined by electron microscopy seem, for the most part, to be considerably rougher than 40 A although some samples do not appear to approach the 40 A criterion for smoothness. None of the films used in this work was examined by this technique.

During the early stages of the vacuum anneal the copper films, and to some extent the nickel ones, showed an increase in the contrast in the x-ray interference pattern. This may be interpreted to mean that the films have become "smoother." As the annealing temperature rose above 200°C the copper films on soft glass had their x-ray interference patterns destroyed. The nickel films and the copper films on Pyrex showed only a small inclination to a diminished interference pattern at the higher temperatures. The disappearance of the x-ray interference pattern for the copper film on the soft glass substrate at temperatures above 200°C might be explained by a failure of the film-substrate bond resulting in a fractured film whose roughened nature would no longer support an x-ray fringe system. Copper on Pyrex, and either nickel or germanium films on Pyrex or soft glass, seem to be relatively stable with respect to vacuum anneal at temperatures up to about 400°C. The thinnest germanium film (240 A) did show a small but significant shift in its critical angle towards larger glancing angles at the highest annealing temperatures. This shift indicates a small increase in the average density of the film.

When the copper films, deposited on Pyrex, were oxidized in air the x-ray interference patterns changed but nevertheless persisted until the oxide appeared to reach the film-substrate interface whereupon the interference pattern disappeared. The interference structures associated with the oxide-coated copper films resemble, but are not identical with, those theoretically predicted for a two-layer film of Cu_2O on copper on Pyrex. Figure 14 contains a theoretical reflection curve for such a system.[18] The details of the interference structure for partially oxidized films, i.e., the heights and spacings of the fringes, depend sensitively on the relative thicknesses and relative densities of the two layers. The theoretical curve presumes that the totally oxidized film is a smooth coherent layer giving rise to an additional single-layer interference pattern characteristic of the layer thickness and the oxide density. Disappearance of the interference pattern with complete oxidation of the copper film may again be associated with the conjecture that the copper oxide film has become rough.

Efforts to oxidize nickel and germanium films in air

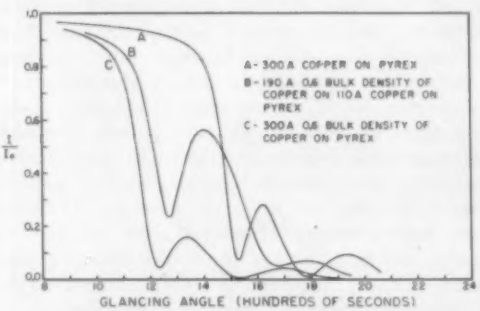
A
B
C
A-300 A COPPER ON PYREX
B-190 A 0.6 BULK DENSITY OF COPPER ON 110 A COPPER ON PYREX
C-300 A 0.6 BULK DENSITY OF COPPER ON PYREX
I/Io
GLANCING ANGLE (HUNDREDS OF SECONDS)

FIG. 14. Theoretical reflection curve for a double layer film.

[15] See photographs in reference footnotes 3 and 8.
[16] R. S. Sennett and G. D. Scott, J. Opt. Soc. Am. 40, 203 (1950).
[17] B. M. Siegel, "Studies on the morphology and structure of copper films deposited by vacuum evaporation," Technical Rept. No. 9, December 15, 1958, Document Nos. AFOSR TN 59-7, ASTIA AD 208 303.
[18] The curve was kindly furnished from some unpublished work of N. J. Scott and L. G. Parratt.

showed little evidence, in the form of the characteristic complex interference patterns, of the formation of a coherent oxide film whose thickness was an appreciable fraction of the original film thickness. It is estimated that, for an 800-A film, the coherent oxide layer must have a thickness at least as great as 15 A in order to change measurably the character of the interference pattern.[19] With both the nickel and germanium films, the contrast in the interference pattern was reduced as a consequence of the air anneal at a temperature between 200° and 400°C. Such anneal of these films also produced a contraction of the fringe spacing. This decrease of fringe spacing could be associated with a small increase in the film thickness due, perhaps, to the oxidation or to the absorption of other materials from the furnace atmosphere.

When a partially oxidized copper film, on either Pyrex or soft glass, was then vacuum annealed, the appearance of the film was restored to its original bright copper mirror finish. However, the x-ray reflection curve, although having the critical angle returned most of the way to its fresh-film value, had lost the interference fringe system characteristic of a smooth film. It appears that the vacuum anneal has reduced the oxide leaving the copper film in a roughened or spongy state. The roughening of copper surfaces by successive oxidations and hydrogen reductions has been reported by several investigators, and perhaps the vacuum reduction of the copper films produces analogous effects.[20] It is believed that no amount of anneal within the temperature and pressure ranges allowed by the present x-ray reflectometer would restore the reduced film to its original x-ray smoothness. A vacuum anneal whose duration was of the order of one week introduced no further changes in the vacuum reduced film. It has been reported that very small quantities of adsorbed gas would prevent films with very small crystallites from annealing to form larger crystals in the film.[21] The vacuum system in the present instrument is not good enough to prevent the adsorption of a small amount of gas even if the films were not exposed to air in the transfer process. Such adsorbed gas may account for the "frozen" characteristics of the roughened films.

The vacuum deposit of selenium produced an amorphous film which was "smooth" to x-ray reflection. Vacuum anneal at temperatures sufficiently high to induce a phase transition to the crystalline form was associated with a destruction of the x-ray interference pattern beyond the critical angle and the introduction of a broad minimum into the reflection curve at glancing angles between 100 and 300 seconds of arc. It has been noted that similar curves have been obtained for heat treated aluminum films.[13] This small-angle minimum in the reflection curve may be associated with a gross breakup of the film in the manner outlined in Sec. II.

The results of the measurements on the rough surfaces and coatings, in the absence of any more complete theory, seem to lend some credance to the speculations of Sec. II. These speculations included a prediction that the reflected beam from a very rough (badly broken up) surface would have an angular spread in it due to small-angle scattering. It has already been noted that such a spread is observed with the synthetic "rough films" (see Fig. 13). The magnitude of this observed spread for the polystyrene spheres is in approximate agreement with the small-angle scattering observed in other experiments[22,23] in which are reported the effect of the angular spread on the apparent absorption coefficients. Note, however, that absorbing foils of copper or of silver showed a much smaller angular spread in the transmitted beam than did absorbing layers of graphite or polystyrene; these results might lead one to expect a smaller spread in the reflected beam for the "broken-up" copper or selenium films than is observed with the "films" of polystyrene latex.

The series of experiments described here were undertaken in order to explore the possibility that anneal and oxidation processes in thin films could be studied by x-ray reflection techniques. It was found that the method is useful in making relative measurements of film "smoothness," in observing the formation and reduction of coherent oxide layers, in observing the stability of various films to heat treatment, and in observing the gross breakup of thin films. It might be expected that, as the physical analysis of ultra-small-angle scattering and reflection from rough surfaces is better developed, even more detailed information about the structure of thin films would be derivable from x-ray reflection curves.

In addition to further analytical work, it is recommended (1) that a cryostat be incorporated in the x-ray reflectometer to allow temperatures well below room temperature, (2) that the lowest attainable ambient pressure be reduced to less than 10^{-9} mm Hg, and (3) that all future films be evaporated in position in the reflectometer vacuum chamber. Then, with these improvements, the x-ray total reflection method promises to be a powerful tool in the investigation of the dynamic behavior of thin films over a wide range of temperature and pressure.

VI. ACKNOWLEDGMENTS

The authors take this opportunity to thank R. Sviedrys and M. W. Hane for their aid in assembling the data and in producing the films, and Miss Nancy J. Scott and Dr. Richard Deslattes for many helpful discussions during the course of the work.

[19] See work cited in reference footnote 7.

[20] W. E. Garner, T. J. Gray, and F. S. Stone, Proc. Roy. Soc. (London) **A197**, 294 (1949).

[21] H. D. Keith, Proc. Phys. Soc. (London) **B69**, Pt. 2, 180 (1956).

[22] L. G. Parratt, J. O. Porteus, H. W. Schnopper, and T. Watanabe, Rev. Sci. Instr. **30**, 344 (1959).

[23] L. G. Parratt, J. O. Porteus, H. W. Schnopper, and T. Watanabe, "Ultra-small-angle x-ray scattering," Technical Rept. No. 2, December 20, 1958, Document Nos. AFOSR TN-58-781 and ASTIA AD 202 002.

Phase Oscillations in High Current Synchrotrons

IRVIN G. HENRY
Hughes Aircraft Company, Culver City, California
(Received March 22, 1960; and in final form May 9, 1960)

The theory of phase oscillations in the synchrotron, first given by Bohm and Foldy, is extended to cover the case where the amplitude of the accelerating voltage is not constant and where the accelerated bunch is itself sufficiently large to produce an appreciable part of the accelerating voltage. It is found that the phase oscillation is more stable when the driving frequency is less than the natural frequency of the accelerating electrode system, and that the plate characteristic of the driving amplifier has a negligible effect on the phase stability.

INTRODUCTION

BOHM and Foldy[1] and Sands[2] showed that a particle traveling with nearly the velocity of light in a synchrotron, whose magnetic field varies as r^{-n}, has the equation of phase oscillation

$$\ddot{y}+k\omega_0\lambda^{-2}(1-n)^{-1}E_0^{-1}(\Delta\dot{E})+E_0^{-1}\dot{E}_0\dot{y}=0. \quad (1)$$

Here y is $\phi-\phi_0$, the deviation from equilibrium of the phase of the particle with respect to the accelerator, k is the harmonic integer of the accelerator, λ is $(2\pi r_0+L)/2\pi r_0$, L is the length of the straight sections, E_0 is the equilibrium energy of the particle, ΔE is the deviation of the energy from equilibrium, and ω_0 is the equilibrium angular velocity in the curved sections, that is $\omega_0=c/r_0$. In the electron synchrotron, or in the proton synchrotron at extreme energy, the bunch traverses the accelerating gap after the peak voltage has passed. The phase is said to be zero if the accelerating voltage is zero at the transit time, it is $\pi/2$ if the accelerating voltage is a maximum at the transit time, that is to say an earlier bunch has a larger phase. Bohm and Foldy and Sands also showed that

$$\Delta\dot{E}=P_{a0}\cot\phi_0\cdot y+(\lambda^2\dot{y}/k\omega_0)(3-4n)P_{\gamma 0}, \quad (2)$$

where P_{a0} is the power imparted to an equilibrium particle by the accelerating electrode and $P_{\gamma 0}$ is the electromagnetic power radiated by an equilibrium particle. One can substitute (2) into (1) to obtain

$$\ddot{y}+[(\dot{E}_0/E_0)+(3-4n/1-n)(P_{\gamma 0}/E_0)]\dot{y} +k\lambda^{-2}(1-n)^{-1}(P_{a0}/E_0)\omega_0\cot\phi_0\cdot y=0. \quad (3)$$

ϕ_0 is determined by the equilibrium power balance

$$(\omega_0/2\pi\lambda)eV\sin\phi_0=P_{a0}=P_{\gamma 0}+\dot{E}_0-P_{\beta 0}, \quad (4)$$

where $P_{\beta 0}$ is the power received by an equilibrium particle from the azimuthal electric field associated with the increasing magnetic field, V is the amplitude of the accelerator voltage, and $\omega_0/2\pi\lambda$ is, of course, the equilibrium rotational frequency.

Our approach will be to introduce additional terms into (1) and (4), which will take into account the voltage induced in the accelerator by the particle bunch. We will also allow the frequency at which the accelerating electrode is driven, $k\omega_0/2\pi\lambda$, to be different from its natural frequency of oscillation, and we will allow the charge delivered by the amplifier to the accelerating electrode to depend on the voltage instantaneously present on the electrode (and hence on the plate of the amplifier). Then we will find the analog of Eqs. (2) and (3).

PHYSICAL ASSUMPTIONS

We will assume that (a) the radio-frequency accelerating electrode has a natural frequency ω_c; (b) it is charged at constant intervals of time $2\pi\lambda/k\omega_0$; $k\omega_0/\lambda$ does not quite coincide with ω_c; $\omega_c=(k/\lambda)(\omega_0+\epsilon)$; in practice ϵ might vary in the range $\pm a$, where a is the damping constant of the electrode system; (c) the bunches are small enough for the electrode voltage not to change by a large fraction during the transit; (d) the driving charge σ delivered by the amplifier to the electrode depends on the voltage W on the electrode; the variation of driving charge will be written $\sigma-\sigma_0=\sigma_0\xi=K(W-W_0)$; (e) the k bunches have total charge Q and, except where otherwise stated, all bunches have the same phase ϕ with respect to the electrode.

ACCELERATOR VOLTAGE

The accelerating electrode voltage arises from two sources. If at time u the amplifier places a charge σ on the accelerator cavity, it excites a voltage at time t of magnitude $(\sigma/C)\epsilon^{-a(t-u)}\cos\omega_c(t-u)$; here C is the accelerator capacity. Also if at time u a bunch of charge Q traverses the electrode gap, it excites a voltage $-(Q/C)\epsilon^{-a(t-u)}\cos\omega_c(t-u)$, where the minus sign denotes the fact that the voltage tends to oppose the passage of the bunch. $W(t)$ is found by summing over all previous passages of the bunches and over all previous driving charges. Since the power dissipated in the accelerator has to be reasonably small, the damping constant a is usually about $10^{-3}\ \omega_c$ or less. Consequently many thousands of waves contribute strongly to W, and the sum of the waves can be accurately represented by an integral.

We distinguish between transit times u_{tr}, t_{tr} and charging times u_{ch}, t_{ch}. We will adopt the convention

[1] D. Bohm and L. Foldy, Phys. Rev. **70**, 249 (1946).
[2] M. Sands, Phys. Rev. **97**, 470 (1955).

that the phase is $+\pi/2$ if the beam transits at a charging time. When $Q=0$ and $\epsilon=0$, this is consistent with the convention of Bohm and Foldy, since the voltage maximum would then coincide with the charging times. Then, if we denote any integer by ν, the following relations hold

$$(k\omega_0/\lambda)(t_{ch}-u_{ch})=2\pi\nu \tag{5a}$$

$$(k\omega_0/\lambda)(t_{tr}-u_{ch})=2\pi\nu+[(\pi/2)-\phi(t)] \tag{5b}$$

$$(k\omega_0/\lambda)(t_{ch}-u_{tr})=2\pi\nu-[(\pi/2)-\phi(u)] \tag{5c}$$

$$(k\omega_0/\lambda)(t_{tr}-u_{tr})=2\pi\nu-[(\pi/2)-\phi(u)]+[(\pi/2)-\phi(t)]. \tag{5d}$$

Since the phase oscillates at a frequency much less than the orbital frequency, ϕ changes but little in a fraction of a turn; consequently one need not distinguish between $\phi(t_{ch})$ and $\phi(t_{tr})$ when t_{tr} and t_{ch} occur in the same turn. A similar remark can be made for u_{tr} and u_{ch}. Thus

$$W(t_{ch})=[k(\omega_0+\epsilon)/2\pi\lambda]\int_{-\infty}^{t}\epsilon^{-\alpha(t-u)}\times[\{\sigma(u)/C\}\cos\{(k\epsilon/\lambda)(t-u)\}+\{Q/kC\}\sin\{(k\epsilon/\lambda)(t-u)+\phi(u)\}]du \tag{6a}$$

$$W(t_{tr})=[k(\omega_0+\epsilon)/2\pi\lambda]\int_{-\infty}^{t}\epsilon^{-\alpha(t-u)}\times[\{\sigma(u)/C\}\sin\{\phi(t)-(k\epsilon/\lambda)(t-u)\}+\{Q/kC\}\cos\{(k\epsilon/\lambda)(t-u)+\phi(u)-\phi(t)\}]du. \tag{6b}$$

Using an obvious notation, we can rewrite these equations

$$W(t_{ch})=W_\sigma(t_{ch})+W_Q(t_{ch})$$
$$W(t_{tr})=W_\sigma(t_{tr})+W_Q(t_{tr}).$$

Note that in computing W_σ we had to use u_{ch} and therefore had to substitute from (5a) and (5b), while in computing W_Q we had to use u_{tr} and therefore had to substitute from (5c) and (5d). The factor before the integral signs occurs simply because the pulses came at mean intervals of time $2\pi\lambda/k(\omega_0+\epsilon)$. Henceforth ϵ will be neglected compared with ω_0 in this factor.

EQUATIONS OF PHASE OSCILLATION

An electron of charge q crossing the accelerator at time t_{tr} receives energy $qW(t_{tr})$, and, averaging this around the turn, one could say that it receives power $[c/(2\pi r+L)]q[W_\sigma(t_{tr})+W_Q(t_{tr})]$. We will define $P_\alpha=[c/(2\pi r+L)]qW_\sigma(t_{tr})$ and $P_r=[c/(2\pi r+L)]qW_Q(t_{tr})$.

It then follows that

$$P_r=[cq/(2\pi r+L)]\int_{-\infty}^{t}(Q/kC)\epsilon^{-\alpha(t-u)}\times\cos[\phi(t)-\phi(u)-(k\epsilon/\lambda)(t-u)](\omega_c/2\pi)du \tag{7a}$$

$$P_\alpha=[cq/(2\pi r+L)]\int_{-\infty}^{t}\{\sigma(u)/C\}\epsilon^{-\alpha(t-u)}\times\sin[\phi(t)-(k\epsilon/\lambda)(t-u)](\omega_c/2\pi)du. \tag{7b}$$

$P_{\alpha 0}$ and P_{r0} are obtained by setting $\phi(t)=\phi(u)=\phi_0$, $\sigma(u)=\sigma_0$ in the right members. ΔP_r and ΔP_α are obtained by differentiating the right members with respect to σ, r, and ϕ, and evaluating the resulting expressions with $\phi=\phi_0$, $r=r_0$, and $\sigma=\sigma_0$. The result is

$$\frac{\Delta P_r}{P_{r0}}=-\frac{\Delta r}{\lambda r_0}+\frac{a^2+\theta^2}{a}\int_{-\infty}^{t}\epsilon^{-\alpha(t-u)}\sin\theta(t-u)\cdot\{y(t)-y(u)\}du \tag{8a}$$

$$\frac{\Delta P_\alpha}{P_{\alpha 0}}=-\frac{\Delta r}{\lambda r_0}+\frac{a^2+\theta^2}{a\sin\phi_0-\theta\cos\phi_0}\left[\int_{-\infty}^{t}z(u)\epsilon^{-\alpha(t-u)}\times\{\sin\phi_0\cos\theta(t-u)-\cos\phi_0\sin\theta(t-u)\}du+\frac{a\cos\phi_0+\theta\sin\phi_0}{a^2+\theta^2}y(t)\right], \tag{8b}$$

where $\theta=k\epsilon/\lambda$. In addition Sands[2] gives us

$$\Delta r/r_0=-\lambda^2\dot{y}/k\omega_0,$$
$$\Delta P_\beta/P_{\beta 0}=[1-(P_{\beta 0}/\dot{E}_0)](\lambda\dot{y}/k\omega_0), \tag{9}$$
$$\Delta P_\gamma/P_{\gamma 0}=-(3-4n-\lambda^{-1})(\lambda^2\dot{y}/k\omega_0).$$

Since

$$\dot{E}=P_\alpha+P_\beta-P_\gamma-P_r, \tag{10a}$$

we have

$$\dot{E}_0=P_{\alpha 0}+P_{\beta 0}-P_{\gamma 0}-P_{r0}, \tag{10b}$$

which is the analog of (4), and also

$$\Delta\dot{E}=\Delta P_\alpha+\Delta P_\beta-\Delta P_\gamma-\Delta P_r. \tag{10c}$$

The equilibrium power Eq. (10b) is illustrated in Fig. 1, which also shows the equilibrium phase of electron passage. We substitute (8a), (8b), and (9) into (10c) and we then eliminate $\dot{E}_0$ by using (10b). Inserting the resulting expression into (1) yields

$$\ddot{y}(t)+R\dot{y}(t)+X^2y(t)-L\int_{-\infty}^{t}\epsilon^{-\alpha(t-u)}[y(t)-y(u)]\sin[\theta(t-u)]du+M\int_{-\infty}^{t}z(u)\epsilon^{-\alpha(t-u)}[\sin\phi_0\cos\theta(t-u)-\cos\phi_0\sin\theta(t-u)]du=0, \tag{11}$$

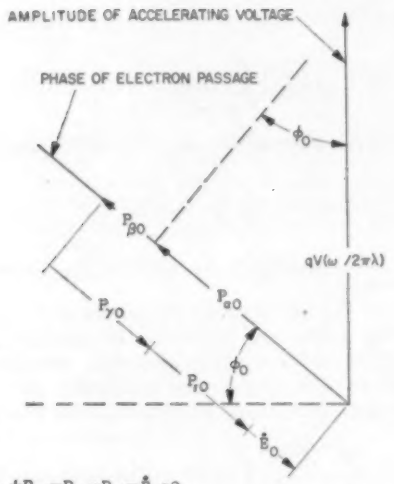

FIG. 1. Stationary phase and power relationships. (*Note.*—In the figure, ω should be given as ω_c.)

where

$$R=(3-4n/1-n)(P_{\gamma 0}/E_0)+(\dot{E}_0/E_0)$$

$$X^2=\frac{k}{\lambda^2(1-n)}\,\frac{a\cos\phi_0+\theta\sin\phi_0}{a\sin\phi_0-\theta\cos\phi_0}\,\frac{P_{a0}}{\omega_0 E_0}$$

$$=\frac{k^2}{(2\pi)^2\lambda^4(1-n)}\,\frac{a\cos\phi_0+\theta\sin\phi_0}{a\sin\phi_0-\theta\cos\phi_0}\sin\phi_0\,\frac{a}{a^2+\theta^2}\,\omega_0^3\frac{q\sigma_0}{CE_0}$$

$$L=\frac{k}{\lambda^2(1-n)}\,\frac{a^2+\theta^2}{a}\,\frac{P_{r0}}{\omega_0 E_0}=\frac{k}{(2\pi)^2\lambda^4(1-n)}\,\omega_0^3\frac{qQ}{CE_0}$$

$$M=\frac{k}{\lambda^2(1-n)}\,\frac{a^2+\theta^2}{a\sin\phi_0-\theta\cos\phi_0}\,\frac{P_{a0}}{\omega_0 E_0}$$

$$=\frac{k^2}{(2\pi)^2\lambda^4(1-n)}\,\frac{a\sin\phi_0}{a\sin\phi_0-\theta\cos\phi_0}\,\omega_0^3\frac{q\sigma_0}{CE_0}$$

$$P=(1/2\pi)(K/C)\omega_c\cong(1/2\pi)(k/\lambda)(K/C)\omega_0$$

$$H=(1/2\pi)(K/C)(Q/k\sigma_0)\omega_c$$

$$\cong(1/2\pi)(K/C)(Q/\sigma_0)\omega_0. \quad (12)$$

Note that the first three terms in (11) give the phase equation of Bohm and Foldy; i.e., if the accelerated charge Q is very small and if the driving charge is independent of the accelerator voltage so that M is zero, then we obtain their result.

In addition to Eq. (11) we have the relation governing the deviation of driving charge

$$\sigma_0 z(t)=K\Delta W(t_{ch}). \quad (13)$$

The right member of (13) is formed by differentiating (6a) with respect to σ and ϕ. This yields

$$z(t)=P\int_{-\infty}^{t}z(u)e^{-a(t-u)}\cos\theta(t-u)du$$

$$-H\int_{-\infty}^{t}y(u)e^{-a(t-u)}[\cos\phi_0\cos\theta(t-u)$$

$$+\sin\phi_0\sin\theta(t-u)]du. \quad (14)$$

By differentiating Eqs. (11) and (14) twice with respect to t, and noting that the integrals recur, one can produce purely differential equations.

$$\dddot{y}+(R+2a)\ddot{y}+\left(X^2-L\frac{\theta}{\theta^2+a^2}+2aR+a^2+\theta^2\right)\dot{y}$$

$$+\left(2aX^2+a^2R-2L\frac{\theta a}{\theta^2+a^2}+\theta^2R\right)\dot{y}+(a^2X^2+\theta^2X^2)y$$

$$+M\sin\phi_0\dot{z}+M(a\sin\phi_0-\theta\cos\phi_0)z=0 \quad \cdots, \quad (15a)$$

$$\ddot{z}+(2a-P)\dot{z}+(a^2+\theta^2-aP)z+H\cos\phi_0\dot{y}$$

$$+H(a\cos\phi_0+\theta\sin\phi_0)y=0 \quad \cdots. \quad (15b)$$

STABILITY

Note in Eqs. (15a) and (15b) that R, X^2, L, P, and H are all positive, while the sign of M depends on the sign and magnitude of θ and hence of ϵ. Also R and X^2 appear in the equation of Bohm and Foldy; P and H are zero unless the driving charge can vary with the instantaneous voltage at the charging time; M appears only in z terms, and z is zero unless the driving charge can vary; L appears if the accelerated charge Q is comparable with the driving charge per turn $k\sigma_0$. Remember, too, that these constants are not quite constant; they change by only a small fraction during one phase oscillation, but some of them change by several orders of magnitude during the complete acceleration period.

Numerical values typical of modern electron synchrotrons such as the Caltech synchrotron are maximum energy about 1.1 Bev, $X\sim 10^6$, $R\sim 10^4\rightarrow 10^1$, a and $\theta\sim 10^4$, L and $M\sim 10^{18}$ at injection and 10^{15} at 1.1 Bev (this assumes $Q\sim k\sigma_0\sim 10^{10}$ electrons), P and H depend on K which is a tube "constant." Now K is by definition $\partial\sigma/\partial W(t_{ch})$. $\partial\sigma/\partial W(t_{ch})$ is of order σ_0/W_0, perhaps three or four times as great since the amplifier has a triode characteristic. But σ_0/W_0 is Ca/ω_c. Thus $(K/C)\omega_c$ is $\sim 10^5$ and, since $Q\sim k\sigma_0$ or less, P and H must be

$\sim 10^6$ or less. It should be pointed out that X, R, a, θ, H, and P were given in units of sec^{-1}, while M and L were given in units of sec^{-3}.

Assuming that y and z vary closely as e^{iXt}, we find from (15b), after discarding very small terms,

$$\dot{z} \cong iXz = Ey.$$

Substituting into (15a), and using $\dot{y} \cong -\dddot{y}/X^2$ give

$$\dddot{y}+\left[R-\frac{a^2R}{X^2}+\frac{2L}{X^2}\frac{a}{a^2+\theta^2}-\frac{\theta^2R}{X^2}+\frac{HM(a\sin\phi_0-\theta\cos\phi_0)}{X^4}\cos\phi_0\right]\ddot{y}$$

$$+\left[X^2-L\frac{\theta}{\theta^2+a^2}+2aR-\frac{HM}{X^2}\sin\phi_0\cos\phi_0\right]\dot{y}=0. \tag{16}$$

Discarding negligible terms, the following equation is finally obtained.

$$\ddot{y}+\left[R+\frac{2L}{X^2}\frac{\theta a}{\theta^2+a^2}\right]\dot{y}+X^2\left[1-\frac{L}{X^2}\frac{\theta}{\theta^2+a^2}\right]y=0. \tag{17}$$

Note that in the last step K, which is contained in H and P, has entirely disappeared, removing the dependence on the plate characteristic K.

Consider first the coefficient of $\dot{y}$. It must be positive for stability. R is about 10^8 at injection, diminishes with the increase of E_0, reaches a minimum of about 20 when E_0 is 325 Mev, and increases with the radiated power $P_{\gamma 0}$ to about 450 when E_0 is 1.1 Bev. But $2L/X^2$ is about 10^5 at injection, about $10^{4.5}$ when E_0 is 325 Mev, and about 10^4 when E_0 is 1.1 Bev. $2L/X^2$ is so much greater than R, particularly midway through the acceleration period, that θ must be positive for stability. But θ is $k\epsilon/\lambda$; therefore ϵ is positive and the driving frequency ω_c is greater than the electrode frequency $k\omega_0/\lambda$. One should remember that L is proportional to the accelerated charge Q, while X^2 is proportional to the driving charge $k\sigma_0$. Thus if Q is reduced by a factor of about 10^4, the condition on θ is removed.

Next consider the coefficient of y. It is helpful to write it in terms of the fundamental machine constants.

$$\frac{L}{X^2}\frac{\theta}{\theta^2+a^2}=\frac{1}{\sin\phi_0}\frac{Q}{k\sigma_0}\frac{x(\sin\phi_0-x\cos\phi_0)}{\cos\phi_0+x\sin\phi_0},$$

where $x=\theta/a=k\epsilon/\lambda a$. It was already seen that θ and, therefore, x cannot be negative. But if θ is too positive, perhaps the coefficient of y will approach zero or change sign, thus invalidating the original assumption that y and z vary as e^{iXt}. Closer examination will show that this cannot occur. $1/\sin\phi_0$ can hardly be greater than 4 or 5; $Q/k\sigma_0$ is at most somewhat less than 1. Examine numerically $x(\sin\phi_0-x\cos\phi_0)/(\cos\phi_0+x\sin\phi_0)$, bearing in mind that x is unlikely to be as great as 1. If $\phi_0=30°$, the maximum of the function occurs when x is 0.3 and has a value of 0.071; if ϕ_0 is 45°, the maximum occurs when x is 0.4 and has a value 0.17. Therefore the coefficient of y remains positive.

OTHER MODES OF OSCILLATION

In the foregoing treatment all bunches were assumed to oscillate with the same phase. If one examines two equal bunches of charge $Q/2$ oscillating with opposite phase, $y_2=-y_1$, certain small differences appear. The voltage amplitude of the accelerating electrode must be constant, hence z must be zero. The analog of Eq. (11) is then

$$\ddot{y}_1+R\dot{y}_1+X^2y_1-(L/2)$$

$$\times\int_{-\infty}^{t}\epsilon^{-a(t-u)}\sin[\theta(t-u)]2y_1(t)du=0$$

and the analog of (17) is

$$\ddot{y}_1+R\dot{y}_1+\left[X^2-L\frac{\theta}{\theta^2+a^2}\right]y_1=0.$$

So with any appreciable (positive) ϵ the damping constant is evidently much smaller when the two bunches oscillate with opposed phase than when they oscillate with parallel phase. Several modes of oscillation are shown in Fig. 2, where the elongation and contraction of each bunch is depicted by showing two half-bunches. Naturally the theory we have presented does not distinguish between modes B, C, and D. But we have shown that the damping of A is stronger than the damping of B, C and D by the factor $L\theta/(\theta^2+a^2)$.

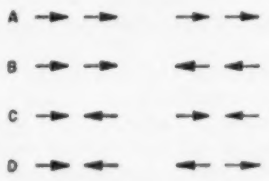

FIG. 2. Modes of phase oscillation.

In one accelerator two ripples were shown with an electric probe, at twice-phase-oscillation frequency and with parallel phase. Each ripple was made by one bunch. Since the ripples were about twice the phase oscillation frequency, they were almost certainly caused by expansion and contraction of each bunch. For

instance, with a bunch composed of only two electrons, the probe would be unable to distinguish which electron was which, so that, if each electron performed phase oscillations at frequency X, the contractions would follow one another at frequency $2X$. Thus mode C was apparently the one observed. Modes A and B were apparently not observed, perhaps because they are not excited in the injection and capture process. Mode C may be preferred to mode D because of nonlinearities not retained in the preceding analysis. One can conclude only that the observations were not in contradiction with the linear theory.

LIMIT OF STABLE OSCILLATION

Now Eq. (10c) will be substituted into Eq. (1). All $\dot{y}$ (damping) terms will be omitted because they are in any case small, but the nonlinear y terms will be retained. Thus the behavior will be that of an energy-conserving anharmonic oscillator. Since the variation of σ has been shown to have only a small effect, we will take $\sigma=\sigma_0$. P_β is always negligible compared with P_α so it will be left out. Then (1) becomes

$$\ddot{\phi}+k\omega_0\lambda^{-2}(1-n)^{-1}E_0^{-1}\Delta\dot{E}=0$$

and (10c) becomes

$$\Delta\dot{E}=\Delta P_\alpha-\Delta P_\gamma-\Delta P_r.$$

Consulting Eqs. (9), one finds that ΔP_γ contributes only $\dot{y}$ terms so it will be dropped. Furthermore, in forming ΔP_α and ΔP_r, one may take $r=r_0$, because the variation in r can lead only to $\dot{y}$ terms. This leaves only

$$\ddot{\phi}+k\omega_0\lambda^{-2}(1-n)^{-1}E_0^{-1}(\Delta P_\alpha-\Delta P_r)=0, \qquad (18)$$

where

$$\Delta P_\alpha=(cq/2\pi r_0+L)(\sigma_0/C)\int_{-\infty}^{t}e^{-a(t-u)}\times[\sin\{\phi(t)-\theta(t-u)\}-\sin\{\phi_0-\theta(t-u)\}]\times(k\omega_0/2\pi\lambda)du$$

$$=(cq/2\pi r_0+L)(\sigma_0/C)(k\omega_0/2\pi\lambda)(\theta^2+a^2)^{-1}\times[a\{\sin\phi(t)-\sin\phi_0\}-\theta\{\cos\phi(t)-\cos\phi_0\}]$$

$$=(cq/2\pi r_0+L)(\sigma_0/C)(k\omega_0/2\pi\lambda)(\theta^2+a^2)^{-\frac{1}{2}}\times[\sin\{\phi(t)-\alpha\}-\sin\{\phi_0-\alpha\}],$$

where α is arctan (θ/a). If $P_r=P_{r0}=0$, and if $\phi-\alpha=\tau$, we have an equation of the form

$$\ddot{\tau}+\Omega^2(\sin\tau-\sin\tau_0)=0.$$

E. M. McMillan has pointed out that this is simply the equation of a pendulum acting under gravity and under an additional constant torque which moves its stable point from $\tau=0$ to $\tau=\tau_0$. Hence by inspection the limit of stable oscillation is $\pi-\tau_0$, because at this angle the gravitational restoring torque is the same as at τ_0 and it just balances the additional constant torque. Hence if the pendulum does not quite reach the angle $\pi-\tau_0$ it will return, but if it passes $\pi-\tau_0$ it will go into accelerated circular motion without possibility of return. So $\phi=\phi_1=\pi-\phi_0+2\alpha$ is the limit of stable oscillation of the bunch. If Q is comparable with σ_0, P_r can no longer be considered negligible compared with P_α. But since we are taking $\phi(t)=\phi(u)=\phi_1$, it follows that $\Delta P_r=P_r-P_{r0}=0$, as we readily verify by examining equation (7a). Thus the limit of stable oscillation is still $\pi-\phi_0+2\alpha$. However one must remember that the numerical value of ϕ_0 still depends on the magnitude of P_{r0}.

CONCLUSIONS

With a large bunch the accelerator must be driven at a frequency slightly less than its natural frequency. The evidence on the modes with several bunches is inconclusive. The plate characteristic of the amplifier has apparently slight effect. Instability through feedback from the bunch to the radio frequency equipment cannot be caused by a normal amplifier characteristic.

Current Noise due to Ohmic Contacts on Cadmium Sulfide*

JAMES J. BROPHY AND ROBERT J. ROBINSON
Physics Division, Armour Research Foundation, Chicago 16, Illinois

(Received February 4, 1960)

Current noise measurements on the same lightly doped cadmium sulfide crystal having indium soldered contacts of different quality are used to demonstrate the strong influence of contacts on the observed noise spectra. The results suggest the presence of shallow trapping states distributed in energy and located near the electrodes. The concentration of these states depends on the quality of the contact. These effects are not contact noise in the usual sense since the shape of the noise spectra is only moderately affected; however, the noise level may change by orders of magnitude.

ELECTRICAL current noise having a $1/f$ power density spectrum is quite generally associated with metal-semiconductor contacts.[1] In fact, the quality of a contact may be experimentally assessed in terms of the magnitude of the observed $1/f$ noise component. In the case of cadmium sulfide, indium electrodes are reported to be ohmic and low noise.[2] However, we have obtained evidence that ohmic contacts to cadmium sulfide may drastically influence the observed current noise in this material even though contact noise, as such, is not present.

In a previous paper[3] we have shown how the current noise spectra of illuminated cadmium sulfide single crystals may be qualitatively understood in terms of electronic transitions between the conduction band and trapped holes together with multiple trapping transitions between the conduction band and shallow traps. At low frequencies the noise current density, S_i, is given by

$$S_i = (4i^2\tau_0/n_0V)\langle\Delta n^2\rangle/n_0, \qquad (1)$$

where i is the dc current, τ_0 is the photoconductive decay constant, n_0 is the conduction band carrier density, V is the crystal volume, and $\langle\Delta n^2\rangle$ is the variance of the conduction electron density. Multiple trapping causes fluctuations in carrier density which are observed as current noise and which may be interpreted using Eq. (1) in terms of the magnitude of $\langle\Delta n^2\rangle/n_0$. This quantity may range from unity to greater than 10^3, depending on the particular crystal and the conditions of measurements.

The noise spectra are of the form $\tau_0/(1+\omega^2\tau_0^2)$ at low frequencies. At high frequencies (for most crystals, >1000 cps) trapping noise dominates and the curves may either show a second relaxation spectra with a time constant characteristic of trapping at a discrete level, or $1/f$ noise due to a distribution of trap levels in energy.[3] Both behaviors may be observed in the same crystal by varying the illumination intensity since the discrete levels are most effective when the quasi-fermi level is near their energy depth.

In the present experiments, a lightly CuCl doped single crystal, 2.4 mm$\times$2.5 mm$\times$0.4 mm, was provided with soldered indium electrodes and illuminated with 5200 A radiation from a tungsten ribbon filament lamp and an interference filter. Noise voltages were observed across a 1.25×10^4 ohm wire-wound load resistor using a standard tunable amplifier-voltmeter system. A single 1.35 v mercury cell in series with the crystal and load resistor supplied the current.

Two current noise spectra initially observed for this crystal at photocurrents of 32 and 6 μa are shown as curve A in Figs. 1 and 2, respectively. The spectrum in Fig. 1 shows a low frequency turnover below 10 cps corresponding to the relaxation time associated with τ_0 and f^{-2} behavior throughout the rest of the frequency range. That of Fig. 2 shows similar low-frequency behavior together with a relaxation frequency of 1300 cps associated with trapping. The position of the quasi-fermi level in the two cases is calculated to be 0.34 and 0.41 v below the conduction band, respectively. The two spectra suggest that there was discrete trap state 0.41 v below the conduction band and that the density of other states, at least those near 0.34 v is so small as to be unobservable in the spectra. The magnitude and shape of these spectra were well reproducible in several experimental runs.

To pursue other studies it became necessary to remove this crystal from the sample holder. This was done without intentionally disturbing the electrodes. However, upon reinsertion, the spectra marked B in the figures were obtained under the identical experimental conditions as previously employed. The noise level of curve B in Fig. 1 is nearly two orders of magnitude greater than that of A, yet the low frequency relaxation shape is preserved. However, beyond 1000 cps trapping noise with a $1/f$ trend appears. Similarly in curve B of Fig. 2, the noise level has increased markedly while the shape of the spectra, even including the effect of the discrete level, is only moderately altered. We attribute these changes in level to increased trapping due to introduction of distributed trapping states presumably caused

* Supported by the Office of Naval Research.

[1] C. J. Christensen and G. L. Pearson, Bell System Tech. J. **15**, 197 (1936). P. H. Miller, Proc. I. R. E. **35**, 252 (1947). R. E. Burgess, Brit. J. Appl. Phys. **6**, 185 (1955).

[2] C. I. Shulman, Phys. Rev. **98**, 384 (1955). K. M. Van Vliet *et al.* Physica **22**, 723 (1956).

[3] J. J. Brophy and R. J. Robinson, Phys. Rev. **118**, 959 (May 15, 1960).

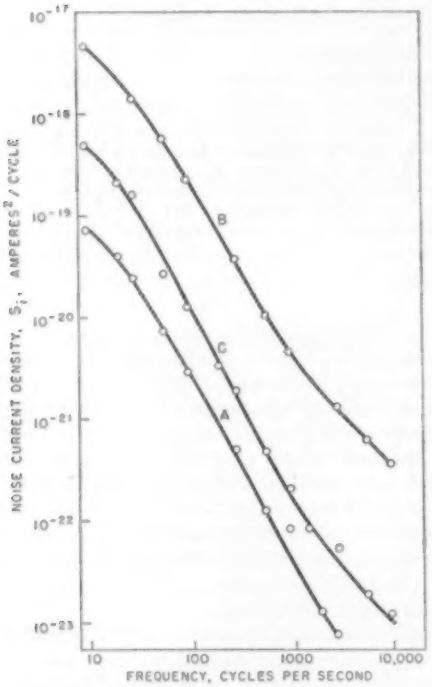

FIG. 1. Current noise spectra of a cadmium sulfide single crystal under 5200 A illumination and for 32-μa photocurrent. Curve *A* is for the original electrodes, curve *B* for the disturbed electrodes, and curve *C* for the repaired electrodes. The quasi-fermi level is 0.34 v below the conduction band for this current.

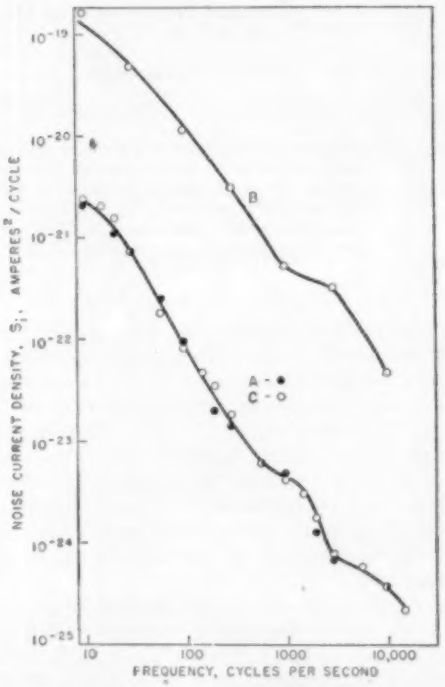

FIG. 2. Current noise spectra of a cadminum sulfide single crystal under 5200 A illumination and for 6-μa photocurrent (curves *A* and *C*) and 8-μa photocurrent (curve *B*). The three curves represent the same electrode conditions as Fig. 1. The quasi-fermi level is near 0.41 v below the conduction band for these currents.

by mechanical disturbance of the electrodes. The increased trapping increases the fluctuations in current carriers and therefore the low frequency noise, as in Eq. (1).

The $1/f$ behavior of the trapping noise shown by curve *B* of Fig. 1 should not be confused with the usual $1/f$ noise associated with poor contacts. A simple $1/f$ noise source at the electrodes would simply add to the total noise without increasing the magnitude of S_i in Eq. (1). In preparing other crystals for noise studies, poor electrodes are quite often produced. These samples show true $1/f$ contact noise over the entire spectrum with a magnitude much greater than that shown in these curves.

After spectra *B* were taken the crystal was provided with new contacts by removing the old electrode material, abraiding the electrode area with a knife, and resoldering with indium. Curves *C* of Figs. 1 and 2 were then obtained. The noise level of *C* in Fig. 1 is smaller than *B* but still larger than *A*. Correspondingly, the high frequency $1/f$ effect is much smaller than in the case of *B*. It appears the reelectroding procedure has succeeded in reducing the concentration or energy extent of the distributed traps.

Curve *C* of Fig. 2 agrees within experimental error with *A*. This is as expected if the discrete level is not influenced by the contacts and if the distributed level density is small, since the discrete level dominates when the quasi fermi is nearby.

The substantial changes in noise level are observed even though the photocurrents and the incident photon fluxes are the same. The incident flux was 6×10^{14} photons/cm^2/sec for the conditions pertaining to Fig. 1 and 1×10^{14} photons/cm^2/sec for those of Fig. 2.

These results suggest the presence of shallow trapping states near the electrodes, which is in agreement with independent evidence from photoconductivity studies.[4] The concentration of these traps depends on the quality of the contact and the traps are evidently distributed in energy. The effects described here are not contact noise in the usual sense since they obviously influence the bulk electronic transition processes. It seems clear that the effects of contacts in the manner shown by these data must be seriously considered in all studies of electrical phenomena in cadmium sulfide.

[4] R. W. Smith, RCA Rev. **20**, 69 (1959).

Growth from the Melt. I. Influence of Surface Intersections in Pure Metals

G. F. Bolling and W. A. Tiller
Westinghouse Research Laboratories, Churchill Borough, Beulah Road, Pittsburgh 35, Pennsylvania
(Received January 5, 1960; and in final form April 28, 1960)

The solid-liquid interface shape during growth from the melt has been determined for pure materials in the vicinity of external and internal surfaces; both the cases of isotropy and anisotropy of solid-liquid interfacial energy have been considered. From these considerations it is possible to determine some effects associated with interface and external surface anisotropy. For example, a preferred direction of growth, a surface layer phenomenon and stray-crystal formation during seeding and normal crystal growth may arise as a result of the solid-liquid interface configuration.

INTRODUCTION

FOR a quantitative understanding of crystal growth it is necessary to obtain a complete description of solid-liquid interface morphology under all possible conditions of growth. Such a description may be conveniently divided into three parts: the macroscopic external shape; the microscopic shape on the size scale of cells and dendrites; and the atomic configuration which includes faceting, layer phenomena and the concept of surface roughness.

For each morphology a complete description requires a knowledge of solute and temperature distributions; energies of external, internal, and solid-liquid surfaces; and the proximity to thermodynamic equilibrium at various regions of the interface. This task is too formidable to undertake at one time. Therefore, we endeaver to describe the solid-liquid interface morphology in the relatively simple case of a pure material in the regions of external and internal surfaces under the assumption of thermodynamic equilibrium maintaining at the interface. We further restrict our attention to a somewhat macroscopic description and do not discuss any atomic scale interface morphology.

GROOVE SHAPE

Here the shape of the solid-liquid interface, $y=g(x)$, is examined in the vicinity of a grain boundary or an external boundary, i.e., a crucible surface or free surface. In a pure material this shape will depend upon (i) the solid-liquid interfacial free energy per unit area γ_{SL}, (ii) the temperature at the interface $T(x,y)$, and (iii) the angle formed by minimizing surface free energy through a "surface tension balance" at the junction of the interface and either the external or internal surface. For simplicity we shall consider two dimensions, assuming that the shape is constant in the third dimension.

In the simplest case when γ_{SL} is isotropic the interface between solid and liquid will be a smooth surface. The shape in Fig. 1 serves to define the interface. Here, $y>0$ represents liquid, and $y=0$, $x\rightarrow\infty$ represents the position of the main solid-liquid interface. The region to the right of the surface is solid and that to the left is either liquid or a boundary surface which makes an angle θ with the main interface. At the groove the interface makes an angle ϕ, with the boundary surface, determined by the equilibrium conditions at the surface. If we apply a condition of equilibrium at the interface, its shape may be determined from the equation

$$T(\infty,0)-T(x,y)=-(\gamma_{SL}/\Delta S)y''[1+y'^2]^{-\frac{3}{2}} \quad (1)$$

where $T(\infty,0)$ is the equilibrium melting point and ΔS is the entropy of fusion per unit volume of the material. For the special case of a pure material with isotropic γ_{SL} this equation may be solved under the condition that $T(x,y)=Gy$ on $y=g(x)$, where G is a constant. Using the notation that $K^2=\gamma/G\Delta S$ Eq. (1) becomes

$$y[1+y'^2]^{\frac{1}{2}}=K^2y''. \quad (2)$$

A simple integration gives

$$y^2/2=-K^2[1+y'^2]^{-\frac{1}{2}}+K^2B, \quad (3)$$

where B is an arbitrary constant of integration. Three solutions may be obtained for Eq. (3) depending upon three possible values of B: I. $B>1$, II. $B=1$, III. $B<1$. Since each of these solutions will be used in subsequent investigations of growth from the melt they are included here. We obtain from a transformation due to Legendre,[1,2]

I. $B\geqslant 1$

$$x=f_1(y)=\pm\frac{2K}{(2[B+1])^{\frac{1}{2}}}\times\{BF(r,s)-(B+1)E(r,s)\}+A, \quad (4)$$

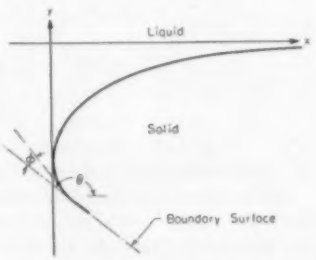

FIG. 1. Schematic illustration of a solid-liquid interface near a boundary surface.

[1] A similar method was used by McNutt and Andes (footnote 8) in solving this problem. However, the solutions they obtain for Eqs. (4) and (5) are less than set forth here by a factor of 2.

[2] W. Gröbner and N. Hofreiter, *Integraltafel, Unbestimmte Integrale* (Springer-Verlag, Vienna, 1948), Vol. 1, p. 64; W. Flügge, *Tables of Transcendental Functions* (Pergamon Press, New York, 1954), pp. 86, 87.

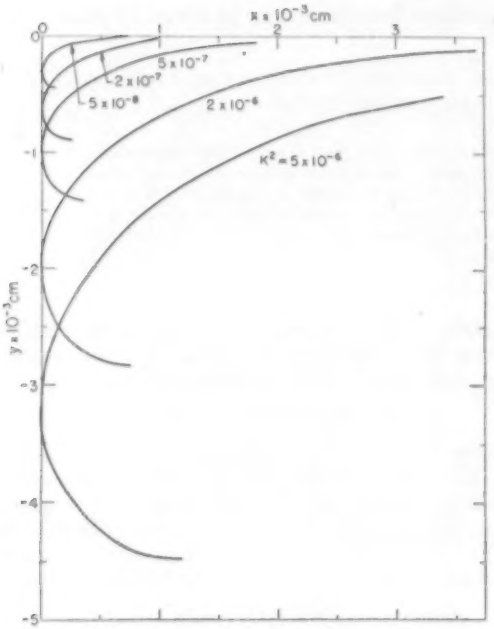

FIG. 2. Interface shape plotted from Eq. (8) for isotropic γ_{SL} and several values of $K^2=\gamma_{SL}/G\Delta S$.

where

$$r=\sin^{-1}[2/(B+1)]^{\frac{1}{2}},$$

$$s=\cos^{-1}\left[\frac{2K^2(1-B)+y^2}{4K^2}\right]^{\frac{1}{2}},$$

and

$$2K^2(B-1)\leqslant y^2\leqslant 2K^2(B+1).$$

II. $B\leqslant 1$

$$x=f_2(y)=\pm K\{F(r,s)-2E(r,s)\}+A, \qquad (5)$$

where

$$r=\sin^{-1}[(B+1)/2]^{\frac{1}{2}}$$

$$s=\cos^{-1}[y^2/2K^2(B+1)]^{\frac{1}{2}},$$

and

$$0\leqslant y^2\leqslant 2K^2(B+1).$$

III. $B=1$

$$x=f_3(y)=K\ln\left[\frac{2K+(4K^2-y^2)^{\frac{1}{2}}}{y}\right]-(4K^2-y^2)^{\frac{1}{2}}+A, \quad (6)$$

where $0\leqslant y^2\leqslant 4K^2$. Here $F(r,s)$ and $E(r,s)$ are elliptic integrals of the first and second kinds, respectively.

If the interfacial energy over the whole of $x=f(y)$ is isotropic, then $y'=0$ when $y=0$ and from Eq. (3) we can see that $B=1$. Thus, the interface shape is described by case III. The constant A may be determined by setting $x=0$ at $y'=\infty$ and using Eqs. (3) and (6). Thus, for this arrangement of the coordinate system, Eq. (6) with $A=K[\sqrt{2}-\ln(\sqrt{2}+1)]$ gives the interface shape. This interface shape is plotted in Fig. 2 for various values of K. We have treated the interface as a semiinfinite line; however, it may be seen that for any reasonable value of K, $y'\to 0$ very closely for $x\sim 0.01$ cm.

The simplest case of anisotropy of interfacial free energy is with the main interface as a singular surface having a low value γ_0 while all other orientations displayed on $x=f(y)$ are isotropic having a value γ_1. Here $y'>0$ when $y=0$, so that the interface shape is given by case II with $B=(1+\tan^2\rho_0)^{-\frac{1}{2}}=\gamma_0/\gamma_1$ and $\rho_0=\cos^{-1}B$=the angle of intersection of the plane surface of energy γ_0 with the curved surface of energy γ_1. The integration constant A is determined by setting $x=0$ at $y'=\infty$. For this case the interface shape is shown in Fig. 3 for several values of γ_0/γ_1 with $K^2=(5\times 10^{-7})$.

The interface shape may also be envisioned for the case where the main solid-liquid interface does not exhibit a singular surface but does exhibit the orientation of lowest γ, (γ_0). This will have a shape between that represented by Figs. 2 and 3 depending upon the variation of γ. Proximity to the shape in Fig. 3 will exist with most other orientations than the main interface having the value γ_1.

It is worthwhile to indicate a method of treating a more general case. The interface may be polyhedral or composed of segments depending upon the variation of γ_{SL} with orientation. The shape of the ith segment may be determined by measuring y relative to the junction of the ith and $(i-1)$th segments, (the 0th segment is the main interface), where some equilibrium constraint must exist. This is an example of case II and the type of anisotropy which has already been treated is the simplest application of this.

In a general case solute may be present and, with γ_{SL} isotropic, the problem may be treated by dividing the interface into segments over which the solute concentration can be approximated by $C_i=\text{const}\times(y-y_{i-1})$, where y_{i-1} is the intersection coordinate of the ith and $(i-1)$th segments. Equation (1) must then be expressed

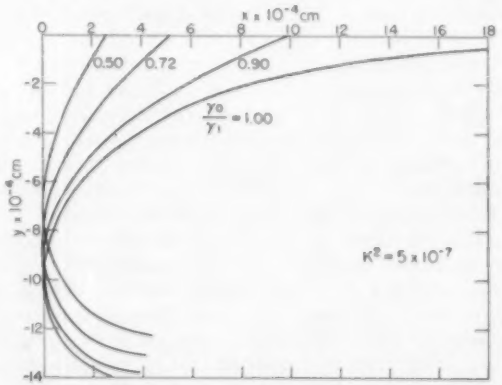

FIG. 3. Interface shape plotted from Eq. (7) for anisotropic γ_{SL}. The x axis beyond the curve intercept represents the face of interfacial free energy γ_0 lower than the curved portion of value γ_1.

in a more general form (to be used in paper II)

$$T(\infty,0)-T(x,y)=m_L\{C(\infty,0)-C(x,y)\}-(\gamma_{SL}/\Delta S)[y''(1+y'^2)^{\frac{3}{2}}]. \quad (7)$$

Here $T(\infty,0)$ is the equilibrium liquidus temperature for the composition $C(\infty,0)$ and m_L is the liquidus slope of the system. Thus, if the solute distribution is known, the effect of solute on the interface shape may be determined. The same reasoning can be applied to variations in γ_{SL} or in G provided that segmenting can be made such that over the ith segment $\gamma_{SL}{}^i=$constant, $C_i=\text{const}(y-y_{i-1})$ and $T_i=\text{const}(y-y_{i-1})$. γ_{SL} will of course be a function of orientation but this may be expressed as a function of position on the shape $y=g(x)$.

THE EFFECTS OF SURFACE JUNCTIONS

In this section we will look at the morphology of a solid-liquid interface as it meets the surface of the crystal at either a crucible wall, a grain boundary or a gas phase. The consequences of such intersections on crystal growth are discussed. The detailed shape of the solid-liquid interface in the contact region does depend upon the assumption that $T[f(y),y]=Gy$, but not enough to impair the following treatment, as shown in Appendix I.

External Boundaries

(*i*) *At a container.* First let us consider interface contacts with an external surface. Assuming a steady-state motion of the interface and isotropy of interfacial energy, the interface shape near the external surface will depend upon the shape of the freezing point isotherm for the main interface; i.e., concave, planar, or convex with respect to a point in the liquid. If we further assume, for the sake of illustration, that the temperature gradient in the solid normal to this isotherm is constant for the three types of isotherms, we may compare the three interfaces. Although the specimen axis will be parallel to the external boundary in each case, we will plot the interface shape with the main interface at $y=0$ so that the external boundaries will not be parallel for the three cases. This is shown in Fig. 4 for a constant value of ϕ (Fig. 1). We see that the angle θ is particularly important in determining the interface shape where θ is the angle between the external boundary and the freezing point isotherm.

Two features of importance can be seen from Fig. 4; both the degree of supercooling of the liquid, ΔT, at the point of contact of the interface and the external surface and the volume of supercooled liquid increases as θ increases ($\Delta T\sim10^{-2}$°C). Thus, the probability per unit time of nucleating a stray crystal will increase with θ. Since we are primarily interested in the probability per unit volume of nucleating a stray crystal, the freezing velocity v is also an important parameter. However, the isotherm shape and the temperature gradient G are not independent of v and the number of stray crystals forming per unit area of external surface will not be simply proportional to $1/v$.

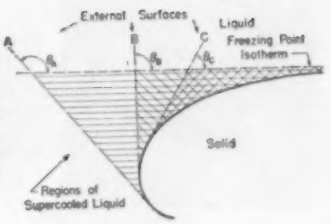

FIG. 4. The volume of supercooled liquid as a function of the freezing-point isotherm shape, i.e., concave, planar or convex to the liquid. The specimen axis is parallel to the external surface.

(*ii*) *At a container during seeding.* Consider a case of crystal seeding where the walls of the crucible slope from a crystal dimension d, at an angle ξ to the specimen axis, to a crystal dimension $d_2(d_2>d_1)$. If the crucible is a better conductor than the crystal, the isotherms will be concave to the liquid and the angle of contact θ between the main interface and the crucible wall, will include the angle ξ in the region of changing dimension. It is obvious that θ will approach 180° as ξ increases, and thus the frequency of stray crystal formation will increase in this region. Therefore, during crystal seeding when one wishes to increase the crystal size, consideration must be given to the angle ξ of the crucible walls in this region.

In the foregoing a situation has been described where all parts of the interface can satisfy the condition of steady-state growth with negligible departure from equilibrium; however, for some anisotropic materials this condition may not be realized. In the groove region near the bounding surface the normal velocity of the interface v_n must be smaller than the axial velocity v_a. Further, for the normal growth of a face at a velocity v_n a certain degree of supercooling δT_n is necessary. The magnitude of δT_n for the same v_n will depend upon the atomic mechanism of freezing and will tend to increase as the face becomes singular. In some cases an imperfection may nucleate on the face itself provided the supercooling it displaces yields enough free energy for its formation. This requires that the imperfection be able to provide, at least in its initial stages, growth at the rate v_n with a smaller supercooling than δT_n. For example, twin formation in Ge appears to satisfy this condition,[3] so that this may provide the mechanism of repeated twin formation during the growth of Ge crystals under certain conditions.

Contact angles and interface shapes must also be considered in analyzing the kinetics of crystal growth on substrates from supercooled liquids. For example, in the growth of ice on substrates from supercooled water,[4] it is found that the growth rate at constant supercooling depends markedly upon the substrate. Since the contact angle at the interface substrate junction greatly influ-

[3] G. F. Bolling, W. A. Tiller, and J. W. Rutter, Can. J. Phys. **34**, 234, (1956).
[4] C. S. Lindenmeyer, G. T. Orrok, K. A. Jackson, and B. Chambers, J. Chem. Phys. **27**, 822 (1957).

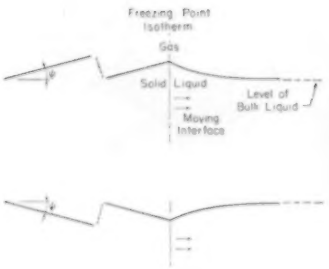

FIG. 5. Schematic representation of positively and negatively stepped surfaces of a freezing crystal and the liquid profile in the interface region (horizontal growth).

ences the morphology of the advancing front, and thus the heat flow conditions, the kinetics should not be simply related to the thermal properties of the substrates.

(*iii*) *At a free surface.* When the bounding surface is a free surface, i.e., solid-gas not solid-crucible, an anisotropy of this bounding surface leads to an interesting phenomenon.[5–7] Under the appropriate energetic conditions (faceting conditions), the solid-gas surface will not form parallel to the liquid-gas surface but will form at some angle ψ so that a low energy surface is exposed.

Several conditions govern the shapes of the free surfaces. First, the solid surface exhibits a particular facet orientation. Secondly, the shape of the solid-liquid interface is subject to the conditions already derived. Thirdly, the liquid-gas surface will have a shape determined by Eq. (2) with $K^2=\gamma_{LG}/\rho g$ for horizontal growth where γ_{LG} is the surface free energy of the liquid, ρ is the density difference between the liquid and gas phases, and g is the gravitational constant. (This shape is similar to the solid-liquid interfaces of Fig. 2 and has been recently discussed by McNutt and Andes.[8]) Finally, if we consider a static situation there must be some minimum free energy configuration at the junction of the three surfaces influenced by the wettability of the solid face, the angle ψ, and the various values of γ.

The balance of forces at the junction cannot be derived without postulating adsorption or rapid curvature changes at the junction. However, as pointed out by Landau and Lifshitz,[9] an equilibrium will indeed exist over a range of contact angles under given conditions. Excluding the junction, the shapes are illustrated in Fig. 5 for positive and negative ψ. Since $\gamma_{LG}/\rho g \gg \gamma_{SL}/G\Delta S$, the curvature at the solid-liquid interface does not appear in the diagrams but would enter the equilibrium configuration at the junction. However, it is most likely that the shape of the solid-liquid interface at the external surface limits the height of the junction, h, above the bulk liquid (Fig. 6). For example, if the maximum value of ϕ for which equilibrium can exist at the edge of the facet is denoted by $\phi_{\max}$, an $h_{\max}$ exists at which an abrupt breakdown of contact at the facet edge must occur. We may write, in general, from meniscus problems[8] that

$$h=K\{2[1-\sin\alpha]\}^{\frac{1}{2}},$$

and in particular when

$$h=h_{\max}, \quad \alpha=\alpha_{\min}=(\pi/2)+\psi-\phi_{\max}, \tag{8}$$

where α is the angle between the curved liquid surface at the junction and the vertical.

For steps of any appreciable size to be observed, the liquid must not completely wet the newly exposed solid-gas interface that is created at the breakdown; otherwise, the liquid would just flow back to the curved portion of the surface which was once the solid-liquid interface and no large steps would result. For a large step, the liquid must drop almost to the bulk level and be unable to climb up the exposed surface. A newly established edge equilibrium allows propagation of a new facet until $\phi_{\max}$ is again reached. If we consider $\psi\approx 10°$, $\gamma_{LG}=400$ ergs/cm^2 and assume that $\phi_{\max}=15°$, from Eq. 8, $h_{\max}$ is calculated to be about 5×10^{-2} cm for Pb. This is in reasonable agreement with step heights observed by the authors for Pb crystals grown slowly in an oxidizing atmosphere.

For a complete treatment of this phenomenon, the velocity of growth must be considered since the ability of the liquid to flow upwards with the facet edge at various rates and maintain its equilibrium shape will depend upon the viscosity of the liquid and the freezing velocity of the crystal.

Internal Boundaries

Let us first consider the case of a bicrystal having a grain boundary energy γ_{GB} under steady-state growth for the case of isotropic solid-liquid interfacial energy where $\gamma_{SL}=\frac{1}{2}\gamma_{GB}$.[10] For this case a curve of Fig. 2 of appropriate K^2 with $\theta=90°$ and $\phi=0$ describes the interface shape on each side of the grain boundary groove and the grain boundary elongates in a direction normal to the freezing point isotherm. Since $B=1$, it can be seen from Eq. (3) that the root of the groove

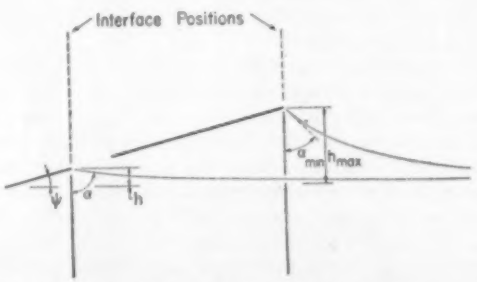

FIG. 6. Change of liquid profile during the development of a surface step to its maximum height.

[5] L. Graf, Z. Metallkunde, **42**, 336 (1951).
[6] H. A. Atwater, A. R. Lang, and B. Chambers, Can. J. Phys. **33**, 352 (1955).
[7] A. Rosenberg, PhD thesis, University of Toronto, 1956.
[8] J. E. McNutt and G. M. Andes, J. Chem. Phys. **30**, 1300 (1959).
[9] L. D. Landau and E. M. Lifshitz, *Statistical Physics* (Pergamon Press, New York, 1958), p. 472.

occurs at $y=\sqrt{2}K$ and that the equilibrium temperature of the root is $\Delta T=\sqrt{2}KG$ deg below the equilibrium temperature for a flat face. Because of the supercooling of the groove liquid there is also a finite probability of nucleating stray crystals here. The case of isotropy for $\gamma_{SL}>\frac{1}{2}\gamma_{GB}$ is an obvious extension of the above, whereas, although the case of isotropy for $\gamma_{SL}<\frac{1}{2}\gamma_{GB}$ has been discussed by Cahn and Hilliard,[11] the interface shape in the groove region is not amenable treatment with our present state of knowledge.

Let us finally consider the case of anisotropic γ_{SL}. Let a bicrystal be grown, one crystal having a singular surface (γ_0) exposed at $y=0$ and an isotropic surface (γ_1) for $y<0$, the other having an isotropic surface (γ_1) exposed for all y. Then, although the energy of the interfaces near the root of the groove is the same, the groove shape will be anisotropic. The groove shape can be constructed by combining a curve from Fig. 2 for one crystal and a curve from Fig. 3 for the other with the proper K and γ_0/γ_1 ratio. This groove shape is illustrated in Fig. 7 for a particular K and two values of γ_0/γ_1. From this we can see that the boundary will not meet the interface isotherm at $\theta=90°$, but at a value of θ that increases as the ratio γ_0/γ_1 decreases. This will lead to the encroachment of the isotropic interface grain by the interface grain with a singular surface. (The same general result will arise without the restriction of a singular surface if the same range of anisotropy is allowed in the dominant grain.) Such an effect will lead to the development of a preferred orientation in a sample where many grains of different orientation nucleate early in the freezing process. In fact, the development of a preferred orientation will occur at a greater rate than that predicted from a knowledge of the angle θ. This is because the boundary, at one end, will tend to be perpendicular to that external surface where the grains originally nucleated and, at the other end, must also make an angle θ with the solid-liquid interface. It follows that at least a portion of a grain boundary must be concave towards the crystal with the nonsingular interface since the solid-liquid interface is parallel to the external surface. This curvature will be a driving force

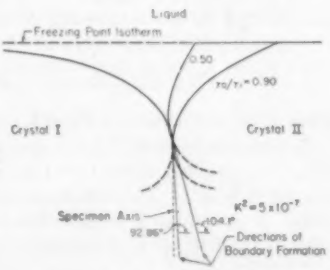

FIG. 7. Direction of formation of the grain boundary when adjacent grains produce an anisotropic boundary groove at the solid liquid interface. The angle of encroachment θ increases as γ_0/γ_1 decreases.

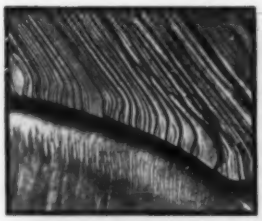

FIG. 8. Photomicrograph of a decanted solid-liquid interface for pure Pb. The grain boundary groove exhibits the type of anisotropy illustrated in Fig. 7. The plateaus are {111} faces so $\gamma_0/\gamma_1<1$. (×233)

to move the boundary laterally along the interface and increase the rate of development of the preferred orientation. The rate of lateral boundary motion will depend upon boundary mobility which is found to be high in the case of zone refined materials.[12,13]

The experiments performed by Rosenberg and Tiller[14] support this explanation for a preferred orientation or growth selection in pure materials. In very pure unidirectionally solidified castings of zone-refined lead, they determined that the preferred orientation was ⟨111⟩. This material seems to fulfil the two conditions prerequisite for this type of preferred orientation; first, there is evidence for a high boundary mobility[12] and secondly, the experiments of Rosenberg[7] would indicate the tendency towards a singular {111} face in pure lead. Moreover, it was observed that additions of 0.0001 wt% Ag to the zone-refined Pb destroyed the tendency for a preferred orientation, while 0.0005 wt% allowed the development of the normal preferred orientation ⟨100⟩ which is the same as the direction of dendritic growth. This is logical for several reasons: The presence of an impurity decreases boundary mobility especially when growth from the melt promotes grain boundary segregation; the boundary groove is forced towards symmetry in the presence of a solute distribution ahead of the interface; and an increasing impurity content leads to the onset of dendritic growth.

As a direct experiment for support of the hypothesis, an interface was exposed in its as-growing condition by rapidly decanting the liquid from the solid during freezing. Figures 8 and 9 are photomicrographs of the grain boundary grooves intersecting the interface. It is observed that the grooves display a marked anisotropy of shape supporting the postulate of anisotropic γ_{SL}

FIG. 9. Photomicrograph of a decanted solid-liquid interface in pure Pb illustrating the grain boundary groove anisotropy in the vicinity of a triple junction. Note that the grain boundary groove between the similar grains is symmetrical. (×233)

[10] D. McLean, *Grain Boundaries in Metals* (Oxford University Press, New York, 1957), p. 76–80.
[11] J. E. Hilliard and J. W. Cahn, Acta Met. **6**, 772 (1958).
[12] G. F. Bolling, W. C. Winegard, Acta Met. **6**, 283 (1958).
[13] K. T. Aust and J. W. Rutter, Trans. A. I. M. E. **215**, 119 (1959).
[14] A. Rosenberg and W. A. Tiller, Acta Met. **5**, 565 (1957).

and preferred crystal orientation; the encroaching grain is nearer the {111} pole than that one encroached upon.

Considerations of grain boundary grooves at a freezing solid-liquid interface also apply to the case of twin boundaries intersecting the solid-liquid interface. The groove surfaces will be given by Fig. 2 for crystals with isotropic γ_{SL}. If β is the angle between the interface at the root of the groove and the normal to the main interface and η is the angle between the twin plane and the normal to the main interface, then by considering the balance of forces only along the twin plane, we have

$$\cos\beta \cos\eta = \gamma_t/2\gamma_{SL} \text{ with } \beta \geqslant \eta \qquad (9)$$

where γ_t is the twin boundary free energy. Since $\gamma_t/\gamma_{SL} > 0.1$ for most metals, it can be readily seen that a twin boundary cannot form at an angle η greater than about 78°.

The presence of a groove at a twin boundary which moves across the solid-liquid interface as growth proceeds may influence dislocation propagation in the crystal. For example, consider a dislocation line ending in the interface of the parent crystal upon which the twin encroaches. When the dislocation line is contacted by the root of the boundary groove, two possibilities must be considered: (i) The dislocation maintains a particular relation to the interface normal or (ii) it is oriented crystallographically or randomly such that it is not influenced by the interface shape. In the latter instances the dislocation could propagate into the twin. However, in the former case a sharp curvature will develop if the dislocation crosses the groove root; this may be sufficient to lock the emergent end of the dislocation firmly in the groove root so that it cannot propagate into the twin. Dash[15] has shown that twin formation in silicon acts as an effective dislocation filter such that dislocations in the parent crystal do not propagate across the twin boundary.

SUMMARY

The solid-liquid interface morphology in the vicinity of intersections with grain boundaries and external surfaces has been examined theoretically. The treatment deals with the steady-state freezing of a pure material under the following assumptions: (i) The solid and the liquid are in thermodynamic equilibrium at the interface, (ii) the solid-liquid interface is smooth with a specific anisotropy of surface free energy, and (iii) the temperature along the solid-liquid interface is linearly dependent upon the y coordinate. The interface morphology calculated on the basis of these assumptions allow one to understand the formation of stray crystals during seeding and general crystal growth, the development of a surface layer phenomenon, the development of a preferred direction of growth and effects related to twin formation and growth on a substrate.

The assumptions made in this treatment may be relaxed without a serious alteration of the general conclusions. A specified departure from thermodynamic equilibrium at the interface could be treated by altering Eq. (2). Likewise, if the temperature along the interface depends on a polynomial in y, Eq. (2) can be modified to deal with it. The solution to such a modified equation is difficult to find; however, for certain polynomials the solution can be evaluated and it leads to the same general conclusions concerning the growth phenomena discussed in the foregoing.[16]

APPENDIX I

In the following treatment we wish to show that the assumption of a linear temperature variation in the y direction along the groove surface is justified. Consider an infinite solid-liquid interface centered by a groove of shape, $x=f(y)$, where $y=0$ represents the main interface and $x=0$ locates the groove center. The temperature distribution in the liquid T_L is given by the Fourier integral

$$T_L - T_0 = \int_0^\infty A(b) \cos bx e^{-\lambda y} db, \qquad (A1)$$

and

$$\lambda = (v/2a) + ([v/2a]^2 + b^2)^{\frac{1}{2}}, \qquad (A2)$$

where T_0 is a constant and a is the thermal diffusivity in the liquid.

In the region where

$$(bx)^2/2 \ll 1 \text{ and } (\lambda y)^2/2 \ll 1,$$

Eq. (A1) is approximated by the linear variation in y,

$$T_L - T_0 = \int_0^\epsilon A(b) db - y \int_0^\epsilon \lambda A(b) db, \qquad (A3)$$

where ϵ is the value of b for which the integrand is essentially zero. ϵ may be determined by representing the temperature distribution at $y=0$ in the form

$$T_L - T_M \simeq \Delta T \exp[-5(xv/a)^2], \qquad (A4)$$

since a/v is the approximate width of the thermal diffusion field about the advancing groove.

The solution of Eqs. (A1) and (A4) for $A(b)$ at $y=0$ is

$$A(b) \simeq a\Delta T/4v \exp[-(ba/4v)^2]. \qquad (A5)$$

Thus $A(b) \to 0$ when $\epsilon > 10v/a$.

For metals $v/a \sim 10^{-1}$ cm^{-1} and since the groove dimensions are less than 10^{-2} cm, $\epsilon x \simeq \lambda y \simeq 10^{-2}$. Thus Eq. (A3) is valid. This arises primarily from the large value of a/v, and a similar treatment should be of general validity for nonsymmetrical grooves.

[15] W. C. Dash, J. Appl. Phys. **30**, 459 (1959).

[16] G. F. Bolling and W. A. Tiller (to be published).

JOURNAL OF APPLIED PHYSICS VOLUME 31, NUMBER 8 AUGUST, 1960

Partition Noise in Electron Beams at Microwave Frequencies

A. Ashkin and L. D. White
Bell Telephone Laboratories, Murray Hill, New Jersey

(Received January 26, 1960)

A study was made at 4080 Mc of the partition noise introduced into a beam by a meshed grid as a function of its position along the beam. Simultaneous information concerning the beam dynamics was obtained by means of a beam analyzer. With cathode magnetic fields somewhat below those corresponding to immersed flow, the partition noise exhibited sharp dips as the grid in moving along the beam passed through the planes which corresponded to image planes of the cathode. These observations confirm the picture of noise smoothing taking place over relatively small areas in the vicinity of the cathode and elucidate the contribution of the random interception of electrons to the partition noise. With small cathode magnetic fields the partition noise varied sinusoidally with the cyclotron periodicity as the grid was moved along the beam. This variation with position is thought to result from the contribution to the partition noise of higher-order mode conversion.

1. INTRODUCTION

It is well known that noise smoothing of electron beams below full-shot noise occurs at microwave frequencies[1] even though the potential depression smoothing as envisioned at lower frequencies[2–4] ceases to operate. This smoothing at microwave frequencies is thought[5] to take place through the action of the space-charge forces within a distance of approximately ten times the cathode to potential minimum spacing. The linear dimensions of the area over which noise smoothing takes place are approximately equal to the cathode to potential minimum spacing. Thus, the beam a short distance from the cathode may be thought of as being made up of many nonoverlapping elementary current filaments, each with its own noise smoothing. The distribution of transverse velocities of the electrons in an elementary filament is random with the spread being determined by the temperature of the cathode. These transverse velocities in general will result in a transverse spreading of the elementary filaments so that they are of finite size and overlap one another in the subsequent beam. Nevertheless, the noise power carried by the electrons of a given filament is still less than that of full shot noise.

The total noise disturbance contained in these elementary smoothed filaments can be expressed in terms of the excitation of normal modes or space-charge waves which then propagate down the beam. From such a picture of noise excitation and propagation, Haus and Robinson[6] have derived the noise figure of microwave amplifiers.

If part of a smoothed beam is intercepted by a grid or aperture, the noise power per unit current in the beam is observed to increase. The corresponding increase in noise is called partition noise. There are two known processes which produce this partition noise. One process[3,7–9] is the random interception of electrons from the individual elementary smoothed filaments. The source of randomness in this interception is the randomness of the electrons' initial transverse velocities which produces a random spatial distribution across the elementary filament. The other process is the conversion of noise power from the higher-order space-charge waves before interception to the fundamental space-charge wave after interception.[9,10] The amount of coupling between a given higher-order space-charge wave and the fundamental depends upon the geometry of the interceptor.

Experimentally, little work has been done to verify the processes which produce partition noise. The reason lies in the difficulty of calculating and measuring effects due to higher-order space-charge waves and the difficulty of knowing the beam dynamics to the extent of being able to calculate the amount of interception of the smoothed elementary filaments. Measurements have been made on the noise figure of traveling wave tubes as a function of the amount of current interception. These measurements, however, yield little information on the fundamental processes. W. R. Beam[9] has done experiments from which he obtains some confirmation of the random interception process. He subtracts from the total partition noise the partition noise at very high magnetic fields, in which the transverse thermal motions are very small. The high-field partition noise is taken as the contribution of higher-order mode conversion to the total partition noise. He then compares the observed dependence of the remaining partition noise upon magnetic field with the dependence predicted on the basis of random interception. Qualitative agreement between experiment and theory was obtained.

[1] C. C. Cutler and C. F. Quate, Phys. Rev. **80**, 875 (1950).
[2] A. J. Rack, Bell System Tech. J. **17**, 592 (1938).
[3] B. J. Thompson, D. O. North, and W. A. Harris, RCA Rev. **4**, 269 (1940); **4**, 441 (1940); **5**, 106 (1940); **5**, 247 (1940); **5**, 371 (1941); **5**, 505 (1941); and **6**, 114 (1941).
[4] D. K. C. MacDonald, Phil. Mag. **41**, 863 (1950).
[5] P. K. Tien and J. Moshman, J. Appl. Phys. **27**, 1067 (1956).
[6] H. A. Haus and F. N. H. Robinson, Proc. I.R.E. **43**, 981 (1955).
[7] F. N. H. Robinson and R. Kompfner, Proc. I.R.E. **39**, 918 (1951).
[8] F. N. H. Robinson, J. Brit. Inst. Radio Engrs. **14**, 79 (1954).
[9] W. R. Beam, RCA Rev. **16**, 551 (1955).
[10] W. W. Rigrod, Bell System Tech. J. **38**, 119 (1959).

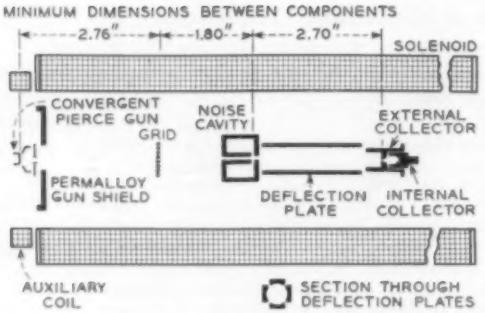

FIG. 1. Cross section of the beam apparatus. The resonant frequency of the noise cavity is 4080 Mc. The dimensions given are the minimum axial separations between the corresponding components.

The present experiment separates the two processes through the use of appropriate electron optics. The experiment was prompted by a previous detailed study of beam dynamics using an electron beam analyzer.[11,12] Images of the cathode were found periodically along beams in which the flux threading the gun cathode was less than that threading the beam in the drift region (partial magnetic shielding). Between images, the electrons which originated at a given small area of the cathode spread out over a relatively large area as a result of their transverse velocity distribution. The distance between successive planes at which the electrons returned to the same configuration they had at the cathode was a cyclotron wavelength. This imaging led to the suggestion that the partition noise introduced by a grid in such a beam would vary periodically with grid position, with the periodicity being equal to the imaging or cyclotron wavelength.

In the present paper the investigation of partition noise produced by a grid with the above experimental conditions is described. Periodic dips in the partition noise vs grid position were observed. These variations are interpreted in terms of random interception from the smoothed elementary filaments. In addition, partition noise obtained with cathode fields corresponding closely to full cathode shielding is described. Sinusoidal variations of partition noise with grid position were observed. These variations have been interpreted by Rigrod[10] as resulting from the higher-order space-charge waves. It is to be noted that no cathode imaging has been observed with such small cathode fields.

2. APPARATUS AND METHOD OF TAKING DATA

The beam apparatus used was essentially that of footnote references 11 and 12. Figure 1 shows its basic features. The system was demountable and operated at a pressure of about 10^{-7} mm Hg. The beam was launched from a Pierce-type gun[13] with a 9:1-area convergence through a partial magnetic shield into the main solenoid field. An auxiliary coil was located outside the shield to permit adjustment of the cathode flux. Full magnetic shielding corresponds to zero-magnetic field B_c at the cathode. B_c equal to one-ninth the main field B_0 gives immersed flow since then the magnetic flux threading the cathode equals the flux threading the beam in the main field B_0. Cases where B_c lies between zero and one-ninth-B_0 correspond to partial magnetic shielding. Within this range of cathode flux there was no current interception on the gun electrodes. The analyzer and cavity were rigidly connected together and could be moved axially along the beam.

The grid was a square mesh of wires at beam potential. Its purpose was to intercept current over the cross section of the beam. It could be moved axially along the beam independently of the cavity and analyzer or could be locked to them permitting the whole assembly to move as a unit along the beam. In addition, the grid could be rotated out of the beam. Actually, either of two grids could be placed across the beam. One grid was made with 0.005-in. wires, 0.017 in. between centers and the other, 0.003-in. wires, 0.011 in. between centers. Each of these grids intercepted approximately 50% of the beam current.

For purposes of noise detection, the beam current was square wave modulated at 100 cps. The noise detecting cavity was tuned to 4080 Mc. Its output was passed through a standard superheterodyne receiver, through a narrow band 100-cps filter and then further amplified. This signal was beaten against the modulating frequency in a phase sensitive detector. The dc output was passed through a filter with a time constant of 2 sec and then read on a milliammeter, designated as the noise meter. The noise meter reading was found to be linear with rf power over the range used.

The data from the beam analyzer was presented on two oscilloscopes. The so-called "P.P.I." scope gave an actual picture of the beam cross section in which the intensity of light from the oscilloscope screen was a measure of the current density. The so-called "A" scope showed the superposition of the current variations as the beam was swept continuously past the pinhole (see footnote references 11 and 12).

The nature of the partition noise introduced by the grid was determined from the results of three different types of noise measurements. The first was the observation of the noise in the fundamental space-charge wave on the beam in the absence of the grid. The second was the observation of the noise in the fundamental space-charge wave following a fixed grid. From the phase of the space-charge wave at the grid, it could be determined whether the noise immediately following the grid was predominantly in the form of current or velocity

[11] A. Ashkin, J. Appl. Phys. **28**, 564 (1957).
[12] A. Ashkin, J. Appl. Phys. **29**, 1594 (1958).

[13] Karl R. Spangenberg, *Vacuum Tubes* (McGraw-Hill Book Company, Inc., New York, 1948), pp. 449–465.

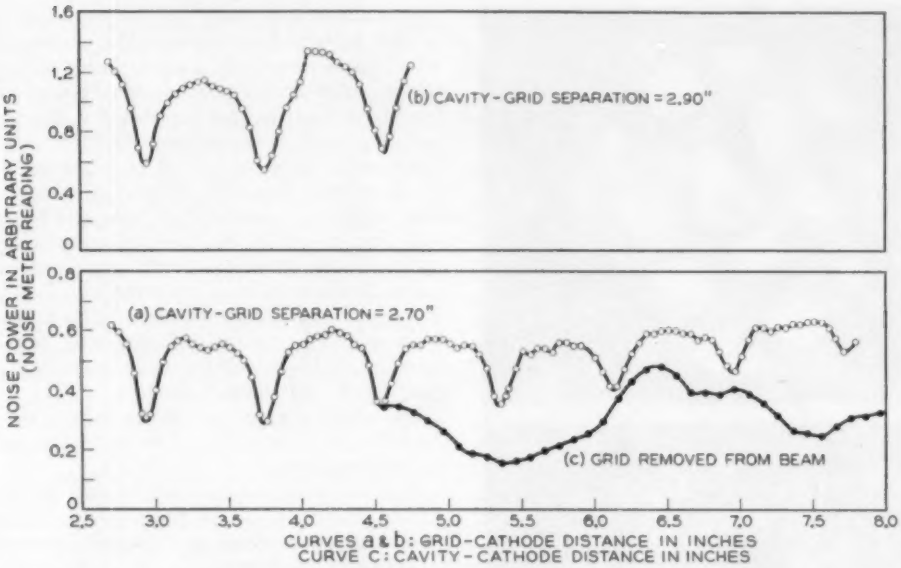
NOISE POWER IN ARBITRARY UNITS (NOISE METER READING)
(b) CAVITY-GRID SEPARATION = 2.90"
(a) CAVITY-GRID SEPARATION = 2.70"
(c) GRID REMOVED FROM BEAM
CURVES a & b: GRID-CATHODE DISTANCE IN INCHES
CURVE C: CAVITY-CATHODE DISTANCE IN INCHES

FIG. 2. Periodic dips. Curves (a) and (b): variation in noise power as grid plus cavity are moved along the beam. Curve (c): variation in noise power as cavity is moved along the beam with grid removed from beam. Beam conditions: beam voltage, 700 v; beam current, 3.2 ma; main magnetic field, 280 gauss; and cathode magnetic field, 30 gauss.

fluctuations. The third type of measurement was made by fixing the grid-cavity separation and observing the noise as the grid plus cavity were moved along the beam.

Information on the shape of the beam and its imaging properties was obtained from the beam analyzer.

3. EXPERIMENTAL DATA AND INTERPRETATION

3.1 Periodic Dips in the Interception Noise

A group of measurements, as described above, is shown in Figs. 2 and 3. The beam conditions were quite similar to those which in the past had yielded good cathode images. (That the cathode was being imaged could be ascertained only when the cathode had aged to the extent that the emission was not uniform over the surface of the cathode.) One of the beam conditions associated with cathode imaging is that the cathode is only partially shielded. Figure 2(c) is a plot of the cavity output vs the cathode-to-cavity distance with the grid removed from the beam and is simply the noise in the fundamental space-charge wave. Figure 2(a) is a plot of the cavity output as a function of grid position with the grid-cavity separation fixed at a half-space-charge wavelength. With this separation the noise at the cavity is approximately that immediately behind the grid. The space-charge wavelength was determined from observations (Fig. 3) of the space-charge waves in the wake of the grid when it was fixed at various positions along the beam. As will be shown shortly, partition noise introduced in the form of current fluctuations is the major part of the noise following the grid. Thus, the variation of noise with grid position obtained with a grid-cavity separation of a half-space-charge wavelength results mainly from the variation of the partition noise with grid position. Figure 2(a) shows sharp periodic dips in the partition noise introduced by the grid. Figure 2(b) is also a plot of cavity output vs grid position. The grid-cavity separation, however, is 0.2 in. larger than that used for Fig. 2(a) but is still approximately a half-space-charge wavelength. The break indicated in the curve shown by the dashed line probably resulted from an undesired increase in amplifier gain. The gain used while taking Fig. 2(b) was different from that used for Figs. 2(a) and 2(c). A comparison of Fig. 2(a) with

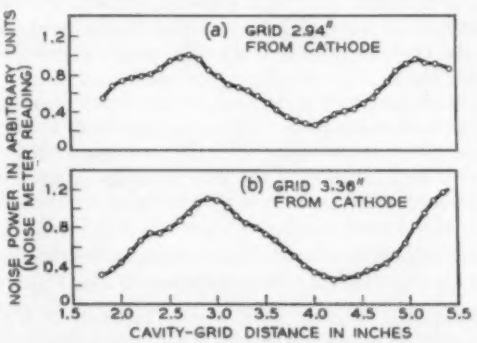
NOISE POWER IN ARBITRARY UNITS (NOISE METER READING)
(a) GRID 2.94" FROM CATHODE
(b) GRID 3.36" FROM CATHODE
CAVITY-GRID DISTANCE IN INCHES

FIG. 3. Space-charge waves following fixed grid. Curve (a): grid fixed at first dip of Fig. 2, 2.94 in. from the cathode. Curve (b): grid fixed midway between first and second dips of Fig. 2, 3.36 in. from the cathode. Beam conditions: same as for Fig. 2.

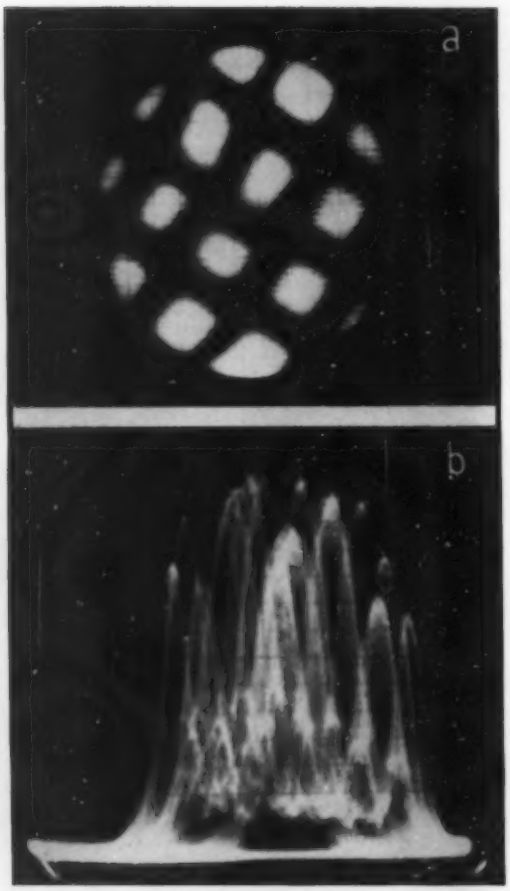

FIG. 4. Excellent grid image. Figure (a): so-called "P.P.I." presentation. Figure (b): so-called "A" presentation. Beam conditions: requires partially shielded cathode.

Fig. 2(b) shows that the noise dips are associated with the grid position and not the cavity position. This fact rules out the possibility of accounting for the noise dips on the basis of variations in cavity coupling to a scalloping beam.

Figure 3(a) shows the noise on the beam following the grid when it was located at the position of the first noise minimum of Fig. 2(a). The cavity output is plotted as a function of the grid to cavity separation. A similar plot for the case of the grid being between the first and second minima is shown in Fig. 3(b). The amplifier gain was changed between taking the Fig. 3(a) and the Fig. 3(b) data. Extrapolations of Fig. 3(a) and Fig. 3(b) yield noise maxima in the vicinity of the grid. The noise as a function of grid position was also measured with fixed grid-cavity separations other than a half-space-charge wavelength. As the grid-cavity separation was changed significantly from a half-space-charge wavelength toward one- or three-quarter wavelengths, both the total noise and the relative size of the noise dips decreased. At a separation of three-quarters plasma wavelength (4.05 in.) the average noise was roughly a third that for a grid-cavity separation of a half wavelength. No cyclotron periodicity could be seen, but a space-charge wave was clearly evident. These results indicate that with the grid at one of the larger dips roughly half, and that with the grid between dips well over a half, of the noise following the grid was partition noise introduced in the form of current fluctuations. This conclusion is consistent with Figs. 2(a) and 2(c) since Fig. 2(c) shows the noise for the unintercepted beam whereas only one-half the beam current and, therefore, only one-half the beam noise in the fundamental mode gets through the grid.

The absolute magnitude of the noise is not known. An attempted calibration by means of shot noise gave an ambiguous result.

Partition noise having characteristics like those described previously was not restricted to only the beam conditions tabulated but was observed at several other sets of beam conditions.

Most of the data were taken with the coarser of the two grids. Limited data taken with the finer grid indicated that similar results would have been obtained.

The beam dynamics associated with these noise patterns was investigated with the analyzer. With the grid fixed with respect to the beam, the analyzer revealed good grid images periodically along the beam. An excellent grid image is shown in Figs. 4(a) and 4(b). The distance between successive images corresponded to a cyclotron wavelength and was the same as that between successive noise dips in Figs. 2(a) and 2(b). Midway between images there were little, if any, signs of a grid image. The quality of the images deteriorated somewhat with increasing distance from the grid and depended slightly upon the position of the grid with respect to the beam scallops. These imaging properties indicate that the electrons from any point in the beam follow helical paths having the same pitch and a distribution in radius.

With the grid removed from the beam, the analyzer showed a beam shape similar to that shown in Figs. 5(a) and 5(b). The current density varied smoothly across the beam and the beam contour varied smoothly with distance. The periodicity of the scalloping was closely that of the noise dips. The miminum diam were about 0.7 that of the maximum diam.

The above data on the imaging of the grid give no indication of whether or not the cathode is being imaged. Fortunately, after a few weeks of operation, the beam showed periodically along its length the spotted appearance characteristic of images of an aging cathode. Figures 5(c) and 5(d) are the photographs of the oscilloscope patterns of such a spotted beam. For comparison, a smooth beam is shown in Fig. 5(a) and 5(b). The

occurrence of beam spots was accompanied by only a slight drop in cathode current due to aging; for example, from 4.3 ma to 4.2 ma for a set of conditions which produced noise dips. The positions of the noise dips with respect to the positions of the planes showing beam spots were investigated. First, the grid was located at a noise dip. Then the analyzer was placed at a grid image. Finally, the grid was removed and the analyzer was relocated at the nearest plane showing beam spots. The resulting shifts in analyzer position were small—about ± 0.05 in. or $\pm 8\%$ of a cyclotron wavelength. These small shifts were comparable in size with the errors to be expected in the measuring of the distances and the determining of the positions of the images. Thus, to within the experimental accuracy, the locations of the beam spots coincided with the locations of the noise dips. The location of the planes showing beam spots with respect to the phase of the beam scallops was arbitrary.

The foregoing data yield information concerning noise smoothing within the beam. At the planes of the noise dips the smoothing in the beam exists not only over the beam as a whole, but also exists over individual small portions of the beam. In particular, there is considerable smoothing over areas the size of the holes in the grid. Between the planes of the noise dips, the noise smoothing still exists over the beam as a whole but does not exist over small portions of the beam. The coincidence of the locations of the cathode images with the locations of the noise dips implies that the initial smoothing, which is produced in the gun, takes place over small areas.

A model which fits the data is the following. At the cathode, or in its vicinity, the beam is made up of a number of small nonoverlapping filaments, each of which is smoothed; i.e., the noise induced in a cavity by a single filament would be considerably less than shot noise. Along the beam the cathode is periodically imaged, as a result of the focusing properties of the magnetic field, and at these images the beam is also composed of a number of nonoverlapping noise-smoothed filaments. Each of these filaments has a random distribution of thermal transverse velocities at the cathode. As a result of these transverse velocities, between images each filament spreads out considerably and overlaps with other filaments so that the current passing through a small area consists of random contributions from many filaments. The linear dimensions of the area over which a filament spreads are larger than the diameter of the grid wire (if this were not true, the images of the grid would not vanish for grid-analyzer separations of an odd number of half-cyclotron wavelengths).

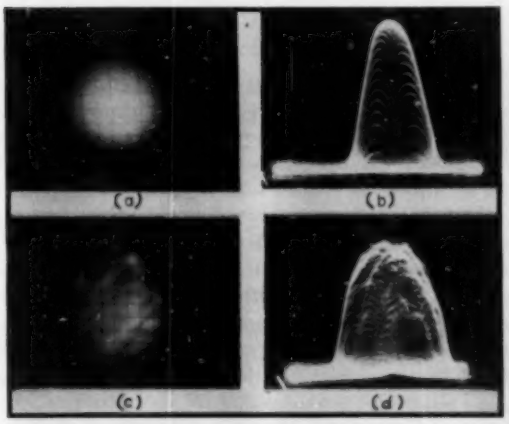

FIG. 5. Images of unintercepted beam. Figures (a) and (b): typical image of beam from new cathode. Figures (c) and (d): typical of images which occur periodically along beam after the cathode has aged sufficiently. Beam conditions: requires partially shielded cathode.

Noise patterns similar to Figs. 2(a) and 2(b) are produced in the following way. When the grid is located at an image plane, it is very probable that any individual filament will be either completely transmitted or completely intercepted. Assume the former. Then the noise contributed by the filament following the grid is the same as that preceding it. As the grid is moved along the filament, the size of the filament increases and the grid begins to intercept some of the electrons in a random manner. This random interception introduces additional noise into the beam which noise has both current and velocity fluctuation components; however, the noise of the current fluctuation is considerably larger than that due to velocity fluctuations. When the grid has been moved along the filament to where the filament has increased to a size comparable to the grid mesh so that on the average half of the filament is being intercepted, the noise introduced by the grid is a maximum. The current fluctuation amounts to one-half of full-shot noise for the current following the grid. As the grid is moved further along the filament, the noise remains constant until the filament size decreases to the extent that, on the average, less than half of the filament is being intercepted, at which location the noise introduced by the grid begins to decrease. Analogous comments can be made in the case of the filament being completely intercepted by the grid when it is at the image plane. Thus, the noise following a grid intercepting a beam made up of such filaments would show minima at the planes where the filaments do not overlap, and would rise on either side of these minima to plateaus extending over the region where the dimensions of the filaments were comparable to those of the mesh.

3.2 Sinusoidal Variation in the Noise Introduced by the Grid

Another type of pattern of grid noise vs grid-cathode distance is shown in Fig. 6. Here, the variation in partition noise with position is approximately sinusoidal. As in Fig. 2(a) and 2(b) the grid-cavity separation is fixed

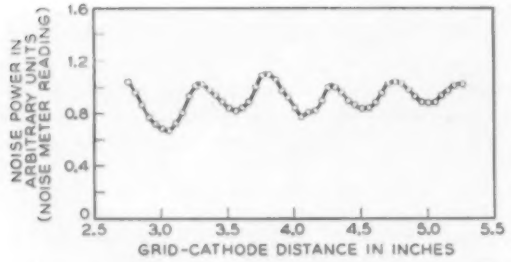

FIG. 6. "Sinusoidal" noise pattern. Curve shows variation of noise power as grid plus cavity are moved along the beam. Beam conditions: beam voltage, 700 v; beam current, 5.5 ma; main magnetic field, 450 gauss; and cathode magnetic field, 10 gauss.

and is about one-half plasma wavelength. The periodicity of the pattern corresponds to the cyclotron wavelength. The main difference in the experimental conditions between those which produced dips and those which produced sinsoidal patterns is the magnetic field at the cathode. The dips were obtained with cathode fields somewhere between half and all of that needed for immersed flow. The sinusoidal patterns were obtained with cathode fields of a quarter or less of that necessary for immersed flow. The minimum cathode field at which sinusoidal variations could be observed was determined by the appearance of growing noise[14] of sufficient magnitude to mask the sinusoidal variations. The growing noise was, of course, not the result of intercepting the beam and is thus not relevant to the present work except to note that the conditions for sinusoidal variations were contiguous with those for growing noise.

The beam dynamics associated with sinusoidal noise patterns were investigated with the analyzer and were found to be very different from those associated with "noise dips." The beam ripple was quite small. The ratio of maximum diameter to minimum diameter was about 10:9. The periodic images of the fixed grid were quite poor. No cathode images, i.e., spotted beams, were observed. Thus, the beam was quite well mixed. If at the cathode the beam were considered to be made up of nonoverlapping filaments, there would be no plane in the beam in which all these filaments would be simultaneously nonoverlapping. With such a beam it might be expected that the partition noise would be independent of the position of the grid in the beam.

An interpretation of the sinusoidal variations can be given in terms of space-charge waves. Rigrod[10] has shown that when the cathode field is zero, the half-space-charge wavelengths of all modes except the fundamental are equal to the cyclotron wavelength. Thus, since all the higher-order modes are excited in phase at a plane close to the cathode, the noise current maxima of these higher-order modes will all coincide in the beam. The grid acts as a transducer, coupling the higher-order modes to the fundamental. Thus, the noise as a function of grid position should have the same shape as would be obtained from observing the higher-order modes directly; namely, a sinusoidal variation in noise current having the cyclotron periodicity.

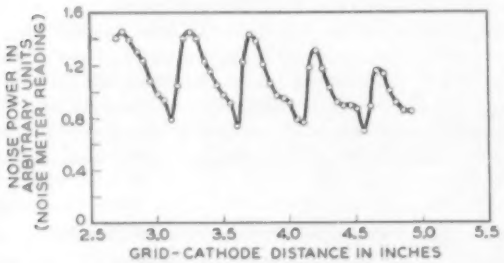

FIG. 7. Complex noise pattern. Curve shows variation of noise power as grid plus cavity are moved along the beam. Beam conditions: beam voltage, 700 v.; beam current, 5.0 ma; main magnetic field, 450 gauss; and cathode magnetic field, 35 gauss.

[14] W. W. Rigrod, Bell System Tech. J. **36**, 831 (1957).

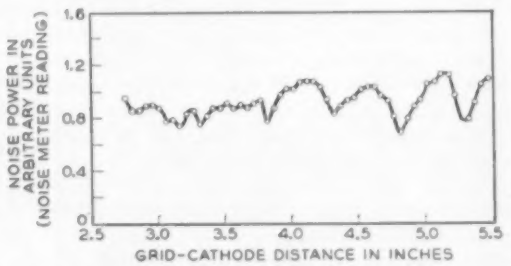

FIG. 8. Noise dips which increase with distance from cathode. Curve shows variation of noise power as grid plus cathode are moved along the beam. Beam conditions: beam voltage, 700 v; beam current, 2.5 ma; main magnetic field, 450 gauss; and cathode magnetic field, 10 gauss.

3.3 Other Types of Noise Patterns

Not all the patterns observed were as simple in form and interpretation as those described above. Another type of distinctive pattern was one which appeared to be made up of two simpler patterns (e.g., dips and sinusoids) having slightly different periodicities. Figure 7 shows such a pattern. Though some of these patterns occurred for cathode fields intermediate between that which gave a sinusoidal pattern and that for dips, leading one to suspect that the pattern resulted from a combination of these two patterns, other similar patterns occurred for cathode fields not in this region and interpretation in terms of electron motions and higher-order modes is much more difficult.

Another interesting pattern, which was not generally seen, is shown in Fig. 8. In this case the dips increase in size with distance from the cathode. The explanation of this behavior is not known.

4. CONCLUSION

Experimental conditions were obtained which yielded information concerning the partition noise resulting from random interception of electrons. In particular, it was observed that as a grid was moved axially through the planes in the beam at which the cathode was imaged, the partition noise went through sharp minima. This variation with position of the partition noise strongly indicates that noise smoothing at these planes exists over relatively small areas. The coincidence of the cathode images and the noise minima implies that the beam at a plane close to the cathode can be regarded as being made up of small nonoverlapping filaments, each with its own smoothing.

Experimental conditions were also obtained which yielded a partition noise dependence upon grid position which is interpreted as resulting from noise power being converted from higher-order space-charge waves into the fundamental.

ACKNOWLEDGMENTS

The authors gratefully acknowledge stimulation and encouragement from R. Kompfner, many helpful discussions with W. W. Rigrod and P. K. Tien, and excellent experimental assistance from J. J. Wiegand.

JOURNAL OF APPLIED PHYSICS VOLUME 31, NUMBER 8 AUGUST 1960

Thermal Expansion Coefficients of Bismuth

E. F. Cave* and L. V. Holroyd
Department of Physics, University of Missouri, Columbia, Missouri
(Received November 13, 1959; and in final form April 25, 1960)

The linear thermal expansion coefficients of the a and c axes of bismuth have been measured from 80°K to 540°K by mechanical means. These same coefficients were determined over a more limited range of temperatures by single crystal and powder x-ray methods. The mechanical and x-ray values did not differ significantly. The expansion coefficient for the c axis was found to be $16.6\pm0.4\times10^{-6}$ $(C°)^{-1}$ at 100°K, $17.3\pm0.2\times10^{-6}$ $(C°)^{-1}$ at 150°K, and $17.6\pm0.2\times10^{-6}$ $(C°)^{-1}$ at 540°K. For the a axis the expansion coefficient was $10.8\pm0.3\times10^{-6}$ $(C°)^{-1}$ at 100°K, $11.6\pm0.2\times10^{-6}$ $(C°)^{-1}$ at 150°K, and $11.8\pm0.2\times10^{-6}$ $(C°)^{-1}$ at 540°K.

INTRODUCTION

In a review article Childs[1] pointed out the need for further measurements of the anisotropic thermal expansion coefficients of bismuth as a function of temperature. Some investigators have reported that the two coefficients were remarkably constant over the interval 100°K to 500°K. Others, however, found large and discontinuous changes in the coefficients at 258°K and 345°K. Figure 1 is reproduced from the article by Childs and is modified by the addition of data taken by the authors of the present work. Included in Fig. 1 are data by Bridgman,[2] Fizeau,[3] Jacobs and Goetz,[4] Jay,[5] Ho and Goetz,[6] and Roberts.[7] The a and c axes referred to are those of the hexagonal triple cell.

Sharp discontinuities in the temperature dependence of the expansion coefficients of bismuth were found by Jacobs and Goetz and by Jay but not by Ho and Goetz or by Roberts. The peculiarity of these discontinuities is enhanced by the observations of Bronson and MacHattie[8] that the specific heat of bismuth is a slowly varying, linear function of the temperature over the interval 193°K to 393°K. Bronson and MacHattie estimate their data to be accurate to about 0.1%.

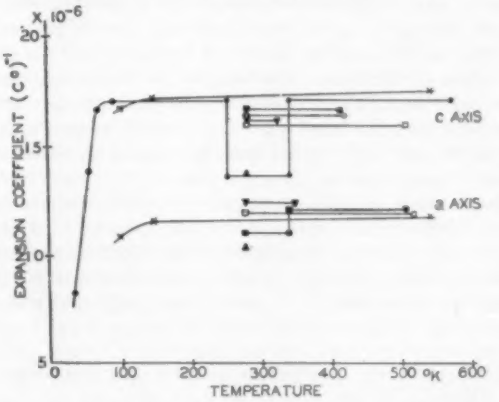

FIG. 1. α for the a and c axes of bismuth. ▲ Bridgman.[2] ▼ Fizeau.[3] ● Jacobs and Goetz.[4] ■ Jay.[5] ○ Ho and Goetz.[6] □ Roberts.[7] ✕ Present work.

---

* Now with Semi-Conductor Division, R. C. A., Somerville, New Jersey.

[1] B. G. Childs, Revs. Modern Phys. **25**, 665 (1953).
[2] P. W. Bridgman, Proc. Am. Acad. Arts Sci. **60**, 305 (1925).
[3] A. H. Fizeau, Compt. rend. **68**, 1125 (1869).
[4] R. B. Jacobs and A. Goetz, Phys. Rev. **51**, 159 (1937).
[5] A. H. Jay, Proc. Roy. Soc. (London) **A143**, 465 (1934).
[6] T. L. Ho and A. Goetz, Phys. Rev. **43**, 213 (1933).
[7] J. K. Roberts, Proc. Roy. Soc. (London) **A106**, 385 (1924).
[8] H. L. Bronson and L. E. MacHattie, Can. J. Research **A16**, 177 (1938).

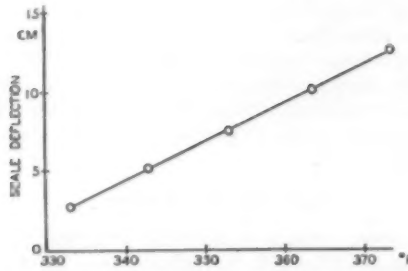

FIG. 2. Scale deflection (change in sample length) vs temperature for the *a* axis. Optical lever method.

The present work was undertaken in an effort to obtain data on expansion coefficients which were accurate and reproducible enough to resolve this question.

APPARATUS AND EXPERIMENTAL METHODS

Preparation of Sample

The single crystals of bismuth were prepared by pulling from a melt of purified bismuth maintained under vacuum. Crystals several cm wide and up to 10 cm long could be grown. Since growth takes place with the *a* axis perpendicular to the melt, crystals for *c*-axis measurements had to be obtained by making transverse cuts. The bismuth was purified by zone refining, and the final product was examined spectroscopically for impurities. Copper and iron were the main impurities and were present to about 1 part per million.

Expansion Determination by Optical Lever

The samples were housed in a cylindrical aluminum bomb. This bomb was kept inside a large Dewar flask so that after being cooled to liquid air temperature, the bomb and sample would warm slowly to room temperature. Temperatures up to the melting point of bismuth could be obtained by means of heater wound on the outside of the bomb. The temperature range was thus from 80°K to 540°K. The differential expansion between the sample and a fused quartz tube of similar length was transmitted to an optical lever by a fused quartz push rod. Corrections for the expansion of the quartz were made using the data of Sosman.[9] A typical operating sensitivity for the optical lever corresponded to a net change in length of the sample of 8.50×10^{-5} cm per mm of scale deflection at 1 meter. Samples oriented for *a*-axis measurements were about 10 cm long while those used for *c*-axis measurements were about 2 cm long.

[9] R. B. Sosman, *The Properties of Silica* (Chemical Catalog Company, New York, 1927).

Expansion Determination by X-Ray Diffraction

The expansion coefficient for the *c* axis was determined by means of the Bragg spectrometer. Single crystals of bismuth were mounted in a cryostat so designed that regardless of expansion the crystal remained centered over the axis of the spectrometer. Only the (001) (hexagonal indices) reflection could be used. Line profiles of the $K\alpha$ line of molybdenum in the fifth and eighth orders were determined at twelve different temperatures distributed over the interval 150°K to 540°K. The shift of a peak could be determined to within about 15 sec of arc.

The *a*-axis measurements were made using a symmetrical back reflection camera with a spherical sample holder. The (500) (hexagonal indices) reflection was studied over the temperature interval 193°K to 373°K. The powder patterns for two temperatures (which differed by 90K°) were recorded on the same film. Typical line shifts of 0.35 cm were obtained and these could be determined to within 0.01 cm.

RESULTS

To obtain data for the *a* axis by means of the optical lever, readings were taken at approximately 10 K° intervals and the least counts of the optical lever and the thermocouple potentiometer would indicate that the slope of a plot of length vs temperature for a 10 K° interval should be determined to within 3%. Data were taken also from 323°K to 373°K, wherein a discontinuity had previously been found, with a higher sensitivity and an indicated accuracy of about 2% over a 10 K° interval (see Fig. 2). There was no evidence of a discontinuity in the expansion coefficients from 80°K to 540°K. Below 100°K the expansion coefficients for both the *c* and *a* axes begin to fall off quite rapidly (see Fig. 1). The average expansion coefficient for the *c* axis was found to be $16.6\pm0.4\times10^{-6}$ $(C°)^{-1}$ at 100°K, $17.3\pm0.2\times10^{-6}$ $(C°)^{-1}$ at 150°K, and $17.6\pm0.2\times10^{-6}$ $(C°)^{-1}$ at 540°K. For the *a* axis the expansion coefficient was $10.8\pm0.3\times10^{-6}$ $(C°)^{-1}$ at 100°K, $11.6\pm0.2\times10^{-6}$ $(C°)^{-1}$ at 150°K and $11.8\pm0.2\times10^{-6}$ $(C°)^{-1}$ at 540°K. The errors quoted originate largely in the lack of reproducibility from sample to sample.

The x-ray data taken over a more limited range of temperature served to verify the mechanical data. The value of the *c*-axis expansion coefficient by the single crystal method was found to be $17.7\pm0.4\times10^{-6}$ $(C°)^{-1}$ in the temperature interval 150°K to 540°K. The *a*-axis expansion coefficient using the powder method was found to be $11.8\pm0.4\times10^{-6}$ $(C°)^{-1}$ in the temperature interval 193°K to 373°K. No discontinuity was found in the temperature dependence of the lattice constants.

JOURNAL OF APPLIED PHYSICS VOLUME 31, NUMBER 8 AUGUST, 1960

Dislocations in Silicon Carbide

S. AMELINCKX* AND G. STRUMANE
Laboratorium voor Kristalkunde; Geologisch Instituut, Rijksuniversiteit Gent, Ghent (Belgium)

AND

W. W. WEBB
Metals Research Laboratories, Union Carbide Metals Company, Division of Union Carbide Corporation, Niagara Falls, New York

(Received March 14, 1960; and in final form April 25, 1960)

The dislocation structure of type 6*H* hexagonal silicon carbide has been studied by etching combined with optical microscopy and by x-ray diffraction microscopy. The validity of the conventional etching technique for identification of the sites of the intersection of dislocations with (0001) surfaces has been established. However, high densities of dislocations lying in (0001) planes and hence heretofore undetected by etching techniques were often observed by diffraction microscopy. Dislocations with $[11\bar{2}0]$ vectors have now been found with evidence for slip both on basal planes and on a "puckered" pyramidal plane. Pileups formed by slip and dislocation walls formed by climb were also observed. Silicon carbide shows many of the characteristics of more conventional plastically deformable materials.

I. INTRODUCTION

IN view of the increasing importance of silicon carbide as a semiconductor and as a high-temperature structural material on the one hand, and the importance of imperfections for semiconductor and high-temperature behavior on the other hand, it seemed worth while to investigate in detail the dislocation structure of silicon-carbide crystals. The influence on the growth of silicon carbide of screw dislocations intersecting crystal surfaces parallel to the basal plane is a classical fact. Even though the existence of extraneous pits on the etched basal surfaces is also known, there has been no investigation of the dislocations that might be involved in plastic deformation. Evidence will be presented here that silicon carbide deforms plastically at high temperature and that it polygonizes in spite of its well-known high hardness at room temperature: Mohs' hardness = 9. Two methods of investigation were applied: etching combined with optical microscopy, and x-ray diffraction microscopy.

II. EXPERIMENTAL

A. Crystals

Use was made of grown faces of industrial crystals grown by reaction presumably combined with sublimation. The majority of crystals are of the hexagonal 6*H* type. No attempt was made to detect contingent polytypes. There are however indications from the symmetry of some of the etch pits that rhombohedral polytypes may have been present in some of the crystals studied only by optical methods.

Some of the crystals examined by etch pit techniques were subsequently thinned by grinding and polishing of material from the rough side of the crystal until the thickness had been reduced to about 0.01–0.05 cm so as to allow x-ray diffraction microscopy. These crystals were again etched before x-ray examination to remove strained material from the ground surface. Other crystals of the 6*H* type grown by D. R. Hamilton[1] were also examined; these were about 0.01–0.05 cm thick and up to 0.2 cm in maximum dimension as grown. The two surfaces (0001) of the crystal were nearly parallel as grown so no thinning was required.

B. X-Ray Diffraction Method for Dislocation Mapping

X-ray diffraction microscopy methods consisting essentially of refined versions of the Berg-Barrett method[2] have been demonstrated by Lang[3] to be capable of resolution of individual dislocations in nearly perfect crystals. Variations of these techniques[4] designed for application to relatively small crystals were used in this investigation. Since x-ray absorption in silicon carbide is relatively small, the values of the product $(\mu/\rho)\rho t$, where (μ/ρ) is the mass absorption coefficient, ρ the density, and t the crystal thickness, were substantially less than one. Under these conditions dislocations are revealed by enhancement of diffracted radiation from regions of the crystal within about five microns of dislocations. The experiment is arranged so that the diffracted x-ray beam leaves the side of the crystal opposite to that entered by the incident beam (as in the "Laue case").

Low index-diffraction planes of the type $(hki0)$ were selected so that the diffraction micrographs recorded on an x-ray sensitive photographic emulsion placed close to the crystal in the diffracted beam are slightly distorted two-dimensional maps of the dislocation structure of the platelets projected nearly on (0001) planes. Thus, dislocation lines in arrays lying nearly parallel with (0001) planes are projected with little distortion onto the emulsion, but dislocation lines lying nearly

* Now at C. E. N. (Centre d'Etudes Nucléairs) Mol-Donk (Belgium).

[1] D. R. Hamilton, J. Electrochem. Soc. **105**, 735 (1958).
[2] C. S. Barrett, *Structure of Metals* (McGraw-Hill Book Company, Inc., New York, 1952), p. 95.
[3] A. R. Lang, J. Appl. Phys. **29**, 597 (1958).
[4] W. W. Webb, J. Appl. Phys. **31**, 194 (1960).

FIG. 1. Spiral structure made visible by carefully etching. Etch pits at centers of spirals mark screw or mixed dislocations; other etch pits mark edge dislocations. (100×)

perpendicular to (0001) planes will be substantially foreshortened in projection.

Since dislocations with Burgers vectors lying in the diffracting planes produce little or no contrast, it is possible to determine the Burgers vectors by comparison of diffraction patterns from several sets of nonparallel diffracting planes.

Dislocations with [0001] Burgers vectors probably would not be seen in the x-ray experiments but they are revealed by etching.

C. Etching Procedure

Two different etchants which are believed to reveal dislocations have been described in the literature:

(1) Fused borax in a platinum crucible at about 800 to 1000°C.[5,6]

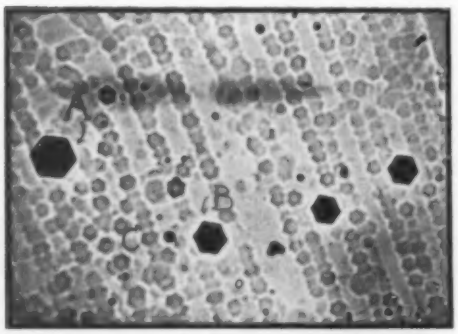

FIG. 2. Pits marking different kinds of defects. Pit *A* marks a screw dislocation (a step ends in *A*), pits *B* edge dislocations; both pits have orientation I. Pits *C* have orientation II; they are believed to mark defects in a silica film on the surface; they are flat-bottomed. (320×)

[5] R. Gevers, S. Amelinckx, and W. Dekeyser, Naturwissenschaften **39**, 448 (1952).
[6] R. Gevers, J. chim phys. **50**, 321 (1953).

(2) Fused alkali carbonates at about 1000°C.[7,8]

We have used the etching procedure given under (1) but in somewhat more carefully controlled circumstances. The crystals were quenched in water after etching, since this greatly facilitates their cleaning.

Suitable etch pits could be developed on only the (0001) face as is common in crystals such as SiC that have nonidentical opposite basal-plane faces. Lateral faces were occasionally examined but seldom etched satisfactorily.

D. Etching of Growth Patterns

In accord with Gevers *et al.*,[5,6] and Horn[7] it was found that the centers of growth spirals are attacked preferentially, as one would expect since these are emergence points of dislocations having a Burgers vector with a component normal to the face under observation (the *c* face). Contrary to Horn (who used the second etchant)

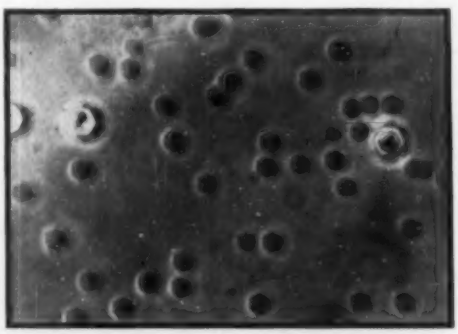

FIG. 3. Pits in both orientations I and II. Notice trigonal symmetry of flat-bottomed pits. (320×)

and in agreement with Gevers[6] it was found that the surface steps are also attacked preferentially. By the use of controlled etching (1 hr at 800°C) one can reveal spiral structures which were not visible in the unetched condition. A fine groove is developed all along the steps, which makes the structure quite visible in phase-contrast microscopy and even in bright-field illumination. Figure 1 shows an example. The interlaced steps are only 7.5 A high[9]; nevertheless they become quite visible after etching.

Fine etch pits are visible in the centers of the spirals, but also elsewhere. The pits not associated with spirals have to be attributed to dislocations with a Burgers vector parallel to the *c* face. We will show that such dislocations result from glide.

[7] F. H. Horn, Phil. Mag. **43**, 1210 (1952).
[8] J. W. Faust, *Methods of Experimental Physics* (Academic Press, Inc., New York, 1959), Vol. 6, p. 147.
[9] S. Amelinckx, Nature **168**, 431 (1951).

E. Etch Pit Shapes

The detailed shape of the etch pits merits some further attention. One can distinguish a number of pit types, differing either in shape, size, or orientation. It is not completely clear at present what they all represent. The points that are presently clear are these:

(1) The deep and centered hexagonal pits, having sides parallel to the edges of the crystal face (i.e., to $[11\bar{2}0]$ directions) mark dislocations. We will call this orientation I. The size differs for edge and screw dislocations. It is significantly larger for screw dislocations, in which case it depends on the stepheight of the spiral centered on it. The size increases with increasing Burgers vector (for the same etching time). The pits marking edge dislocations are uniform in size. (See Fig. 2.)

(2) The flat-bottomed shallow pits which have sides turned 30° with respect to the edges of the crystal face (we will call this orientation II) very probably mark

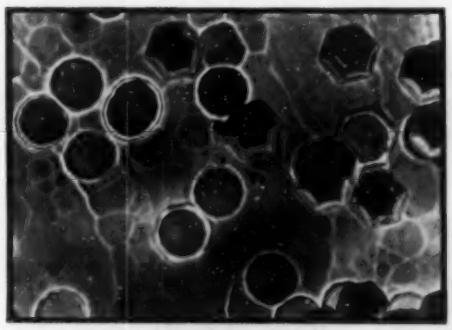

FIG. 4. Twelve-sided pits. (300×)

defects in a silica film, which covers silicon-carbide crystals and is apparently not entirely removed by the etchant. This will be discussed further in detail. When small these pits are perfectly hexagonal, but in fact exhibit trigonal symmetry. (See Fig. 3.)

(3) The shape of pits, not their number, seems to be a function of the etching temperature also. At high temperatures (900–950°C), all pits tend to have orientation I. At intermediate temperatures (850–900°C), however, the shallow pits tend to be twelve-sided (apparently rounded). (Fig. 4.) Some of the deeper flat-bottomed pits exhibit a gradual change from one orientation into the other, giving rise to the shape shown in Fig. 5 at the left. At low temperature (800°C), all flat-bottomed pits have orientation II.

(4) The dislocation pits always remain hexagonal. Those with orientation I occasionally develop small secondary edges, especially after longer etching times. (Fig. 5.)

FIG. 5. Differently shaped pits which result after long etching times: 3 hr at 900°. (300×)

III. DISCUSSION OF RESULTS

A. Density of Dislocations

The density of dislocation etch pits in well-formed crystals is usually very low. In extreme cases this may be 1–10 cm^{-2}; in other cases it may be as much as 10^4 cm^{-2} due to plastic deformation. Most of the pits are *not* associated with spirals and exhibit linear arrangements; they are therefore most probably due to deformation. The x-ray diffraction method indicates, however, that many dislocations are present in the c planes. Dislocation densities in the c plane vary between zero and 10^4 cm^{-2}. Areas as large as 0.1 cm^2 have been observed to be free of any dislocations. Since the dislocations in c planes are not revealed either by etch pits or by growth spirals the two experimental methods are complementary.

B. Determination of Glide Elements from Etch Pit Patterns

The pyramidal glide plane was determined in the following way. The specimen shown in Fig. 6 was used. Careful examination of the glide trace delineated by

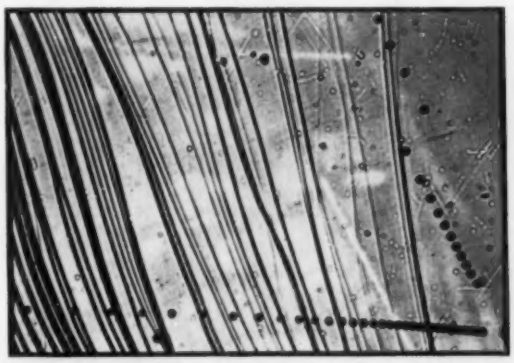

FIG. 6. Pileups of dislocations in pyramidal glide planes shown by etch pits on stepped surface nearly parallel to basal plane. (125×)

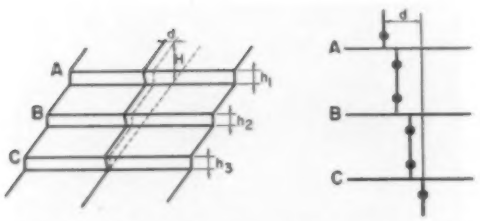

FIG. 7. Glide trace intersecting surface steps; illustrating the derivation of the glide plane orientation.

the line of dark etch pits at the bottom of the photograph reveals that it is slightly curved. Since the other simultaneously formed glide traces on this face are perfectly straight, it is justifiable to assume that no climb has occurred and that the observed curvature is a consequence of surface curvature resulting from the presence of the high surface steps which are clearly visible. If the glide plane is not perpendicular to the plane of observation, the glide trace is laterally displaced every time a step is intersected, as shown in Fig. 7. Measurement of the total stepheight $H=h_1+h_2+h_3+\cdots$ and of the lateral displacement d gives $\alpha=\arctan(d/H)$. H was measured by means of multiple beam interferometry[10] whereas d was measured from an enlarged micrograph.

Since the measurement of d is not very precise, we found for α the range of values 60–70°. The proportional increase of d and H along the glide trace confirmed that the dislocations are still in their glide plane. Since we also know the direction of the trace on the $c(0001)$ plane, we can now deduce the slip plane.

Alternatively, the slip plane may in principle be determined from the eccentricity of the etch pits as shown in Fig. 8. The angle $\alpha=\tan^{-1}2h/(D_1-D_2)$.

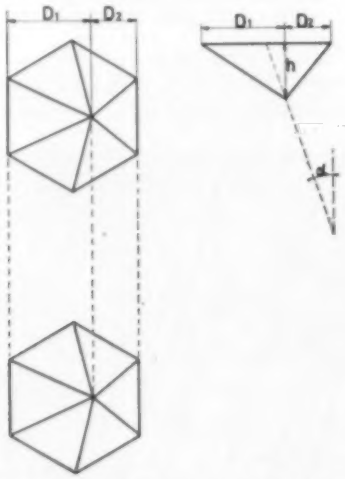

FIG. 8. Illustrating the derivation of the slip plane from deep etch pits.

[10] S. Tolansky, *Multiple Beam Interferometry of Surfaces and Thin Films* (Oxford University Press, New York, 1948).

The geometry of the pyramidal slip plane is shown in Fig. 9. It is clear that this is not a "flat" plane but instead looks like a corrugated surface, with corrugations parallel to the slip vector. It can best be described in terms of a cubic analogy in which it consists of alternate strips of (111) and (100) plane. Each strip is three layers wide and lies alternately along (111) or the most nearly parallel (100) plane. The indices of the two planes in the 6*H* structure on a hexagonal lattice are $(1\bar{1}01)$ and $(4\bar{4}01)$; the resulting puckered plane lies essentially along the $(3\bar{3}01)$ plane. From the absence of steps along the slip trace one can conclude, as just stated, that the slip vector in this glide plane is parallel to (0001), i.e., it is in the $[11\bar{2}0]$ direction.

In the 6*H* structure no really flat planes exist other than the *c* planes. This explains why straight slip steps on the *c* face are only very rarely observed. Such steps result from glide with a vector which has a component perpendicular to the *c* face, i.e., which crosses the corrugations. They give rise to spirals if growth occurs. Since spirals are observed, this means that at high temperature such glide is possible, but only occasionally at temperatures where growth has ceased, so that the step remains undeformed.

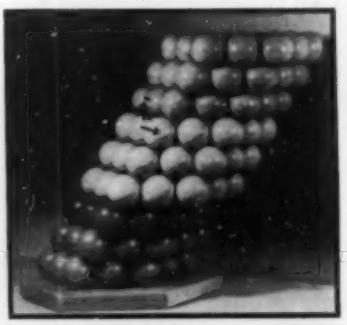

(a)

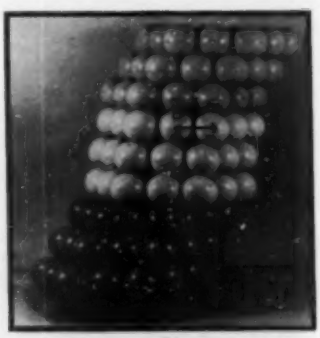

(b)

FIG. 9. The structure of SiC-6*H*, showing the pyramidal glide plane (balls represent only silicon atoms). (a) Side view; (b) front view.

C. Dislocations Revealed by X-Ray Microscopy

Figure 10 is a diffraction micrograph taken using $(11\bar{2}0)$ type planes and it shows dislocations lying in basal planes of a laboratory-grown crystal of Type 6*H* structure. In Fig. 11 diffraction micrographs of the same crystal using $(\bar{1}100)$, $(0\bar{1}10)$, and $(\bar{1}010)$ planes, respectively, are shown. Here it can be seen that the complex dislocation structure of Fig. 10 has been resolved into three sets of dislocations. In each of the diffraction micrographs of Fig. 11 two of the three possible sets appear, the third being eliminated by selection of diffracting planes parallel to the Burgers vector. The arrow indicates the direction of the diffraction vector (perpendicular to the diffracting planes). Dislocations with a component of their Burgers vectors parallel to the arrow appear. Thus, in Fig. 11(a) there are two sets of regular nearly parallel edge dislocations with $[2\bar{1}\bar{1}0]$ and $[\bar{1}2\bar{1}0]$ Burgers vector directions.

In both Figs. 11(b) and 11(c) are seen one set of irregular, crooked dislocations with $[\bar{1}\bar{1}20]$ Burgers vector directions. In addition, each one of the two regular sets is clearly visible in one of these two diffraction micrographs.

These observations establish the existence of $[11\bar{2}0]$ Burgers vectors for dislocations lying in or nearly in (0001) planes. This direction connects nearest neighbor, like atoms in the basal plane, so is the expected Burgers vector orientation. The $[11\bar{2}0]$ dislocations lying in screw orientation can presumably cross slip from (0001) planes to the $[3\bar{3}01]$ glide plane.

Figure 12 shows a pair of diffraction micrographs of another crystal with quite different dislocation structure. Here there are nearly straight dislocations. There is a preference for 90°, 60°, and 30° angles between the dislocation line directions and Burgers vectors. Inspection of a complete set of diffraction micrographs indicates that some pure screw dislocations are also present in (0001) planes.

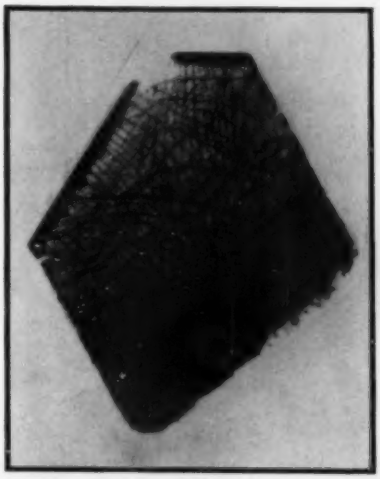

FIG. 10. Diffraction micrograph of laboratory grown crystal showing complex network of dislocations in the basal plane. (34×)

It is not certain whether these dislocations were propagated by growth or generated by plastic deformation. It does appear that all of the dislocations originate on the rough edges at which the crystals nucleated and were propagated by growth of the crystals from these edges. This is particularly evident in the case shown in Fig. 12.

The observation on basal plane surfaces of etch pits without associated surface steps suggests the presence

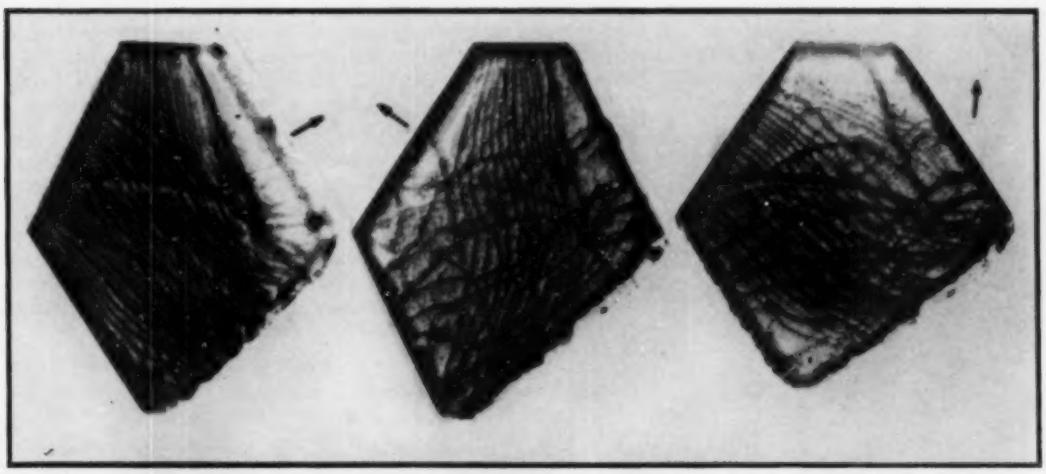

(a) (b) (c)

FIG. 11. Resolution of the network shown in Fig. 10 by choice of three different $(3\bar{3}00)$ diffraction vectors shown by arrows. (34×)

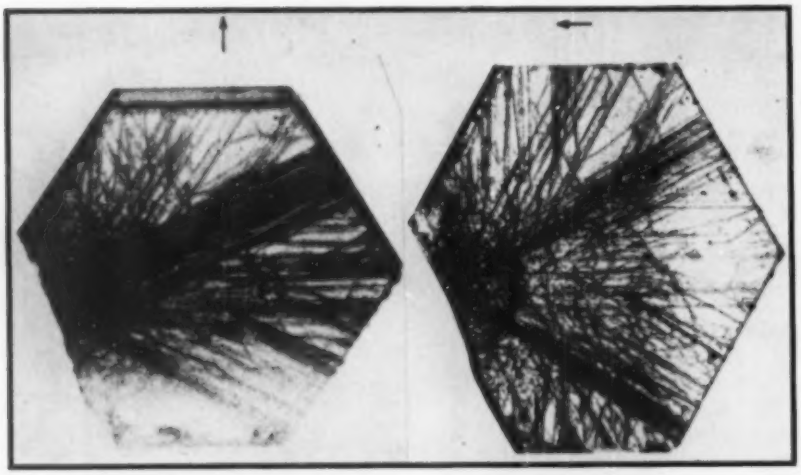

FIG. 12. Another type of dislocation configuration in a laboratory grown crystal with two different diffraction vector directions. (32×)

of dislocation lines with Burgers vectors in the basal plane, but with slip planes lying at an angle to the basal plane. To test this hypothesis, commercial silicon-carbide crystals with etch pit arrays similar to those shown in Fig. 6 were studied by x-ray diffraction microscopy. Typical results are presented for part of one crystal. Figure 13 shows an etch pit pattern and a corresponding diffraction micrograph of this region.

Two types of etch pits are visible: hexagonal flat-bottomed pits that appear light, and hexagonal pyramidal pits that appear dark. Only the pyramidal pits are customarily assumed to mark the intersections of dislocations with the surface. Direct comparison of the etch pit patterns with terminations of dislocations shown in diffraction microscopy patterns permits testing of this assumption. The bottom surfaces of these crystals were mechanically polished before etching. Etch pits invariably appeared on only one surface of the crystals regardless of whether smooth surfaces were available on both sides of those crystals without polishing as was true of the laboratory grown crystals. Thus, only those dislocations terminating in one surface of the crystal show a corresponding etch pit.

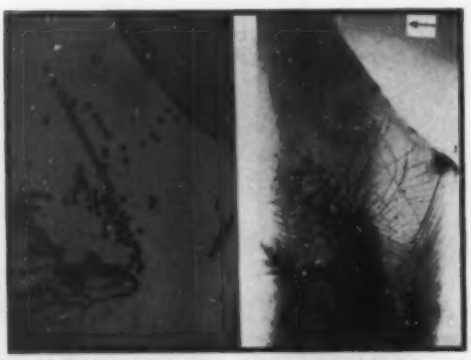

FIG. 13. Etch pit figure and corresponding diffraction micrograph of heavily deformed section of thinned commercial crystal. (14×)

The diffraction micrograph shows that a high density of dislocation lines lies nearly parallel with (0001) planes in this typical crystal. The etch pit density has no relationship to the total dislocation density. Complex networks are visible particularly near the bottom of the picture. A disturbance at the bottom center of the photograph has evidently led to the generation of many dislocations lying nearly parallel with the basal plane. The etch pit pattern suggests that slip has also occurred on nonbasal planes, resulting in a pileup of nonbasal dislocations just above the heavily deformed region. At right center of the diffraction micrograph, terminations of dislocations that should correspond to their intersections with the surface are apparent. Details of this area are shown in Fig. 14 in two diffraction micrographs (with the diffraction vectors indicated by arrows) and in an etch pit pattern.

Each pyramidal etch pit corresponds in the diffraction micrographs to either a short dark line indicating a nonbasal dislocation line that passes through the crystal or to the termination of a long dark line indicating the intersection of a quasi-basal dislocation at the surface. One set of nearly parallel dislocation lines visible at the right in Fig. 13 intersects the bottom surface of the crystal where no etch pits form, so not all of the dislocation line intersections have a corresponding etch pit.

In the dislocation pileup each etch pit clearly corresponds to a single dislocation line lying roughly perpendicular to the basal planes. Some climb has occurred so this array is not an ideal pileup and the dislocations do not lie in the slip plane. The directions and lengths of the dark lines marking these dislocations in the diffraction micrographs are determined by the diffraction

geometry. To the right of the pileup are several other etch pits corresponding to individual dislocations that lie at a large angle to the basal plane. Several of these are not perpendicular to the basal plane and the direction of these short dislocation lines suggests that they lie at about a 60° angle to the basal plane. One pair of closely spaced pits appears to be due to a small dislocation loop.

As predicted, there are no dislocations associated with the flat-bottomed etch pits.

The dislocation configuration giving rise to the short linear array of five pits just to the right of the pileup is somewhat surprising. All except the top pit appear to be due to dislocations that lie mostly parallel to the basal planes but suddenly turn sharply upward near the end where they intersect the crystal surface. Apparently these basal dislocations have either climbed or cross-slipped out of the basal plane. Unfortunately, determination of the Burgers vector directions of these dislocations was somewhat uncertain. If the dislocation lines are in pure screw orientation in the basal plane they can have cross-slipped onto planes with indices of the type $(h\bar{h}oj)$, but climb could also have produced the observed configuration regardless of the Burgers vector direction in the basal plane.

D. Polygonization

The strong interaction between edge dislocations in parallel glide planes is favorable for polygonization, since it brings them one on top of the other. This most probably occurs during deformation at high temperature; it is the very first stage in polygonization. All further stages can readily be observed in silicon carbide.

Figure 14 shows a typical example. A trace of a glide plane is indicated. It is clear that the walls are perpendicular to these glide traces.

Several features typical for polygonization structures have been observed. Figure 15 shows the effect of annealing on the structure of short finite walls. The edge dislocations are in equilibrium with respect to glide if on a plane perpendicular to their glide plane. However, they repel one another in a direction parallel to the wall. During annealing they will therefore tend to disperse, since the stress induces them to climb. Figures 14 and 15 suggest that equilibrium displacement takes

FIG. 14. Detail of dislocation pileup and surface intersections in crystal shown in Fig. 13. Arrows indicate diffraction vector directions. (17×)

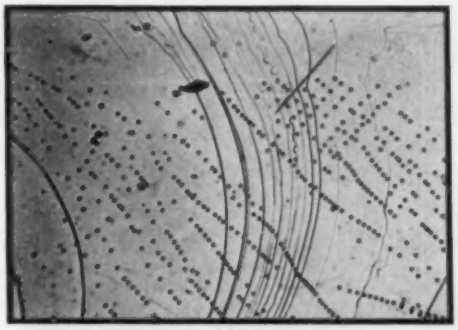

(a)

(b)

FIG. 15. (a) Polygon walls as observed on the c plane. The trace of the glide planes is indicated. (60×) (b) Finite polygon walls. (120×)

place at both ends in a sense away from the center of the wall. This implies that at one end of the wall dislocations climb by addition and at the other end by subtraction. We assume like Friedel,[11] for the case of a semi-infinite wall, that the displacement after a given interval of time is proportional to the net force to which a given dislocation was subjected in the equidistant configuration. One can then derive a relation characterizing their geometry.

Let there be N dislocations in the wall. We assume them to be originally at a constant spacing h. (See Fig. 16.) The force to which dislocation p is subjected is then given by

$$F_p=\frac{D}{h}\Big[\sum_{i=1}^{p-1}(i-p)^{-1}+\sum_{i=p+1}^{N}(i-p)^{-1}\Big],$$

where $D=Gb/2\pi(1-\nu)$.

A similar expression can be derived for F_{p+1}. Thus

$$F_{p+1}-F_p=\frac{D}{h}\Big[\frac{1}{N-p}+\frac{1}{p}\Big]=\frac{D}{h}\frac{N}{p(N-p)}.$$

[11] J. Friedel, *Les Dislocations* (Gauthiers-Villars, Paris, 1956).

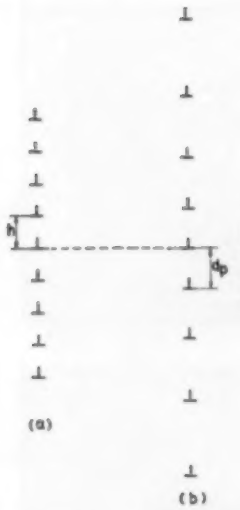

FIG. 16. (a) Dislocations in finite walls of the kind shown in Fig. 15 immediately after slip followed by rearrangement in the slip planes. (b) The same wall after climb has occurred.

We now apply the assumption made by Friedel, i.e., that the increase in distance between the dislocations with index p and $p+1$, which we call d_p, is proportional to $F_{p+1}-F_p$. Unlike Friedel, we cannot neglect the original separation h; so we have the relation

$$d_p = h + m(t)N/[p(N-p)],$$

where $m(t)$ is a proportionality constant which increases with time but is constant for a given observed configuration. The plotting of d_p vs $N/[p(N-p)]$ should yield a straight line, allowing us to deduce the values of h and m. Figure 17 shows such plots for some of the walls shown in Fig. 15.

Neglecting h and assuming $N \gg p$ leads to $d_p \sim 1/p$, Friedel's relation. The latter relation, valid for semi-infinite walls, has been verified in the case of polygonized silicon iron[12] and potassium chloride.[13]

Other interesting configurations which lend themselves to theoretical verification of the interaction forces between dislocations are visible in Figs. 15 and 18.

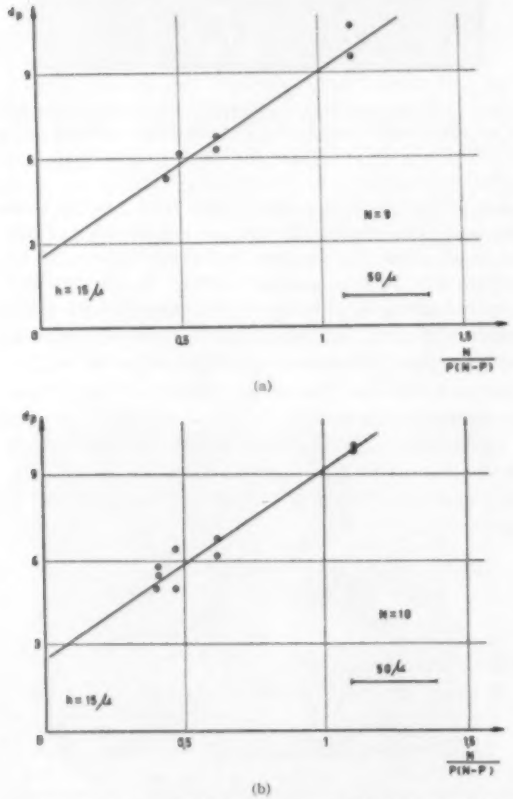

FIG. 17. Plots verifying the geometry of finite walls after climb has occurred.

FIG. 18. Peculiar configurations (doublets and quadruplets) of dislocations in a polygon wall. The configuration is in equilibrium with respect to glide, not with respect to climb. (120×)

Similar ones have been observed previously in germanium[14,15] and in zinc.[16] Gilman has analyzed such configurations in detail; they are stable with respect to glide but not with respect to climb.

E. Plastic Deformation

Very often linear arrays of pits are observed, the direction of the lines being [11$\bar{2}$0], i.e., parallel to the close-packed direction in the c plane. We will present evidence that these are glide traces, i.e., the result of plastic flow. Gevers *et al.*,[5] and Gevers[6] observed several years ago such linear arrangements, but they did not

[12] G. G. Dunn and W. R. Hibbard, Acta Met. **3**, 409 (1955).
[13] S. Amelinckx and R. Strumane, Acta Met. (to be published).
[14] J. J. Oberly, J. Metals **6**, 1025 (1954).
[15] Y. Uemura, J. Phys. Soc. Japan **10**, 1020 (1955).
[16] J. Gilman, General Electric Research Rept., 55-RL-1434 (1955).

interpret them as being due to plastic deformation. The most striking evidence comes from Figs. 6 and 19. Dislocations are plied up behind an obstacle clearly marked by etch pits. Observation in phase contrast reveals that the obstacle is a dislocation or a dislocation group on which a growth spiral is centered. Such dislocations seem to be very effective barriers for edge dislocations since similar configurations have been observed frequently. We have observed grown-in screw dislocations which resisted up to 20–30 piled-up dislocations (Fig. 6). Note also that the leading dislocation in the longer pileup approaches nearer to the obstacle than the corresponding dislocation in the shorter pileup, which is of course what one would expect since the stress on the leading dislocation is smaller in the latter case.

Eshelby, Frank, and Nabarro,[17] and Leibfried[18] have calculated the equilibrium configuration, under applied stress, of edge dislocations in a glide plane when stopped by an obstacle. Their theory yields the following approximate relation. If i is the index of a dislocation, counted from the leading one, we have

$$i(\pi/2)=(2n\tau_0 x/D)^{\frac{1}{2}} \quad D=Gb/2\pi(1-\gamma)$$

where n is the number of dislocations in the pileup, x the distance measured from the leading one, τ_0 the applied shear stress, and b, G, and ν have their usual meaning. This relation is easily verified by plotting $x^{\frac{1}{2}}$ vs i; this should yield a straight line. Such a plot has been made for the pileups of Fig. 6 and the results are shown in Fig. 20. It is clear that the slope increases when n, the number of piled-up dislocations, decreases. The agreement is such that little doubt is left that we are dealing with dislocations in their glide plane.

The values of τ_0 obtained from the plots shown in Fig. 20 are surprisingly small. However, the temperature at which these pileups formed is not known.

Very often a pileup in one glide plane is accompanied by a pileup in another glide plane intersecting the first one in the obstacle. (See Fig. 6.) This is of course no coincidence. It has been shown by Eshelby, Frank, and Nabarro that the stress concentration at the end of a pileup is equivalent to the one existing at a crack tip. This means that there are large stress components in the direction of the intersecting glide planes. The resolved shear stress has a relative maximum in a given family of glide planes, for the particular glide planes passing through the obstacle. If a source is present in that or a nearby glide plane, this stress will be relieved and a second pileup against the same obstacle results. This is shown schematically in Fig. 21.

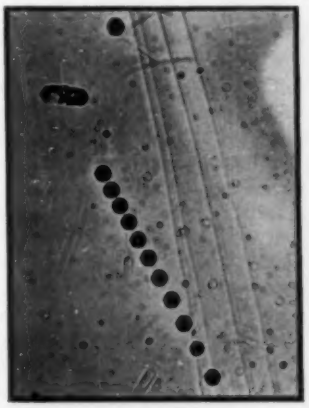

FIG. 19. Pileup of dislocations against an obstacle. (225×)

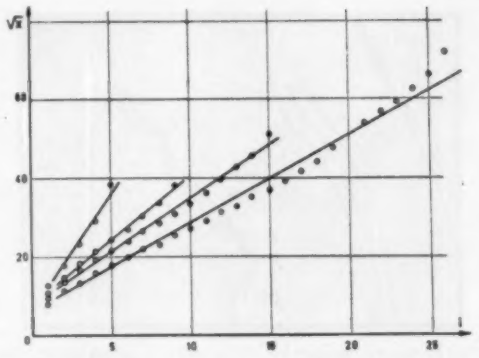

FIG. 20. Plot of the square root of the distance of a given dislocation, from the leading dislocation, vs the index of this dislocation. The unit along the ordinate is (microns)$^{\frac{1}{2}}$. The slope decreases with the total number of dislocations in the pileup.

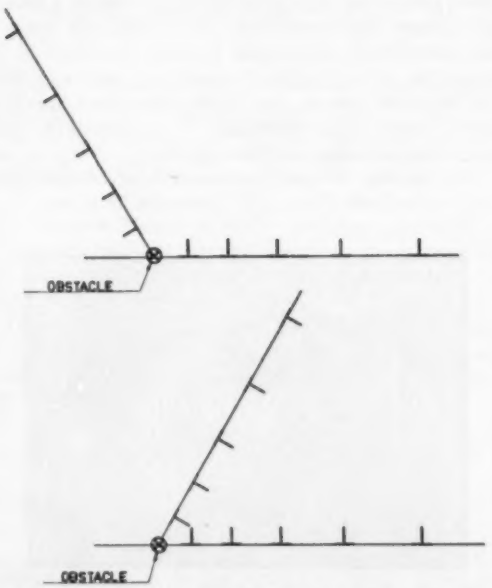

FIG. 21. Relief of stress in one pileup by glide on a second glide plane.

[17] J. D. Eshelby, F. C. Frank, and F. R. N. Nabarro, Phil. Mag. **42**, 351 (1951).
[18] G. Leibfried, Z. Physik **130**, 214 (1951).

FIG. 22. Interaction between dislocations in parallel glide planes. Note the tendency to take positions "one on top of the other." (180×)

F. Interaction between Dislocations in Parallel Glide Planes

It is clear from Fig. 22 that dislocations in parallel glide planes interact with one another. The distance over which interaction can be observed is larger than in most other substances as a consequence of the extreme hardness of silicon carbide.

The dislocations line up in a direction perpendicular to the glide planes. This is of course exactly what one would expect from theory if they are edge dislocations of the same sign. Since they also repel one another in their glide plane, the actual position may sometimes be a compromise, especially if unequal densities of dislocations are present in the parallel glide planes.

It is often observed that dislocations in one glide plane are held up by a grown-in dislocation in a nearby glide plane. This is visible in Fig. 6 where the obstacle has undoubtedly also helped. In some cases part of the procession of dislocations escaped past such a barrier, but since this relieves part of the stress along the glide plane, some of the following dislocations were held up by the same barrier. (See Fig. 23.)

In a number of cases opposite ends of different glide traces interfered. Since it is reasonable to assume that the shear stresses have been of the same sign along the two glide traces, it is clear that we now have to do with dislocations of opposite sign. (See Fig. 24.)

According to theory, two dislocations of opposite sign in parallel glide planes are in unstable equilibrium if they are "one on top of the other" and in stable equilibrium if the line connecting their positions is at 45° to the glide plane. This is true of course only if interaction with other dislocations in the same glide plane can be neglected. This however is not the case in Fig. 24, and it is clearly visible that the adopted positions are a compromise between the mutual repulsion in their glide planes and the tendency to adopt the equilibrium positions described. Some climb has taken place in Fig. 24 and in accordance with the assumption of dislocations of opposite sign, stresses induce climb in a sense that brings them closer together.

G. Origin of Flat-Bottomed Pits

The small and very shallow etch pits, which have the orientation II (see Fig. 2), are not found on all crystals. For most crystals on which they are present they exhibit curvilinear arrangement, which at first sight constitutes a fine scale substructure. They also form along scratches and along surface steps of such crystals.

It is well known that silicon-carbide crystals are often covered by a SiO_2 film which, according to the circumstances of formation, is crystobalite or tridymite. This film probably grows epitaxially since its (111) lattice planes fit with a small degree of misfit on the (0001) planes of SiC, as shown in Fig. 25. It is therefore suggested that the linear arrangements of pits probably mark defects in the SiO_2 film due to the differential contraction on cooling and in view of the small misfit. Since scratches and surface steps would be weak spots, it is natural that pits would form there too.

Figure 25 also shows that the close-packed directions of the SiO_2 film form angles of 30° with those of the SiC substrate. Since etching tends to develop pits with sides parallel to close-packed directions, this hypothesis

FIG. 23. Dislocations piled up against a barrier; some dislocations escaped past the barrier. (60×)

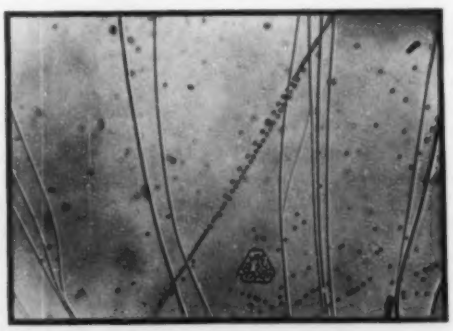

FIG. 24. Interaction between dislocations of opposite sign in parallel glide planes. (120×)

also explains the difference in orientation with dislocation etch pits.

IV. CONCLUSION

From the observations discussed here we are able to describe the various dislocations and glide elements in silicon carbide.

At least two different types of Burgers vectors are present: basal plane vectors and vectors having a component perpendicular to the c plane.

A. Dislocations Having Basal Plane Burgers' Vectors: $b=a[11\bar{2}0]$

Evidence for dislocations with $[11\bar{2}0]$ Burgers vectors was derived from the x-ray diffraction microscopy using selected diffraction vectors and from the absence of steps along slip traces as observed on the c plane by means of etch pits. Exact correspondence was established between the x-ray diffraction micrographs and pyramidal etch pits formed where dislocations intersect the crystal surface.

There are many dislocations in the basal plane, at least some of which are probably due to glide on this plane. There seems to be a preference for pure edge orientation although straight dislocations forming angles of 0°, 30°, and 60° with the Burgers vector are also common. However, many smoothly curved dislocations are evident. These dislocations were found by the x-ray method and by occasional observations of etch pits on prism faces.

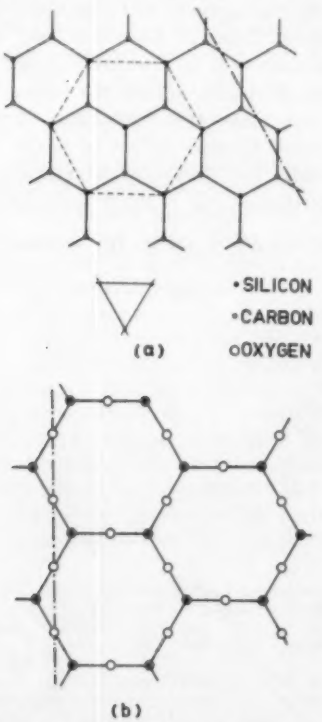

FIG. 25. Epitaxial relation between silicon carbide and silica film.

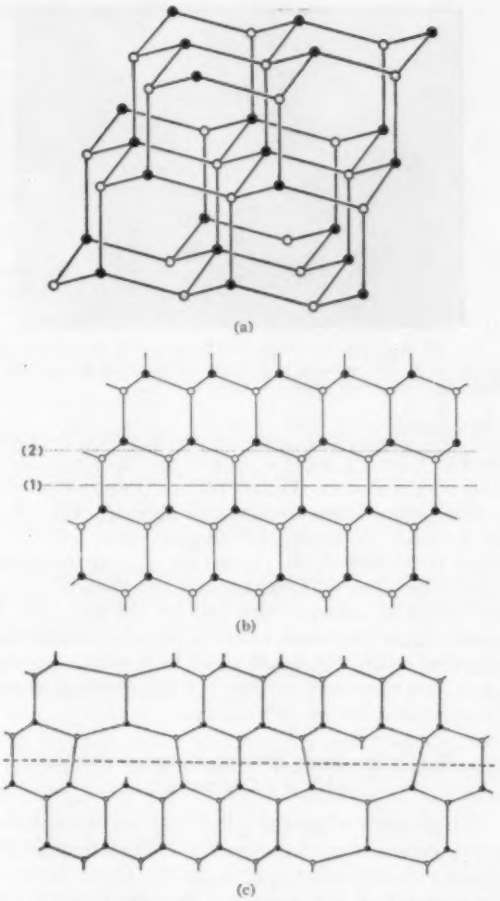

FIG. 26. Illustration of edge dislocations in the SiC structure. (a) Perspective view of the SiC lattice. (b) View of the two conceivable positions of the slip planes in SiC; only position (1) is likely. (c) Section of the two kinds of edge dislocations likely in SiC: in one case supplementary half-plane ends in a row of silicon atoms, the other in a row of carbon atoms.

Dislocations with the same $[11\bar{2}0]$ Burgers vectors in the basal plane are revealed intersecting the basal planes by both experimental methods. Slip traces give indication of pyramidal slip, the slip plane being the corrugated $(3\bar{3}01)$ pseudo plane composed of $(1\bar{1}01)$ and $(4\bar{4}01)$ strips as shown in Fig. 9. The slip vector is however in the same $[11\bar{2}0]$ direction. Therefore, in principle pencil-glide and cross-slip are possible in the SiC structure.

In view of the polar nature of the SiC structure, two types of dislocations can be distinguished. These are shown schematically in Fig. 26. Figure 26(a) represents

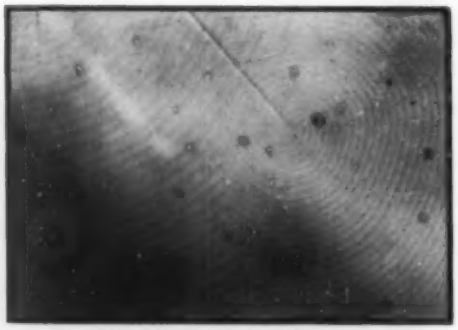

FIG. 27. Slip step on c face. The step ends in the center of a group of growth spirals. The indicated direction is parallel to the close packed row of atoms. (100×)

the SiC structure in space. Looking along the close-packed rows one sees the section shown in Fig. 26(b). The indicated lines (1) and (2) are traces either of a c (0001) plane in the 6H structure or of any (111) plane in the cubic modification. The glide plane will be located at the dashed line (1) and not, e.g., at the dotted line (2) because for the latter plane three bonds have to be broken in contrast with one for the first kind of plane. Figure 26(c) represents the two edge dislocations of opposite sign that would result from glide along this plane; it is clear that one ends in a row of silicon atoms, the other in a row of carbon atoms.

B. Dislocations Having Burgers Vectors with a c Component

The presence of growth spirals and the observations of slip steps on the c face (see Fig. 27) both require the presence of dislocations with a Burgers vector having a c component. It is known that the component in the c-direction of these dislocations, which is equal to the stepheight of the "elementary" growth spirals, is in general one third of the c-repeat distance for the rhombohedral types and $\frac{1}{2}c$ or c for the hexagonal types.

The traces on the c plane of the glide planes associated with this Burgers vector are parallel to the $[11\bar{2}0]$ direction; its indices could not be determined.

Hamilton[19] has determined the magnitude of the [0001] component of the Burgers vector of axial dislocations in some 4H type silicon carbide whiskers from measurements of the corresponding lattice twists. These observations lead to c components of Burgers vectors in agreement with those found from the step height of growth spirals. Our x-ray diffraction microscopy studies of the screw dislocation in an especially large 4H whisker grown by Hamilton showed no contrast associated with the axial dislocation on diffracting from $(11\bar{2}0)$, $(1\bar{2}10)$, and $(\bar{2}110)$ planes but showed clear contrast on diffracting from (0004) planes. This indicates that the axial dislocation is purely screw with a [0001] Burgers vector. The same Burgers vector direction should occur in the 6H structure.

ACKNOWLEDGMENTS

Two of us (S. Amelinckx and G. Strumane) would like to thank Professor W. Dekeyser for his interest and I.R.S.I.A. for support of this work. We would like to thank the management of Union Carbide Corporation, European Research Associates, and the Gordon Research Conferences for the various opportunities for meeting and discussion in both the United States and Belgium that made this transatlantic collaboration possible. It is a pleasure for one of us (W. W. Webb) to acknowledge the inspired cooperation and assistance of N. P. Bertolone on all of the x-ray experiments.

[19] D. R. Hamilton, J. Appl. Phys. 31, 112 (1960).

Three-Dimensional Space Charge Flow*

JORGE ROSENBLATT
Comisión Nacional de Energía Atómica, Buenos Aires, Argentina
(Received January 27, 1960; and in final form April 12, 1960)

The general theory of stationary beams of prescribed shape is developed taking into account the electrostatic interaction between the particles. The Hamilton-Jacobi equation, expressed in a particular system of coordinates, allows the determination of the potential distribution inside the beam. Compatibility conditions for the equations are obtained, as well as a general rule for the determination of the feasibility of arbitrarily chosen trajectories. A theoretical expression results for the proportionality coefficient k in Child's law ($J=kV^{\frac{3}{2}}$) which relates current density J with the potential difference V between electrodes. The theory was applied to the particular case of a plane beam with hyperbolic boundaries. The beam was experimentally reproduced, providing values for k in close agreement with the theoretical ones.

INTRODUCTION

THE effects of space charge on electron or ion beams have not been exactly calculated except for simple cases.[1-3] Assuming rectilinear motion, Pierce[4] obtained the potential distributions for beams bounded in space and was able to find by analytical means, or with the aid of an electrolytic trough, the equipotential surfaces in the region devoid of space charge. This means, in effect, that an assumption must be made about the shape of a beam to obtain the electrodes which produce it. A noniterative method[5] has also been described to plot equipotentials in cases of axial symmetry.

Spangenberg[6] has pointed out the importance of the action function to obtain a general equation for three-dimensional beams. It is, in vector form,

$$\nabla\cdot(\nabla^2 W\cdot\nabla W)=0, \tag{1}$$

where W is the action function (Hamilton's characteristic function). However, Spangenberg was unable to solve cases other than the one-dimensional (rectilinear) one. Expansion of the vector operators for the x, y coordinates provides a 22-term fourth order, third degree partial differential equations.

We shall presently show how Eq. (1) can be generally solved, and how, at least in principle, the potential distribution inside the beam can be found once the shape of the beam is assumed to be known. This means that certain trajectories (subject to conditions which will be derived later on) are imposed, as Pierce did in the particular rectilinear case. Knowledge of the inside potential then allows the determination of the external electrodes. Thus, the production of beams of any (allowed) shape can be considered as a theoretically solved problem, but may still remain as a mathematical and technical difficulty.

In what follows we shall treat only electrostatic interactions, neglecting relativistic effects[7] such as the magnetic force exerted by the beam on itself.

THE ELECTROSTATIC POTENTIAL INSIDE THE BEAM

We *impose* a certain family of curves as the possible paths of the particles in the beam. Each of these curves is given by two equations

$$g(x,y,z)=\eta \tag{2a}$$

$$h(x,y,z)=\zeta. \tag{2b}$$

The variation of the parameters η and ζ describes the whole family. Now suppose that $g(x,y,z)$ and $h(x,y,z)$ are such that we can form an orthongonal system of coordinates (ξ,η,ζ) with $\xi=f(x,y,z)$; in which, obviously, a trajectory is defined by

$$\eta=\text{const}, \tag{3a}$$

$$\zeta=\text{const}, \tag{3b}$$

and $f(x,y,z)$ is found from the requirement that $\xi=$const is the equation for the orthogonal surfaces to the family of curves. In this coordinate system, (1) η and ζ are constants of the motion and (2) the corresponding conjugate momenta are cyclic variables in the Hamiltonian of a particle. The Hamilton-Jacobi equation for such a particle should be written

$$H(\xi,\eta,\zeta,dW/d\xi)=E, \tag{4}$$

where E is the total energy of the particle. The action function depends only on the coordinate ξ. This is another way of stating the well-known fact that the surfaces $W=$const are normal to the trajectory of the particle.

Let $ds^2=h_1^2d\xi^2+h_2^2d\eta^2+h_3^2d\zeta^2$ be the line element in our coordinate system. The kinetic energy of a particle moving along the coordinate line ξ is

$$T=\tfrac{1}{2}p^2/mh_1^2,$$

* Based on a thesis submitted to the Universidad Nacional de La Plata in partial fulfillment of the requirements for the degree of Doctor in Physical Sciences.

[1] C. E. Fay, A. L. Samuel, and W. Shockley, Bell System Tech. J. **17**, 49 (1938).
[2] I. Langmuir and K. Blodgett, Phys. Rev. **22**, 374 (1923).
[3] I. Langmuir and K. Blodgett, Phys. Rev. **24**, 49 (1924).
[4] J. R. Pierce, J. Appl. Phys. **11**, 548 (1940).
[5] Kuo-Chu Ho and R. J. Moon, J. Appl. Phys. **24**, 1186 (1953).
[6] K. Spangenberg, J. Franklin Inst. **232**, 365 (1941).
[7] R. D. Fowler and G. E. Gibson, Phys. Rev. **46**, 1083 (1934).

where p is the conjugate momentum to the coordinate ξ. We can write explicitly, instead of Eq. (4),

$$q\varphi+(1/2mh_1^2)(dW/d\xi)^2=E; \tag{5}$$

in which φ is the electrostatic potential; q and m, the charge and mass of the particles. It can be assumed without restriction that $E=0$, and then

$$\varphi=-\Phi/h_1^2, \tag{6}$$

where $\Phi=(1/2qm)(dW/d\xi)^2$ *depends only on* ξ.

We have thus reduced the problem of finding the electrostatic potential to that of calculating a function Φ *of only one variable* ξ. In order to do this, let us apply the Laplacian operator to both members of Eq. (6). From Poisson's equation

$$\nabla^2(-\Phi/h_1^2)=-J/v\epsilon_0. \tag{7}$$

We are using the mks system throughout this paper. J is the current density and v the velocity of the particles. But

$$\mathbf{v}=(1/m)\nabla W \tag{8a}$$

and

$$v=(1/mh_1)(dW/d\xi)=(1/h_1)[(2q/m)\Phi]^{\frac{1}{2}}. \tag{8b}$$

Therefore,

$$J=\epsilon_0[(2q/m)\Phi]^{\frac{1}{2}}(1/h_1)\nabla^2(\Phi/h_1^2). \tag{9}$$

The fact that $\nabla\cdot\mathbf{J}=0$ in the steady state can be expressed as

$$(\partial/\partial\xi)[h_2h_3(\Phi^{\frac{1}{2}}/h_1)\nabla^2(\Phi/h_1^2)]=0 \tag{10}$$

because the only component different from zero in $\mathbf{J}$ is in the direction of ξ. Equation (10) is essentially the same as Eq. (1), and has been obtained by similar steps. However, our particular choice of coordinate system enables us not only to express it directly in scalar form but to proceed immediately to a first integration,

$$(\Phi^{\frac{1}{2}}/h_1)\nabla^2(\Phi/h_1^2)=K(\eta,\zeta)/h_2h_3. \tag{11}$$

The function $K(\eta,\zeta)$ results from the partial integration of Eq. (10). Equation (9) shows its physical meaning: the right-hand member of Eq. (11) is proportional to the current density J.

When the Laplacian operator in Eq. (11) is expanded, one obtains

$$\nabla^2(\Phi/h_1^2)=(1/h_1^2)\nabla^2\Phi+2\nabla(1/h_1^2)\cdot\nabla\Phi+\Phi\nabla^2(1/h_1^2),$$

where, in turn

$$\nabla^2\Phi=(1/h_1h_2h_3)(\partial/\partial\xi)[(h_2h_3/h_1)\Phi'],$$

and

$$2\nabla\Phi\cdot\nabla(1/h_1^2)=(2/h_1^2)\Phi'(\partial/\partial\xi)(1/h_1^2)=\Phi'(\partial/\partial\xi)(1/h_1^4).$$

The primes denote total differentiation with respect to ξ. These expressions result in

$$\frac{h_2h_3}{h_1}\nabla^2\left(\frac{\Phi}{h_1^2}\right)=\frac{1}{h_1^4}\frac{\partial}{\partial\xi}\left(\frac{h_2h_3}{h_1}\Phi'\right)+\frac{h_2h_3}{h_1}\Phi'\frac{\partial}{\partial\xi}\left(\frac{1}{h_1^4}\right)+\Phi\frac{h_2h_3}{h_1}\nabla^2\left(\frac{1}{h_1^2}\right)$$

$$=\frac{\partial}{\partial\xi}\left(\frac{h_2h_3}{h_1^5}\Phi'\right)+\Phi\frac{h_2h_3}{h_1}\nabla^2\left(\frac{1}{h_1^2}\right).$$

When this equation is placed in Eq. (11), the latter is transformed into

$$\Phi^{\frac{1}{2}}[(\partial/\partial\xi)(A\Phi')+B\Phi]=K(\eta,\zeta), \tag{12}$$

where the functions A and B are given by

$$A=h_2h_3/h_1^5 \tag{13a}$$

$$B=(h_2h_3/h_1)\nabla^2(1/h_1^2). \tag{13b}$$

COMPATIBILITY AND SOLUTION OF THE FUNDAMENTAL EQUATION

We have now derived a differential equation [Eq. (12)] with *two* unknown functions in which Φ depends only on ξ; and K, on the two other coordinates. The fact that the left-hand member of Eq. (12) depends upon the three coordinates and the right-hand one, upon only two, indicates *a priori* that the functions A and B cannot be arbitrarily chosen; that is, certain conditions must hold for the allowed trajectories (which ultimately determine the h_i's and thus, A and B).

We shall now show how these "compatibility conditions" can be obtained and provide the solution for Φ. For the sake of brevity in our formulas we shall derive them for a two-dimensional case with coordinates (ξ,η). The extension to three dimensions is immediate.

It is easily shown that Eq. (12) is equivalent to a system of first-order partial differential equations. In fact, defining a new function by $\Psi=A\Phi'$, the system is

$$\partial\Phi/\partial\xi=\Psi/A \tag{14a}$$

$$\partial\Psi/\partial\xi=(K/\Phi^{\frac{1}{2}})-B\Phi \tag{14b}$$

$$\partial K/\partial\xi=0 \tag{14c}$$

$$\partial\Phi/\partial\eta=0. \tag{14d}$$

From these equations, the following two can be derived:

$$\partial\Psi/\partial\eta=\Psi\partial\ln A/\partial\eta, \tag{14e}$$

$$\frac{\partial K}{\partial\eta}=\left[\left(\frac{\partial^2\ln A}{\partial\xi\partial\eta}\right)\Psi+\left(\frac{K}{\Phi^{\frac{1}{2}}}-B\Phi\right)\frac{\partial\ln A}{\partial\eta}+\Phi\frac{\partial B}{\partial\eta}\right]\Phi^{\frac{1}{2}}. \tag{14f}$$

Equations (14) allow us to write the total differentials of the functions Ψ, Φ and K,

$$d\Psi=[(K/\Phi^{\frac{1}{2}})-B\Phi]d\xi+\Psi(\partial\ln A/\partial\eta)d\eta \tag{15a}$$

$$d\Phi=(\Psi/A)d\xi \tag{15b}$$

$$dK=\Phi^{\frac{1}{2}}\left[\Psi\frac{\partial^2\ln A}{\partial\xi\partial\eta}+\left(\frac{K}{\Phi^{\frac{1}{2}}}-B\Phi\right)\frac{\partial\ln A}{\partial\eta}+\Phi\frac{\partial B}{\partial\eta}\right]d\eta. \tag{15c}$$

Now the necessary and sufficient condition for an expression

$$f(\xi,\eta,\omega)d\xi+g(\xi,\eta,\omega)d\eta$$

to be an exact differential $d\omega$ is that

$$(\partial f/\partial\eta)+(\partial f/\partial\omega)g=(\partial g/\partial\xi)+(\partial g/\partial\omega)f.$$

If similar conditions hold identically for the differential coefficients in the right-hand members of Eqs. (15) once the derivatives of the functions are replaced by its expressions given by the system (14), this system will be compatible. Accordingly, the restrictions on the functions A and B shall be found.

The integrability conditions, when applied to Eqs. (15), provide identities except for Eq. (15c). In this case one obtains, after some algebraic manipulations,

$$4\Phi\left(\frac{K}{\Phi^{\frac{1}{2}}}-B\Phi\right)\frac{\partial^2\ln A}{\partial\xi\partial\eta}+\frac{\Psi^2}{A}\frac{\partial^2\ln A}{\partial\xi\partial\eta}+\Psi\Phi\left[3\frac{(\partial B/\partial\eta)-B(\partial\ln A/\partial\eta)}{A}+2\frac{\partial^2\ln A}{\partial\xi^2\partial\eta}\right]+2\Phi^2\left(\frac{\partial^2 B}{\partial\xi\partial\eta}-\frac{\partial B}{\partial\xi}\frac{\partial\ln A}{\partial\eta}\right)=0. \tag{16}$$

If we let $\partial^2\ln A/\partial\xi\partial\eta=0$, then A can be written as the product of two functions

$$A=X(\xi)Y(\eta).$$

Also, if the definition of Ψ is taken into account, we can now write instead of Eq. (16), that

$$\Phi'/\Phi=-\tfrac{2}{3}(\partial/\partial\xi)\ln[(\partial B/\partial\eta)-BY'/Y]. \tag{17}$$

This equation has meaning only if the right-hand member is a function of the single variable ξ. In such a case, Eq. (17) can be immediately integrated, yielding

$$\Phi=\Phi_0[L(\xi)]^{-\frac{1}{2}}. \tag{18}$$

Here Φ_0 is a constant and $L(\xi)$ appears in

$$(\partial/\partial\eta)(B/Y)=L(\xi)M(\eta), \tag{19}$$

the necessary condition, with $M(\eta)$ an arbitrary function, in order that the right-hand member of Eq. (17) depend only on ξ. Conversely, if Eq. (19) holds, the compatibility of our system is assured with the solution (18).

Suppose now $\partial^2\ln A/\partial\xi\partial\eta\neq0$. We can eliminate K between Eqs. (16) and (14b) and form a new system with only two unknown functions, Φ and Ψ,

$$\partial\Phi/\partial\xi=\Psi/A \tag{20a}$$

$$\partial\Phi/\partial\eta=0 \tag{20b}$$

$$\frac{\partial\Psi}{\partial\xi}=-\left\{\frac{\Psi^2}{4A\Phi}+\frac{\Psi}{4A}\times\frac{3[(\partial B/\partial\eta)-B(\partial\ln A/\partial\eta)]+2A(\partial^3\ln A/\partial\xi^2\partial\eta)}{(\partial^2\ln A/\partial\xi\partial\eta)}+\frac{\Phi}{2}\frac{(\partial^2 B/\partial\xi\partial\eta)-(\partial B/\partial\xi)(\partial\ln A/\partial\eta)}{(\partial^2\ln A/\partial\xi\partial\eta)}\right\} \tag{20c}$$

$$\partial\Psi/\partial\eta=\Psi(\partial\ln A/\partial\eta), \tag{20d}$$

to which similar integrability conditions can be applied. We obtain, after some tedious but straightforward algebra, the condition that

$$\frac{2\left[\dfrac{\partial^2 B}{\partial\xi\partial\eta}\dfrac{\partial B}{\partial\xi}\dfrac{\partial\ln A}{\partial\eta}\Big/(\partial^2\ln A/\partial\xi\partial\eta)\cdot\dfrac{\partial\ln A}{\partial\eta}-\dfrac{\partial}{\partial\eta}\left[\dfrac{\partial^2 B}{\partial\xi\partial\eta}\dfrac{\partial B}{\partial\xi}\dfrac{\partial\ln A}{\partial\eta}\Big/(\partial^2\ln A/\partial\xi\partial\eta)\right]\right]}{\dfrac{\partial}{\partial\eta}\left[\dfrac{3\left(\dfrac{\partial B}{\partial\eta}-B\dfrac{\partial\ln A}{\partial\eta}\right)+2A\dfrac{\partial^3\ln A}{\partial\xi^2\partial\eta}}{(\partial^2\ln A/\partial\xi\partial\eta)}\right]-\dfrac{3\left(\dfrac{\partial B}{\partial\eta}-B\dfrac{\partial\ln A}{\partial\eta}\right)+2A\dfrac{\partial^3\ln A}{\partial\xi^2\partial\eta}}{(\partial^2\ln A/\partial\xi\partial\eta)}\cdot\dfrac{\partial\ln A}{\partial\eta}+4A\dfrac{\partial^2\ln A}{\partial\xi\partial\eta}}=F(\xi) \tag{21}$$

must be a function of the only variable ξ. In such a case Φ satisfies the differential equation

$$\Phi'/\Phi=F(\xi) \tag{22}$$

with the general solution

$$\Phi=\Phi_0 e^{\int F(\xi)d\xi}, \tag{23}$$

where Φ_0 is an arbitrary constant.

CHILD'S LAW

The dependence of current density on the three-halves power of the potential difference between electrodes is one of the well-established facts of space-charge flow of any type. It was derived theoretically by Child[8] for rectilinear flow between parallel plane

[8] C. D. Child, Phys. Rev. **23**, 492 (1911).

electrodes. It will be shown how the expressions obtained indicate its general validity, and how the proportionality coefficient depends upon the particular shape of the beam. In fact, replacement of (23) in (12) gives

$$K=\Phi_0^{\frac{1}{2}}e^{\frac{1}{2}}\int F(\xi)d\xi\left[A(F'+F^2)+F\frac{\partial A}{\partial\xi}+B\right]. \quad (24)$$

Equation (24) together with (6) and the aforementioned meaning of K, gives for the current density in the three-dimensional case

$$J=\epsilon_0(2q/m)^{\frac{1}{2}}(h_1^2/h_2h_3)[A(F'+F^2)+F(\partial A/\partial\xi)+B]\varphi^{\frac{1}{2}}. \quad (25)$$

The metric coefficients, as well as the whole expression in square brackets appearing in Eq. (25), depend only on the geometry of the coordinate system in use, that is, on the *shape* of the beam. If φ is the potential difference between electrodes, Eq. (25) allows the determination of the proportionality coefficient between the current density and the three-halves power of the accelerating potential.

Unfortunately, the validity of Eq. (25) cannot be checked against the already known solutions of rectilinear motion between parallel plane electrodes, concentric cylinders, and concentric spheres. In fact, Eq. (16) holds identically for such cases, and the function $F(\xi)$ cannot be calculated. On the other hand, one obtains from Eq. (12) the already known equations for the potential.

For the foregoing reasons, the theory was applied to a particular case with the view of its experimental reproduction.

POTENTIAL DISTRIBUTION FOR A PARTICULAR BEAM

Let us consider an electron beam with hyperbolic paths. The beam is supposed unbounded in the z direction. The equation for the trajectories is

$$xy=\eta, \quad (26)$$

where η is a constant for each trajectory. The family of orthogonal trajectories is given by the equation

$$\tfrac{1}{2}(x^2-y^2)=\xi=\text{const}. \quad (27)$$

In the coordinate system ξ, η, the metric coefficients are

$$h_1^2=h_2^2=(x^2+y^2)^{-1}=\tfrac{1}{2}(\xi^2+\eta^2)^{-1} \quad \text{and} \quad h_3=1.$$

Formulas (13) now give

$$A=4(\xi^2+\eta^2); \qquad B=4$$

and Eq. (21) shows immediately that $F(\xi)=0$. Then, by Eq. (23),

$$\Phi=\Phi_0=\text{const}.$$

For the potential distribution inside the beam, we have from Eq. (6)

$$\varphi=-\Phi_0(x^2+y^2)=-\Phi_0r^2. \quad (28)$$

The constant Φ_0 is negative for electrons. In Eq. (28), r is the distance from the z axis to the point under under consideration. The equipotentials are concentric cylinders.

According to Eq. (25), the current density is

$$J=4\epsilon_0(2q/m)^{\frac{1}{2}}(\varphi^{\frac{1}{2}}/r^2). \quad (29)$$

To obtain it in vector form we first calculate the charge density ρ from Eq. (28) by application of the Laplacian operator

$$\rho=4\epsilon_0\Phi_0. \quad (30)$$

The action function W follows from the definition of Φ by integration

$$W=(2qm\Phi_0)^{\frac{1}{2}}\xi+\text{const},$$

and because of Eqs. (8a) and (27) the velocity is given by

$$\mathbf{v}=(2q\Phi_0/m)^{\frac{1}{2}}(x\mathbf{i}-y\mathbf{j}). \quad (31)$$

Multiplication of (30) and (31) gives

$$\mathbf{J}=\rho\mathbf{v}=4\epsilon_0\Phi_0^{\frac{1}{2}}(2q/m)^{\frac{1}{2}}(x\mathbf{i}-y\mathbf{j}). \quad (32)$$

Now suppose our beam is not unbounded in the x, y plane, but is limited by the hyperbolic cylinders $xy=\lambda$ and $xy=-\lambda$ and the plane $x=0$. This is shown by the dotted curves of Fig. 1. In such a case the total current (per unit length in the z direction) is

$$I=\int_{-\lambda/x}^{\lambda/x}J_x\,dy=8\epsilon_0\Phi_0^{\frac{1}{2}}(2q/m)^{\frac{1}{2}}\lambda. \quad (33)$$

In the case illustrated in Fig. 2, the lower limit of integration must be 0, and we have

$$I=\int_{0}^{\lambda/x}J_x\,dy=4\epsilon_0\Phi_0^{\frac{1}{2}}(2q/m)^{\frac{1}{2}}\lambda. \quad (34)$$

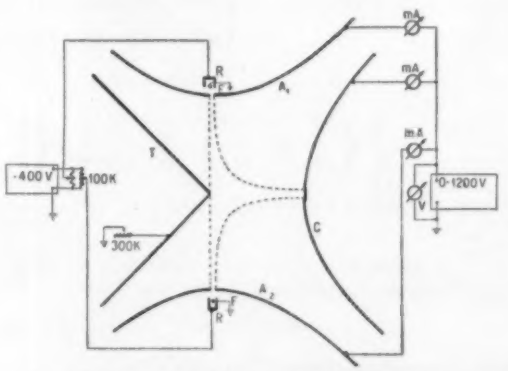

FIG. 1. Beam shape and electrical connections in the first experiment performed. The dotted curves show predicted beam limits. A_1, A_2, and C are high-tension electrodes. R, electron reflectors. F, filaments. T, grounded electrode.

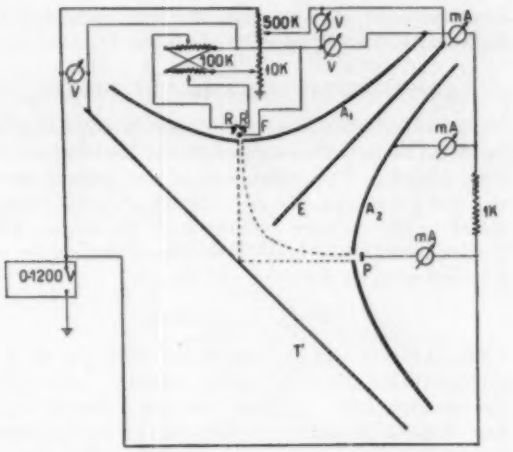

FIG. 2. Beam shape and electrical connections in the second experiment performed. The dotted curves show predicted beam limits. A_1 and A_2 are high-tension electrodes. P, collector plate. R and R', electron reflectors. F, filament. T', low-tension electrode. E, intermediate-tension electrode.

ELECTRODE ARRANGEMENT

The electrodes producing our particular beam must be equipotential surfaces in the region outside the beam. The mathematical problem involved is then the solution of Laplace's equation for the potential. The boundary conditions result from continuity of the potential and its normal derivative; this last requirement is a consequence of the fact that the centrifugal force on an electron depends only upon the velocity and the curvature of the path, irrespective of whether it is a boundary or an internal one.

Let us define now

$$u=\xi \qquad v=\eta-\lambda$$
$$w=u+iv \qquad w^*=u-iv.$$

The region devoid of charge corresponds to the half-plane $v>0$ in the complex plane w. The solution of Laplace's equation is then[9]

$$\varphi(u,v)=\mathrm{Re}\,\varphi_0(w)+\mathrm{Im}\int_0^w N_0(\zeta)\,d\zeta \tag{35}$$

with the following boundary conditions:

$$\varphi_0(u)=\varphi(u,0)=-2\Phi_0(u^2+\lambda^2)^{\frac{1}{2}} \tag{36a}$$

$$N_0(u)=\partial\varphi/\partial v\big]_{v=0}=-2\Phi_0\lambda/(u^2+\lambda^2)^{\frac{1}{2}}. \tag{36b}$$

Expressions (35) and (36) allow the calculation of the function φ.

$$\varphi=-2\Phi_0\Big\{1/\sqrt{2}\big[\{(u^2+\lambda^2-v^2)^2+4u^2v^2\}^{\frac{1}{2}}+(u^2+\lambda^2-v^2)\big]^{\frac{1}{2}}$$
$$+\lambda\,\mathrm{tg}^{-1}\frac{v+(1/\sqrt{2})\big[\{(u^2+\lambda^2-v^2)^2+4u^2v^2\}^{\frac{1}{2}}-(u^2+\lambda^2-v^2)\big]^{\frac{1}{2}}}{u+(1/\sqrt{2})\big[\{(u^2+\lambda^2-v^2)^2+4u^2v^2\}^{\frac{1}{2}}+(u^2+\lambda^2-v^2)\big]^{\frac{1}{2}}}\Big\}. \tag{37}$$

We have thus obtained the potential distribution for the region devoid of charge of the first quadrant in the x, y plane. For a beam like the one illustrated in Fig. 1, it is evident from symmetry arguments that the same distribution holds in the fourth quadrant. The boundary conditions for the other two quadrants are

$$\varphi_0(y)=-\Phi_0y^2$$
$$N_0(y)=\partial\varphi/\partial x\big]_{x=0}=0,$$

and we obtain for the potential

$$\varphi(x,y)=\mathrm{Re}\,\varphi_0(y+ix)=-\Phi_0(y^2-x^2).$$

The equipotentials are equilateral hyperbolas, whose asymptotes correspond to the equipotential $\varphi=0$.

A similar argument holds for the fourth quadrant in the case of Fig. 2. The potential is

$$\varphi=-\Phi_0(x^2-y^2).$$

We have still to plot the equipotential surfaces corresponding to (37). We shall obtain a parametric representation of them. The parameter will be

$$\alpha=\mathrm{tg}^{-1}\frac{v+(1/\sqrt{2})\{\big[(u^2+\lambda^2-v^2)^2+4u^2v^2\big]^{\frac{1}{2}}-(u^2+\lambda^2-v^2)\}^{\frac{1}{2}}}{u+(1/\sqrt{2})\{\big[(u^2+\lambda^2-v^2)^2+4u^2v^2\big]^{\frac{1}{2}}+(u^2+\lambda^2-v^2)\}^{\frac{1}{2}}}. \tag{38}$$

If we express the potential as

$$\varphi=-2\Phi_0\lambda\psi,$$

with ψ a dimensionless variable, and then multiply (37) and $\mathrm{tg}\alpha$ [given by (38)], we obtain the parametric equation for v

$$v=\lambda(\psi-\alpha)\mathrm{tg}\alpha. \tag{39}$$

Similarly, the parametric expression for u is given by

$$u=\pm\lambda\big[(\psi-\alpha)^2-\cos^2\alpha\big]^{\frac{1}{2}}. \tag{40}$$

It is easily seen that $0\leqslant\alpha\leqslant\psi$ if $\psi\leqslant\pi/2$ and $0\leqslant\alpha\leqslant\pi/2$ if $\psi>\pi/2$. Moreover $\psi\geqslant1$. The justification for the

[9] P. M. Morse and H. Feshbach, *Methods of Theoretical Physics* (McGraw-Hill Book Company, Inc., New York, 1953), Vol. 1, p. 689.

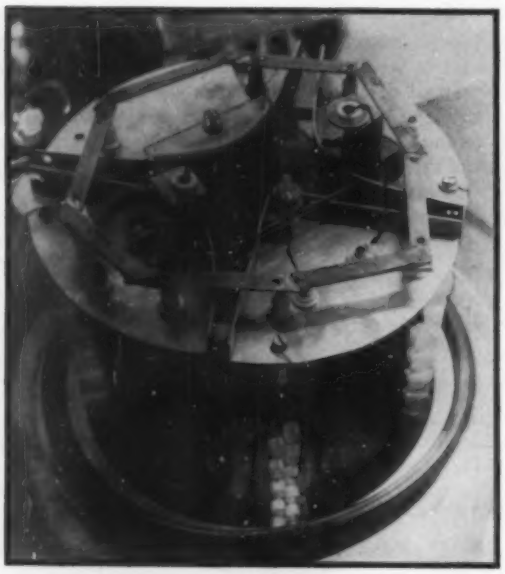

(a)

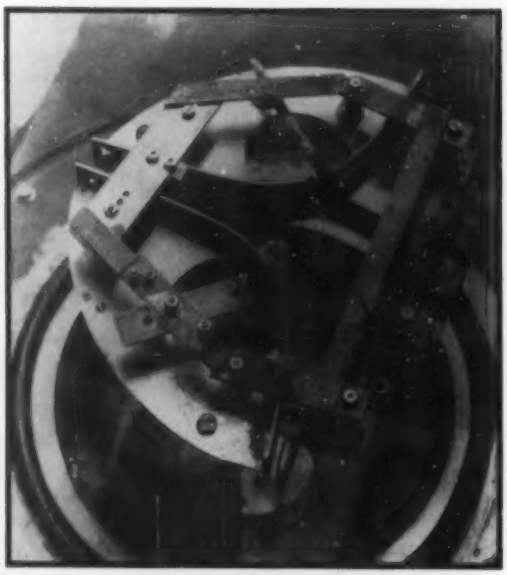

(b)

FIG. 3. Electrode arrangements. (a) First experiment, corresponding to Fig. 1. (b) Second experiment, corresponding to Fig. 2. In case (b), the crystal plates were taken off before photographing.

additional electrode E of Fig. 2, corresponding to $\psi=\pi/2$, arises from the fact that when α varies from 0 to $\pi/2$, v varies from 0 to ∞, unless $\psi=\pi/2$. In that case $u\to 0$ when $\alpha\to\pi/2$, and v can be made to tend to any value from λ to infinity when ψ approaches $\pi/2$ from the right. The electrode E corresponds then to the conditions $u=0$, $\lambda\leqslant v<\infty$, $\psi=\pi/2$.

EXPERIMENTAL CHECK OF THE THEORY

Two experiments were performed corresponding to predicted beam limits as shown by the dotted curves of Figs. 1 and 2. The equipotentials were plotted from the above formulas. The electrodes A_1, A_2 and C correspond to the distance $r=5$ cm from the origin. The particular choice $\lambda=1$ cm^2 allows the determination of ψ according to its definition and Eq. (28)

$$\psi=r^2/(2\lambda)=12.5.$$

Through slits 3.2 cm high and 2 mm wide, a beam 3.2 cm high (in the z direction) was produced by collimating the electrons from thoriated-tungsten filaments F in Figs. 1 and 2. In order to reduce edge effects the beam was made to flow between two parallel crystal plates; their job was to become electrically charged until they were able to repel any electron tending to deviate from the plane path. These plates as well as the electrode arrangements of both experiments can be seen in the photographs of Fig. 3.

In the first experiment U-shaped, negative electrodes (R in Fig. 1) surrounded the filaments, and were used as electron reflectors. By properly adjusting the potential of the electrodes, it was possible (1) to reduce to a minimum the currents to A_1 and A_2 and (2) to obtain a close agreement between experimental and theoretical values of current in C for *one* value of the potential in electrodes A_1, A_2 and C. From then on the tension in R remained fixed and the accordance was conserved for other values of tension in A_1, A_2, C. Variation of the 300 kΩ resistance connected to the grounded electrode T produced no change in the collected current, showing that no measurable current was flowing through it. Of course, a complete proof of the theory could only be achieved if it could be known that the electrons escaping from the slits in A_1 and A_2 had not only the correct magnitude of the velocity but also the proper *direction*. Nevertheless, the very fact that the expected current was obtained is a qualitative verification of the theory. Moreover, Eq. (25) is verified by the calculation of a least-square value of $I/V^{\frac{1}{2}}$

$$(I/V^{\frac{1}{2}})_{\text{exp}}=(11.2\pm 0.1)\times 10^{-7}\text{amp}/(\text{v})^{\frac{1}{2}}.$$

This can be compared with the theoretical value obtained from Eq. (33),

$$(I/V^{\frac{1}{2}})_{\text{theor}}=10.76\times 10^{-7}\text{ amp}/(\text{v})^{\frac{1}{2}}.$$

The deviation observed can be ascribed to: (1) edge effects not completely removed by the crystal plates; (2) unavoidable mechanical misalignments; (3) the fixed tension of R producing a different over-all effect for different values of tension in A_1 and A_2.

The second experiment, schematically shown in Fig. 2, was designed to obtain information also about

the *shape* of the beam. This was done by collecting a considerable fraction of the beam in a plate (P on Fig. 2) after the slit of A_2. To obtain a differential effect on the beam, variable with the total current emitted by the filament, the reflectors R were replaced by two plates R and R′, connected as shown in Fig. 2. From the experimental results the following value has been obtained:

$$(I/V^{\frac{3}{2}})_{\text{exp}} = (5.5 \pm 0.2) \times 10^{-7} \text{ amp}/(\text{v})^{\frac{3}{2}}.$$

This is in close agreement with

$$(I/V^{\frac{3}{2}})_{\text{theor}} = 5.38 \times 10^{-7} \text{ amp}/(\text{v})^{\frac{3}{2}}.$$

A further evidence of the correctness of the theory is derived from the large fraction (30%) of the total current emitted from the slit in A_1 collected in the electrode P; moreover, less than 0.2% of that current reached the electrode E. It was, therefore, concluded that the shape of the beam was very close to the predicted one.

ACKNOWLEDGMENTS

The author wants to express his thanks to Dr. J. G. Roederer for his continued support and helpful discussions, to Dr. E. Roxin for his useful suggestions, and to S. V. Tejero for his skillful assistance in preparing the experiments.

JOURNAL OF APPLIED PHYSICS VOLUME 31, NUMBER 8 AUGUST, 1960

Stress Waves in Solids*

C. R. CASSITY†
Research and Development Division, New Mexico Institute of Mining and Technology, Socorro, New Mexico
(Received October 28, 1959; and in final form March 28, 1960)

Several experimental tests dealing with the effects of stress waves initiated in solids by high explosives or by impacts are described. The tests indicate that stress waves which are initiated solely as compression commonly acquire tensile components which are not due to reflections.

I. INTRODUCTION

THE present work concerns the effects of stress waves initiated in solids by explosives or by impacts. Most of the stress waves were initiated by detonating the explosive C-3 in direct contact with the solid; but in a few cases the explosives C-4 or TNT, or impact of solid upon solid at relative velocities of several thousand feet per second were used. Much of the work has immediate ordnance applications, and most of it developed from questions raised in ordnance. However, the tests and results *per se* are fundamental in nature.

This work was begun before Rinehart and Pearson's book[1] was published, but much of their early work was known through other publications and has influenced these experiments both before and since the publication of the book. Those tests and results which are described herein were selected solely because they appear to be unusual or not well-known.

II. DESCRIPTION OF TESTS

1. One of the first experiments in which the results differed from those of Rinehart is sketched in Fig. 1 and should be compared with Fig. 10 of Rinehart.[2] His statement is " . . . if . . . a solid steel rod is coated with a thin layer of explosive, and the explosive is detonated, the rod fragmentizes as though it had been blown outward by a high pressure originating along the axis of the rod. . . . In this case, the explosive was ¼ in. thick and the rod was of mild steel, 1 in. in diam. Increasing the thickness of the explosive, and hence the magnitude of the stress as well as its duration, causes the rod to fragmentize into even finer pieces." A number

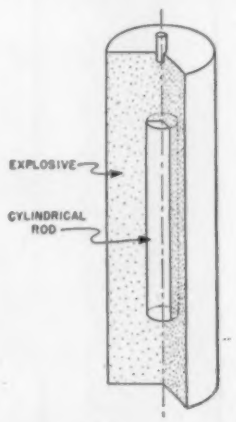

FIG. 1. Metal rod and surrounding explosive.

* The results presented in this paper were obtained under a contract with the Bureau of Ordnance, U. S. Navy Department.
† Now at Space Sciences Laboratory, Missile and Space Vehicle Department, General Electric Company, Philadelphia, Pennsylvania.
[1] John S. Rinehart and John Pearson, *Behavior of Metals Under Impulsive Loads* (American Society for Metals, Cleveland, Ohio, 1954).
[2] John S. Rinehart, Navord Rept. 1183 (1949).

FIG. 2. Cross sections of recovered mild-steel plates. Left: 2½-in. thickness of explosive on each side of plate. Center: 2-in. thickness of explosive on each side of plate. Right: 1½-in. thickness of explosive on each side of plate (only half of plate is shown).

of experiments have established that a "thin" layer of explosive (specifically C-3) is a layer thinner than the diameter of the mild steel rod. In fact, a mild steel rod remains intact if the explosive is thicker than the diameter of the rod. Similarly, a flat steel plate whose two faces are covered with layers of explosive splits if, and only if, the thickness of the explosive layer is less than the thickness of the plate. This is shown in Fig. 2 which shows the cross sections of three 2-in. thick plates whose faces had been covered with 2½-, 2-, and 1½-in. thicknesses of explosive.

2. An interesting result ensues from the detonation of a thick layer of C-3 around a brass rod. Figure 3 shows a longitudinal section of a 1-in. diam by 8-in. long rod, the composition of which was Cu 60.5%, Zn 36.5%, Pb 3.1%. The rod was enclosed along the axis of a 4-in. diam by 14-in. long charge. The point of initiation of detonation was 1 in. off center at one end of the charge. A $\frac{1}{16}$-in. diam hole is produced which extends along the rod from near the detonator end to the opposite end. Deposited on the upper end of the cavity is a light-colored material which chemical tests show to be principally lead. The photomicrographs of Fig. 4 show the grain structure in the vicinity of the hole. Material immediately adjacent to the hole was reamed out and assayed. The analyses of three samples are given in Table I.

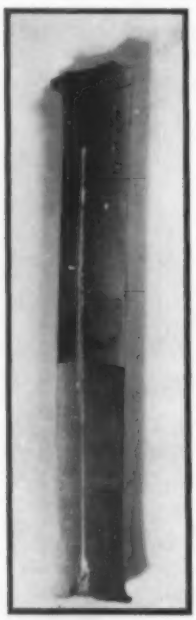

FIG. 3. Longitudinal section of brass rod with hole

The percentage of zinc near the hole has increased sufficiently so that phase diagrams indicate either free zinc or β-brass, yet the x-ray diffraction pattern shows only α-brass. A possibility which might be expected in view of the rapidity of the action is that whatever free zinc or β-brass is present is too finely divided to affect the x rays.

Walsh *et al.*[3] have calculated the temperatures to be expected in various materials when subjected to shocks up to 500 kbars. Although the magnitude of the shock which arrived at the center of the rod is unknown, it may have been considerably above 500 kbars, and the presence of dendrites indicates the existence of a melted phase. This whole experiment is a suitable subject for further study.

3. A hole similar to those produced in brass rods has also been produced in copper and in bronze. However, the pronounced metallurgical changes around the hole are not found in copper and are much less pronounced,

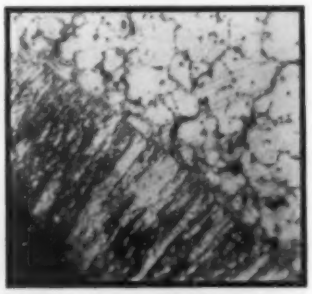

FIG. 4. Photomicrograph of transverse section of brass rod.

if not nonexistent, in bronze. Attempts to produce the well-defined hole in aluminum and steel have met with indifferent success, the nearest approach consisting of a circular central area more or less filled with cracks. Whether this apparent difference in behavior of different materials really represents a qualitative difference in the materials or merely indicates a failure to find a combination of explosive, geometry, etc., appropriate to each material is unknown.

4. A type of fracture which is not new, but for which no satisfactory explanation has been published, occurs

TABLE I.

Sample	Weight (g)	Cu (g)	Zn (g)	Pb (g)	% Zn
A	0.0845	0.02717	0.0365	0.000493	46
B	0.0632	...	0.0353	0.000576	56
C	0.0773	0.03886	0.0365	0.000411	47.2

[3] John M. Walsh, Melvin H. Rice, Robert G. McQueen, and Frederick L. Yarger, Phys. Rev. **108**, 196 (1957).

under the test arrangements of Fig. 5 and is shown in Figs. 6 and 7. In Fig. 6 the two charges were detonated simultaneously and induced approximately spherical waves. The result shown in Fig. 7, in which the upper charge was detonated first, disproves the hypothesis stated by Evans[4]: "The compression pulses are reflected from the original faces in tension and reinforce as such to produce a characteristic region of fracture. No Hopkinson region of fracture can be observed by reflection of the returning compression pulse at the original surfaces, but though the magnitude of the pulse has decayed sufficiently not to produce these, collision at the center once more increases the effective amplitude, this time sufficiently to cause fracture." If Evans' explanation were correct, the lower charge would have to be the one detonated first.

5. Although it does not seem to have appeared in print, another "explanation" for the type of fracture shown in Figs. 6 and 7 has frequently been given. This is that the compression waves meet and combine to create a region of such high compressive stress that

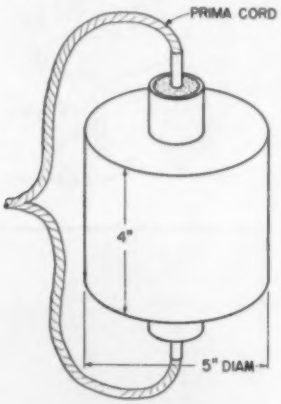

FIG. 5. Cylinder loaded at both ends by cylindrical charges of explosive.

the tendency of the material to relieve this stress gives rise to tensile waves propagating from the edges of the compressed region toward the center of the region. When these tensile waves reach the center, they have reduced the compression to zero, but they combine as tension and pull the material apart. A test of this hypothesis was made using a test piece of the same over-all dimensions as the two previously mentioned, but with an interface between each charge and the central region where the compressive waves meet. Figure 8 shows the absence of any central fracture, thus demonstrating that this hypothesis is false.

6. The type of fracture discussed in Secs. 4 and 5 has been produced in mild steel, brass, and lead. One attempt with copper failed; several attempts with aluminum were indecisive. A probable explanation of the fracture is based upon theoretical findings of Allen and

[4] W. M. Evans, Research **5**, 502 (1952).

FIG. 6. Cold-rolled steel cylinder, 5-in. diam by 4-in. long. Fracture at center results from collision of waves from simultaneously detonated charges.

FIG. 7. Cold-rolled steel cylinder, 5-in. diam by 4-in. long. Fracture below center is result of later detonation of lower charge.

Goldsmith,[5] Selberg,[6] and others, who have shown that a spherically expanding compression wave may be expected to acquire a tension tail. The superimposition of the two tensile tails from the two compression waves initiated at the two ends of the test piece might give rise to sufficient tension to cause fracture. If this were the case, the fracture described in Sec. 4 would be expected to occur where it does occur; furthermore, the interfaces in Sec. 5 would remove the tension tails and the fracture would not be expected. Another method of testing for the existence of a tension tail is shown in Fig. 9. The face at 45 deg to the axes of the charges

FIG. 8. Cold-rolled steel cylinder, 5-in. diam by 4-in. long, made in three sections. Interfaces have prevented formation of fracture at center.

[5] William A. Allen and Werner Goldsmith, J. Appl. Phys. **26**, 69 (1955).
[6] H. L. Selberg, Arkiv Fysik **5**, 97 (1952).

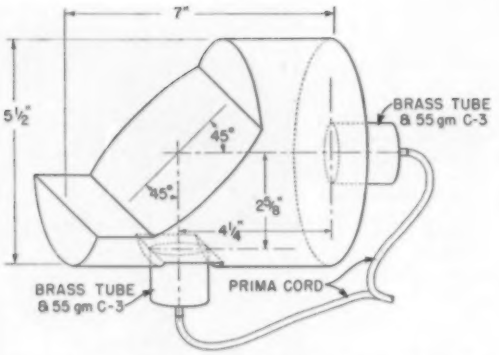

FIG. 9. Design of test piece for demonstrating the existence of tension tail to spherical compression wave.

FIG. 10. Fracture (z) caused by collision of wave from right-hand charge with inverted wave from charge at bottom.

inverts the compression wave from the lower charge and causes head-on collision of the inverted tension front with the compression from the other charge. Unless the compression wave has associated tensile phases, there should be no fracture. The sectioned test piece in Fig. 10 exhibits ordinary scabs along the left-hand portion of the wave at x and y, where the distance to the charge is insufficient to attenuate the wave below the dynamic strength of the material. These scabs prevent further propagation of this portion of the reflected tensile wave, but the right-hand portion is reflected and meets the wave originating at the right-hand charge. A fracture is evident at z, which is $\frac{5}{16}$ in. to the right from the midpoint of the path between the two charges. This is

FIG. 11. Cold-rolled steel cylinder, 5-in. diam by 4-in. long, impacted by ½-in. thick steel plate.

evidence of the existence of a tension tail of significant magnitude $\frac{5}{8}$ in. behind the compression front.

7. The results of one of a series of experiments involving impacts are represented by Fig. 11. In this particular test, a 2-in. diam by ½-in. thick steel plate was driven by a 4-in. thick charge of composition C-4 into one end of a 5-in. diam by 4-in. long steel cylinder. The impact velocity is unknown, but it must have been several thousand feet per second. There is a single scab at the free surface and an irregular piece of roughly hemispherical shape, 1 in. in diam, which has been separated at a position directly under the area of impact. The reason for the separation of this piece is unknown,

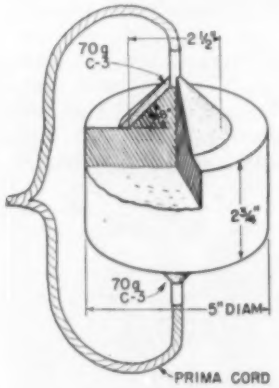

FIG. 12. Cold-rolled steel cylinder with cones at ends for generating plane waves.

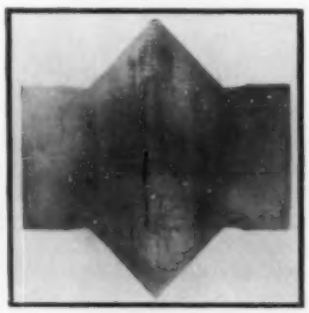

FIG. 13. Cold-rolled steel cylinder, 5-in. diam by 2¾-in. long, with cones for generating plane waves. Transverse fractures at center result from collision of waves.

but it may be related to the occurrence of a fracture reported by Rinehart and Pearson[1] as being found below the craters of explosive charges and attributed by them to the inability of material to expand rapidly on release of load. We suggest as an equally likely cause the development of a tension tail of sufficient magnitude to cause fracture.

8. Another case in which the conversion of a compression wave into a tensile wave may be anticipated is discussed by Kolsky and Shearman.[7] By their demonstration, the energy of a compression wave which moves into a corner, specifically into the vertex of a cone, is

[7] H. Kolsky and A. C. Shearman, Research **2**, 384 (1949).

converted totally into that of a tensile wave. Among the numerous firings which have been conducted here, including some specifically intended to produce this result, nothing like the corner fractures or loss of cone tips has been observed. However, a very interesting indirect consequence of the various experiments and hypotheses has developed. This came about through the self-imposed question as to whether there are still other circumstances, as, for example, in connection with plane or converging compression waves, in which tension tails are developed. That such circumstances do exist was established on the first try by a test involving the head-on collision of two plane waves. The plane waves were generated by machining cones on the ends of a cold-rolled steel cylinder, as in Fig. 12. The cones were covered with a layer of C-3, which was detonated at the apex of the cone. The half-angle of the cones, 42 deg, is selected so that the wave, which stands at 48 deg to the explosive-steel interface, emerges as a plane wave at the base of the cone. The sectioned cylinder is shown in Fig. 13. There are two distinct parallel fractures about $\frac{1}{4}$ in. apart which, from considerations of symmetry, must have occurred simultaneously. One possible explanation of these, though one which is not yet verified, is that the colliding stress waves have the appearance shown in Fig. 14. Assuming two tension

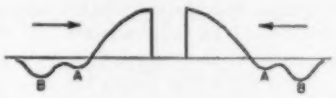

FIG. 14. Hypothesized stress time curve associated with plane compression wave.

tails A and B, as shown, if the magnitude $\sigma(A)$ of the first tension tail is less than half the dynamic strength of the material, the meeting of the two first tension tails from left and right would not give rise to tension in excess of the strength of the material, and no fracture would result. If, however, $\sigma(B)$ is sufficiently larger than $\sigma(A)$, and $\sigma(A)+\sigma(B)$ exceeds the dynamic strength of the material, the simultaneous meeting of the first tension tail from either side with the second tension tail from the other side would cause the simultaneous formation of two fractures separated by the distance between A and B. The results for β-brass and aluminum are shown in Figs. 15 and 16.

This experiment has been repeated a number of times with test pieces varying in length from $2\frac{1}{4}$–3 in. The only difference noted in the general character of the

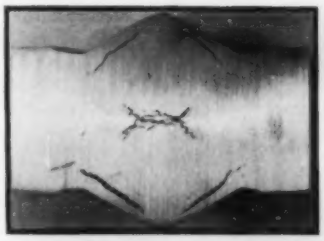

FIG. 15. Cylinder of β-brass, 5-in. diam by $2\frac{1}{4}$-in. long, with cones for generating plane waves. Scabs at ends result from reflection of waves at end opposite the charge.

FIG. 16. Aluminum cylinder, 5-in. diam by 3-in. long, with cones for generating plane waves. Transverse fractures at center result from collision of waves.

fractures is that, for the 3-in. length, there exists a third fracture midway between and less prominent than the other two. Increasing the amounts of explosive from 70–110 g increases the number of parallel fractures to five. An explanation of these last-mentioned results by a stress-time curve similar to that of Fig. 14 would require a considerable complication of that curve. However, if such a complication is rejected, there seems to remain no way to explain the results. That the existence of two or more parallel fractures is not an incidental consequence of the generation of plane waves by cones has been established by other means of generating the waves. The result, therefore, is assignable with greater certainty as a manifestation of some property of plane waves in general.

ACKNOWLEDGMENT

The author is grateful to the Bureau of Ordnance, U. S. Navy Department for permission to publish the results of these experimental tests.

Spectral Emissivity, Total Emissivity, and Thermal Conductivity of Molybdenum, Tantalum, and Tungsten above 2300°K

ROBERT D. ALLEN, LOUIS F. GLASIER, JR., AND PAUL L. JORDAN
Aerojet-General Corporation, Azusa, California

(Received November 9, 1959)

The emissivities and thermal conductivities of high purity arc melted molybdenum and tantalum and powder metallurgy tantalum and tungsten were measured between 2300°K and their respective melting points. A method is presented for the determination of spectral and total emissivities from the determination of brightness temperature at the center of an electrically heated rod as a function of heat flow rate. The method does not depend on the experimental achievement of blackbody conditions. Spectral emissivities were also determined by measurement of brightness temperatures at the respective melting points. Thermal conductivities of electrically heated rods were determined by the Jain and Krishnan longitudinal heat flow method. The spectral emissivities of tantalum and tungsten decrease linearly with increase in temperature. The spectral emissivity of molybdenum is constant. The total emissivities of molybdenum, tantalum, and tungsten increase with increasing temperature. For any of the metals the spectral and total emissivities are closest to each other at the melting point. The melting point of tantalum is significantly lowered by small increase in impurity content. The thermal conductivities of molybdenum, tantalum, and tungsten decrease linearly with increasing temperature. The ranges of spectral emissivity, total emissivity, and thermal conductivity above 2300°K are as follows:

	ϵ_λ	ϵ_T	K (cal. cm^{-1} sec.$^{-1}$ °K^{-1})
Molybdenum	0.30	0.271–0.285	0.34–0.32
Tantalum	0.361–0.350	0.288–0.324	0.15–0.11
Tungsten	0.37 –0.36	0.268–0.352	0.38–0.30

I. INTRODUCTION

THE emissivities and thermal conductivities of refractory metals must be known to permit their intelligent use in high-temperature missile applications such as nozzles and jetevators. For instance, the temperature profile reached by a particular material is dependent upon its thermal conductivity and the rate at which heat flows through it; the heat flow rate, in turn, is dependent upon the emissivity (absorptivity) of the material.

Emissivity and thermal conductivity data in the literature show appreciable discord. Furthermore, calculation of thermal conductivity usually depends upon knowledge of spectral and total emissivity to permit necessary temperature corrections and heat flow rate determinations. Thus, it is desirable to measure emissivities and thermal conductivity on the same materials.

A new method for the determination of spectral and total emissivities from a single experimental procedure, involving the determination of brightness temperature as a function of heat flow rate, has been applied for the first time. Spectral emissivities have also been separately determined by measurement of the brightness temperatures of the respective metals at melting.

Thermal conductivities have been determined by the Jain and Krishnan[1] method. This technique is based upon the experimental determination of the distribution of temperature along a thin rod which is electrically heated. The method assumes that heat is radiated from the rod's surface to an effectively black environment.

TABLE I. Material designations and details of manufacture of molybdenum, tantalum, and tungsten.

Material designation	Manufacturer	Methods of manufacture
Molybdenum	Fansteel Corp.	Cast, under inert gas, in watercooled copper mold using consumable electrode. Hot worked and hot rolled.
Tantalum No. 1	Fansteel Corp.	Pressed and sintered metal powder. Hot and cold rolled.
Tantalum No. 2	National Research Corp.	Cast, in vacuum, in water-cooled copper mold using consumable electrode. Cold rolled, swaged and cold drawn.
Tungsten No. 1	Fansteel Corp.	Pressed and sintered metal powder. Hot worked.
Tungsten No. 2	Wah Chang Corp.	Pressed and sintered metal powder. Hot worked.

II. MATERIALS

All the materials were reasonably typical of commercial purity. The molybdenum was made by arc melting, under inert gas; the tantalum materials were produced by powder metallurgy procedures and vacuum arc melting; and the tungsten materials were produced by powder metallurgy procedures only. The material designations, details of manufacture, and chemical analyses are supplied in Tables I and II.

III. DEFINITIONS AND THEORY

The total emissivity of a radiating body is the ratio of the heat flow rate from that body to the heat flow rate from a blackbody of the same dimensions at the same absolute temperature. Total emissivity, ϵ_T, may also be defined by the equation

$$\epsilon_T = Q/\sigma A(T_m^4 - T_o^4), \quad (1)$$

[1] S. C. Jain and K. S. Krishnan, Proc. Roy. Soc. (London) A222, 167–180 (1954).

TABLE II. Chemical analyses of molybdenum, tantalum, and tungsten.

Material designation	Fe	Mn	Ti	Ni	Si	Cu	Nb	C	O_2	N_2	Mo	Ta	W	Others
Molybdenum	0.18	0.036	···	···	0.073	···	···	0.04	0.005	···	bal.	···	···	0.01
Tantalum No. 1	0.005	···	···	···	<0.02	···	···	0.0008	···	···	0.003	bal.	···	0.052
Tantalum No. 2	0.0028	···	···	···	···	···	0.0035	0.0016	0.0032 to 0.0050	<0.0010	···	bal.	···	0.0175
Tungsten No. 1	0.004	···	0.005	0.005	···	···	···	···	0.006	···	0.04	···	bal.	0.027
Tungsten No. 2	···	···	···	···	···	0.002	···	···	···	···	0.04	···	99.95	0.008

where Q is the heat flow rate, A is the area through which the heat flows, σ is the Stefan-Boltzmann constant, T_m is the temperature of the radiating element in degrees Kelvin, and T_e is the temperature of the environment in degrees Kelvin. In practice, T_e may be neglected if the environmental temperature is low.

Spectral emissivity, ϵ_λ, is defined by Wien's law:

$$\ln\epsilon_\lambda = C_2/\lambda\{1/T - 1/T'\}, \tag{2}$$

where C_2 is the second constant of Planck's law, λ is the wavelength of the pyrometer filter, T is the true temperature, and T' is the brightness temperature. The spectral emissivity must be determined in order to convert an experimental brightness temperature into a true temperature, since pyrometric temperature measurement is carried out at a single effective wavelength.[2]

Spectral emissivity may be expressed as a function of brightness temperature, heat flow rate, and the derivative of brightness temperature with respect to heat flow rate. The derivation is given below.

Neglecting the environmental temperature T_e, Eq. (1) becomes

$$Q = \epsilon_T \sigma A T^4. \tag{3}$$

By substituting Eq. (3) in Eq. (2)

$$\ln\epsilon_\lambda = \frac{C_2}{\lambda\{Q/\epsilon_T\sigma A\}^{\frac{1}{4}}} - \frac{C_2}{\lambda T'}. \tag{4}$$

By partial differentiation,

$$\frac{\partial T'}{\partial Q} = \frac{(\epsilon_T\sigma A)^{\frac{1}{4}}(T')^2}{4Q^{5/4}}, \tag{5}$$

$$\frac{\partial T'}{\partial \epsilon_T} = -\frac{(\sigma A)^{\frac{1}{4}}(T')^2}{4Q^{\frac{1}{4}}\epsilon_T^{\frac{1}{4}}}, \tag{6}$$

$$\frac{\partial T'}{\partial \epsilon_\lambda} = \frac{(T')^2\lambda}{\epsilon_\lambda C_2}. \tag{7}$$

[2] The single effective wavelength is an average over a narrow band in the visible spectrum. The spectral emissivity shows negligible variation over the width of this band at a given temperature.

On combining the preceding,

$$dT' = \frac{(\epsilon_T\sigma A)^{\frac{1}{4}}(T')^2}{4Q^{5/4}}dQ - \frac{(\sigma A)^{\frac{1}{4}}(T')^2}{4Q^{\frac{1}{4}}\epsilon_T^{\frac{1}{4}}}d\epsilon_T + \frac{(T')^2\lambda}{\epsilon_\lambda C_2}d\epsilon_\lambda. \tag{8}$$

Upon factoring (8) and upon substituting from (3),

$$\frac{dT'}{(T')^2} = \frac{dQ}{4TQ} - \frac{d\epsilon_T}{4T\epsilon_T} + \frac{\lambda d\epsilon_\lambda}{C_2\epsilon_\lambda}. \tag{9}$$

Since the sum of the second and third terms on the right is small relative to the first term, the equation may be written

$$1/T = [4Q/(T')^2][dT'/dQ]. \tag{10}$$

By substituting in (2),

$$\ln\epsilon_\lambda = \frac{C_2}{\lambda}\left[\frac{4Q}{(T')^2}\left(\frac{dT'}{dQ}\right) - \frac{1}{T'}\right]. \tag{11}$$

Equations (3) and (11) permit solutions for ϵ_T and ϵ_λ. Their approximate rates of change with heat flow rate or temperature can be readily calculated by solutions at a number of power levels.

If necessary, a complete solution of Eq. (9) can now be obtained. On dividing, it becomes

$$\frac{1}{(T')^2}\frac{dT'}{dQ} = \frac{1}{4TQ} - \frac{1}{4T\epsilon_T}\frac{d\epsilon_T}{dQ} + \frac{\lambda}{C_2\epsilon_\lambda}\frac{d\epsilon_\lambda}{dQ}. \tag{12}$$

This may be rewritten

$$\frac{1}{(T')^2}\frac{dT'}{dQ} = \frac{1}{4TQ} + \alpha; \tag{13}$$

therefore,

$$\frac{1}{T} = 4Q\left[\frac{1}{(T')^2}\frac{dT'}{dQ} - \alpha\right], \tag{14}$$

and

$$\ln\epsilon_\lambda = \frac{C_2}{\lambda}\left[4Q\left(\frac{1}{(T')^2}\frac{dT'}{dQ} - \alpha\right) - \frac{1}{T'}\right]. \tag{15}$$

Successive solutions of Eqs. (15) and (3) will lead to successively more accurate determinations of α, ϵ_λ, and ϵ_T. The relaxation procedure should be carried out

at several power levels since α is a function of several temperature dependent variables. Finally, ϵ_λ and ϵ_T can be plotted as functions of temperature.

The thermal conductivity of a substance, a numerical quantity which specifies its ability to conduct heat, is defined as the proportionality constant k in the equation

$$Q=-kA(dt/dx), \tag{16}$$

where Q is the heat flow rate, A is the area through which the heat passes, and dt/dx is the temperature gradient in a direction perpendicular to A. This equation may be used to determine the thermal conductivity of a rod-shaped specimen with a measurable temperature gradient parallel to its length, a constant heat flow rate perpendicular to all cross sections and a constant temperature parallel to any one cross section. In practice, such conditions are extremely difficult to obtain.

The Jain and Krishnan method makes possible the determination of the thermal conductivity of a long rod electrically heated between electrode-holders. Thermal conductivity is calculated from temperatures measured along the length of the rod. The following equation applies:

$$k=\frac{16\epsilon_T\sigma T_m^3x^2}{D\left[\ln\tau+\frac{\tau}{2T_m}+\frac{\tau^2}{16T_m^2}-\frac{\tau^3}{240T_m^3}-\ln t-\frac{t}{2T_m}-\frac{t^2}{16T_m^2}-\frac{t^3}{240T_m^3}\right]^2}, \tag{17}$$

where ϵ_T is the total emissivity, σ is the Stefan-Boltzmann constant, D is the diameter of the specimen, T_m is the temperature at the center, τ is the temperature difference between the center and end of the rod, and t is the temperature difference between the center and a point x distance from the end of the rod. Measured brightness temperatures must be corrected to true temperatures with the appropriate spectral emissivities. All temperatures are in degrees Kelvin. In practice, the cube terms in the denominator of Eq. (17) are usually small enough to be omitted.

The principal theoretical shortcoming of the method is that it does not take into account the radial component of the temperature gradient within the rod. This radial component, however, will be relatively less important if the test material has a positive temperature coefficient of resistivity. (Molybdenum, tantalum, and tungsten have positive coefficients.)

IV. EQUIPMENT AND PROCEDURES

Experimental determinations of total and spectral emissivity and thermal conductivity were carried out in a Pyrex bell jar in a protective atmosphere of argon or in partial vacuum. The base plate was machined from a glass-bonded synthetic mica. Test temperatures were achieved by direct current electrical self resistance heating of test specimens. Power leads, voltage measurement leads, and atmosphere control ports through the base were sealed with epoxy cement.

Test specimens were 0.125 in. in diam and 10 in. long. They were successively polished with No. 1-, 0-, 00-, 000-, and 0000-abrasive papers. Each specimen was connected in a vertical position between a rigid copper bus bar at the top and a flexible copper lead at the bottom (to allow for thermal expansion). The vertical distance between electrical connections was 8 in. Two voltage leads of 0.020-in. diam tungsten wire were spot welded 1 in. apart, symmetrically on either side of the center of each emissivity specimen.

Direct current was supplied by a 60-v 2000-amp motor generator set. Temperatures were measured with a disappearing filament pyrometer. Observed temperatures were corrected to brightness temperatures with an experimental "window factor." Electrical measurements were made with a recording dc ammeter and a vacuum tube voltmeter. Measurements of temperature and electrical quantities were not recorded until a steady state had been reached. After any change in electrical power setting, continuous readings of the center temperature were made until it stopped changing.

Oxidation and/or sublimation of molybdenum, tantalum, and tungsten were difficult to overcome. The most damaging consequence of these reactions was accumulation of a translucent deposit on the bell jar wall. Such a deposit seriously lowered the observed temperatures and decreased the quantity of radiant energy leaving the jar. To reduce the sublimation and subsequent deposition, emissivity runs on molybdenum were carried out in a partial pressure of argon; the inert gas flowed through the jar at the rate of 10 cu ft/hr. Emissivity runs on tungsten and tantalum and all thermal conductivity runs were carried out in argon at a pressure slightly greater than one atmosphere. (The argon flowed through the jar at the rate of 10 cu ft/hr and bubbled through 0.1 in. of water at the system's exit.)

The test procedures for emissivity were of two types: (1) measurement of brightness temperature at the melting point by slowly increasing power and closely following the sample temperature until melting broke the circuit. This procedure was carried out a minimum of three times for each metal. (2) Simultaneous measurements of brightness temperature, current, and potential drop across the test section at a series of power levels. These readings were recorded at 10-amp intervals within the brightness temperature range between 1500°C and 2800°C.

Spectral and total emissivities were calculated with the following steps:

1. The spectral emissivity for 0.65 μ was obtained at each melting point[3] by substitution of brightness and true temperatures into Eq. (2).

2. Heat flow rates at the various power levels were calculated from Eq. (18),

$$Q=JEI \tag{18}$$

in which Q is the heat flow rate, J is a conversion factor, E is potential drop, and I is current.

3. The spectral emissivities (0.65 μ) and total emissivities at temperatures below melting were obtained from Eqs. (3), (11), and (15) according to the procedures described under "Definitions and Theory."

The test procedures for thermal conductivity are described below. At each power level, temperature readings were obtained at the center of the specimen, and distance readings were obtained at a point 100°C cooler than the center. The approximate temperature

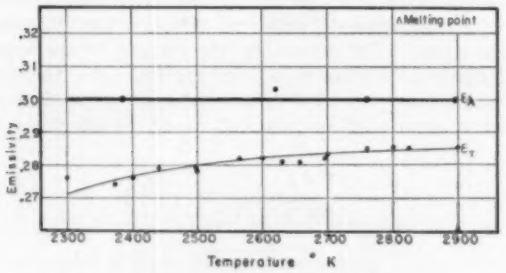

FIG. 1. Total and spectral emissivities (at 0.65 μ) of molybdenum above 2300°K.

of the upper copper clamp was determined with a chromel-alumel thermocouple, immediately after each power shutoff.

In detail, a temperature was first read at the center. Then the pyrometer reading was decreased by 100°C and the pyrometer rotated through a vertical angle until a match was obtained with the specimen at some point between center and end. The linear distance between the latter point and the end was measured by observation, through the pyrometer, of a stainless steel scale affixed to the outside of the bell jar. This scale reading was corrected with a calibration curve which had been obtained by substituting a second steel scale for the sample and correlating the corresponding readings from the two scales. The measuring procedure was repeated several times to obtain an average temperature at the center and an average location of a temperature 100°C less. The power was then turned off and the temperature of the sample grip immediately

[3] Melting points were taken from *Metals Handbook*, edited by Taylor Lyman (The American Society for Metals, 1948), pp. 20–21.

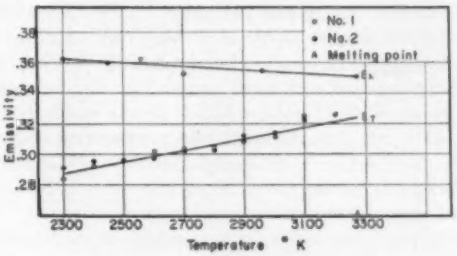

FIG. 2. Total and spectral emissivities (at 0.65 μ) of tantalum above 2300°K.

determined with a thermocouple. The true temperature of the clamp was obtained by extrapolation from a temperature-time curve established from successive readings during cooling.

Thermal conductivities were calculated from Eq. (17).

V. RESULTS AND DISCUSSION

Total and spectral emissivities are plotted vs true temperature in Figs. 1–3. The total emissivities of molybdenum, tantalum, and tungsten increase with increasing temperature. Total emissivities of tantalum No. 1, tantalum No. 2, and tungsten No. 1 are linear functions of temperature over the respective temperature intervals from 2300°K to melting. The total emissivity of tungsten No. 2 increases with temperature at an increasing rate. The total emissivity of molybdenum increases with temperature at a decreasing rate from 2300°K to melting.

The spectral emissivities of tantalum and tungsten decrease with increase in temperature between 2300°K and the respective melting points; the relationships are linear. The rates of variation with temperature are appreciably less than those determined for total emissivity. The spectral emissivity of molybdenum is constant, within limits of experimental error, between 2300°K and the melting point.

For any one of the three metals, the spectral and total emissivities are closest to each other at the melting point.

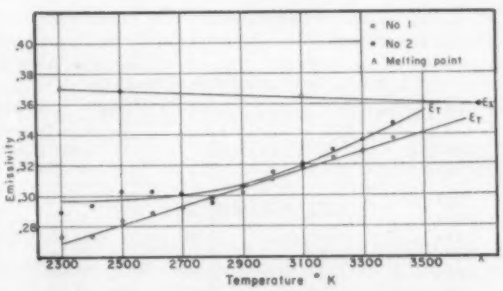

FIG. 3. Total and spectral emissivities (at 0.65 μ) of tungsten above 2300°K.

Tantalum No. 1 and tantalum No. 2 yielded emissivities which were identical within experimental error, in the temperature region below melting; this was true of both spectral and total emissivity. The brightness temperature of tantalum No. 1 at the melting point was 43°C less than the brightness temperature of No. 2. This discrepancy is probably indicative of an actual difference in melting point. The lower purity of tantalum No. 1 supports this interpretation of the data.

The mathematical analyses employed to determine spectral emissivity at temperatures below the melting point and total emissivities at all temperatures assume that all energy supplied to a sample within the central portion is dissipated by radiation. Two departures from this condition are considered: (1) convective heat transfer from the specimen to the inert gas flowing through the bell jar and (2) conductive heat transfer from the specimen through the voltage leads. The percentage of heat transferred to the gas was very small. A calorimetric calculation showed that less than 0.5% of the total heat generated in the test section at 2500°C was removed by convection. Calculations based on temperature profiles along the voltage leads indicated that only about 0.5% of the heat generated within the test section was removed by conduction through the leads. The amount of heat lost by conduction through the voltage leads was sufficient, however, to produce a slight temperature drop at the points where these were spot-welded to the specimen. The temperature drop from midway between the voltage leads to either lead averaged less than one percent. Temperature profiles along the test section indicated that the temperature at the midpoint did not differ from the mean temperature by more than 0.3%.

TABLE III. Total emissivities of molybdenum.

Temperature (°K)	This investigation	Worthing[a]
2400	0.277	0.248
2600	0.282	0.265
2800	0.285	0.281
2895	0.286	0.290

[a] See footnote reference 4.

TABLE IV. Total emissivities of tantalum.

Temperature (°K)	This investigation	Worthing[a]
2400	0.292	0.269
2600	0.300	0.287
2800	0.308	0.304

[a] See footnote reference 4.

TABLE V. Total emissivities of tungsten.

Temperature (°K)	This investigation No. 1	This investigation No. 2	*American Institute of Physics Handbook*, 1957
2400	0.277	0.294	0.296
2600	0.289	0.298	0.311
2800	0.300	0.304	0.323
3000	0.312	0.314	0.334
3200	0.323	0.329	0.341
3400	0.335	0.347	0.348
3600	0.347	...	0.354

The total emissivity data from this investigation are in reasonable accord with published values. Worthing[4] determined the total emissivities of molybdenum and tantalum from experimental measurements of radiation intensity at various temperatures. His results are compared with this investigation in Tables III and IV. Comparative tungsten data are given in Table V.

The spectral emissivities (at 0.65 μ) determined during the present investigation are somewhat lower than values published by Worthing.[4,5] The differences are least at the melting points of the metals and greatest at the lowest temperature considered (2300°K).

In order to theorize about these discrepancies, it is necessary to briefly describe Worthing's method. Tubular specimens with openings in the walls were electrically heated and outside and inside temperatures were determined with a disappearing filament pyrometer. To determine the actual temperature difference between inside and outside walls, thermal conductivity, electrical resistivity, and current density were substituted into the well-known Angell equation

$$\Delta T=\frac{i^2\rho}{2K}\left(r_i\ln\frac{r_0}{r_i}-\frac{r_0^2-r_i^2}{2}\right), \tag{19}$$

where ΔT is the temperature difference between inner and outer surfaces, i is the current density, ρ is the resistivity, k is the thermal conductivity, r_i is the internal radius, and r_0 is the external radius. The temperature difference was subtracted from the inside temperature to obtain the true outside temperature.

Spectral emissivity was obtained from Eq. (2) by substitution of the outside brightness and true temperatures. The method assumes that blackbody conditions obtain at the inside temperature stations.

Worthing[6] has mentioned three factors which produce high emissivities: (1) use of poorly polished specimens, (2) insufficient approach to blackbody conditions, and (3) use of impure specimens. Without question, the tube method of determining spectral emissivity is subject to error due to departure from perfect blackbody conditions. Furthermore, departure from blackbody conditions within a tube is probably greater at lower temperatures because the length of the constant temperature zone is a function of temperature; therefore, an inside temperature station "sees" a larger cold area at low temperature than at high. For this

[4] A. G. Worthing, Phys. Rev. **28**, 190–210 (1926).
[5] A. G. Worthing, Phys. Rev. **10**, 377–394 (1917).
[6] A. G. Worthing, Phys. Rev. **25**, 846–857 (1925).

reason, higher apparent spectral emissivities would be obtained at lower temperatures.

The method employed in this investigation does not depend on the experimental achievement of blackbody conditions.

The comparative spectral emissivity data are presented in Tables VI–VIII.

Thermal conductivities of molybdenum, tantalum, and tungsten decrease with increasing temperature from 2300°K to their respective melting points. Thermal conductivity temperature curves for all three metals are linear with relatively slight slopes. The data are shown in Figs. 4–6. Single curves obtain for both tantalum

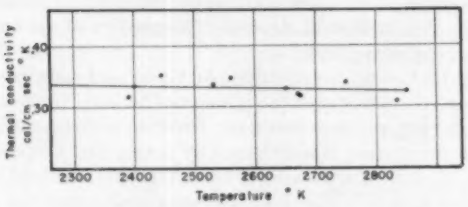

FIG. 4. Thermal conductivity of molybdenum above 2300°K.

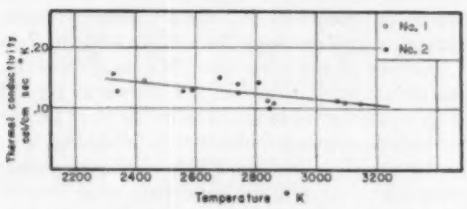

FIG. 5. Thermal conductivity of tantalum above 2300°K.

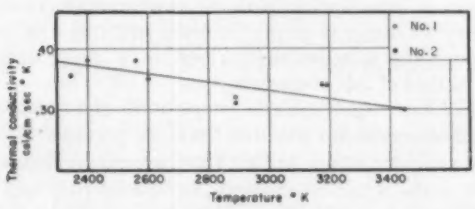

FIG. 6. Thermal conductivity of tungsten above 2300°K.

materials and both tungsten materials. Thus, differences in purity were insufficient to produce measureable differences in thermal conductivity.

Very limited comparison of these thermal conductivities with published data has been made because of the paucity of data on very pure metals at these very high temperatures. Available data are characterized by inconsistencies among the reported magnitudes and temperature coefficients of thermal conductivity. For instance, thermal conductivities of molybdenum reported by Zuikker[7] are not in agreement with values

[7] C. Zuikker, Physica 7, 71–74 (1927).

TABLE VI. Spectral emissivities (0.65 μ) of molybdenum

Temperature (°K)	This investigation	Worthing[a]
2400	0.30	0.341
2600	0.30	0.336
2800	0.30	0.331
2898	0.30	0.328

[a] See footnote reference 4.

TABLE VII. Spectral emissivities (0.65 μ) of tantalum.

Temperature (°K)	This investigation	Worthing[a]
2400	0.361	0.404
2600	0.358	0.397
2800	0.356	0.390
3000	0.353	0.384
3269	0.350	0.375

[a] See footnote reference 4.

TABLE VIII. Spectral emissivities (0.65 μ) of tungsten.

Temperature (°K)	This investigation	Worthing[a]
2400	0.370	0.429
2600	0.368	0.425
2800	0.367	0.420
3000	0.365	0.415
3200	0.364	0.410
3400	0.363	0.405
3683	0.360	0.397

[a] See footnote reference 4.

reported by Rasor and McClelland[8] either with respect to magnitude or temperature dependence. The thermal conductivities determined in this investigation are in better agreement with Zuikker's results.

Similar discrepancies exist among the published thermal conductivities for tantalum and tungsten.

VI. CONCLUSIONS

1. The total emissivities of molybdenum, tantalum, and tungsten increase with temperature, usually at a decreasing rate, between 2300°K and the respective melting points.

2. The spectral emissivities of tantalum and tungsten decrease linearly with temperature between 2300°K and the respective melting points. The spectral emissivity of molybdenum is constant within this temperature span.

3. The thermal conductivities of molybdenum, tantalum, and tungsten decrease linearly with temperature from 2300°K to the respective melting points.

VII. ACKNOWLEDGMENTS

This work was carried out under U. S. Navy contract. Technical assistance was rendered by D. R. Blair and A. H. Hussung.

[8] N. S. Rasor and J. D. McClelland, WADC Tech. Rept. 56-400, Pt. I (1957).

Exchange Anisotropy Memory Effect

I. S. JACOBS AND P. E. LAWRENCE
General Electric Research Laboratory, Schenectady, New York

(Received April 14, 1960)

A magnetic memory effect is observed in a low Curie point ferrimagnetic spinel ($\sim NiFe_{0.15}Cr_{1.85}O_4$) containing a coherent antiferromagnetic impurity (NiO) with a high Néel point. It is explained in terms of the Meiklejohn-Bean exchange anisotropy coupling the two phases. The past magnetic history is remembered in the spontaneous reacquisition of a fraction of the past remanent state despite prolonged storage at temperatures above the ferrimagnetic Curie point. A feature of the explanation is the condition that antiferromagnetic domains in NiO rotate irreversibly in accessible fields.

INTRODUCTION

AN interesting magnetic memory effect is observed in a mixed nickel ferrite-chromite ferrimagnetic spinel containing antiferromagnetic nickel oxide as an impurity. The material remembers its past magnetic history, in the sign and magnitude of a spontaneously acquired remanent magnetization, despite long retention at temperatures *above* the ferrimagnetic Curie point. The explanation of the phenomenon derives from the exchange anisotropy discovered by Meiklejohn and Bean[1] resulting from an interaction between the antiferromagnetic and the ferrimagnetic, supplemented by properties of NiO domains recently observed by Roth and Slack.[2]

CONVENTIONAL MAGNETIC BEHAVIOR

The material of interest has the nominal composition $NiFe_{0.15}Cr_{1.85}O_4$ and was obtained through the cooperation of T. R. McGuire of the U. S. Naval Ordnance Laboratory. It was prepared in powder form by standard ceramic techniques for studies[3] of the magnetic and crystallographic properties of the system $NiFe_{2-t}Cr_tO_4$ ($0 \leqslant t \leqslant 2$). The same material was used in a high-pulsed field magnetization study[4] of chromite spinels. The crystal structure is cubic spinel at room temperature, but distorts to a tetragonal modification and then to an orthorhombic one as the temperature is lowered.[3] The presence of the NiO impurity was established by x-ray examination. Its magnitude is estimated at 2% by comparison of the observed intensities of resolved reflections with those expected from the two phases.

The magnetization of the dominant ferrimagnetic component is shown in Fig. 1 for low temperature and high fields. In the previous study,[4] the failure of this curve to saturate was interpreted as evidence for a ferrimagnetic arrangement with angles between ionic magnetic moments. The spontaneous moment at 4.2°K was estimated (neglecting dilution by the NiO) at 56 emu (volume), or 40 emu, depending on the sign of the ferrimagnetic anisotropy.[4]

In an earlier investigation, McGuire and Greenwald reported a zero spontaneous moment for this compound, i.e., a compensation point as a function of composition. The discrepancy is understood by noting that this compound showed a remanence coercivity (reverse field required to reduce the previously saturated remanence to zero) equal to 13 koe at 77°K and 16 koe at 20.4°K. (These were measured with undirectional pulsed fields having a half-period of 100 msec.) Measurements of the previous authors were limited to fields of 7 koe. The behavior of the remanence M_R as a function of the maximum applied field H_{max} is shown in Fig. 2 for the two temperatures noted. The initial state for these curves is the isothermal remanence, saturated (or nearly so) in the negative direction. Fields of 50 koe or greater are required to saturate the remanence or to reverse it completely. The observed coercivities are rather higher than those of similar ferrimagnetics, suggesting possible magnetic complications with the antiferromagnetic impurity.[4] Alternatively, the distorted structure and low spontaneous moment might allow an intrinsic anisotropy field of this magnitude.

The ferrimagnetic Curie temperature of this nickel ferrite-chromite is estimated from the previous work[3] to be slightly under 200°K. The temperature dependence of the remanent moment can be used to obtain a

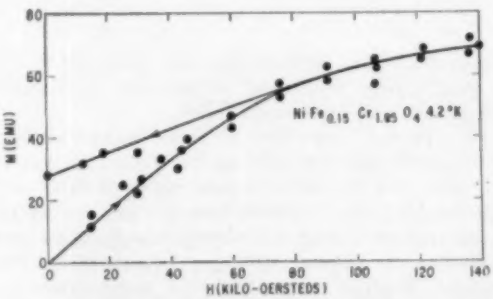

FIG. 1. Magnetization per unit volume M vs field H at 4.2°K for powder of nominal composition $NiFe_{0.15}Cr_{1.85}O_4$.

[1] W. H. Meiklejohn and C. P. Bean, Phys. Rev. **102**, 1413 (1956); **105**, 904 (1957).
[2] W. L. Roth and G. A. Slack, J. Appl. Phys. **31**, 352S (1960); also, unpublished work.
[3] T. R. McGuire and S. W. Greenwald, Bull. Am. Phys. Soc. Ser. II, **2**, 22 (1957); II, **3**, 43 (1958); *Solid State Physics in Electronics and Telecommunications*, edited by M. Désirant and J. L. Michiels (Academic Press, Inc., New York, 1960), vol. 3, p. 50.
[4] I. S. Jacobs, J. Phys. Chem. Solids (to appear in 1960).

lower limit to the Curie temperature. In view of its stability, and the memory features described below, this method probably gives a good estimate of that temperature. Figure 3 shows the isothermal remanences at 4.2°, 20°, and 77°K saturated by pulsed fields of 140 koe, and the decrease of the 77°K remanence with increasing temperature. The Curie temperature obtained thereby is about 250°K, reflecting a possible shift in composition of the ferrimagnetic toward a higher iron content.

MAGNETIC MEMORY BEHAVIOR

If a virgin sample of the material is cooled in the earth's field to a temperature below its ferrimagnetic Curie point (e.g., 77°K), it acquires a remanent volume moment of about 0.5 emu. Exposure to high-pulsed fields creates isothermal remanences saturating at 19 emu and 28 emu for 77°K and 20.4°K, respectively. When the sample, isothermally saturated by 140 koe

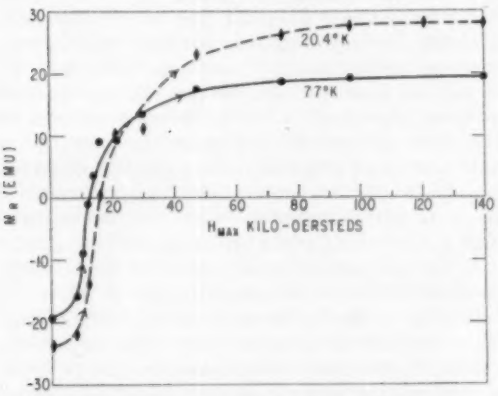

FIG. 2. Behavior of the remanent magnetization M_R as a function of maximum magnetic field H_{max} at 77° and 20.4°K for the powder of Fig. 1. The initial condition at 77°K is a remanent state created by $H_{max}=-140$ koe, while that at 20.4°K is the state created by $H_{max}=-45$ koe.

at low temperature, is warmed to room temperature in the earth's field, no remanence is detected ($M_R<0.05$ emu). On subsequent cooling to 77° or 20.4°K in the earth's field, it spontaneously reacquires a remanent moment of about one-fourth of the previous saturation remanence. This "memory" remanence takes its sign from the remanent state at low temperature just prior to warming. This sign is independent of the direction of the earth's field, thus removing any suggestion that this is a normal thermoremanence in the earth's field.[5] The cycle of cooling and warming between 77° and 300°K, without reapplying pulsed fields, may be repeated a number of times with the recovered remanence remaining a constant fraction of the original saturated remanence. Overnight or several week intervals at room temperature have no effect on this memory.

[5] For a discussion of thermoremanence, see, e.g., L. Néel, Advances in Phys. 4, 191 (1955).

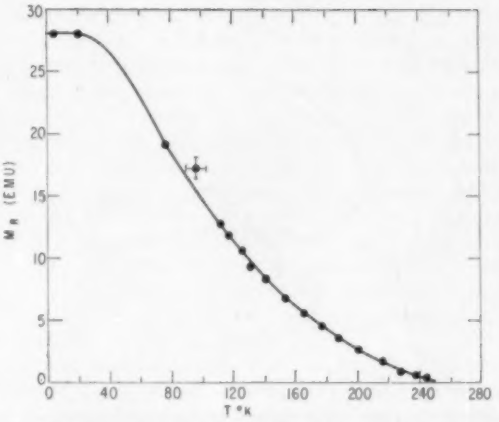

FIG. 3. Remanent magnetization M_R vs temperature T for the powder of Fig. 1. The points at 4.2°, 20.4°, and 77°K are saturated remanences created by $H_{max}=140$ koe, while those above 77°K are the natural decrease of the last named with increasing temperature.

If we tentatively ascribe the observed effect to the presence of the antiferromagnetic NiO impurity, it is of interest to look for an experimental connection with the properties of NiO. The fraction of remanent moment spontaneously recovered on cooling below the Curie point is a function of the thermal history above the Curie point. Figure 4 shows the recovered moment M'_R measured at 77°K, as a function of the maximum exposure temperature, T_{max}. The initial state was a saturated remanence at 77°K, and subsequent heating and cooling was all in the earth's field. The memory effect thus disappears at about 525°K, or approximately at the antiferromagnetic Néel temperature of the NiO ($T_N=525°\pm10°$K). This result confirms the assumption that the memory arises from the presence of the NiO.

An additional experiment was carried out to investigate the effect of the magnetic history at 300°K; i.e.,

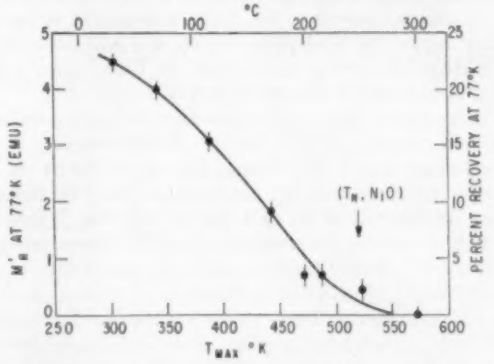

FIG. 4. Remanent magnetization M'_R spontaneously recovered at 77°K as a function of maximum exposure temperature T_{max} for the powder of Fig. 1. The initial state was a saturated remanence at 77°K, and subsequent heating was all in the earth's field only. Indicated percentages refer to the initial state.

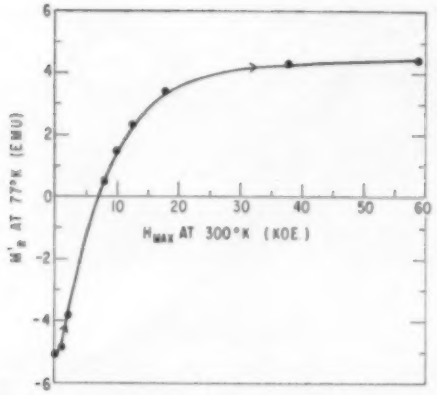

FIG. 5. Remanent magnetization M'_R spontaneously recovered at 77°K as a function of the maximum magnetic field. H_{max}, applied at 300°K, for the powder of Fig. 1. The initial state was a negative saturated remanence at 77°K.

above the ferrimagnetic Curie point but below the antiferromagnetic Néel point. In Fig. 5 is shown the behavior of the recovered remanent moment M'_R measured at 77°K, as a function of the maximum magnetic field applied at 300°K. The initial state was a negatively saturated remanence (−140 koe) at 77°K, and all heating and cooling occurred in the earth's field. The fields applied were dc up to 2 koe and pulsed from 8 koe upward. Thus the memory can be reversed at this temperature by a process whose coercivity is about 7 koe. The magnitude of the maximum recovered remanence is essentially unchanged by this reversal.

DISCUSSION

An explanation of this effect is readily obtained in terms of the exchange anisotropy of Meiklejohn and Bean.[1] The two phases of interest here have nearly identical lattice parameters so that magnetic exchange contact acting across an interface is quite likely. We need only assume that the antiferromagnetic arrangement below the Néel point nucleates a portion of the ferrimagnetic arrangement below its Curie point and thus determines its preferred direction.

A necessary part of the explanation is an accounting of how a preferentially directed antiferromagnetic arrangement comes into being, since it is absent in a virgin specimen, or in one heated above the Néel point. As a consequence of the data presented in Fig. 5, attention is focused on the properties of NiO. The magnetic structure[2,6] of NiO consists of ferromagnetic sheets in (111) planes, with reversed directions of magnetization in alternate sheets. These planes are the likely ones for exchange anisotropy coupling. Roth and Slack[2] have recently reported an irreversible magnetization process in the (111) plane of an untwinned NiO crystal, starting at fields in excess of 2.4 koe. The mean coercivity for this process at 300°K is about 5 koe, in rough agreement with the 7 koe observed in Fig. 5. In unpublished work, they note that the easy directions of the low field torque curve in the (111) plane depend on the previous magnetic history. The magnetization process may be irreversible rotation of antiferromagnetic domains. We thus propose that this rotation is the origin of the preferential antiferromagnetic arrangement responsible for nucleating the ferrimagnetic memory.

We now consider a specific model, which may operate at 300°K. The antiferromagnetic moment arrangement has n equivalent easy directions distributed in the (111) plane making angles $2\pi/n$ with each other. When a field is applied in excess of that required for domain rotation, the antiferromagnetic moments become oriented nearly perpendicular to the field. Upon removal of this field, the antiferromagnetic moments relax to the easy direction in the (111) plane most nearly perpendicular to the field direction. If n is even, there are two equivalent choices for this easy direction, 180° out of phase with each other. We may imagine a sharp interface between the spinel and NiO phases, parallel to the (111) plane. We assume that the antiferromagnet picks that one of these equivalent directions for which the first ferromagnetic (111) sheet of the NiO, nearest to the spinel, has a positive moment component along the field direction. This choice would be influenced by a weak coupling over a transition region between the paramagnetic spinel, partially magnetized by the applied field, and the antiferromagnet aligned nearly perpendicular thereto. When the system is subsequently cooled below the Curie point of the ferrimagnetic spinel, the ferrimagnetic moment array is nucleated by exchange coupling to the antiferromagnet. We assume here that the ferrimagnetic moment array is collinear with the antiferromagnet. The coupling to the net ferrimagnetic moment is assumed to be ferromagnetic at the interface. This may be expected through an antiparallel coupling between the octahedral moments of the NiO and the tetrahedral moments of the spinel, whose net ferrimagnetic moment is probably dominated by its octahedral contribution, opposing its tetrahedral one.[4] This spontaneously acquired magnetization lies nearly perpendicular to the original field direction, but has a positive component along that direction. Following the method used by Wohlfarth and Tonge,[7] it is easy to show that the expected remanence for a random powder is given by $M'_R = M_s(n/4)[1-\cos(\pi/n)]$, where M_s is the spontaneous magnetization at the final temperature of the cooling process. If n is six, as suggested by the symmetry of the (111) plane and the observed ⟨110⟩ moment directions therein,[6] we expect a maximum acquired remanence of $M'_R(\text{theor}) = 0.20 M_s$. On the experimental side, the value of M_s is uncertain as noted,[4] but is estimated from the remanences shown in Fig. 3, by dividing by 0.5 or 0.707, depending on the sign of the ferrimag-

[6] W. L. Roth, Phys. Rev. **110**, 1333 (1958); **111**, 772 (1958).

[7] E. P. Wohlfarth and D. G. Tonge, Phil. Mag. **2**, 1333 (1957)

netic anisotropy. We thus obtain from the data of Fig. 5 for 300°K, $M'_R(\text{expt}) = (0.015 \pm 0.03)M_s$ in satisfactory agreement with the model. If n is lower, perhaps caused by strains, the agreement is poorer. The predictions of the model, however, are not exceeded, and the deviations therefrom are in the direction of imperfect fulfillment of its assumptions. These would not be surprising. For example, if the anisotropy axis systems of the two phases are not collinear, the remanence will be lower by a factor which, in simple cases, is the cosine of the angle between the two systems.

We now apply this model to the experiment in which the ferrimagnetic remanence is saturated at low temperature, before warming above the Curie temperature, and subsequently recooling. To attain the relatively high remanences observed at low temperature, the ferrimagnetic moments must take up the easy directions in the spinel nearest the applied field direction. For these directions to be different, from those acquired in the foregoing, there should be more than two easy magnetization directions in the ferrimagnetic phase. The antiferromagnetic arrangement, however, must take up the same kind of configuration as just described for the room temperature experiment. This is required by the equality of the remanences spontaneously acquired in the two cases upon cooling. Between the interior of the ferrimagnetic phase aligned near to the field direction and the interior of the antiferromagnetic phase aligned almost perpendicular thereto, there is a transition region comprising a partial ferrimagnetic domain wall and a partial antiferromagnetic one. To achieve this condition, the thicknesses of the separate phases must be much greater than that required for the transition region. The field thus acts nearly independently on the interiors of the two magnetic components, their coupling serving only to influence favorable choices in the near-perpendicular antiferromagnetic array. Upon heating above the ferrimagnetic Curie temperature, the transition wall would move out into the paramagnetic spinel and disappear there. The antiferromagnetic phase is left with lowered energy in a uniformly magnetized near-perpendicular state.

If the antiferromagnetic phase were not thick enough to support its partial domain wall, it would be aligned by the coupling to be parallel to the magnetized ferrimagnetic spinel. This array would be able to nucleate a full recovery of the relatively large low temperature remanence. This favorable condition is contrary to the observed results. Alternatively, if the ferrimagnetic phase were too thin, it would be aligned with the near-perpendicular antiferromagnetic phase when the field is removed. This would mean a small saturated remanence at low temperatures, but a full recovery thereof, after warming and recooling. This is also contrary to observation. The existence of sharp x-ray diffraction lines of both phases is in accord with the requirement of sufficiently thick separate phases.

In the model adopted, the coercivity of the ferrimagnetic phase at low temperature is governed in part by its magnetocrystalline anisotropy and in part by the antiferromagnetic anisotropy, to both of which the crystallographic distortions probably contribute. The relative contribution of the antiferromagnetic phase depends on the ratio of coupled surface to volume of the ferrimagnetic.

CONCLUSION

A magnetic memory effect in a ferrimagnetic spinel with low Curie point containing a coherent antiferromagnetic impurity with high Néel point is observed and explained in terms of the Meiklejohn-Bean exchange anisotropy coupling the two phases. An important feature of the explanation is the condition that antiferromagnetic domains in NiO rotate irreversibly in accessible fields. The memory effect enables the spinel to regain spontaneously a fraction of its past remanent state despite prolonged storage at temperatures above its ferrimagnetic Curie point.

ACKNOWLEDGMENT

The authors wish to thank W. L. Roth and G. A. Slack for permission to quote some of their results prior to publication. They are also indebted to C. P. Bean, W. L. Roth, and W. H. Meiklejohn for stimulating discussions.

Forces on Ion-Bombarded Electrodes in a Low-Pressure Plasma*

G. K. Wehner
Mechanical Division of General Mills, Incorporated, Minneapolis, Minnesota
(Received April 11, 1960)

Forces arising on ion-bombarded electrodes have been measured with a torsion balance immersed in a low-pressure Hg plasma. The force curves obtained for 22 metals in the range of 20 to 300 ev bombarding energy indicate that Hg^+-ions are completely accommodated ($\alpha=1$) on clean metal surfaces and the forces originate essentially from the ejection of sputtered atoms. On comparing the forces with the sputtering yields, one obtains information on the average ejection velocities of sputtered atoms which are found to be much higher than those of thermally evaporated atoms. Oxide-covered surfaces exhibit a quite different behavior inasmuch as the accommodation coefficient for Hg^+-ions seems to be less than unity.

INTRODUCTION

WHEN a thin metal foil is bombarded with ions from a low gas pressure plasma, the foil is pushed away from the plasma and the forces increase with increasing energy of the bombarding ions. Some early studies on these forces were made in connection with the forces which arise at cathodes of vacuum arcs, in particular at Hg pool cathodes.[1–3] More directly related is a paper by Lamar[4] who studied the momentum transfer on an ion-bombarded Mo surface by measuring the deflection of a pendulum suspended in a He-plasma. A major difficulty in Lamar's experiments resulted from the large superimposed radiometer forces (gas pressure 0.2-mm Hg).

It is shown here that interfering radiometer forces can be kept negligibly small in a Hg-discharge operated at sufficiently low gas pressure ($<0.2\mu$). One can then directly obtain information on the accommodation coefficients of Hg^+-ions as well as on the ejection of sputtered atoms. Accommodation coefficients are very sensitive to surface layers. This, together with the fact that surface layers can be removed readily by ion bombardment, makes the forces a sensitive indicator for determining whether a metal surface is atomically clean and how long it remains so.

Force Considerations

A negative electrode (the target) immersed in a low gas pressure plasma of high density such as in the positive column of a Hg pool cathode discharge behaves like a large negative Langmuir probe. It becomes covered with an ion sheath which arises because the plasma has such a high electrical conductivity that the potential difference between plasma and target is confined to the immediate vicinity of the target. Plasma electrons are rejected at the sheath edge; plasma ions are accelerated in the sheath toward the electrode. With the ion mean free path large compared to the ion sheath thickness, one can neglect collisions with gas atoms and the ions arrive at the flat metal surface under normal incidence with a kinetic energy which is equal to the potential difference between target and plasma. While the ion crosses the sheath, the target is pulled toward the ion, i.e., in a direction toward the plasma. The impinging ion, however, transfers momentum and pushes the target away from the plasma. It can easily be shown that these two forces would cancel each other exactly if the ion would stick to the target surface. Consequently, if any forces arise, they must be caused by such other effects as the following:

1. Rebounding neutralized ions would cause a reaction force pushing the target away from the plasma. The analysis of this force furnishes information on the accommodation of the bombarding ions.

2. A similar reaction force arises from ejected neutral sputtered atoms. Sputtering sets in significantly only above certain ion energies, hence this force must become negligibly small below the sputtering onset energy. The sputtering force furnishes information on the average ejection velocities of sputtered atoms.

3. Radiometer forces arise either from the impingement or the evaporation of neutral gas atoms and temperature differences at the walls or between front and back sides of the target. Fortunately, these forces can be kept small enough to prevent serious interference by operating the tube at a low gas pressure ($<0.2\,\mu$) with the target seeing as much as possible a symmetrical plasma and temperature environment.

Positive ions released from the surface would be pulled back to the target and would not enter into force considerations—unless their ejection energy is higher than the bombarding energy of the ions—a case which does not exist. Negative ions, released from the surface, are accelerated in the sheath toward the plasma and would push the electrode away from the plasma. Negative ion formation at ion-bombarded clean metal surfaces, however, is very inefficient[5] and can hardly enter into the picture here. The same is true for electrons released from the surface under ion or photon bombardment. γ coefficients in Hg up to several 1000-ev ion

* Work was partly supported by ONR contract.
[1] R. Tanberg, Phys. Rev. **35**, 1080 (1930).
[2] K. T. Compton, Phys. Rev. **36**, 706 (1930).
[3] E. Kobel, Phys. Rev. **36**, 1636 (1930).
[4] E. S. Lamar, Phys. Rev. **43**, 169 (1933).
[5] H. S. W. Massey and E. H. S. Burhop, *Electronic and Ionic Impact Phenomena* (Clarendon Press, Oxford, 1952).

energy rarely exceed 0.02. This, combined with their small mass, makes them unable to compete with rebounding or sputtered neutral atoms.

Thus, the only conceivably significant forces are those described under (1) and (2). A significant advantage in using ions for these force measurements is the fact that the primary force caused by the impinging ions cancels out. This allows a much more accurate determination of the forces resulting from the rebounding or sputtered part than would be possible if the bombardment were performed with neutral atoms.

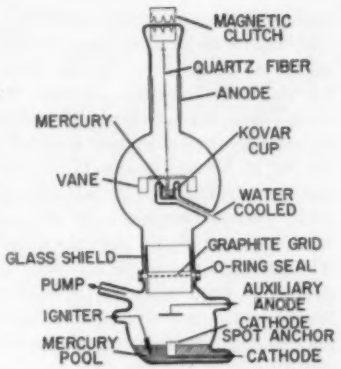

FIG. 1. Discharge tube for force measurements

Experimental Setup

Figure 1 is a schematic of the demountable tube. The lower part is essentially the same as used in our Hg sputtering studies and has been described in more detail elsewhere.[6] A dc Hg discharge with a current of ~ 3 amp is maintained between the pool cathode and a main anode (voltage drop ~ 30 v) and fills the tube above the stabilizing grid with a Hg plasma of high density. The tube is immersed up to the O-ring seal in an antifreeze solution which by means of a refrigeration unit is kept at a temperature of 0°C, setting the Hg gas pressure to $\sim 0.2\,\mu$. Immersed in the plasma is a "radiometer-like" torsion balance suspended from a quartz fiber. The zero position of the balance can be adjusted by means of a magnetic clutch. Voltage can be applied to the vanes through their connecting rod by a wire which dips into a small bowl filled with a liquid metal. Gallium was used for this purpose in the first experiments because of its low vapor pressure. It was found that liquid gallium is somewhat sluggish, however, interfering with the completely free movement of the balance, as evidenced by a not exactly reproducible zero position and hysteresis effects. Much improvement was noted when the Ga was replaced by Hg. The Hg had to be cooled, however, in order to prevent its evaporation. Cooling was accomplished by pumping part of the 0°C antifreeze solution through a glass finger which extends into the tube and ends in a Kovar cup which holds the Hg.

One of the tubes had two sidearms from which two additional electrodes could be pushed into the plasma magnetically. These electrodes were used to deposit different metals by sputtering onto the vane surfaces.

From the sputtering work in Hg it is known that metal surfaces become covered with a Hg film unless the target is kept above a certain critical temperature. Above this temperature, which for most metals is around 300°C, the dwelling time of Hg atoms on a metal surface is short enough not to interfere. A Hg film has a marked influence on the forces. Not only does the accommodation of ions change but very pronounced additional forces arise from sputtered Hg atoms. Under these circumstances it is very important to keep the target temperature above the critical value. This can be accomplished in several ways: (1) operating the tube at high power levels so that the target vanes are in a high temperature gas-and-plasma environment; (2) additional heating of the tube walls (heating tape) from the outside; (3) making measurements immediately after the target temperature has been raised by ion or by electron bombardment. Above the critical target temperature the forces become essentially independent of temperature. This fact, together with a check as to whether the forces are proportional to the bombarding ion current, as they should be, makes it possible to verify whether these temperature requirements have been fulfilled.

After some experience in operating the balance has been gained, one learns how to bring the balance to a fast stop and how to avoid the overswing by applying a braking voltage pulse at the proper moment. This eliminates the necessity for a special damping provision.

The balance was calibrated by measuring the periods of oscillation with and without the addition of known weights to the vanes. The torque of the 21.5 cm long and ~ 70-μ diameter quartz fiber was found to be 0.065 dyne-cm per degree of rotation.

EXPERIMENTS

When the vanes are made from one metal only, the forces are equal at the front and back sides of the vanes and the balance stays in zero position whether the discharge is switched on or off and regardless of the potential applied to the vanes. This situation is changed when front and back sides of the vanes are made of different metals. For example, one can make the vanes of Mo and then, by inserting two Au electrodes through two sidearms, deposit a thin Au layer by sputtering onto the front side of one vane and the back side of the other. Strong forces now arise and can be measured as a function of the bombarding ion energy. As soon as the Au layer has been sputtered off, the balance returns to zero position. The same force curve can be obtained when the vanes are prepared by spot welding thin Au and Mo sheets together. If different metals are used on the front

[6] G. K. Wehner, Phys. Rev. **108**, 35 (1957).

and back sides of a vane, one measures, of course, only the difference in the forces between two metals and learns nothing about the absolute force curve of one metal. Interchanging different front and back side metals does not help here either. For instance, when one determines the force curve for Au vs Mo in one run, then for Au vs Ni and finally Mo vs Ni in succeeding runs, one curve is found to be the difference of the other two, which merely proves the reliability of the measurement but does not give the absolute force curve for one metal. The problem would be solved if the plasma could be prevented from reaching the back side of a vane. This would create an unsymmetrical environment, however, and would introduce superimposed radiometer forces resulting from the fact that the vane sees a hot plasma on one side and a cooler gas and tube wall on the other.

The best that can be done under these circumstances is to keep the forces on the back side constant, i.e., independent of the bombarding energies on the front side, by covering it with an insulating layer. Such a layer assumes the floating potential of a probe, i.e., it becomes somewhat negatively charged in the plasma. It is consequently under low velocity ion bombardment and subject to a small constant force. This force can be kept the same for all measurements by always operating the discharge with the same discharge parameters (voltage, current, pressure) and using the same insulating material. The behavior of different insulating materials was checked by covering front and back sides of the vanes with different insulators and measuring the shift of the balance when the discharge was switched on. In one experiment we checked microscope cover slides vs quartz paper, in another mica vs quartz paper. In both cases the balance moved somewhat toward the quartz paper side when the plasma was established. Reversing the insulators gave the same result, indicating that possible unsymmetries in the plasma do not enter into the picture. With the force on mica or glass obviously somewhat larger than that on quartz paper, the latter was chosen for all measurements. The quartz paper clings fairly well to a metal when pressed on with a drop of distilled water. It was found, as will be discussed below, that all the force curves for clean metals tend to converge at low ion energy to the same value. It is reasonable to assume that this value is identical with force zero on the metal side.

Experiments with insulators on both sides of the vanes gave information on the extent of ion leakage current to parts of the balance other than the vanes, e.g., to the Hg surface in the bowl. All other parts, e.g., the outside of the bowl, the balance crossbar and the exposed part of the wire dipping into the Hg bowl, were insulated in order to prevent their contact with the plasma. The leakage current was found to amount to roughly 15% of the current measured in the case of metal vanes with quartz backs. Taking this correction into account, the actual ion current to the vanes is $\sim$7.5 ma at -50 v and $\sim$8.5 mm at -300 v bombarding voltage. For bombarding voltages smaller than 20 v the measured current drops rapidly because of the superimposed electron current, and the ion current has to be estimated by extrapolating the fairly well saturated ion current from higher negative voltages down to the low voltage value. With vanes 1.4 cm$\times$1.5 cm in size as used in these experiments, the average ion current density is roughly 2 ma/cm^2.

Probe measurements showed that the plasma potential in vane vicinity does not differ from anode potential by more than $\sim$5 v. Thus, the bombarding voltage can always be measured directly with respect to the anode.

The order of magnitude of the radiometer force arising from temperature differences of front and back sides of the vanes in a region where the mean free path of Hg atoms is large or comparable to the tube dimensions can be estimated from

$$F=0.43nkT^{\frac{1}{2}}(T_1^{\frac{1}{2}}-T_2^{\frac{1}{2}}),$$

where F = force per unit area, n = number of Hg atoms per cm^3 in the tube, k = Boltzmann constant, T = tem-

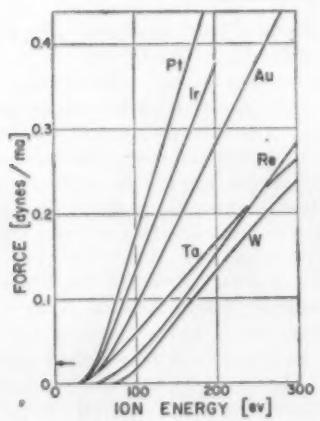

FIG. 2. Forces on Period VI metals as a function of Hg^+-ion energy.

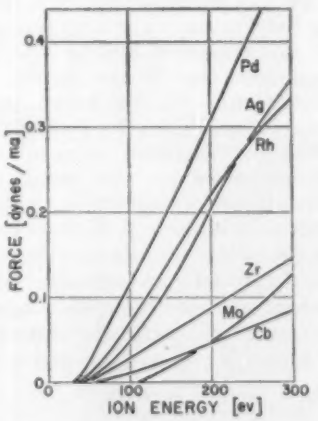

FIG. 3. Forces on Period V metals as a function of Hg^+-ion energy.

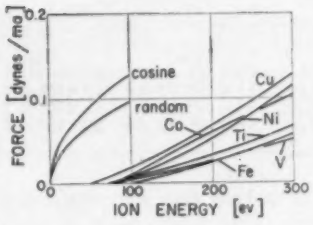

FIG. 4. Forces on Period IV metals as a function of Hg^+-ion energy. Curves marked "random" and "cosine" would arise if only 10% of the Hg^+-ions were reflected with full kinetic energy.

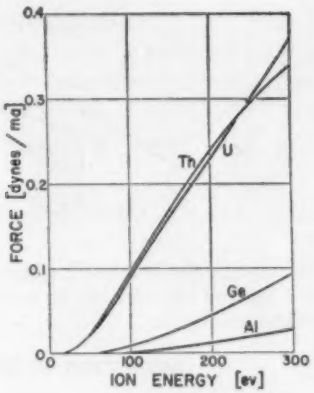

FIG. 5. Forces on Th, U, Ge, and Al as a function of Hg^+-ion energy.

perature of the gas on the walls, and T_1 and T_2 are the temperatures of front and back sides of the vanes. In deriving this equation, it is assumed that the number of atoms which evaporate with a spatial cosine distribution from the vanes is equal to the number arriving at the vanes from the gas. The evaluation for $T=400°K$, $T_1=700°K$, $T_2=500°K$, a Hg gas pressure of 0.2 μ, and 2 cm^2 area for each vane yields a combined force for the two vanes of ~ 0.1 dyne. With a distance of 8.6 cm between the centers of the two vanes, as used in all experiments, the torque would amount to 0.43 dyne-cm or the balance would turn by roughly 7°. This is about the amount of zero shift observed experimentally immediately after the vanes had been bombarded with ions of ~ 300-ev energy. The vanes have sufficient heat capacity so that in a fast measurement this zero shift can be roughly determined and taken into account. Normally, however, as the ionic heating of the vanes stays within reasonable limits (<0.4 w/cm^2), the zero shift becomes small and can be neglected. Serious difficulties arise, however, at very low ion energies (<15 ev) where the forces become very small; the zero shift consequently becomes relatively more important and substantial heating of the vanes results from the collected electrons. In this region the measurements become less reliable.

The bombarding ion current density can be changed with the main discharge current. The forces are found to be roughly proportional to the ion current provided the vanes stay hot enough to prevent Hg from accumulating at the vane surfaces.

In measuring the force curves of different metals a pronouncedly different behavior is noted between noble and non-noble metals. With noble metals the curves are always reproducible; in non-noble metals the forces depend markedly on the previous treatment of the target or the condition of the surface. More specifically, the force curves for non-noble metals begin to show the same characteristics as those of the noble metals as soon as the oxide layer has been removed by sputtering. When keeping the vanes at a low potential, however, the sputtering rate by the low velocity ions is so small that the formation of oxide layers from background impurities in the tube cannot be overcome and the force curve changes gradually over into that found for a new or unsputtered target.

Different metals not only require different bombarding ion energies and different times to remove surface layers effectively but they show different rates of conversion from the clean to the oxide covered state as well. In some metals the process proceeds so fast that one hardly has time enough to measure the forces in the clean state. With W as it comes from stock, for instance, it takes about 10 minutes bombardment at -300 ev (2 ma/cm^2) for the force curve to change to the clean curve. At a voltage of -20 v the curve changes back to the original state in only a matter of a few seconds, and the surface now becomes covered supposedly with at least a monolayer of oxide. Much improvement is noted when a getter material such as U, Th, or Ti is sputtered in a sidearm of the tube. One can then increase the time during which the surface remains clean to more than 30 minutes, even with the valve to the pump closed. Thus, the forces actually turn out to be a very sensitive and useful indicator of surface layer formation caused for instance by background impurities in the discharge.

Figures 2 to 5 show the experimentally determined forces in d/ma as a function of the bombarding ion energy for 22 metals after cleaning by sputtering. All curves tend to converge at low ion energy to the same constant force. In other words, at sufficiently low ion energies, the balance always goes back to the same position P with respect to "zero." "Zero" is the position which the balance has before the discharge is switched on (indicated in Fig. 2 by an arrow). Position P is always in such a direction as if a small constant force were pushing on the quartz paper side. It is reasonable to assume that this force represents the unknown force resulting from the ion bombardment of the insulator backs. Consequently, position P was identified with zero force on the metal sides and in accordance with this the graphs in Figs 2 to 5 have been drawn so that position P coincides with the origin of the force ordinate.

Figure 6 shows as a typical example the two curves obtained with a non-noble metal such as Zr. One of the two curves is characteristic of the metal immediately after a thorough sputtering treatment (-300 v, 30 min),

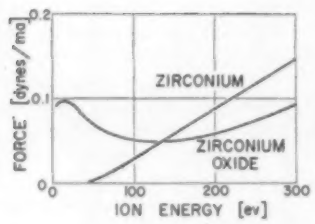

FIG. 6. Force curves for clean and oxide-covered Zr surfaces.

the other of the metal as it comes from stock or after it has had an opportunity to become covered with an oxide layer again.

DISCUSSION OF RESULTS

The force curves for the clean metals and their onset energy rather closely resemble the corresponding sputtering yield curves.[6,7] This indicates that the forces which arise on ion-bombarded clean metals are caused by the ejected sputtered atoms. With the known data on sputtering yields[6,7] and the angular distribution of atoms sputtered from a polycrystalline target under normal Hg^+-ion incidence,[8] one can determine from the forces the average kinetic energy of the ejected sputtered atoms. Approximating the angular distribution with a cosine law, the average velocity $\bar{v}$ of sputtered atoms is

$$\bar{v}=\frac{3\times10^8 F}{2AY},$$

where $\bar{v}$=velocity in cm/sec, F=force in d/ma, A=atomic weight number, and Y=sputtering yield (atoms/ion).

Results for the noble metals are listed in Table I, which gives the average velocities in cm/sec and the corresponding kinetic energies at 100, 200, and 300 ev bombarding energies. These results are in fairly good agreement with recently published data[9] obtained with another method.

The average velocities from other metals are higher and have a tendency in some cases to increase with decreasing bombarding energy to unbelievably high values. This discrepancy is partly caused by the fact that the sputtering yields at low ion energies are in many cases, in particular in those metals which tend to form sputtering-resistant oxide layers, higher than previously reported, as we found with a recently developed spectroscopic method which makes it possible to eliminate surface contamination difficulties[10] in sputtering yield measurements. Furthermore, one cannot completely rule out the possibility that part of the Hg^+-ions become imbedded in the target during bombardment and are then sputtered together with the target atoms. This would result in additional forces which could be misinterpreted as higher ejection energies of sputtered target atoms.

TABLE I.

	Cu	Ag	Au
100 ev	3×10^5 (3.0 ev)	3.1×10^5 (5.4 ev)	2.4×10^5 (5.9 ev)
200 ev	3.1×10^5 (3.2 ev)	3.3×10^5 (6.1 ev)	2.1×10^5 (4.5 ev)
300 ev	3.3×10^5 (3.6 ev)	2.9×10^5 (4.7 ev)	2.2×10^5 (5 ev)

Below the sputtering onset the forces on a clean metal were always found to be close to zero, indicating that the accommodation coefficient of Hg^+-ions must be very close to unity. In Fig. 4 the two curves indicate, for instance, the forces which would arise if only 10% of the Hg^+-ions were reflected as neutrals with full kinetic energy, in one case assuming a cosine and in the other a random distribution.

Strikingly different is the situation with oxide-covered metals. The low energy hump, shown in Fig. 6 for instance, becomes less and less pronounced the closer the target metal's position in the periodic table is to one of the noble metals. Thus, the maximum at around 20 ev decreases in height in the order Ti, V, Cr, Mn, is barely noticeable in Fe and disappears in Co, Ni, Cu. The same behavior is observed in the 5th period with Zr, Cb, Mo and no hump in Rh, Pd, Ag and in the 6th period with Ta, W, Re, and zero forces in the case of Ir, Pt, and Au. It is not clear yet what the reasons are for this force behavior. One cannot completely exclude the possibility that negative ion formation at oxide-covered target surfaces plays a role here. Such ions, as discussed above, would be accelerated in the sheath and push the target away from the plasma. If one interprets these forces in terms of accommodation coefficients, one would have to assume that oxide-covered surfaces do not accommodate Hg^+-ions as well as clean metals. This is not in agreement with other results concerning the difference of thermal accommodation coefficients between clean and oxide covered surfaces.[11] From Fig. 6, for instance, one would have to conclude that at 20 ev bombarding energy the accommodation coefficient has decreased from unity for the clean metal to roughly 0.8 for the oxide-covered metal. The decrease beyond the maximum in the curves would indicate that the accommodation coefficient increases with higher ion energy until the force curve finally rises again because of the oxide sputtering. The region below 20 ev would be of much interest but the measurements here become rather unreliable, unfortunately, because of the heating of the vanes by the superimposed electron current.

It will be of much interest to extend these same measurements to other gases, in particular to the lighter gas ions. We should expect a quite different force behavior

[7] G. K. Wehner, Phys. Rev. **112**, 1120 (1958).
[8] G. K. Wehner and D. Rosenberg, J. Appl. Phys. **31**, 177 (1960).
[9] G. K. Wehner, Phys. Rev. **114**, 1270 (1959).
[10] R. Stuart and G. Wehner, Phys. Rev. Letters **4**, 409 (1960).
[11] H. Mayer, *Physik duenner Schichten*, (Wissenschaftliche Verlagsgesellschaft, M. B. H. Stuttgart, Germany, 1955), Vol. 2.

in the low ion energy region when a light ion bombards a material of much heavier atoms because the accommodation coefficients here are expected to become substantially less than unity.

ACKNOWLEDGMENT

The skillful and patient work of B. Richelman, R. Moseson, and our glass experts, Emil Benz and Arthur Haut, is gratefully acknowledged.

JOURNAL OF APPLIED PHYSICS VOLUME 31, NUMBER 8 AUGUST, 1960

Contribution of Anode Emission to Space Charge in Thermionic Power Converters

ANTHONY F. DUGAN
Lockheed Missiles and Space Division, Sunnyvale, California
(Received December 16, 1959; and in final form April 6, 1960)

The space charge theory of Langmuir has been extended to include the effects of anode emission on the performance of a vacuum thermionic power converter. The basic equation is similar to Langmuir's $\xi-\eta$ equation, but it involves two additional parameters which depend on the temperatures and thermionic properties of the electrodes. An iterative technique is described for obtaining solutions in specific cases, and some sample calculations based on hypothetical diodes are presented. The calculations indicate that the effect of the anode temperature is considerably more pronounced if the cathode-anode work function difference is large.

I. INTRODUCTION

IN the treatment of space charge effects in vacuum thermionic diodes, it is usually assumed that the anode emission is sufficiently small to be neglected. An analysis based upon this assumption leads to the familiar Langmuir space charge equation.[1,2] This equation has been used by several authors, for example, Webster,[3] to determine performance characteristics of thermionic power converters. In many cases, however, neglect of anode emission cannot be justified; for instance, in space applications it is desirable to reject waste heat by radiation directly from the anode in order to minimize the weight of the system. A converter operating at 20% efficiency and producing 3 w/cm² requires the anode to reject 12 w/cm². Assuming black body conditions, the anode temperature would have to be greater than 1200°K. At this temperature, the anode emission can be appreciable and should, therefore, be considered in determining the expected performance.

The effects of anode back current on the efficiency of a thermionic diode have been considered by Houston.[4] In his paper, however, he did not consider the contribution of the anode to cathode current to the space charge. The purpose of the present paper is to describe a method of calculating space charge when both cathode and anode are emitting.

II. ANALYSIS

Figure 1 is a schematic representation of the potential energy of an electron in a thermionic power converter. ϕ_c and ϕ_a are the true work functions of cathode and anode, respectively. V_0 is the effective output voltage of the converter and is determined in actual practice by matching the external electrical load to the operating characteristics of the converter. V_m is the potential energy maximum, and is determined by the distribution of electrons between the electrodes. The following derivation of the space charge distribution employs an analytical approach similar to that used by Fry.[2]

If a surface is at temperature T, it will emit electrons with a Maxwell velocity distribution characteristic of T. For a single surface, say the cathode, the number of

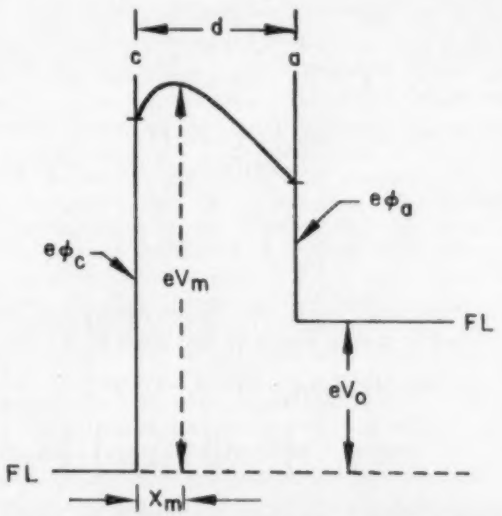

FIG. 1. Schematic representation of an electron's potential energy in a thermionic power converter. FL denotes the Fermi level.

[1] I. M. Langmuir, Phys. Rev. 21, 419 (1923).
[2] T. C. Fry, Phys. Rev. 17, 441 (1921).
[3] H. F. Webster, J. Appl. Phys. 30, 488 (1959).
[4] J. M. Houston, J. Appl. Phys. 30, 481 (1959).

electrons emitted per unit time per unit area with velocity components normal to the surface between v_0 and v_0+dv_0 is

$$dN_c=N_c\frac{mv_0}{kT_c}\exp(-mv_0^2/2kT_c)dv_0. \quad (1)$$

The charge density at a point x where the potential is V can be found from

$$\rho_c=e\int_{v_0'}^{\infty}\frac{dN_c(v_0)}{v}, \quad (2)$$

where

$$v=\left[v_0^2-\frac{2e(V-\phi_c)}{m}\right]^{\frac{1}{2}} \quad (3)$$

is the velocity which an electron whose initial velocity was v_0 has when it reaches x. Equation (2) must be integrated over the appropriate velocities. If $x<x_m$, one finds at x, in addition to those electrons whose initial velocities were sufficient to carry them past x_m, a reverse current consisting of those electrons whose initial velocities were sufficient to carry them past x, but not past x_m. For $x>x_m$, one finds these electrons missing. The charge density is, therefore,

$$\rho_c=eN_c\frac{m}{kT_c}\exp\left(-\frac{e(V-\phi_c)}{kT_c}\right)\left[\int_0^{\infty}\exp\left(-\frac{mv^2}{2kT_c}\right)dv \pm\int_0^{[2e(V_m-V)/m]^{\frac{1}{2}}}\exp\left(-\frac{mv^2}{2kT_c}\right)dv\right], \quad (5)$$

in which the upper and lower signs refer, respectively, to $x<x_m$ and $x>x_m$. Equation (3) has been used to change the variable of integration v_0 to v. The result of integrating Eq. (4) is:

$$\rho_c=eN_c(\pi m/2kT_c)^{\frac{1}{2}}\exp[-e(V-\phi_c)/kT_c]\times[1\pm\mathrm{erf}\{[e(V_m-V)/kT_c]^{\frac{1}{2}}\}], \quad (5)$$

where

$$\mathrm{erf}(z)=\frac{2}{(\pi)^{\frac{1}{2}}}\int_0^z\exp(-y^2)dy.$$

When the anode emits, the charge density will be increased by a term similar to that given by Eq. (5).

$$\rho_a=eN_a(\pi m/2kT_a)^{\frac{1}{2}}\exp[-e(V-\phi_a-V_0)/kT_a]\times\left[1\mp\mathrm{erf}\left\{\left[\frac{e(V_m-V)}{kT_a}\right]^{\frac{1}{2}}\right\}\right]. \quad (6)$$

Poisson's equation relates the potential to the charge density:

$$d^2V/dx^2=-4\pi\rho, \quad (7)$$

$$\frac{d^2V}{dx^2}=-4\pi e\left\{N_c\left(\frac{\pi m}{2kT_c}\right)^{\frac{1}{2}}\times\exp\left[-\frac{e(V-\phi_c)}{kT_c}\right]\left[1\pm\mathrm{erf}\left\{\left[\frac{e(V_m-V)}{kT_c}\right]^{\frac{1}{2}}\right\}\right]+N_a\left(\frac{\pi m}{2kT_a}\right)^{\frac{1}{2}}\exp\left(-\frac{e(V-\phi_a-V_0)}{kT_a}\right)\times\left[1\mp\mathrm{erf}\left\{\left[\frac{e(V_m-V)}{kT_a}\right]^{\frac{1}{2}}\right\}\right]\right\}. \quad (8)$$

With the following changes of variables:

$$\eta=e(V_m-V)/kT_c,$$
$$\xi=\left[\frac{8\pi e^2N_c}{kT_c}\left(\frac{\pi m}{2kT_c}\right)^{\frac{1}{2}}\right]^{\frac{1}{2}}(x-x_m)\exp(-\tfrac{1}{2}\eta_c), \quad (9)$$
$$\alpha=T_c/T_a,$$

and some manipulations, Eq. (8) can be put into the form:

$$\frac{d^2\eta}{d\xi^2}=-\frac{1}{2}\left\{e^{\eta}(1\pm\mathrm{erf}\eta^{\frac{1}{2}})+\alpha^{\frac{1}{2}}\frac{N_a}{N_c}e^{\eta_c-\eta_a}(1\mp\mathrm{erf}(\alpha\eta)^{\frac{1}{2}})\right\}, \quad (10)$$

where η_c and η_a are the values of η at cathode and anode, and the upper signs are to be used for $\xi<0$ and the lower signs are to be used for $\xi>0$. Equation (10) is readily seen to reduce to Langmuir's equation if the anode temperature goes to zero. N_a and N_c are simply proportional to the saturation current densities which can be computed from Richardson's equation:

$$I_s=AT^2\exp(-e\phi/kT),$$

where A is the emission coefficient in amp/cm² °K². For the purpose of demonstrating the method, values of A and ϕ were chosen which were obtained from Richardson plots for some materials. Strictly speaking, one should use the true work functions and set $A=120$ amp/cm² °K². In the calculations described below, however, the empirical values of A and ϕ were used throughout and no temperature dependence was considered. The calculations, therefore, describe hypothetical diodes for which the true work function and the Richardson work function are identical. The main features of the results are not seriously effected by this assumption, and the computational procedure is the same if the true work functions are used.

A first integral of Eq. (10) can be obtained, but from there on one must use numerical methods. Letting I_{se} and I_{sc} be the saturation currents from anode and cathode, and integrating Eq. (10),

$$d\eta/d\xi=\{e^{\eta}(1\pm\mathrm{erf}\eta^{\frac{1}{2}})-[1\pm(2/\pi^{\frac{1}{2}})\eta^{\frac{1}{2}}]+B(e^{\eta_a}[1\mp\mathrm{erf}(\alpha\eta)^{\frac{1}{2}}]-[1\mp(2/\pi^{\frac{1}{2}})(\alpha\eta)^{\frac{1}{2}}])\}, \quad (11)$$

where $B=(I_{sa}/I_{sc})\alpha^{-\frac{1}{2}}\exp(\eta_c-\alpha\eta_a)$. The net current drawn by the diode is

$$I=I_{sc}e^{-\eta_c}-I_{sa}e^{-\alpha\eta_a}. \tag{12}$$

Since η_c and η_a involve V_m, an iterative procedure is required to solve for V_m. If the anode-cathode separation is d, then

$$\xi_a-\xi_c=\left(\frac{8\pi e^2}{k}\right)^{\frac{1}{2}}\left(\frac{\pi m}{ke^2}\right)^{\frac{1}{2}}\frac{I_{sc}^{\frac{1}{2}}}{T_c^{\frac{1}{2}}}de^{-\frac{1}{2}\eta_c} \tag{13}$$

$$=9.188\times10^{5}\frac{I_{sc}^{\frac{1}{2}}}{T_c^{\frac{1}{2}}}de^{-\frac{1}{2}\eta_c} \tag{14}$$

with I_{sc} in amp/cm² and d in cm.

The procedure for finding V_m is as follows: Calculate $\eta_c-\eta_a=e(V_0+\phi_a-\phi_c)/kT_c$. V_0 is the output voltage of the converter and is a known quantity. Webster[3] assumes that the current is known, and calculates V_0. With the anode emitting, however, it is more convenient to assume V_0 and calculate the current. Now, $\eta_c=e(V_m-V)/kT_c>\eta_c-\eta_a$. Choose, therefore, a value of $\eta_c>\eta_c-\eta_a$, and find η_a. Using Eq. 14, $\xi_a-\xi_c$ can be calculated. Using the values of η_c and η_a, Eq. (11) can be numerically integrated to obtain ξ_c and ξ_a. Next, compare the value of $\xi_a-\xi_c$ obtained by integration of Eq. 11 with the value obtained from Eq. 14. Let $\delta=(\xi_a-\xi_c)_{14}-(\xi_a-\xi_c)_{11}$ where the subscript refers to the number of the equation by which the quantity is calculated. δ will be zero for the correct value of η_c. If δ is not zero, η_c should be improved by decreasing or increasing according to whether δ is negative or positive. The process can usually be made to converge in five or six iterations. A program was set up for the IBM 709 to perform the calculations, and several performance curves were obtained.

III. DISCUSSION

It would appear worthwhile to be able to generate a family of solutions of Eq. 11 for various values of α and B. If B were a function of α only, it would be possible to generate such a family, but B depends on ϕ_c, ϕ_a, T_c, and T_a through I_{sc} and I_{sa}. The result of this situation is that each converter under consideration must be treated as a special case. The usefulness of the method lies in the fact that it furnishes a way of determining under what conditions anode emission becomes a serious problem. This is demonstrated by some calculations based on the properties of some materials from which typical converters might be constructed.

In the calculations described below, the cathode has the emission properties of the L-metal cathode, $\phi_c=1.65$ volt, and $A_c=3$ amp/cm² °K². The usual type of converter has an anode with a low work function, therefore, calculations were made for $\phi_a=1.0$ v and $A_a=6.5$ amp/cm²°K². In order to determine the effects of changing the anode work function, some computations were made for the case in which the anode was the same material as the cathode.

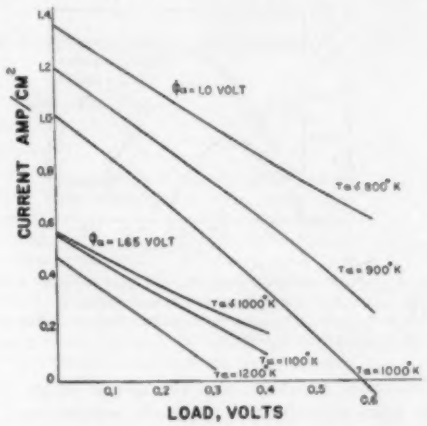

FIG. 2. Current voltage characteristics for two types of thermionic power converters. In the upper three curves, the anode has a work function of 1.0 v and emission coefficient of 6.5 amp/cm² °K². In the lower three curves, the anode has the same properties as the cathode, work function 1.65 v and emission coefficient 3.0 amp/cm² °K². The electrode separation is 0.002 cm and the cathode temperature is 1400°K.

The effect of anode work function can be seen from Fig. 2 where current is plotted vs output voltage for various anode temperatures. The curves for which $\phi_a=1.0$ v start at higher currents than those for $\phi_a=1.65$ v. As the anode temperature increases, the current drops more noticeably for the upper curves ($\phi_a=1.0$ v) than for the lower curves. The threshold temperature beyond which anode emission is appreciable is lower for a diode with a low anode work function. The drop in current as V_0 is increased is attributable to two mechanisms. First, the forward current from cathode to anode decreases. Second, the back current from anode to cathode increases. Both these effects are readily understood from Fig. 1. Increasing V_0 increases V_m, and also causes V_m to move closer to the anode. The limiting position of V_m is at the anode surface. This implies that as V_0 increases, $(V_m-\phi_a-V_0)$ decreases which in turn increases the anode emission. The forward current on the other hand decreases exponentially with increase in V_0. At higher temperatures, the effect of increased back emission is greater than the effect of decreased forward emission. Figure 2 demonstrates this fact. If there is no anode emission, $T_a\leq800$°K and $T_a\leq1000$°K for $\phi_a=1.0$ v and 1.65 v, respectively, the current asymptotically goes to zero as V_0 is increased. At temperatures at which anode emission is appreciable, however, the current decreases more rapidly as V_0 is increased, and becomes negative at some voltage which is not particularly large. Figures 3 and 4 are power output as a function of load voltage for the two types of converters. In Fig. 4, the anode has

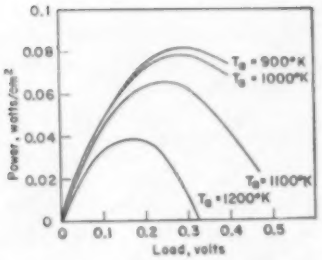

FIG. 3. Output power as a function of load voltage. Anode and cathode have the same thermionic properties $\phi=1.65$ v and $A=3.0$ amp/cm² °K². Electrode separation is 0.002 cm and cathode temperature is 1400°K.

the low-work function, and the power output is seen to be quite sensitive to the anode temperature. Even at $T_a=900$°K, the power peak has dropped to about two-thirds of what it was at $T_a=0$°K. With the high anode work function, an anode temperature of 900°K causes only a slight diminution in power, and then only at higher voltages.

The effect of cathode-anode separation is quite interesting. It is usually stated in discussions of thermionic power converters that one way to eliminate space charge is to use very small separations. Figure 5 shows the effect of spacing on the power output for the low-work function anode type of converter. There is a crossing of the power curves. This is understandable by the same argument that was used to explain the fact that increasing V_a increases the anode emission. Reducing the spacing causes a reduction in the height of the potential energy maximum, and also reduces the values of V_a for which the maximum reaches its limiting

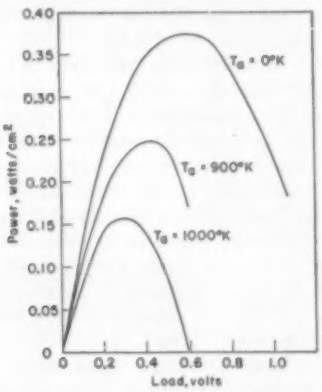

FIG. 4. Power output as a function of load voltage for $\phi_a=1.0$ v, $A=6.5$ amp/cm² °K², $\phi_c=1.65$ v, $A_c=3.0$ amp/cm² °K². Electrode separation is 0.002 cm. Cathode temperature is 1400°K.

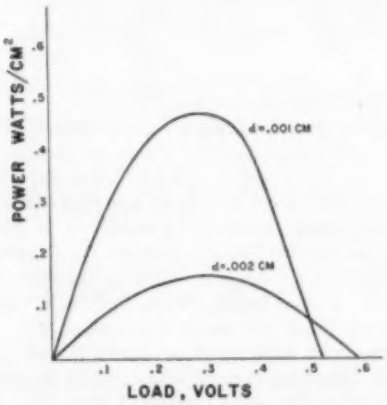

FIG. 5. Comparison of power output for spacings of 0.001 cm and 0.002 cm. The anode properties are $\phi_a=1.0$ v, $A_a=6.5$ amp/cm² °K², $T_a=1000$°K. For the cathode, $\phi_c=1.65$ v, $A_c=3.0$ amp/cm² °K², and $T_c=1400$°K. Whereas the peak is considerably higher for $d=0.001$ cm, note the much sharper drop as the peak voltage is passed.

position—the anode surface. As a result, for higher voltages, the net current drops as the spacing is decreased. This occurs however, at such a voltage that the net power output is too low to be of interest.

The anode emission problem, it can be concluded, becomes most serious at voltages beyond that which yields peak power output. Radiation can, therefore, still be effectively used to reject waste heat, but if the anode work function is much lower than the cathode work function, one is limited to low operating voltages.

Electromagnetic Theory of dc Effects in Ferromagnetic Resonance*

H. J. JURETSCHKE
Polytechnic Institute of Brooklyn, Brooklyn 1, New York
(Received April 14, 1960)

Effects of magnetoresistance and extraordinary Hall effect on the propagation of electromagnetic waves through very thin sheets of ferromagnetic conductors are studied. These contributions to the conductivity produce electric fields varying like products of current and magnetization and introduce nonlinear interactions, which are particularly large in the neighborhood of ferromagnetic resonance. Detailed first-order dc electric fields are obtained for the configuration of a very thin ferromagnetic sheet very close to a conducting wall. The results predict signals strictly proportional to incident microwave power, and mostly inversely proportional to film thickness, becoming independent of thickness for the thinnest films. Their magnetic field or frequency dependence gives typical resonance curves modulated by slowly varying amplitudes. The maxima and zeros of these amplitudes are very sensitive to the local field configuration. Once this latter is well known, however, these effects can be employed to study conveniently the high-frequency conduction and magnetic properties of the thinnest films.

1. INTRODUCTION

ELECTRICAL conduction in a ferromagnetic metal generally depends on the direction of the magnetization $\mathbf{M}$. The simplest phenomenological description of such dependence in an isotropic conductor takes the form[1]

$$\mathbf{J}=\sigma\mathbf{E}-(\Delta\rho/\rho M^2)(\mathbf{J}\cdot\mathbf{M})\mathbf{M}+R\sigma\mathbf{J}\times\mathbf{M}. \quad (1)$$

Here R is the extraordinary Hall constant, and $\Delta\rho=\rho_{\parallel}-\rho_{\perp}$, where the resistivity components refer to the two principal directions of $\mathbf{J}$ with respect to $\mathbf{M}$; $\sigma=1/\rho$ is, strictly, $\sigma_{\perp}$. $\Delta\rho$ is generally positive, while R may have either sign. Expression (1) neglects the applied field-dependent galvanomagnetic effects occurring in all metals. In ferromagnetics these are normally much smaller than the spontaneous effects of interest here, and begin to play a role at very large applied fields.

If the average direction of $\mathbf{M}$ is fixed by an applied static magnetic field $\mathbf{H}_0$, a superimposed electromagnetic field will produce two effects in the metal: (1) Its magnetic field causes the magnetization to precess at the applied frequency about its average direction, and (2) its electric field excites oscillating conduction currents. As a consequence of the nonlinear terms in Eq. (1) these effects are coupled and will produce, among other results, time-independent fields and currents. Direct current effects accompanying ferromagnetic resonance have been observed experimentally,[2] and are in qualitative agreement with the interpretation outlined. The present paper develops a more detailed theory of the effects to be expected on this basis.

2. GENERAL FORMULATION

Formally, the interaction of an electromagnetic field with a conducting ferromagnetic is described by Maxwell's equations subject both to the nonlinear current-voltage relation of Eq. (1), and to the equation of motion of $\mathbf{M}$. Since the nonlinear terms in Eq. (1) are small, however, the solutions to this problem do not differ radically from those of the corresponding linear one, and can be obtained by iteration. In particular, for a discussion of the lowest-order effects due to the correction terms in Eq. (1) it suffices to substitute in these the zero-order solutions for $\mathbf{J}$ and $\mathbf{M}$, obtained with $\Delta\rho=R=0$.

Let the first-order fields be designated by lower case letters, while capital letters now refer to zero-order fields. In addition, because of the small angle of precession, it is useful to introduce the oscillating component of the magnetization $\mathbf{M}_1$ such that

$$\mathbf{M}=\mathbf{M}_0+\mathbf{M}_1, \quad \mathbf{M}_0\cdot\mathbf{M}_1=0, \quad |\mathbf{M}|\doteq|\mathbf{M}_0|.$$

If only first powers of M_1 are retained, the first-order contribution of Eq. (1) takes the form

$$\mathbf{j}=\sigma\mathbf{e}-(\Delta\rho/\rho M^2)(\mathbf{J}\cdot\mathbf{M}_0)\mathbf{M}_0+R\sigma\mathbf{J}\times\mathbf{M}_0 -(\Delta\rho/\rho M^2)\{(\mathbf{J}\cdot\mathbf{M}_0)\mathbf{M}_1+(\mathbf{J}\cdot\mathbf{M}_1)\mathbf{M}_0\} +R\sigma\mathbf{J}\times\mathbf{M}_1. \quad (2)$$

The first line of Eq. (2) lists the corrections to the zero-order solution of the same frequency. The second line contains the nonlinear effects, which generate both time-independent fields and fields of double frequency.

The discussion of both types of field is similar, and here we will concentrate on the time-independent, or dc fields. These are obtained from the time average of Eq. (2);

$$\langle\mathbf{j}\rangle=\sigma\langle\mathbf{e}\rangle+\sigma\mathbf{e}_0, \quad (3)$$

with

$$\mathbf{e}_0=-(\Delta\rho/M^2)(\langle\mathbf{J}\cdot\mathbf{M}_1\rangle\mathbf{M}_0+\langle\mathbf{J}\times\mathbf{M}_1\rangle\times\mathbf{M}_0) +R\langle\mathbf{J}\times\mathbf{M}_1\rangle. \quad (4)$$

Hence, for given microwave fields, we must find the averages $\langle\mathbf{J}\cdot\mathbf{M}_1\rangle$ and $\langle\mathbf{J}\times\mathbf{M}_1\rangle$. Once these are known,

* Supported by the Office of Naval Research.

[1] J.-P. Jan, *Solid State Physics* (Academic Press, Inc., New York, 1957), vol. 5, Secs. II and V.

[2] W. Egan and H. J. Juretschke, Bull. Am. Phys. Soc. Ser. II 3, 194 (1958); P. E. Tannenwald and M. H. Seavey, Jr., J. Physique radium 20, 323 (1959).

they define $\mathbf{e}_0$ which can then be considered as an impressed field.

Since from now on we will be concerned only with average values of first-order quantities, it is convenient to drop the brackets. Let $\langle\mathbf{j}\rangle\rightarrow\mathbf{j}$, $\langle\mathbf{e}\rangle\rightarrow\mathbf{e}$. These first-order fields obey Maxwell's time-independent equations;

$$\nabla\times\mathbf{e}=0, \quad \nabla\cdot\mathbf{j}=0. \tag{5}$$

Because of Eqs. (5) and (3) we can define a potential v satisfying the equations

$$-\nabla v=\mathbf{e}, \quad \nabla^2 v=\nabla\cdot\mathbf{e}_0. \tag{6}$$

Thus, the first-order time-independent fields derive from a potential satisfying Poisson's equation and subject to boundary conditions obtainable from Eq. (3) through the boundary conditions on $\mathbf{j}$. It is of interest to note that in general, therefore, the modified Ohm's law, Eq. (1), allows for the existence of a time-independent charge density in the interior of a metal.

Because $\mathbf{e}_0$ is obtained by averaging products of electromagnetic fields, it becomes cumbersome to work out the problem in its most general form. It is more convenient to specialize immediately to electromagnetic fields of interest in waveguides and cavities, and we will consider primarily the simplest possibility of a completely transverse wave falling at normal incidence on the ferromagnetic material.

Let the surface normal be along z, the static fields $\mathbf{H}_0$ and $\mathbf{M}_0$ along y, and the microwave magnetic field H_1 along x of a Cartesian coordinate system. Then $\mathbf{J}=(0,J,0)$, and $\mathbf{M}_1=(M_x,0,M_z)$, and $\mathbf{e}_0$ has the components:

$$\mathbf{e}_0=\{-(\Delta\rho/M)\langle JM_x\rangle+R\langle JM_z\rangle, \quad 0, \quad -(\Delta\rho/M)\langle JM_z\rangle-R\langle JM_x\rangle\}. \tag{7}$$

The computation of dc effects therefore consists of determining the averages $\langle JM_x\rangle$ and $\langle JM_z\rangle$ for a particular combination of waves traveling along z, and of then solving the electrostatic problem defined by Eq. (6).

3. ZERO-ORDER FIELD CONFIGURATION

It is clear that dc effects can be detected only in ferromagnetic films which are thin compared to the skin depth of the radiation, because of the shorting effect of the part of the metal not penetrated by microwaves. It should be noted that films in this thickness range may have thicknesses which are small compared to the bulk mean free path of their electrons. However, the skin effect remains normal under these conditions,[3] so that the local relation (1) continues to apply.

Very thin film samples require dielectric backing, such as glass for support, and their surface must be electrically insulated from any waveguide walls. By taking into account these requirements, the simplest field and film configuration is one in which a dielectric layer separates the film from a perfectly conducting short. The idealized situation is then as follows: At a distance D above the perfectly conducting plane $z=-D$ sits a ferromagnetic film, of thickness Δ and of infinite extent in the other directions. In the region $z>-D$, there exist microwave fields H_x and E_y having a space and time dependence given by $\exp i(\pm kz-\omega t)$. The propagation constant k has values in the three different regions, $-D\leq z\leq 0$, $0\leq z\leq\Delta$, $\Delta\leq z$, determined by their respective electromagnetic properties.

If the propagation constant in the region above the short is k_1, a compatible set of fields is given by

$$H_x=H_1\cos k_1(z+D)e^{-i\omega t}$$
$$E_y=(\omega/ck_1)H_1\sin k_1(z+D)e^{-i(\omega t+\pi/2)}, \quad -D\leq z\leq 0. \tag{8}$$

Because of the spatial variation of the magnetization in a metallic ferromagnetic such a field will generally excite in the film three modes of widely differing propagation constants and composition.[4] However, in materials for which spin-exchange effects are small under the conditions of standard resonance experiments, and, according to MacDonald, nickel falls in this class, Eq. (8) can be connected to a single mode in the film. If this mode is characterized by a complex propagation constant k_2 and a normal skin depth $\delta=c/(2\pi\sigma\omega)^{\frac{1}{2}}$, the fields in the film compatible with Eq. (8) are

$$H_x=H_1\cos k_1D\{\cos k_2z-(2i/k_1k_2\delta^2)\times\tan k_1D\sin k_2z\}e^{-i\omega t}, \quad 0\leq z\leq\Delta. \tag{9}$$
$$E_y=(\omega/ck_1)H_1\sin k_1D\{\cos k_2z-\tfrac{1}{2}ik_1k_2\delta^2\times\cot k_1D\sin k_2z\}e^{-i(\omega t+\pi/2)},$$

If $|k_2|\Delta\ll 1$, the trigonometric functions can be expanded, and since also $k_1\ll|k_2|$, $\Delta\ll D$, Eq. (9) can be simplified for very thin films as follows:

$$H_x=H_1\cos k_1D\{1-2iz(1/k_1\delta^2)\tan k_1D\}e^{-i\omega t},$$
$$E_y=(\omega/ck_1)H_1\sin k_1De^{-i(\omega t+\pi/2)}. \tag{10}$$

The approximations leading to Eq. (10) are valid except for D in the immediate neighborhood of a magnetic field node in the standing wave pattern above the short. If $|D-n\pi/k_1|\ll\frac{1}{2}\Delta|k_2^2\delta^2|$ the expression for E_y must be modified. Thus, for instance, at $D=n\pi/k_1$, the fields become

$$H_x=H_1e^{-i\omega t},$$
$$E_y=-(\omega/2c)k_2^2\delta^2H_1ze^{-i\omega t}. \tag{10'}$$

This condition may be realized for $n\geq 1$. However, immediately above the short the effective D is given by the skin depth of the short, and for even the best

[3] R. B. Dingle, Physica **19**, 1187 (1953); B. M. Bolotovskii, Soviet Phys. JETP **5**, 465 (1957).

[4] J. R. MacDonald, Phys. Rev. **103**, 280 (1956); W. S. Ament and G. T. Rado, Phys. Rev. **97**, 1558 (1955).

conductors at normal temperatures the foregoing inequality cannot be obtained for Δ of the order of 10^{-5} cm or less. Hence Eq. (10) applies for $k_1D<\pi$, and only this range of D will be considered in the following.

The fields in the region $z>\Delta$ can be established by a similar procedure. They are of interest mainly to relate the amplitude H_1 to that of the incident radiation. If the propagation constant in this region is k_0, and the inequalities apply to k_0 as well as to k_1, this relation is

$$H_1\cos k_1D = \frac{2H_{\text{inc}}}{\{1+(k_0/k_1)^2[1+(2\Delta/k_0\delta^2)]^2\tan^2 k_1D\}^{\frac{1}{2}}}. \quad (11)$$

The foregoing fields have been assumed to be entirely transverse and at normal incidence. Neither condition is met in most guided waves, but it can be corrected for. In the regions $z<0$ and $z>\Delta$ this merely requires adjusting the propagation constant k for the angle of incidence. Thus, for a TE_{10} mode in a rectangular guide of long dimension a_0 in its cross section

$$k^2=(\epsilon\omega^2/c^2)-(n\pi/a_0)^2,$$

where ϵ is the dielectric constant of the region. Within the ferromagnetic film $k_2\delta$ is of order unity and since the skin depth is very small compared to a_0, all lateral boundary conditions play but a small role in defining the mode. Hence k_2 can be computed for normal incidence, this approximation implying that all quantities of order $1/k_2a_0$ have been neglected.

The sample must, of course, be located in a region in which the microwave fields taken into account are practically uniform and are large compared to the remaining field components.

4. THE ELECTROSTATIC PROBLEM

The quantities $\langle JM_x\rangle$ and $\langle JM_z\rangle$ in Eq. (7) are obtained by multiplying σE_y of Eq. (10) with M_x and M_z and taking the time average. Since M_x and M_z are proportional to the H_x of Eq. (10) these averages will at most have a linear dependence on z. It is most convenient to solve the electrostatic problem posed by Eq. (6) for a general dependence of this form, since the exact values of the constants arising from the averages depend on the particular equation of motion assumed for the magnetization. Therefore, let Eq. (7) be of the form

$$\mathbf{e}_0=(A+Bz, 0, C+Dz). \quad (7')$$

Then we want to solve the equation

$$\nabla^2 v=D, \quad (6')$$

subject to certain boundary conditions.

Two types of boundary conditions are of interest. If the film is truly of infinite lateral extent, all field quantities can only depend on z, and Eq. (5) can be satisfied only if $e_x=e_y=0$, $j_z=0$. In that case the solution of Eq. (6′) satisfying the boundary condition $j_z=0$, at $z=0$, is

$$v=Cz+\tfrac{1}{2}Dz^2, \quad (12)$$

and we obtain the following full solution for the currents and fields

$$\begin{aligned} &j_x=\sigma(A+Bz), \quad j_y=j_z=0,\\ &e_z=-(C+Dz), \quad e_x=e_y=0. \end{aligned} \quad (13)$$

Thus, there are no transverse electric fields, but there exists a volume charge density in the steady state, accompanied by a transverse current. It should be noted that these arguments for the infinite film are independent of the particular form (7′) and apply to a general $\mathbf{e}_0$ whose components depend only on z.

The other practical boundary condition occurs when dc currents are prevented from flowing across specified boundaries in the otherwise infinite film. By making these dc barriers sufficiently thin, the plane microwave field configuration remains practically undisturbed.

Let us specify that no current flows across the rectangular slab specified by $x=\pm a$, $y=\pm b$, $z=0$, Δ, where a and b are of macroscopic dimensions while the film thickness Δ is very small. In that case we want to solve Eq. (6′) subject to the boundary conditions

$$\begin{aligned} &\frac{\partial v}{\partial x}(\pm a, y, z)=A+Bz, \quad \frac{\partial v}{\partial y}(x, \pm b, z)=0,\\ &\frac{\partial v}{\partial z}(x,y,0)=C, \quad \frac{\partial v}{\partial z}(x,y,\Delta)=C+\Delta D. \end{aligned} \quad (14)$$

By using Eq. (12), we can write a y-independent solution

$$v=(Cz+\tfrac{1}{2}Dz^2)+A'x+v_2(x,z), \quad (15)$$

where v_2 obeys Laplace's equation and has a normal derivative $\pm[(A-A')+Bz]$ at $x=\pm a$ and vanishing normal derivatives at $z=0$, Δ. $(A-A')$ is so far not specified. This solution for v_2 is obtainable in terms of the general series solution satisfying the boundary conditions at $z=0$, Δ. The coefficients in this series are determined by matching $(\partial v_2/\partial x)_{\pm a}$ to the series expansion of z.[5] The result is

$$A-A'=-\tfrac{1}{2}B\Delta$$

and

$$v_2=-\frac{4\Delta^2B}{\pi^3}\sum_{m=1}\frac{1}{(2m-1)^3}\frac{\sinh(2m-1)\pi x/\Delta}{\cosh(2m-1)\pi a/\Delta}\times\cos(2m-1)\pi z/\Delta. \quad (16)$$

We obtain the potential difference in the x- direction across the slab by combining Eqs. (15) and (16):

[5] B. O. Pierce, *Short Table of Integrals* (Ginn and Company, Boston, Massachusetts, 1929), No. 810.

$$v(a,y,z)-v(-a,y,z)$$
$$=2a(A+\tfrac{1}{2}B\Delta)-\frac{8\Delta^2 B}{\pi^3}\sum_{m=1}\frac{1}{(2m-1)^3}$$
$$\times\tanh(2m-1)\pi a/\Delta\cos(2m-1)\pi z/\Delta. \quad (17)$$

According to Eq. (17) the potential difference varies with z. Let us estimate the magnitude of the z-dependent term. First of all, its average value vanishes. The sum in Eq. (17) will have its maximum when $z=0$, and since $a/\Delta\gg 1$, the order of magnitude of the z-dependent term is

$$\frac{8\Delta^2 B}{\pi^3}\sum_{m=1}\frac{1}{(2m-1)^3}\simeq\frac{17}{2\pi^3}\Delta^2 B.$$

Thus, it is at most a fraction Δ/a of the z-independent term and can be neglected. On the other hand, from earlier arguments leading to Eq. (10), A and $B\Delta$ may be of the same magnitude.

Hence we conclude that for very thin slabs the boundary conditions (14) are satisfied to a high degree of approximation by an electric field which sets up a uniform ohmic current density equal and opposite to the average value of the current density, Eq. (13), existing in a slab of infinite lateral extent.

The same argument will apply for $\mathbf{e}_0$ more general than (7′) so that it includes also a y- component linear in z.

If the boundaries at $y=\pm b$ are required to be at constant potential, the result (17) still applies, for $y=0$, as long as $b/a>4$.[6]

5. PROPAGATION IN A FERROMAGNETIC CONDUCTING MEDIUM

Most of the material in this section follows earlier analyses[7] and is included mainly for completeness and unity of notation. The zero-order solutions of interest in the preceding sections are superpositions of plane waves propagating in a ferromagnetic conductor whose magnetization interacts both with the electromagnetic field and a static uniform field $\mathbf{H}_0$. These waves obey Maxwell's equations

$$\nabla\times\mathbf{H}=4\pi/c\mathbf{J}, \quad \nabla\times E=-1/c\dot{\mathbf{B}}, \quad (18)$$

where $\mathbf{J}=\sigma\mathbf{E}$, and $\mathbf{H}$ and $\mathbf{B}$ are related both by the constitutive equation and by the equation of motion of the magnetization. In this section we will assume for this the Bloch equation

$$\mathbf{M}_1=\gamma\mathbf{M}\times\mathbf{H}-\mathbf{M}_1/\tau, \quad (19)$$

where $\mathbf{M}_1$ is the oscillating part of $\mathbf{M}$ defined in Sec. 2. Combining the two equations of (18), and assuming the space-time dependence $\exp i(kz-\omega t)$, we obtain

$$k^2H_x=(2i/\delta^2)B_x, \quad k^2H_y=(2i/\delta^2)B_y, \quad (20)$$
$$0=B_z.$$

For $\mathbf{H}_0=(0,H,0)$, and $\mathbf{M}_0=(0,M,0)$ the linearized form of Eq. (19) becomes

$$-i\omega M_x=\gamma(MH_z-M_zH)-M_x/\tau, \quad i\omega M_y=0,$$
$$-i\omega M_z=\gamma(M_xH-MH_x)-M_z/\tau, \quad (21)$$

and leads to the solutions

$$\frac{M_x}{H_x}=\frac{\gamma^2BMe^{-i\phi_2}}{[(\omega_0^2-\omega^2)^2+4\omega^2/\tau^2]^{\frac{1}{2}}}$$
$$\frac{M_z}{H_z}=-\left[\frac{\omega^2+1/\tau^2}{(\omega_0^2-\omega^2)^2+4\omega^2/\tau^2}\right]^{\frac{1}{2}}\gamma Me^{i(\phi_1-\phi_2)}, \quad (22)$$

where $\omega_0^2=\gamma^2BH+1/\tau^2$, and

$$\tan\phi_1=-\omega\tau, \quad \tan\phi_2=-\frac{2\omega/\tau}{\omega_0^2-\omega^2}. \quad (23)$$

Substitution of Eq. (22) into the first part of Eq. (20) gives the propagation constant

$$k=\pm\frac{1}{\delta}(1+i)\left[\frac{(\tilde{\omega}_0^2-\omega^2)^2+4\omega^2/\tau^2}{(\omega_0^2-\omega^2)^2+4\omega^2/\tau^2}\right]^{\frac{1}{4}}e^{i(\phi_2-\phi_2)/2}, \quad (24)$$

where

$$\tilde{\omega}_0^2=\gamma^2B^2+1/\tau^2, \quad \tan\phi_2=-\frac{2\omega/\tau}{\tilde{\omega}_0^2-\omega^2}. \quad (25)$$

Equation (22) relates the magnetization to the local magnetic field, while Eq. (24) establishes the propagation constant for the x and z components through which the local fields can be related to the incident fields, as in Eq. (10).

With the arrangement of the static field as given, the second part of Eq. (20) yields another propagation constant for waves whose magnetic field has only a y component

$$k=\pm(1/\delta)(1+i). \quad (26)$$

Such waves are completely unaffected by the resonating magnetization.

6. dc FIELDS IN FERROMAGNETIC RESONANCE

The two averages occurring in Eq. (7) can now be evaluated. By combining the real parts of Eqs. (10) and (22) and taking the time average, we get

$$\langle JM_x\rangle=\frac{\sigma\omega}{ck_1}\frac{\gamma^2BM}{[(\omega_0^2-\omega^2)+4\omega^2/\tau^2]^{\frac{1}{2}}}\frac{1}{4}H_1^2\sin 2k_1D$$
$$\times\left(\sin\phi_2+\frac{2\tan k_1D}{k_1\delta^2}\cos\phi_2\,z\right), \quad (27)$$

$$\langle JM_z\rangle=-\frac{\sigma\omega}{ck_1}\gamma M\left[\frac{\omega^2+1/\tau^2}{(\omega_0^2-\omega^2)^2+4\omega^2/\tau^2}\right]^{\frac{1}{2}}\frac{1}{4}H_1^2\sin 2k_1D$$
$$\times\left[\sin(\phi_2-\phi_1)+\frac{2\tan k_1D}{k_1\delta^2}\cos(\phi_2-\phi_1)\,z\right].$$

[6] J. Volger, Phys. Rev. **79**, 1023 (1950).
[7] C. Kittel, Phys. Rev. **73**, 155 (1948); N. Bloembergen, Phys. Rev. **78**, 572 (1950).

The constant terms in Eq. (27) are to be identified with the A of Eq. (7′), while the coefficient of z is B. With this assignment we can immediately write down the observed voltage along x. By using the first part of Eq. (17),

$$v(a,y,z)-v(-a,y,z)$$

$$=\frac{ac}{4\pi k_1\delta^2}H_1^2\sin 2k_1D[1+\tan^2\phi_4]^{\frac{1}{2}}$$

$$\times\frac{1}{[(\omega_0^2-\omega^2)^2+4\omega^2/\tau^2]^{\frac{1}{2}}}[-\gamma^2B\Delta\rho\sin(\phi_2+\phi_4)$$

$$-\gamma MR(\omega^2+1/\tau^2)^{\frac{1}{2}}\sin(\phi_2+\phi_4-\phi_1)], \quad (28)$$

where ϕ_1 and ϕ_2 are defined by Eq. (23) and

$$\tan\phi_4=\frac{\Delta}{k_1\delta^2}\tan k_1D. \quad (29)$$

Equation (28) contains the full ω or H_0 dependence of the voltage. The complete D dependence at constant microwave power requires eliminating H_1 by means of Eq. (11).

The magnitude of the electric field predicted by Eq. (28) can be estimated from values of the parameters known from conventional resonance and other experiments. For thin nickel films at X band, this field is of the order of 10^{-3} H_1^2 v/cm, when H_1 is in oersteds, so that an incident power of 1 w/cm^2 will give about 20 μv/cm. Both magnetoresistance and Hall effect give similar contributions.

Let us consider Eq. (28) at a fixed value of D and ω, as a function of the applied static field H_0. The common factor contains the resonance denominator of the magnetization, which is closely related to that observed in the usual resonance absorption experiment. The magnetoresistance and Hall effect contributions modulate this factor through slowly varying trigonometric functions, whose detailed nodes and antinodes depend on ϕ_4 and ϕ_1, but must be such that the magnetoresistance term may change sign when $\omega_0/\omega>1$, and has a maximum for $\omega_0/\omega\leq 1$, while the opposite applies to the Hall effect term.

If, in particular, $\phi_4\cong 0$, the magnetoresistance shows a typical resonance behavior and the Hall effect a dispersive curve. However, for films of reasonable properties, even if located close to the short, ϕ_4 is usually not negligible. For instance, if $D=10^{-2}$ cm, and $\omega=6\times10^{10}$/sec, and we consider a film of an area resistivity $1/\sigma\Delta$ of 10 ohms/square, then, with $\tan k_1D \doteq k_1D$, we obtain $\tan\phi_4=0.377$. Thus appreciable shifts of the observed curves may be expected even for very thin films. If the distance D from the short is increased, such phase shifts become more pronounced, and will, in fact, approach $\pi/2$ for k_1D of the order of unity. Thus, the observed signals are very sensitive to the film location in a standing wave pattern.

At fixed D, the amplitude of the signals is directly proportional to H_1^2 and therefore to the power of the incident microwaves. For fixed microwave power, the signal amplitude of Eq. (28) apart from the resonance denominator is, within the usual approximation, given by

$$\frac{ac}{2\pi k_1\delta^2}\tan k_1D\cdot\frac{\sec\phi_4}{\tan^2\phi_4+\frac{1}{4}}H_{\text{inc}}^2. \quad (30)$$

For very small D, Eq. (30) approaches $(2acD/\pi\delta^2)H_{\text{inc}}^2$, and is proportional to D, while for large D (i.e., $\tan^2\phi_4>1$), it reaches the constant value $(ac/2\pi\Delta)H_{\text{inc}}^2$. When $\tan_1D=k_1\delta^2/\sqrt{2}\Delta$, Eq. (30) has its maximum value $(\frac{8}{9})^{\frac{1}{2}}(ac/\pi\Delta)H_{\text{inc}}^2$. For the film just considered, this maximum occurs at $D=0.02$ cm, so that in this case, the amplitude (30) is nearly constant over the whole range of accessible values of D. For films of higher resistivity, however, Eq. (30) predicts an appreciable change of amplitude with increasing D.

Expression (30) is valid for $\Delta\gg\frac{1}{2}k_0\delta^2$. The foregoing discussion indicates that, in the whole range of Δ for which this inequality holds, the signal amplitude for large D is inversely proportional to Δ, so that the largest amplitude occurs for the thinnest films. In the limit as Δ approaches zero, the signal amplitude becomes independent of Δ and has the value

$$-\frac{2ac}{k_1\pi\delta^2}\frac{\tan k_1D}{1+(k_0/k_1)^2\tan^2k_1D}$$

which attains its maximum value, $-(ac/\pi k_0\delta^2)$, when $\tan k_1D=k_1/k_0$. In that case Eq. (28) goes over into an expression of the form already discussed by Seavey[8] for traveling waves.

7. OTHER STATIC FIELD ORIENTATIONS

Both terms appearing in Eq. (28) reverse with the static field. In order to separate the two contributions experimentally it is most convenient to vary the direction of the static field with respect to the microwave fields.

If the average magnetization is not normal to the microwave magnetic field, an incident wave will usually break up into two parts traveling in the medium with the propagation constants given by Eqs. (24) and (26), respectively. However, within the approximations leading to Eq. (10), this difference can be ignored, and we need consider only a single wave. We can then take over all the results of Sec. 3, and also of Sec. 5 if M_x and M_z of that section are identified with the precessing components of the magnetization $\mathbf{M}_1$ perpendicular to $\mathbf{M}_0$, and also H_x is to be the component of the microwave field perpendicular to $\mathbf{M}_0$.

[8] M. H. Seavey, Jr., J. Appl. Phys. **31**, 216S (1960).

In particular, if $\mathbf{M}_0=(M\sin\theta,\ M\cos\theta,\ 0)$, Eq. (4) has the three components

$$\begin{aligned} e_{x0}&=\{-(\Delta\rho/M)\langle JM_x\rangle\cos2\theta+R\langle JM_x\rangle\}\cos\theta,\\ e_{y0}&=(\Delta\rho/M)\langle JM_x\rangle\sin2\theta\cos\theta,\\ e_{z0}&=\{-(\Delta\rho/M)\langle JM_x\rangle+R\langle JM_x\rangle\}\cos^2\theta, \end{aligned} \tag{31}$$

where $\langle JM_x\rangle$ and $\langle JM_x\rangle$ are given by Eq. (27).

Depending on the boundary conditions, Eq. (31) gives rise to various dc voltages and currents. If, as before, we allow no current across boundaries normal to x, we obtain a voltage difference in the x direction, $\Delta v=2ae_{0x}$. Apart from the common factor $\cos\theta$, this differs from Eq. (28) only in that the first term is multiplied by $\cos2\theta$.

Hence, by studying the observed signal as a function of θ, or using in particular the configurations $\theta=0,\ \pi/4$, it is possible to separate the two terms appearing in Eq. (28).

Directions of the applied magnetic field giving an out-of-the-plane component can also be considered for separating these terms. However, they are of interest mainly to determine the value of γ.[9]

8. DISCUSSION

The theory developed in this report makes a number of predictions regarding the experimental aspects of the dc effects accompanying ferromagnetic resonance. Some of these, such as the strict proportionality of the amplitude to incident microwave power, are completely general. Others, depending on the electrical and magnetic properties of the film, may differ in practice from the particular case discussed here.

The electrical properties are determined by σ, R, and $\Delta\rho$. Although it has been established that the microwave behavior of thin films is determined by their effective dc conductivity, this applies only if the added scattering in the film is either due to the film surfaces or to microscopic impurities. Macroscopic porosity and other capacitative channels[10] may well make the dc and microwave conductivities unequal. There is no definitive theory of the extraordinary Hall effect in films. Evidence indicates that at dc R becomes very large in thin films,[11] but the exact values are sensitive to the method of preparation.[12] $\Delta\rho$, on the other hand, is less sensitive to film thickness,[13] so that a test of the $1/\Delta$ variation of the amplitude should concentrate on the magnetoresistance contribution. The same qualifications about the microwave behavior of σ also apply to R and $\Delta\rho$.

The magnetic response of the film depends on its relaxation mechanism, and on other contributions to its magnetic energy besides that due to the externally applied field. The results, Eq. (28), would be modified in some details if instead of the Bloch formulation Landau-Lifshitz damping had been considered, but, within the limits of the linear approximation of Eq. (21), the differences are slight. Magnetic anisotropy will influence both the apparent resonant field and the phase lag between the magnetization and the magnetic field,[14] and will therefore affect the over-all amplitude and the relative contribution from $\Delta\rho$ and R. Such corrections can be supplied whenever the nature of the anisotropy energy is known.

It must be stressed that the dc effects depend directly on the *local* electromagnetic fields. Hence it is extremely important to carry out tests under conditions in which these can be accurately established. In general a knowledge of the far-field characteristics of the film within a guide will be insufficient for predicting the details of the dc fields. In fact, once these latter are understood they may well be used as local field probes for metallic obstacles.

Since the results depend on both magnetic and electrical properties of the film, measurement of the dc effects does, in fact, allow a study of all of these in thin films. This is of use to corroborate measurements of these quantities by other techniques, to study the magnetic resonance properties of films not amenable to conventional experiments because of poor signal to noise, and to investigate the magnetization-dependent galvanomagnetic effects at high frequency.

[9] P. E. Tannenwald and M. H. Seavey, Jr., Phys. Rev. **105**, 377 (1957).
[10] R. S. Sennett and G. D. Scott, J. Opt. Soc. Am. **40**, 203 (1950).
[11] R. Coren and H. J. Juretschke, J. Appl. Phys. **28**, 806 (1957).
[12] L. Reimer, Z. Physik **150**, 277 (1958).
[13] W. Hellenthal, Z. Physik **151**, 421 (1958); H. J. Juretschke, *Structure and Properties of Thin Films* (John Wiley & Sons, Inc., New York, 1959), p. 410.
[14] J. R. MacDonald, Phys. Rev. **106**, 890 (1957).

Temperature Dependence of Young's Modulus of Vitreous Germania and Silica*

S. SPINNER AND G. W. CLEEK
National Bureau of Standards, Washington, D. C.

(Received April 14, 1960)

The temperature dependence of Young's modulus of vitreous GeO_2 has been determined by a dynamic resonance method from −195°C to 540°C. The modulus increases with increasing temperature from about −120°C to 400°C. Below and above this range the modulus decreases with increasing temperature. Young's modulus for vitreous SiO_2 also increases from about −190°C to 1175°C and decreases with increasing temperature outside this range.

In view of the similarity in structures and bond energies of these two materials, the similarity in the elastic modulus-temperature relations is believed to be significant; especially when contrasted with the lack of agreement in another commonly measured anharmonic property, thermal expansion.

I. INTRODUCTION

IT has recently been pointed out by J. D. Mackenzie[1] that vitreous SiO_2 and GeO_2 possess similar structures. In addition, the structures and the magnitudes of the flow parameters of the two liquids are alike; and further, the Si-O and Ge-O bond energies are "almost identical." These facts led Mackenzie to redetermine the linear thermal expansivity of vitreous GeO_2 in order to check a previously reported value of 7.7×10^{-6} per °C, which differed markedly from that of vitreous SiO_2 (0.5×10^{-6} per °C). He found, however, a value of 7.5×10^{-6} per °C, in good agreement with the previously reported value, rather than the unusually low value for vitreous SiO_2.

Considerations of this type led the present authors to inquire whether the temperature relation of elastic modulus of vitreous GeO_2 might not be similar to that of vitreous SiO_2. Such a comparison could be most instructive, since SiO_2 is known to have an anomalous positive temperature coefficient of elastic modulus in contrast not only with other glasses, but also with most other materials—ceramic or metallic. In fact, the only glasses also known to have positive temperature coefficients are those having a high percentage of SiO_2 (e.g., Vycor—96% SiO_2, Pyrex No. 7740—about 80% SiO_2). There are also theoretical reasons for believing that the temperature coefficient of elastic modulus is at least as reliable a reflection of the intrinsic structure of a material as the coefficient of expansion. The former depends upon the odd and even powered terms of the anharmonic expansion whereas the latter depends only on the odd powered terms.[2,3]

II. EXPERIMENT

a. Specimens

The germania specimens were prepared from rods formed by drawing from a platinum crucible containing molten germania immediately after the crucible had been withdrawn from a furnace. The molten germania was produced by heating the batch in the furnace to about 1500°C. The GeO_2 which constituted the batch for this melt was obtained from the Eagle-Pitcher Company, Semi-Conductor Branch, Miami, Oklahoma. It was specified as "electronic grade." Spectrographic analysis of the GeO_2 batch revealed faint traces (less than 0.0001%) of Ca, Fe, and Pb, and traces (less than 0.001%) of Mg and Si. The detection of Cu and Al was questionable.

The final specimens were roughly cylindrical in shape, about 6 in. long and about $\frac{1}{8}$ in. diam. Because of the manner in which they were formed, the dimensions of the specimens were not uniform; the cross section especially was not circular, but elliptical.

The fused silica specimen measured for comparison was also cylindrical in shape, about 7 in. long and about $\frac{1}{2}$ in. in diam. It was from the same source as the specimens used in a previous investigation.[4]

b. Method and Calculations

Measurements of elastic modulus both below and above room temperature were performed by a dynamic resonance method. The procedure for making the measurements at room temperature and above has already been described by Wachtman and Lam.[5] The modification of the equipment for determinations at low temperature was designed by Wachtman[6] and will be described by him in a forthcoming publication.

The basic procedure at both high and low temperatures is to excite an detect one of the flexural resonance frequencies of the specimen. Then the ratio of Young's modulus at any temperature to its room temperature, or base value, (E_t/E_0) is related to the ratio of the flexural resonance frequencies at the same two temperatures (f_t/f_0) by the following well-known equation

$$\frac{E_t}{E_0}=\left(\frac{f_t}{f_0}\right)^2\Big/\left(1+\frac{\Delta l}{l}\right). \qquad (1)$$

* This investigation was sponsored by the Division of Research, U. S. Atomic Energy Commission.

[1] J. D. Mackenzie, J. Am. Ceram. Soc. **42**, 310 (1959).
[2] Charles Kittel, *Introduction to Solid State Physics* (John Wiley & Sons, Inc., New York, 1957), 2nd. ed., p. 152.
[3] E. A. Stern, Phys. Rev. **111**, 786–797 (1958).
[4] S. Spinner, J. Am. Ceram. Soc. **37**, 229–34 (1954).
[5] J. B. Wachtman, Jr., and D. G. Lam, Jr., J. Am. Ceram. Soc. **42**, 254–260 (1959).
[6] J. B. Wachtman, Jr. (private communication).

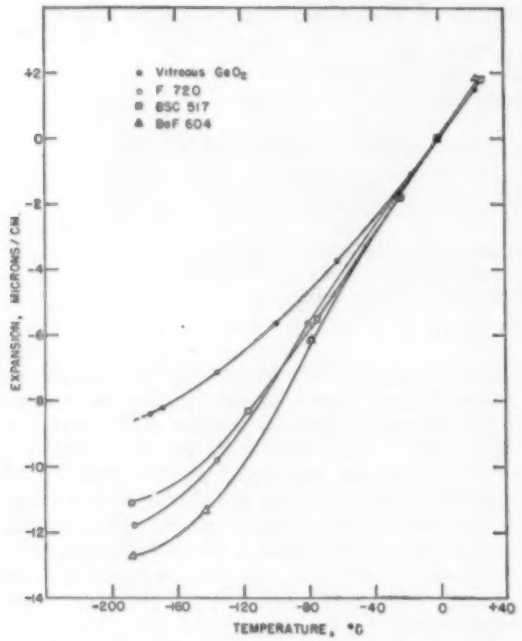

FIG. 1. Low-temperature thermal expansion of vitreous GeO_2 and some other glasses.

The factor $(1+\Delta l/l)$ is the correction for thermal expansion, $\Delta l/l$, from room temperature to the temperature of measurement (whether above or below room temperature). The values of $\Delta l/l$ obtained by Mackenzie for GeO_2 were used for this correction above room temperature. Below room temperature, corresponding data obtained here by an interferometric method were used. This thermal expansion data for GeO_2 below room temperature is given in Fig. 1, along with that for several other glasses for comparison.

It should be noted that, as long as the shape of the specimen remains unchanged during the course of the experiment, accurate values of the dimensions are not required for obtaining accurate values of (E_t/E_0). Thus (E_t/E_0) could be obtained with an accuracy of about $\pm 0.1\%$ over most of the temperature range, even though, because of the lack of uniformity of the GeO_2 specimens, the absolute value at room temperature E_0 could only be obtained to about $\pm 10\%$. The best estimate of E_0, derived from the fundamental flexural resonance frequencies of the two GeO_2 specimens, was 535 kilobars. The relations given by Pickett[7] were used for this determination. By comparison, the SiO_2 specimen, which was used in the previous investigation,[4] was more regular in shape, so that the value of $E_0 = 730$ kilobars reported in that study is believed to be at least as accurate as the (E_t/E_0) values for any of the specimens measured here.

The GeO_2 data above room temperature are based on separate runs on two different specimens. The noncircular cross section led to two flexural resonance frequencies in any particular mode of vibration (fundamental or overtones); one associated with vibrations in the direction of the short axis of the cross section and the other with those in the direction of the long axis (of the cross section). Each point above room temperature is usually based upon four flexural resonance frequencies, the two vibrations for the fundamental and the two for the first overtone. The degree of agreement in (E_t/E_0) based on these four resonance frequencies, serves as an internal check on the consistency of the data. The total spread in (E_t/E_0), based on these four types of flexural vibration, was usually on the order of 0.1%, and justified the use of the average of (E_t/E_0) from these four resonances, for the points shown above room temperature.

The GeO_2 measurements below room temperature were made during two separate runs on the same specimen. In this case, it was experimentally more feasible to base the values of (E_t/E_0) only on one fundamental flexural frequency.

c. Effect of Heat Treatment

Since the GeO_2 specimens were quenched from a relatively high temperature in the process of drawing, the value of Young's modulus at room temperature increased as a result of the first heating as indicated by an increase in the flexural resonance frequencies. This type of behavior is in accordance with previous investigations[8,9] which show that the room temperature values of elastic moduli of glasses, as well as other properties, can be changed by the time and temperature of annealing. This increase in E_0 can be determined with an accuracy comparable with (E_t/E_0), since its determination is subject only to the same condition (i.e., retention of the shape of the specimen).

The specimens measured were, therefore, first annealed at 475°C for four hours and then cooled at a rate of about 10°C per hr. This annealing process raised the room temperature modulus by about 3%. This procedure sufficiently stabilized the room temperature value of Young's modulus E_0 so that after subsequent heatings, the specimens returned to values of resonance frequency and, hence E_0, not significantly different from the value after the first annealing. Consequently, one was reasonably certain that the elastic modulus-temperature curve was truly an instantaneous (and instantaneously reversible) temperature effect not confused by time dependent changes in elastic modulus associated with changes in the fictive temperature.

[7] Gerald Pickett, Am. Soc. Testing Materials **45**, 846 (1945).

[8] G. E. Stong, J. Am. Ceram. Soc. **20**, 16–22 (1937).

[9] S. Spinner and Albert Napolitano, J. Am. Ceram. Soc. **39**, 390–394 (1956).

However, the increased spread in the experimental points above about 350°C is probably due to continued annealing affecting the value of E_t in this region.

The upper temperature limit of the elastic modulus determinations for GeO_2 was fixed by the fact that the specimens sagged under their own weight between the suspension fibers. This occurred somewhere between 500 and 545°C, depending on the times involved. It is interesting that at the temperature at which this sagging took place, the resonance frequency responses were not seriously reduced in amplitude. Sagging was indicated by a fairly sharp change in the pattern of the resonance frequency-temperature curve. (Resonance frequencies obtained after sagging occurred, of course, are not acceptable, since the condition of retention of shape previously mentioned is no longer satisfied.)

III. RESULTS

The curve of (E_t/E_0) for GeO_2 as a function of temperature from −195°C to 540°C is shown in Fig. 2. Young's modulus is seen to increase with increasing temperature from about −120°C to +400°C, and to decrease with increasing temperature above and below this range. Probably even more noteworthy than the increase in modulus with temperature is the unusually rapid drop that occurs between −195°C and −120°C. At −195°C the modulus is already higher than the maximum attained above room temperature (around 400°C) and, from the shape of the curve in this low-temperature region, it appears that the modulus would rise considerably more, if the temperature were lowered still further. That this rapid drop and reversal in the low-temperature region is not due to experimental error is assured by the fact that several single-crystal sapphire rods of the same approximate dimensions as the GeO_2 specimens, when similarly measured in the same apparatus, showed no such minimum in this temperature region, but rather, the "normal" decrease in modulus with increasing temperature.

It is also noted from Fig. 2, that not only does the curve formed by the experimental points in the low-temperature apparatus fit nicely with the one formed by the points using the high-temperature apparatus, also that in the temperature region where the points from both sets of apparatus overlap, from 20°C to about 90°C, these points fall on the same line. Both these agreements are good evidence of the reliability of the data.

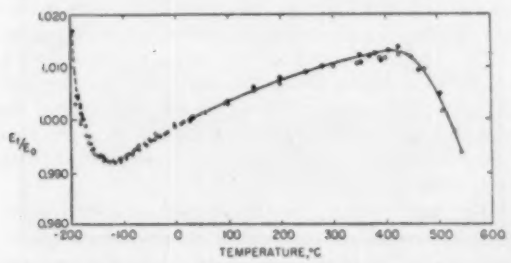

FIG. 2. Temperature dependence of Young's modulus of vitreous GeO_2. E_t/E_0 is the ratio Young's modulus at temperature of test to Young's modulus at room temperature. $E_0 \approx 530$ kilobars. The four different symbols represent two sets of determinations both above and below room temperature.

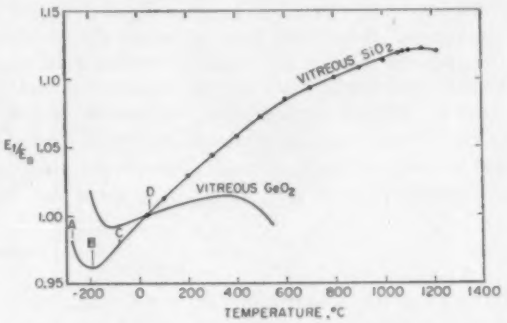

FIG. 3. Temperature dependence of Young's modulus of vitreous SiO_2. E_t/E_0 is the ratio of Young's modulus at temperature of test to Young's modulus at room temperature. $E_0 = 730$ kilobars. Data from *A* to *C* are taken from Fine *et al.*, from *B* to *D* from McSkimin. Curve for vitreous GeO_2 is reproduced from Fig. 1 for comparison.

Although the value of the coefficient of expansion of GeO_2 is somewhat lower than that of the glasses with which it is compared (Fig. 1), the shape of the curve is similar to that for these glasses and shows none of the thermal expansion anomalies characteristic of SiO_2 in this general temperature region.

Young's modulus as a function of temperature for vitreous SiO_2 is shown in Fig. 3. Since the previous publication of such data for this material,[10] the method for measuring Young's modulus at elevated temperatures has been improved and the temperature range extended. The curve of (E_t/E_0) vs temperature is seen to depart from linearity even around room temperature. Successive increases in temperature result in smaller increases in Young's modulus until a maximum is reached around 1175°C. The value of E_t at this temperature is 819 kilobars.

The low-temperature values from about +40°C to about −195°C are taken from McSkimin,[11] and from −73°C to −271°C, from Fine, Van Duyne, and Kenney.[12]

As was the case for GeO_2, the low-temperature curve fits well with the high-temperature one, and in the short temperature range of overlap, the curves coincide. Furthermore, the absolute value of Young's modulus at room temperature from McSkimin is in agreement with the one given here.

---

[10] S. Spinner, J. Am. Ceram. Soc. **39**, 113–118 (1956).
[11] H. J. McSkimin, J. Appl. Phys. **24**, 988–97 (1953).
[12] M. E. Fine, H. Van Duyne, and N. T. Kenney, J. Appl. Phys. **25**, 402–405 (1954).

The curve for GeO_2 is included in Fig. 3 to facilitate comparison. It is clear that, although the absolute values of the positive and negative slopes are different for the two materials, and that the maxima and minima occur at different temperatures, the over-all patterns of the Young's modulus-temperature curves for GeO_2 and SiO_2 are essentially alike. It appears then, that the similarities in these two materials pointed out by MacKenzie are significantly reflected in the similarity of the temperature dependence of Young's modulus.

ACKNOWLEDGMENTS

The authors are grateful to T. G. Scuderi and D. G. Lam, Jr., for their assistance in making the low-temperature thermal expansion and low-temperature elastic modulus measurements, respectively.

JOURNAL OF APPLIED PHYSICS VOLUME 31, NUMBER 8 AUGUST, 1960

Thermal Conductivity of Eight Halide Crystals in the Temperature Range 220°K to 390°K*

KATHRYN A. MCCARTHY AND STANLEY S. BALLARD†
Department of Physics, Tufts University, Medford, Massachusetts
(Received July 20, 1959; and in final form April 4, 1960)

The thermal conductivity of eight halide crystals has been measured over the temperature range 220°K to 390°K. The thermal conductivities of potassium bromide, potassium chloride, and sodium chloride vary inversely with temperature for the lower part of this temperature range, and are nearly independent of temperature for the higher temperatures of the range measured. The thermal conductivities of cesium bromide, cesium iodide, and silver chloride are nearly independent of temperature throughout the entire temperature range. The thermal conductivities of barium fluoride and calcium fluoride vary more rapidly with temperature than anticipated from a T^{-1} relationship; however, the accuracy of the data is not sufficient to establish the exact form of the variation of the thermal conductivity with temperature. The comparative method used for these measurements is described.

THE thermal conductivities of eight halide crystals have been measured over the temperature range 220°K to 390°K, using two equipments based on a comparison method previously described.[1] The method is a comparative one, in which the thermal conductivity of a material (called the "unknown") is determined as a function of the thermal conductivity of a material (called the "known") for which data are well established. Z-cut quartz crystals were used for the measurements of barium fluoride, calcium fluoride, potassium bromide, potassium chloride, and sodium chloride. Pyrex No.7740 supplied by the Corning Glass Works was used for the measurements of cesium bromide, cesium iodide, and silver chloride.

The equipment used for measurements from 220°K to about 320°K is shown in Fig. 1. The two samples, one known and the other unknown, are placed one above the other between a heat source and a heat sink. The heat source is a brass cylinder with a copper base that is heated by a resistor supported just above the copper base. The heat sink is a brass cylinder with a copper top; the temperature of the heat sink is controlled by an auxiliary heat exchanger that is not shown in the photograph. A copper plate is placed between the crystals to support the thermocouple which measures the interface temperature. Thermocouples are also located near the surfaces of the heat source and heat sink that contact the faces of the samples. Each of the copper surfaces is polished to establish good thermal contact when the crystal pile is assembled; the mechanical contact of the crystals with the copper surfaces has been found to be so good that the crystals cannot be lifted from the surfaces, but must be slid from the surfaces. Tests have shown that excellent thermal contact is thus obtained. The counterweight shown to the right of the crystal pile is used to balance the weight of the heat source, so that the crystals are not strained during test. The entire equipment is mounted on a vacuum plate and covered by a glass bell jar; the air surrounding the apparatus is evacuated.

The equipment used for measurements from 300°K to 390°K is similar to the one shown in Fig. 1, except that the temperatures of both the heat source and the heat sink are electrically controlled. The data reported below were determined from measurements made with both equipments.

Heat may be lost from the system in several ways. Heat losses due to convection are prevented by the vacuum; the use of the vacuum also makes possible the measurement of hygroscopic crystals, such as cesium iodide, potassium bromide, and sodium chloride. Heat may be lost from the crystal pile by conduction along

* Assisted by a grant from the Penrose Fund of the American Philosophical Society and a Frederick Gardner Cottrell grant from the Research Corporation.
† Now at the Department of Physics, University of Florida, Gainesville, Florida.
[1] S. S. Ballard, K. A. McCarthy, and W. C. Davis, Rev. Sci. Instr. 21, 905 (1950).

the thermocouple wires; a calculation of this loss shows it to be negligible.

Heat may also be lost by radiation from the crystal pile. These losses have been calculated by the method used by Stuckes and Chasmar[2] for a similar apparatus. It can be shown that for the crystals with higher values of thermal conductivity, i.e., barium fluoride, calcium fluoride, potassium bromide, potassium chloride, and sodium chloride, the heat loss due to radiation is small. However, for the crystals with lower thermal conductivity, cesium bromide, cesium iodide, and silver chloride, the heat losses must be considered.

In the equipment shown in Fig. 1, the bell jar surrounding the crystal pile is at approximately ambient temperature. The heat loss H_r per unit time due to radiation from the surfaces of the two crystals has been estimated from the following equation:

$$H_r=\sigma(\epsilon_1+\epsilon_2)2\pi rs[T_c^4-T_a^4],$$

where σ is Stefan's constant, ϵ_1 and ϵ_2 are the emissivities of the two crystals, r and s are the radius and the thickness, respectively, of either the "known" or the "unknown" crystal, T_c is the average temperature of the crystal pile, and T_a is the temperature of the surroundings of the crystal pile. The copper plate between the samples has been neglected in this calculation, the crystals are assumed to be of the same size, and the emissivity of the bell jar bell is taken as unity.

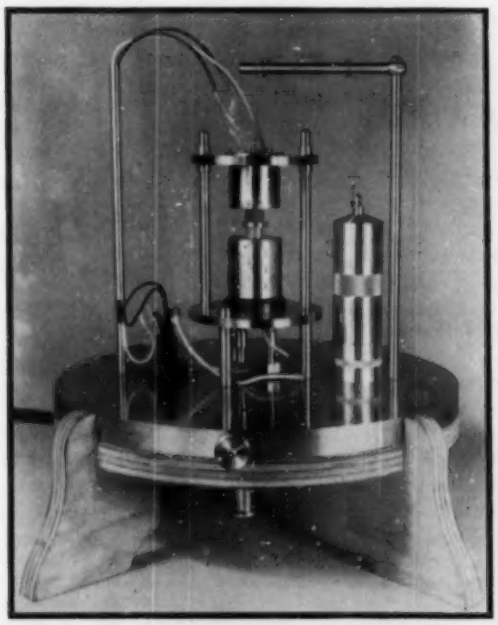

FIG. 1. Equipment for measuring the thermal conductivity of small samples in the temperature range 220°K to 320°K.

[2] A. D. Stuckes and R. P. Chasmar, *Report of the Meeting on Semiconductors* (The Physical Society, London, 1956), p. 119.

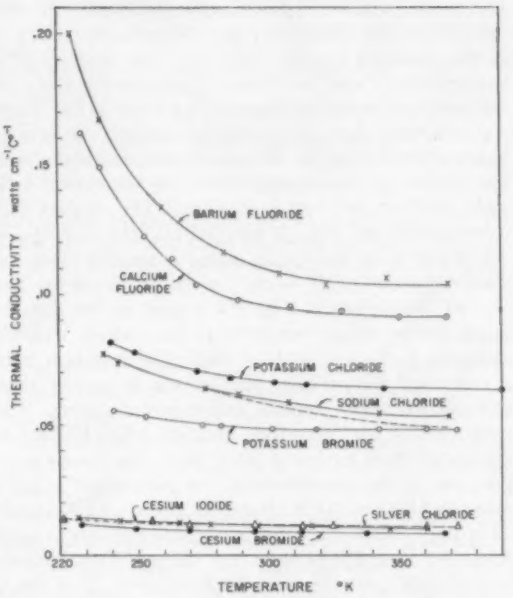

FIG. 2. Thermal conductivity as a function of temperature, for eight halide crystals.

The heat conducted through the crystal pile per unit time H_c equals the heat conducted through one crystal per unit time when steady-state conditions exist, and is given by $H_c=k\pi r^2 s^{-1}\Delta T$, where k is the thermal conductivity of the crystal and ΔT is the temperature difference across the crystal. The dimensions of the crystalline samples were approximately 1 cm in radius and 0.5 cm in thickness; the temperature difference across the pile was maintained at 5°C or less. The ratio H_r/H_c for these samples equals $\sim 10^{-12}(T_c^4-T_a^4)(\epsilon_1+\epsilon_2)(2k)^{-1}$. At 350°K, for potassium chloride the radiation loss is less than 10% of the heat conducted through the crystal. At 350°K, for silver chloride the radiation loss is estimated to be less than 20%; the radiation losses for cesium bromide and cesium iodide should be of the same magnitude.

The crystals for which data are given were obtained from various sources. The barium fluoride and the calcium fluoride were provided by the Optovac Company. The cesium bromide, cesium iodide, potassium bromide, potassium chloride, and sodium chloride were provided by the Harshaw Chemical Company. The silver chloride crystals were drawn from a melt that was initially c.p. silver chloride powder, by a technique previously described.[3]

The thermal conductivity values determined experimentally for these eight crystals are plotted in Fig. 2. Eucken[4] has shown that at temperatures above the

[3] K. A. McCarthy and B. Chalmers, Can. J. Phys. **36**, 1645 (1958).

[4] A. Eucken, Ann. Physik **34**, 185 (1911).

Debye temperature the thermal conductivity of nonmetallic crystals should be proportional to the reciprocal of the absolute temperature; thus, the product of a temperature T and the thermal conductivity k at that temperature should be constant for a particular material. Klemens[5] has calculated this product for several halide crystals from the data of Eucken and Kuhn[6] and has compared these results with the theoretical estimates of Leibfried and Schlömann.[7] The product $\Theta_D k$ calculated from Fig. 2 for sodium chloride ($\Theta_D \sim$ 280°K) is 17 w cm^{-1}; this value is smaller than the observed value of 27 w cm^{-1} given by Klemens. The dashed line shown in Fig. 2 is a plot of the thermal conductivity versus temperature for sodium chloride assuming $\Theta_D k$ equal to 17 w cm^{-1}; the deviation from a reciprocal temperature relationship is greater than anticipated from possible experimental errors. The product $\Theta_D k$ for potassium bromide ($\Theta_D \sim 170$°K) as calculated by Klemens is 10 w cm^{-1}; the lowest temperature of the measurements on potassium bromide given in Fig. 2 is 241°K. However, Tk at 241°K equals 13 w cm^{-1}, and thus is in reasonable agreement with Klemens' data. The product $\Theta_D k$ for potassium chloride ($\Theta_D \sim 230$°K) as calculated by Klemens is 28 w cm^{-1}, which is larger than Tk of 20 w cm^{-1} given by the Fig. 2 value for k at 240°K.

The thermal conductivity values for calcium fluoride ($\Theta_D \sim 474$°K) given in Fig. 2 are approximately the same as those reported by Eucken for natural calcium fluoride, and are in agreement with recent measurements by Slack.[8] The values reported by Charvat and Kingery[9] are about half as large. The measurements for calcium fluoride in the lower part of the temperature range indicate that Tk is greater than predicted by the Eucken relationship and is decreasing with increasing temperature; at $\sim$300°K Tk approaches a constant value. The product Tk for calcium fluoride at 369°K equals 34 w cm^{-1}, which is in reasonable agreement with $\Theta_D k$ of 30 w cm^{-1} calculated by Klemens. The values for barium fluoride show a similar relationship with temperature. However, since these data are new to the literature and Θ_D is unknown, no comparison with either theory or other experimental data can be made.

The unusual behavior of the thermal conductivity of sodium chloride at temperatures above the Debye temperature suggested that measurements should be made on materials with Θ_D less than the lowest temperature reached with the present equipment. It was expected that such a material would have low thermal conductivity following the Θ_D^3 dependence predicted by Leibfried and Schlömann.

Data are given in Fig. 2 for cesium bromide, cesium iodide, and silver chloride. For silver chloride, Θ_D equals 150°K, as calculated from the elastic constants measured by Arenberg[10] and using the method of calculation of Quimby and Sutton.[11] For cesium bromide, Θ_D equals 134°K, and for cesium iodide, Θ_D equals 137°K; these values are determined from the recent elastic data of Bolef and Menes,[12] and of Reinitz and Huntington.[13] For each of these crystals, at temperatures above the Debye temperature, the thermal conductivity is nearly independent of temperature; radiation losses and experimental errors do not satisfactorily explain this deviation from the Debye T^{-1} relationship. The results for cesium iodide supplement those of Berman and Tirmizi[14]; it is believed that the results for cesium bromide and silver chloride are new to the literature.

ACKNOWLEDGMENTS

The authors of this paper wish to thank David W. MacLeod who constructed the two thermal conductivity equipments, and Elizabeth A. Bray who assisted in some of the measurements.

[5] P. G. Klemens, *Solid State Physics* (Academic Press, Inc., New York, 1958), Vol. 7, p. 47.
[6] A. Eucken and G. Kuhn, Z. physik. Chem. (Leipzig) **134**, 193 (1928).
[7] G. Leibfried and E. Schlömann, Nachr. Akad. Wiss. Göttingen, Math.-physik. Kl. IIa, No. 4, **71** (1954).
[8] G. A. Slack (private communication, 1959).
[9] F. R. Charvat and W. D. Kingery, J. Am. Ceram. Soc. **40**, 306 (1957).
[10] D. L. Arenberg, J. Appl. Phys. **21**, 941 (1950).
[11] S. L. Quimby and P. M. Sutton, Phys. Rev. **91**, 1122 (1953); P. M. Sutton, *ibid.* **99**, 1826 (1955).
[12] D. I. Bolef and M. Menes, Bull. Am. Phys. Soc. Ser. II, **4**, 427 (1959).
[13] K. Reinitz and H. B. Huntington, Bull. Am. Phys. Soc. Ser. II, **5**, 40 (1960).
[14] R. Berman and S. M. A. Tirmizi, *Low temperature Physics and Chemistry* (University of Wisconsin Press, Madison, Wisconsin, 1958), p. 382.

Dislocations in Metal Crystals Grown from the Melt

C. ELBAUM*
Division of Engineering and Applied Physics, Harvard University, Cambridge, Massachusetts
(Received August 28, 1959; and in final form April 6, 1960)

Dislocation densities and arrangements were studied, as a function of specimen thickness, in metal crystals grown from the melt. Aluminum crystals containing fewer than 10^4 dislocations per cm^2 were produced by this method. The results of this study are consistent with the mechanism of collapsing vacancy disks for generating dislocations in crystals grown from the melt.

It was found, in aluminum, that below a dislocation density of about 10^6 lines per cm^2, dislocations remain in a random network and do not form sub-boundary arrays. The range of effective interaction between dislocations, to form arrays, thus appears to be limited to the average distance between dislocations when the density is about 10^6 lines per cm^2, or about 10 μ.

INTRODUCTION

A STUDY of dislocation densities and arrangements as a function of crystal thickness was carried out on thin aluminum single crystals grown from the melt. This investigation was undertaken in an attempt to obtain evidence of the origin of dislocations in metal crystals.

It has been suggested in the past[1–3] that dislocations in crystals grown from the melt are likely to originate from the collapse of vacancy disks formed by precipitation of these imperfections. This precipitation takes place under conditions of supersaturation during cooling of the specimen. However, supersaturation of vacancies must be defined with respect to specific sinks and will occur only if such sinks are absent or inaccessible. The likely sinks for vacancies are external surfaces, grain boundaries and dislocations containing jogs. In the present case thin single crystals were used and therefore the external surfaces may be considered as the most probable sinks for vacancies.

Under usual laboratory conditions crystals are grown from the melt with a temperature gradient (along the growth direction of the crystal) $dT/dx=G$ of about 20°C/cm and at a rate $dx/dt=v$ of about 10^{-3} cm/sec. Near the melting point the diffusion coefficient for vacancies is of the order of 10^{-6} cm^2/sec for most metals.[3] With the usual values of activation energy for vacancy diffusion the diffusion coefficient will not change by more than a factor of 2 or 3 with a temperature drop of 10°C from the melting point. For the above conditions the rate of temperature change $Gv=dT/dt$ will lead to a time t of about 10^3 sec for a 10°C temperature drop. In this time the vacancies can diffuse over a distance of approximately $x\cong(Dt)^{\frac{1}{2}}\cong10^{-1.5}$ cm or of the order of a fraction of 1 mm. Of course for higher rates of growth this distance will be correspondingly smaller.

The above calculation is obviously very rough and is presented only for the purpose of illustration. It does indicate, nevertheless, that a supersaturation of vacancies, with respect to external surfaces is likely to occur for crystal thicknesses in excess of a fraction of a millimeter.

Under these circumstances attainment of the required value of the supersaturation will depend on the distance over which vacancies will have to diffuse to a free surface, i.e., the crystal dimensions. The thinner the crystal, the more difficult it should be to build up the required supersaturation to nucleate collapsible disks and consequently the fewer dislocations should be found.

In this study crystal thickness was chosen as the main variable. This choice was made because, for a constant rate of growth and temperature gradient, it appears to be the most significant parameter in deciding on the validity of the idea that collapsing vacancy disks constitute an important mechanism for producing dislocations. Particularly significant is the fact that, for chosen values of G and v, there is a crystal thickness below which an appreciable vacancy supersaturation with respect to an external surface cannot build up.

Let us represent qualitatively the supersaturation of vacancies, as a function of crystal thickness, by the continuous line in Fig. 1. Let the supersaturation necessary to nucleate dislocations by the collapsing vacancy mechanism be represented by the dashed, horizontal line. δ represents the distance from the external surface over which no appreciable supersaturation can buildup. For thicknesses smaller than 2δ the mechanism of collapsing vacancy disks should be essentially inoperative. When the actual thickness of the crystal is in excess of several times this critical value, the dislocation density attributable to the above mechanism should no longer vary with thickness (at least at distances from the surface in excess of the critical value). For intermediate thicknesses the dislocation density should vary as a function of thickness. If no other dislocation generating mechanism operated a study of this variation could, in principle, allow one to determine the vacancy supersaturation necessary to produce dislocations by collapsing vacancy disks.

* Now at Brown University, Richardson Hall, Providence 12, Rhode Island.

[1] F. Seitz, Phys. Rev. **79**, 890 (1950).

[2] F. C. Frank, *Symposium on the Plastic Deformation of Crystalline Solids* (Mellon Institute, Pittsburgh, Pennsylvania 1950), p. 89.

[3] F. C. Frank, *Deformation and Flow of Solids* (IUTAM Colloquium, Madrid, 1955), p. 73.

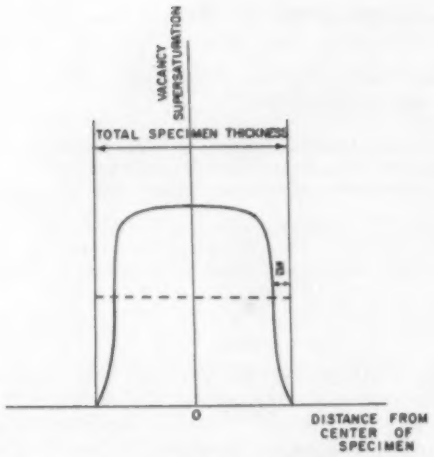

FIG. 1. Vacancy supersaturation with respect to an external surface as a function of specimen thickness. Solid line—assumed vacancy supersaturation distribution. Dashed line—assumed supersaturation necessary to produce dislocations.

EXPERIMENTAL PROCEDURE AND RESULTS

The Czochralski technique modified by Teal and Little[4] was used to grow aluminum single crystals in the shape of a carrot, about 30 mm long and ranging in diameter from about 1 mm to 2.5 mm. The axis of the crystals (the direction of growth) was parallel to a ⟨110⟩ crystallographic direction. The metal was 99.995% pure.

Dislocation densities and arrangements were studied using an x-ray diffraction technique recently developed by A. R. Lang.[5,6] This technique reveals individual dislocations in crystals in which the dislocation density does not exceed about 10^6 lines/cm^2.

The details of the x-ray diffraction technique and the visibility of dislocations are treated in detail by Lang.[6] Briefly, the visibility of invidual dislocations is based on the difference in the integrated intensity of an x-ray beam diffracted by a "perfect" and "imperfect" crystal. The diffraction of x-rays from nearly perfect crystals can be considered on the basis of the Darwin model. According to this model the intensity of a beam diffracted by a "perfect" lattice is rapidly attenuated through destructive interference with multiply reflected rays. The integrated intensity of such a beam is therefore small and may be a factor of ten or more smaller than the intensity obtained from an "ideally imperfect" crystal of the same dimensions. Localized imperfections that disturb the lattice periodicity in a crystal and thus the coherence of reflections, will act as regions of imperfect crystal with a consequent enhancement of diffracted intensity. The region of high strain surrounding a dislocation fulfills the above requirements. Thus when a Bragg reflection from a chosen set of lattice planes is recorded photographically, lines of enhanced intensity corresponding to dislocation lines can be found in the image. This will be so provided that the dislocation density is low enough for these lines to be individually distinguishable and that the regions between dislocations are otherwise sufficiently perfect to approximate the conditions of diffraction by a perfect crystal.

It is found experimentally, that when the dislocation density is about 10^4 lines/cm^2 the imperfect regions around a dislocation extend over a radius of approximately 5 μ (the precise value depends somewhat on the total dislocation density and decreases with increasing density). Since individual dislocations can be resolved only when these regions do not overlap, the upper limit of dislocation density for which individuals can be distinguished is about 10^6 lenes/cm^2.

Figure 2 shows a (111) transmission picture from an aluminum crystal, using MoKα_1, radiation and Ilford film with Nuclear Emulsion type L4 (resolution about 1.5 μ) which was used throughout this study. This image was obtained from a region of the crystal about 1 mm in diam and shows a dislocation density of about 10^4 lines/cm^2.

Figure 3 shows a similar reflection from a region about 1.5 mm in diam. Individual dislocations are still easy to distinguish. The dislocation density is about 10^5 lines/cm^2.

Figure 4 shows a similar reflection from a region about 2 mm in diameter. In this case individual dislocations are no longer clearly resolved except near the surface. The dislocation density in the center of the specimen is estimated to be roughly 10^6 lines/cm^2. It

FIG. 2. X-ray transmission image from Al crystal about 1 mm in diameter. Dislocations are seen as dark segments. Magnification about 80×.

[4] G. K. Teal and J. B. Little, Phys. Rev. **78**, 647 (1950).
[5] A. R. Lang, J. Appl. Phys. **29**, 597 (1958).
[6] A. R. Lang, J. Appl. Phys. **30**, 1748 (1959).

should be pointed out that the highest density is found in the central region of the crystal.

In this photograph the first indications are found of what might be interpreted as sub boundary arrays of dislocations (arrow).

In all three figures narrow regions of enhanced intensity can be seen along the surface of the crystal. Although it is not entirely clear what causes these local intensity enhancements, they are tentatively attributed to surface damage that might have occurred during the handling of the specimens.

Results similar to those shown in Figs. 2–4 were obtained on each of the three specimens that were investigated.

DISCUSSION

The results of the present study are consistent with the idea that collapsing vacancy disks constitute an important mechanism for generating dislocations. The dislocation density increases rapidly with the diameter of the specimens as is predicted by the foregoing theory.

It must, nevertheless, be pointed out that qualitatively similar results would be expected if thermal strains were responsible for the increase in dislocation density with increasing diameter of the crystal. However, thermal strains increase from the axis of the crystal outward. Under these circumstances the dislocation density would be expected to increase in the same manner as the thermal strains. Figure 4 shows that the opposite effect is found; the highest dislocation density is found toward the center of the specimen. This observation further suggests that the surface acts as a vacancy sink, whereas beyond a certain distance the vacancy supersaturation becomes sufficient to produce dislocations.

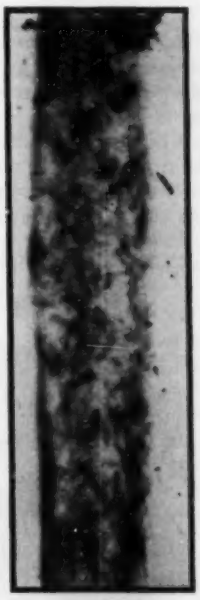

FIG. 3. X-ray transmission image from Al crystal about 1.5 mm in diameter. Magnification about 80×.

FIG. 4. X-ray transmission image from Al crystal about 2 mm in diameter. Magnification about 80×.

It is also interesting to note that no sub-boundary arrays of dislocations are found in the regions where the dislocation density is less than about 10^6 lines/cm^2. The first evidence of such arrays is found in Fig. 4. It therefore appears that a minimum dislocation density is required before such arrays start forming. The range of effective interaction between dislocations, to form arrays, thus appears to be limited to the average distance between dislocations when the density is about 10^6 lines/cm^2, or about 10 μ.

ACKNOWLEDGMENTS

The author would like to thank Professor A. R. Lang and Dr. N. Kato for helpful discussions concerning the x-ray technique used in this work.

Spiral Dislocations on Glass Fracture Surfaces

W. C. LEVENGOOD AND T. S. VONG
Ball Brothers Research Corporation, Muncie, Indiana
(Received September 21, 1959)

Within a certain range of composition spiral defects were observed on etched soda-lime-silica glasses. The patterns described spirals of Archimedes and appeared to originate from interstitial defects in the glass. Mutual stress influence effects were observed. The hypothesis of an existing torque field around the interstitial defects was useful in explaining the spiral mechanism. Application of mechanical torque stresses produced the spiral effect. In some cases it appeared feasible to apply stress energy relationships developed from dislocation theories to these minute flaw patterns.

A dynamic spherical indenter technique was developed to study structural variations in these glasses. The lengths of flaws produced by a rolling indenter were found to be sensitive to changes in the silica content of the glasses and less affected by variations in the soda-lime ratio. The effects of heating and crystallization were also studied.

I. INTRODUCTION

UNUSUAL radially symmetric flaw patterns were observed during the course of an investigation of the effect of composition variations on minute flaw patterns in glass. The particular system being studied was a simple three-component soda-lime-silica glass. Two different series of glasses were studied; in one, the soda-lime ratio was held constant and the silica varied, and in the second, the soda-lime ratio varied with the silica constant. The minute flaw patterns in these glasses were developed with an etching technique which has been previously described.[1] The defects made visible with this etchant have previously shown characteristics and reacted to applied stresses in a manner analogous to dislocations in crystalline material.

The fresh fracture surfaces of regular commercial glasses, for example, have shown interesting flaw displacement effects when subjected to various types of externally applied stresses. A wave or cyclic type of flaw formation has been found[2] between parallel diamond traces, and this effect was attributed to stress wave interactions created by the scratching tool. Circular matching flaws were also discovered on the surfaces of induced body cracks which had exhibited spontaneous closure. These patterns were attributed to localized shear forces around zones of reaction products on the fracture surfaces. On the glasses discussed here, intricate spiral flaw patterns formed without introducing externally applied forces. The detailed structure and peculiarities of this defect pattern indicated an internal mechanism similar to that producing "Frank-Read" sources in crystalline material. The results were compared to a limited degree, with dislocation theories.

A dynamic stress application technique was used to determine the extent or range through which structural readjustment occurred as the result of known applied forces. It was found that there were considerable variations within a "zone of stress influence" formed on glasses which were only slightly different in composition. This zone of stress influence was determined by the distance through which flaws spread from a load region created by a rolling steel ball. This technique was found to be a useful method for obtaining quantitative information regarding the effect of network formers and modifiers in the glass structure.

II. EXPERIMENTAL

All glasses were made from reagent grade materials. The grit size of the pulverized silica was approximately 200. Melting was carried out in platinum at a temperature of 1430°C with a melting time of approximately one-half hour. In the first series of glasses the soda-lime ratio (calculated percent Na_2O/CaO) was held constant at 1.14 and the silica varied between 55% and 80%. In the second series the silica was held constant at 60% and the soda-lime ratio varied between the limits of 0.1 to 4.0. The glasses were all annealed and the fresh fracture surfaces were created by cutting the slugs of glass in half with a glass cutter.

It was found advantageous to investigate the effect of externally applied forces on the flaws by making traces using a rolling ball technique. A $\frac{5}{16}$ in. diameter steel ball was mounted in a slot in a steel plate and allowed to rotate freely along this slot. This device was mounted on a simple lever arm stylus so the ball could be drawn horizontally over the surface of the glass. The loads were applied normal to the surfaces and the rolling velocity was kept at a low value (approximately 0.5 cm per sec).

III. RESULTS

Only pertinent photomicrographs of the flaw patterns are shown. It was not feasible to include photographs of all the samples; however, one would almost have to do this to clearly demonstrate the subtle changes in the flaw patterns. When mention is made of "ordinary" or "typical" flaw patterns in the following discussion, reference is made to the type of defects originally found[1] in commercial soda-lime-silica glasses such as container glass, sheet glass et cetera.

[1] W. C. Levengood, J. Appl. Phys. **30**, 378–386 (1959).
[2] W. C. Levengood and T. S. Vong, J. Chem. Phys. **31**, 1104–1110 (1959).

A. Soda-Lime Ratio Constant (1.14)

The glasses containing silica in amounts greater than 65% disclosed flaw patterns typical of ordinary commercial glasses; however, the number appeared to decrease with increasing silica. The 65% silica melt contained flaws which, after etching, appeared to be more pronounced or sharper in outline.

From 58% to 60% silica a spiral type of flaw formation was observed at random locations on both the free melt surface and the cleavage surfaces. These spiral defects were very similar in appearance to dislocation patterns found in crystals which are known as "Frank-Read" sources. In crystals, this effect may occur when the critical shear stress is exceeded and dislocation lines spiral outward from fixed points in the crystal. An example of one of these spiral patterns on the fracture surface of a 60% SiO_2 glass is shown in Fig. 1. The lines appear to extend outward from the short horizontal segment at the center of the spiral.

The appearance of the spiral formations suggested that the defect lines may be described by known mathematical laws of spiral formation. An investigation disclosed that the etch patterns form "Spirals of Archimedes." In terms of polar coordinates, the empirical equation is

$$\rho = k\theta, \tag{1}$$

where ρ is the radius vector, θ the angle of this vector, and k is a constant. The origin points were placed at the ends of the central straight segment in Fig. 1, and the two spirals radiated outward from these origin points. The radius vector was mesaured through 3π rotations and k was found to be constant at an average value of 0.029 with a random average variation of $\pm 10\%$. The approximate radius of these defects is given by

$$r \simeq 3\pi k \simeq 0.27 \text{ mm}. \tag{2}$$

The interaction of two spiral dislocation regions is shown in Fig. 2. Here the dislocation lines of one region have completely encircled those of the other. In this type of radial formation the stress influence effects became quite apparent. This can be distinguished as long range interactions of the elastic stress fields surrounding each source.

By applying Eq. (1) to the spiral defects in Fig. 2, it is interesting to note that k remains constant at the average value of 0.029 until about 3π rotations of the radius vector. At this point there is a marked increase in the constant, indicating that the flaw was affected by the stress field from the neighboring source. This stress field appeared to exert an influence on the flaws over a distance of about 0.29 mm which is comparable with the critical radius given in Eq. (2). This effect can be seen in Fig. 2 by following a given spiral line and noting the inflection point.

Typical random etch lines on glass surfaces appear to be the edges of slip planes normal to the surface, terminating in the glass at a dislocation line (as previous experiments have indicated[2]). The direction of the slip vector with respect to the line would suggest an edge type dislocation. The spiral flaw patterns on the other hand indicate the presence of a screw-type mechanism with the slip vector parallel to the surface and the flaw lines.

If it is assumed that the source of the spiral creates a torque parallel to the surface then a screw mechanism becomes feasible. By considering the short linear segment at the center of the spiral as a radial element of a right circular cylinder oriented at a right angle with the fracture surface and under a torsion stress, the incremental shear ds at the ends of this radial section is given as,

$$ds = r\phi = \gamma, \tag{3}$$

where r is the radius or one-half the length of the linear spiral origin, ϕ the angle of twist per unit length of the cylindrical element. The shear strain γ is also equal to

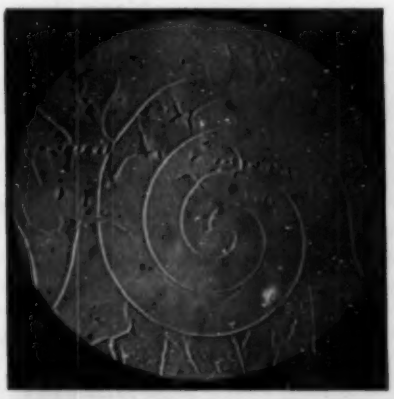

FIG. 1. Typical spiral flaw patterns on a fracture surface, 70× (60% SiO_2, $R=1.14$).

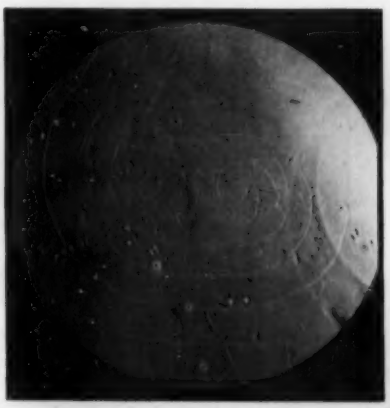

FIG. 2. Interacting spiral patterns, 34× (60% SiO_2, $R=1.14$).

the shear stress divided by the shear modulus or,

$$\gamma = \tau/G. \tag{4}$$

Equating (3) and (4) gives the maximum torque stress at the spiral origin,

$$\tau_{max} = rG\phi. \tag{5}$$

This stress field is similar in form to the actual observed shape of the spirals [Eq. (1)]. The maximum number of spiral turns are observed when the spiral source is located at a free surface. Many examples have been found where only one or two turns spiral outward from the origin. These are undoubtedly cases where the maximum torque field is located at a greater depth below the cleavage surface. Again employing the cylindrical element[3]; for a constant twist θ in a section of vertical depth d below the surface, the shear stress varies inversely with the depth,

$$\tau = rG\theta/d. \tag{6}$$

In actuality, the variation of shear stress with depth is perhaps far more complex, since we have a torque field embedded in an elastic medium which in localized regions may be anisotropic.

If this hypothesis of an existing localized torque stress is correct, then it should be possible to mechanically reproduce these patterns. An experiment was subsequently devised whereby a vertically loaded narrow knife edge (approximately 1 mm wide) was applied to a fracture surface, then given a twist or torque amounting to approximately a 5° rotation. After the applied torque field, the samples were etched and it was found that the spiral patterns were initiated at the end of the narrow load region. In the example shown in Fig. 3 the spade was rotated clockwise. In no case was the spiral effect produced by using only vertical loading stresses. For an experimental verification it was necessary to apply the torque component of stress.

FIG. 3. Spiral formations produced by an applied torque stress. Vertical load on fracture surface approximately 1 kg; rotated clockwise on a 60% SiO_2, $R=1.14$ glass (54×).

[3] R. B. Lindsay, *Physical Mechanics* (D. Van Nostrand Company, Inc., Princeton, New Jersey, 1950), p. 309.

B. Zone of Stress Influence Around Dynamic Load Regions

In a previous study[2] the shear stress found necessary to form the flaws was determined by using static loading tests. With the types of glasses discussed here this type of experiment proved unsatisfactory for several reasons. The primary disadvantage in these static tests is the difficulty in locating the exact load point and separating the flaws caused by the loading from those which ordinarily form during the cleavage process. In glasses with reduced silica, the number of random fracture surface flaws appear to become much greater.

This same argument holds true for dynamic scratches with diamond points and steel needles, however, to a lesser degree. Here one can observe flaws which definitely radiate out from the scratches. The stress conditions are complicated by the shearing and fracturing caused by the dragging action. If, however, one rolls a spherical indenter across the surface, the associated flaws may be seen in a zone on either side of the trace without the chipping and tearing effect.

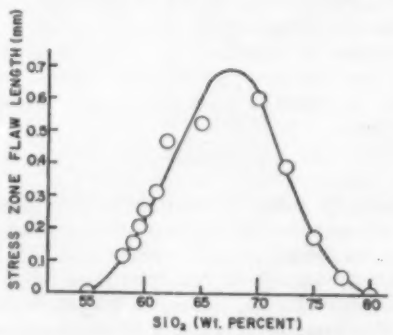

FIG. 4. Effect of silica on length of flaws produced by a rolling spherical indenter (max shear = 4.46×10^4 psi, $R=1.14$).

On regular commercial flint and sheet glasses, parallel traces made by this rolling ball technique (with loads greater than the critical shear stress) create cyclic type flaw formations (footnote 2). The ball trace appears to exert an influence on the flaw formation over a distance of several millimeters. This was not the case however in the series of glasses containing variable silica. Here the flaws could only be seen for a short distance on either side of ball traces made on the fresh fracture surfaces. These flaws originate at the edge of the contact region, which is the point of maximum normal shear, and in most cases spread perpendicular to the trace line.

The lengths of these stress zone flaws were measured in the series of glasses containing variable silica. This length is the distance from the edge of the ball contact trace line to the end of the stress zone flaw. Only those flaws were measured which were definitely associated with the ball trace line. A satisfactory load on the $\frac{5}{16}$ in.

ball was found to be 500 g and the average radius of the ball contact trace was 0.071 mm. Assuming static conditions (low rolling velocity) one may calculate the maximum shear stress at the edge of the contact region using the method of Timoshenko.[4] The ball contact region was easily located after etching due to the fact that the ball produced a path of very fine etch crystals. The maximum shear stress (τ max) at the edge of the contact zone, with these loading conditions, was 4.46×10^4 psi.

Measurements of the zone of stress influence are shown in Fig. 4; the points represent the average of about thirty measurements. It may be seen that with varying silica there are pronounced variations in flaw lengths. Long range slip occurs only in a limited composition region. With high silica the structure has a high bond strength and slip is limited. High alkali oxide content appears to produce a weak structure which does not support excessive slip.

C. Silica Constant (60%), Soda-Lime Ratio Varied

In these glasses the soda-lime ratio was varied from 0.2 to 4.0 with the silica held constant at 60%. The spiral flaw formation was observed in practically all of these glasses, with the ratio limits for spiral formation from 0.33 to 2.0.

TABLE I. Effect of melting time on flaw formation (60% SiO_2, $R=1.14$).

Melting time	Length of stress zone flaws (av)	Spirals per cm²
5 min	0.119 mm	0.73
10 min	0.165 mm	2.11
15 min	0.204 mm	4.82
30 min	0.259 mm	4.12
16 hr	0.264 mm	0.00

In the high CaO glass ($R=0.2$) no flaw patterns could be located on the crack surfaces and in the high soda ($R=4$) glass flaws were found, but no spiral formations. Well-formed spiral flaws were found in the glasses with a soda-lime ratio around 1.0; however, there were no rapid changes in flaw characteristics as was found in the variable silica glasses. It was also interesting to note that the stress zone flaws were not as extensive as in the silica series. The measured values were within the same range as those found for the variable silica glasses containing spiral flaws. The average lengths of the stress zone flaws in these glasses are shown in Fig. 5. The structure appears to be much less sensitive to variations in the soda-lime ratio than the silica content.

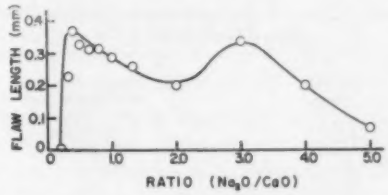

FIG. 5. Variation in flaw lengths with soda-lime ratio (max shear $=4.46\times10^4$ psi, 60% SiO_2).

D. Time-Temperature Effects

The fact that the sources for these spiral patterns are believed to be defects within the glass structure, suggested an additional series of experiments to determine the effect of internal molecular order on the flaw formation. It is well known that if glasses are held at the liquidus or crystallization temperature for long periods of time they will show a high degree of structural order in the form of crystal masses. This variation in lattice energy may also be observed in glasses heated above the crystallization temperature as evidenced by changes in density, index of refraction, etc., with heat soaking (see for example Morey,[5] pp. 260–262).

A 60% SiO_2 batch ($R=1.14$) was held for various lengths of time at the melting temperature (1430°C). After annealing, the slugs of glass were split open and the rolling ball technique applied again using the 500 g load. The average lengths of the flaw zones are shown in Table I. The right column in Table I shows the number of spiral flaws per unit area on the fresh fracture surfaces.

It may be seen in Table I that the average lengths of the stress zone flaws more than double as the melting time increases from 5 minutes to 30 minutes, whereas there is very little change from 30 minutes to 16 hours melting time. The maximum number of spiral flaws occurs in the neighborhood of 15 minutes melting time. At 16 hours, no spirals were seen, possibly because internal molecular rearrangement reduced the localized stress field below the critical value.

There was also one other effect in this glass which should be mentioned; namely a gradual discoloration of the glass with increased heating time. The 5-minute melt sample was a very clear or colorless glass, whereas the other glasses were obviously darker in color. The 16 hour sample disclosed a definite brownish discoloration. The exact reason for this is not known. Perhaps it is the gradual formation of color centers created by sodium in the glass.

A quantity of this same base composition was held below the liquidus temperature (760°C) until it became a solid crystalline mass. After pulverizing, approximately 30 g portions of this crystallized glass were reheated at 1200°C for various lengths of time. After annealing, the rolling ball load was applied to the frac-

[4] S. Timoshenko and J. W. Goodier, *Theory of Elasticity* (McGraw-Hill Book Company, Inc., New York, 1951).

[5] G. W. Morey, *The Properties of Glass* (Reinhold Publishing Corporation, New York, 1954).

TABLE II. Flaw formation in reheated precrystallized glass (60% SiO_2, $R=1.14$).

Melting time	Length of stress zone flaws (av)
10 min	0.107 mm
15 min	0.184
30 min	0.263
16 hr	0.266

ture surfaces. The average lengths of the load zone flaws are shown in Table II. Again an increase in length of flaws may be seen with increased time of heating. The magnitude of the changes and actual flaw lengths are about the same as found in the melt samples made from raw ingredients. This may be readily seen by comparing Tables I and II.

IV. DISCUSSION OF RESULTS

The critical shear stress found necessary to move or produce a flaw in regular commercial flint glass was previously determined experimentally.[2] Since in the present work we are also discussing similar type flaws in a soda-lime-silica system, it was thought that it might be to the point to compare this experimentally determined value,

$$\tau_c \simeq 6.0\times10^7 \frac{\text{dynes}}{\text{cm}^2} \text{ (experimental)}, \tag{7}$$

with the shear stresses calculated from dislocation theory. The critical shear stress necessary to move a dislocation is given by Cottrell[6] as,

$$\tau_c = \frac{2G}{(1-\nu)} \exp -\frac{2\pi a}{b(1-\nu)}, \tag{8}$$

where G is the shear modulus ($G\sim4\times10^6$ psi) and ν is Poisson's ratio ($\nu\sim0.3$). The slip vector is b and this is assumed to occur in glass over several interatomic distances or around 10 A (the average silicon-oxygen bond distance in glass is about 1.62 A). The a in Eq. 8 is a function of the dislocation length and in this case is assumed to be equal to b. After substitution in (8) this gives,

$$\tau_c \simeq 9.7\times10^7 \frac{\text{dynes}}{\text{cm}^2} \text{ (theory)}. \tag{9}$$

This value is of the same order of magnitude as the observed shear stress [Eq. (7)] found necessary to form or move a defect line on fresh glass surfaces. This critical stress is of considerably less magnitude than the observed yield stress of glass.[7]

We may now obtain information regarding the order of magnitude of the rotational strain at the spiral source by equating the Cottrell shear stress with the spiral stress field equation,

$$\frac{2G}{(1-\nu)} \exp -\frac{2\pi a}{b(1-\nu)} \simeq r G\phi. \tag{10}$$

On solving for ϕ, we get

$$\phi \simeq \frac{2}{r(1-\nu)} \exp -\frac{2\pi a}{b(1-\nu)}. \tag{11}$$

The length of the source was obtained from the photomicrographs and the remainder of the values as previously indicated. The approximate rotation of the source is,

$$\phi \simeq 0.036 \text{ radian}. \tag{12}$$

This rotation is of the same order of magnitude as the angle of twist used on the spade to mechanically reproduce the spiral effect. The larger angle of rotation in the torque experiments may be the result of some elastic yield in the metal spade and a slight slippage on the glass surface.

As to the actual form of these internal sources it is believed that they are produced by interstitial groupings in the glass network. A spiral growth originating from an internal source in a sapphire microcrystal was recently shown by May.[8] In the glasses showing the spiral formation, large additions of the alkali metal oxides produced an interesting disruption in the silicon-oxygen network. A precise explanation for the existence of the torque stress created by the interstitial groupings awaits further experimentation.

Some speculative calculations were made to examine the types of glasses resulting from additions of the alkali oxides to a sodium disilicate ($Na_2O\cdot2SiO_2$) type of structure. Each mole of Na_2O was assumed to combine with two moles of SiO_2, and one mole of CaO with one of silica. On this basis it was interesting to note that the spiral flaws occurred in those glasses in which there was either an excess of alkali oxide or very little excess silica. With excessive moles of silica, either the regular type flaw pattern was observed or the glass crystallized. In the glasses with high alkali content the solute atoms may group during the melting process and form interstitial dislocations.

It appeared from these speculations that the cation-oxygen coordination in these glasses is an important factor to be considered in terms of the observed structural changes. In accordance with the electrostatic valence rule of Pauling[9] the strength of the electrostatic bond of the cation to each coordinated anion (oxygen

[6] A. H. Cottrell, *Dislocations and Plastic Flow in Crystals* (Oxford University Press, Oxford, 1953).
[7] W. C. Levengood and T. S. Vong, J. Opt. Soc. Am. 49, 61–66 (1959).
[8] J. E. May, J. Am. Ceram. Soc. 42, 391–393 (1959).
[9] L. Pauling, *The Nature of the Chemical Bond* (Cornell University Press, New York, 1948).

in this case) is given by the ratio of the valence charge to the coordination number. This is based on a tetrahedral type structure as found in silica crystals. For the ions involved in this study, Pauling's ratio gives for the bond strengths:

Ion	Electrostatic bond strength
Si^{+4}	1
Ca^{+2}	$\frac{1}{2}$
Na^{+1}	$\frac{1}{4}$

From this one would expect the most pronounced change in structure to occur with variations in the Si—O bonds and Fig. 4 shows this to be the case. Qualitatively then, this model predicts a more rigid structure with increasing number of silicon-oxygen bonds, a structure capable of transmitting stresses over large distances; however, when the Si—O bonds become numerous the structure supports large stresses with only very limited slip.

Replacing the weak Na—O bonds with Ca—O should also produce a slight increase in the sensitivity of the structure to applied stresses. This was also shown by the curve in Fig. 5.

Pauling pointed out (footnote reference 9, pp. 385) that the electrostatic valence rule has been useful in the case of silicate minerals. In the studies here we have a silicate glass; however, it appears that the valence rules may be applicable at least in a limited sense. The spiral formation occurs in a transition state between a rigid glass with high bond strength and an extremely weak structure in which readjustments due to applied stresses are localized.

The importance of the field strength of ions in relation to their effect on the elastic properties of glass has been recently pointed out by Deeg.[10] In simple silicate glasses a decrease in the modulus of elasticity was obtained by replacing high field strength silicon-oxygen bonds with alkali ions of lower field strength. We are now in the process of making alkali oxide substitutions in simple glasses and noting the effect on the flaw formation.

[10] E. Deeg, Glastech. Ber. **31**, 229–240 (1958).

V. CONCLUSION

Spiral defect patterns were found on the etched fracture surfaces of soda-lime-silica glasses. The spiral formations were sensitive to variations in the silica content of the glass and fairly insensitive to changes in the soda-lime ratio. The spiral defects were similar in appearance to "Frank-Read" type dislocations in crystals and morphologically the patterns described spirals of Archimedes with the origins at internal dislocations in the glass. The spiral sources were believed to be interstitial groupings of alkali oxides which caused localized torque stress regions. The spiral patterns were reproduced by mechanically applying torque stress fields to glass surfaces.

Externally applied stress effects were studied by using a rolling ball technique. The flaws which formed normally to ball trace regions on fresh fracture surfaces were observed to vary in length in relation to the particular composition being used. With soda-lime ratio constant, the length of flaws disclosed a peak at medium percentages of silica and a minimum at the high and low percentages. With silica constant, the length of the flaw zone changes only slightly with varying soda-lime ratio. Increasing CaO caused a slight increase in the width of the flaw zone. The spiral flaws formed in a composition region between glasses with a rigid or high bond strength and a weak type of structure.

Increased heat-soak-time at the melting temperature produced a reduction and final disappearance of the spiral patterns as well as an increase in the length of the stress zone flaws. Heat soaking also caused an increase in the lengths of stress zone flaws in glass which had been precrystallized. These temperature effects were attributed to changes in the lattice energy of the network.

Characteristic Energy Losses of Electrons in Carbon*

LEWIS B. LEDER† AND J. A. SUDDETH
National Bureau of Standards, Washington, D. C.

(Received February 15, 1960; and in final form April 25, 1960)

The values reported for the characteristic energy losses of electrons in carbon vary by as much as 50%. In an attempt to resolve this discrepancy the electron energy losses have been remeasured for evaporated carbon and natural graphite, and it is found that there is a large difference for these two forms of carbon. Electron diffraction patterns of evaporated carbon show it to be highly amorphous. Annealing of the films causes growth of the crystallites, and also an increase of the energy loss toward the loss values for graphite. It is shown by calculation that the difference in the energy losses for the two forms is due to a difference in density, and that annealing increases the density of the evaporated carbon and, therefore, the energy loss value.

INTRODUCTION

ONE of the principal problems in the investigation of the characteristic energy losses of electrons is that of attempting to determine the causes for the discrepancies in the energy loss values as reported by the various investigators and even by the same investigator. Examination of the data shows that for some materials there is good agreement among the reported values, but for many there are rather large differences and, in some cases, the differences are so great that the loss values would appear to correspond to different materials. Some small differences can probably be accounted for by differences in the acceptance angles of the different apparatus used, the purity of the specimens, presence of oxides on the surface of the specimens, strains introduced in the films on mounting, and so forth; but only one source of a large difference is apparent to us at present. This is a difference in density of specimens.

One instance of discrepancy which we felt would lend itself to some clarification is that of carbon. The first measurements were made by Rudberg,[1] and more recently by Leder,[2] Jull,[3] Klein,[4] and Watanabe.[5] The spectrum consists of two losses: a weak, low-lying one and a stronger one at a higher value. The values reported have ranged from 5–7.6 ev for the low-lying loss, and from 19–26 ev for the higher one. Study of the published data indicated that, in general, the lower values of the two losses were obtained using evaporated carbon films, whereas the higher values were obtained using natural graphite.

We have remeasured the characteristic energy losses in both natural graphite and in evaporated carbon to determine if the difference did exist, and if it did whether it could be ascribed to a difference in density of the two forms of carbon. We have also studied the energy loss in evaporated carbon films under various conditions to determine how it changes.

EXPERIMENTAL

Most of the measurements were made using a cylindrical-lens energy analyzer described earlier.[6] The acceptance angle was 10^{-7} sr. Because the electron transmission of the graphite and annealed carbon samples was low (due to thickness) the integrating properties of photographic recording was used rather than the combination of a phosphor and photomultiplier.[7] Electron diffraction patterns of each sample were taken in a separate apparatus.

Graphite originating in India and Ceylon was used for the bulk of the measurements on graphite.[8] No attempt was made to purify the samples, although it was noted that some foreign material was imbedded between the layers of the typical lamellar graphite structure. However, two samples of highly purified graphite flakes[9] were also used, and no difference was observed in the loss values. Films thin enough for transmission of 30-kv electrons were obtained by slicing pieces from the bulk specimen or flake using the point of a sewing needle honed to the shape of a chisel. The India and Ceylon graphite yielded both polycrystalline and single crystal samples. The flakes gave only polycrystalline samples.

The evaporated carbon films were obtained using the Bradley[10] carbon-arc technique. Microscope slides were first prepared by evaporating a thin coating (approximately 50 A) of sodium chloride on the surface of the slide. Carbon was then evaporated over the NaCl, and the films were floated off onto water by carefully dipping the slide in the water and dissolving the NaCl.

Since we wished to anneal the carbon specimens

* This work was in part supported by the U. S. Atomic Energy Commission.

† Now at RCA Laboratories, Princeton, New Jersey.

[1] E. Rudberg, Svenska Vet. Akad. Handl. **7**, No. 1 (1929).

[2] L. B. Leder, Phys. Rev. **103**, 1721 (1956).

[3] G. Jull, Proc. Phys. Soc. (London) **B69**, 1237 (1956).

[4] W. Kleinn, Optik, **11**, 226 (1954).

[5] H. Watanabe, J. Electronmicroscopy **4** (Ann. ed.), 24 (1956).

[6] G. Mollenstedt, Optik, **5**, 499 (1949).

[7] L. Marton, L. B. Leder, and H. Mendlowitz, Advances in Electronics and Electron Phys. **7**, 183 (1955); L. B. Leder, Phys. Rev. **103**, 1721 (1956).

[8] We wish to thank Dr. Paul E. Desautels, Associate Curator, Division of Mineralogy and Petrology, Smithsonian Institution for several graphite samples.

[9] Dr. V. R. Deitz of the Bone Char Research group of the National Bureau of Standards was kind enough to supply us with this graphite which had been treated to spectroscopic purity.

[10] D. E. Bradley, Brit. J. Appl. Phys. **5**, 65 (1954).

directly on the holder which was to be inserted into the analyzer; and, since the graphitization temperature of carbon is 2800–3300°C,[11] the specimen holder was made of spectroscopically pure artificial graphite. We started with $\frac{3}{8}$-in. diam rod. A center section $\frac{3}{4}$ in. long was milled flat to a $\frac{3}{32}$-in. thickness. A 13-mil hole, over which the carbon film was mounted, was drilled in the center of this section. The region about the hole was further thinned by reducing the width from $\frac{3}{8}$ in. to $\frac{3}{16}$ in. and the thickness from 3/32 to 3/64 in. The details are shown on Fig. 1. Clamping of this heater-holder was impractical since it was quite fragile. Therefore, it was held by spring tension between two $\frac{3}{8}$-in. copper rods. Shallow semicircular slots were cut in the ends of the copper rods and bosses were cut on the ends of the holder to fit these slots. These kept the holder from slipping out from between the rods during heating. The bosses were cut at 90° to each other to reduce the possibility of breakage due to bending of the holder.

The films were picked up from the water and dried over the hole in the graphite holder. The annealing was accomplished by passing current through the holder mounted in an evacuated bell jar. The temperature of the film was measured by observing the black-body color of the 13-mil hole in the holder with an optical pyrometer corrected for the absorption of the bell jar. The pyrometer was preset to a desired temperature and then the current through the holder was increased until the hole color was the same as that of pyrometer filament. At this point the current was turned off and the holder allowed to cool. Because of the difficulty of estimating the color temperature under these conditions, the annealing temperatures are taken to be accurate to ±100°C.

All the measurements with evaporated carbon were made on films obtained in one evaporation process. The thickness of these evaporated carbon films was measured with a Tolansky interferometer[12] to be 780±70 A. They were light brown in transmission. It was noted that they changed color on heating, and became black in transmission and silvery appearing in reflection at quite low temperatures. Above 2200°C the films became opaque and were black in reflection. The electron transmission properties paralleled the optical properties. Initially, and up to about 2200°C annealing temperature, the transmission to 30-kv electrons was high and good diffraction patterns were obtained. Above 2200°C annealing temperature a weak diffraction pattern in a diffuse background was obtained, and at about 2500°C and above the films became opaque to the 30-kv electrons. We have not been able to explain this apparent thickening of the films. It could be reasonably assumed that the sample film over the hole was at a lower temperature than at the edge of the hole and that carbon from the holder diffused over the surface of the film. Another possible explanation is that carbonaceous material was deposited on the carbon films as the result of high temperature decomposition of hydrocarbons (e.g., diffusion pump fluid, gasket grease, etc.) present in the bell jar. For those annealing temperatures at which the carbon film became opaque to electrons, a piece of the film was removed from the surface of the holder close to the hole. Quite often it was found that electrons would go through such pieces when mounted on one of our standard specimen holders. All measurements above 2400°C annealing temperature were made on such pieces.

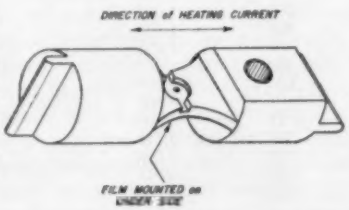

FIG. 1. Carbon film holder made from spectroscopic carbon rod. During the annealing process, it is clamped between copper supports in an evacuated bell jar.

RESULTS

Electron Diffraction Measurements

The lattice of graphite is made up of hexagonal layers arranged in such a way that the projection from the center of a hexagon in one layer passes through an atom in the next layer. The lattice constants are[13] $a_0 = 2.456$ A and $c_0 = 6.694$ A. Plane spacings for graphite were calculated from the electron diffraction pattern obtained from the Ceylon graphite [Fig. 2(a)], and agree quite well with the values given by Finch and Wilman[14] although we did not obtain as many diffraction rings as they did. However, the "extra" rings which they reported did not give spacings representative of any normal identity spacings in the structure assigned to graphite by x-ray diffraction, and were explained by them as being due to fractional l indices.

The diffraction pattern obtained for evaporated carbon consisted of three diffuse rings [Fig. 2(b)] indicating that the structure was nearly amorphous. Because of the diffuse character of the rings, it was difficult to obtain accurate plane spacings, but they were sufficiently accurate to indicate that only one of the three corresponded to a graphite spacing. This was for the (100) plane. The half-width of the rings indicated that the crystallites were of the order of 40 A in size.

Heating of the evaporated carbon film changed the character of the diffraction pattern quite radically. For an annealing temperature of 1000°C, new rings which were considerably narrower appeared. The sharpening

[11] J. Biscoe and B. E. Warren, J. Appl. Phys. **13**, 364 (1942); H. T. Pinnick, *Proceedings of the Conference on Carbon*, Buffalo, New York, 1956.

[12] S. Tolansky, *Multiple-beam Interferometry of Surfaces and Films* (Oxford University Press, New York, 1947).

[13] J. B. Nelson and D. P. Riley, Proc. Phys. Soc. (London) **A57**, 477 (1945).

[14] G. I. Finch and H. Wilman, Proc. Roy. Soc. (London) **A155**, 345 (1936).

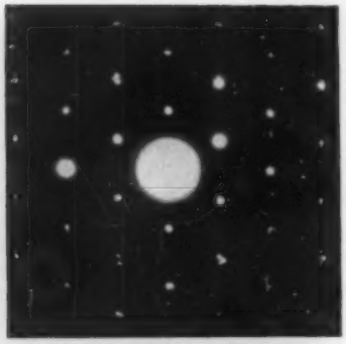

(a)

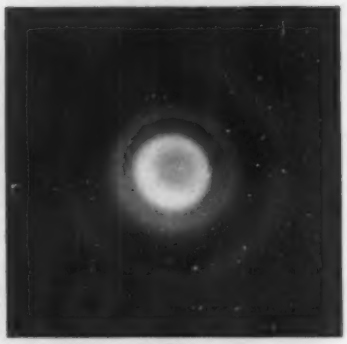

(b)

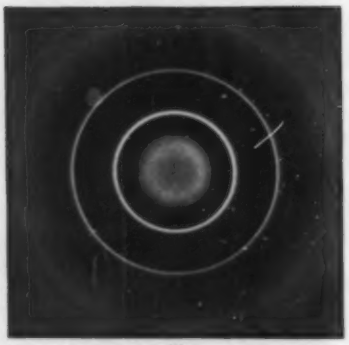

(c)

FIG. 2. (a) is the electron diffraction pattern obtained from Ceylon graphite; (b) is the diffraction pattern of an evaporated carbon film; and (c) is the diffraction pattern of an evaporated carbon film annealed at 1000°C for approximately 30 sec.

of the rings indicated growth of the crystallites, and measurements gave an approximate size of 300 A. Increased temperature did not appear to change the pattern further, although this may have been due to the fact that we heated the films at any given temperature for only a few seconds. The diffraction pattern is shown on Fig. 2(c). The lattice spacings obtained from this pattern show quite strikingly that the structure of the film has changed. The first and third spacings of the unannealed carbon have disappeared, and all the spacings correspond exactly to those obtained for natural graphite. In Table I we have listed the calculated plane plane spacings and the corresponding indices of diffraction.

Low-Temperature Measurements

It has been shown by Blue and Danielson[15] that the temperature dependence of the resistivity of evaporated carbon shows a T^{-5} dependence in the temperature range 300° to 77°K. If the characteristic energy losses were in some manner connected with the dc conductivity, a relatively large change in the energy loss should be observed in this same temperature range. Such measurements were made in a different apparatus[16] from that used for the annealing measurements. A change in the energy loss of less than 0.1 ev (the effective resolving power of the analyzer) was found for the change in temperature from 300° to 78°K; this is the order of magnitude expected to result from thermal expansion only.

Energy Loss Measurements

The energy losses for graphite were measured with both single crystal and polycrystalline specimens. No noticeable difference in the characteristic-energy-loss value was found. The energy-loss spectrum consists of a weak loss at 7.2 ev and a much stronger, rather broad loss at 24.7 ev. These values agree very well with the losses of 7.3 ev and 25.0 ev found by Watanabe[5] using natural graphite.

The energy-loss spectrum obtained using evaporated carbon films looks the same as that for graphite. However, the loss values were found to be 5.8 ev and 19.8 ev.

TABLE I. Plane spacings in angstroms obtained from electron diffraction patterns of natural graphite, evaporated carbon, and annealed evaporated carbon.

Indices of diffraction	Graphite	Evaporated carbon	Annealed carbon
...	...	4.44	...
002	...	...	3.23
100	...	2.13	2.124
...	2.091	...	...
110	1.231	...	1.231
...	...	1.18	...
112	1.156	...	...
200	1.065	...	1.067
201	1.055	...	...
...	1.045	...	...
204?	...	...	0.868
120	0.806	...	0.810
...	0.803	...	...
121	0.800	...	...
300	0.711	...	0.713
302	0.696	...	...
220	0.615	...	0.612
222	0.605	...	...

[15] M. D. Blue and G. C. Danielson, J. Appl. Phys. **28**, 583 (1957).

[16] L. B. Leder and L. Marton, Phys. Rev. **112**, 341 (1958); L. B. Leder and J. A. Simpson, Rev. Sci. Instr. **29**, 571 (1958).

Jull,[3] also using evaporated carbon films, found loss values of 5.5 ev and 23.0 ev.

Energy-loss measurements were made for several annealing temperatures. There appeared to be a trend for the energy-loss values to increase with increased annealing temperature, although there were some inconsistencies at the higher temperatures. These inconsistencies can probably be traced to the fact, as stated earlier, that we used specimen pieces stripped from near the hole in the carbon holder-heater. It can be reasonably surmised that the films were not uniformly heated so that some of the samples taken from the holder, which had been heated to a given temperature, had not reached that temperature. In Table II we have listed the energy-loss values and the temperature to which the heater had been brought. We have also indicated whether the specimen was taken off the holder or measured on the holder.

TABLE II. The energy losses in evaporated carbon as a function of annealing temperature. The errors shown are standard deviations from several runs. The large deviations for the second loss are due to the large halfwidth of this loss while that for the 2500°C annealing temperature reflects the fact that the films had to be removed from the holder to be measured, as explained in the text.

Annealing temp. °C	Loss 1 ev	Loss 2 ev	Remarks
1000	5.6±0.2	20.6±0.3	Measured on holder
2000	5.7±0.1	21.6±0.3	Measured on holder
2200	6.5±0.05	22.6±1.2	Measured on holder
2300	6.6±0.2	24.9±0.6	Measured on holder
2400	6.1±0.1	24.2±0.1	Measured on holder
2500	6.5±0.6	24.0±0.9	Removed from holder
2800	6.3±0.1	24.6±0.5	Removed from holder

Calculation of the Energy Losses

If the value of the strongest energy loss can be expressed[17] by $E_2=\hbar(4\pi ne^2/m)^{\frac{1}{2}}$, we can then also write this equation as

$$E_2=[\hbar e/(1.6\times10^{-12})](4\pi N_0 zd/Am)^{\frac{1}{2}}\text{ ev}, \quad (1)$$

where $\hbar$ is Planck's constant divided by 2π, n is the density of electrons, e is the electronic charge, m is the electron mass, N_0 is Avogadro's number, d is the density, z is the number of participating electrons, and A is the atomic number. For carbon, if z is arbitrarily taken to be equal to 4 (the number of valence electrons), $E_2=16.6(d)^{\frac{1}{2}}$ ev. We can then calculate the energy-loss value using the densities for three forms of carbon as given in the handbooks,[18] and the density of evaporated carbon as measured by Langbein.[19] In Table III we have listed the four types of carbon in column one; in the second column are shown the densities, in the third column the calculated energy losses, and in the fourth column the measured energy losses for graphite and evaporated carbon. The agreement between the calculated and measured values is excellent. The loss value of 23.3 ev found by Kleinn[4] using lampblack can possibly be explained as being due to the fact that lampblack has a density in the range given for so-called "amorphous" carbon. However, Rudberg[1] found a loss of 26.0 ev using the deposit from burning camphor. We have not been able to find any published information about the density of such a deposit although it would be expected to be somewhat less than that of graphite.

TABLE III. The main energy loss for different forms of carbon.

Carbon form	Density	Calc loss—ev	Measured loss—ev
Evaporated	1.35	19.3	19.8
"Amorphous"	1.8–2.1	22.3–24.1	...
Graphite	2.25	24.9	25.1
Diamond	3.51	31.1	...

The low-lying loss in graphite has been explained by Ichikawa[20] as being due to the π electrons of carbon. For a polycrystalline film he gives the equation

$$E_1=\hbar\left(\frac{4\pi ne^2}{m}\right)^{\frac{1}{2}}\left\{1-\frac{ma^2\gamma_0}{3\hbar^2}\left[1+\frac{\gamma_1}{4\gamma_0}\left(\frac{c}{a}\right)^2\right]\right\}^{\frac{1}{2}}\text{ ev}. \quad (2)$$

Here γ_0 is the resonance energy between nearest neighbors in a plane, γ_1 is the resonance energy of nearest neighbors in adjacent planes, and a and c are the lattice parameters. The part of the equation outside the brackets is identical with Eq. (1). By taking z equal to 1 (the number of π electrons per atom) and γ_0 and γ_1 equal to 1.63 and 0.42 ev, respectively (Ichikawa found a value of 0.32 for γ_1 using a value of $c=7.72$ A instead of $c=6.694$), 7.5 ev is found as the magnitude of the low-lying loss in graphite as compared to the value of 7.2 ev measured by us. The calculated value for evaporated carbon can then be obtained by using the density of 1.35 found by Langbein[18] if it can be assumed that the same values for γ_0 and γ_1 can be used. In Table IV we have listed the results in the same way as in Table III. Again it is seen that the calculated value for evaporated carbon fits the measured value very well. Kleinn's value for lampblack of 5.7 ev is too low for "amorphous" carbon, but Rudberg's value of 7.0 ev for camphor smoke does come in the proper range.

CONCLUSIONS

The characteristic-energy losses measured for graphite were found to be in excellent agreement with the values found by Watanabe.[5] The energy losses found for

TABLE IV. The low-lying energy loss for different forms of carbon.

Carbon form	Density	Calc loss—ev	Measured loss—ev
Evaporated	1.35	5.8	5.8
"Amorphous"	1.8–2.1	6.7–7.2	...
Graphite	2.25	7.5	7.2
Diamond	3.51	9.4	...

[17] L. Marton, L. B. Leder, and H. Mendlowitz, Advances in Electronics and Electron Phys. **7**, 183 (1955).

[18] *Handbook of Chemistry and Physics* (Chemical Rubber Publishing Company, Cleveland, Ohio, 1946), 30th ed., p. 396.

[19] W. Langbein, Naturwissenschaften, **45**, 510 (1958).

[20] Y. H. Ichikawa, Phys. Rev. **109**, 653 (1958).

evaporated carbon were considerably less than those for graphite. Annealing of the evaporated films caused an increase in the crystallite size and also caused the films to become more graphitic as evidenced by the diffraction pattern. The energy losses increased with increased annealing temperature so that at an annealing temperature of 2300°C the energy losses were nearly equal to those in graphite. Above this temperature the losses remained fairly constant, on the average, although individual measurements for some specimens showed the full graphite loss values. This is explained by the necessity of having to remove samples from the heater-holder in order to make measurements at these higher temperatures so that we were not measuring pieces which had reached the measured heater temperature.

Measurements of the energy losses for single-crystal and polycrystalline graphite showed no difference for these two crystalline forms. On this basis, it is likely that the difference in energy loss between evaporated carbon and graphite is not due to a difference in crystal structure. On the other hand, the difference is well explained by a difference in density of the two forms of carbon, and the measured loss values fit very well to the loss values calculated on this basis. Annealing of the films changes the density and thereby the energy loss, intermediate loss values being due to intermediate density values. The values measured by Kleinn[4] using lampblack can also be explained on this basis since lampblack corresponds to what is often loosely called an "amorphous" carbon; but the loss value of 23.0 ev found by Jull[3] for evaporated carbon cannot be explained without knowing more about the method of preparation and treatment after preparation since these would affect the density.

Measurement of the energy losses in evaporated carbon films held at liquid nitrogen temperature showed less than a 0.5% change from the room temperature values. From this, it would appear that the energy losses are only slightly related, if at all, to the dc resistivity of the films since it has been shown[18] that in the same temperature interval the resistivity changes by a factor greater than 700%.

We wish to thank Dr. L. Marton, Chief of the Electron Physics Section, for his constant advice and encouragement, and L. E. Mann for the fine job he did in making the graphite heaters.

JOURNAL OF APPLIED PHYSICS VOLUME 31, NUMBER 8 AUGUST, 1960

Elastic Constants of Single-Crystal Aluminum Antimonide

D. I. Bolef and M. Menes
Westinghouse Research Laboratories, Pittsburgh 35, Pennsylvania
(Received March 28, 1960)

The ultrasonic cw resonance technique was used to measure the adiabatic elastic constants of single-crystal aluminum antimonide at 27°C. The values for the elastic stiffness constants, in units of 10^{11} d/cm^2, are: $c_{11}=8.939$, $c_{12}=4.427$, and $c_{44}=4.155$. A theoretical density of 4.36 g/cc was used. The values of c_{11} and c_{44} for single crystal GaSb obtained by the cw resonance technique are compared with previous values obtained by pulse-echo techniques.

I. INTRODUCTION

THE elastic constants of several Group III–Group V compounds of the zinc blend structure have been reported in recent years.[1–4] Interpretation of some of these data on the basis of degree of covalent bonding has been attempted by Potter.[5] This paper reports the results of measurements of the adiabatic elastic constants of single-crystal aluminum antimonide at 27°C.

The three elastic stiffness constants, c_{11}, c_{12}, and c_{44}, were determined from the velocities of sound waves propagated along the [100] and [110] axes of the crystal. Since five independent velocities were measured, two cross checks of the elastic constants were provided. The ultrasonic cw resonance technique was used at a frequency of 10 Mc. Measurements were also made at

TABLE I. Wave velocities in AlSb at 27°C.

Direction of propagation	Mode	Equation for velocity	Velocity (10^5 cm/sec)
100	Longitudinal	$(c_{11}/\rho)^{\frac{1}{2}}$	4.528±0.004
100	Transverse	$(c_{44}/\rho)^{\frac{1}{2}}$	3.087±0.003
110	Longitudinal	$\left[\frac{1}{2\rho}(c_{11}+c_{12}+2c_{44})\right]^{\frac{1}{2}}$	4.977±0.004
110	Transverse	$(c_{44}/\rho)^{\frac{1}{2}}$	3.085±0.003
110	Transverse	$\left[\frac{1}{2\rho}(c_{11}-c_{12})\right]^{\frac{1}{2}}$	2.276±0.002

[1] H. J. McSkimin, W. L. Bond, G. L. Pearson, and H. J. Hrostowski, Bull. Am. Phys. Soc. Ser. II 1, 111 (1956).
[2] R. F. Potter, Phys. Rev. 103, 47 (1956).
[3] L. J. Slutsky and C. W. Garland, Phys. Rev. 113, 167 (1959).
[4] T. B. Bateman, H. J. McSkimin, and J. M. Whelan, J. Appl. Phys. 30, 544 (1959).
[5] R. F. Potter, J. Phys. Chem. Solids 3, 223 (1957).

TABLE II. Elastic stiffness constants at 27°C. Units of 10^{11} d/cm².[a]

	Propagation [100][b]	[110]
c_{11}	8.939±0.02	8.907±0.04
c_{12}	4.425±0.02	4.393±0.02
c_{44}	4.155±0.008	4.150±0.008

[a] $\rho = 4.360$ g/cc used to calculate c.
[b] ($\frac{1}{2}$) $(c_{11}-c_{12})$ used to calculate c_{12}.

TABLE III. Comparison of elastic stiffness constants of GaSb at 27°C. Units of 10^{11} d/cm².

	Present work 10 Mc	30 Mc	McSkimin *et al.*[a] 50 Mc
c_{11}	8.828±0.02	8.840±0.02	8.849±0.025
c_{12}			4.037±0.02
c_{44}	4.319±0.01	4.319±0.01	4.325±0.013

[a] Footnote reference 1.

tained using the expression:

$$v_S = \frac{2l_S}{n}\left[\nu_{C,n} - \frac{m_T}{m_S}(\nu_T - \nu_{C,n})\right], \tag{1}$$

where l_S is the acoustic path length in the specimen, $\nu_{C,n}$ the observed resonance frequency, ν_T the transducer frequency, $m = \rho l$ where ρ is the density, and the subscripts T and S refer, respectively, to transducer and specimen. n is the effective number of half-wavelengths of sound in the specimen at a measured resonance frequency $\nu_{C,n}$,

$$n = \frac{\nu_{C,n}}{\Delta\nu_C}\left(1 - \frac{m_T}{m_S}\right), \tag{2}$$

where $\Delta\nu_C$ is the observed frequency separation between adjacent half-wave resonances. That the bond can be neglected under the present experimental conditions has been shown.[7]

TABLE IV. Elastic properties of Group III–Group V compounds. $T = 25$°C. Units of 10^{11} d/cm².

Crystal	ρ (g/cc)	c_{11}	c_{12}	c_{44}	Anisotropy $2c_{44}/(c_{11}-c_{12})$	$(c_{12}-c_{44})/(c_{12}+c_{44})\times 100$	Bulk modulus $B=(c_{11}+2c_{12})/3$	Text footnote reference
GaAs	5.307	11.88	5.38	5.94	1.83	−4.9	0.755	4
AlSb	4.360	8.94	4.42	4.15	1.84	2.8	0.590	Present work
GaSb	5.619	8.85	4.04	4.32	1.80	−3.3	0.539	1
InSb	5.789	6.72	3.67	3.02	1.98	9.7	0.469	1

10 Mc and at 30 Mc on single crystal gallium antimonide oriented along the [100] axis.

II. EXPERIMENTAL

The single crystal AlSb was obtained from the Ohio Semiconductor Company. The cylindrical specimen, oriented along the [100] crystallographic axis, was roughly 0.35 in. in length and 0.5 in. in diameter. The crystallographic orientation was checked by means of the x-ray Laue back-reflection technique.[6] The (100) faces were ground on a cast-iron lap using AO 303 ½ carborundum and kerosene. After etching for five minutes in 1:1 HCl and HNO_3, the faces were given a final polish on AO 303 ½. The (110) faces were rough-ground on 4–0 emery paper and then polished on AO 303 ½. Both sets of faces were flat and parallel to within 0.05 mil. The acoustic path lengths were: parallel [100] axis, 0.3402 in.; parallel [110] axis, 0.460 in. The cross sections were such that ½-in. transducers could be used on both sets of faces.

The wave velocities in the crystal were determined by the cw resonance technique.[7] The velocities were ob-

III. RESULTS AND DISCUSSION

The wave velocities measured at 10 Mc are given in Table I. The estimated probable errors are primarily due to uncertainties in the values of the specimen length and frequencies. Values of the elastic stiffness constants derived from the velocities are given in Table II. The theoretical density of 4.360 g/cc was used, assuming for the value of the lattice constant $a = 6.0950$ A at 26°C.[8]

In order to compare the cw results with those obtained by careful pulse techniques, measurements were made on a single crystal of GaSb. The (100) faces of this crystal were exposed, thus permitting measurement of c_{11} and c_{44} only. A comparison of the cw results at 10 Mc and at 30 Mc with results of McSkimin[1] obtained at 50 Mc by use of a phase comparison technique is given in Table III.

A comparison of the present results for AlSb with other Group III–Group V compounds is given in Table IV. The fifth column is a measure of the crystal anisotropy while the sixth is a measure of departure from the Cauchy relation.

IV. ACKNOWLEDGMENT

We wish to thank R. Farich for his valuable aid in sample preparation.

[6] We are indebted to Dr. A. Taylor and Miss Brenda Kagle for the x ray.
[7] D. I. Bolef and M. Menes, J. Appl. Phys. **31**, 1010 (1960).
[8] R. F. Blunt, W. R. Hosler, and H. P. Frederikse, Phys. Rev. **96**, 578 (1954).

Heat Treatment of Gallium Arsenide

J. T. EDMOND*
Services Electronics Research Laboratory, Baldock, Hertfordshire, England
(Received January 5, 1960; and in final form March 4, 1960)

Specimens of N-type GaAs were found to become P-type or less strongly N-type as a result of heat treatment. The heat treatment was carried out in small quartz tubes, of two grades of purity. The magnitude of the changes was much less in high-purity quartz. The effect in ordinary quartz was shown to be due in part to copper contamination, the copper originating in the quartz; the changes could be reduced by annealing.

CHANGES have been observed in the electrical properties of a number of semiconductors after heat treatment. Such changes have been discussed in the case of germanium, silicon, and lead sulphide and among III-V compounds InAs[1-3] and InSb[4]. The effect of heat treatment on N-type GaAs has been to make the material less strongly N-type or change it to P-type.

The basic experimental procedure was as follows—single crystal specimens were obtained of approximate size 10×2.5×1.5 mm. The Hall constant (R) of each was measured and the specimen cleaned, etched in a mixture of 5 parts hydrochloric acid to 1 part nitric acid and washed. The specimen was sealed in an evacuated quartz tube of about 1.5 cc volume. Two grades of quartz were used, ordinary purity Vitreosil[5] or very pure Spectrosil[5]; the purity is shown later to be very significant. After heat treatment, mostly at 1000 °C, the specimen was taken from the furnace and quenched. Thereafter, the specimen was ground slightly on all sides to eliminate surface effects and the Hall constant remeasured.

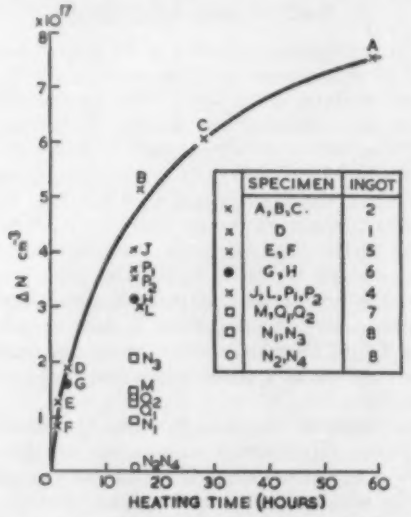

FIG. 1. Effect of heat treatment on number of centers in GaAs (see also Table I).

Table I shows a number of results obtained and also the estimated change in carrier concentration, ΔN (in the exhaustion range). Most of the specimens were finally P-type, but it is clear from measurements at different temperatures that the acceptor levels were sufficiently far above the top of the valence band that only some of the centers were ionized. Hence, it is not possible to obtain the number of carriers in the extrinsic range directly from room-temperature measurement. In a few cases in which the measurements were extended above room temperature the number of carriers at 300°C (apparently in the exhaustion range) was about three times that at room temperature. This factor has been assumed and applied in all cases; although this procedure is not rigorous it is sufficiently accurate for the present purpose. Figure 1 shows ΔN plotted against the time of treatment at 1000°C for a number of specimens. With the exception of N_2 and N_4, the specimens were heated in Vitreosil tubes; these tubes, however, were not specially selected and may have been from different batches of quartz. A to F and J, L, P_1, and P_2 were made from similar ingots, the others from ingots believed to be more pure. A to F show the same behavior (ΔN as a function of time of treatment) as that described by Dixon and Enright[1] for InAs. The mechanism, proposed originally by Kurtz and Kulin,[6] is as follows—the heat treatment effects are caused by the movement of impurities collected initially around dislocations; at high temperatures the impurities escape into the lattice and may be quenched therein; during annealing the impurities diffuse back to the dislocations. It is assumed that in lattice sites the impurities are electrically active in the sense of producing carriers but not active at dislocations.

A number of other mechanisms were considered, however, and further experiments performed. A section of ingot 33×6×12 mm was heat treated at 1000°C for 16 hours. The ingot proved to have a P-type surface but N-type interior. Sections were taken and electroplated with silver as shown in Fig. 2—the silver depositing on the P-type regions. As a result of this experiment, it was believed that an acceptor impurity

* Now at C. E. G. B., Friars House, Blackfriars Road, London, S. E. 1, England.
[1] J. R. Dixon and D. P. Enright, J. Appl. Phys. **30**, 753 (1959).
[2] J. R. Dixon and D. P. Enright, J. Appl. Phys. **30**, 1462 (1959).
[3] C. Hilsum, Proc. Phys. Soc. (London) **B73**, 685 (1959).
[4] K. F. Hulme, R. R. E. Memorandum 1581 (1959).
[5] Supplied by The Thermal Syndicate Ltd., Wallsend, England.
[6] A. D. Kurtz and S. A. Kulin, Acta Met. **2**, 352 (1954).

TABLE I. Heat treatment of GaAs—change in electrical properties as a function of time of treatment, etc.

GaAs ingot	Specimen	R_1[a] cm^3 $coul^{-1}$	n_1[c] cm^{-3} $\times10^{-16}$	R_2[b] cm^3 $coul^{-1}$	n_2[e] cm^{-3} $\times10^{-16}$	n_2'[d] cm^{-3} $\times10^{-16}$	ΔN[e] cm^{-3} $\times10^{-16}$	Temperature °C	Time hours
2	*A*	(− 20.4)	−30.6	+ 41.6	+15.0	45.1	75.7	1000	59
2	*B*	− 30.5	−20.5	+ 60.6	+10.3	30.9	51.4	1000	16½
2	*C*	− 31.3	−19.9	+ 46.1	+13.6	40.7	60.6	1000	28
1	*D*	−111	− 5.6	+146	+ 4.28	12.8	18.4	1000	3
5	*E*	− 90	− 6.9	+340	+ 1.8	5.5	12.4	1000	1
5	*F*	−186	− 3.4	+403	+ 1.55	4.6	8.0	1000	1
6	*G*	−285	− 2.2	+135	+ 4.6	13.9	16.1	1000	3
6	*H*	−268	− 2.3	+ 64	+ 9.8	29.3	31.6	1000	15
3	*I*	− 43.4	−14.4	∞	0	0	14.4	900	15
4	*J*[f]	− 36.5	−17.1	+ 79.6	+ 7.85	23.0	40.1	1000	15
4	*L*[g]	− 65.1	− 9.6	+ 91.3	+ 6.8	20.5	30.1	1000	16
7	*M*	−236	− 2.7	+161.5	+ 3.9	11.6	14.3	1000	15
8	N_1	−657	− 0.95	+227	+ 2.75	8.25	9.2	1000	15
8	N_2[h]	−333	− 1.88	−535	− 1.17	...	0.71	1000	15½
8	N_3	−344	− 1.82	+101	+ 6.2	18.6	20.4	1000	15
8	N_4[h]	−366	− 1.70	−685	− 0.91	...	0.79	1000	15
4	P_1	− 87.5	− 7.1	+ 63.4	+ 7.8	29.5	36.6	1000	15
4	P_2	− 66.6	− 9.4	+ 71.7	+ 8.7	26.1	35.5	1000	15
7	Q_1	−257	− 2.43	+175.7	+ 3.55	10.7	13.1	1000	15
7	Q_2	−415	− 1.51	+153.6	+ 4.06	12.2	13.7	1000	15

[a] R_1 is the Hall constant before heat treatment.
[b] R_2 the Hall constant after heat treatment.
[c] n_1 and n_2 are the corresponding number of carriers (negative for electrons, positive for holes).
[d] $n_2' = 3n_2$ (See text).
[e] ΔN is the difference between n_2' and n_1.
[f] *J* was heated in an ambient arsenic pressure of about 3.8 atmospheres (cf. P_1 and P_2).
[g] *L* was only ground and washed, not etched, before heat treatment (cf. P_1 and P_2).
[h] N_2 and N_4 were heat treated in Spectrosil, all others in Vitreosil.

was diffusing into the material from the surface of the ingot and that the cross section of the specimens, previously used, had been sufficiently small to allow almost complete diffusion throughout. One or two specimens had shown slightly higher *P*-type values when thinned to half-thickness.

Various surface treatments of the specimens were tried, but without altering the effects of heat treatment; therefore, it was then suspected that the impurity might come from the quartz (Vitreosil). Keller and Pettit[7] believe that in their preparation of ZnS there is contamination by 1 to 10 parts per million of copper, lead, tin, and iron from the quartz.

Four specimens were treated, N_1 and N_3 in Vitreosil and N_2 and N_4 in Spectrosil, all at 1000°C (Table I). It is clear that the use of Spectrosil reduces the value of ΔN observed by an order of magnitude or more; this has been confirmed using specimens from other ingots. It is possible, of course, that Spectrosil contains an extra donor impurity, but this is considered to be unlikely. Assuming, therefore, that the acceptor impurity originates in the quartz, one may account for the shape of the curve in Fig. 1 if this is a function of the rate of escape of impurity from the quartz (Vitreosil). It is also noted that the magnitude of the effects found in GaAs were about 7×10^{17} cm^{-3} at 1000°C; in InAs,[1] 1×10^{17} cm^{-3} at 850°C; and in InSb,[4] 3×10^{15} cm^{-3} at 500°C; all for 60-hours treatment. This too may be consistent with the foregoing theory in that the rate of escape from quartz is likely to increase with temperature. However Dixon and Enright[2] find a close connection between the effects of heat treatment in InAs and the electron mobility before heat treatment, indicating that in this case at least the behavior depends also on the quality of the material. Something of the same nature may appear in Fig. 1 in which specimens *A–F*, *J*, *L*, P_1, P_2 show greater values of ΔN than *M*, Q_1, Q_2, N_1, N_3 from more recent and purer ingots.

It was suspected that the impurity involved in these effects was copper, which is an acceptor impurity in GaAs and also is known to have a sufficiently high diffusion constant, about 10^{-5}–10^{-6} cm^2 sec^{-1}, to permeate the specimens shown in Table I.[8] Accordingly an analysis was made of a number of samples by means of the square wave polarograph (Table II).

Specimen N_3 has been contaminated markedly with copper and N_4 slightly. The amounts shown in Table II are in possible agreement with those estimated in

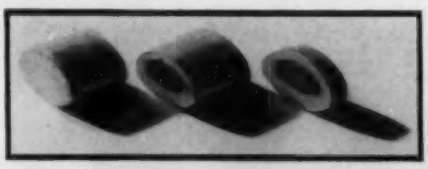

FIG. 2. Ingot of GaAs heat treated and sectioned. Sections electroplated with silver showing *p*-type regions on the surface.

[7] S. P. Keller and G. D. Pettit Phys. Rev. **115**, 526 (1959).

[8] C. S. Fuller and J. M. Whelan, J. Phys. Chem. Solids **6**, 173 (1958).

TABLE II. Analysis of copper content of GaAs specimens by square-wave polarograph.

Sample	ppm copper (atomic)	Remarks
Sample, from ingot (2)	0.1	Untreated sample
Sample, from ingot (8)	0.1	Untreated sample
N_4, from ingot (8)	0.3	After heating in Spectrosil
N_3, from ingot (8)	11	After heating in Vitreosil

Table I, bearing in mind the doubts already expressed about the true value of ΔN. It is interesting to note that the sample from ingot (2) did not contain any copper detectable by this means. Yet specimens from this ingot showed the behavior already illustrated in Fig. 1.

Additional evidence of the presence of copper after heat treatment in specimens E and F was obtained by comparing the variation of resistivity with temperature (100–250°K) with that of two copper doped specimens. All showed an activation energy of about 0.14 ev. Subsequently, however, other specimens were examined for which the value was much smaller, ~0.03 ev.

Annealing has been carried out in Vitreosil on specimens heat treated in Vitreosil, and in Spectrosil on specimens heat treated in Spectrosil. The results are shown in Table III.

TABLE III. Change in Hall constant on annealing heat treated GaAs.

Type of quartz	Specimen	R_1[a] cm^3 $coul^{-1}$	R_2[b] cm^3 $coul^{-1}$	R_3[c] cm^3 $coul^{-1}$	Annealing procedure
Vitreosil	B	− 30.5	+ 60.6	+ 86.6	1 hour at 1000°C. Cooled to room temperature at 36°C per hour.
Vitreosil	H	−268	+ 64	+190	Cooled from 1000°C at 24°C per hour.
Vitreosil	O_3	−415	+153.6	+158	47 hours at 600°C. Cooled to room temperature at 11°C per hour.
Spectrosil	S_1	−143	−226	(−268)	Cooled from 1000 °C at 24°C per hour.
Spectrosil	S_2	−184	−295	(−1000)	Cooled from 1000°C at 20°C per hour.

[a] R_1 is the Hall constant before heat treatment.
[b] R_2 is the Hall constant after heat treatment and before annealing.
[c] R_3 is the Hall constant after annealing.

There is a tendency for P-type specimens heat treated and annealed in Vitreosil to return to their original state. This could be due to the movement of copper to dislocations according to the theory of Dixon and Enright, although the copper may have originated in the quartz. It would be expected, however, that since the same type of Vitreosil is used in preparation of GaAs, a little copper would be present in the prepared ingots. It is assumed that it is present in smaller concentration only since the relative size of ingot to specimen is much greater than the corresponding tube sizes used for preparation and heat treatment.

The importance of the purity of the quartz has also been demonstrated in the heat treatment and annealing of InAs. The change in carrier concentration is again much less in Spectrosil than in Vitreosil. These results will be reported later in detail.

It is concluded that:

(1) The changes due to heat treatment in GaAs depend on the purity of the quartz employed in the process.
(2) To a smaller degree, the effects are a function of the quality of the GaAs.
(3) The contaminant in some cases at least is copper.
(4) The results on annealing GaAs may be consistent with the mechanism suggested by Dixon and Enright for InAs.
(5) For general purposes, preparation of GaAs, etc., the importance of using the purest quartz is indicated.

ACKNOWLEDGMENTS

It is a pleasure to thank Mrs. M. Garner for much help in the preparation of specimens and measurements, Mr. W. Harding for supplying GaAs, Dr. V. Jennings for the analysis by polarograph, Dr. C. Hilsum for suggesting the work on InAs, and also the Admiralty for permission to publish.

Analog Study of Large-Signal High-Frequency Diodes

C. L. ANDREWS
General Electric Research Laboratory, Schenectady, New York
(Received April 11, 1960)

A rolling-ball analogue for the motion of electrons in a high-frequency longitudinal field has been developed in which the balls, injected at regular time intervals, plotted photographically a family of graphs of distance against time, indicated the electron bunching, velocity modulation, and density modulation. From these graphs the current densities were found as a function of time for a series of equally spaced positions between cathode and anode, and the plate current induced by the electron stream was computed. Graphs of conductance against transit angle revealed that the conductance was independent of the size of signal for indices of modulation 0.25, 0.50, and 0.75. When the transit angle was 2π the induced plate current was almost pure first harmonic plus dc. When the transit angle was 3π the first harmonic disappeared.

INTRODUCTION

DISTANCE-TIME graphs, known as Applegate diagrams, of a stream of electrons crossing a field-free space showing the conversion of velocity modulation to density modulation, have been commonly used in describing electron ballistics in drift spaces of klystrons. The purpose of this report was to describe a rolling-ball analog for obtaining distance-time graphs for a stream of electrons in an alternating longitudinal electric field with transit times of the order of a period of the oscillating field.

The first studies were of an analog for large signals in a diode tube without space charge. The diode was a simple case in which to test the analog methods. Moreover, no analysis seems to have been made of the electron ballistics in diodes at large signal except for zero bias.[1]

APPARATUS

The rotating cylinder of Fig. 1 fed the balls at constant rate from the funnel to the track. A precise motor-driven mechanical oscillator with adjustable amplitude and frequency caused the slope of the straight track to vary sinusoidally. The device was analogous to a temperature-limited diode with an ac signal superposed on a dc field. An image of the groove in the track fell on a slot in the hard-rubber shield in the back of the camera. The film of a film pack (Kodak Tri-X) was pulled by motor at constant speed by the slot. The track was illuminated by a stroboscope (General Radio strobolux). The track was painted flatblack and the bottom of the groove was covered with a white plastic strip which was photographed as a constant time line on the graph. Thus, in the series of pictures of the balls on the track, each ball plotted a graph of its distance along the track against time. The image of the light source observed in the ball was a small point at the center of a dark circle.

If the track did not oscillate but had a constant slope, the graphs traced by the balls were a set of identical parabolas as shown in Fig. 2. The slope of the track in this case was one to 20. Figure 3 was obtained by oscillating the slope of the track with 100% modulation; that is, the amplitude of the ac signal equaled the dc bias.

TESTS FOR ERRORS

In treating the rolling-ball analog, we assumed that the ball acquired only translational kinetic energy plus rotational kinetic energy about an axis through the center of gravity parallel to the plane of the track and perpendicular to the direction of the groove. For this ideal case, the acceleration $a=5/7\ g\sin\theta$, g is the acceleration of a freely falling body, and θ the angle that the inclined plane makes with the horizontal. Unless precautions were taken, even the balls that followed the grooves sometimes acquired other rotations. In the groove of Fig. 4(a) the ball acquired spin components about the vertical axis. In the groove of Fig. 4(b) the ball will oscillate laterally with angular velocities about an axis parallel to the direction of the groove. Harries[2] has reported, in developing launching tracks for the rubber membrane analogue, that the best track was a rectangular slot of width small com-

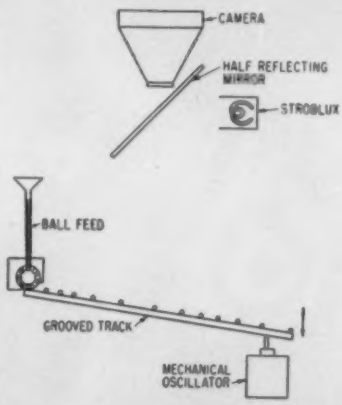

FIG. 1. Diagram of apparatus for making distance-time graphs of rolling balls.

[1] C. C. Wang, Proc. I.R.E. **29**, 200 (1941).

[2] J. H. D. Harries, Proc. I.R.E. **44**, 242 (1956).

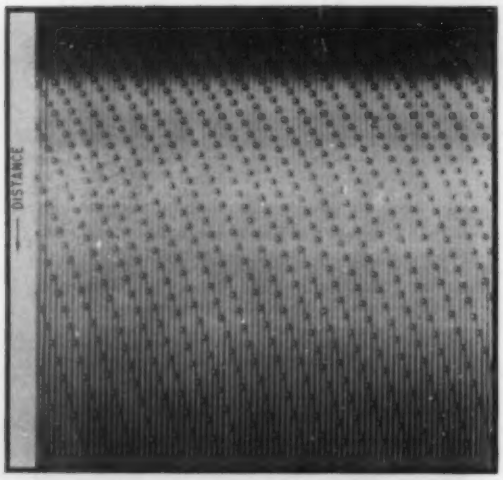

FIG. 2. Distance-time graphs plotted by balls undergoing constant acceleration provide a check on the precision of the method.

pared to the diameter of the ball, as shown in Fig. 4(c). Even with this groove, care had to be taken to avoid vibrations which would cause the ball to oscillate laterally, rolling alternately on the two edges of the slot.

We obtained a minimum of frictional loss by using two plates of tool steel for track, as in Fig. 4(d). The upper edges of the two plates and the steel separator between were milled and polished in one plane, after which the separator was lowered to produce a groove.

A test of frictional loss was made by oscillating the track about the zero bias (level) position and observing the lag of the sinusoidally varying velocity behind the applied sinusoidally alternating force. Figure 5 was a photographic plot of a ball undergoing such a forced oscillation on the track. The alternating velocity lagged 76 deg behind the alternating applied force. The reactive component of the mechanical impedance was four times the resistive component. The frequency of oscillation was 0.40 cps and the frequency of the stroboscope was 30 flashes/sec, giving 75 flashes or time coordinate lines per cycle. The phase lag of velocity behind the alternating force could be made more nearly 90 deg by (1) reducing the friction of the track to reduce the resistive component, or (2) increasing the frequency of oscillation to increase the reactive component.

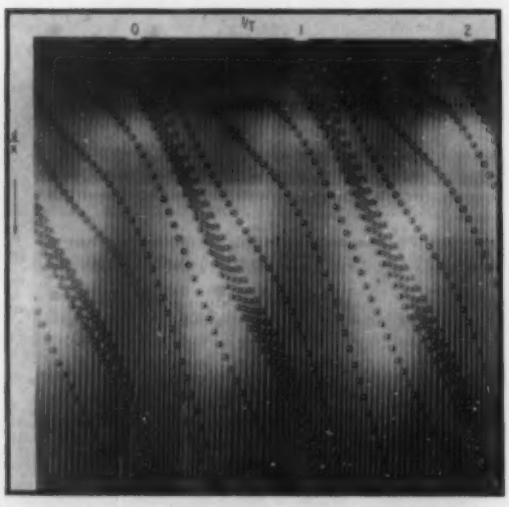

FIG. 3. Distance-time graph plotted by balls when the slope of the incline was modulated by a signal of 100% modulation.

OBSERVATIONS

The graphical plots of distance against time for a series of balls launched at regular time intervals during the cycle were made in (1) sets of 12 different frequencies and thus 12 different values of mean transit time of electrons crossing the tube, and (2) for sets of 12 different percentages of modulation. Twelve was the number of films in a pack. A set of 12 such pictures was taken in as many minutes while calculated plots of any one of the families of graphs in the set required a day of computations.

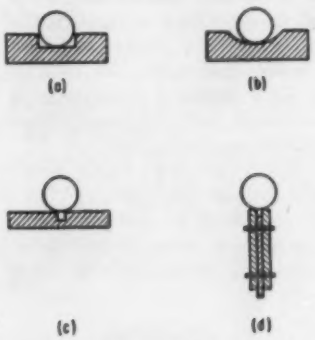

FIG. 4. Groove (a) causes erratic losses to spin energy about the vertical axis. Groove (b) causes the balls to oscillate laterally with angular velocities about an axis parallel to the groove. Groove (c) restricts the rotation to that about an axis perpendicular to the plane in which the groove oscillates. Groove (d) made of separate tool-steel plates gave the least frictional loss.

With time the calculated plots were made more precisely than the photographed ones. Thus the series of photographic plots was used to indicate the desirability of calculating one of those in the set. For instance, all of the sets indicated that those electrons which remained at the center of the bunches had been launched when the instantaneous value of the ac potential difference was near a minimum; that is, the launching phase of electrons at the center of the bunch was 180 ± 10 deg. The phase reference was that of the applied potential difference. Calculations for special cases showed that the electrons which remained at the

center of the bunch has been launched when the ac potential was precisely a minimum.

The distance-time graph of Fig. 6 indicated how the velocity modulation was converted largely to density modulation as the electrons crossed the tube with transit angles of 360 deg.

The distance along the track from "cathode to anode" was divided into a number of sections of equal length and the velocities found from the slopes of the curves at the centers of each of three sections for a series of times during the cycle. Likewise, the charge density was measured as the inverse of the distance between balls on the track at the same positions and times. The electron current densities were then computed as products of the charge densities and velocities. The total current density at any instant is $j_{\text{inst}}=\rho v+\epsilon_0(\partial E/\partial t)$. The first term is the electron current density expressed as a product of charge density and velocity v. The

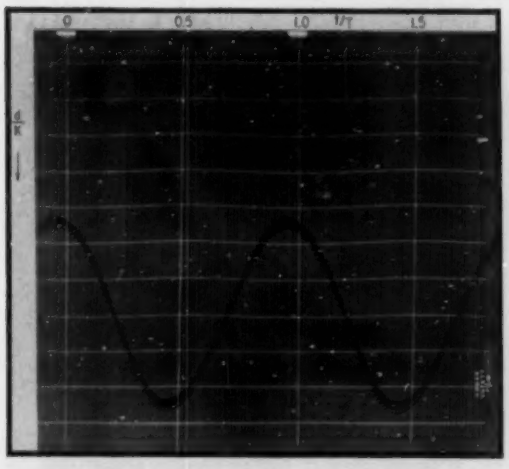

FIG. 5. A test for frictional loss by oscillating the track about the zero bias position.

second term is the displacement current expressed as a product of permittivity and the time rate of change of electric field intensity. Since the latter term is always 90 deg ahead of the alternating emf in phase, we treated only the electron current density.

A series of plots was made of electron current density j against time t/T expressed as a fraction of a period. As a check on the calculation, we noted that the current averaged over time, indicated by the area under the curve, was the same at any position in the tube.

The plate current induced by the electron stream was computed as the average of the current densities at evenly spaced positions between cathode and anode for a series of 20 times during the cycle. Some of the problems to be solved were (1) the determination of the transit times which would yield predominance of the first and second harmonics, and (2) the determination of how the plots of conductance against transit

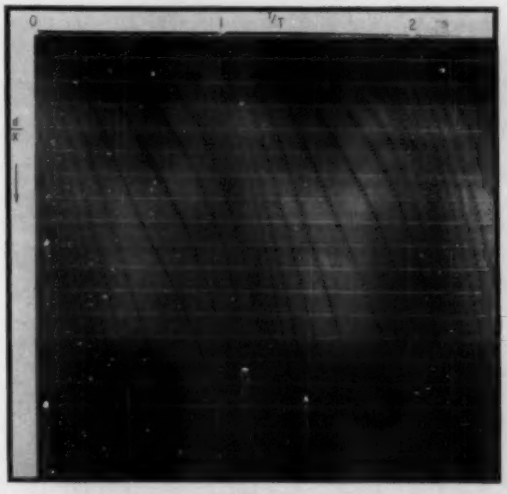

FIG. 6. Distance-time graph indicating how the velocity modulation was converted to density modulation as the electron crossed the tube with transit angle of 360 deg. $M=0.50$. Incidentally, the specular reflection from the track caused a wave form across the graph which was a hazy plot of the alternating potential difference against time.

angle varied with modulation M. Modulation indices of 0.25, 0.50, and 0.75 were employed. The most precise values of conductance were determined from calculated distance-time plots.

CALCULATION OF DISTANCE-TIME PLOTS

If A is the constant acceleration of the electron because of dc bias alone, M is the modulation index, the angular frequency and d is distance from the cathode, then the acceleration

$$a=d^2/dt^2(d)=A(1+M\cos\omega t). \quad (1)$$

On solving for d, we obtain the velocity $v=d/dt(d)=A[t+(M/\omega)\sin\omega t+\text{const}]$.

We may evaluate the constant by noting that a particular electron starts with zero velocity at its launching time t_a. Thus we obtain

$$v=d/dt(d)=A[(t-t_a)+(M/\omega)(\sin\omega t-\sin\omega t_a)]. \quad (2)$$

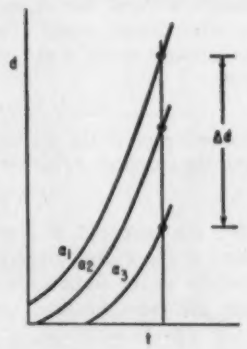

FIG. 7. The charge density is inversely as the distance between electrons measured along the constant time coordinate.

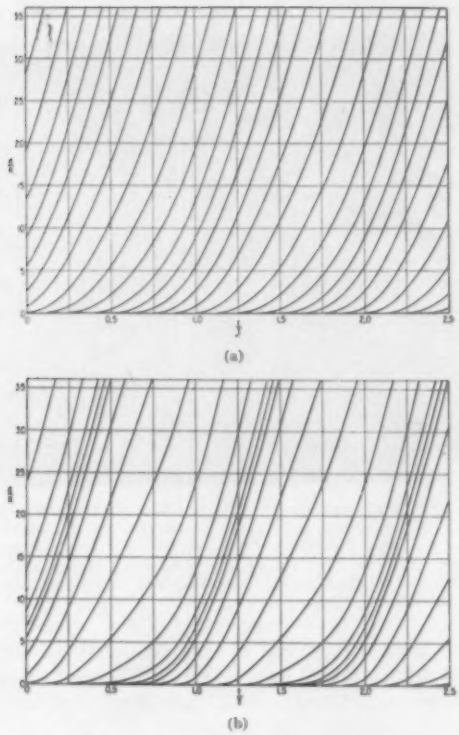

(a)

(b)

FIG. 8. (a) and (b) Computed distance-time graphs for modulation indices $M=0.25$ and 0.75.

On solving for the distance d and finding the constant of integration, by noting that $t=t_s$ when $d=0$, we obtain

$$d=\frac{A}{2\omega^2}\{(\omega t-\omega t_s)^2+2M[\cos\omega t_s-\cos\omega t-(\omega t-\omega t_s)\sin\omega t_s]\}, \quad (3)$$

where $t-t_s$ is the transit time of an electron and $\omega t-\omega t_s$ the transit angle. Each electron has a different transit angle. We may describe the properties of the tube in terms of the mean transit angle or still more simply in terms of the dc transit angle which is nearly equal to the mean transit angle. The dc transit angle is the transit angle taken in the limit as M approaches zero. Thus

$$d(2\omega^2/A)=(\omega t-\omega t_s)^2.$$

We shall express the dc transit angle by the symbol θ and the constant $A/2\omega^2$ by K. Thus

$$d/K=\theta^2.$$

We are prepared to solve for the instantaneous values of the charge density ρ. The charge density is inversely as the distance between electrons measured along the constant time coordinate of Fig. 7. Thus

$$C/\rho=\Delta d, \quad (4)$$

where C is a constant. For convenience we may represent the phase angle of launching ωt_s by the letter α. The constant α distinguishes each curve on the distance-time plot. The increment

$$\Delta d=(\partial d/\partial\alpha)_t\Delta\alpha. \quad (5)$$

By substituting in Eq. (4), we obtain

$$C/\rho=(\partial d/\partial\alpha)_t\Delta\alpha. \quad (6)$$

By taking the partial of d with respect to α in Eq. (3) and substituting Eq. (6), we obtain

$$C\omega^2/\rho A\Delta\alpha=(\alpha-\omega t)(1+M\cos\alpha). \quad (7)$$

If ρ_0 is the charge density at zero modulation

$$(1/\rho_0)(C\omega^2/A\Delta\alpha)=\alpha-\omega t, \quad (8)$$

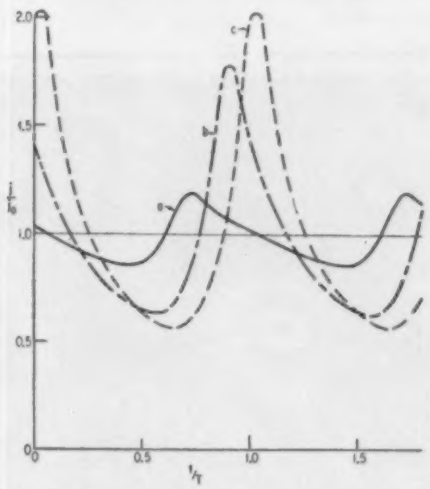

FIG. 9. Sample plots of current densities against time for (a) $d/K=0.25$, (b) $d/K=4.25$, and (c) $d/K=8.25$. In each case $M=0.5$.

and the relative value of the instantaneous charge density is

$$\rho/\rho_0=1/(1+M\cos\alpha). \quad (9)$$

We note that the relative charge density ρ/ρ_0 is independent of the transit angle. If v_0 is the limiting value of the instantaneous velocity as the modulation approaches zero

$$v_0/A=t-t_s \quad (10)$$

and the instantaneous relative velocity

$$v/v_0=1+M[(\sin\omega t-\sin\alpha)/(\omega t-\alpha)]. \quad (11)$$

We note that for large transit angles $\omega t-\alpha$ the relative velocity v/v_0 approaches the constant unity so that the modulation is only density modulation. The instantaneous current density, relative to the dc current density is the product of the relative charge density

and velocity so that

$$\frac{j}{j_0}=\frac{1+M[(\sin\omega t-\sin\alpha)/(\omega t-\alpha)]}{1+M\cos\alpha}. \qquad (12)$$

CURRENT DENSITIES

Our next purpose was to plot the relative current density j/j_0 against time t/T for values of d/K at the centers of elements of equal length between the cathode and anode. Although any given position d/K and time t/T defined a unique value of α, we failed in all attempts to express α as a simple function of d/K and t/T. Thus we were compelled for any value of d/K to pick those times t/T which fell on a distance-time curve for an electron of given phase of launching α. Thus α could be read from the time coordinate and j/j_0 computed for any given d/K and a series of time t/T. The distance-time plots, either photographed or computed from Eq. (3), were not only of pictorial pedagogic value but a necessity in computing current densities. Figures 8(a) and 8(b) were computed distance-time graphs for modulation indices $M=0.25$ and 0.75.

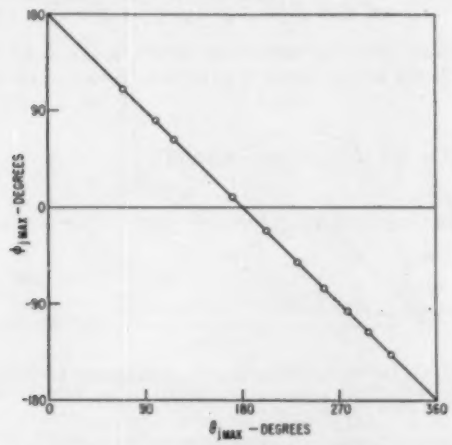

FIG. 10. Graph of phase of peak of current density against transit angle of the electron at the position of maximum current density.

Since the final plots of conductance were made against dc transit angle which was equal to the square root of d/K, it was found best to make a series of distance-time plots for the total cathode-to-plate spacing of d/K, equal to 1, 10, and 100 and to divide each of those spaces into 20 equal elements of length. The current densities were computed at the centers of each of these elements. Figure 9 was a sample of current densities plotted against time for three values of d/K and a modulation index of $M=0.5$.

Graphs of phase of peak current density $\phi_{j\,max}$ against the transit angle $\theta_{j\,max}$ of the electron which is at the position of maximum current density revealed that, for all values of M,

$$\phi_{j\,max}=\pi-\theta_{j\,max}$$

as shown in Fig. 10. Thus, when the transit angle of the electron at the position of maximum density was π, the peaks of the current density were in phase with the signal potential.

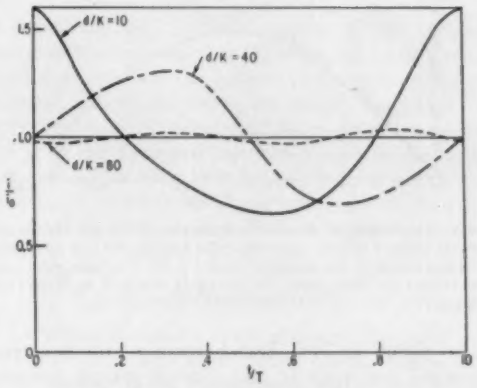

FIG. 11. Induced plate current plotted against time for grid-anode spacing $d/K=10$, 40, and 80.

INDUCED PLATE CURRENT

That portion of the plate current per area of plate surface which was induced by the stream of electrons was computed at 20 equally spaced times during the cycle as the average of the current densities at those times at equally spaced distances between cathode and anode. Figure 11 was a sample of induced plate currents i/i_0 plotted against time t/T for a series of values of electrode spacings d/K. Interesting observations were made from the series of graphs of instantaneous plate currents even before a Fourier analysis of the plate currents was completed. When d/K was 10 and thus the transit angle approximately π, the fundamental component of current was in phase with the applied ac potential. When d/K was 40 and thus the transit angle approximately 2π, the harmonics above the first had nearly disappeared and the current lagged the potential by $\pi/2$. When d/K was 80 and the transit

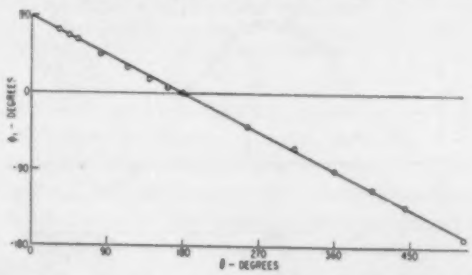

FIG. 12. The phase of the first harmonic in the induced plate current plotted against transit angle.

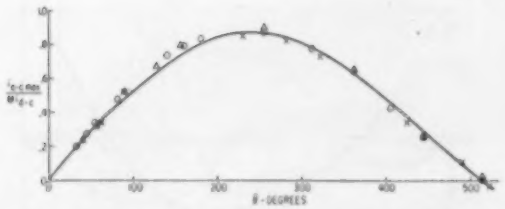

FIG. 13. Graph of relative admittance Y/Y_0 for the induced current plotted against angle reveals that the relative admittance is independent of the modulation index M. The triangles, circles and crosses are data points for the cases $M=0.25$, 0.50, and 0.75, respectively. The curve is computed from Eq. (16).

angle about 3π, the first harmonic had completely vanished and only dc and a small second harmonic remained.

A Fourier analysis was made for the amplitude and phase of the first harmonic of the plate current. A plot of the phase of the current taken relative to the potential against transit angle gave the simple linear relation of Fig. 12. The phase was independent of the modulation index M. The phase ϕ was related to the transit angle θ by

$$\phi=(\pi-\theta)/2. \tag{13}$$

Thus the power factor

$$\cos\phi=\cos(\pi-\theta)/2=[(1-\cos\theta)/2]^{\frac{1}{2}}=\sin(\theta/2).$$

For simplicity we defined β as the *half transit angle* so that the power factor was $\sin\beta$.

Plots of the ratio of maximum of the first harmonic $I_{ac\ max}$ in the plate current to the dc plate current i_{dc} against dc transit angle revealed a maximum when the transit angle was 240 deg and the first zero at 518 deg. For a given transit angle, $I_{ac\ max}/I_{dc}$ was proportional to the modulation index M.

CONDUCTANCE

The ratio obtained by dividing the admittance Y of the tube for the current induced by the electron stream by the dc admittance Y_0 is

$$\frac{Y}{Y_0}=\left(\frac{I_{ac\ max}}{E_{ac\ max}}\right)\Big/\left(\frac{I_{dc}}{E_{dc}}\right). \tag{14}$$

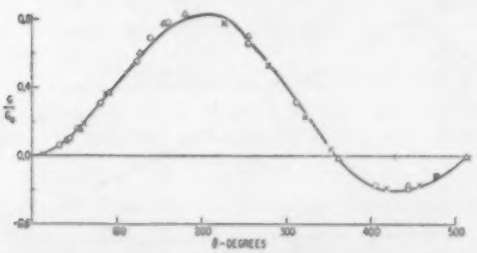

FIG. 14. Graph of relative conductance plotted against transit angle. The triangles, circles and crosses are data points for the cases $M=0.25$, 0.50, and 0.75, respectively.

Since $M=E_{ac\ max}/E_{dc}$, we obtain on substitution in Eq. (14)

$$Y/Y_0=(1/M)(I_{ac\ max}/I_{dc}) \tag{15}$$

Figure 13 is a plot of $1/M\ I_{ac\ max}/I_{dc}$ against transit angle. Within the limits of error of our calculation Y/Y_0 is the same for modulation indices $M=0.25$, 0.50, and 0.75.

The calculated values are compared in Fig. 13 with the expression

$$Y/Y_0=2[(\sin\beta/\beta^2)-(\cos\beta/\beta)]; \tag{16}$$

β is the half transit angle. This equation fits the calculations within the limits of their error. The relative conductance is

$$G/G_0=(Y/Y_0)(\cos\phi)=(Y/Y_0)(\sin\beta). \tag{17}$$

Substituting for Y/Y_0 from Eq. (16), we obtain

$$G/G_0=2[(\sin\beta/\beta)-\cos\beta]\sin\beta/\beta. \tag{18}$$

There are two conditions which make $G/G_0=0$: (1) If the second factor is to be zero, $\beta=n\pi$ where n is

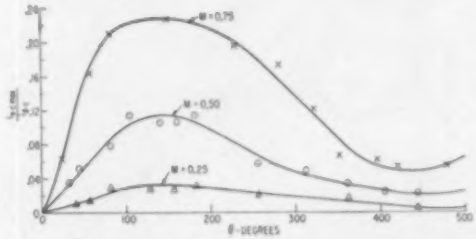

FIG. 15. The ratio of the amplitude of the second harmonic to the dc plate current plotted against the transit angle for the three cases of $M=0.25$, 0.50, and 0.75.

any positive integer; (2) if the first factor is to be zero, $\tan\beta=\beta$. This occurs when $\beta=0$, 1.43π, 2.46π, 3.47π. The case $\beta=1.43\pi$ corresponds to $d/K=80$ when the first harmonic in the induced plate current was zero. Approximately $\tan\beta=\beta$ when $\beta=(2n+1)\pi/2$ where n is any positive integer. The approximation is closer as n increases. Figure 14 is a graph of the relative conductance G/G_0 against the transit angle θ. The solid curve is a plot of Eq. (18) and is identical with that of Mihran[3] for the case of zero space charge and small signal.

SECOND HARMONIC

Fourier analyses were made for the amplitudes of the second harmonics in the induced plate currents for modulations M equal to 0.25, 0.50, and 0.75. Figure 15 was a series of plots of the ratio of the amplitude of the second harmonic to the dc plate current $i_{ac\ max}/i_{dc}$ against the transit angle θ. The precision of the determination of the amplitudes of the second harmonics

[3] T. G. Mihran, Proc. I. R. E. 42, 862 (1954).

was not sufficient to justify trying to find the equations of the curves of Fig. 15. For a given transit angle the amplitudes of the second harmonics $i_{ac\ max}$ were approximately proportional to the square of the modulation index M for this range of modulations. We noted that the second harmonic content was a minimum in the range of transit angles for which the plate conductance shown in Fig. 14 was negative.

CONCLUSIONS

The rolling-ball analogue for electrons in a high-frequency, large-signal diode provided a rapid means of obtaining plots of distance against time for electrons emitted at regular time intervals during a cycle. A large number of such plots were made in a short time with varying modulations and transit times to suggest the most important cases for which the more time-consuming calculations were made.

Calculations and Fourier analysis of the induced plate currents revealed that (1) when the transit angle of the diode was 2π, the current was almost pure first harmonic plus dc; (2) when the transit angle was 3π the first harmonic disappeared leaving almost pure dc; (3) the second harmonic was a minimum in the range of transit angles from 360 to 520 deg for which the conductance of the diode is negative, and (4) the relative conductance G/G_0 of a diode was independent of the size of the signal.

ACKNOWLEDGMENTS

The author is pleased to acknowledge the assistance and ingenious ideas of P. E. Pallett, R. E. Abbey, and W. B. Halstead of the Photographic Laboratory of the General Electric Research Laboratory; and E. D. McArthur, R. A. Dehn, L. A. Harris, and T. G. Mihran for discussions and criticism of the manuscript.

JOURNAL OF APPLIED PHYSICS VOLUME 31, NUMBER 8 AUGUST, 1960

Plasma Propulsion by a Rapidly Varying Magnetic Field*

MILTON M. KLEIN
Missile and Space Vehicle Department, General Electric Company, Philadelphia, Pennsylvania

AND

KEITH A. BRUECKNER†
University of Pennsylvania, Philadelphia, Pennsylvania

(Received March 22, 1960)

An investigation has been made of the motion of a plasma under the action of a rapidly varying magnetic field from a stationary coil. The analysis has been done for two cases: (1) the plasma is assumed completely diamagnetic so that the ionization history of the plasma may be ignored and (2) the nondiamagnetic case where the ionization process is considered in detail. For the diamagnetic case the analysis yields a coupled set of nonlinear ordinary differential equations which have been put in similarity form and solved for a wide range of the similarity parameters. An illustrative example is given to show how to use the results to obtain detailed information for a given physical system. The calculations indicate that, for field frequencies of about one megacycle, velocities of the order 10^7 cm/sec may be attained, but the efficiency of conversion of stored energy into kinetic energy is rather low (about 5–10%) and cannot be varied much by possible changes in the physical and geometrical parameters of the system.

Because of the complexity of the analysis, a systematic series of solutions has not been made for the nondiamagnetic case. Instead, a typical example has been worked out to indicate the major differences to be expected. The results show that the nondiamagnetic plasma yields an efficiency slightly less than that obtained for the corresponding diamagnetic plasma. The ionization process inside the plasma levels off very rapidly so that the electron density increases by only a few percent during the motion of the plasma, but the amount of ionization has very little effect upon the efficiency of the system. The indications are that the efficiency of a plasma driven by a magnetic field from a stationary coil is probably too low for practical applications.

1. INTRODUCTION

CONSIDERABLE attention has been devoted in recent years to the possible use of a plasma propulsion system for guidance and control in space travel. Because of the many difficulties inherent in maintaining a plasma, most experimental work on plasmas has been directed toward instrumentation and technique while only a limited effort, experimental or theoretical, has been given to the performance of a plasma propulsion system.[1] A theoretical investigation has therefore been made of the performance of a simple plasma propulsion

* Based on work performed under the auspices of the U. S. Air Force, Ballistic Missiles Division under contract.

† Consultant, General Electric Company; Present Affiliation: University of California, School of Science and Engineering, La Jolla, California.

[1] W. H. Bostick, *Plasma Motors: The Propulsion of Plasma by Magnetic Means, IXth International Aeronautic Congress, Amsterdam 1958* (Springer-Verlag, Berlin, Germany, 1959), pp. 794–808.

system in which a rapidly varying magnetic field originating in a circular coil interacts with a plasma which has been injected into a confining cylinder.

The plasma absorbs energy from the magnetic field, starts to ionize rapidly, and becomes a good conductor, thus limiting the penetration of the magnetic field into its interior. A current sheath is therefore formed which is propelled forward into the neutral gas by the pressure of the magnetic field. The study of the motion of a plasma in terms of its ionization history is a fairly complicated one and we have therefore, for convenience, separated the analysis into two parts: (1) the plasma is assumed completely diamagnetic so that the ionization history may be disregarded, and (2) the ionization process is accounted for (nondiamagnetic case).

For the diamagnetic case the force on the plasma may be obtained from consideration of the change in energy occurring when the plasma is introduced into the system, or alternatively from a study of the pressure of the magnetic field acting on the plasma. The resulting equations of motion and energy then yield a coupled set of nonlinear ordinary differential equations which can be solved numerically. We have put these equations in convenient similarity form and obtained solutions covering a wide range of the physical and geometrical parameters of the system from which the details for a given physical system may be obtained.

For the nondiamagnetic case we study in detail the heating and ionization of the plasma, and the formation of the current sheath. The motion of the plasma is then obtained by making use of a snow-plow model of acceleration in which the current sheath moves forward into the neutral gas. During this process further ionization of some neutrals occurs inside the sheath while others are lost by diffusion from the rear of the sheath. Because of the greater complexity of the analysis for the nondiamagnetic case, we have not obtained a systematic series of solutions of the type given for the diamagnetic case. Instead we have worked out a typical example to indicate the major differences to be expected between the diamagnetic and nondiamagnetic cases.

2. DIAMAGNETIC CASE

2.1 Gradient Method

We consider a plasma, which has been injected into a confining cylinder, acted on by a magnetic field from a circular coil, the coil being supplied by the discharge of a capacitor; the plasma is situated along the axis of the coil and near the plane of the coil (Fig. 1). The magnetic field due to a circular coil, for a point on the axis of the coil, is along the axis of the coil and of magnitude (we use MKS units in this report)

$$B=\frac{\mu_0}{2}\frac{b^2 I}{(b^2+x^2)^{\frac{3}{2}}}, \tag{1}$$

where B is the flux density in web/m^2; b is the radius of the coil, meters; x is the distance along axis from coil to plasma, meters; I is the current in the coil, amp. For points near the axis the component of the field normal to the axis is much smaller than the component along the axis. We have therefore assumed that the field **B** has the value given by Eq. (1) at the position x, over the cross section of the plasma.

The force F acting as a plasma in an electro-magnetic field is given by[2]

$$F=\partial U/\partial x, \tag{2}$$

where U is the magnetic energy of the system as a function of current and position and the derivative is to be evaluated with the current kept constant. For our case $U=(\frac{1}{2})LI^2$ where L is the inductance of the system. Since L is the sum of the coil inductance L_c and the change in inductance ΔL due to the plasma ($L=L_c+\Delta L$), Eq. (2) becomes

$$F=\frac{I^2}{2}\frac{\partial(\Delta L)}{\partial x}. \tag{3}$$

To obtain ΔL we consider for simplicity a sphere of relative permeability K immersed in an initially uniform field **B**, the current I of the system being kept constant. By evaluating the change in energy through the volume of the sphere and comparing it to the variation in energy of the system due to change in inductance we obtain[3]

$$\Delta L=\frac{4\pi a^3}{\mu_0}\frac{K-1}{K+2}\frac{B^2}{I^2}, \tag{4}$$

where a is the radius of the plasma. For an initially uniform field, the field inside the diamagnetic sphere is found to be uniform. It is therefore best, in applying Eq. (4) to initially nonuniform fields to consider only small plasmas so that the field does not vary appreciably over the plasma.

If we calculate the force from Eq. (3) using the field B from Eq. (1) the equation of motion of the plasma is

$$m\ddot{x}=3\pi\mu_0\frac{1-K}{2+K}a^3b^4\frac{x}{(b^2+x^2)^4}I^2, \tag{5}$$

where m is the mass of the plasma.

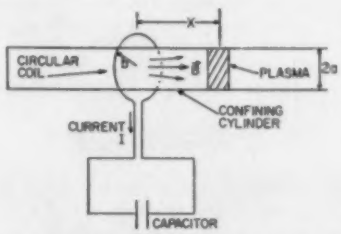

FIG. 1. Schematic diagram of system for plasma propulsion by a magnetic field.

[2] M. Abraham and R. Becker, *Classical Electricity and Magnetism* (Hafner Publishing Company, New York, 1932), p. 162.
[3] W. R. Smythe, *Static and Dynamic Electricity* (McGraw-Hill Book Company, Inc., New York, 1950), 2nd ed., pp. 59 and 322.

The additional necessary relation between the current I and the position x is obtained from energy considerations. The field frequencies relevant to the analysis (10^6-10^7/sec) are considerably lower than those occurring in electromagnetic waves so that the system is quasi-stationary, the field instantaneously distributing itself in space at each instant of time. The law of conservation of energy in its steady state is therefore applicable to our system and we may write

$$\frac{q_0^2-q^2}{2C}=\tfrac{1}{2}L\dot{q}^2+\tfrac{1}{2}m\dot{x}^2, \tag{6}$$

where q and q_0 are the charges on the capacitor at time t and at the initial time $t=0$, and C is the capacitance in farads. Equations (5) and (6) are a coupled set of ordinary nonlinear differential equations in the distance x and charge q. It is convenient at this point to replace the variables x, q, and t by new dimensionless variables $\xi=x/b$, $\rho=q/q_0$, $\tau=\omega t$ so that Eqs. (5) and (6) become

$$\ddot{\xi}=C_2\rho^2\frac{\xi}{(1+\xi^2)^4} \tag{7}$$

$$1-\rho^2=LC\omega^2\alpha^2+(mb^2C\omega^2/q_0^2)\dot{\xi}^2, \tag{8}$$

where

$$C_2=3\pi\mu_0\frac{1-K}{2+K}\frac{a^3}{b^4}\frac{q_0^2}{m}, \tag{9}$$

and a dot now denotes $d/d\tau$. The constant ω may be arbitrarily chosen to make Eq. (8) as simple as possible. We therefore set $\omega=1/(L_0C)^{\frac{1}{2}}$, where L_0 is the inductance at $x=0$, and Eq. (8) becomes

$$1-\rho^2=(L/L_0)\dot{\rho}^2+C_1\dot{\xi}^2, \tag{10}$$

where

$$C_1=mb^2/q_0^2L_0. \tag{11}$$

Except for the slowly varying term L/L_0, Eqs. (7) and (10) exhibit the similarity form of the governing equations of the problem in terms of the similarity constants C_1 and C_2 whose relation to the various physical and geometrical parameters is given by Eqs. (9) and (11). The solution of Eqs. (7) and (10) for a range of values of C_1 and C_2 will therefore give the desired information for a given physical system. Because of the nonlinearity of these equations a numerical method of solution was employed.

Although the equations of motion are not analytically tractable, a useful approximate solution for the maximum velocity of the plasma may be obtained. Calculations indicate that the kinetic energy term in Eq. (10) is small compared to the magnetic energy term. In addition, since L/L_0 is a slowly varying function of ξ, we may, for the purpose of this calculation, take $L/L_0=1$. The charge ρ then varies harmonically with time, $\rho=\cos\tau$ and Eq. (7) becomes[5]

$$\ddot{\xi}=C_2\sin^2\tau\frac{\xi}{(1+\xi^2)^4}. \tag{12}$$

We now assume that $\sin^2\tau$ may be replaced by an average value of $\frac{1}{2}$ so that Eq. (12) may be integrated with respect to ξ to yield a maximum velocity

$$\tfrac{1}{2}\dot{\xi}_{\max}^2=\frac{C_2}{2}\int_0^\infty\frac{\xi d\xi}{(1+\xi^2)^4}=\frac{C_2}{12}, \tag{13}$$

and a maximum kinetic energy

$$\tfrac{1}{2}mv_{\max}^2=\frac{C_2}{12}\frac{mb^2}{L_0C}=\frac{\pi}{2}\frac{1-K}{2+K}\frac{\mu_0}{L_0}\frac{a^3}{b^2}\frac{q_0^2}{2C}, \tag{14}$$

where $v=dx/dt$ is the plasma velocity. We note, from Eq. (14), that the kinetic energy may be increased by increasing the size of the plasma (radius a) and decreasing the coil inductance L_c. The size of the plasma is limited by the size of the coil (radius b) and the inductance L_c is a slowly varying function of coil radius and thickness. Thus, aside from the obvious factor $q_0^2/2C$, the kinetic energy cannot be varied greatly. We also note that the kinetic energy is independent of mass.

We define the coupling efficiency η of the process as the fraction of stored energy $q_0^2/2C$ that is, converted into kinetic energy. We then have, from Eq. (10),

$$\eta=\frac{\mathrm{KE}_{\max}}{q_0^2/2C}=C_1\dot{\xi}_{\max}^2. \tag{15}$$

If we use the approximate value of $\dot{\xi}_{\max}$ in Eq. (13) we obtain

$$\eta\cong\tfrac{1}{6}C_1C_2, \tag{16}$$

showing that the coupling efficiency depends linearly upon C_1 for constant C_2. Since the reactance term $C_1\dot{\xi}_{\max}^2$, which was neglected in deriving Eq. (16) is small so long as C_2 is not large, we expect this equation to be most accurate for small C_2.

2.2 Pressure Method

The calculation of the force acting on a plasma may be simplified by working in terms of the pressure due to an electromagnetic field. Since the diamagnetism of the plasma prevents the magnetic field from penetrating appreciably into the plasma, we may assume that the field acts only on the front side of the plasma, and write for the force F moving the plasma to the right in the x direction

$$F=(B^2/2\mu_0)\pi a^2. \tag{17}$$

The diamagnetic constant K does not appear in Eq. (17) since we have assumed a perfectly diamagnetic sphere ($K=0$) in this approximation. For a diamagnetic sphere immersed in a uniform field $\mathbf{B}_0$, the field $\mathbf{B}$ on the surface

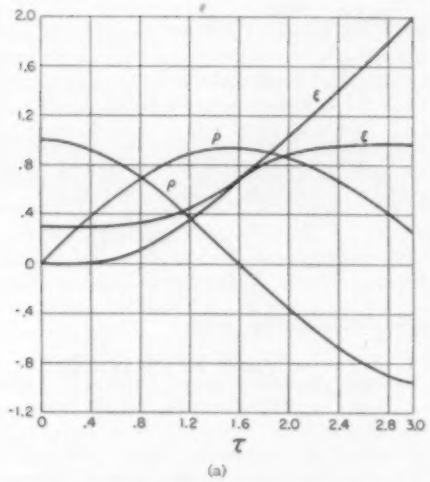

(a)

FIG. 2(a). Variation of ξ, $\dot{\xi}$, ρ, and $\dot{\rho}$, with τ for $C_2=5.0$ and for small damping ($C_1=0$); gradient method.

of the sphere is, on the average, slightly larger than $\mathbf{B}_0$. An integration of the pressure over the front surface of the sphere for this case yields a result similar to Eq. (17), but with a correction factor of 9/8. Since, the correction factor, although difficult to obtain for a non-uniform field, is evidently not too different from unity and may be incorporated in the similarity constant of the equation of motion we shall use Eq. (17) and take for the magnitude of the field B the value given by Eq. (1). The equation of motion of the plasma is then

$$m\ddot{x}=-\frac{\pi}{8}\mu_0\frac{a^2b^4}{(b^2+x^2)^3}I^2, \tag{18}$$

which has the dimensionless form

$$\ddot{\xi}=C_2'\frac{\dot{\rho}^2}{(1+\xi^2)^3}, \tag{19}$$

where

$$C_2'=-\frac{\pi}{8}\mu_0\frac{a^2}{b^3}\frac{q_0^2}{m}. \tag{20}$$

The energy equation is unaffected by this approximation and is given, as in the gradient method, by Eq. (10).

To obtain approximate expressions for the maximum velocity and kinetic energy we proceed in the same manner as that employed in the gradient method to obtain

$$\tfrac{1}{2}\dot{\xi}_{\max}^2=\frac{C_2'}{2}\int_0^\infty\frac{d\xi}{(1+\xi^2)^3}=\frac{3\pi}{32}C_2' \tag{21}$$

$$\tfrac{1}{2}mv_{\max}^2=\frac{3\pi}{32}C_2'\frac{mb^2}{L_0C}=\frac{3\pi^2}{128}\frac{\mu_0}{L_0}\frac{a^2}{b}\frac{q_0^2}{2C} \tag{22}$$

$$\eta\cong\frac{3\pi}{16}C_1C_2'. \tag{23}$$

2.3 Comparison of the Two Methods

The determination of the force acting on a plasma by the gradient method (Sec. 2.1) makes use of the change in inductance of a system with an initial uniform field, due to the presence of the plasma. Since a circular coil has a far from uniform field, the gradient method will be most accurate when the plasma is small compared to the coil. The pressure method, on the other hand, assumes that the field suffers a large decrease in going from the front to the rear of the plasma, and is therefore more appropriate for a plasma not too small compared to the coil.

An estimate of the comparative efficiences by the two methods may easily be obtained by use of the approximate equations for the efficiency. By setting $K=0$ and comparing Eqs. (16) and (23) we obtain

$$\eta_{\text{grad}}/\eta_{\text{press}}\cong(32/3\pi)a/b, \tag{24}$$

a result which shown that the gradient method will, in general, yield higher efficiencies (and velocities) unless the coil radius b is at least about 3.5 times the plasma radius a.

2.4 Method of Calculation

The equations of motion corresponding to the gradient method [Eqs. (7) and (10)] and those corresponding to the pressure method [Eqs. (10) and (19)] were integrated numerically for several values of the similarity constants. Because of the variable inductance term L/L_0, which depends explicitly upon the plasma and coil geometry, Eq. (10) is not in similarity form. Since L/L_0 is a slowly varying term and changes only by about 15% for the entire motion of the plasma, it will have very little effect upon the similarity solution. We have therefore evaluated L/L_0 for the case discussed in the illustrative example section and used these values in constructing our similarity solutions.

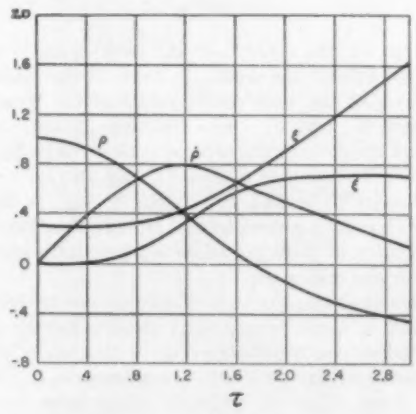

(b)

FIG. 2(b). Variation of ξ, $\dot{\xi}$, ρ, and $\dot{\rho}$ with τ for $C_2=5.0$ and for large damping ($C_1=1.5$); gradient method.

Starting values for small τ were obtained by noting that, since ξ is small in this region, the reactance term $C_1\xi^2$ is negligible so that the harmonic solutions for ρ and $\dot{\rho}$ are valid. In addition, since ξ is also negligible for small τ, simple analytic solutions were obtainable for $\ddot{\xi}$ and $\dot{\xi}$. For larger values of τ subsequent values of $\ddot{\xi}$ were obtained by converting the force equation for $\ddot{\xi}$ into a difference equation; the corresponding values of $\dot{\xi}$ were then obtained from the increments in $\ddot{\xi}$. The succeeding values of $\dot{\rho}$ were obtained from the energy equation and the corresponding values of ρ by numerical integration.

For the pressure method case, since the space function in Eq. (19) has a maximum at $\xi=0$, the optimum increase in kinetic energy occurs when the plasma is placed next to the coil ($\xi=0$) at $t=0$. For the gradient method, since the space function in Eq. (7) is zero at $\xi=0$, the kinetic energy increases very little if the plasma is placed close to the coil at the beginning of the

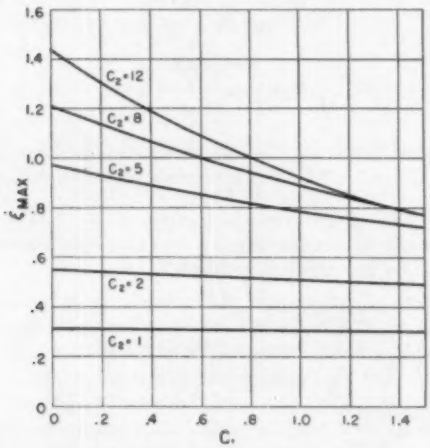

FIG. 3. Maximum velocity $\dot{\xi}_{max}$ as a function of C_1 for several values of C_2; gradient method.

acceleration. Trial calculations indicated that the increase in kinetic energy had a maximum near $\xi=0.3$, but varied very little in the range $\xi=0.2$ to 0.4, and dropped sharply outside this interval. The value $\xi_0=0.3$ was therefore chosen for the initial position of the plasma.

2.5 Results

Some typical results obtained by the gradient method are presented in Fig. 2 where we have plotted position, velocity, charge, and current as a function of time for a given value of C_2 and for several values of C_1. The curves show the typical rapid rise in $\dot{\xi}$ for small τ and the gradual bending over and approach to an asymptotic value at the distance ξ becomes large. The variations in ρ and $\dot{\rho}$ are almost but not quite harmonic (because of the variation in the inductance) for the value $C_1=0$; for

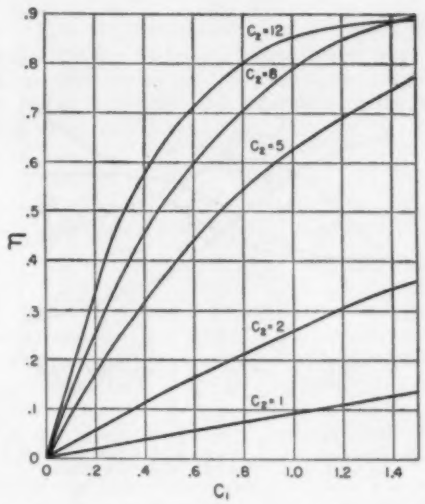

FIG. 4. Efficiency η as a function of C_1 for several values of C_2; gradient method.

the larger value of 1.5, the damping effect of the reactance term $C_1\xi^2$ is very marked.

The explicit variation of $\dot{\xi}_{max}$ with C_1 is presented in Fig. 3 where we have plotted $\dot{\xi}_{max}$ as a function of C_1 with C_2 as parameter. The curves are practically horizontal for small C_2 but start to decrease rapidly for large C_2; for sufficiently large C_2 and C_1 the damping effect becomes large enough to yield lower values of $\dot{\xi}_{max}$ for higher values of C_2. The increased damping for large C_2 may be anticipated from the almost direct dependence of $\dot{\xi}_{max}$ upon C_2 for small C_1 [see Eq. (13)]. The efficiency curves are presented in Fig. 4 as a function of C_1 with C_2 as parameter. The curves are linear

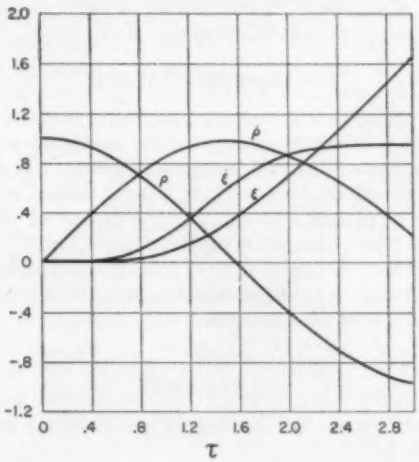

(a)

FIG. 5(a). Variation of ξ, $\dot{\xi}$, ρ, and $\dot{\rho}$, with τ for $C_2'=1.0$ and for small damping ($C_1=0$); pressure method.

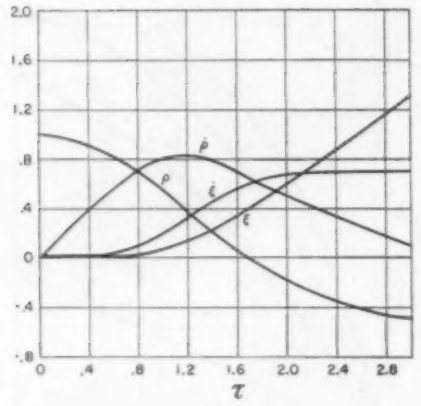

(b)

FIG. 5(b). Variation of ξ, $\dot{\xi}$, ρ, and $\dot{\rho}$, with τ for $C_2'=1.0$ and for large damping ($C_1=1.5$); pressure method.

for small C_2 and start to bend over as C_2 increases; these results may be expected from the discussion for the $\dot{\xi}_{max}$ curves and the relation $\eta=C_1\dot{\xi}_{max}^2$.

The corresponding results obtained by the pressure method are presented in Figs. 5 through 7. The typical results for ρ, $\dot{\rho}$, ξ, and $\dot{\xi}$ in Fig. 5 exhibit the same general dependence of ξ and $\dot{\xi}$ upon τ and the damping effect of large C_1 upon ρ and $\dot{\rho}$ as shown for the gradient method in Fig. 2. The maximum velocity and efficiency curves given in Figs. 6 and 7 show the same general form and effect of damping as do the corresponding curves for the gradient method (Figs. 3 and 4) but the effects become evident at values of C_2' considerably lower than the corresponding values of C_2. This result is to be expected since a given value of C_2 is much larger than the corresponding value of C_2' (see definitions of C_2 and C_2'), and will be brought out in the illustrative example following this discussion.

2.6 Illustrative Example

To show the use of the maximum velocity and efficiency curves in solving for the motion of a given plasma we consider the following example: coil radius $b=5$ cm; coil thickness $r=1$ cm; plasma radius $a=3$ cm; length of plasma $l=3$ cm; particle density of plasma $N=10^{16}/\text{cm}^3$; charge on capacitor $q_0=1.5\times10^{-2}$ coul; capacitance of capacitor $C=1.5$ μf. If we consider the plasma as made up of protons of mass $m_a=1.67\times10^{-24}$ g, the mass m of the plasma is

$$m=\pi a^2 l N m_a$$
$$=1.41\times10^{-9}\text{Kg}.$$

The inductance of the coil in the presence of the plasma is

$$L=L_c\left(1+\frac{\Delta L}{L_c}\right),$$

where

$$\Delta L=-\frac{\pi}{2}\mu_0\frac{a^2b^4}{(b^2+x^2)^3}$$

$$L_c=\mu_0 b\left(\ln\frac{8b}{r}-\frac{7}{4}\right).$$

On substituting numerical values we obtain

$$L_c=1.22\times10^{-7}\text{ henries}$$

$$L=L_c\left(1-\frac{0.175}{(1+\xi^2)^3}\right)$$

$$L_0=1.01\times10^{-7}\text{ henries}.$$

The similarity constants then have the values

$$C_1=\frac{mb^2}{q_0^2L_0}=0.155$$

$$C_2=\frac{3}{2}\pi\mu_0\frac{a^2}{b^4}\frac{q_0^2}{m}=3.38$$

$$C_2'=\frac{\pi}{8}\mu_0\frac{a^2}{b^3}\frac{q_0^2}{m}=0.47.$$

From the maximum velocity and efficiency curves we obtain by the gradient method

$$\dot{\xi}_{max}=0.74$$
$$v_{max}=b\omega\dot{\xi}_{max}=0.95\times10^7\text{ cm/sec}$$
$$\eta=0.085,$$

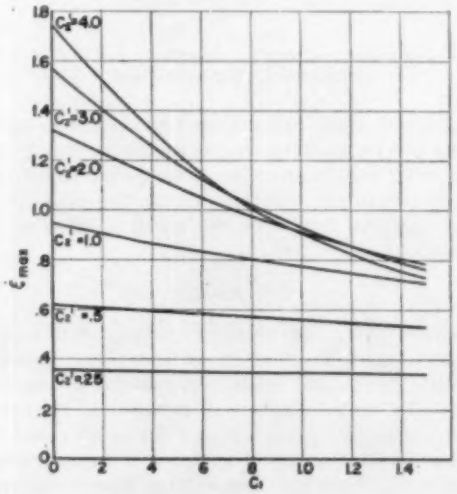

FIG. 6. Maximum velocity curve, $\dot{\xi}_{max}$ as a function of C_1 for several values of C_2'; pressure method.

and by the pressure method

$$\xi_{max}=0.58$$
$$v_{max}=0.75\times10^7 \text{ cm/sec}$$
$$\eta=0.050.$$

The values of ξ_{max} and η obtained by the gradient method are higher than those by the pressure method, a result to be expected here since the plasma radius is not much smaller than the coil radius (see comparison of efficiencies in Sec. 2.3). In view of the large plasma radius, the results by the pressure method are probably more accurate. It is also worth noting here that, because of the small value of C_1, the approximate formulae for the maximum velocity and efficiency should give fairly good results for this case. For example, for the efficiency we have by the gradient method, Eq. (16)

$$\eta\cong\tfrac{1}{8}C_1C_2=0.087,$$

and by the pressure method, Eq. (23)

$$\eta\cong\frac{3\pi}{16}C_1C_2'=0.042,$$

results which indicate the validity of the approximate formulas for small values of C_1.

3. NONDIAMAGNETIC CASE

3.1 Plasma Ionization

We no longer assume that the plasma is completely diamagnetic and consider the ionization process in detail in obtaining the motion of the plasma. We determine first how the energy from a magnetic field B, which is changing at the rate $\dot{B}$, goes into heating of electrons before ionization occurs. An electron moves in a circular orbit under the action of the magnetic field and gains energy by betratron action from the induced electric field. If we assume that the energy gained in one revolution is small so that the radius of the orbit may be considered constant we have, from Faraday's law

$$\Delta E=e\pi r^2\dot{B}, \tag{24}$$

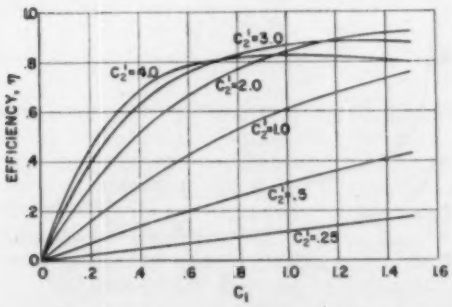

FIG. 7. Efficiency curves as a function of C_1 for several values of C_2'; pressure method.

where ΔE is the increase in energy per orbit, e is the magnitude of the electronic charge, and we have taken $\dot{B}$ as constant. For an electron of mass m_e and velocity v moving in a circular orbit the radius of the path is related to the field B by

$$v/r=eB/m_e. \tag{25}$$

Since the time required to complete an orbit is $\Delta t=2\pi(r/v)$, we have, from Eqs. (24) and (25),

$$\dot{E}/E=\dot{B}/B, \tag{26}$$

where we have taken E as the kinetic energy of the electron and set $\dot{E}=(\Delta E/\Delta t)$. This result gives the relation between the magnetic field and the electron energy when the field energy goes solely into heating of electrons.

We now consider the more general case in which electrons are gaining energy from the magnetic field and losing energy by collisions and ionization. The fraction of energy of an electron transferred to a neutral atom of mass m_a in an elastic collision is $2(m_e/m_a)(1-\cos\theta)$, where θ is the angle of scattering. We shall assume a uniform scattering distribution so that $2(m_e/m_a)$ is the fraction of energy lost per collision.[4] The number of collisions per sec is $\bar{v}/\lambda_e$, where $\bar{v}$ and λ_e are the average velocity and collision mean free path of the electron. The rate of transfer of energy by collisions is then

$$(dE/dt)_{coll}=2(m_e/m_a)n\bar{E}(\bar{v}/\lambda_c), \tag{27}$$

where n is the electron density and $\bar{E}$ is the mean energy of the electrons. In the same manner the rate of transfer of energy by ionization is

$$(dE/dt)_{ion}=n_i(\bar{v}_i/\lambda_i)(\Delta E)_i, \tag{28}$$

where n_i and $\bar{v}_i$ are the density and average velocity of the ionizing electrons, λ_i is the mean free path for ionization and $(\Delta E)_i$ is the energy transferred during an ionizing collision. In order to utilize Eq. (28) we need the fraction of ionizing electrons n_i/n as a function of the electron temperature. Because of the high frequency of collisions with each other the electrons are always close to a Maxwellian distribution and we may write

$$n_i/n=\int_{E_i}^{\infty}e^{-E/\theta}E^{\frac{1}{2}}dE\Big/\int_0^{\infty}e^{-E/\theta}E^{\frac{1}{2}}dE, \tag{29}$$

where $\theta=kT$ is the modulus for a Boltzmann distribution, k is the Boltzmann constant, and E_i is the energy required to ionize an atom. The integral in the numerator of Eq. (29) may be evaluated approximately by noting that, since $E_i\gg\theta$, the principal contribution to the integral comes from the region $E\cong E_i$. We may then replace $E^{\frac{1}{2}}$ by $E_i^{\frac{1}{2}}$ in which case the integral is

[4] H. Massey and E. Burhop, *Electronic and Ionic Impact Phenomenon* (Oxford University Press, London, England, 1952), pp. 14–15.

elementary and Eq. (29) takes the form

$$\frac{n_i}{n}=\frac{2}{\pi^{\frac{1}{2}}}\beta^{\frac{1}{2}}e^{-\beta}, \tag{30}$$

where $\beta=E_i/\theta$. Since the energy supplied per particle by the magnetic field is $(\dot{B}/B)\bar{E}$ conservation of energy gives

$$\frac{\dot{B}}{B}\bar{E}=2\frac{m_e}{m_a}\bar{E}\frac{\bar{v}}{\lambda_e}+(\Delta E)_i\frac{\bar{v}_i}{\lambda_i}+\frac{d\bar{E}}{dt}, \tag{31}$$

where the last term represents the heating of electrons. In addition, the equation for the rate of electron production by ionization is, by particle conservation,

$$dn/dt=n_i(\bar{v}_i/\lambda_i). \tag{32}$$

We now simplify Eqs. (31) and (32) by assuming that $(\Delta E)_i$ may be replaced by the ionization energy E_i; λ_e depends only on the density of neutrals in the undisturbed gas N_0, and λ_i only on the neutral density in the current sheath N. We shall assume, in our approximation, that the cross sections for collision and ionization σ_e and σ_i are constant and equal to each other. By making use of Eq. (30) and of $\lambda_e=1/N_0\sigma_e$, $\lambda_i=1/N\sigma_i$, we can write Eqs. (31) and (32) in the form

$$\frac{1}{B}\frac{dB}{dt}=\alpha\left(\frac{3\pi}{2}\right)^{\frac{1}{2}}\frac{m_e}{m_a}\beta^{-\frac{1}{2}}+\frac{2}{3}\alpha\beta^{\frac{1}{2}}e^{-\beta}-\frac{1}{\beta}\frac{d\beta}{dt} \tag{33}$$

$$\frac{1}{n}\frac{dn}{dt}=\alpha\beta^{-\frac{1}{2}}e^{-\beta}\frac{N}{N_0}, \tag{34}$$

where $\alpha=(2/\pi^{\frac{1}{2}})(\bar{v}_i/\lambda_c)$ and we have used $(\bar{E}=3\theta/2.)$ The collision term is, in general, small compared to the other terms and will be neglected here.

Approximate solutions to these equations may be obtained for the case of rapid field variation. At the beginning of the process, since the electrons are fairly cool ($\beta\gg1$), they transfer ionization energy slowly and the ionization term in Eq. (33) may be dropped. During this period β drops (as $\bar{E}$ rises) and Eq. (33) becomes

$$\frac{1}{B}\frac{dB}{dt}=-\frac{1}{\beta}\frac{d\beta}{dt}, \tag{35}$$

while Eq. (34) reduces to $dn/dt=0$. Equation (35) is, of course, the same as Eq. (26) where only heating of electrons is considered. As the temperature rises, the rate of ionization increases rapidly and the temperature begins to level off as the neutral gas ionizes. During this ionization period we may neglect the heating term in comparison with the ionization term, and our equations become

$$\frac{1}{B}\frac{dB}{dt}=\frac{2}{3}\alpha\beta^{\frac{1}{2}}e^{-\beta}\frac{N}{N_0} \tag{36}$$

$$\frac{1}{n}\frac{dn}{dt}=\alpha\beta^{\frac{1}{2}}e^{-\beta}\frac{N}{N_0}. \tag{37}$$

We may combine Eqs. (36) and (37) to express dn/dt directly in terms of B by

$$\frac{1}{n}\frac{dn}{dt}=\frac{3}{2\beta}\frac{1}{B}\frac{dB}{dt}. \tag{38}$$

As a typical example, we take the ionization energy $E_i=10$ ev; the corresponding electron ionization velocity $\bar{v}_i=1.88\times10^8$ cm/sec. For a density $N_0=10^{17}$ atoms/cc and collision cross section $\sigma_c=10^{-16}$ cm^2, the collision mean free path $\lambda_i=0.1$ cm and the parameter $\alpha=2.12\times10^9$/sec. The solution to Eq. (36) for the mean electron energy at the start of ionization $\bar{E}_1=(3/2\beta_1)E_i$, is given in Fig. 8 as a function of neutral density for several rates of rise of the magnetic field. The mean electron energy rises slowly with increasing $(1/B)(dB/dt)$ and decreasing N/N_0, except for low values of the neutral density.

3.2 Early Stage Ionization and Heating

We now consider in detail the process of early stage heating and ionization. At early stages of the acceleration the motion of the plasma is small and we can solve for the increase in electron density neglecting the motion of the plasma. We will also neglect the space variation of the magnetic field since we are restricting ourselves to regions near the point of gas injection where the plasma is formed. The electrons will not absorb energy from the magnetic field by betatron action until the Larmor radius becomes of the same order or smaller than the mean free path. The heating of electrons will therefore start at the value B_0 given by

$$B_0=m_e v_0/e\lambda_c, \tag{39}$$

where v_0 is the initial electron velocity, taken here as the average of the thermal velocity distribution. We shall assume that, for the early stage heating, the magnetic

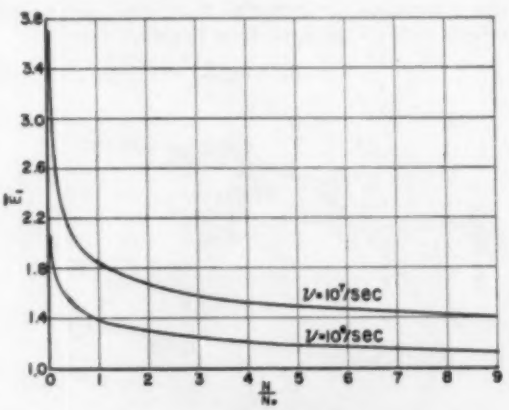

FIG. 8. Mean electron temperature $\bar{E}_1$ as a function of neutral density N/N_0 for several frequencies.

field rises linearly with time, and may therefore write

$$B/B_m = t/t_m, \tag{40}$$

where t_m is the characteristic rise time for the field and B_m is the maximum value attained by the field. The time at which heating starts t_0 is therefore obtained by using for B_0 in Eq. (40) the value given in Eq. (39) to yield

$$t_0 = \frac{m_e v_0}{e\lambda_c}\frac{t_m}{B_m} = \frac{1}{e\lambda_c}(3m_e kT_0)^{\frac{1}{2}}\frac{t_m}{B_m}. \tag{41}$$

For $t > t_0$, electrons gain energy from the magnetic field until ionization sets in, after which the energy from the field goes into production of additional electrons. To determine the electron density during ionization we first obtain the time t_1 which separates the heating and ionization regions. During the heating period the temperature-time relation is, from Eqs. (26), (40), and (41)

$$t = t_0\frac{\beta_0}{\beta} = \frac{E_i}{e\lambda_c}\left(\frac{3m_e}{kT_0}\right)^{\frac{1}{2}}\frac{t_m}{B_m}\frac{1}{\beta}, \tag{42}$$

while the ionization period relation is, from Eqs. (26) and (36),

$$\frac{1}{t}\frac{2}{3} = -\alpha\beta^{\frac{1}{2}}e^{-\beta}, \tag{43}$$

in which, since the fraction ionized is assumed small, we have set $N/N_0 = 1$. The time t_1 and the corresponding temperature β_1 are then obtained by solving Eqs. (42) and (43) simultaneously at the common time t_1. The electron density during the ionization period is now obtained by integrating Eq. (38) with $(1/B)(dB/dt) = (1/t)$. We obtain an approximate integral of this equation by first expressing β in terms of t by Eq. (43), and Eq. (38) becomes

$$\frac{1}{n}\frac{dn}{dt} = \frac{3}{2}\frac{1}{t\ln(\gamma t)}, \tag{44}$$

where $\gamma = \frac{2}{3}\alpha\beta^{\frac{1}{2}}$. We may now integrate Eq. (44) approximately by neglecting the slow variation inside the logarithm to obtain

$$\frac{n}{n_1} = \left(\frac{\ln\gamma t}{\ln\gamma t_1}\right)^{\frac{3}{2}}, \tag{45}$$

where n_1 is the electron density at the beginning of ionization. In view of the derivation, the value of γ used is the average in the interval. The results obtained with this equation are valid only if the fraction ionized remains considerably less than unity. The maximum growth in electron density is seen to occur, from Eq. (45), when the time of ionization t_1 is a minimum; the corresponding value of β_1 is, from Eq. (43), $\beta_1 = 1.5$. As a typical example we take $E_i = 10$ ev, $t_m = 10^{-6}$ sec, and $\alpha = 2.12\times 10^9$/sec. A plot of n/n_1 as a function of time

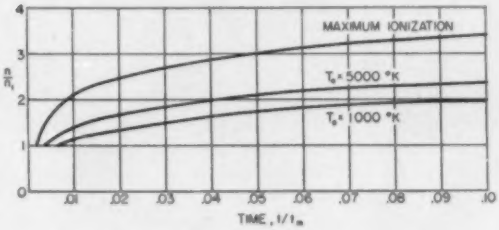

FIG. 9. Growth in electron density n/n_1 during early ionization period.

during the early ionization period is given in Fig. 9 for electron energies corresponding to $T_0 = 1000°$ and 5000°K and a field strength $B_m = 5\times 10^4$ gauss, and in addition, for the case of maximum growth of electron density. The electron density rises rapidly at first and then starts to level off; the results show only a mild dependence upon the initial electron energy and the curve for maximum growth in electron density is not significantly above those corresponding to the other cases. The possibilities of efficient preionization by rapidly varying magnetic fields appear therefore to be quite limited.

3.3 Sheath Formation

As the magnetic field rises and ionization begins, the high conductivity of the partially ionized plasma will prevent the magnetic field from penetrating into the plasma interior and a current sheath will form. We shall make the rough approximation that the depth d to which the magnetic field penetrates is the same as the skin-depth of a conductor acted on by an oscillating field and given by[5]

$$d = \left(\frac{\eta}{2\pi\omega}\right)^{\frac{1}{2}}, \tag{46}$$

where η is the resistivity in emu and ω is the angular frequency of the field. For an ionized gas the resistivity is[6]

$$\eta = 6.53\times 10^{12}\frac{\ln\Lambda}{T^{\frac{3}{2}}}\text{ emu}, \tag{47}$$

where $\ln\Lambda$ is a slowly varying function of temperature and density. The skin-depth may therefore be written as

$$d = \frac{4.07\times 10^5}{T^{\frac{3}{4}}}\left(\frac{\ln\Lambda}{\nu}\right)^{\frac{1}{2}}, \tag{48}$$

where ν is the frequency in reciprocal seconds. For a typical case with $T = 10^4$ °K, $\nu = 10^6$/sec, and $\ln\Lambda = 10$, d = 1.30 cm.

[5] L. Spitzer, Jr., *Physics of Fully Ionized Gases* (Interscience Publishers, Inc., New York, 1956), Chap. 4, p. 52.

[6] L. Spitzer, Jr., *Physics of Fully Ionized Gases* (Interscience Publishers, Inc., New York, 1956), Chap. 5, p. 84.

3.4 Snow Plow Model of Acceleration

As ionization begins, the current sheath which forms on the surface of the plasma is accelerated forward into the neutral gas by the magnetic field pressure.[7] During this process conditions inside the sheath will change as neutral material is picked up, ionized, and partially lost by diffusion through the rear of the sheath. We now analyze this process in detail.

We utilize here the pressure method for obtaining the force on the plasma [see Eq. (16)]; the equation of motion for the sheath is, accordingly,

$$\frac{d}{dt}\left(M_A\frac{dx}{dt}\right)=\frac{B^2}{2\mu_0}, \tag{49}$$

where M_A is the mass per unit area inside the sheath. The value of M_A is determined by the amount of neutral material picked up by the moving sheath and by the loss of neutral material by diffusion, through the rear of the sheath. We thus have,

$$M_A=m_aN_0\int_0^t vdt-m_a\int_0^t Fdt, \tag{50}$$

where F is the flux of neutrals out of the sheath and $v=dx/dt$ is the sheath velocity. For the neutral flux F we use the standard formula for the flux of molecules with a Maxwellian distribution past a plane area,

$$F=(D/4)N\bar{v}_N, \tag{51}$$

where $\bar{v}_N$ is the mean thermal velocity of the neutrals inside the sheath and D is a diffusion factor to account for the decrease, by the diffusion process, in the density of neutrals in the rear of the sheath. The neutral density N is governed by the influx of neutrals, the loss by diffusion of neutrals and the rate of ionization of neutrals and may therefore be obtained from the rate equation

$$\frac{dN}{dt}=\left(\frac{dN}{dt}\right)_{\text{influx}}+\left(\frac{dN}{dt}\right)_{\text{loss}}+\left(\frac{dN}{dt}\right)_{\text{ion}}. \tag{52}$$

To determine the influx and loss terms we assume that the incoming particles and the material diffusing out are distributed uniformly over a depth d and may therefore write

$$\left.\begin{aligned}\left(\frac{dN}{dt}\right)_{\text{influx}}&=\frac{1}{d}N_0\bar{v}\\ \left(\frac{dN}{dt}\right)_{\text{loss}}&=-\frac{F}{d}\end{aligned}\right\}. \tag{53}$$

The ionization rate is the same as the rate at which electrons are produced [see Eq. (38)] and Eq. (52) may therefore be expressed as

$$\frac{dN}{dt}=\frac{N_0\bar{v}}{d}-\frac{F}{d}-\frac{3}{2\beta}\frac{1}{B}\frac{dB}{dt}. \tag{54}$$

The thermal velocity for neutrals $\bar{v}_N$ needed in the calculations of the neutral flux F may be obtained by consideration of the energy balance for neutrals. The incoming neutrals, as they are picked up by the sheath, deposit a quickly thermalized kinetic energy per particle of amount $(\frac{1}{2})m_av^2$. The incoming energy flux and the energy flux due to loss of neutrals are then, from Eq. (53)

$$\tfrac{1}{2}m_av^2\left(\frac{dN}{dt}\right)_{\text{influx}}=\tfrac{1}{2}m_av^2\frac{N_0}{d}, \tag{55}$$

$$\bar{E}_N\left(\frac{dN}{dt}\right)_{\text{loss}}=-\bar{E}_N\frac{F}{d}, \tag{56}$$

where $\bar{E}_N$ is the mean thermal energy of the heavy particles in the sheath. The collisions with fast electrons inside the sheath also heats the neutrals, but this is a small effect compared with the rate of energy influx, Eq. (55). The net energy input thus goes into heating the neutrals in the sheath together with the ions already formed, the heavy particles all thermalizing quickly to the same temperature. The mean thermal energy $\bar{E}_N$ is therefore determined from the energy balance

$$\frac{d}{dt}(N_t\bar{E}_N)=\frac{N_0\bar{v}}{d}\tfrac{1}{2}m_av^2-\bar{E}_N\frac{F}{d}, \tag{57}$$

where N_t is the total number of neutrals and ions in the sheath. The number N_t is determined from Eq. (52) with the ionization term missing, i.e.,

$$\frac{d}{dt}N_t=\frac{N_0}{d}\bar{v}-\frac{F}{d}. \tag{58}$$

If we expand the left-hand side of Eq. (57) and make use of Eq. (58) we obtain the somewhat simpler equation for determining $\bar{E}_N$

$$N_t\frac{d}{dt}\bar{E}_N=\bar{v}\frac{N_0}{d}\left(\frac{m_a}{2}v^2-\bar{E}_N\right), \tag{59}$$

a result more readily obtained if we note that the left side is the rate of change of energy of all the heavy particles inside the sheath while the right side gives the net rate at which energy enters the sheath.

In the derivation of Eq. (59) we have not considered the possible ionization of the neutrals inside the sheath by the neutrals entering the sheath. Since the energy of these entering heavy particles exceeds the binding energy of the neutrals inside the sheath over a considerable range of the plasma motion, the ionization process

[7] M. Rosenbluth, *Magnetohydrodynamics*, edited by Rolf Landshoff (Stanford University Press, Stanford, California, 1957), "Dynamics of a pinched gas," Sec. 1, p. 57.

should not be neglected. Since we are principally interested in how the overall efficiency of the process is affected by not making the assumption of a completely diamagnetic plasma, and in view of the additional complications introduced by consideration of the ionization process, we have, instead, made two limiting calculations. In one of these we assume that no ionization takes place so that leakage of neutrals occurs as described in the foregoing discussion. In the other calculation we assume that the ionization of neutrals is complete so that the current sheath is completely diamagnetic and no leakage of neutrals occurs. The results for these two limiting calculations will be presented later.

In the foregoing we have also ignored the effect of the shock wave which will be produced by the disturbance emanating from the front of the sheath. Because of the extremely high velocities of the sheath front, the shock would not recede from the sheath so that the complications of shock reflection from the end of the gas may be ignored. The shock would therefore, at most, partially ionize and increase the temperature of the gas entering the sheath. Since this effect would tend to make the gas more diamagnetic and would be covered by our limiting calculations, we have omitted consideration of the shock wave in our calculations.

3.5 Final Form of Equations of Motion

To summarize the results of Sec. 3 we collect the relevant equations and express them in convenient dimensionless form. As in the diamagnetic case we measure the time in units of $\tau=\omega t$, where $\omega=1/(L_0C)^{\frac{1}{2}}$ is the natural frequency of the external circuit; the distance is measured as a fraction of the coil radius b by $\xi=x/b$. The electron and neutral concentrations are defined by, $s=n/N_0$, $y=N/N_0$. From the results for the diamagnetic case we have seen that only a small part of the energy from the magnetic field goes into kinetic energy of the plasma. Because of the complexity of the analysis for the nondiamagnetic case we have assumed, for simplicity, that the harmonic solutions for charge, current and field, although strictly valid only for the plasma free case, may be used here. We have, in addition, used the simplified pressure method for determing the equation of motion of the plasma and have neglected the small variation of inductance due to the presence of the plasma. The governing equations are then the following:

Equation of motion

$$\frac{d}{d\tau}(M\dot{\xi})=C_3\frac{\sin^2\tau}{(1+\xi^2)^3}, \tag{60}$$

where

$$M=\frac{M_A}{m_aN_0b}=\xi-\frac{D}{4}\int_0^\tau y\dot{\xi}_N d\tau \tag{61}$$

$$C_3=\frac{\mu_0q_0^2}{8m_aN_0b^4}, \tag{62}$$

and $\dot{\xi}_N$ is the thermal velocity of the neutrals.

Production of electrons

$$\frac{1}{s}\frac{ds}{d\tau}=\frac{3}{2\beta}\cot\tau. \tag{63}$$

Production of neutrals

$$\frac{dy}{d\tau}=\frac{3s}{2\beta}\cot\tau+\frac{b}{d}\left(\dot{\xi}-\frac{D}{4}y\dot{\xi}_N\right). \tag{64}$$

Electron temperature

$$\beta^{\frac{1}{2}}e^{-\beta}=\frac{3\omega}{2\alpha}\frac{\cot\tau}{y}. \tag{65}$$

Skin depth

$$d=206\frac{\beta^{\frac{1}{2}}}{\nu^{\frac{1}{2}}}, \tag{66}$$

where we have taken $\ln\Lambda$ [Eq. (47)] as constant and used 10 as an average value.

Thermal velocity of neutrals inside the sheath

$$d/d\tau(\xi_N^2)=(\xi/M)(\xi^2-\xi_N^2). \tag{67}$$

By making use of Eq. (61) for M and an integration by parts, Eq. (67) may be expressed in the more convenient form for calculation

$$\xi_N^2=\frac{1}{M}\int_0^\tau\left(\xi^2-y\frac{D}{4}\xi_N^2\right)d\tau. \tag{68}$$

3.6 Method of Calculation

For convenience, the calculations were started at $\tau=0.1$, the earlier values being readily obtainable from the equations developed for the early ionization period (Sec. 3.2). For small values of τ the plasma and thermal velocities are linear in τ allowing one to calculate the first few values directly. The electron temperature β and skin depth d were determined from Eqs. (65) and (66). The rate of production of electrons $ds/d\tau$ and the rate of production of neutrals $dy/d\tau$ were next obtained from Eqs. (63) and (64). The values of s and y were then integrated out to the next value of τ by linear formulas, using the values of the derivatives at the midpoint of the interval. For higher values of τ, where the linear approximation was no longer applicable, the velocities $\dot{\xi}$ and $\dot{\xi}_N$ were obtained by numerical integration of Eqs. (60) and (68). The diffusion factor D in Eq. (51) may, in principle, be obtained by solving the steady-state diffusion equation for the distribution of neutrals inside the sheath. To simplify the calculation we have, instead, assumed an average value of D.

Because of the complexity of the calculations for the nondiamagnetic case, a systematic series of calculations similar to those obtained for the diamagnetic case have not proved feasible here. Instead we have made a calculation of the motion of the plasma for typical values of the physical and geometrical parameters of

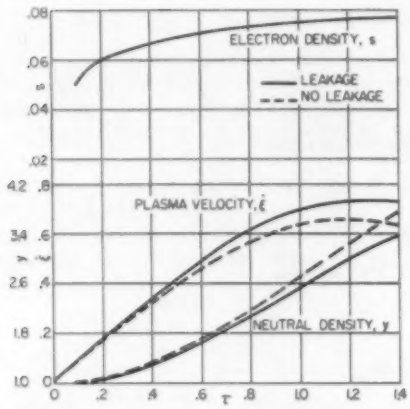

FIG. 10. Electron density s, neutral density y, and plasma velocity ξ as functions of time τ for leakage and no leakage.

the system to give an indication of the differences to be expected for the diamagnetic and nondiamagnetic cases. The values chosen were coil radius $b=5$ cm; coil thickness $r=1$ cm; plasma radius $a=3$ cm; similarity constant $C_3=1.0$; diffusion factor $D=0.5$; constant $\alpha=2.12\times10^9$/sec; magnetic field frequency $\nu=10^6$/sec; ionization energy $E_i=10$ ev; initial electron concentration $s_0=0.05$. As indicated previously the calculations were made for both leakage and no leakage of neutrals from the rear of the sheath.

3.7 Results

The results obtained for the nondiamagnetic case are presented in Fig. 10 where we have plotted electron density s, neutral density y and sheath velocity ξ as functions of time τ. The electron density rises rapidly at first and then slows down to a practically constant value. The distinction between leakage and no leakage is negligible with regard to electron density. The sheath velocity increases linearly for small τ and then starts to bend over due to the mass picked up by the plasma. The velocity curve for the no leakage case is, of course, below that for the leakage case because of the greater rate of increase in mass of the plasma. The neutral density y rises rapidly at first and then slows down to an almost constant rise as the plasma acceleration decreases. The no leakage case gives higher values of y than does the leakage case despite the lower corresponding plasma velocity, a result to be expected since the decrease in sheath velocity for no leakage is a secondary effect due to the increased mass picked up by the plasma.

If the sheath continues to move forward into the neutral gas its velocity will reach a maximum and then start to decrease. Since the kinetic energy of the plasma depends upon the square of the velocity is desirable to cutoff the neutral gas near the point of maximum velocity and allow the plasma to finish its acceleration without influx of neutral gas. A calculation has been made, therefore, of the final motion of the plasma for a neutral gas cutoff at $\tau=1.2$. The results give $\xi_{max}=1.11$ for the leakage case and 1.03 for no leakage. The corresponding efficiencies are almost the same and slightly under 4%. The efficiency for the corresponding diamagnetic case is about 7%. We thus see that the assumption that the plasma is completely diamagnetic will yield efficiencies which are slightly too high. Therefore, the results for both the diamagnetic and nondiamagnetic plasmas indicate that for a plasma driven by a magnetic field from a stationary coil, the fraction of electromagnetic energy converted into kinetic energy of the plasma may be too low for practical applications.

ACKNOWLEDGMENTS

We wish to express our appreciation to Dr. Howard Greyber for many stimulating and informative discussions, and to Miss Janice Furey for her competent help in carrying out the required computations.

Parametric Amplifier Theory for Plasmas and Electron Beams*

G. S. KINO
Microwave Laboratory, W. W. Hansen Laboratories of Physics, Stanford University, Stanford, California
(Received February 4, 1960; and in final form May 6, 1960)

A theory is given for a new type of parametric amplifier which uses a gas discharge plasma as a nonlinear propagating medium. This theory is based on a zero-temperature plasma assumption. The nonlinear coupling between traveling waves passing through the plasma is determined by taking second-order terms in the velocity into account. A simplified normal mode theory is used to describe the effect on the propagation constants of the individual modes due to coupling between them. The theory is carried out in detail for a plasma in an infinite magnetic field and for a plasma in a zero magnetic field. The final propagation equation for the traveling waves is found in terms of the fields in the plasma of the small-signal pumping wave, signal wave, and idler wave. In the Appendix the theory is extended to cover the case of beam-type parametric amplifiers. It is shown that the theory is applicable both to beam-type amplifiers which use space-charge waves for all three modes of propagation or to waves which are partially those of a circuit and of the beam itself. The results obtained are in agreement with the theory of Louisell and Quate for the principal waves of a space-charge wave parametric amplifier.

LIST OF SYMBOLS

A, dA — cross-sectional area

a, b — subscripts denoting parameters of the signal idler waves, respectively

a' — parameter denoting the difference in velocities of space charge waves

$$\omega_{q0} = 2a'\omega_{q1} = 2a'\omega_{q2}$$

B — ac magnetic flux density

D — dimensionless parameter denoting the strength of coupling between the signal and idler waves; D is proportional to the square root of the pump power and is analagous to Pierce's parameter C; also used as a subscript denoting the dc parameters of an electron beam

$\bar{e}, \bar{e}_T$ — electric fields which are functions only of the coordinates transverse to the direction of propagation; these parameters denote the difference between the fields of perturbed and unperturbed waves

$\bar{E}, E_n$, etc. — ac electric fields

$\bar{h}, \bar{h}_T$ — ac magnetic-field quantities analagous to $\bar{e}$ and e_T

$\bar{H}$ — ac magnetic-field intensity

J, J — current density

j — square root of minus one

l, dl — distances along the inside surface of a plasma described in a plane perpendicular to the direction of propagation; l is used to denote a complete line integral around this surface

M, N — $\bar{E}_a = M(\bar{E}_1 + \bar{e})$ and $\bar{E}_b = N(\bar{E}_2 + \bar{e})$

m — parameter denoting the magnitude of the pumping power in a pure space charge wave parametric amplifier:

$$m^2 = \left| \int_A (J_0'/J_D) E_{1z} E_{2z} dA \right|^2 \Big/ \left| \int_A E_{1z}^2 dA \int_A E_{2z}^2 dA \right|.$$

n — subscript denoting a component of field normal to the surface of a plasma

P — total power flowing through the cross section of the system

T — subscript used to denote the components of a vector in a plane perpendicular to the direction of propagation

t — time

$\bar{v}, v$ — velocity of an electron

z — distance along the direction of propagation; also used as a subscript to denote the z component of a vector

β — propagation constant of a wave

δ — parameter denoting the phase error between the three waves of interest; $\beta_1 + \beta_2 = \beta_0(1+2\delta)$

η — e/m for an electron

μ — parameter denoting the rate of increase of the growing wave in a beam-type parametric amplifier. $\beta = (\omega_1/v_D) - a'\beta_q \pm j\mu\beta q_q$

ω — radian frequency

ω_p — plasma frequency

ω_q — reduced plasma frequency of an electron beam

0 — subscript denoting the parameters of the pump wave

1, 2 — subscripts denoting the parameter of the signal and idler waves, respectively, when the pumping power is negligible

$*$ — superscript denoting complex conjugate quantities

$', ''$ — Superscripts denoting first- and second-order quantities, respectively, of the ac electric fields; however, the $'$ superscript does not have this meaning with a $'$, which was a notation chosen to conform with that of Louisell and Quate.[1]

$\rightarrow$ — a superscript indicating a vector

* The research reported in this document has been sponsored by the Air Force Cambridge Research Center, Air Research and Development Command, U. S. Air Force.

I. INTRODUCTION

IT has been shown by Tien[1-3] and others that it is possible to make a traveling-wave parametric amplifier which makes use of the nonlinear properties of a transmission system. If this system can propagate two waves of frequencies ω_1, ω_2 with propagation constants β_1, β_2, respectively, it is necessary to vary some parameters of the system; for instance, the dielectric constant or permeability at a frequency ω_0 with a phase delay of β_0 per unit of length, with

$$\omega_1+\omega_2=\omega_0, \tag{1}$$

$$\beta_1+\beta_2\simeq\beta_0, \tag{2}$$

to obtain appreciable gain at frequencies ω_1 and ω_2. Earlier forms of this device, suggested in the past, make use of the nonlinear properties of an electron beam, of a ferrite, or of a series of junction diodes placed across a transmission line. In this paper we shall deal with the theory of yet another form of the device, one which makes use of the nonlinear properties of a gas discharge plasma. The theory of this device is somewhat similar to that of the electron beam parametric amplifier, with some important differences, because the plasma frequency is now comparable with the working frequency. For simplicity we shall consider only two possibilities, that of a plasma in an infinite magnetic field, a restriction which limits the motion of electrons in a plasma to the direction of the magnetic field; and the other extreme, a plasma in zero magnetic field, which allows the electrons in a plasma to move freely in the direction of the electric field. The case of a finite magnetic field is considerably more complicated and will not be dealt with here.

In order to further simplify our treatment we shall make the assumption that all waves of frequency $n\omega_0+m\omega_1$, except the one for which $n=-m=1$, are of incorrect phase velocity to interact strongly with the pump wave of radian frequency ω_0 and the signal wave of radian frequency ω_1. Thus we shall only consider the interaction between three waves of radian frequencies ω_0, ω_1, and $\omega_0-\omega_1=\omega_2$, respectively. We shall also find it necessary to make the additional assumptions that the pump wave of radian frequency ω_0 is of large amplitude compared with the signal wave of radian frequency ω_1 and the idler wave of frequency ω_2, and that the gain per unit wavelength is small, an assumption equivalent to the small C assumption of traveling-wave tube theory. We shall, however, take account of the finite diameter of the plasma, the fact that the fields may vary over the cross section of the plasma and may not have the identical cross-sectional variation for all three modes. The treatment will not be restricted to pure modes of the plasma; any mode that is dealt with may be partially a mode of a circuit placed near the plasma.

[1] W. H. Louisell and C. F. Quate, Proc. I. R. E. **46**, 707 (1958).
[2] P. K. Tien and H. Suhl, Proc. I. R. E. **46**, 700 (1958).
[3] P. K. Tien, J. Appl. Phys. **29**, 1347 (1958).

Nonlinear Coupling Equations

We shall neglect the motion of ions in the plasma and make the assumption that electrons in the plasma are initially stationary, that is, at zero temperature. Let us consider as our first example the equation of motion of the electrons in a plasma which is placed in an infinite z directed magnetic field, that is

$$dv_z/dt=\eta E_z, \tag{3}$$

where

$$\eta=e/m.$$

This equation can be written in the form

$$(\partial v_z/\partial t)+v_z(\partial v_z/\partial z)=\eta E_z. \tag{4}$$

Equation (4) is a nonlinear equation in v_z which may be solved for v_z by writing v_z in the form

$$v_z=v_z'+v_z''\cdots \tag{5}$$

where v_z' is first-order in E_z, v_z'' second-order in E_z, etc. By considering only first-order terms in Eq. (4) we may write

$$\partial v_z'/\partial t=\eta E_z \tag{6}$$

which is the usual form of the small-signal equation for the velocity of the electrons in a plasma. As we are interested in the interaction of one wave with another, we need to take account of second-order quantities. By substituting Eq. (5) into Eq. (4) and making use of Eq. (6) we can solve for v_z'' by neglecting all quantities higher than the second order. Thus we obtain the following relationship between v_z'' and v_z'

$$(\partial v_z''/\partial t)+v_z'(\partial v_z'/\partial z)=0. \tag{7}$$

If we assume that the form of the modes of a plasma are known, that is, that we have solved the small-signal equations of the type of Eq. (6), in conjunction with Poisson's equation, the equation of continuity, and Maxwell's equations, we may then make use of these solutions to find the interaction between two individual waves, and hence find the necessary second-order terms. For a plasma, we can divide the ac convection current into first- and second-order terms in E_z in a similar way, and so write

$$J_z=J_z'+J_z''\cdots, \tag{8}$$

where

$$J_z'=\rho_D v_z', \tag{9}$$

and

$$J_z''=\rho_D v_z''+\rho' v_z', \tag{10}$$

where ρ_D is the dc electron charge density of the plasma, and the ac component of charge is given by the expression

$$\rho=\rho'+\rho''\cdots. \tag{11}$$

It follows from the equation of continuity that

$$(\partial J_z'/\partial z)+(\partial\rho'/\partial t)=0 \tag{12}$$

$$(\partial J_z''/\partial z)+(\partial\rho''/\partial t)=0. \tag{13}$$

Thus by making use of Eqs. (6), (7), (9), (10), and (12), it is possible, in principle, to solve for J_z'' in terms of E_z.

We shall take the pump, signal, and idler fields to be of the respective forms

$$\begin{aligned}
\bar{E}_{\omega 0}(x,y,z,t) &= \tfrac{1}{2}[\bar{E}_0(x,y)e^{j(\omega_0 t-\beta_0 z)}+\bar{E}_0^*(x,y)e^{-j(\omega_0 t-\beta_0 z)}]\\
\bar{E}_{\omega 1}(x,y,z,t) &= \tfrac{1}{2}[\bar{E}_a(x,y)e^{j(\omega_1 t-\beta_a z)}+\bar{E}_a^*(x,y)e^{-j(\omega_1 t-\beta_a^* z)}]\\
\bar{E}_{\omega 2}(x,y,z,t) &= \tfrac{1}{2}[\bar{E}_b(x,y)e^{j(\omega_2 t-\beta_b z)}+\bar{E}_b^*(x,y)e^{-j(\omega_2 t-\beta_b^* z)}]
\end{aligned} \tag{14}$$

with β_0 taken to be real and

$$\beta_a+\beta_b^*=\beta_0=\beta_a^*+\beta_b. \tag{15}$$

It should be noted that if there were no interaction between the individual waves, that is, if all signals were of very small amplitude, the propagation constants of the signal and idler waves at frequencies ω_1, ω_2 would be β_1 and β_2, respectively. To obtain gain, then β_1 and β_2 would have to satisfy Eq. (2). It follows that it will be our aim to find the propagation constants β_a, β_b in terms of the original propagation constants β_1, β_2, and β_0 and the field distributions of the individual waves. We shall resolve the velocity, current, charge density, and other quantities into components of the same form as the electric fields. We may then write, for instance, that

$$\begin{aligned}
j\omega_0 v_{0z}' &= \eta E_{0z}, \quad -j\omega_0 v_{0z}'^* = \eta E_{0z}^*\\
j\omega_1 v_{az}' &= \eta E_{az}, \quad -j\omega_1 v_{az}'^* = \eta E_{az}^*\\
j\omega_2 v_{bz}' &= \eta E_{bz}, \quad -j\omega_2 v_{bz}'^* = \eta E_{bz}^*.
\end{aligned} \tag{16}$$

We can then use Eq. (7) to find that

$$\begin{aligned}
&\omega_1 v_{az}''+\tfrac{1}{2}(\beta_b^*-\beta_0)v_{0z}'v_{bz}'^*=0\\
&\text{and}\\
&\omega_2 v_{bz}'^*+\tfrac{1}{2}(\beta_a-\beta_0)v_{0z}'^*v_{az}'=0.
\end{aligned} \tag{17}$$

By using Eq. (15) we may simplify Eq. (17) and write

$$\begin{aligned}
v_{az}'' &= \tfrac{1}{2}(\beta_a/\omega_1)v_{0z}'v_{bz}'^*\\
v_{bz}'^* &= \tfrac{1}{2}(\beta_b^*/\omega_2)v_{0z}'^*v_{az}'.
\end{aligned} \tag{18}$$

By substituting Eq. (18) in Eq. (10) we find J_{az}'' in the form

$$J_{az}''=\tfrac{1}{2}[(\beta_a/\omega_1)\rho_D v_{0z}'v_{bz}'^*+\rho_0'v_{bz}'^*+\rho_b'^*v_{0z}']. \tag{19}$$

It follows from Eqs. (9) and (12) that

$$\begin{aligned}
&\rho_0'=(\beta_0/\omega_0)J_{0z}'=(\beta_0/\omega_0)\rho_D v_{0z}'\\
&\text{and}\\
&\rho_b'^*=(\beta_b^*/\omega_2)J_{bz}'=(\beta_b^*/\omega_2)\rho_D v_{bz}'^*
\end{aligned} \tag{20}$$

so that we may write Eq. (19) as

$$J_{az}''=\tfrac{1}{2}\rho_D v_{0z}'v_{bz}'^*[(\beta_0/\omega_0)+(\beta_a/\omega_1)+(\beta_b^*/\omega_2)] \tag{21}$$

which may also be written in the more convenient form

$$\begin{aligned}
J_{az}'' &= (\eta^2 E_{0z}E_{bz}^*\rho_D/2\omega\omega_2)\\
&\quad\times[(\beta_0/\omega_0)+(\beta_a/\omega_1)+(\beta_b^*/\omega_2)].
\end{aligned} \tag{22}$$

By making use of Eq. (6), it follows similarly that

$$\begin{aligned}
J_{bz}''^* &= (\eta^2 E_{0z}^*E_{az}\rho_D/2\omega_0\omega_1)\\
&\quad\times[(\beta_0/\omega_0)+(\beta_a/\omega_1)+(\beta_b^*/\omega_2)].
\end{aligned} \tag{23}$$

We have therefore found a relationship between the second-order currents and the exciting field, or what might be called the coupling currents and the exciting fields, for the case of a plasma in an infinite magnetic field. Similar expressions for a plasma in a zero magnetic field are derived in Appendix I and are of the form

$$\begin{aligned}
J_a'' &= (\eta^2\rho_D/2j\omega_0\omega_1\omega_2)\\
&\quad\times[\nabla_T(\bar{E}_0\cdot\bar{E}_b^*)-j\beta_a\bar{i}_z(\bar{E}_0\cdot\bar{E}_b^*)]
\end{aligned} \tag{24}$$

$$\begin{aligned}
J_b''^* &= -(\eta^2\rho_D/2j\omega_0\omega_1\omega_2)\\
&\quad\times[\nabla_T(\bar{E}_0^*\cdot\bar{E}_a)-j\beta_b^*\bar{i}_z(\bar{E}_0^*\cdot\bar{E}_a)]
\end{aligned} \tag{25}$$

where ∇_T denotes the transverse component of the gradient, and $\bar{i}_z$ is the unit vector in the z direction.

II. DETERMINATION OF THE PROPAGATION CONSTANTS OF THE COUPLED SYSTEM

It is now necessary to find further relationships between the second-order coupling currents J_a'' and $J_b''^*$ so as to be able to solve for the propagation constants β_a and β_b of the parametric system. What we need is an equivalent of the circuit equation of traveling-wave-tube theory. One natural way of obtaining this equation would be to use a normal mode expansion.[4] As we are only interested in small perturbations from the original transmission modes of the system, it will be easier to derive a simple approximate formula which neglects the presence of other modes.

We shall first consider the change in propagation constant of a mode at radian frequency ω_1 of propagation constant β_1, which is caused by an exciting current J_a'' with propagation constant β_a flowing through the system. We shall take the fields of the unperturbed mode of propagation constant β_1 to be

$$\begin{aligned}
\bar{\mathcal{E}}_1(x,y,z,t) &= \bar{E}_1(x,y)e^{j(\omega_1 t-\beta_1 z)}\\
\bar{\mathcal{H}}_1(x,y,z,t) &= \bar{H}_1(x,y)e^{j(\omega_1 t-\beta_1 z)}
\end{aligned}$$

and the fields of the slightly perturbed mode of frequency ω_1 and propagation constant β_a to be

$$\begin{aligned}
\bar{\mathcal{E}}_a(x,y,z,t) &= \bar{E}_a(x,y)e^{j(\omega_1 t-\beta_a z)}\\
\bar{\mathcal{H}}_a(x,y,z,t) &= \bar{H}_a(x,y)e^{j(\omega_1 t-\beta_a z)}
\end{aligned}$$

with an exciting current flowing through the system, which is

$$\dagger J_a''(x,y,z,t)=J_a''(x,y)e^{j(\omega_1 t-\beta_a z)}.$$

We now consider the integral

$$\int_A \nabla\cdot[(\bar{\mathcal{E}}_a\times\bar{\mathcal{H}}_1^*)+(\bar{\mathcal{E}}_1^*\times\bar{\mathcal{H}}_a)]dA$$

[4] G. S. Kino, Electronics Research Laboratory, Stanford University, Tech. Rept. No. 84, May 2, 1955.

taken over the cross-sectional area of the transmission system. We may use the following form of Gauss's theorem

$$\int_A \nabla\cdot\bar{F}dA=\int_A\frac{\partial F_z}{\partial z}dA+\oint_l F_n dl$$

and the vector identity

$$\nabla\cdot(\bar{A}\times\bar{B})=\bar{B}\cdot\nabla\times\bar{A}-\bar{A}\cdot\nabla\times\bar{B}$$

to write

$$\begin{aligned}\int_A\nabla\cdot[(\bar{E}_a\times\bar{H}_1^*)+(\bar{E}_1^*\times\bar{H}_a)]dA&\\ =j(\beta_1-\beta_a)\int_A[(\bar{\mathcal{E}}_{aT}\times\bar{\mathcal{H}}_{1T}^*)+(\bar{\mathcal{E}}_{1T}^*\times\bar{\mathcal{H}}_{aT})]\cdot\bar{\imath}_z dA&\\ =\int_A[(\bar{H}_1^*\cdot\nabla\times\bar{E}_a)-(\bar{E}_a\cdot\nabla\times\bar{H}_1^*)&\\ +(\bar{\mathcal{H}}_a\cdot\nabla\times\bar{\mathcal{E}}_1^*-\bar{\mathcal{E}}_1^*\cdot\nabla\times\bar{\mathcal{H}}_a)]dA,&\quad(26)\end{aligned}$$

where we have taken the unperturbed mode of the system to be lossless, and the subscript T to stand for the transverse components of field. It follows, then, by using Maxwell's equations, that Eq. (26) reduces to the very simple expression

$$\beta_a-\beta_1=\frac{-j\int_A J_a''\cdot\bar{E}_1^*dA}{\int_A[(\bar{E}_{aT}\times\bar{H}_{1T}^*)+(\bar{E}_{1T}^*\times\bar{H}_{aT})]\cdot\bar{\imath}_z dA}.\quad(27)$$

Equation (27) is an exact expression, but is not in the most convenient form to use because it is expressed in terms of both the perturbed and unperturbed field quantities. In order to put Eq. (27) in a more convenient form we write

$$\begin{aligned}\bar{E}_a&=M(\bar{E}_1+\bar{e})\\ \bar{H}_a&=M(\bar{H}_1+\bar{h})\end{aligned}\quad(28)$$

where M is an arbitrary constant, and it is assumed that for small perturbations the contribution of $\bar{e}$ and $\bar{h}$ to the denominator of Eq. (27) is only of first order. Thus, by making this substitution and assuming that $|\beta_a-\beta_1|\ll\beta_1$ it will be seen that the contribution of the terms $\bar{e}_T$ and $\bar{h}_T$ to the right-hand side of Eq. (27) is of second order, so, we may write Eq. (27) in the more convenient but approximate form

$$\beta_a-\beta_1=\frac{-j\int_A J_a''\cdot\bar{E}_1^*dA}{M\int_A[(\bar{E}_{1T}\times\bar{H}_{1T}^*)+(\bar{E}_{1T}^*\times\bar{H}_{1T})]\cdot\bar{\imath}_z dA}.\quad(29)$$

It should be noted that the denominator on the right-hand side of Eq. (29) is four times the power flowing down the system in the unperturbed mode of radian frequency ω_1. Thus we can write Eq. (29) in the form which we will use hereafter:

$$\beta_a-\beta_1=-j\int_A J_a''\cdot\bar{E}_1^*dA\Big/4P_1M,\quad(30)$$

where

$$4P_1=\int_A[(\bar{E}_{1T}\times\bar{H}_{1T}^*)+(\bar{E}_{1T}^*\times\bar{H}_{1T})]\cdot\bar{\imath}_z dA.$$

A similar expression may be found for the propagation constant β_b^* in terms of β_2. This expression is

$$\beta_b^*-\beta_2=j\int_A J_b''^*\cdot\bar{E}_2 dA\Big/4P_2N^*,\quad(31)$$

where

$$4P_2=\int_A[(\bar{E}_{2T}\times\bar{H}_{2T}^*)+(\bar{E}_{2T}^*\times\bar{H}_{2T})]\cdot\bar{\imath}_z dA,$$

N is defined in the same way as M, and $\beta_2^*=\beta_2$ for a lossless system. Equations (30) and (31) are therefore the required circuit equations, which, in combination with either Eqs. (22) and (23) or (24) and (25), may be solved to give the propagation constants β_a and β_b of a parametric amplifier.

We shall illustrate this procedure, first, by solving for the propagation constants β_a and β_b of a plasma parametric amplifier in which the plasma is placed in an infinite magnetic field. We first substitute Eq. (22) in Eq. (30) to obtain the expression

$$\beta_a-\beta_1=\frac{-j\eta^2}{\omega_0\omega_2}\left(\frac{\beta_0}{\omega_0}+\frac{\beta_a}{\omega_1}+\frac{\beta_b^*}{\omega_2}\right)\frac{N^*}{M}\times\frac{\int_A\rho_D E_{0z}E_{1z}^*E_{2z}^*dA}{8P_1},\quad(32)$$

the further approximation having been made that $E_{bz}=NE_{2z}$ over the region of integration, an approximation which should be valid for small perturbations.

As a last step in this process, because the perturbation is small, it is reasonable to replace β_a by β_1 and β_b^* by β_2 in the right-hand side of Eq. (32). We finally obtain the formal expression that we require, which is

$$\beta_a-\beta_1=\frac{-j\eta^2}{\omega_0\omega_2}\left(\frac{\beta_0}{\omega_0}+\frac{\beta_1}{\omega_1}+\frac{\beta_2}{\omega_2}\right)\frac{N^*}{M}\times\frac{\int_A\rho_D E_{0z}E_{1z}^*E_{2z}^*dA}{8P_1}.\quad(33)$$

The similar expression for the difference between β_b^*

and β_2 will be

$$\beta_b^*-\beta_2=\frac{j\eta^2}{\omega_0\omega_1}\left(\frac{\beta_0}{\omega_0}+\frac{\beta_1}{\omega_1}+\frac{\beta_2}{\omega_2}\right)\frac{M}{N^*}\times\frac{\int_A\rho_D E_{0z}^*E_{1z}E_{2z}dA}{8P_2}. \quad (34)$$

We may now take the product of Eqs. (34) and (33) to eliminate M and N^*, and so obtain the following dispersion equation

$$(\beta_a-\beta_1)(\beta_b^*-\beta_2)=\frac{\eta^4}{\omega_0^2\omega_1\omega_2}\left(\frac{\beta_0}{\omega_0}+\frac{\beta_1}{\omega_1}+\frac{\beta_2}{\omega_2}\right)^2\times\frac{\left(\int_A\rho_D E_{0z}^*E_{1z}E_{2z}dA\right)\left(\int_A\rho_D E_{0z}E_{1z}^*E_{2z}^*dA\right)}{64P_1P_2}. \quad (35)$$

For β_1 and β_2 corresponding to lossless modes, with no loss in generality, we can write this equation in the following form

$$(\beta_a-\beta_1)(\beta_b^*-\beta_2)=\frac{\eta^4}{\omega_0^2\omega_1\omega_2}\left(\frac{\beta_0}{\omega_0}+\frac{\beta_1}{\omega_1}+\frac{\beta_2}{\omega_2}\right)^2\times\frac{\left(\int_A\rho_D E_{0z}E_{1z}E_{2z}dA\right)^2}{64P_1P_2}. \quad (36)$$

Thus, we have obtained a dispersion equation which is stated entirely in terms of field quantities of the original propagating modes of the system under small-signal conditions. As might be expected, the right-hand side of the equation, which expresses the change in the propagation constants from their unperturbed values, depends in its magnitude on a product of the field quantities over the plasma, and on the density of the plasma itself. No assumption is made that the density is constant within the plasma.

We shall now show how the similar expression for a plasma in zero magnetic field may be derived, and in the next section we shall discuss the implications of these dispersion equations.

In order to proceed with the derivation for zero magnetic field, we must substitute Eq. (24) in Eq. (30), to find the expression analogous to Eq. (32) for $\beta_a-\beta_1$. This expression is

$$\beta_a-\beta_1=\frac{-\eta^2\rho_D}{\omega_0\omega_1\omega_2}\times\frac{\int_A[-j\beta_a(\bar{E}_0\cdot\bar{E}_b^*)E_{1z}^*+\bar{E}_{1T}^*\cdot\nabla_T(\bar{E}_0\cdot\bar{E}_b^*)]dA}{8P_1M}. \quad (37)$$

As before, we may substitute β_1 for β_a, $N^*\bar{E}_2^*$ for $\bar{E}_b^*$, on the right-hand side of this equation, provided that the perturbations are small, and so obtain the following expression for $\beta_a-\beta_1$

$$\beta_a-\beta_1=\frac{-\eta^2\rho_D}{\omega_0\omega_1\omega_2}\frac{N^*}{M}\times\frac{\int_A[-j\beta_1(\bar{E}_0\cdot\bar{E}_2^*)E_{1z}^*+\bar{E}_{1T}^*\cdot\nabla_T(\bar{E}_0\cdot\bar{E}_2^*)]dA}{8P_1}, \quad (38)$$

the assumption having been made in this case that ρ_D is constant.

We may write Eq. (38) in a simpler form by expressing the second term in the numerator of Eq. (38) as follows

$$\bar{E}_{1T}^*\cdot\nabla_T(\bar{E}_0\cdot\bar{E}_2^*)=\nabla_T\cdot[\bar{E}_{1T}^*(\bar{E}_0\cdot\bar{E}_2^*)]-(\bar{E}_0\cdot\bar{E}_2^*)\nabla_T\cdot\bar{E}_{1T}^*. \quad (39)$$

We may then substitute the divergence equation for the field $\bar{E}_1^*$ in a plasma in zero magnetic field, which is

$$\nabla_T\cdot\bar{E}_{1T}^*+j\beta_1^*E_{1z}^*=0 \quad (40)$$

in Eq. (39) to write

$$\bar{E}_{1T}^*\cdot\nabla_T(\bar{E}_0\cdot\bar{E}_2^*)=\nabla_T\cdot[\bar{E}_{1T}^*(\bar{E}_0\cdot\bar{E}_2^*)]+j\beta_1^*E_{1z}^*(\bar{E}_0\cdot\bar{E}_2^*). \quad (41)$$

Substitution of Eq. (41) in Eq. (38), and use of the lossless mode assumption, $\beta_1=\beta_1^*$ then yields the required simplified form of Eq. (38)

$$\beta_a-\beta_1=\frac{-\eta^2\rho_D}{\omega_0\omega_1\omega_2}\frac{N^*}{M}\times\frac{\int_A\nabla_T\cdot[\bar{E}_{1T}^*(\bar{E}_0\cdot\bar{E}_2^*)]dA}{8P_1}. \quad (42)$$

Finally, by using the two-dimensional form of Gauss's theorem, it will be seen that the numerator of Eq. (42) may be expressed entirely in terms of conditions at the surface of the plasma. Thus we have

$$\beta_a-\beta_1=\frac{-\eta^2\rho_D}{\omega_0\omega_1\omega_2}\frac{N^*}{M}\times\frac{\oint_l(\bar{E}_0\cdot\bar{E}_2^*)E_{1n}^*dl}{8P_1}, \quad (43)$$

where n denotes the component of field normal to the surface of the plasma, and l denotes a line integral taken just inside the surface.

It should be noted that this line integral has been derived by assuming that the equations of motion we have used are obeyed everywhere throughout the region of integration. This assumption is only true within a region where there is still plasma present under ac conditions, i.e., to within a small distance inside the

unperturbed surface of the plasma. Consequently the integral of Eq. (42) can only be correctly evaluated within this region, and the thin region between the unperturbed surface and perturbed surface must be considered separately. It can be shown, however, that this additional contribution is of higher order than the main integral and so may be neglected. It is therefore reasonable to consider the surface integral of Eq. (43) to be taken just inside the unperturbed surface of the plasma. The required field quantities in this expression may then be obtained by the usual method of replacing the rippled surface by a surface charge layer at the original surface of the unperturbed plasma, or by using the concept of continuity of the total current normal to the surface.

We are now in a position to write down, as before, the final dispersion equation for a parametric amplifier using a plasma in zero magnetic field. This equation is

$$(\beta_a-\beta_1)(\beta_b{}^*-\beta_2) = \frac{\eta^4\rho_D{}^2}{\omega_0{}^2\omega_1{}^2\omega_2{}^2}\frac{\left[\oint_l (\bar{E}_0\cdot\bar{E}_2{}^*)E_{1n}{}^*dl\right]\left[\oint_l (\bar{E}_0{}^*\cdot\bar{E}_1)E_{2n}dl\right]}{64P_1P_2}. \tag{44}$$

Thus, as before, we have obtained the final dispersion equation entirely in terms of field quantities of the original small-signal modes of the unperturbed system.

III. DISCUSSION OF THE DISPERSION EQUATIONS

The two dispersion equations which we have obtained, Eqs. (36) and (44), may be expressed in the simple form,

$$(\beta_a-\beta_1)(\beta_b{}^*-\beta_2)=\beta_0{}^2D^2 \tag{45}$$

where

$$D=\frac{\eta^2}{8\omega_0(\omega_1\omega_2)^{\frac{1}{2}}\beta_0}\left(\frac{\beta_0}{\omega_0}+\frac{\beta_1}{\omega_1}+\frac{\beta_2}{\omega_2}\right)\frac{\int_A \rho_D E_{0z}E_{1z}E_{2z}dA}{(P_1P_2)^{\frac{1}{2}}}, \tag{46}$$

for a plasma in an infinite magnetic field, and

$$D=\frac{\eta^2\rho_D}{8\omega_0\omega_1\omega_2\beta_0}\times\frac{\left\{\left[\oint_l E_{an}{}^*(\bar{E}_0\cdot\bar{E}_2{}^*)dl\right]\left[\oint_l E_{bn}(\bar{E}_0{}^*\cdot\bar{E}_1)dl\right]\right\}^{\frac{1}{2}}}{(P_1P_2)^{\frac{1}{2}}}, \tag{47}$$

for a plasma in zero magnetic field.

In order to solve Eq. (45), it is necessary to know the relationship between β_1, β_2, and β_0. We will find it convenient to write this relationship in the form

$$\beta_1+\beta_2=\beta_0(1+2\delta) \tag{48}$$

where δ expresses the relative differences in phase between the three propagating waves of the system. Thus, with δ zero, it is to be expected that maximum interaction between the three waves would occur.

By using Eq. (48) with Eqs. (15) and (45) it is possible to express the equation which defines β_a in the following form

$$(\beta_a-\beta_1)(\beta_a-\beta_1+2\delta\beta_0)=-\beta_0{}^2D^2. \tag{49}$$

This equation has the simple solution

$$\beta_a=\beta_1-\delta\beta_0\pm j\beta_0(D^2-\delta^2)^{\frac{1}{2}} \tag{50}$$

which implies from Eqs. (15) and (48) that $\beta_b{}^*$ has the simple solution

$$\beta_b{}^*=\beta_2-\delta\beta_0\mp j\beta_0(D^2-\delta^2)^{\frac{1}{2}} \tag{51}$$

and therefore

$$\beta_b=\beta_2-\delta\beta_0\pm j\beta_0(D^2-\delta^2)^{\frac{1}{2}}. \tag{52}$$

Thus, it will be seen that if $D>\delta$ there will be a possible growing wave and a possible decreasing wave which can propagate along the system, and hence in a forward wave traveling-wave parametric amplifier there will be gain. Moreover, the gain will be maximum when δ is zero.

We may deal with backward wave traveling-wave parametric amplifiers in a similar fashion, backward waves being represented by reversing the sign of the relevant power flow, P_1 or P_2 in Eqs. (46) or (47). We see that the solutions are exactly the same in form as those given by Tien,[1,2] and as might be expected, the boundary conditions will also be of exactly the same form. The reader is referred to the papers of Tien for this information.

The parameter D may then be evaluated in terms of the fields of the waves which can propagate through the system. These waves are assumed known and so there is no inherent difficulty involved. This process has been carried out for the type of amplifier to be described in the next section, with the result that for a few decibels of gain, it would be expected that the pumping powers necessary would be of the order of a few watts.

IV. EXPERIMENTAL WORK

In order to test the theory, an experimental parametric traveling-wave amplifier was made by B. Ludovici.[5] He used a mercury vapor gas-discharge tube that took the form shown in Fig. 1. The tube, which had a hot cathode, also had a long positive column with an envelope of precision glass tubing about 1-cm o.d. and 50 cm long. For convenience, the discharge column was enclosed in an outer metal cylinder with a longitudinal slot cut in it. A probe could be inserted through this slot and moved along the length of the column to

[5] B. Ludovici (private communication).

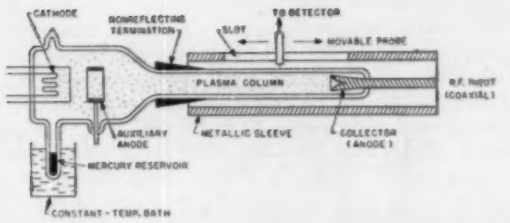

FIG. 1. Schematic of an experimental plasma parametric amplifier.

sample the rf fields present. Signals below the plasma frequency were introduced on the anode of the tube and propagated as slow waves along the long uniform discharge column. This type of propagating mode has been described by Gould and Trivelpiece,[6] and our measurements of their properties are in substantial agreement with theirs. Without any termination present standing waves could be measured on the system. However by using a termination of resistance paper wound around the tube, it was possible to obtain pure traveling waves on the system and so measure their amplitude.

The slow waves which can propagate along this column have a phase velocity, which over a certain range is almost independent of frequency. Thus within a limited frequency range, it was possible to choose a suitable signal frequency ω_1, idler frequency ω_2, and pump frequency ω, so as to keep the phase error parameter δ very small. In order to observe traveling wave parametric amplification, a pump signal ω of the order of 50 w and a small signal ω_1 were introduced on the anode of the discharge tube. The amplitude of the small signal ω_1 and the idler signal $\omega-\omega_1=\omega_2$ could then be measured at any point along the column by means of the movable probe. Typically, it was observed that with a pump frequency of 750 Mc, and a signal frequency of 300 Mc, the idler frequency of 450 Mc would increase rapidly in amplitude from the collector to the gun end of the tube. Moreover, with sufficient pumping power, the signal wave at frequency ω_1 was observed to increase in amplitude along the length of the tube, although the total increase in amplitude from one end of the tube to the other was only of the order of 2 db.

Thus the type of parametric effects predicted in the first part of this paper have been observed experimentally, although their magnitude is very small. With the experimental working conditions, the theory would predict that with no loss, and no velocity dispersion ($\delta=0$) the gain from one end of the tube to the other would be about 17 db. However with the observed value of $\delta=0.035$, the theory would predict only marginal gain. So far it has not been possible to obtain ideal experimental conditions. What has been observed, however, is that when the theory predicts marginal gain (a few db) the gain is indeed marginal. And under conditions when the theory would predict negligible parametric effects, the effects are indeed negligible.

At the present time the design of the experimental tube is being modified in order to lower the velocity dispersion. With better experimental conditions, it is hoped to obtain a more complete check on the theory given in the first part of this paper.

[6] A. W. Trivelpiece, Electron Tube and Microwave Laboratory, California Institute of Technology, Tech. Rept. No. 7, May, 1958.

APPENDIX I. DERIVATION OF THE ZERO MAGNETIC FIELD NONLINEAR COUPLING EQUATIONS

We shall derive here the nonlinear coupling equations for a plasma free to move in any direction, that is, a plasma in zero magnetic field. As before, we neglect the motion of the ions and make the assumption that the electrons in the plasma are initially stationary. The equation of motion for the electrons in the plasma is therefore

$$d\bar{v}/dt=\eta(\bar{E}+\bar{v}\times\bar{B}). \tag{A1.1}$$

This equation may be written in the form

$$(\partial\bar{v}/\partial t)+\bar{v}\cdot\nabla\bar{v}=\eta(\bar{E}+\bar{v}\times\bar{B}), \tag{A1.2}$$

which may then be solved into first- and second-order terms in $\bar{E}$, as before, by writing $\bar{v}$ in the form

$$\bar{v}=\bar{v}'+\bar{v}''+\cdots, \tag{A1.3}$$

with a similar expansion for all components of current, charge, etc.

Following the previous derivation for the infinite magnetic field case, we may equate first-order terms, regarding $\bar{v}\times\bar{B}$ to be of second-order, or higher, to find a small-signal expression for the velocity of an electron, which is

$$\partial\bar{v}'/\partial t=\eta\bar{E}. \tag{A1.4}$$

We may then equate the second-order terms to derive the necessary coupling equations. The second-order equation then takes the form

$$(\partial\bar{v}''/\partial t)+\bar{v}'\cdot\nabla\bar{v}'=\eta(\bar{v}'\times\bar{B}). \tag{A1.5}$$

By using the vector identity

$$\tfrac{1}{2}\nabla(v'^2)=\bar{v}'\cdot\nabla\bar{v}'+\bar{v}'\times\nabla\times\bar{v}',$$

we can write Eq. (A1.5) in the form

$$\partial\bar{v}''/\partial t=-\tfrac{1}{2}\nabla(v'^2)+\bar{v}'\times(\nabla\times\bar{v}'+\eta\bar{B}). \tag{A1.6}$$

It follows from Eq. (A1.4) that

$$\nabla\times(\partial\bar{v}'/\partial t)=\eta\nabla\times\bar{E}, \tag{A1.7}$$

so that from Maxwell's equation we may put[1]

$$\nabla\times(\partial\bar{v}'/\partial t)=-\eta\partial\bar{B}/\partial t, \tag{A1.8}$$

and therefore

$$\nabla\times(\partial\bar{v}'/\partial t)+\eta\partial\bar{B}'/\partial t=\partial/\partial t(\nabla\times\bar{v}'+\eta\bar{B})=0. \tag{A1.9}$$

And so for ac or dc signals

$$\nabla\times\bar{v}'+\eta\bar{B}'=0. \tag{A1.10}$$

Equation (A1.6) may therefore be written in the simplified form

$$\partial \bar{v}''/\partial t = -\tfrac{1}{2}\nabla(\bar{v}'^2). \quad \text{(A1.11)}$$

We may then find the second-order coupling current term by writing

$$J'' = \rho_D \bar{v}'' \quad \text{(A1.12)}$$

because in a zero magnetic field the first-order space-charge term is zero.

It is now convenient to split the field into three component waves of the type given by Eq. (14), then substitute to find that

$$J_a'' = \frac{\eta^2 \rho_D}{2j\omega_0\omega_1\omega_2}[\nabla_T(\bar{E}_0 \cdot \bar{E}_b) - j\beta_a \bar{i}_z(\bar{E}_0 \cdot \bar{E}_b^*)], \quad \text{(A1.13)}$$

and

$$J_b''^* = -\frac{\eta^2 \rho_D}{2j\omega_0\omega_1\omega_2} \times[\nabla_T(\bar{E}_0^* \cdot \bar{E}_a) - j\beta_b^* \bar{i}_z(\bar{E}_0^* \cdot \bar{E}_a)], \quad \text{(A1.14)}$$

where ∇_T denotes the transverse component of the gradient, and $\bar{i}_z$ is the unit vector in the z direction. Equations (A1.13) and (A1.14) are therefore the required nonlinear coupling equations which give the coupling currents in terms of the ac fields.

APPENDIX II. THEORY OF BEAM-TYPE PARAMETRIC AMPLIFIERS

The theory for plasma parametric amplifiers which has been given in the main part of this paper may be extended to deal with beam-type parametric amplifiers. The advantage of the procedure used here over that used by Louisell and Quate is that this type of theory may be applied to beam-type parametric amplifiers in which the propagating modes are not necessarily pure space-charge waves of the beam.

To extend the original theory given in the main body of this paper, we shall only consider the case of an electron beam in an infinite magnetic field; although the alternative case of a positive ion focused electron beam or an electron beam in Brillouin flow may also be dealt with by these methods. We shall consider an electron beam with dc velocity v_D. By using the equations of motion of the electron beam, the second-order currents J_{az}'' and $J_{bz}''^*$ may be found by following the same procedure as before. Thus, the equations for the second-order coupling currents J_{az}'' and $J_{bz}''^*$ become

$$J_{az}'' = \frac{\eta^2 \rho_D \omega_1 E_{0z} E_{bz}^*}{2(\omega_0 - \beta_0 v_D)(\omega_1 - \beta_a v_D)(\omega_2 - \beta_b^* v_D)} \times\left(\frac{\beta_0}{\omega_0 - \beta_0 v_D} + \frac{\beta_a}{\omega_1 - \beta_a v_D} + \frac{\beta_b^*}{\omega_2 - \beta_b^* v_D}\right), \quad \text{(A2.1)}$$

and

$$J_{bz}''^* = \frac{\eta^2 \rho_D \omega_2 E_{0z}^* E_{az}}{2(\omega_0 - \beta_0 v_D)(\omega_1 - \beta_a v_D)(\omega_2 - \beta_b^* v_D)} \times\left(\frac{\beta_0}{\omega_0 - \beta_0 v_D} + \frac{\beta_a}{\omega_1 - \beta_a v_D} + \frac{\beta_b^*}{\omega_2 - \beta_b^* v_D}\right). \quad \text{(A2.2)}$$

On the other hand, the circuit Eqs. (30) and (31) remain in exactly the same form as before except that the term denoting power flow P_1 in Eq. (30), for instance, should now be replaced by a more complicated form

$$P_1 = \tfrac{1}{2}\,\mathrm{Re}\left\{\int_A \left[(\bar{E}_{T1} \times \bar{H}_{T1}^*) \cdot \bar{i}_z + \frac{v_D}{\eta} v_{1z} J_{1z}^*\right]\right\} dA. \quad \text{(A2.3)}$$

Thus, we have now added a term denoting the kinetic power flow within the beam itself. In a pure space-charge wave, the second term which we have added will be of much greater importance than the term denoting electromagnetic power flow.

We may now combine Eqs. (A2.1) and (A2.2) with Eqs. (30) and (31) to form a dispersion equation for a parametric amplifier using an electron beam as the nonlinear medium. This dispersion equation is

$$(\beta_a - \beta_1)(\beta_b^* - \beta_2) = \frac{\eta^4 \omega_1 \omega_2}{(\omega_0 - \beta_0 v_D)^2(\omega_1 - \beta_1 v_D)^2(\omega_2 - \beta_2 v_D)^2} \times\left(\frac{\beta_0}{\omega_0 - \beta_0 v_D} + \frac{\beta_1}{\omega_1 - \beta_1 v_D} + \frac{\beta_2}{\omega_2 - \beta_2 v_D}\right)^2 \times\frac{\left|\int_A \rho_D E_{0z} E_{1z} E_{2z} dA\right|^2}{64 P_1 P_2}, \quad \text{(A2.4)}$$

the assumption having been made, as in the main part of this paper, that β_a may be replaced by β_1 and β_b^* by β_2 on the right-hand side of the equation. Equation (A2.4) is then the correct dispersion equation for a parametric beam-type amplifier; the original modes which are coupled by the nonlinearities in the beam may either be pure space-charge waves or modes which are partially those of a beam and a circuit. As in the treatment in the main part of this paper, the assumption has been made that the perturbation from the original propagation constants by the coupling of one wave to another is small, in this case somewhat less than the difference in phase constant between, say, the slow and fast space-charge waves of an electron beam. Such an assumption is necessary for the validity of this treatment and of any other treatment suitable for a finite electron beam which is known to the author, because otherwise if the perturbations in propagation constant are greater than these very small values, the field distribution in the beam itself will change, and it is there-

fore necessary to form a field theory to find this field distribution. Such a theory would be much more complicated than the ones that have been given heretofore.

As an illustration of the usefulness of Eq. (A2.4) we shall solve it for the same case as that of Louisell and Quate, that is with all three waves to be pure space-charge waves of the beam. We shall show that by using the approach given here it is possible to find purely analytic solutions which are valid over most of the range of interest. These solutions are more accurate than the Louisell-Quate solution over some parts of the range, and less over other parts, but always simpler in form. For pure space-charge waves, we may neglect the first term in Eq. (A2.3) and write

$$P_1=\frac{v_D}{2\eta}\,\mathrm{Re}\left\{\int_A v_{1z}J_{1z}^*dA\right\}$$

$$=\frac{1}{2}\,\frac{\omega_1 v_D\eta}{(\omega_1-\beta_1 v_D)^2}\int_A \rho_D E_{1z}^2 dA, \quad \text{(A2.5)}$$

where A now denotes the area of the beam. On substituting Eq. (A2.5) and the similar expression for P_2 in Eq. (A2.4) then, we find the new form of the dispersion equation, which is

$$(\beta_a-\beta_1)(\beta_b^*-\beta_2)=\frac{\eta^2(\omega_1-\beta_1 v_D)(\omega_2-\beta_2 v_D)}{(\omega_0-\beta_0 v_D)^2 v_D^2}$$

$$\times\left(\frac{\beta_0}{\omega_0-\beta_0 v_D}+\frac{\beta_1}{\omega_1-\beta_1 v_D}+\frac{\beta_2}{\omega_2-\beta_2 v_D}\right)^2$$

$$\times\frac{\left|\int_A \rho_D E_{0z}E_{1z}E_{2z}dA\right|^2}{\left|16\int_A \rho_D E_{1z}^2 dA\int_A \rho_D E_{2z}^2 dA\right|}. \quad \text{(A2.6)}$$

Equation (A2.6) is, therefore, the dispersion equation for a parametric amplifier in which the signal and idler waves are pure space-charge waves of the electron beam, but the pump wave is still arbitrary. In order to correspond to the case which Louisell and Quate take, we shall consider the pump wave to be a pure space-charge wave and ρ_D to be uniform in the electron beam. For convenience, we shall write

$$|\omega_1-\beta_1 v_D|=\omega_{q1},\quad |\omega_2-\beta_2 v_D|=\omega_{q2},\quad |\omega_0-\beta_0 v_D|=\omega_{q0},$$

and we use the first-order theory to obtain E_{0z} in the following form

$$E_{0z}=(j\omega_{q0}^2 v_D/\eta\omega_0)(J_0'/J_D) \quad \text{(A2.7)}$$

where J_0' is the ac convection current density of the pump wave at any point on the electron beam, and J_D is the dc current density in the beam. We shall than find it convenient to define a parameter m as follows

$$m^2=\left|\int_A (J_0'/J_D)E_{1z}E_{2z}dA\right|^2\Big/$$

$$\left|\int_A E_{1z}^2 dA\int_A E_{2z}^2 dA\right|. \quad \text{(A2.8)}$$

This parameter m is then equivalent to Louisell and Quate's[1] parameter m, the difference being that account is now taken of field variations over the electron beam. For if the pump wave, signal wave and idler wave do not have uniform fields in the beam, the parameter m defined by Louisell and Quate, which is based on the total current in the beam, is not very meaningful.

After substitution of Eqs. (A2.7), (A2.8) and the space-charge factors in Eq. (A2.6) it takes the much simpler form

$$(\beta_a-\beta_1)(\beta_b^*-\beta_2)$$

$$=\frac{m^2\omega_{q0}^2\omega_{q1}\omega_{q2}}{16\omega_0^2 v_D^2}\left(\frac{\omega_0}{\omega_{q0}}+\frac{\omega_1}{\omega_{q1}}+\frac{\omega_2}{\omega_{q2}}\right)^2, \quad \text{(A2.9)}$$

the assumption having been made that all three waves have approximately a phase velocity equal to the beam velocity. Thus we have arrived at the final dispersion equation that we require, and it may be solved in exactly the same way as were Eqs. (45)–(47) in the main body of this paper. However, it is interesting to compare the results of solving Eq. (A2.9) with the theory of Louisell and Quate.[1] To compare our results directly with theirs, we shall assume that $\omega_0=2\omega_1=2\omega_2$, and write $\omega_{q0}=2a'\omega_{q1}=2a'\omega_{q2}$, $\beta_q=\omega_{q1}/v_D$, $\beta_a=\beta_b=\beta$, $\beta_1=\beta_2$, so that Eq. (A2.9) takes the form

$$(\beta-\beta_1)(\beta^*-\beta_1)=(m^2a'^2/16)[2+(1/a')]^2\beta_q^2. \quad \text{(A2.10)}$$

We may then use the phase condition

$$\beta+\beta^*=\beta_0, \quad \text{(A2.11)}$$

and the conditions

$$\begin{aligned}\beta_1&=(\omega_1/v_D)-(\omega_{q1}/v_D),\\ \beta_0&=(2\omega_1/v_D)-(\omega_{q0}/v_D),\end{aligned} \quad \text{(A2.12)}$$

assuming that we are dealing with fast waves, to write the final dispersion equations as follows:

$$[\beta+\beta_q-(\omega_1/v_D)][\beta-\beta_q(1-2a')-(\omega_1/v_D)]$$

$$=-(a'^2m^2/16)[2+(1/a')]^2\beta_q^2. \quad \text{(A2.13)}$$

The solution of this equation is

$$\beta=(\omega_1/v_D)-a'\beta_q\pm j\mu\beta_q, \quad \text{(A2.14)}$$

where

$$\mu=[(m^2/16)(2a'+1)^2-(1-a')^2]^{\frac{1}{2}}.$$

Like Louisell and Quate, we have found a growing wave and a decreasing wave both traveling at the phase

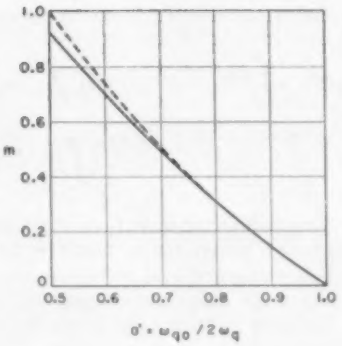

FIG. 2. The value of the minimum depth of modulation which will produce gain vs a'. The full line refers to the solution of Louisell and Quate, the dashed line refers to the solution given in this paper.

velocity of the fast pumping wave. Louisell and Quate's other two solutions would not be expected to appear in this solution, as we have assumed that we are interacting only with the fast space-charge wave, and we are looking for the perturbed forms of the fast space-charge wave. Naturally, the slow space-charge waves in the electron beam will be there whether there is or is not second-order interaction; because there is a slow space-charge wave present in the electron beam, there will be a new wave, be it ever so weak, which arises from the interaction of the slow space-charge wave with the fast pump wave and will therefore be the fourth solution to which Louisell refers. However, such a solution is, of course, unimportant. To compare the solution we have obtained more closely with Louisell, let us look first at the case of $a'=1$. We then find that $\mu=3m/4$, which is exactly the solution given by Louisell. Finally, we may determine the value of m for zero gain, that is, for $\mu=0$. This is given by the following expression

$$m=4(1-a')/(1+2a'), \qquad \text{(A2.15)}$$

which is plotted against Louisell's result in Fig. 2. It will be seen that the two expressions compare well. However, both theories might be expected to be subject to error. In Louisell and Quate's theory, there is no correction for change of field across the electron beam. In our theory, there is no provision for interaction with the slow space-charge wave. Thus, Louisell and Quate's expression might be expected to be correct when $a'=1$, because here the field is uniform across the beam. For our theory we would not expect perfect results. On the other hand, for smaller values of gain, that is, for small values of the parameter m, with beams of the finite diameter, our expressions should be correct, as the effect of variation of the fields over the cross section of the beam is taken into account in Eq. (A2.8). Finally, it should be noted, that here we have only presented the application of these expressions to a pure space-charge wave parametric amplifier. It should be apparent to the reader from the work in this paper that the theory may also be applied to other cases where the propagating modes are not pure space-charge waves of the beam.

JOURNAL OF APPLIED PHYSICS VOLUME 31, NUMBER 8 AUGUST, 1960

Determination of Surface Structure using Ultra-High Vacuum Replication

L. BACHMANN,* W. H. ORR, T. N. RHODIN, AND B. M. SIEGEL
Department of Engineering Physics, Cornell University, Ithaca, New York

(Received April 15, 1960)

Electron microscopy has been applied to the problem of characterizing the distribution of preferred sites for nucleation and growth on clean surfaces of evaporated films of magnesium metal. The films were deposited, platinum-shadowed, and carbon-backed in the same system under ultra-high vacuum conditions to minimize surface contamination and to improve the fidelity of surface replication. Upon examination of both clean and oxidized films in the electron microscope, the distribution of the platinum deposit was observed to be markedly influenced by the vacuum conditions used in the replication procedure. In addition, the particle size and separation of the platinum grains and their distribution, with relation to the substrate, indicated an enhanced surface mobility on cleaved mica and an apparent reaction on magnesium. These observations may have bearing on both the surface properties of metal deposits and on the development of high-resolution replication techniques.

INTRODUCTION

THE nucleation and growth processes by which deposits form by condensation of reaction on solid surfaces are sensitive to the surface properties of the substrate in the early stages of deposition. High-resolution electron microscopy provides direct information on the nature and distribution of the surface structures characteristic of the nucleation phenomena. Where the nucleation process is complicated by chemical reaction such as in the early stages of oxidation, studies of oriented nucleation are particularly difficult. Nevertheless, interesting studies have been made on nucleation and growth associated with oxidation by Bardolle and Benard,[1] by Gulbransen, McMillan, and Andrew,[2] by Harris, Ball, and Gwathmey,[3] by Menzel and Stössel,[4] by Martius,[5] by Moreau and Benard,[6] and by Basset,

* Now at the Institute of Physical Chemistry, University of Innsbruck, Austria.

Menter, and Pashley.[7] The latter have also demonstrated the occurence of preferred structures associated with the oriented nucleation of gold deposits on cleavage faces of alkali halides. This work thus provides information on the relationship of nucleation structures to various surface singularities of the substrate.

The application of electron microscopy to heterogeneous nucleation requires special procedures to achieve adequate resolution and to avoid uncertainties produced by surface contamination. For oxide nucleation studies on reactive metals like magnesium, the technique is further complicated by the small size of the oxide nuclei and by the sensitivity of the surface to contamination at pressures as low as 10^{-7} mm. In this case the surface preparation and replicating techniques employed by previous investigators are not adequate since the evaporation, shadowing and backing of the metal deposits must be carried out at vacuums of 10^{-8} mm or better. This study was directed primarily towards the characterization of metal surfaces evaporated and replicated under ultra-high vacuum conditions. The techniques used and the resulting observations have interesting implications both with reference to the characterization of surface properites and to the nucleation behavior of surface deposits.

These observations have a general bearing on the effect of minute surface contamination on the mobility and hence the size and distribution of the shadowing film and also on the chemical reactivity of the freshly deposited metal film itself. Furthermore the influence of ultra-high vacuum has a direct practical significance in the development of effective procedures for replica preparation in the application of high-resolution electron microscopy to the characterization of surfaces of reactive metals. It is the purpose of this paper to present some of the more significant procedures and results observed in the preliminary stages of this study.

APPARATUS

The general requirements characteristic of a good shadowed replica,[8] require that the shadowing material be inert, dense, stable, and dispersed uniformally on the finest possible scale. Platinum has been shown to have very low granularity and to provide high resolution of details in surface structure.[9,10] In addition, its relatively low vapor pressure at the melting point enhances thorough outgassing and makes evaporation in ultra-high vacuum possible.

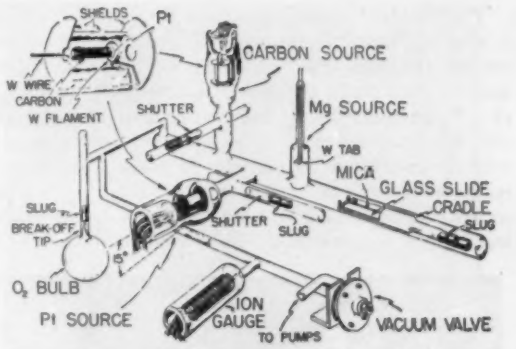

FIG. 1. Diagram of the apparatus used to deposit a metal film in an ultra-high vacuum and to replicate separate halves of this film before and after exposure to oxygen.

Electron bombardment of a drop of platinum placed at the end of a carbon rod proved to be effective in producing an adequately high evaporation rate. In comparison, bombardment of a pendant drop on the end of a platinum rod[11] is unsuitable for raising the temperature of the platinum much above its melting point. Calculations, using the evaporation rate of platinum at its melting point,[12] indicate that for the geometry used in the experiment about two hours would be required to deposit a monolayer. The conventional method of shadowing using a tungsten filament charged with platinum was also unsatisfactory for evaporation in ultra-high vacuum. Molten platinum alloyed readily with the tungsten and large amounts of gas were evolved. Gas evolution due to alloying of the platinum was also observed with other support metals such as molybdenum and tantalum.

It was desirable for the purpose of this experiment to deposit several monolayers in a few minutes to avoid surface changes during deposition. Hence it was necessary to heat the platinum several hundred degrees above its melting point and to hold it at this temperature for several minutes. Carbon does not react with molten platinum and it is possible to outgas it sufficiently to carry out the platinum evaporation in an ultra-high vacuum. By using higher electron bombardment intensities the carbon itself was also satisfactorily evaporated under the same conditions.

The design used for electron bombardment indicated in Fig. 1 is similar to that originated by Inghram.[13] The platinum was placed on one end of a 1-mm carbon rod. A tungsten wire coiled around the other end supported the rod and minimized heat losses from the anode. The cathode-filament was a tungsten ribbon bent in a loop around the end of the anode. Tantalum shields minimized heat losses and masked the substrate from the hot filament.

[1] J. Bardolle and J. Benard, Compt. rend. **232**, 231 (1951); Rev. mét. **49**, 613 (1952).
[2] E. A. Gulbransen, W. R. McMillan, and K. F. Andrew, Trans. AIME **200**, 1027 (1954).
[3] W. W. Harris, F. R. Ball, and A. T. Gwathmey, Acta Met. **5**, 574 (1957).
[4] E. Menzel and W. Stössel, Naturwissenschaften **41**, 302 (1954).
[5] U. M. Martius, Can. J. Phys. **33**, 466 (1955).
[6] J. Moreau and J. Benard, J. chim phys. **53**, 787 (1956).
[7] G. A. Basset, J. W. Menter, and D. W. Pashley, Discussions Faraday Soc., **No. 28** (1959).
[8] D. E. Bradley, J. Appl. Phys. **27**, 1399 (1956).
[9] R. C. Williams and R. C. Backus, J. Appl. Phys. **20**, 98 (1949).
[10] C. E. Hall, Proc. Natl. Acad. Sci. U. S. **42**, 801 (1956).
[11] J. C. Kelley, J. Sci. Instr. **36**, 89 (1959).
[12] O. S. Heavens, J. Sci. Instr. **36**, 95 (1959).
[13] M. G. Inghram and R. J. Hayden, *Handbook on Mass Spectroscopy* Natl. Research Council Natl. Acad. Sci. (U. S.), Nuclear Sci. Abstr. Ser. Rept. No. 14 (1954).

The platinum source was one of three stations along a long horizontal Pyrex tube in which the substrate moved (Fig. 1). The substrate was a Pyrex slide, mounted in a cradle and moved magnetically by means of a Pyrex-encased iron slug and an external solenoid coil. The first station was an evaporation source charged with the metal to be studied. In these experiments magnesium was evaporated from a tungsten tab in a source like that used by Cohen.[14] The second station was the platinum source which was mounted on an axis 15° above the horizontal plane and 14 cm from the substrate. About half way between the platinum and the substrate, there was a side tube containing a Pyrex shutter actuated by a Pyrex encased iron slug. This shutter was extended slightly into the platinum beam during evaporation to determine how much platinum had been deposited on the substrate. The third station along the substrate tube was a carbon source. By depositing a carbon film on the shadowcast surface in an ultra-high vacuum, the replica was completed without exposure to any contaminating atmosphere. The carbon source was constructed in the same way as the platinum source with omission of the platinum charge. There was also a side tube with a shutter for determining the amount of carbon deposited on the substrate.

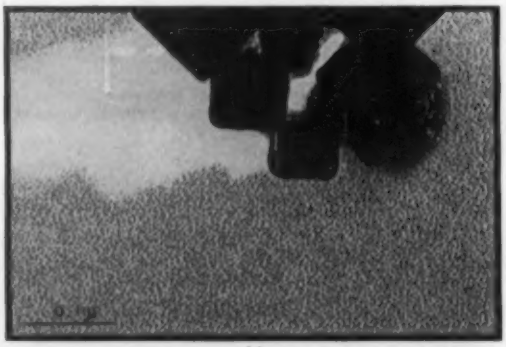

(a)

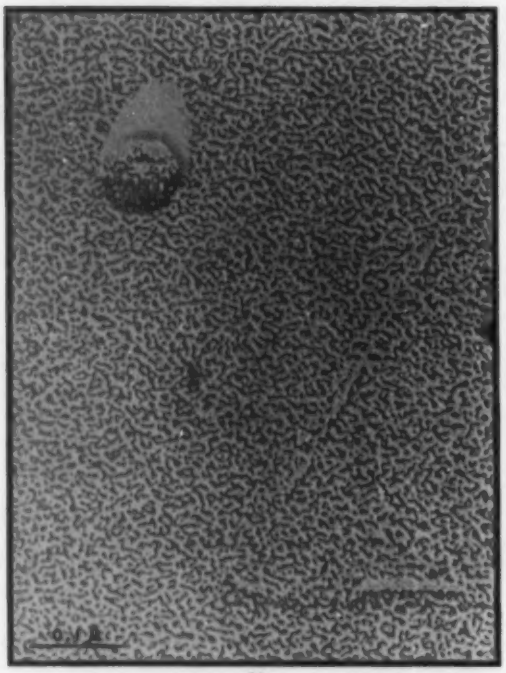

(b)

FIG. 2(a). Electron micrograph of platinum deposited on a cleaved mica surface at a pressure of 10^{-5} mm of Hg. The shadowing angle was 15°. Magnification 150 000×. (b) Electron micrograph of platinum deposited on a cleaved mica surface at a pressure of 10^{-6} mm of Hg. The shadowing angle was 15°. Magnification 150 000×.

[14] M. S. Cohen, Acta Met. (to be published).

The magnesium source was designed so that it covered about two square inches of the substrate with a deposit several thousand angstroms thick. The platinum and carbon beams were apertured so that they covered only half of this area. Thus, one-half of the magnesium surface could be shadowed with platinum and backed with carbon before the surface was exposed to higher pressures while the other half could be shadowed and backed after such exposure. An oxygen bulb with a breakoff tip was used to expose the second half of the magnesium surface to oxygen. The entire system including a Bayard-Alpert ionization gauge and a bakeable high-vacuum valve was arranged for bakeout and ion-pumping using the procedures described by Alpert.[15]

PROCEDURE

Prior to assembly all three sources were outgassed in another system at 10^{-5} mm. The glass system itself including the glass substrate was cleaned with boiling nitric acid and thoroughly rinsed. Half of the glass substrate was covered with a freshly cleaved mica strip and positioned at the end of the assembly. After the assembly was baked out at 320°C, the platinum and carbon sources and the shields were outgassed by electron bombardment at the highest temperatures to be used. With the sources kept just below the evaporation temperature, the bakeout was repeated, the assembly was then isolated from the diffusion pump and ion-pumped to below 10^{-8} mm. The first experiment was made on substrates of Pyrex and mica prepared as described but without deposition of magnesium to investigate the influence of the substrates themselves on the platinum deposit.

In the next experiment the substrates were first positioned under the magnesium source for deposition of the magnesium film and subsequently positioned under the other sources so that half the magnesium film was first platinum-shadowed and then backed with carbon. The operating pressure was 10^{-8} mm and at no time exceeded 5×10^{-8} mm. The unshadowed and unbacked magnesium surface was then oxidized *in situ* by introduction of high-purity oxygen at 20 mm and 25°C for

[15] D. Alpert, J. Appl. Phys. **24**, 860 (1953).

two hours. From the experiments of Addiss,[16] the nominal thickness of the oxide film formed under these conditions was estimated to be 30 A. After removal of the oxygen, the oxidized surface was shadowed and backed as before. The samples were then removed from the vacuum system, stripped in 3% HCl solution and placed in the electron microscope for examination.

RESULTS AND DISCUSSION

The first experiments were made to determine the influence of the ultra-high vacuum on the nature of the platinum-shadow deposit itself. Comparison was made between deposits on two substrates, Pyrex glass cleaned in hot acid and freshly cleaved mica, and for two vacuum conditions, 10^{-5} mm (obtained by conventional kinetic pumping) and 10^{-8} mm (obtained by bakeout and ion-pumping). The effect of vacuum on the nature of the deposit on chemically cleaned Pyrex varied slightly among samples and no significant effect of vacuum on granularity was observed. This may be associated with the difficulty of preparation of a clean reproducible surface on glass. In the case of the deposit on mica, a significant difference in granularity was observed as indicated in Fig. 2(a) and (b). The grain size is remarkably uniform and approximately an order of magnitude greater for the ultra-high vacuum deposit. The grains of this deposit are also larger than the grains on either Pyrex substrate. It is most likely that[17] the freshly cleaved mica substrate in an ultra-high vacuum is smoother and cleaner than the Pyrex substrate in the better vacuum as well as the mica in the poorer vacuum. Thus, the rates of nucleation and growth of the deposits are considerably different. The very sharp shadow-profile associated with the unidentified spherical particle observed on the mica substrate in the better vacuum is interpreted to result from an enhanced grain growth of platinum nuclei just outside this region by surface diffusion of platinum atoms from the penumbra of the shadow region. In comparison, the shadow-profile of the cubic particles on the mica substrate in poorer vacuum is significantly more diffuse. This diffuseness was also observed on both Pyrex substrates. In addition, decoration of the triangular singularity present on the mica surface, showing a linear alignment of nuclei even in the shadowing direction, resembles effects attributed by Basset, Menter, and Pashley[18] to oriented nucleation on edge faces on cleaved rock salt. The nature of the deposit and the character of the substrates are consistent with an interpretation requiring a lower nucleation rate and higher mobility of the platinum deposited on the mica surface in an ultra-high vacuum.

Additional complications were introduced upon replication of the magnesium films deposited by evaporation

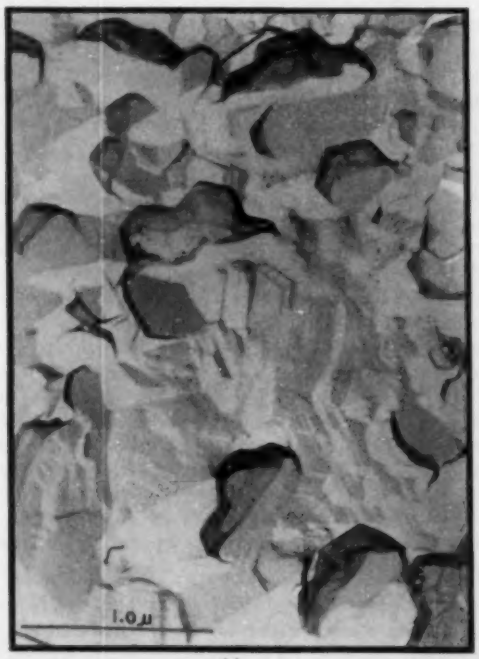

(a)

(b)

FIG. 3(a). Electron micrograph of platinum deposited on an oxidized magnesium surface with a shadowing angle of 15°. The magnesium film, several thousand angstroms thick, was deposited on Pyrex at a pressure of 10^{-8} mm of Hg, and then exposed to an oxygen pressure of 20 mm of Hg for two hours. Magnification 30 000×. (b) Same as Fig. 3(a). Magnification 150 000×. Area *A* shows anomalous deposition of the platinum. Area *B* shows some oriented nucleation of the platinum deposit.

[16] R. R. Addiss, Jr., Acta Met. (to be published).
[17] J. S. Courtney-Pratt, Research (London) 3, Suppl. 47 (1950).
[18] See footnote reference 7.

FIG. 4. Electron micrograph of platinum deposited on a clean magnesium surface. The magnesium film, several thousand angstroms thick, was deposited on mica and shadowed with platinum while the pressure remained at 10^{-6} mm of Hg. Magnification 50 000×. The magnesium film shown in Fig. 3(a), Fig. 3(b), and Fig. 4 was formed in a single evaporation.

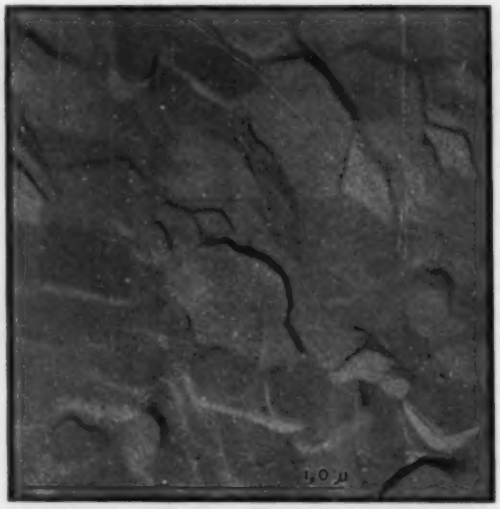

FIG. 5. Electron micrograph of a postshadowed carbon replica of a clean magnesium surface. The magnesium film, several thousand angstroms thick, was deposited on Pyrex and covered with carbon while the pressure remained at 10^{-6} mm of Hg. The carbon replica was removed and shadowed with platinum at an angle of 15°. Magnification 50 000×.

in the ultra-high vacuum. These films were replicated in both the clean and oxidized condition as described. The replicas of the oxidized magnesium are relatively free of complications as indicated in the electron micrograph of Fig. 3(a) and (b). Its structure is similar to that obtained by Cohen[19] by replication outside of the system in which the magnesium was deposited. The small hexagonal crystals with preferred orientation of the basal planes parallel to the substrate are typical of magnesium evaporated under these conditions. The degree of basal plane orientation and hence the roughness of the magnesium surface varies with the substrate. For example, deposits on mica are smoother with a higher degree of orientation than those on Pyrex glass.

The electron micrographs of the oxidized magnesium surfaces contain interesting details of surface structure. There is a tendency for the platinum to exhibit rearrangements in some areas on the basal planes indicating a growth of the platinum grains promoted in these areas [see Fig. 3(b), area *A*]. Indications of steps or rows characteristic of oriented nucleation have also been observed [see Fig. 3(b), area *B*]. The mode of deposition of the platinum may be influenced by a corresponding distribution of preferred nucleation sites for the platinum on certain areas of the oxidized magnesium surface. It is possible that this phenomenon may be more effectively demonstrated by using a shadowing metal with a higher surface mobility such as gold (see Basset[20]).

If the platinum is deposited directly on the clean magnesium, the electron micrographs show artifacts as indicated in Fig. 4. Although the outlines of the hexagonal magnesium crystals can still be distinguished, the platinum deposit has been completely disarranged. The anomalous redistribution of the platinum may be associated with a tendency of the platinum to alloy with the clean magnesium and to be redistributed on the backing film of carbon when the replica is stripped. It is significant that this effect seems to be characteristic of magnesium deposited under conditions of minimum contamination. This suggests that the effect may be used as a new method for the characterization of clean metal surfaces with a higher sensitivity than is available by other methods.

A clean magnesium surface can be satisfactorily replicated by another method. It is necessary to cover the surface in an ultra-high vacuum with a layer of carbon and then postshadow this replica in the usual manner. An electron micrograph of a clean surface obtained in this manner is shown in Fig. 5. It is observed that the oriented nucleation effects present on the oxidized surface are greatly reduced. The effect of the carbon may be to alter significantly the interfacial energy of the platinum deposit with the substrate or the absence of the oxide may have an important influence on the platinum nucleation. Further studies of the oxidation effect with other shadowing techniques are in progress.

[19] See footnote reference 14.
[20] G. A. Basset, Phil. Mag. 3, 1042 (1958).

ACKNOWLEDGMENTS

This work was supported by the United States Navy through the Metallurgy Branch of the Office of Naval Research under contract, and by the United States Air Force through the Air Force Office of Scientific Research of the Air Research and Development Command under contract.

Negative Glow Plasma as a Cathode for Electron Tubes

J. M. Anderson and L. A. Harris
General Electric Research Laboratory, Schenectady, New York
(Received March 14, 1960; and in final form, April 4, 1960)

The plasmas of the negative glow region of a cold-cathode discharge in helium and neon are examined for their ability to supply free electrons for operation of a "vacuum" amplifier tube. The plasma replaces the conventional oxide-coated hot cathode in a tube with closely-spaced fine-mesh grids. At gas pressures ~1-mm Hg the volt-ampere characteristics of the amplifier portion of the total discharge tube are essentially the same as found in the high-vacuum, hot-cathode counterpart.

The noise content of the plate current of the "glow-cathode" tube, defined by equivalent noise-diode current, was examined from 50 kc to 50 Mc. At the lower frequency this equivalent current is ~10 times the actual plate current flowing. At frequencies approaching 50 Mc the equivalent current drops to a factor ~0.5 and may be considerably lower for unexamined frequencies above 50 Mc.

INTRODUCTION

RECENTLY a quite low temperature (~400°K) has been reported[1] for the "ultimate" electrons[2] present in the negative glow plasma of a cold-cathode discharge in helium. This electron group has relatively high density (~10^{10} to 10^{13} electrons/cc) attainable with moderate power requirements from a dc voltage source. Interest is quite naturally aroused concerning the applicability of this plasma in certain electron devices, in particular as the effective cathode for a multi-electrode "vacuum" tube of the conventional type.

Maintenance of a glow discharge, in helium, having the desired properties requires a gas pressure in the range of a few mm of mercury. This appears incompatible with the description of the conventional amplifier vacuum tube. However, by closely spacing the electrodes with techniques developed in recent years, electron collisions with gas atoms within the gas-filled "vacuum" tube can be virtually eliminated. For reference, the mean free path for a room temperature electron in helium at 1-mm Hg is approximately 0.5 mm or 0.020 in. The following text describes a preliminary experimental investigation of the dc properties of such a glow cathode tube (GCT), and, of considerable current interest, the noise content of the plate current as a function of frequency.

HISTORICAL PRECEDENCE

The concept of supplying free electrons from the plasma of an electrical gaseous discharge, in lieu of a heated cathode, was described by Nienhold[3] in Germany in 1916. He envisioned a cold cathode, two spaced grids, and an anode all in parallel planes. The first grid acted as anode to the discharge tube section and cathode to the amplifying section. About the same time W. Schottky (see reference 7 below) proposed a "wall" amplifier utilizing the flow of electrons to the conducting walls of a cylindrical discharge tube. Modulation of this current of ambipolar diffusion was accomplished by a grid spaced close to the tube wall.

In the early 1930's the idea was revived with many public announcements and some experimental work by Hund,[4] Boumeester and Druyvesteyn,[5] and LeVan and Weeks.[6] These tubes used hot cathodes and right cylindrical configurations but in all essential points followed the patents of Nienhold. It is doubtful that any GCT described to date has been marketed, and the reason is most probably summarized by Schröter[7] who claims such tubes are inefficient and nonreproducible. Recent gas construction techniques,[8] however, have led to stability of operation and reproducibility. Since the early work the sensitivity of currently-used electronic equipment places an increasing demand for low noise amplification. Present knowledge of gaseous discharge plasmas would predict considerable internal noise generation for these earlier devices. It should be noted in passing that a somewhat similar tube, the Plasmatron, developed by Johnson and Webster[9] is not strictly to be included here since the source of electrons for the amplifying section is not from the plasma proper.

In contrast with past efforts, the present work attempts to achieve low noise content in the amplifying tube by taking advantage of the low-temperature group of electrons in the helium cold-cathode discharge.

TUBE CONFIGURATION AND dc OPERATION

In these tests two discharge tube configurations were employed and one amplifier tube assembly, used with both discharge tubes, allowed comparison of results. Designs of the plasma-containing portions of the total tube must be based on the properties of a cold-cathode

[1] J. M. Anderson, J. Appl. Phys. **31**, 511–515 (1960).
[2] G. Francis, *Handbook of Physics* (Springer-Verlag, Berlin, 1956), Vol. 22, p. 111.
[3] J. Nienhold, German Patents No. 319,806; 331,029; 345,921; and 345,276, 1916 through 1919.
[4] A. Hund, Electronics **6**, p. 6 (1933).
[5] H. G. Boumeester and M. J. Druyvesteyn, Philips Tech. Rev. **1**, p. 367 (1936).
[6] J. D. LeVan and P. T. Weeks, Proc. I.R.E. **24**, 180 (1936).
[7] F. Schröter, Electronics **8**, 131 (1935).
[8] J. M. Lafferty, I.R.E. Trans. on Electron Devices **ED-5**, 143–147 (1958).
[9] E. O. Johnson and W. M. Webster, Proc. I.R.E. 40, 645–659 (1952).

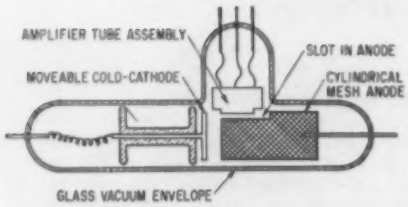

FIG. 1. Simplified sketch of electrode arrangement in the glow-cathode tube with movable cold cathode.

gaseous discharge. One requirement is that the amplifier portion must have its grid in "contact" with the negative glow region of the discharge which begins to form at a specific distance from the cold cathode. The intervening space, the cathode fall, is a region of high potential gradient dropping almost the whole of the potential applied to the discharge tube electrodes. Electrons liberated by positive ions or photons striking the cold cathode are accelerated through this field and enter the negative glow with relatively high energy. These primary electrons excite and ionize the gas to form the visible light and the plasma of the negative glow. Secondary electrons, products of the ionization, form a group of electrons at high mean energy (almost Maxwellian velocity distribution) which further ionizes and excites the helium gas. Collisions with the gas finally spend the high energy of the primary and secondary electrons and they "cool" to near gas temperature. These ultimate electrons are finally removed by recombination with positive ions or diffusion to the anode or tube walls.

To realize minimum noise, the electrons used in the amplifier tube must be drawn from this reservoir of cool electrons. For this reason, the amplifier tube must be disposed to avoid interception of the fast primary electrons. In both discharge tube configurations the plane of the amplifier grid was placed normal to that of the cold cathode. The positive column region was excluded from both tubes by placing the discharge tube anode sufficiently close to the negative glow. Helium (Linde rare gases, MSC grade) was used for most tests and was introduced to the tube through activated charcoal at liquid nitrogen temperature to remove impurities. Traces of neon, ~1 ppm, remained, however. Later, neon was introduced for comparison of discharge noise contribution with a different gas.

The first discharge tube configuration tested (see Fig. 1) had a movable cold cathode allowing optimum positioning of the negative glow with respect to the amplifier. The amplifier tube was composed of two molybdenum grids with 50% optical transmission, 90 mesh size, and 0.001 in. thickness. The grids were aligned [see Fig. 2(b)] one above the other to maintain maximum transmission and spaced approximately 0.003 in. The distance of the anode from the second grid was again about 0.003 in. For most purposes the first grid was maintained slightly positive in potential with respect to the discharge tube anode. In this condition the first grid collects an appreciable portion of the total discharge maintenance current. The second grid becomes the control grid for triode operation. If the first grid is utilized as a control grid the characteristics of the tube resemble those of a tetrode vacuum tube.

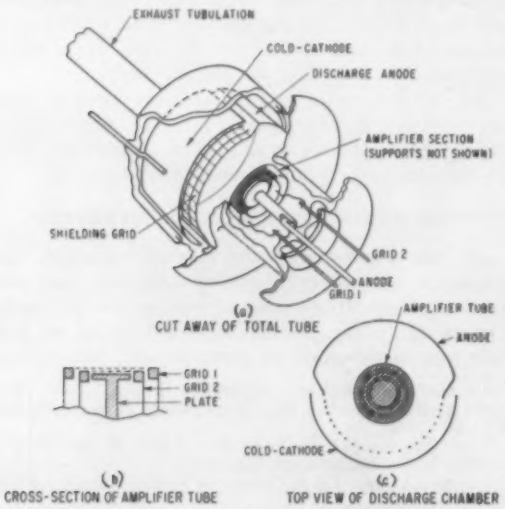

FIG. 2. Details of the glow-cathode tube where the negative glow plasma forms within the anode structure.

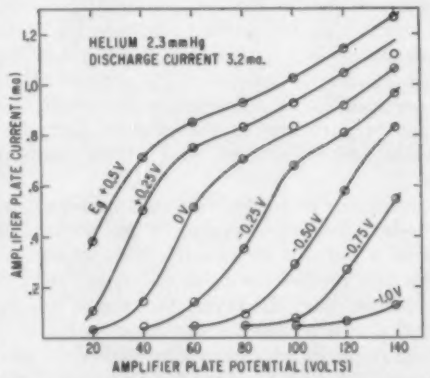

FIG. 3. Volt-ampere characteristics of a glow-cathode tube with triode connection (grids tied together electrically.)

The second discharge-tube configuration is shown on Fig. 2. Here the object is to contain the negative glow plasma within a shielded anode cage with the hope that certain of the higher frequency components of noise might be shunted around the amplifier portion of the tube.

Static volt-ampere measurements on the amplifier tube show that the characteristic curves are similar to those obtained for the conventional vacuum tube. If the grids are electrically tied together and operation is

as a triode with the discharge as an effective cathode the curves of Fig. 3 are obtained. The gain of the tube in the usable portion of the characteristics is approximately 100. The plate current in this instance was rather low, a fraction of a ma, while the discharge current was 3.2 ma and discharge maintenance potential approximately 400 v.

Maintaining the first amplifier grid at a fixed potential with respect to the discharge tube anode and varying the second-grid potential, now the control grid, would appear to be a more desirable electrical arrangement. Better shielding from the vagaries of the plasma would be expected. Further, the first grid could be set at a somewhat positive potential relative to the discharge anode, which would increase positively the plasma space potential and tend to "channel" discharge current to the amplifier tube. Typical characteristics

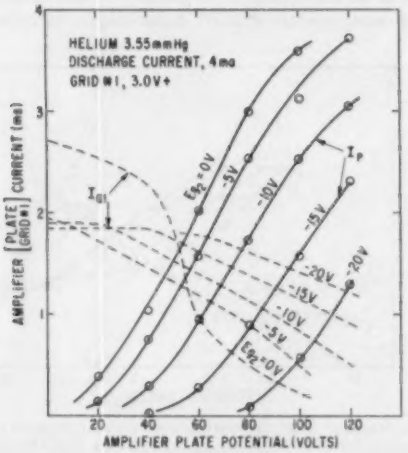

FIG. 4. Volt-ampere characteristics of a glow-cathode tube with the first grid as a virtual cathode and the second grid as the control grid (triode connection).

under these conditions (grid No. 1 is 3.0 v+with repect to the discharge anode) are shown on Fig. 4 where the helium gas pressure was 3.55-mm Hg and the discharge current was 4 ma. Note that almost the entire discharge current is caused to flow through the amplifier tube. However, the gain under this operation is quite low; for this example it is approximately 4. Such a low gain would be expected from purely geometrical considerations, since the second grid, shadowed by the first grid, becomes less effective in controlling the electric field gradient at the plasma surface. On Fig. 4 the current taken by the first grid is also shown as the dotted curves, for each bias potential of the second grid. Note that there is an expected decrease in current as the plate voltage increases.

The tube was next operated as a tetrode with the second grid at a potential of 45 v positive with respect to the discharge anode. Characteristic curves so obtained, but not shown here, indicate a relatively low transconductance, $\sim$400 μmhos.

It has been naively assumed in this and previous work that the plasma emits electrons from its surface much as would be expected from a conventional oxide-coated hot cathode. It is well known that a sheath containing a surplus of positive ions exists in the interface between the plasma and its container creating a potential gradient which tends to restrain the flow of electrons from the plasma. Under the condition of ambipolar diffusion, the oppositely charged particles leave the plasma in equal numbers to the walls and there recombine. The situation is altered adjacent to the anode or most positive electrode in contact with the negative glow, where more electrons diffuse from the plasma than positive ions, to give the net discharge maintenance current. Thus, we might expect the effect of the control grid of the amplifier to be an alteration in potential gradient in the plasma sheath which modulates the electron flow to the amplifier plate. Electrons drifting in a gas under the influence of an electric field will gain thermal energy through collisions with gas atoms. For lowest noise operation of the amplifying tube the sheath should be made as thin as possible, a condition obtained with the greatest plasma electron density. The high density in the negative glow is a further reason for selecting this region of the cold-cathode gaseous discharge.

RADIO FREQUENCY NOISE MEASUREMENTS

The noise content of the plate current of the GCT was measured by comparison with the noise content of temperature-limited current in a vacuum diode. The results are expressible in terms of the equivalent noise diode current which by substitution will produce the same output indicator response in the receiving apparatus.

For the super audio and low radio frequencies an amplifier with maximum response at $\approx$50 kc and with an effective bandwidth of $\approx$145 kc was constructed. This battery-operated post-amplifier had an equivalent noise resistance of 1050 ohm. As will be seen this value is sufficiently low for our purposes in view of the relatively high-noise voltages being measured. Noise content at frequencies below 10 kc was not measured but less noise would not be expected in this range.[10] Noise from a resistance or a standard noise diode and measured with the 50-kc amplifier agreed with calculated noise to within about 6%. This amplifier calibration allows its use in measuring equivalent diode currents greater than the capability of the diode noise source.

For higher radio frequencies, narrow bandwidth spot measurements were made at 0.5, 1, 5, 20, and 50 Mc. Measurements at higher frequencies were not pursued in this preliminary work because unavoidable capacities

[10] A. van der Ziel and E. R. Chenette, Physica **23**, 943–952 (1957).

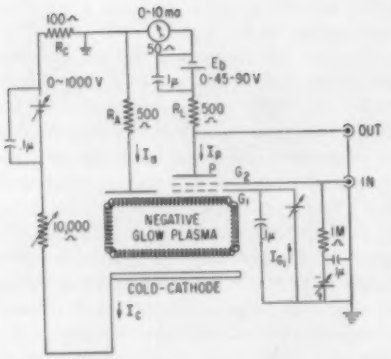

FIG. 5. Circuit schematic for connections to the glow-cathode tube used in these measurements.

in the GCT and circuitry would throw doubt on their validity. Low-noise cascode post-amplifiers at 5, 20, and 50 Mc preceded a conventional communications receiver.

Measurements at 50 kc were made on the earlier configuration of discharge tube with movable cathode, see Fig. 1. The openness of construction of this tube did not allow interpretable results at higher frequencies. For measurement purposes the circuit was that shown on Fig. 5. It is evident from the diagram that noise currents flowing from the cold cathode must return through R_A and R_L according to the relative admittances of the two circuits. Noise currents also return through G_1 which may take an appreciable portion of the total discharge tube current. It was shown experimentally that noise voltages developing across R_A and R_C are in proportion to the respective direct currents flowing in each resistance. At these low frequencies, $\sim$50 kc, the circuit impedances are essentially the resistances indicated and the discharge behaves as a current generator for noise. It was further shown that the noise voltage developing across R_L is more than would be expected from the appropriate dc current. This latter fact points to an additional contribution of noise from the amplifier tube over that from the discharge alone. Generally, with other parameters constant, this additional noise increases for increasing gas pressure.

TABLE I. Typical measurements in the region about 50 kc.

Gas pressures	5 mm Hg	3.2 mm Hg	2 mm Hg	2 mm Hg
I_c (ma)	7.0	2.7 ma	2.0 ma	1.0 ma
I_p (ma)	0.85	1.17	0.85	0.17
I_{G1} (ma)	2.3	0.42	0.31	0.19
I_a (ma)	3.85	1.1	0.84	0.64
I_{eq} in R_L (ma)	13.2	8.5	3.74	2.34
I_{eq} in R_A (ma)	1.4	2.58	2.4	2.2
Ratios				
I_{eq} in R_L, I_p	15.6	7.22	4.4	13.8
I_{eq} in R_A, I_A	0.36	2.32	2.86	3.44

Table I summarizes typical measurements in the region about 50 kc. Tube potentials were set at $E_b = 90$ v and $E_{G1} = 1.5$ v above the discharge anode, and $E_{G2} = 7.5$ v below E_{G1}. Grid No. 2 was grounded for radio frequencies. It will be noted that for reasonably equal I_p's the noise generated in the amplifier tube tends to decrease for lower gas pressures. With neon introduced to the discharge tube instead of helium, the results are essentially the same as above. In the course of the experiment, it was noted that an anode glow forms at the amplifier plate for $E_b \lesssim 40$ v, the intensity of the glow decreasing as gas pressure decreases. Undoubtedly this evidence of collisions within the amplifier explains some of the additional noise over that inherent in the primary discharge plasma. Generally, it may be concluded that the tube as constructed and operated in these experiments showed $\sim$10 times more mean square noise current in a frequency range about 50 kc than a temperature-limited noise diode carrying the same direct current. The minimum noise content obtainable is apparently set by that in the cold-cathode current of the primary glow discharge. Efforts to reduce these noise currents by introducing high impedances at $\sim$50 kc in the cathode circuit are of only little help, confirming the relatively high internal impedance for the discharge at these frequencies as mentioned earlier.

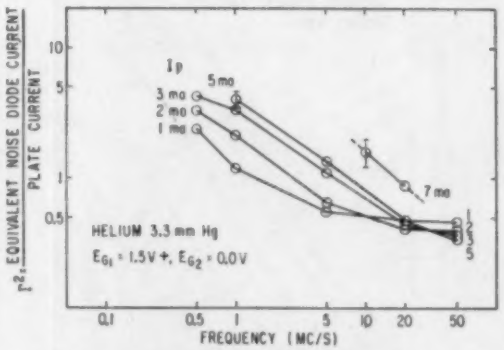

FIG. 6. Ratio of equivalent noise diode current to plate current in the amplifier-tube plate circuit for various radio frequencies and for various glow discharge currents (helium gas filling).

Comparison of the above results with noise measurements on type OA3 tubes by van der Ziel and Chenette[10] show I_{eq} to be a factor one-tenth less in our work than in theirs. Measurements on the type OA3 tube with our equipment give $I_{eq} \approx 100$ ma at 50 kc, in good agreement with van der Ziel and Chenette. The difference between results from the GCT and the OA3 are probably accountable to different discharge conditions.

A measurement of the ratio of equivalent noise diode current to plate current, describing noise output of the amplifier at higher radio frequencies, is plotted on Fig. 6 for helium gas at a pressure of 3.3-mm Hg. The discharge tube structure was that shown in Fig. 2. Cer-

tainly the most interesting feature of the curve on Fig. 6 is the decrease in noise as frequency increases. For $I_p = 1.0$ ma the equivalent noise current is seen to flatten out for high frequencies at about one-half the tube plate current. At larger plate currents the ratio is smaller but does not reach its final value below 50 mc. It might reasonably be estimated to be less than ~ 0.3 for frequencies above 50 mc. However, to reach this lowest noise point requires progressively higher frequency as I_p increases. Introduction of high impedance in the cold-cathode circuit has no effect on the magnitude of noise, probably reflecting the high discharge impedance as well as a shielding action by the anode cage. The above "quieting" factor of ~ 0.3 may be compared with the conventional space-charge-limited oxide cathode where it has been exhaustively determined in past work that this factor is ~ 0.1 or less.

Different gas pressures in helium lead to different variations of noise content in I_p with frequency as seen

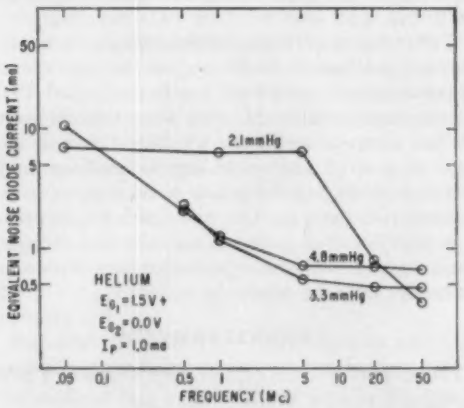

FIG. 7. Equivalent noise diode current in the amplifier-tube plate circuit for various helium gas pressures.

on Fig. 7. At 3.3- and 4.8-mm Hg the negative glow occupied space both inside and outside the anode cage assembly. At 2.1-mm Hg the appearance of the negative glow was wholly within the cage. All curves on Fig. 7 decrease with increasing frequency but with different shapes, and for the lowest pressure it is not certain in these restricted measurements just where a minimum in this curve might be.

Measurements under similar conditions in neon give the results plotted on Fig. 8. Equivalent noise diode currents are higher here than for helium and although the highest frequency used was 20 Mc the curves will probably reach a lower limit at a considerably higher frequency. From the standpoint of electron collisions with gas atoms the probability of collision in neon is less than that in helium for electrons having energies $\gtrsim 15$ ev, but experiments have shown the ultimate electron temperature in neon to be considerably higher than

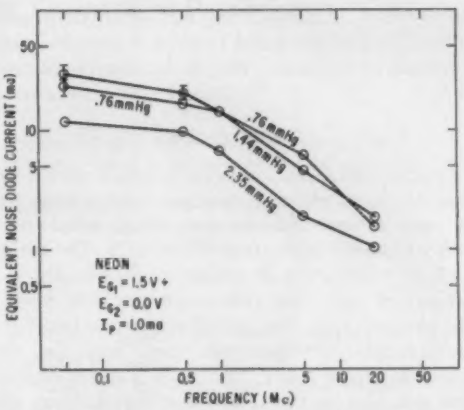

FIG. 8. Equivalent noise diode current in the amplifier-tube plate circuit for various neon gas pressures.

that found in the helium negative glow plasma.[1] It is probable that a lower limit for I_{eq} must include consideration of the electron temperature, in which case helium would be a preferred gas.

The GCT in all of the preceding tests was battery operated to minimize any external contribution of noise. For total discharge currents above ~ 5 ma there was a tendency for transition to arc discharge, preventable by a large value of discharge voltage dropping resistance. The back of the cathode was glass covered to prevent formation of glow except where desired. At the higher currents, irregular "spray" discharges tended to form at the boundary between the glass and the exposed part of the cathode. Upon their appearance the noise content of the amplifier plate current jumped to an enormously larger value. Some effort will have to be made to rid the cathode of these spurious discharges before significantly higher discharge and amplifier plate currents can be achieved.

The inter-electrode capacities of the amplifier tube were measured in the absence of a discharge. Capacity G_1 to G_2 was found to be 22 $\mu\mu$f, G_1 to amplifier plate was 10 $\mu\mu$f, and G_2 to amplifier plate was 15 $\mu\mu$f. These relatively high capacities made noise measurements beyond 50 Mc of doubtful value with an impedance level of 70 ohm. Capacities of G_1, G_2, and the amplifier plate to the discharge anode were each approximately 7 $\mu\mu$f. Capacity of the cold cathode to discharge anode was 15 $\mu\mu$f. Capacities could not be measured simply in the presence of the discharge because of the relatively large component of loss, a point which should be more carefully studied in any further work to determine input impedance of such a tube.

For all the above measurements the signal grid, G_2, was grounded for radio frequencies, contrary to a condition of practical operation. When this grid is returned to its bias source through resistance values up to 20 000 ohm there is a barely noticeable decrease in the noise

content of I_p. Changing the bias of G_1 from zero to minus 7.5 v (but grounded to radio frequencies) causes, in general, an increase $\sim 10\%$ in the noise power present on I_p.

CONCLUSIONS

Results of these tests as well as previous work indicate that the characteristic volt-ampere curves expected of the conventional vacuum amplifying tube are also readily obtained in the case of the GCT. The presence of gas at relatively high pressures, $\lesssim$1-mm Hg, is not detrimental to its function as an amplifier when the tube electrodes are close spaced one to another. For the discharge-tube configurations used here the direct current available in the "vacuum" tube was limited to a few ma. Also the power necessary for discharge maintenance was generally greater than that required for similar performance of an oxide-coated cathode by a factor of the order of 10 or less, which is likewise accountable to the glow-type discharge and its configuration. It is certain that other high-current discharge types would make available more amplifier tube current, but for the present work the aspect of low noise was of most importance. A further improvement in design of the cold-cathode electrode structure would most probably lead to higher direct currents if this is desired.

Measurement of the noise content of the amplifier plate current of the GCT gave greater equivalent noise diode current by a factor ~ 3 or more than the conventional space-charge-limited diode with oxide-coated cathode at $\sim$10–50 Mc. Since noise in the latter is generally smoothed by a factor of 10 or more (compared to the temperature limited diode), we may presume that there is a degree of "space-charge smoothing" by the plasma, but the effect is not as great as would be initially imagined. Whatever smoothing is accomplished by the plasma is presumably due to a compensating mechanism at the sheath edge similar to that occurring at the potential minimum in a conventional tube. A detailed model to explain the observed degree of smoothing has not been worked out at this time.

The observed frequency dependence of noise is quite similar to that found by van der Ziel and Chenette and most probably may be explained in its significant features according to the mechanisms proposed by them. Briefly these processes are (1) passage of positive ions into the cathode fall region from the negative glow plasma, (2) random release of electrons from the cold cathode by positive ions (similar to partition noise), and (3) production of new charges by ionizing collisions in the cathode fall region. The large increase in noise at lower frequencies compared to full shot noise has been attributed by van der Ziel and Chenette to current multiplication processes characteristic of the normal glow discharge. Our operation is in the abnormal glow region, but it would be expected that noise processes active for the normal glow would also be found in the abnormal glow since the transition between the two discharge types is gradual. It is doubtful that $1/f$ noise (flicker noise) is observed in these experiments since the noise from the GCT tends to flatten at lower frequencies. The frequency range in which the observed variation occurs is, moreover, considerably higher in the GCT.

While these results are not immediately encouraging, a firmer conclusion should perhaps be reserved until measurements above 100 Mc can be completed. Helium gas was emphasized in this work since it was hoped that the low temperature of the ultimate electrons in the negative glow plasma would lead to low noise content in the amplifier tube.[11] The few measurements in neon, also reported here, tend to substantiate this premise. It is probable that glow plasmas established in other gases, such as nitrogen or hydrogen, can show an improvement over the results for helium.

ACKNOWLEDGMENTS

The authors wish to express their thanks for helpful conversations with W. N. Coffey and for loan of his noise measuring equipment. We would further like to acknowledge assistance in tube construction by A. N. DeTommasi, W. Garwacki, and H. A. Poran, all of this Laboratory.

[11] *Note added in proof.*—Cooling of the helium gas by artificial means should be effective in further reducing the ultimate electron temperature.

Permanent Magnets Obtained by Drawing Compacts of Parallel Iron Wires

F. P. Levi*
Rola Company Pty. Ltd., Melbourne, Australia
(Received March 16, 1959; and in final revised form May 3, 1960)

A method of producing permanent magnets, which is believed to be novel, is briefly described. The method consists of drawing a compact containing parallel iron wires spaced by a copper alloy matrix until the iron wires become extremely small.

Intrinsic coercive forces of 400 oe have been measured in samples drawn from compacts in which the initial spacing between the iron wires corresponded to an iron packing fraction p of about 0.45. Annealing of cold-drawn samples generally increased both the coercive force and the squareness of the demagnetizing curve.

INTRODUCTION

THE typical property of permanent magnet materials is their high coercive force H_c. According to theory, high coercive forces are caused by the presence of minute "particles" having suitable characteristics.[1]

It can be broadly stated that in known permanent magnet materials, the "particles" are either generated within the material by means of metallurgical processes or are first manufactured as particles and then compacted to produce magnets of the desired shape and size.

Theoretically, a material containing parallel iron filaments, or elongated particles, having equal circular cross sections with a critical diameter of the order of 0.02 μ and suitably spaced from each other by a nonferromagnetic matrix, should have excellent permanent magnetic properties. The characteristics of compacts of elongated iron and iron-cobalt particles, obtained by electrodeposition in mercury and aligned in a magnetic field, are generally in agreement with the theoretical conclusions.[1-3]

The results described here show that an alternative approach is to reduce mechanically a material originally containing much larger iron filaments. In this manner, the production and handling of individual submicroscopic particles is avoided and the alignment of the filaments is automatically achieved.[4]

EXPERIMENTAL PROCEDURES AND RESULTS

Basically, all experiments consisted of: (a) assembling a "first compact," that is a nonferromagnetic tube containing parallel iron wires spaced by a nonferromagnetic matrix; (b) drawing the first compact to a diam between 0.002 and 0.030 in.; (c) assembling a "second compact," that is another nonferromagnetic tube containing parallel fine first compacts; (d) drawing this second compact; and so on.

Provided the individual iron filaments do not break during the process, the cross sectional area of each iron filament and its "equivalent diameter" (that is, its diameter if the cross section remained circular) can be estimated at any given stage from geometrical considerations. Microscopic measurements showed good correlation with these estimated sizes, up to the limit of optical microscope resolution.

In the early experiments, the first compact consisted of a copper tube containing copper plated iron wires embedded in a brazing alloy. The other compacts were similarly made. Figure 1 shows a typical microstructure after drawing to an estimated equivalent diameter of about 1 μ.

Notwithstanding the poor shapes and very low iron content in these preliminary experiments, which increased the difficulty of magnetic measurements, the following phenomena were observed:

When the estimated equivalent diameter was approximately 0.1 μ, the coercive force remained at about 20 oe, both before and after annealing, and the demagnetizing curve appeared fairly square. With filament diameters substantially larger or smaller than 0.1 μ, the coercive

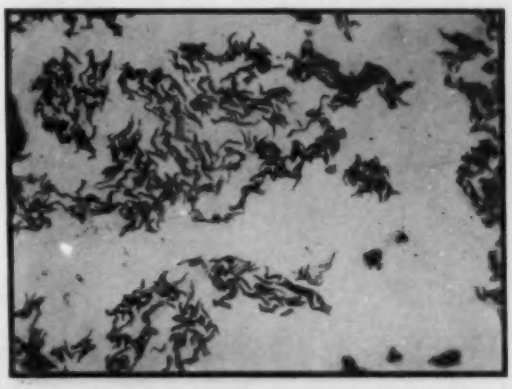

FIG. 1. Deformed filaments cross sections of about 1 μ estimated equivalent diameter obtained in early experiments. (750×)

* Now with Olympic Cables Pty. Ltd., Melbourne, Australia.

[1] T. O. Paine, *Proceedings of the Conference on Magnetism and Magnetic Materials, Boston, 1956* (American Institute of Electrical Engineers, New York, 1957) AIEE Spec. Publ. T-91, pp. 101–117. Includes a bibliography with 79 references.

[2] P. C. Lever, E. J. Yamartino, and R. B. Falk, J. Appl. Phys. 29, 304 (1958).

[3] F. E. Luborsky, T. O. Paine, and L. I. Mendelsohn, Powder Metallurgy, No. 4, 57, (1959).

[4] Patent applications have been filed in Australia and oversea countries in respect of these methods and materials.

force was about 20 oe in the cold-worked sample but decreased to a few oersteds after annealing.

The process was progressively modified, on the basis of considerations described later on, and significant coercive forces were obtained by the following general procedure. One-fourth-in. diam hydrogen-purified-iron wire was drawn to about $\frac{1}{16}$-in. diam and a copper alloy tube was drawn over it. The wall thickness of this tube determined the packing fraction p of the iron filaments in the first compact. This packing fraction was computed geometrically, and then checked both microscopically and magnetically.

With appropriate anneals, the composite wire thus obtained was drawn to a 0.0025-in. diam. The first compact consisted of from 1500 to 1800 composite wires, 0.0025 in. in diam, over which a copper alloy tube was drawn. Again with suitable anneals, the first compact was drawn to 0.0025 in., the iron filaments diam was then about 1 μ. The second compact consisted of another copper alloy tube drawn over 1500 to 1800 first compacts, 0.0025 in. in diam.

Figure 2 and 3 show portions of a second compact, with the iron filaments having a diam of the order of 0.7 μ. It can be seen that the drawing process has not progressed sufficiently to close all the voids between the first compacts. Beyond this stage of reduction, the shapes, sizes, and spacings of the iron filaments could not be clearly followed because electron micrographs were difficult to obtain and interpret.

By drawing further the second compact, coercive forces exceeding 50 oe were obtained for estimated equivalent diameters of 0.4 μ and smaller. The actual values depend upon: the filament size, the annealing sequence and temperatures, the packing fraction p, and the copper alloys used for the matrix. Figure 4 shows the coercive forces measured in a variety of samples.

It was also found that, as a rule, annealing a cold-worked sample increased its coercive force and squareness of the demagnetizing curve. Figure 5 shows the J/H curves, before and after annealing at 420°C, of the sample marked X in Fig. 4.

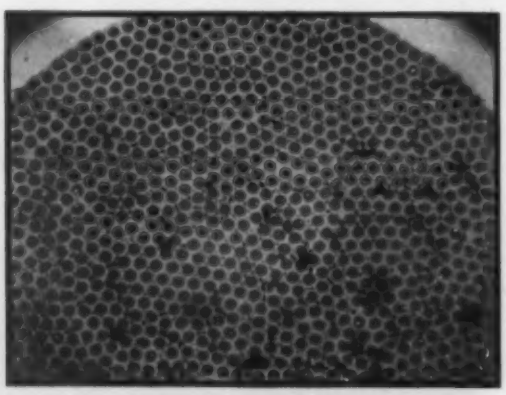

FIG. 2. Portion of second compact containing about 1500 first compacts. (37.5×)

MAGNETIC MEASUREMENTS

The samples used for magnetic measurements were assemblies of second compacts. Since only the material inside the tube surrounding the first compact had the permanent magnetic structure, and all the nonferromagnetic tubes except those used to space the original iron wires had purely mechanical functions, the measurements were, in fact, performed on assemblies of parallel thin permanent magnets (the insides of the first compacts) spaced and surrounded by substantial amounts of nonferromagnetic materials.

The aim of the experiments reported here was to find a process producing high coercive forces and square demagnetizing curves with a packing fraction between 0.40 and 0.50. Accordingly, values of magnetization

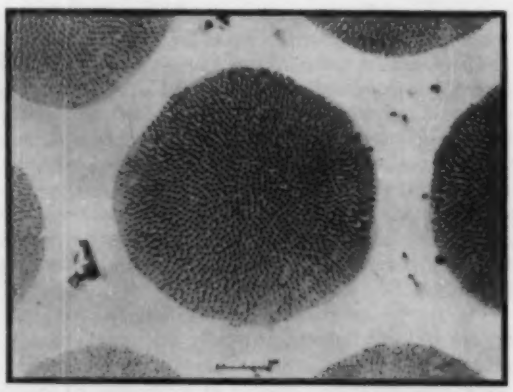

FIG. 3. Same specimen as in Fig. 2, enlarged further to show the iron filaments (approximately 1800 filaments of 0.7 μ) within a first compact. (750×)

intensity J_H at any field H, following saturation, relative to the intensity of magnetization J_S at saturation were considered sufficient. These relative intensities of magnetization were measured as follows:

The samples were inserted in a coil connected to a ballistic galvanometer, both coil and samples being immersed in a field of adjustable intensity H. The galvanometer swing following withdrawal of the sample when the field was 3500 oe in the positive direction was taken as the relative measure of the saturation intensity J_S of the magnets. The galvanometer swing following withdrawal of the sample after the field had been first brought to 3500 oe in the positive direction and then reduced to a given value H was taken as the relative measure of the intensity of magnetization J_H.

SOME METALLURGICAL AND MAGNETIC CONSIDERATIONS

To achieve the best results, the iron and the non-ferromagnetic matrix should apparently possess similar mechanical and recrystallization properties throughout the process. Furthermore, the cold reductions as well as the annealing stages and temperatures should be selected so as to obtain sufficient ductility of the compacts with the smallest possible grain size of both iron and matrix.

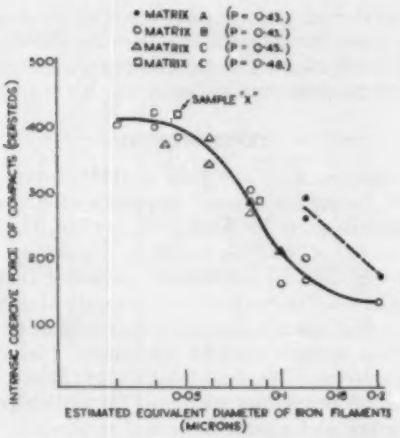

FIG. 4. Intrinsic coercive forces measured in some samples vs estimated equivalent iron filament diameter. Packing fraction p refers to the original iron wires spacing within the first compact.

Suitable annealing temperatures depend upon various factors, but there seems to be a maximum limit to their value for filament sizes below 0.2 μ. For best magnetic properties, the maximum annealing temperature has been found to decrease from about 460°C at an estimated filament equivalent diameters of 0.15 μ to about 380°C at 0.02 μ.

Some early experiments,[5] carried out with extreme cold work and varying packing fractions, indicated that

[5] F. P. Levi, Nature, **183**, 1251 (1959).

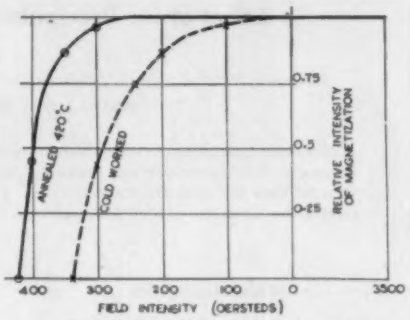

FIG. 5. J/H curves of sample X in Fig. 4.

the approximate relation: H_{ci} compact $= H_{ci}$ particles $(1-p)$ was fairly well satisfied for $0.10 \leq p \leq 0.37$. (H_{ci} compact = intrinsic coercive force of the sample; H_{ci} particles = median intrinsic coercive force of the particles at infinite dilution.) Also, the values of H_{ci} particles estimated with the above relation were somewhat higher than those corresponding to the data shown in Fig. 4 at filament estimated sizes greater than 0.05 μ. These results are not reported in details since they were not consistently reproducible and the measuring technique was then not sufficiently accurate.

ACKNOWLEDGMENTS

The author wishes to thank the Management of the Rola Company for permitting the publication of this information. He is indebted to the scientists of various Australian laboratories who gave advice and assistance; particularly, to: Dr. Hargreaves and Dr. Clarebrough of the Division of Tribophysics of the Commonwealth Scientific and Industrial Research Organization for their competent scientific guidance; G. Perger of the same organization for the many microphotographs, including those illustrating this paper; and to Dr. Rachinger of the Aeronautical Research Laboratories for assistance in the preparation of the manuscript. A sampe of extremely pure iron wire was kindly supplied by the British Iron and Steel Research Association and proved useful for controlled experiments.

Effect of Cu Precipitation on Dislocation Etch Pits in Ge

HOWARD SAVAGE
Electronic Material Sciences Laboratory, Air Force Cambridge Research Center, Bedford, Massachusetts

(Received July 6, 1959; and in final form April 17, 1960)

Measured quantities of copper were introduced into *n*-type germanium single crystals by diffusion. Subsequently, both quenching and annealing heat treatments were performed on the samples. The effect on etch pit sizes and resistivity was recorded. It is shown that saturation with copper does not inhibit completely the formation of etch pits, although they are altered in size.

INTRODUCTION

RECENT work has established that Cu can act as an acceptor in a Ge crystal.[1,2] When Cu is made to precipitate at edge dislocations by thermal treatment, changes in resistivity and strain energy occur.[1,3] The energy of a dislocation cannot be measured directly. However, an etch pit nucleated at a dislocation will undergo etching at a rate determined by the magnitude of the strain energy associated with the dislocation.[4–6] This investigation shows the effect of Cu on resistivity and etch pit formation in Ge.

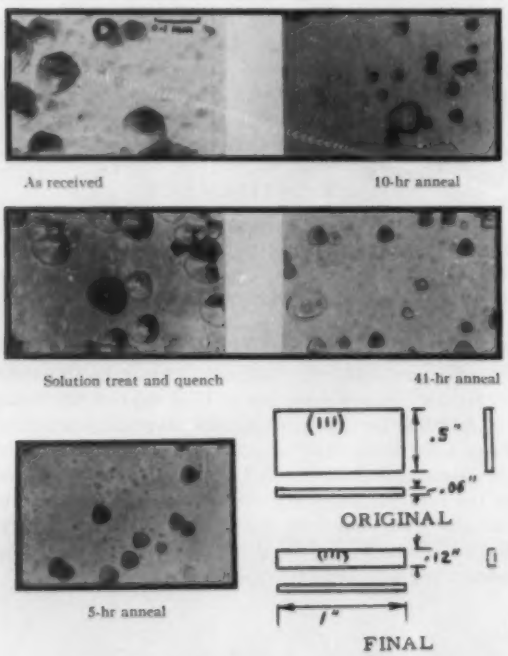

FIG. 1. As-received, etch pit structure and distribution representative of the material without any thermal treatment. Note the symmetry and depth of pits. Quenched, etch pit structure is hardly changed from the as-received condition. Size and number of pits remains constant. 5-hr anneal, size of pits is markedly reduced, but number and distribution are constant. 10-hr anneal, size of pits is just slightly reduced from that of the 5-hr anneal. However, a trend toward shallower pit depth is apparent. 41-hr anneal, pit width and distribution is the same as before but depth is greatly reduced. This effect of depth reduction is most pronounced for the higher copper concentrations.

EXPERIMENTAL

Ge samples were cut from a ⟨111⟩, *n*-type single crystal, having an average resistivity of 6.0 ohm-cm and approximately 10^4 dislocations per cm^2. The sample size was 1.0 in.×0.50 in.×0.06 in. Cu doping by the sealed-tube diffusion method was performed at elevated temperatures. Prior to heat treatment, the samples were cut to a final size of 1.0 in.×0.12 in.×0.06 in. to permit quenching without cracking the sample. (See Fig. 1.) All measurements were made on a (111) face.

Standard procedures were used for surface preparation before and after all thermal treatments. Initial lappings through 600 SiC slurry prepared the samples for 4-probe resistivity measurements. The following procedure yielded reproducible etch pits. Samples were: (1) placed in modified CP-4[7] for three minutes; (2) polished on a diamond lap to a mirror finish; and, (3) finally etched in Ellis No. 7[8] for three hours. Etch pit size was determined by measuring pit width by lineal analysis.

TABLE I. Etch pit diameters measured in mm at 150×.

Thermal treatment	Sample number I	II	III	IV	V
As received	10.0	10.2	10.2	10.2	10.2
550°C, 5 min.	9.0	11.0	11.0	11.0	11.0
500°C, 5 hr	10.0	6.5	5.0	4.5	x
500°C, 10.0 hr	x	4.0	4.5	5.0	6.0
500°C, 41 hr	x	5.0	6.0	6.5	7.5

The Cu concentration was varied by placing 0, 1, 2, 3, and 4 calibrated drops of aqueous $Cu(NO_3)_2$ solution on samples I, II, III, IV, and V, respectively. Diffusion was performed at 900°C for one-half hour. A concentra-

[1] R. A. Logan, Phys. Rev. **100**, 615 (1955).
[2] L. S. Grenier, P. Briedt, Jr., F. N. Hobstetter, and W. C. Ellis, J. Metals **9**, 813, Sec. II (1957).
[3] S. Mayburg, Phys. Rev. **95**, 38 (1954).
[4] A. D. Kurtz and S. A. Kulin, Acta Met. **2**, 354 (1954).
[5] B. A. Bilby, Proc. Phys. Soc. (London) **A63**, 191 (1950).
[6] A. G. Tweet, Phys. Rev. **106**, 221 (1957).
[7] 25 HNO_3, 15 $HC_2H_3O_2$, 15 HF by volume.
[8] 15 ml of 0.8 NKOH to which chlorine was added to give a ph of 8 or 9; mixed with 60 ml of deionized water to which was added 3 small pellets KOH.

tion of 1.39×10^{12} atoms of Cu per drop was selected on the basis of a calculated number of dislocation "sites" in a typical sample. A dislocation "site" is defined as the void existing at each intersection of a dislocation line with a puckered (111) plane.

The remaining heat treatment consisted of heating the samples for 5 min at 550°C and then quenching in vacuum oil. After quenching, the samples were annealed at 500°C for 5, 10, and 41 hr. Precautions were taken during these processes to prevent sample contamination by additional Cu or compensating impurities.

ETCH PIT MEASUREMENTS

Etch pit measurements are shown in Table I. An increased Cu concentration shows an effect after 5 hr,

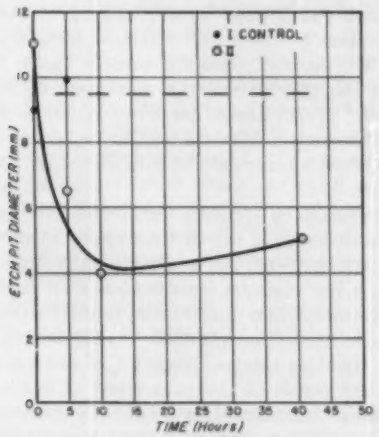

FIG. 2. Decreased in the width of etch pits with time. Note a slight increase after longer annealing times.

and an apparent reversal after 41-hr anneal. A change in width is also noticeable for a single Cu concentration. Figure 2 shows a minimum in the etch pit width after a 15-hr anneal. This minimum is attributed to a nucleation phenomenon, where random Cu atoms just begin to collect at dislocation sites during annealing and then these precipitates grow into "stars." This action is paralleled by a decrease and then a slight increase in strain energy at the dislocation. Experimental verification of these "stars" was sought by a micro-infrared technique,[9] but no such clusters could be observed.

[9] The precipitation of Cu in Si has been studied by P. H. Keck (private communication). The precipitate has the form of needles and/or plates arranged in either ⟨110⟩ or ⟨100⟩ directions in ⟨100⟩ planes. The precipitation is strongly influenced by such parameters as dislocations, oxygen content, copper concentration, and temperature treatment.

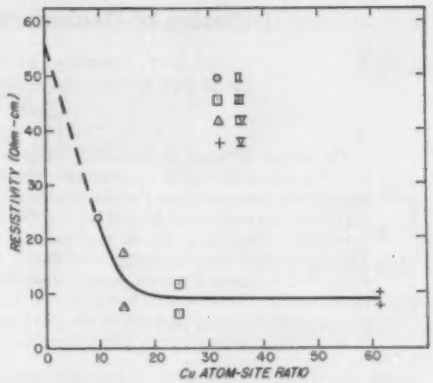

FIG. 3. Resistivity vs Cu atom to site ratio in Ge. Conductivity is n type in all cases. Samples II, III, IV, and V were treated with 1, 2, 3, and 4 calibrated drops of $Cu(NO_3)_2$, respectively.

RESISTIVITY MEASUREMENTS

Figure 3 is a plot of resistivity vs the ratio of Cu atoms to available dislocation sites for a 41-hr anneal. The resistivity drops rapidly until a ratio of approximately 15 atoms per site is reached, at which point the concentration of Cu is 2.5×10^{13} per cm^3. Beyond this concentration, there is little or no resistivity change.

The resistivity changes with time for sample II (see Fig. 2) are as follows: for as quenched, and after annealing for 5, 10, and 41 hr at 500°C; the resistivities are 24.0, 21.8, 5.4, and 1.8 ohm-cm. The maximum change in resistivity occurs with the maximum change in etch pit width. After 10 hr, little change occurs in either value.

CONCLUSION

Cu atoms migrate to dislocations and precipitate in a manner that relieves strain energy. The decrease in etch pit size with annealing time is paralled by a decrease in resistivity. Approximately 15 atoms of Cu per dislocation site produces a minimum etch pit diameter and a maximum change in the resistivity.

ACKNOWLEDGMENT

The author wishes to acknowledge many helpful discussions of this work with J. R. O'Conner and B. D. Lichter. He also wishes to acknowledge the help of W. A. McLaughlin during the initial experimental period.

Diffusion of Deuterium in Deuteron-Irradiated Copper

MARK T. ROBINSON, A. L. SOUTHERN, AND WILLIAM R. WILLIS*
Solid State Division, Oak Ridge National Laboratory,† Oak Ridge, Tennessee
(Received February 15, 1960)

The rate of diffusion of deuterium in metals can be studied by measuring the counting rate of neutrons from the $D(d,n)He^3$ reaction occurring in metals irradiated with low energy deuterons. A method of analyzing the time-dependence of the observed neutron counting rate is presented and applied to experiments on Cu in the temperature range $-46°$ to $+20°C$. It is concluded from the results that grain boundary diffusion is primarily responsible for the movement of deuterium in polycrystalline Cu in this temperature range. The apparent activation energy for diffusion of deuterium in polycrystalline 99.999% Cu is found to be 0.12 ± 0.02 ev/atom. Chemical purity appears to play an influential role in deuterium diffusion in Cu, the rate in OFHC Cu being significantly lower than that in the more pure material. A surface resistance effect, independent of the crystallinity of the specimen but proportional to the deuteron beam current, was found to be of major importance in determining the rate of escape of deuterium from the targets.

I. INTRODUCTION

THE rates of diffusion of the hydrogen isotopes in metals have generally been determined either from high temperature gas permeability data or from data obtained in electrolyses at ordinary temperatures. The application of these methods frequently requires concomitant data on the solubility of hydrogen in the metal as a function of temperature. Because of the difficulties associated with both the permeability and solubility measurements, most of the presently available data were obtained on the transition metals in which both the hydrogen solubility and its diffusion coefficient are reasonably large. Data obtained by these methods are summarized in several places.[1–3]

This communication describes a novel method of studying the diffusion of deuterium in metals over a wide range of temperature which generally requires no knowledge of the equilibrium solubility. The method depends on the large cross-section for the $D(d,n)He^3$ nuclear reaction at low deuteron energies. A beam of deuterons from an accelerator is focused at normal incidence onto the planar surface of a metal target. The stopping of the energetic deuterons in the metal provides the source of diffusing matter as well as the analytical probe for following the changes of its concentration with time. The neutron counting rate from the $D(d,n)He^3$ reaction is recorded as a function of time. Analysis of the resulting curves allows deduction of the diffusion coefficient of deuterium in the metal target. Experiments of this sort have been performed by Fiebiger,[4] by Arnold and Curtis,[5] and by Fink *et al.*[6] The latter two groups have preferred to count the protons from the $D(d,p)T$ reaction, from which the $D(d,n)He^3$ neutron counting rate is easily derived. Fiebiger has pointed out the connection between the data obtained and deuterium diffusion, but he made no attempt to analyze his data and, in fact, employed an inappropriate solution to the diffusion equation in his discussion.

In the following sections, the time-dependent diffusion equation will be solved for a model of the experimental arrangement. An analytical approximation to the $D(d,n)He^3$ reaction cross-section as a function of deuteron penetration into the target will be presented. From these results, an expression can be derived for the neutron counting rate as a function of time. A method of deriving values of the parameters of the counting rate equation from the observed data by means of high-speed digital computing machinery is presented. The analytical procedure is then applied to data obtained by irradiating copper with 176 kev deuterons in the temperature range from $-46°$ to $+20°C$. This is an especially interesting case, since earlier work has shown that the diffusion rate of ordinary hydrogen is immeasurably small in copper when the electrolysis method is employed.[7]

A word should be said about the possible influence of radiation damage on the results of these experiments. The maximum kinetic energy which can be imparted by a 176 kev deuteron to a Cu atom is 21 kev. The range of 25 kev Cu atoms in Cu has been measured by Schmitt and Sharp[8] as about 160 A. Only near the end of the deuteron range will significant numbers of displaced Cu atoms be produced, and these will have

* Consultant to Solid State Division, ORNL, from West Virginia Wesleyan College, Buckhannon, West Virginia.

† Oak Ridge National Laboratory is operated by Union Carbide Corporation for the U. S. Atomic Energy Commission.

[1] F. E. Jaumot, Jr., "A Bibliography of Diffusion of Gases, Liquids, and Solids in Solids, 1890 to 1955," U. S. Atomic Energy Commission Report TID-3071 (April, 1958). pp. 91–117.

[2] D. P. Smith, Hydrogen in Metals (University of Chicago Press, Chicago 1948), *passim*.

[3] R. M. Barrer, Diffusion in and through Solids (Cambridge University Press, London, 1951), pp. 144–238.

[4] K. Fiebiger, Z. angew. Phys. **9**, 213 (1957); Z. Naturforsch. **11a**. 607 (1956).

[5] R. T. Arnold, thesis, Vanderbilt University, Nashville, Tennessee (1955); C. D. Curtis, Vanderbilt University, private communication (1958).

[6] R. W. Fink, *et al*, University of Arkansas Annual Progress Report, under a U. S. Atomic Energy Commission contract (March 1, 1958).

[7] G. Charpy and S. Bonnerot, Compt. rend. **154**, 592 (1912); D. Alekseev and L. Savinina, Zhur. Russ. Fiz. Khim. Obshchestva **56**, 560 (1924); R. Dumpelmann and W. Hein, Z. Physik **22**, 368 (1924). Cf. also footnote reference 2.

[8] R. A. Schmitt and R. A. Sharp, Phys. Rev. Letters **1**, 445 (1958).

ranges much less than 160 A. It is concluded that only a very thin region at the end of the range, probably less than 0.01 μ thick, will be significantly disturbed by the irradiation. Since this is $<1\%$ of the range, it seems quite unlikely that radiation effects on the diffusion rate would be of any importance.

II. THEORY

A. Model of the Diffusion Process

The geometry assumed in analyzing the diffusion process is shown in Fig. 1. The deuteron beam, of initial energy E_0 and current density i, is normally incident on the planar surface of the target, $x=0$. It is assumed that the target thickness ($>1000\,\mu$) is enough greater than the range of the incident deuterons ($\sim 2\,\mu$) that the target may be regarded as infinitely thick. It is also assumed that the deuteron beam is large in diameter ($\sim 1000\,\mu$) compared to the deuteron range and uniform in current density over its cross-section, permitting application of the one-dimensional diffusion equation. In particular, broadening of the beam in the slowing-down process is ignored. As the beam particles penetrate the target, their mean energy E decreases until it reaches zero at the mean deuteron range, $x=R$, producing there a planar source of diffusing deuterium. Straggling of the deuterons is ignored (but see the discussion below).

According to this model, the deuterium concentration in the target obeys the differential equation

$$\partial c/\partial\vartheta=(\partial^2 c/\partial u^2)+S(u), \tag{1}$$

where $c(u,\vartheta)$ is the deuterium concentration, $u=x/R$, $\vartheta=Dt/R^2$, t is the time, D is the deuterium diffusion coefficient, independent of concentration, and the source is

$$\begin{aligned} S(u)&=iR/D \qquad u=1 \\ &=0 \qquad\quad u\neq 1. \end{aligned} \tag{2}$$

The target is assumed to be free of deuterium initially and $c(u,\vartheta)$ is required to vanish at large distances from the source. That is,

$$c(u,0)=0 \tag{3a}$$

$$\lim_{u\to\infty} c(u,\vartheta)=0. \tag{3b}$$

Statement of the problem is completed by specifying the conditions at the boundary $u=0$. It is assumed that the flux of matter escaping from the metal into the vacuum system is proportional to the deuterium concentration in the metal surface. That is,

$$\frac{D}{R}\left(\frac{\partial c}{\partial u}\right)_{u=0}=hc(0,\vartheta), \tag{3c}$$

where h is a mass transfer film coefficient. With the abbreviation

$$\gamma=D/hR \tag{3d}$$

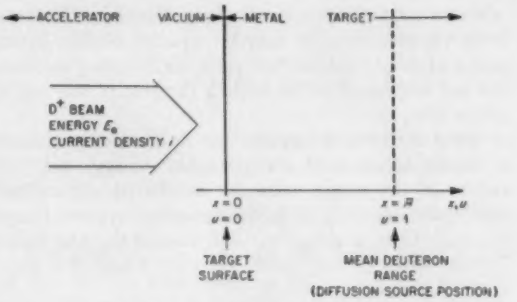

FIG. 1. The geometry of the diffusion model.

the boundary condition becomes

$$c(0,\vartheta)=\gamma\left(\frac{\partial c}{\partial u}\right)_{u=0}. \tag{3e}$$

Some justification of this condition is appropriate. The precise form which should be used depends upon the detailed path whereby deuterium escapes from the metal into the vacuum system. In writing Eq. (3c) it has been assumed that the pressure in the vacuum system is kept sufficiently low that return of deuterium to the target from the gas may be ignored. Other than this, it does not appear possible to make firm statements about the mechanism of escape of deuterium from the metal. Among the possible rate-controlling processes are the combination of deuterium atoms (presumably the diffusing species) into molecules, reaction of deuterium with surface layers on the metal (e.g., Cu_2O on Cu), and the process of desorption of deuterium or reaction products from the surface. All of these phenomena are known to be rate-controlling in one heterogeneous process or another. A general boundary condition might be written as

$$\frac{D}{R}\left(\frac{\partial c}{\partial u}\right)_{u=0}=a_1+a_2c(0,\vartheta)+a_3[c(0,\vartheta)]^2.$$

Unfortunately, the differential Eq. (1) cannot be integrated in useful form with so general a boundary condition as this, on account of the c^2 term. Hence, the present analysis is based on the approximation given in Eq. (3c). The parameter γ will be referred to as the "surface resistance."

If the Laplace transform of the differential Eq. (1) with respect to ϑ is integrated, with the source (2) and subject to the conditions (3), the solution is

$$\bar{c}(u,s)=\frac{iR}{2Ds^{\frac{1}{2}}}\exp(-s^{\frac{1}{2}})\left[\exp(s^{\frac{1}{2}}u)-\frac{1-\gamma s^{\frac{1}{2}}}{1+\gamma s^{\frac{1}{2}}}\exp(-s^{\frac{1}{2}}u)\right] \qquad 0\leqslant u\leqslant 1 \tag{4a}$$

$$=\frac{iR}{2Ds^{\frac{1}{2}}}\left[\exp(s^{\frac{1}{2}})-\frac{1-\gamma s^{\frac{1}{2}}}{1+\gamma s^{\frac{1}{2}}}\exp(-s^{\frac{1}{2}})\right]\exp(-s^{\frac{1}{2}}u) \qquad 1\leqslant u\leqslant\infty, \tag{4b}$$

where $\bar{c}(u,s)$ is the transform of $c(u,\vartheta)$ and s is the transform variable. Eq. (4) may be inverted readily by the use of standard tables,[9] but since the inverted solutions are not employed in the sequel, the results will not be given here.

Since the cross section for the $D(d,n)He^3$ reaction is a strong function of the deuteron energy, only the region of the target near the irradiated surface will contribute importantly to the measured neutron counting rate. Thus, it is legitimate to expand Eq. (4a) into a Taylor series in the space variable, about the point $u=0$. If the definitions

$$\bar{C}_n(s)=\frac{s^{n-\frac{1}{2}}}{1+\gamma s^{\frac{1}{2}}}\exp(-s^{\frac{1}{2}}) \tag{5}$$

are employed, the series may be written as

$$\bar{c}(u,s)=\frac{iR}{D}\sum_{n=0}^{\infty}\left[\frac{\gamma u^{2n}}{(2n)!}+\frac{u^{2n+1}}{(2n+1)!}\right]\bar{C}_n(s) \quad 0\leqslant u\leqslant 1. \tag{6}$$

The desired solution to the differential Eq. (1) is, therefore,

$$c(u,\vartheta)=\frac{iR}{D}\sum_{n=0}^{\infty}\left[\frac{\gamma u^{2n}}{(2n)!}+\frac{u^{2n+1}}{(2n+1)!}\right]C_n(\vartheta) \quad 0\leqslant u\leqslant 1, \tag{7}$$

where the $C_n(\vartheta)$ are the inverse Laplace transforms of the $\bar{C}_n(s)$. The first few $C_n(\vartheta)$ may be found from standard tables[9] and the rest from the recursion relation

$$C_n(\vartheta)=\frac{\partial}{\partial\vartheta}C_{n-1}(\vartheta). \tag{8}$$

Some additional relations, useful in numerical computations, are given in the Appendix.

B. The $D(d,n)He^3$ Cross Section

The total cross-section for the reactions $D(d,n)He^3+D(d,p)T$ obeys the well-known Gamow relation quite accurately, and the ratio of the two cross sections depends only weakly on the deuteron energy.[10] Thus, to a good approximation, the $D(d,n)He^3$ cross section may be written as:

$$\sigma(\epsilon)=\epsilon^{-1}\exp\left[-\frac{A}{E_0^{\frac{1}{2}}}\cdot\frac{1-\epsilon^{\frac{1}{2}}}{\epsilon^{\frac{1}{2}}}\right], \tag{9}$$

where $\epsilon=E/E_0$ is the relative deuteron energy, A is the Gamow slope, and the cross section is normalized to $\sigma(1)=1$. From experimental data on deuteron (or proton) energy loss rates, $(-dE/dx)$, ϵ can be determined as a function of the penetration of deuterons into a target and, hence, a function $\sigma(u)$ can be derived. Unfortunately, data on the slowing down of protons and deuterons in metals do not extend to sufficiently low energies for this procedure to be applied over the entire energy range, and recourse must be had to theory.

Below the limit of the experimental data, the Fermi-Teller relation[11] has been employed in the form

$$-dE/dx=BE^{\frac{1}{2}}, \tag{10}$$

where B is a constant. Integration of this expression yields

$$\begin{aligned}\epsilon&=(1-u)^2 \quad 0\leqslant u\leqslant 1\\ &=0 \quad 1\leqslant u\leqslant\infty,\end{aligned} \tag{11}$$

if Eq. (10) is assumed to apply over the entire deuteron energy range (as it certainly does not do). From Eqs. (9) and (11),

$$\begin{aligned}\sigma(u)&=(1-u)^{-2}e^{-ku/(1-u)} \quad 0\leqslant u\leqslant 1\\ &=0 \quad 1\leqslant u\leqslant\infty,\end{aligned} \tag{12}$$

where k would be $AE_0^{-\frac{1}{2}}$ if Eq. (10) were applicable for $0\leqslant E\leqslant E_0$. Eq. (12) cannot be expected to be especially accurate due to the inadequacy of Eq. (10), but if the parameter k is *empirically adjusted*, surprisingly good agreement can be obtained between values of $\sigma(u)$ based on Eq. (12) and values computed using experimental $(-dE/dx)$ data extrapolated to low energies by Eq. (10). Table I illustrates this agreement for 176 kev deuterons incident on Cu. The "empirical" values of $\sigma(u)$ were obtained by graphical integration of $(-dE/dx)$ vs E for $E\geqslant 100$ kev, using the "best" values recommended by Allison and Warshaw[12] for the slowing down of protons in Cu, coupled with use of Eq. (10) for $E<100$ kev. The integration produced values of the deuteron range, R, and of $\epsilon(u)$, from which the table was constructed using the theoretical Gamow slope.[10] Similarly gratifying agreement has been obtained both for the $D(d,n)He^3$ reaction and for the $Be^9(d,n)B^{10}$ reaction[13] with 176 kev deuterons incident on Be.

TABLE I. $D(d,n)He^3$ cross-section vs penetration into copper. Range (calc) = 1.63 μ. $AE_0^{-\frac{1}{2}}=3.347$. k (Eq. 12) = 3.2662.

u	E (kev)	$\sigma(u)$ "Empirical"	$\sigma(u)$ Eq. 12	u	E (kev)	$\sigma(u)$ "Empirical"	$\sigma(u)$ Eq. 12
0.00	176	1.000	1.000	0.50	45	0.147	0.153
0.05	160	0.934	0.933	0.55	37	0.088	0.091
0.10	145	0.863	0.860	0.60	29	0.043	0.047
0.15	130	0.783	0.778	0.65	22	0.017	0.019
0.20	115	0.691	0.691	0.70	16	0.007	0.005
0.25	100	0.590	0.598	0.75	11	0.001	0.001
0.30	88	0.500	0.503	0.80	7	0.000	0.000
0.35	76	0.403	0.408	0.85	4	0.000	0.000
0.40	65	0.313	0.315	0.90	2	0.000	0.000
0.45	55	0.228	0.228	0.95	1	0.000	0.000
0.50	45	0.147	0.153	1.00	0	0.000	0.000

[9] A. Erdelyi, Editor, *Tables of Integral Transforms*, Bateman Manuscript Project (McGraw-Hill Book Company, Inc., New York, 1954), Vol. I, pp. 245–247.

[10] W. R. Arnold, J. A. Phillips, G. A. Sawyer, E. J. Stovall, Jr., and J. L. Tuck, Phys. Rev. **93**, 483 (1954).

[11] M. Gryzinski, Phys. Rev. **107**, 1471 (1957); E. Fermi and E. Teller, *ibid.*, **72**, 399 (1947).

[12] S. K. Allison and S. D. Warshaw, Rev. Modern Phys. **25**, 779 (1953).

[13] D. C. Ralph and F. E. Dunham, Phys. Rev. **93**, 249 (1954).

It is convenient to define the integrals

$$B_n(k)=(k/n!)\int_0^\infty u^n\sigma(u)du. \tag{13}$$

Inserting Eq. (12), performing one integration by parts, and substituting $v=k/(1-u)$, Eq. (13) is transformed into

$$B_n(k)=\frac{e^k}{n!}\int_k^\infty\left(1-\frac{k}{v}\right)^n e^{-v}dv. \tag{14}$$

Straightforward integration produces

$$\begin{aligned}&B_0(k)=1\\&B_1(k)=1-ke^kE_1(k)\\&\quad\vdots\\&B_n(k)=\frac{[2(n-1)+k]B_{n-1}(k)-B_{n-2}(k)}{n(n-1)},\end{aligned} \tag{15}$$

where $E_1(k)$ is the exponential integral function

$$E_1(k)=\int_k^\infty v^{-1}e^{-v}dv.$$

Table II lists values of the first ten $B_n(k)$ for 176 kev deuterons incident on Cu. Their rapid decrease with increasing n reflects the rapid decrease in the $D(d,n)He^3$ cross section with increasing penetration of deuterons into the metal target.

C. The Neutron Counting Rate Function

The rate of production of neutrons from $D(d,n)He^3$ reactions in a target, which are detected by a counter, is

$$P(t)=iR\sigma_0AF\int_0^\infty\sigma(u)c(u,\vartheta)du, \tag{16}$$

where σ_0 is the nuclear reaction cross section at the incident deuteron energy, A is the cross-sectional area of the deuteron beam, and F is a factor describing the efficiency and geometry of the detector. Defining the scale factor

$$\alpha=i^2R^2\sigma_0AF\gamma/Dk, \tag{17}$$

and introducing Eqs. (7) and (12) into (16), after use of (13), there is obtained

$$P(t)=\alpha\sum_{n=0}^\infty[B_{2n}(k)+B_{2n+1}(k)/\gamma]C_n(\vartheta). \tag{18}$$

Table II. Cross-section integrals $B_n(k)$. $k=3.2662$.

n	$B_n(k)$	n	$B_n(k)$
0	1.00000000	5	0.00003808
1	0.20164399	6	0.00000313
2	0.03034879	7	0.00000023
3	0.00387268	8	0.00000002
4	0.00041135	9	0.00000000

Eq. (18) is fitted to experimental data by the method of least squares,[14] adjusting the three parameters α, γ, and

$$\delta=D/R^2. \tag{19}$$

It is of some interest to examine the asymptotic form of Eq. (18) for long times. As long as $\vartheta\gg\gamma/2$, the error functions in Eq. (A3) may be replaced by their asymptotic expansions,[15] while those in Eqs. (A1), (A2), and (A4) may be replaced by their convergent expansions.[15] Thus, for sufficiently long times, Eq. (18) may be approximated by

$$P(t\to\infty)=a-bt^{-\frac{1}{2}}+ct^{-1}-O(t^{-\frac{3}{2}}), \tag{20}$$

where

$$a=\alpha[B_0(k)+B_1(k)/\gamma], \tag{21a}$$

$$b=\frac{a(1+\gamma)}{\pi^{\frac{1}{2}}\delta^{\frac{1}{2}}}, \tag{21b}$$

$$c\cong\frac{a}{12\pi^{\frac{1}{2}}\delta^{\frac{1}{2}}}\{1+3\gamma[\gamma^2+(1+\gamma)^2]\}. \tag{21c}$$

A small contribution to Eq. (21c) from the functions $C_1(\vartheta)$ and $C_2(\vartheta)$ has been omitted. The usefulness of Eq. (20) is severely restricted since, in the region where the $t^{-\frac{1}{2}}$ term is significant, the condition $\vartheta\gg\gamma/2$ is already deficient. If γ were known to be $\ll1$, though, Eq. (20) would provide a rapid and easy method for determining δ from experimental data. A plot of $P(t)$ vs $t^{-\frac{1}{2}}$ becomes linear for sufficiently small values of the independent variable. From the slope and intercept of this line, using Eq. (21b), the value of δ could be derived. Use of this equation would also be independent of the assumptions made above regarding the form of the cross-section function.

III. EXPERIMENTAL PROCEDURE

The deuteron beam employed in the experiments was extracted from a conventional rf ion source, accelerated to 176 kev by a Cockroft-Walton generator set, and magnetically analyzed to select the D^+ (and H_2^+) component. Because of the considerable neutron background originating in the analyzing magnet, the beam was directed through a 10-ft-long drift tube and focused onto the target by an electrostatic lens. A liquid nitrogen cooled section was provided in the drift tube to prevent collection of organic materials on the target surface. This effectively eliminated the carbon deposits which

[14] See, for example, W. E. Deming, *Statistical Adjustment of Data* (John Wiley & Sons, Inc., New York, 1943), pp. 128–171.

[15] A. Erdelyi, Editor, *Higher Transcendental Functions*, Bateman Manuscript Project (McGraw-Hill Book Company, Inc., New York, 1953), Vol. II, p. 147.

had invariably appeared on the target surface before the cold section was introduced. The deuteron current was measured by making the target part of a Faraday cage, the collected current being passed to ground through a recording microammeter. The Faraday cage was provided with a guard ring maintained at about -250 v to prevent escape of secondary electrons. Measurements of current as a function of guard ring bias showed -60 v to be adequate to suppress the electron current. The cross-sectional area of the deuteron beam could not be defined by apertures close to the target because of the considerable neutron background from $D(d,n)He^3$ reactions occurring in the aperture material. This fact and the great length of the drift tube resulted in a rather poorer stability of the beam current than was really desirable. Several experiments were ruined by current changes apparently associated with movement of the beam within the drift tube.

The neutron detector consisted of a 20-in. cube of paraffin contained in an open aluminum can. Three proportional counters (1-in. diam by 5 in. long) were located on 3-in. centers in a plane 2 in. below the top surface of the paraffin. The counters were filled to 71 cm Hg pressure with $B^{10}F_3$. The three counters were connected in parallel through an AlD preamplifier and an AlD linear amplifier to a Berkeley model 7360 timer-scaler. The output of the scaler was recorded automatically on adding machine tape by a Berkeley model 1452 digital print-out unit. The scaler could be programmed to count for a specified interval of time (generally 1 sec), at the end of which the accumulated count was recorded and the scaler cleared to await the start of the next cycle. The time between print-out stages was generally about 10 sec. Since this time was variable with the temperature of the room and other factors, it was measured for each run by frequent comparison with an electric clock. The dead-time of the detector was found by the two-source method to be 4.33 μsec. The counter was so arranged with respect to the target that neutrons in the angular range (laboratory system, measured from the forward direction) 10° to 155° were detected. Slightly under half of the particles emitted in this range were within the view of the detector surface.

The targets were of three types. The majority were cut from a 0.050-in. thick rolled sheet of 99.999% Cu obtained from the American Smelting and Refining Company. One was a 0.050-in. thick single crystal grown from a melt of similar material. The remaining target was a 0.75-in. block of OFHC grade Cu. This latter target was cooled by flowing water running through channels drilled within it. The temperature was monitored by copper-constantan thermocouples cemented into wells drilled from the back of the target to within $\frac{1}{32}$ in. of the irradiated face. The other targets irradiated at 17° to 19°C were cooled by spraying water onto the back of the target, the temperature being monitored by thermocouples soft-soldered to the back of the target. Targets irradiated below room temperature were cooled by spraying the back of the target with ethanol circulated in a closed system. The ethanol was chilled by a dry ice-ethanol slush and then heated to the desired temperature by a small electric tube furnace. Temperature control was achieved by a Brown Air-o-line proportional controller actuated by one of the target thermocouples. The controller adjusted the voltage applied through a Variac autotransformer to the tube furnace. Temperatures were controlled to about ± 1°C except where noted.

The targets were prepared for irradiation by washing with soap and water, heated by dipping in hot water, etched briefly in 50% aqueous nitric acid, then rinsed in 5% nitric acid and distilled water. After completion of the irradiations, the diamond penetration hardness of each target was determined at a load of 1 kg on a Tukon microhardness tester.

After the series of experiments at 17° to 19°C had been completed, it was found necessary to move the Cockroft-Walton accelerator to another location. On account of major modifications made in the machine at this time, the pressure in the drift tube was lowered significantly in the new arrangement. The pressure at the target after modification of the accelerator was in the range of 5 to 10×10^{-6} mm Hg. The pressure at the target was not measured in the earlier experiments, but from the pressure at other points in the system it is estimated to have been about 1 to 3×10^{-4} mm Hg. The background pressure in the system without the ion beam was about 5×10^{-6} mm Hg. Hence, the arrival rate of background gas molecules, presumably air, was about 10^{15} cm^{-2} sec^{-1}. This is about twice the maximum rate of escape of deuterium from the target surface.

IV. ANALYSIS OF DATA

Each set of experimental data consisted of a list of numbers proportional to the neutron counting rate, obtained at equal intervals of time, from which it was desired to deduce the values of the three parameters: α, a scale factor; γ, the surface resistance; and δ, the scaled diffusion coefficient. The necessary operations were carried out by two digital computer programs.

The original data were transcribed from printed adding machine tape onto 7-channel punched paper tape which was used as input to a program performed on the ORACLE. This program corrected the observations for counter dead-time losses and for background and converted them to true counting rates. Two output tapes were produced. One of these was used in conjunction with a Moseley paper tape programmed x-y recorder to prepare plots of the experimental data. The other was used to transmit the observations to the second computer program. The contents of this paper tape were transcribed onto punched cards by an IBM 46 paper tape to card converter and then onto magnetic

tape which was used as input to a program carried out on an IBM 704 digital computer.

The IBM 704 program consisted of two parts. In the first, the asymptotic Eq. (20) was fitted to all but the first 128 points of the data set by the method of least squares. The data were then examined for points with residuals more than nine times the mean minimized residual of the set (the 99.73% confidence level). If such points were found, another least-squares fit of Eq. (20) was made, omitting the "bad" points. The entire procedure was repeated until the same number of points was rejected on two successive cycles. A typical rejected point may be seen in Fig. 3 at about 9000 sec. The number of points rejected in this way ranged from none (out of 297) to 29 (out of 1354). These points were generally associated with failure of the digital print-out unit to operate correctly. The parameters of Eq. (20) were then used to obtain preliminary estimates of the parameters α, γ, and δ. These estimates were not especially reliable, although α and the quantity $(1+\gamma)/\delta^{\frac{1}{2}}$ (see Eq. (21b)) were fairly accurately estimated. This unreliability results from failure of the approximation on which Eq. (20) is based just in the region where the $t^{-\frac{1}{2}}$ term is becoming significant.

The principal part of the IBM 704 program consisted of fitting Eq. (18) to the data using the method of least squares. The series in (18) was truncated after five terms, this being sufficient to obtain adequate convergence. Since Eq. (18) is nonlinear in the parameters γ and δ, repetitive application of least squares was required to obtain the best fit. The program allowed for varying any combination of the three parameters (with the others held constant) in order to avoid difficulties which often arise in nonlinear least-squares problems. The most important such difficulty encountered with Eq. (18) is concerned with the initial estimate of γ. If too small a value is chosen, the refinement invariably leads to a physically absurd negative result. This does *not* indicate that $\gamma=0$ is the best choice but merely that Eq. (18) is a multiple valued function of γ in the least-squares residual-parameter space.

Since the initial observations are necessarily integral, they are presumably samples of Poisson-distributed populations. For this reason, each observation $P(t)$ was assigned a weight $P^{-1}(t)$. These weights are the true ones only where the data were originally counts accumulated in 1 second but are proportional to the true ones otherwise. The effect of this weighting scheme is to emphasize the values at small times. Agreement of the computed curve with the observed set of data is expressed by an "agreement index"

$$R(\%)=100[\sum w(P_{\text{obs}}-P_{\text{calc}})^2/\sum wP_{\text{obs}}^2]^{\frac{1}{2}}, \quad (22)$$

where w is the weight of an observation, and the summations extend over all observations.

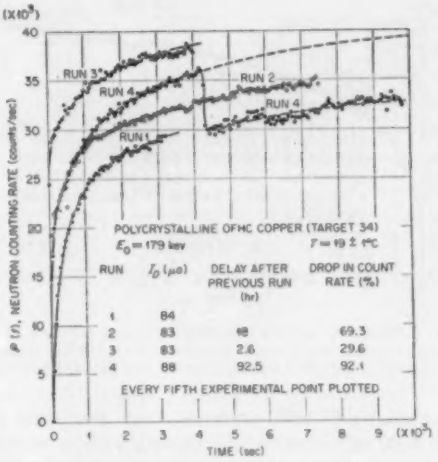

FIG. 2. Observed neutron counting rate as a function of time for the D(d,n)He^3 reaction in Cu. The four curves were obtained on successive runs on the same target.

V. EXPERIMENTAL RESULTS

In Fig. 2 are shown the experimental data obtained during four successive irradiations of a polycrystalline Cu target at 18°C. The data are not corrected for dead-time losses or for background. It may be seen from the curves that the initial counting rate is larger when the off-time of the beam is shorter, illustrating the continued diffusion of deuterium from the target when the beam is not on. The initial rate of rise of the curves is also greater when the off-time is smaller, showing that deuterium is still present within the metal. For times $>\sim 2000$ sec, the slopes of all four curves are about equal. The levels of the various curves are in the order expected from the off-times. The sudden drop in the counting rate at about 4200 sec of the fourth run is believed to be associated with a short period of elevated temperature which expelled some deuterium from the target. Both before and after this drop, the slope of the curve is about the same as in the other curves. An examination of Eq. (18) shows that during the first part of an irradiation the concentration gradient in the region $0\leqslant u\leqslant 1$ rapidly approaches linearity. After such linearity is achieved, the time-dependence of the counting rate results from an increase of the linear gradient due to the gradual filling up with deuterium of the region of the target $u>1$ and from the gradual increase of the concentration at the irradiated surface due to the surface resistance. These considerations satisfactorily explain the relationships of the curves in Fig. 2. It may be noted that the finding of deuterium loss in the absence of the beam agrees with the result of Arnold and Curtis[5] and is in contradiction to that of Fiebiger,[4] who reported no loss of deuterium after allowing his irradiated targets to remain for a week in vacuum.

In every experiment which has been performed, the

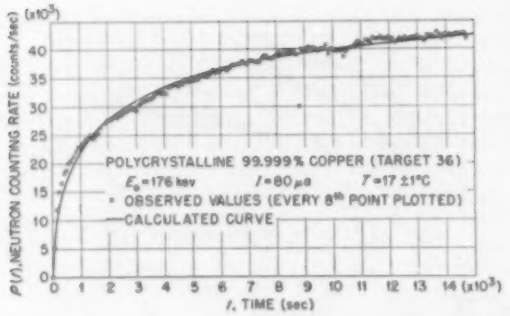

FIG. 3. Observed neutron counting rate as a function of time for a polycrystalline Cu target irradiated with 176 kev deuterons at 17°C. The solid curve was calculated from Eq. (18).

asymptotic Eq. (20) represents the long-time data ($t > \sim 1500$ sec) very well. In Table III are listed values of the parameter $\delta/(1+\gamma)^2$ obtained for a number of specimens of Cu irradiated at 17° to 19°C. The parameter varies over a range of more than a factor of 10, no correlation with the deuteron beam current or the properties of the individual targets being evident. This wide variation must be attributed in large measure to variations of the resistance of the target surfaces to escape of deuterium.

In Figs. 3 and 4 are shown the observed neutron counting rates (corrected for counter dead-time losses and for background) as functions of time for two targets irradiated at 17°C, one polycrystalline, the other a monocrystal. The solid curves were computed from Eq. (18). The agreement of the calculated curves with the observations is generally excellent. Near the knee of the curve for the polycrystalline target, Fig. 3, small systematic derivations occur between the calculated curve and the observations. This behavior is typical of polycrystalline targets. These systematic deviations appear to be absent in the monocrystal data.

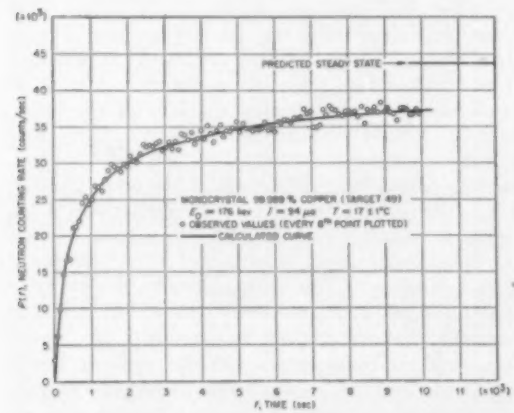

FIG. 4. Observed neutron counting rate as a function of time for a Cu monocrystal irradiated with 176 kev deuterons at 17°C. The solid curve was calculated from Eq. (18).

Table IV summarizes the parameters deduced from observations on several targets. The values of δ are plotted vs $1/T$ in Fig. 5, and those of δ/γ are plotted vs the beam current in Fig. 6. The uncertainties listed are standard deviations as estimated from the method of least squares.

VI. DISCUSSION

The model of the diffusion process developed above appears to provide a quite satisfactory explanation of the form of the neutron counting-rate vs time curves obtained in deuteron irradiations of copper. An attempt was made to improve the agreement of the calculated curves with the observations by including the "straggle" of the deuteron range[16] in the model. A detailed account of this attempt is given elsewhere.[17] It was found that assuming a straggling greater than about 5% of the mean range caused noticeably poorer agreement of the model with observation. This seems entirely reasonable on the basis of existing straggling data.[16] Since an assumed straggling of 5% led to diffusion parameters very close to those obtained when straggling was ignored, no further attempts have been made to include this effect in the model.

TABLE III. Diffusion parameter of deuterium in copper at 17° to 19°C from asymptotic analysis.

Target	$\delta/(1+\gamma)^2$(sec$^{-1}\times10^6$)	R(%)
34	1.93 ±0.26	0.80
36	0.364±0.004	1.00
41	0.429±0.011	3.94
47	0.472±0.021	2.36
49	1.16 ±0.08	2.03
51	0.133±0.005	3.68
55	0.938±0.084	3.78

It will be evident from Figs. 2–4 that no steady-state neutron counting rate is achieved in these irradiations, at least up to 1.5×10^4 sec (4.2 hr). This differs sharply from Fiebiger's work.[4] Since the neutron counting rates observed in the present work are about 100 times greater than Fiebiger's, it would appear that his "steady-states" result only from his inability to measure the small changes occurring in the counting rate for long times. This, in turn, led him to propose a diffusion model which is appropriate only for targets exactly two ranges thick, with no surface resistance at either face.

The data in Table IV show a remarkable correlation between the values of δ deduced from the observations and the DPH hardness of the polycrystalline samples at 18°C. The OFHC sample (Target 34) was much finer grained than the 99.999% samples, suggesting

[16] H. A. Bethe and J. Ashkin *in Experimental Nuclear Physics*, edited by E. Segre (John Wiley & Sons, Inc., New York, 1953), Vol. I, pp. 242–248.

[17] M. T. Robinson, A. L. Southern, and W. R. Willis, Oak Ridge National Laboratory Solid State Division Annual Progress Report for Period Ending August 31, 1959, U. S. Atomic Energy Commission Rept. ORNL-2829, pp. 97–109.

TABLE IV. Diffusion parameters of deuterium in copper.

Target	Hardness (DPH)	Beam current (μamp)	Temperature (°C)	α (cts/sec×10^{-4})	γ	δ (sec^{-1}×10^{2})	δ/γ (sec^{-1}×10^{2})	R(%)
34[a]	98±5	84	19±1	3.70±0.04	1.58±0.10	1.32 ±0.07	8.44±0.71	2.75
36[b]	48±2	80	17±1	5.36±0.02	7.48±0.31	2.54 ±0.15	3.40±0.24	3.17
47[b]	52±1	137±3	18±1	5.37±0.04	3.13±0.23	2.46 ±0.21	7.85±0.89	4.79
49[c]	37±2	94	17±1	3.67±0.01	1.04±0.02	0.580±0.013	5.59±0.18	2.59
55[b]	91±25	49	17±1	2.54±0.02	8.46±0.79	1.03 ±0.44	1.22±0.53	5.36
70[b]	44±1	82	−26±1	4.22±0.04	1.69±0.11	1.40 ±0.09	8.32±0.75	6.92
71[b]	48±2	81	−34±2	5.15±0.07	2.58±0.20	1.05 ±0.08	4.06±0.44	4.77
73[b]	47±3	80	−46±1	5.59±0.03	2.69±0.12	0.536±0.020	1.99±0.11	3.43

[a] OFHC grade, 0.750-in. thick polycrystalline.
[b] 99.999% Cu, 0.050-in. thick polycrystalline.
[c] 99.999% Cu, 0.050-in. thick monocrystal; irradiated surface lay 8.5° from (311).

that both the hardness of this sample and the low diffusion coefficient result from segregation of impurities in the grain boundaries or other imperfections. The wide range of hardness listed for Target 55 is real. Twelve values obtained on this target varied from about 80 to about 130 DPH. We are at a loss to understand this variation but feel that it probably resulted from chemical contamination of the target (most likely oxidation) at some stage in its handling.

The very low diffusion coefficient obtained for the monocrystal suggests that the diffusion of deuterium in polycrystalline copper in the region near room temperature proceeds mainly along grain boundaries or related imperfections. This grain boundary diffusion may be reduced by the presence of impurities as seems to have occurred with the OFHC sample. From the values for the five "soft" polycrystalline targets, the activation energy for diffusion of deuterium in copper is estimated to be 0.12±0.02 ev/atom (2.8±0.5 kcal/mole). The curve in Fig. 5 shows the calculated dependence of δ on temperature with its estimated standard deviation. In view of its considerable uncertainty, there seems to be no point in attempting to interpret the preexponential factor. The right-hand scale of Fig. 5 indicates the values of D, the diffusion coefficient, obtained using a deuteron range of 1.62 μ.

Values of the mass transfer film coefficient δ/γ [cf. Eq. (3d)] are plotted against the deuteron beam current for the 18±1°C runs in Fig. 6. (Actually, the current density should be used as abscissa, but since the diameters of our beams were roughly independent of current the distinction is of secondary importance.) The plot shows that for $I>30$ μamp, δ/γ is approximately proportional to the current. No correlation with crystallinity or hardness is evident. The deviation of the OFHC sample is probably due to a different beam diameter or to different vacuum conditions resulting from the different sample holder employed during its irradiation. There is a possibility (see Table IV) that δ/γ is strongly temperature dependent, but on account of the major changes made in the accelerator between the running

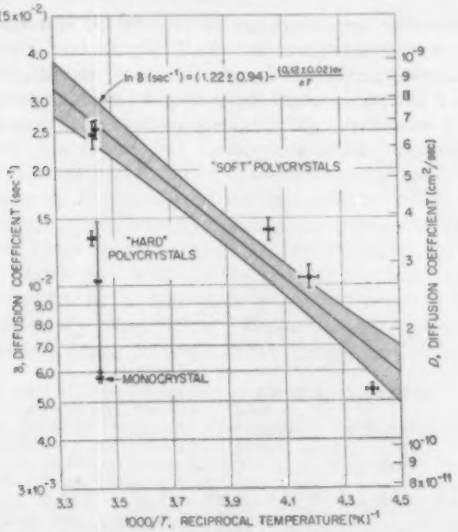

FIG. 5. The diffusion coefficient δ as a function of of reciprocal temperature.

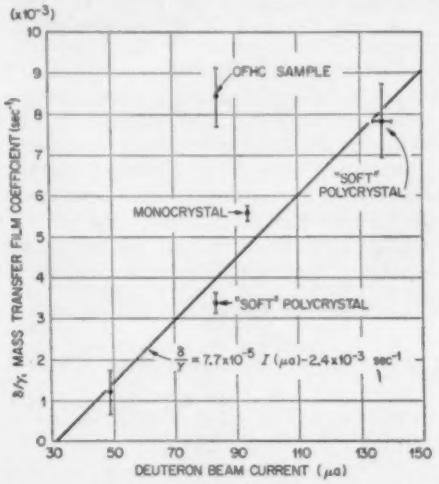

FIG. 6. The mass transfer film coefficient δ/γ as a function of deuteron beam current at 18±1°C.

of the 18°C experiments and the low temperature ones little certainty can be placed in this.

It seems inappropriate to speculate on the nature of the surface resistance observed on these Cu specimens, other than to suggest that it may well be due to the presence of the very thin (~50 A) oxide film which certainly is present on them. Rather, future work must take the direction of attempting to remove the resistance in order to avoid the necessity of the elaborate analysis required of our present data.

The magnitudes of the diffusion coefficients and the activation energy deduced from our data are reasonable. For comparison, it may be noted that the diffusion coefficient of hydrogen in iron at room temperature is about 2×10^{-9} cm^2/sec, some five times greater than is found here for polycrystalline copper. The activation energies reported for diffusion of hydrogen in Ni and Fe are 8.7 and 9.2 kcal/mole, respectively.[3]

VII. ACKNOWLEDGMENTS

The assistance of P. B. Wood, W. D. Plengey, E. B. Carter, and Gladys Walker of the Oak Ridge Gaseous Diffusion Plant Central Data Processing Facility with with the writing of IBM 704 programs and their execution is gratefully acknowledged. R. L. Tanner assisted in the early stages of the experimental program. The authors are indebted to several of their colleagues, especially F. W. Young, Jr., D. K. Holmes, and H. C. Schweinler, for many helpful discussions. The hardness measurements were made by E. J. Manthos. The Cu single crystal was grown by L. H. Jenkins. The neutron detector was based on a design suggested by P. R. Bell of the ORNL Thermonuclear Experimental Division.

VII. APPENDIX

Numerical Evaluation of the $C_n(\vartheta)$

From the definition of the $\bar{C}_n(s)$, Eq. (5), using standard tables,[9] the first two $C_n(\vartheta)$ are found to be

$$C_0(\vartheta)=\operatorname{erfc}(1/2\vartheta^{\frac{1}{2}})-W(\vartheta), \tag{A1}$$

$$C_1(\vartheta)=(1/2\nu\vartheta^{\frac{1}{2}})\operatorname{erf}'(1/2\vartheta^{\frac{1}{2}})-(1/\gamma^2)W(\vartheta), \tag{A2}$$

where

$$W(\vartheta)=\frac{\operatorname{erf}'(1/2\vartheta^{\frac{1}{2}})\operatorname{erfc}[(1/2\vartheta^{\frac{1}{2}})+(\vartheta^{\frac{1}{2}}/\gamma)]}{\operatorname{erf}'[(1/2\vartheta^{\frac{1}{2}})+(\vartheta^{\frac{1}{2}}/\gamma)]}, \tag{A3}$$

and the error functions are defined by

$$\operatorname{erfc}x=1-\operatorname{erf}x=2\pi^{-\frac{1}{2}}\int_x^\infty \exp(-u^2)du$$

$$\operatorname{erf}'x=\frac{d}{dx}\operatorname{erf}x=2\pi^{-\frac{1}{2}}\exp(-x^2).$$

The remaining $C_n(\vartheta)$ may be found from the recursion relationships

$$C_n(\vartheta)=\frac{1}{\gamma^2}C_{n-1}(\vartheta)+\frac{1}{4\gamma\vartheta^{\frac{1}{2}}}\left[\frac{1}{\gamma}X_n(\vartheta)+Y_n(\vartheta)\right]\operatorname{erf}'\frac{1}{2\vartheta^{\frac{1}{2}}}, \tag{A4}$$

where

$$X_n(\vartheta)=1/2\vartheta[Y_{n-1}(\vartheta)-2(n-1)X_{n-1}(\vartheta)] \quad n\geq 3 \tag{A5}$$

$$Y_n(\vartheta)=1/2\vartheta[X_n(\vartheta)-(2n-1)Y_{n-1}(\vartheta)] \quad n\geq 3 \tag{A6}$$

$$X_2(\vartheta)=1 \tag{A7}$$

$$Y_2(\vartheta)=(1/2\vartheta)-1. \tag{A8}$$

These relations lend themselves to ready evaluation on electronic digital computers. In applying the method of least squares to the data fitting problem, it is also necessary to compute $\partial C_n(\vartheta)/\partial\vartheta$ and $\partial C_n(\vartheta)/\partial\gamma$. From Eq. (18) it follows that

$$[\partial C_n(\vartheta)/\partial\vartheta]=C_{n+1}(\vartheta).$$

The other derivatives can be constructed in a manner similar to that given for the $C_n(\vartheta)$. In fact, the two recursion procedures for the $C_n(\vartheta)$ and the $\partial C_n(\vartheta)/\partial\gamma$ may be very conveniently arranged into a single iterative procedure, which is very easily carried out on a high speed digital computer.

Simple Theory Concerning the Reflection of Electrons from Solids

T. E. EVERHART*
Engineering Laboratory, University of Cambridge, Cambridge, England
(Received March 15, 1960; and in final form April 29, 1960)

A simple theory concerning the reflection of electrons from solid targets is derived, based on the following assumptions: (1) the primary cause of electron reflection from a solid material is Rutherford scattering through angles greater than 90°; (2) the energy loss of electrons penetrating a solid target is given by the Thomson-Whiddington law, or a modified version of it; (3) no multiple scattering is allowed. An expression for the reflection coefficient r is derived that agrees surprisingly well with experimental data, in view of the above simplifying assumptions. In particular, the correct variation of r with atomic number Z is obtained, and the observed value of the fractional escape energy is calculated in the limit as $Z \to 0$, where the theory is most accurate. A critical discussion of the simplifying assumptions is given, and the range of validity of the theory is estimated. This theory leads to a better understanding of the related phenomena of secondary emission at primary electron energies between 2 and 50 kev.

1. INTRODUCTION

WHEN an electron beam impinges on a plane target, the electrons that emerge from the target may be divided into two groups, secondary electrons and reflected electrons. The secondary electrons typically have energies of only a few volts, and for purposes of measurement are usually taken as all electrons with energies less than 50 v. The reflected electrons have energies between 50 v and the primary energy, which in this paper will be taken to be at least several hundred volts. As is customary, the secondary-emission coefficient δ is defined as the ratio of the total electron current leaving the target to the primary electron current striking the target. Thus δ has two components: δ_s, the ratio of the secondary electron current leaving the target to the primary electron current striking the target; and r, the ratio of the reflected electron current leaving the target to the primary current striking the target. It follows that $\delta = r + \delta_s$.

Secondary electrons have been the subject of several theories[1-3]; a simple theory of secondary emission (which may be found in Dekker[4]) successfully predicts how the number of secondary electrons varies with primary-beam energy for any plane metal target. Jonker[5] has shown that clean plane metal targets do exhibit a universal variation of secondary emission with primary-electron energy, if the experimental values of the secondary emission coefficient δ and primary energy E_0 are correctly normalized. The experimental curve agrees fairly well with the theoretical curve when the primary-electron energy E_0 is below that required for maximum secondary emission $E_{0_{max}}$. ($E_{0_{max}}$ is typically between 200 and 1000 v.) Above the primary energy required for maximum secondary emission, theory predicts that δ should decrease with increasing E_0 more quickly than experiments indicate.

The above theories of secondary emission totally neglect the reflected electrons, although recently Dobretsov and Matskevich[6] have made an attempt to improve this situation. However interest in reflected electrons has been increasing, with published experimental work by Sternglass,[7] Holliday and Sternglass,[8] Kanter,[9] and Matskevich[10] within the last few years. These papers verify and extend earlier work by Palluel[11] and others. (Sternglass[7] gives a comprehensive list of references to earlier theoretical and experimental work on this subject.) The experiments show that the fraction r of the primary electron current that is reflected from a plane target is virtually independent of the primary-beam energy over a wide energy range. For elements of of atomic number $Z \leqslant 30$, the energy range extends from about 200–500 ev at the low end to a few hundred kev at the high end. For elements of atomic number $Z \geqslant 30$, the lower limit is increased somewhat, but even for the heaviest elements, it lies below 5 kev.[12] In this wide primary energy range, where the reflection coefficient r is practically constant for a given target, it is found to depend primarily on the atomic number of the target material Z, increasing with Z. It is also a function of the angle between the primary beam and the normal to the target surface, increasing as this angle increases.

It is somewhat surprising that little theoretical consideration has been given to the reflected electrons. A diffusion theory by Bothe[13] has been proposed for primary electrons of very high energy, but for lower

* Present address: Department of Electrical Engineering, University of California, Berkeley 4, California.

[1] H. Bruining, *Physics and Applications of Secondary Electron Emission* (Pergamon Press Ltd., London, 1954).

[2] K. G. McKay, *Advances in Electronics I*, 66 (Academic Press, Inc., New York, 1948).

[3] A. J. Dekker, *Solid State Physics Vol. VI* (Academic Press, Inc., New York, 1958), pp. 251–311.

[4] See footnote reference 3, p. 263.

[5] J. L. H. Jonker, Philips Research Repts. **9**, 391 (1954).

[6] L. N. Dobretsov and T. L. Matskevich, Soviet Phys.—Tech. Phys. **2**, 663 (1957).

[7] E. J. Sternglass, Phys. Rev. **95**, 345 (1954).

[8] J. E. Holliday and E. J. Sternglass, J. Appl. Phys. **28**, 1189 (1957).

[9] H. Kanter, Ann. Physik **20**, 144 (1957).

[10] T. L. Matskevich, Soviet Phys.—Tech. Phys. **2**, 255 (1957).

[11] P. C. R. Palluel, C. R. Acad. Sci. Paris **224**, 1492 and 1551 (1947).

[12] See footnote reference 7, Fig. 7.

[13] W. Bothe, Z. Naturforsch. **4a**, 542 (1949); Ann. Physik **6**, 44 (1949).

energies this theory seems to be inappropriate. Dobretsov and Matskevich[6] make an attempt at this problem, but their assumption that the most probable direction of reflection is back toward the source is in disagreement with Kanter.[9] The present paper presents a highly simplified analysis of this extremely complicated subject, the reflected electrons. The theory presented here parallels the simple theories of secondary emission, and is based on the same assumptions.

Table of Symbols

A gram atomic weight
E electron energy, measured in joules or electron volts
E_e escape energy of electron leaving target
E_i K shell ionization energy, ev
E_0 initial electron energy (before striking target)
I mean excitation energy, ev
N number of atoms in a unit target volume (dimensionless)
N_A Avogadro's number (6.023×10^{23} atoms/mole)
P scattered intensity/unit solid angle due to Rutherford scattering (dimensionless)
R range of primary electrons in target material, cm
S unit of area used in Rutherford scattering formula, cm^2
Z atomic number
a dimensionless constant introduced to simplify equations in theory
a_0 $\hbar^2/me^2=0.528\times10^{-8}$ cm
b constant defined in text: dimensions are cm^5/g sec^3
c constant in Thomson-Whiddington law: dimensions are cm^6/g sec^4
e electronic charge: 4.8×10^{-10} esu
$i(y)/i_0$ ratio of electron beam current at depth y to initial electron beam current (dimensionless)
k fractional energy of reflected electrons (dimensionless)
$\bar{k}$ mean fractional energy of reflected electrons (dimensionless)
m electronic mass: 9.1×10^{-28} g
n_0 electron density/S sq cm: dimensions, cm^{-2}
r reflection coefficient
r' nuclear radius, cm
s distance between nucleus and initial electron direction, cm
v electron velocity, cm/sec
v_0 initial electron velocity, cm/sec
x distance coordinate, cm
y fractional range, x/R (dimensionless)
δ secondary-electron coefficient
θ supplement of deflection angle
θ_0 maximum value of θ for given depth of reflection
ρ density, g/cm^3
ϕ angle of deflection
$\bar{\phi}$ mean angle of deflection

Note: cgs electrostatic units are used in this paper, with the exception that the electron volt is often used as a unit of energy.

2. CALCULATION OF REFLECTION COEFFICIENT r

A high-energy electron passing through matter loses energy primarily through inelastic collisions with atomic electrons. The variation of electron velocity v with distance x traveled in the target is given by the Thomson-Whiddington law as

$$v^4=v_0^4-c\rho x=c\rho(R-x), \tag{1}$$

where v_0 is the initial electron velocity, c is assumed constant, ρ is the target density, and R is the range of electrons in the target material, i.e., the value of x when $v=0$,

$$R=v_0^4/c\rho. \tag{2}$$

The Thomson-Whiddington law, derived by Thomson[14] in 1906 is discussed in the light of more recent knowledge in Sec. 4.

Large-angle scattering of high-energy electrons passing through matter is assumed to result from elastic collisions between the electrons and atomic nuclei. Massey and Burhop[15] show that the Rutherford scattering formula is valid when electrons with energies greater than a few hundred volts are elastically scattered by inert gas molecules through angles greater than about 20°. Section 5 assesses the minimum voltage consistent with the Rutherford theory. For a 135° deflection, the minimum incident electron energy for aluminum is about 170 ev; for gold, about 1900 ev.

The Rutherford formula predicts that if n_0 electrons per S sq cm are incident on a bare nucleus of charge Ze, the scattered intensity per unit solid angle is

$$P(\phi)=(n_0Z^2e^4/4S\hbar^2v^4)[1/\sin^4(\phi/2)], \tag{3}$$

where ϕ is the angle of deviation of the scattered electron, and e and m are the electronic charge and mass, respectively. Equation (3) must be multiplied by dN, the number of atoms present in the incremental target volume considered. If this volume consists of an area of S sq cm and is dx cm thick, then

$$dN=N_A\rho Sdx/A, \tag{4}$$

where N_A is Avogadro's number, and A is the gram atomic weight of the target material.

Substituting Eq. (1) into Eq. (3), multiplying by Eq. (4) and for future convenience, writing the distance variable as the fractional range $y=x/R$, the incremental

[14] J. J. Thomson, *Conduction of Electricity Through Gases* (Cambridge University Press, Cambridge, England, 1906), 2nd ed.
[15] H. S. W. Massey and E. H. S. Burhop, *Electronic and Ionic Impact Phenomena* (Oxford University Press, London, 1952), pp. 128–130.

number of electrons at depth y deflected through an angle $\phi=\pi-\theta$ into the incremental solid angle $2\pi\sin\theta d\theta$ may be written in terms of y and θ as

$$dn(y,\theta)=\frac{Z^2e^4N_A}{4m^2cA}\frac{n_0(y)dy}{(1-y)}\frac{2\pi\sin\theta d\theta}{\cos^4(\theta/2)}, \tag{5}$$

where $n_0(y)$ is the number of electrons incident on a plane at depth y in the target,

$$n_0(y)=n_0-\int_0^y\int_0^{\pi/2}dn(y,\theta). \tag{6}$$

Because many incident electrons are deflected through angles smaller than $\pi/2$, the angle of incidence on a plane at depth y is not well defined. It is implicitly assumed in Eqs. (5) and (6) that all electrons not deflected through angles greater than $\pi/2$ have not been deflected at all, and therefore, when Eq. (5) is integrated to give the reflection coefficient r, a value somewhat smaller than is observed experimentally should be expected, since the probability of reflection increases somewhat as the direction of electron motion departs from the incident-beam axis. Integration of Eq. (6) over θ gives

$$n_0(y)=n_0-a\int_0^y n_0(y)dy/(1-y), \tag{7}$$

where

$$a=\pi Z^2e^4N_A/m^2cA. \tag{8}$$

Since Z/A is nearly constant for different target materials, a is very nearly proportional to Z. Solution of Eq. (7) for $n_0(y)$ yields

$$n_0(y)=n_0(1-y)^a, \tag{9}$$

which allows the incremental value of r to be written as

$$dr(y,\theta)=\frac{dn(y,\theta)}{n_0}=\frac{a}{2}(1-y)^{a-1}dy\frac{\sin\theta d\theta}{\cos^4(\theta/2)}. \tag{10}$$

The limits of integration must now be chosen. In Fig. 1, the total distance traveled by an electron reflected at depth x through an angle ϕ is $(x+x\sec\theta)$. This distance must be less than the range R, or the electron will not escape from the target. The limits of the θ integration are therefore 0 and θ_0, where θ_0 is found from the relationship

$$y(1+\sec\theta_0)=1; \tag{11}$$

y then varies between 0 and $\frac{1}{2}$. Integrating over θ first, and then y, we find the equation for r is

$$r=(a-1+0.5^a)/(a+1). \tag{12}$$

This expression predicts that r is independent of primary-electron energy, and depends only on the position of the target material in the periodic table. This result agrees well with experimental observation.

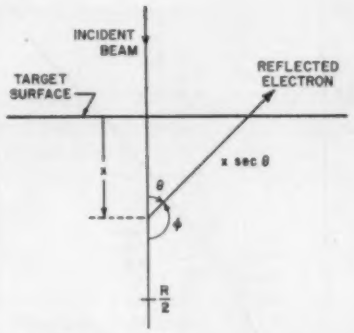

FIG. 1. Idealized electron path in target, illustrating variables discussed in the text.

So far, only one large-angle reflection has been allowed. A certain fraction of the electrons reflected back toward the target surface experience a second large-angle deflection, and do not escape from the target. Hence the predicted variation of r vs Z should increasingly exceed the measured variation as Z becomes large, because the correction owing to these second reflections becomes more important as Z increases. These second reflections are neglected in this simple theory (as are third- and higher-order reflections).

3. COMPARISON OF THEORY WITH EXPERIMENT

Equation (12) shows that r is a function only of a, which in turn is a function of the atomic number Z, fundamental constants, and the constant c from the Thomson-Whiddington law. The generally accepted value of c is 5.05×10^{12} cm^6/g sec^4, and results from careful measurements by Terrill[16] of the *most probable* exit velocity of an electron beam that had penetrated a foil of given thickness.

In Fig. 2, two curves of r vs Z are shown; the lower curve was computed by using Terrill's value of c, and the upper curve was computed by adjusting the value of c to obtain the best fit with experimental results. The qualitative agreement between the upper curve and experiment is surprisingly good, in view of the simplified approach.

It is tempting at this point to find reasons why Terrill's constant does not give the correct magnitude for the reflection coefficient. Alternatively, we might wonder why such good qualitative agreement is obtained when the problem has been so oversimplified. First, the velocity-spread of the electrons penetrating the target has been totally neglected; this spread can become appreciable even after a foil thickness of $0.1R$ has been traversed. Second, the angular distribution of the primary electrons caused by both inelastic collisions has been ignored. Clearly, if the distribution function which represents the velocity spread and angular dis-

[16] H. M. Terrill, Phys. Rev. **22**, 101 (1923).

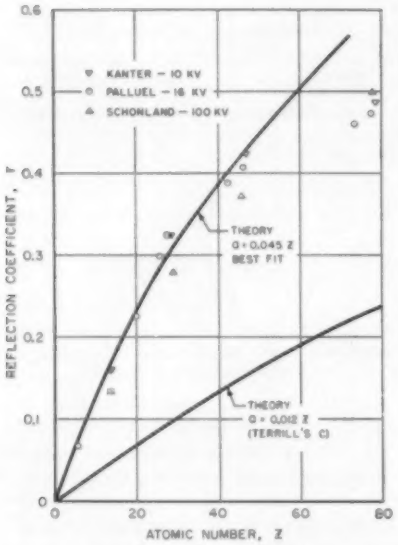

FIG. 2. Reflection coefficient r vs atomic number Z; comparison of theory with experiment.

tribution in velocity of electrons penetrating a solid were known, a much better treatment of this problem would be possible. Without this knowledge, the present simple treatment, plus insights gained from experimental results, seems a reasonable first step.

Terrill shows two curves that are pertinent here. Both are curves of electron intensity emerging from a thin-foil vs the energy of these transmitted electrons for a constant primary electron energy. For values of $t/R \approx 0.3$, the *most probable* transmitted electron energy is well above the *mean* transmitted electron energy. However, for $t/R \sim 0.6$, the *most probable* and *mean* electron energies are much closer together. In both cases, a large spread in the energies of the transmitted electrons is apparent. In the first case, for the thinner foil, note that the most electrons have energies (velocities) below that predicted by the Thomson-Whiddington law. From Eq. (3), there is therefore a greater probability of reflection for the average electron, and since most electrons reflected near the target surface escape, a greater number of reflected electrons is obtained in this case; i.e., the velocity spread causes r to be larger than predicted by the simple theory. In the second case, for the thicker foil, the wide energy spread and nearly symmetric distribution about the most probable energy (now lower since more of the primary energy has been lost) means that there are many primaries with energies considerably greater than the Thomson-Whiddington value, and which have sufficient energy therefore to escape the target if reflected from this deep inside the target. Once again, the velocity spread causes r to be larger than predicted above from the simple theory using Terrill's constant.

A third source of error, particularly for heavier atoms, becomes apparent when multiple large-angle elastic collisions are allowed. A second large-angle collision suffered by an electron traveling toward the target face reduces the value of r, for example. These second collisions are more numerous for heavier atoms, for the same reason that first elastic collisions occur more often in the heavier atoms. The most likely effect of second collisions, therefore, is to reduce the value of r at the larger values of Z, where the greatest discrepancy in the form of the curve in Fig. 2 exists.

4. THOMAS-WHIDDINGTON LAW

The Thomson-Whiddington law gives a simple relationship between the most probable velocity of an electron penetrating a solid target in terms of the electron's initial velocity, the distance traveled through the target, and the target density [see Eq. (1)]. This law can be derived from the energy loss per unit distance of a nonrelativistic electron which results from a quantum-mechanical treatment,[17,18] and is stated by Birkhoff[19] to be

$$-\frac{dE}{dx}=\frac{4\pi N_A e^4 Z\rho}{mv^2 A}\ln\left(\frac{mv^2}{I}\right), \tag{13}$$

where E is the electron energy at depth x, and I is a mean excitation energy. Taking the energy as $mv^2/2$, this relationship may be written in terms of velocity

$$2v^2 d(v^2)=-\frac{16\pi N_A e^4 Z\rho}{m^2 A}\ln\left(\frac{mv^2}{I}\right). \tag{14}$$

The mean excitation energy I is constant only if the energy of the impinging electron is substantially greater than the K-shell ionization energy, which is given approximately by the following modified form of Moseley's law

$$E_i=11.3(Z-1)^2 \text{ ev}. \tag{15}$$

Typical values of E_i for various elements are shown in Table I. If the electron energy E is of the order E_i or lower, I decreases as E decreases. If this decrease is assumed to be *linear*, then Eq. (14) may be integrated to

$$v^4=v_0^4-\left[\frac{16\pi N_A e^4 Z\rho}{m^2 A}\ln(\text{const})\right]x. \tag{16}$$

This is exactly the Thomson-Whiddington law. Since Z/A is roughly constant, the coefficient of x varies mainly with the density, as Terrill found experimentally. The above derivation points out the assumptions necessary for this law to hold.

[17] R. D. Birkhoff in *Handbuch der Physik*, edited by E. Flügge (Springer, Berlin, 1958), Vol. 34, p. 53.
[18] A. Nelms, Natl. Bur. Standards Circ. **No. 577**, 1 (1956).
[19] See footnote reference 17, Eq. (7.10).

TABLE I.

Element	Z	E_i (kev)
Carbon	6	0.28
Aluminum	13	1.6
Copper	29	8.8
Silver	47	24
Gold	79	69

The order of magnitude of the constant in the logarithmic term may be evaluated as follows: I cannot reach its maximum and constant value if $E<E_i$, and therefore if a linear relationship is assumed, the constant of proportionality may be set equal to I_{max}/E_i. This factor varies somewhat for different materials, but a mean value is about 0.1. Thus for $E<E_i$,

$$I\sim 0.1E. \tag{17}$$

The constant in the logarithmic term is therefore of the order of 20, and $\ln 20\approx 3$. The calculated value of c from the bracketed term in Eq. (16) then is about 3×10^{12}, which is within a factor of 2 of Terrill's value of 5.05×10^{12}. Thus this rough evaluation of c results in a reasonable number.

If the electron energy E is much greater than I, the logarithmic term increases slowly with E and the validity of Eq. (16) is questionable. The early experiments of Whiddington[20] and Terrill[16] seemed to verify the Thomson-Whiddington law, and the range-energy relation derived from it, $R\propto E_0^2\propto v_0^4$, follows the experimental curve of Katz-Penfold[21] over the energy range $10\text{ kev}\leqslant E_0\leqslant 100$ kev. However, Lane and Zaffarano[22] and Young[23] have more recently found range-energy relations with powers less than 2. By measuring the energy of electrons that had passed through thin films of Al_2O_3, Young deduced the range-energy relation to be $R\propto E_0^{1.35}$, for the energy range $2.5\text{ kev}\leqslant E_0\leqslant 10$ kev. Note that the lowest primary energy is greater than the K-shell ionization energy of either aluminum or oxygen. The low value of the exponent in this case may be due to the restricted angular range of the electrons measured; only those with velocities nearly parallel to the incident beam passed through the collimating aperture into the velocity analyzer.

Because of these recent observations, it is of qualitative interest to determine how the equation for r is modified if R is proportional to $E_0^{1.5}$, for example, instead of E_0^2. The Thomson-Whiddington law can be easily modified in this case by assuming that $c=bv_0$, where b is a constant. Equation (1) becomes

$$v^4=v_0^4-bv_0\rho x=bv_0\rho R(1-y), \tag{18}$$

where R is now defined as

$$R=v_0^3/b\rho\propto E_0^{1.5}, \tag{19}$$

and y is defined as x/R as before. If the calculations of Sec. 4 are repeated, the same answer is obtained except that a now involves v_0,

$$a=\frac{\pi Z^2e^4N_A}{m^2Abv_0}. \tag{20}$$

Thus in this case a and r decrease as v_0 increases. An experimental curve published by Palluel[11] shows that in the case of carbon, r decreases from 0.1 to 0.075 as the incident energy increases from 4 to 16 kev. According to Sternglass[7] r is constant below 5 kev for carbon. Thus the observed decrease starts well above the K-shell binding energy, and can be qualitatively understood by this modification of the theory. For elements of $Z\geqslant 20$, Palluel observed no decrease as E_0 increased to his maximum value of 16 kev, but if values of r found at 10 kev and 100 kev are compared (see Fig. 2) the higher energy values of r are almost always lower (the only exceptions being for elements of very high atomic number, with K-shell binding energies greater than 50 kev).

Young also measured the fraction of the primary beam current transmitted through foils of different thicknesses and observed an almost linear decrease in current as the foil thickness increased. This result is in sharp disagreement with the exponential law usually associated with absorption, but agrees fairly well with Eq. (9).[24] Since the current, $i(y)$, at depth y and the incident current i_0 are proportional to $n_0(y)$ and n_0 respectively, the fraction of the incident current transmitted through a foil of thickness y is

$$i(y)/i_0=(1-y)^a. \tag{21}$$

If the value of c that gives the best agreement between theory and experiment in Fig. 2 is used, and the effective atomic number of Al_2O_3 is taken as 10, giving $a=0.45$, a theoretical curve of $i(y)/i_0$ vs y is obtained that agrees fairly well with Young's experimental curve.[25]

The stopping power of conduction electrons in metals has not been included in this treatment because Holliday and Sternglass[8] have shown that the variation of r with Z is obeyed by insulators as well as metals; a stopping power applicable to both is therefore indicated.

[20] R. Whiddington, Proc. Roy. Soc. (London) **A89**, 554 (1914).
[21] L. Katz and A. S. Penfold, Revs. Modern Phys. **24**, 28 (1952).
[22] R. O. Lane and D. J. Zaffarano, Phys. Rev. **94**, 960 (1954).
[23] J. R. Young, J. Appl. Phys. **28**, 524 (1957).

[24] The reason why this theory does not predict an exponential absorption law should be made clear. An exponential law results if the probability of reflection remains constant with distance in the target material. However, this probability increases as the electron velocity decreases [Eq. (3)], and thus an exponential absorption law is not expected. However, if only the electrons that have lost no energy are considered on the exit side of the foil, then an exponential law would be expected, for the probability of both reflection and energy-loss per unit path length remains constant with x.

[25] See footnote reference 23, Fig. 3.

5. RUTHERFORD SCATTERING OF HIGH-ENERGY ELECTRONS

A short discussion of Rutherford scattering of kilovolt-energy electrons will indicate the minimum energy for which the above results are expected to be valid. Massey and Burhop[26] show that when a beam of electrons with energies of several hundred electron volts is scattered by an inert gas, the scattered intensity for elastic collisions is correctly predicted by the Rutherford scattering formula, for angles of deviation greater than about 20°. When this formula is applied to a solid material, it is necessary to estimate the minimum electron energy for which it may be expected to be valid.

Let a nucleus of charge Ze esu be at the origin, and let s be the minimum distance between the nucleus and the initial direction of an electron with energy E electron volts. Since the electron trajectory is one branch of a hyperbola with the nucleus at one of the foci, s is also the minimum distance between nucleus and asymptote. If the electron is deflected through an angle $\phi=180°-\theta$,

$$s=(150Ze/E)\tan(\theta/2), \tag{22}$$

(this relationship is proved in many books; see, for example, Goldstein[27]).

By specifying a maximum value of s, a minimum value of electron energy may be computed as a function of θ. The maximum value of s may be taken as the distance where electronic screening of the nucleus becomes negligible; from the Fermi-Thomas statistical model of the atomic field,

$$s\leqslant a_0/Z^{\frac{1}{3}}=(0.528/Z^{\frac{1}{3}})10^{-8}\text{ cm}. \tag{23}$$

For Rutherford scattering, the electron energy must therefore satisfy the following equation,

$$E\geqslant 13.7Z^{\frac{1}{3}}\tan(\theta/2)\text{ ev}. \tag{24}$$

Table II gives the estimated minimum electron energy consistent with Rutherford scattering for representative elements at $\theta=45°$ and $\theta=90°$. If s exceeds the value given in Eq. (23), the electron is deflected by a screened Coulomb field, and the Rutherford formula is no longer correct.

Sternglass[7] shows that for elements $Z\leqslant 30$, r is nearly constant from low values of primary energy ($\sim$500 ev).

TABLE II.

Element	Z	$E_{\min}$(ev) 45°	$E_{\min}$(ev) 90°
Carbon	6	62	150
Aluminum	13	170	420
Copper	29	500	1200
Silver	47	950	2300
Gold	79	1900	4600

[26] See footnote reference 15, p. 130.

[27] H. Goldstein, *Classical Mechanics* (Addison-Wesley Press, Inc., Cambridge, Massachusetts, 1951), p. 84.

For elements $Z\gtrsim 40$, however, r is still increasing at much higher energies, and reaches a more constant value at 2 to 10 kev. The above values of $E_{\min}$ qualitatively explain this observed behavior of r at low primary energies. The $\theta=45°$ column of Table II is probably a good indication of the minimum energies at which the theory is valid. Since relativity corrections have been neglected, the maximum energy might be taken as 25 to 50 kev; however, because the velocities drop out of the general equation for r, the upper limit may be substantially higher, and certainly experiment indicates that r varies little between 10 and 100 kev.

The minimum value of s is determined by the nuclear radius r', which may be written

$$r'=1.5\times 10^{-13}A^{\frac{1}{3}} \tag{25}$$

where A is the integer nearest to the gram atomic weight of an element. If the incident electron is not to strike the nucleus, θ must satisfy the relationship

$$\theta>\frac{2EA^{\frac{1}{3}}}{Ze}10^{-15}\text{ radian}. \tag{26}$$

$\theta_{\min}$ will be maximum for light elements and high electron energies. For carbon ($Z=6$, $A=12$) and an incident energy of 5 kev, $\theta_{\min}$ is 0.08 radian. Therefore little error in r was incurred by taking $\theta=0$ as the lower limit of the θ integration.

6. SMALL-ANGLE DEFLECTIONS

The simplifying assumption made in deriving r, that electrons not deflected through angles exceeding $\pi/2$ are not deflected at all will now be discussed. It seems obvious that electrons are deflected through small angles, and an exact theory should involve the probable mean angle of incidence on a plane parallel to the surface at depth y in the target. The most probable angle of total deflection $\bar{\phi}$ is given by Zworykin *et al.*[28] as

$$\bar{\phi}=\frac{4\cdot 10^5}{E_0}Z\left(\frac{\rho x}{A}\right)^{\frac{1}{2}}, \tag{27}$$

This equation can be written in a much simpler form by using the Thomson-Whiddington law,

$$\bar{\phi}=\begin{bmatrix}0.4\\0.8\end{bmatrix}(yZ)^{\frac{1}{2}}, \tag{28}$$

where the upper and lower numerical constants are obtained by using the Terrill and "best fit" constants, respectively. In deriving Eq. (9), the number of electrons deflected through $\phi\geqslant\pi/2$ by distance y was subtracted from the number of incident electrons n_0, and the mean angle of deviation by depth y applicable to the

[28] V. K. Zworykin, G. A. Morton, E. G. Ramberg, J. Hillier, and A. W. Vance, *Electron Optics and the Electron Microscope* (John Wiley & Sons, Inc., New York, 1945), p. 685.

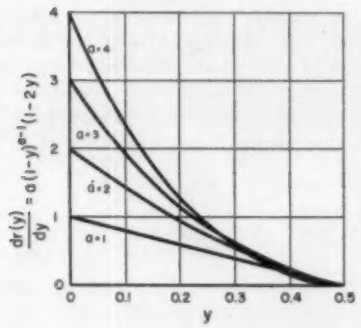

FIG. 3. Rate of change of deflection coefficient r with respect to normalized penetration distance into the target, vs normalized penetration distance.

theory is therefore the mean angle that all electrons deflected through $\phi<\pi/2$ make with the beam axis. This angle is considerably less than $\bar{\phi}$ given by Eq. (28), which includes all deflections.

For small y and Z, Eq. (28) shows that little uncertainty is introduced into the angle of incidence at depth y. As y and Z become large, the angle of divergence increases; and the value of r predicted by the theory becomes smaller than one would expect, since the probability of reflection increases as the angle of incidence varies from normal incidence. This increase possibly counteracts the decrease due to second reflections, which also increase with Z, and may help explain the fairly good agreement between the "best fit" theoretical curve and experiment at large Z.

It is well to point out that as Z increases, an increasingly larger fraction of the reflected electron current comes from nearer the target surface, i.e., from smaller y. This effect is shown in Fig. 3, where the area under the respective curves is equal to r. Thus the average distance traveled by the reflected electrons in the target decreases as Z increases; this relationship reduces the effect of increasing angular beam divergence as y increases.

It is only when the incident electrons have been scattered many times by the target material that all directions of electron velocity become equally probable, and a diffusion theory proposed by Bothe[13] becomes strictly valid. An exact theory would probably lie between the simple theory presented here and Bothe's theory, and it is interesting to note that Bothe's theoretical curve is somewhat above the measured points, whereas the theoretical curve of this paper (obtained using Terrill's constant) is below them.

7. MEAN ENERGY OF REFLECTED ELECTRONS

The energy of a reflected electron escaping from the target at an angle θ after being deflected at depth y is

$$E_e=\tfrac{1}{2}mv^2=\tfrac{1}{2}mv_0^2[1-y(1+\sec\theta)]^{\frac{1}{2}}. \quad (29)$$

The ratio of the energy of escape to the primary energy is termed the fractional energy k, and is therefore

$$k=[1-y(1+\sec\theta)]^{\frac{1}{2}}. \quad (30)$$

The mean fractional energy $\bar{k}$ is calculated in the usual manner:

$$\bar{k}=\int_{y_1}^{y_2}\int_{\theta_1}^{\theta_2} k\,dn(y,\theta) \Big/ \int_{y_1}^{y_2}\int_{\theta_1}^{\theta_2} dn(y,\theta) \quad (31)$$

where the limits may be chosen to correspond with measurements found in the literature. Figure 4 shows $\bar{k}$ evaluated for a small $\Delta\theta$ at $\theta=0$, $\pi/4$, and $\pi/2$. Experimental points by Sternglass and Brand (taken from Sternglass[7]) and by Kanter[9] are also plotted. Using the Sternglass-Brand data, this simple theory predicts only the limiting value of $\bar{k}$ as $Z\to 0$ with accuracy. However, if Kanter's curves of r vs k are weighted and numerically integrated to find the first moment, which is $\bar{k}$, a better agreement with theory is apparent. Both Sternglass and Kanter observe that if the primary energy is increased to the order of 100–400 kev, $\bar{k}\propto Z^{\frac{1}{2}}$. This observation probably indicates that multiple reflections are becoming dominant in this energy range, and Bothe's theory[13] is more appropriate. For electron energies from 2 to 20 kev, both Sternglass and Kanter observe that $\bar{k}$ varies little with Z, but the spread in their observed values of $\bar{k}$ are such that points predicted by this simple theory are bracketed nicely.

8. CONCLUSIONS

In the energy range for which it is valid, this simple theory correctly predicts that r should not vary with primary-electron energy, and it predicts the variation of r with target atomic number Z as well as could be expected in the light of the many simplifying assumptions. Although the approximate value of mean fractional energy is also correctly indicated, perhaps the

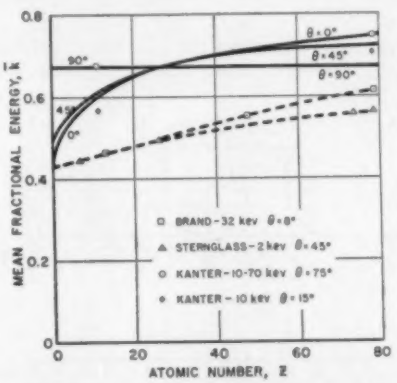

FIG. 4. Mean fractional energy of reflected electrons $\bar{k}$ vs atomic number Z; comparison of theory with experiment.

most important contribution of this treatment is an insight into the physical phenomena that determine the reflection coefficient of a given target.

9. ACKNOWLEDGMENTS

The encouragement of Mr. C. W. Oatley, and constructive suggestions by both Mr. Oatley and Dr. V. E. Cosslett on possible extensions of the approach presented here, were of great value to the author in the preparation of this paper. This work was completed while the author was a Marshall Scholar at the University of Cambridge, and he is grateful to the Marshall Aid Commemoration Commission for their financial support.

JOURNAL OF APPLIED PHYSICS VOLUME 31, NUMBER 8 AUGUST 1960

Spreading Resistance in Cylindrical Semiconductor Devices

DAVID P. KENNEDY
International Business Machines Corporation, Poughkeepsie, New York
(Received December 7, 1959; and in final form April 6, 1960)

For cylindrical semiconductor components, computation of spreading resistance is considered a boundary value problem of the solid circular cylinder. Solutions of this problem may be used, for example, to characterize the thermal spreading resistance within the package of a semiconductor device, the electrical spreading resistance in a mesa type parametric diode, and the extrinsic collector resistance of a mesa transistor. Equations describing the thermal (or electrical) spreading resistance are presented in graphical form for a range of geometrical parameters applicable to many practical situations. Further, examples are given for the potential distribution within each cylindrical structure considered in this analysis.

INTRODUCTION

MANY aspects of semiconductor device design present problems of spreading resistance for which no elementary solution is available. This situation is encountered, for example, in the investigation of heat conduction within the package enclosing a semiconductor device. The base of a high-current diode, Fig. 1(a), can be in intimate contact with its heat sink, yet spreading resistance may result in a substantially elevated junction temperature. A similar design difficulty is encountered when calculating the thermal resistance of a transistor package, Fig. 1(b). Only the outer edge of this cylindrical heat conductor is in thermal contact with its external heat sink; this situation presents a completely different analytical problem.

Comparable situations arise in the electrical design of semiconductor devices. A mesa transitor, Fig. 2(a), exhibits a collector-region voltage drop capable of modifying the electrical characteristics of this device. An accurate analysis is often required to establish the magnitude of this collector-region potential since an extensive amount of flux-line spreading can exist between the collector junction and the ohmic contact. Similarly, a low-frequency spreading resistance is present in the mesa-type parametric diode, Fig. 2(b), which, except for minor details, is identical to the transistor. Many electrical properties of this variable-reactance device are extremely dependent upon the magnitude of extrinsic resistance in series with its junction capacity.

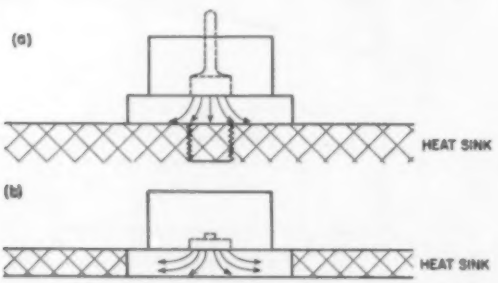

FIG. 1(a). Heat flux spreading in base of high-current diode package. (b). Heat flux spreading in base of transistor package.

This paper presents a steady-state analysis of the temperature distribution within a homogeneous solid cylinder, Fig. 3, which approximates many situations encountered in the design of semiconductor devices. A constant-density heat flux, f, is assumed to enter the cylindrical conductor throughout a region of circular symmetry located at one surface ($0<r<A$; $z=0$); the remainder of this surface ($A<r<B$; $z=0$) is assumed insulated. Analytical similarities between problems of heat and electrical conduction permit the interchange of electrical potential for temperature and electrical conductivity for thermal conductivity. This analysis, therefore, is applicable to problems of thermal and electrical spreading resistance in semiconductor device design.

Previous authors[1] have considered the problem of heat conduction within an infinite solid cylinder having a

[1] A. Gray and G. Matthews, *Treatise on Bessel Function* (Macmillan and Company, Ltd., London, 1952).

circular heat source located at one end. In this paper the thermal characteristics are established for a finite solid cylinder with a circularly symmetrical heat source at one surface and a combination of boundary conditions at the others:

Boundary conditions	$(r=B; 0<z<W)$	$(0<r<B; z=W)$
Case I	adiabatic	isothermal
Case II	isothermal	adiabatic
Case III	isothermal	isothermal

Thermal resistance throughout this analysis has been defined as a ratio of the maximum cylinder temperature—which appears at the center of its circular heat source—and the total heat entering this cylindrical conductor. Equations are presented to establish the magnitude of spreading resistance and also the normalized temperature distribution for each case; numerical evaluation of these equations must be done on a large electronic computer.[2] Computational difficulties, therefore, have been minimized by the introduction of graphs which establish the thermal resistance for a wide range of geometrical parameters. Further, graphical examples are given to illustrate the temperature distribution within cylinders characterizing each combination of boundary conditions.

GENERAL TEMPERATURE DISTRIBUTION

The temperature distribution within a homogeneous solid cylinder of isotropic media must satisfy the Laplace equation,

$$\nabla^2 T(r; z; \theta)=0, \tag{1}$$

when no internal heat sources—or sinks—are present. Use of Eq. (1) limits this analysis to situations where heat enters the solid from an external source. Heat generation resulting from an electric current within the conductor, for example, has been excluded.

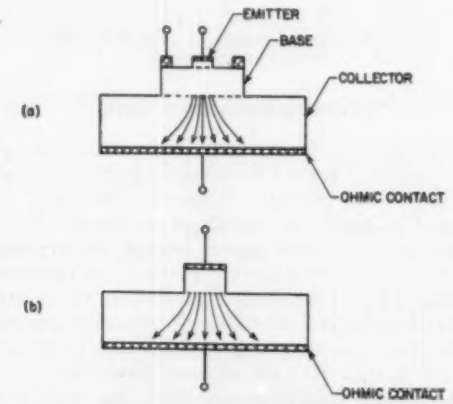

FIG. 2(a). Electric flux spreading in extrinsic collector region. (b). electric flux spreading in paramagnetic diode.

[2] D. P. Kennedy, "Heat conduction in a homogeneous solid cylinder of isotropic media," IBM-TR00. 15072.699. (All computer programs used in this analysis are available in this report).

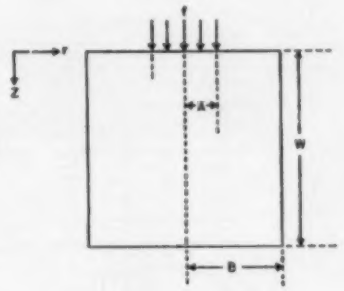

FIG. 3. Cross section of analytical model.

The geometrical configurations considered here are solid circular cylinders in which circular symmetry is maintained. Equation (1), therefore, can be written in cylindrical coordinates of two spatial variables

$$\frac{\partial^2 T}{\partial r^2}+\frac{1}{r}\frac{\partial T}{\partial r}+\frac{\partial^2 T}{\partial z^2}=0. \tag{2}$$

Separation of variables in Eq. (2) is accomplished by assuming a solution of the form

$$T(r; z)=\psi_0+\psi_1 z+U(r)V(z). \tag{3}$$

Substitution of Eq. (3) into Eq. (2) yields the separated

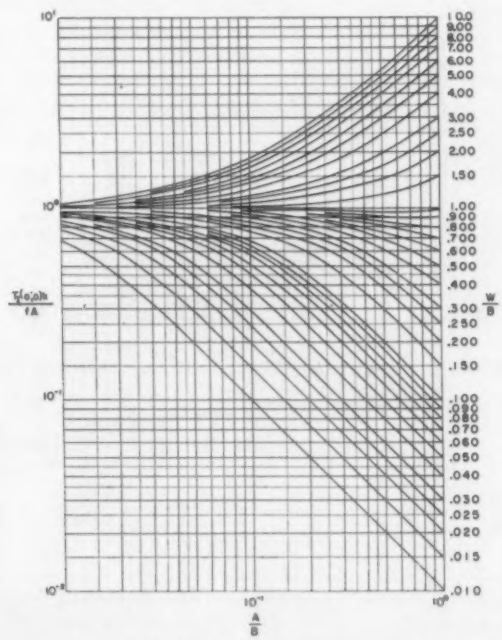

FIG. 4. Maximum cylinder temperature—case I.

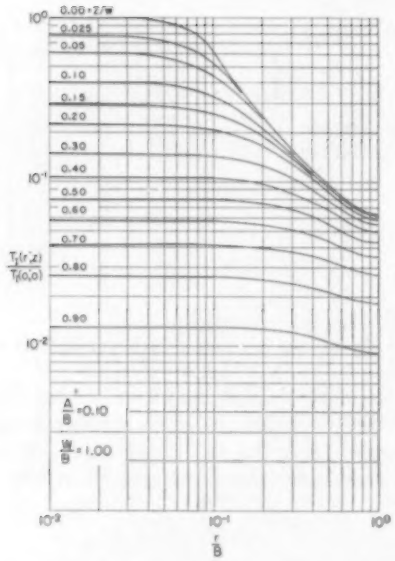

FIG. 5. Temperature distribution—case I—when $(0.10 = A/B;\ 1.00 = W/B)$.

equations

$$\frac{\partial^2 U}{\partial r^2}+\frac{1}{r}\frac{\partial U}{\partial r}+\lambda^2 U(r)=0 \tag{4a}$$

$$\frac{\partial^2 V}{\partial z^2}-\lambda^2 V(z)=0, \tag{4b}$$

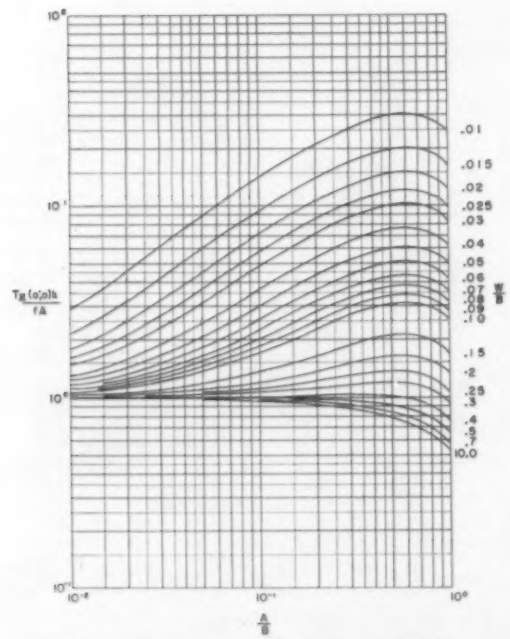

FIG. 6. Maximum cylinder temperature—case II.

where λ is the constant of separation. The physical nature of this type boundary value problem restricts solutions of Eq. (4a) to Bessel functions of zero order. Solutions involving Neumann functions are excluded since the desired temperature distribution must be well behaved at the origin ($r=0$). From Eq. (3) and Eq. (4) we obtain

$$T(r;z)=\psi_0+\psi_1 z+\psi_2[c_1\cosh(\lambda z)+c_2\sinh(\lambda z)]J_0(\lambda r). \tag{5}$$

Equation (5) is a general type of cylindrical harmonic which is used in this analysis to characterize the thermal potential distribution. Application of Eq. (5) to a specific problem results in an infinite summation of such harmonic functions in which the constants are adjusted to satisfy the boundary conditions imposed by practical considerations.

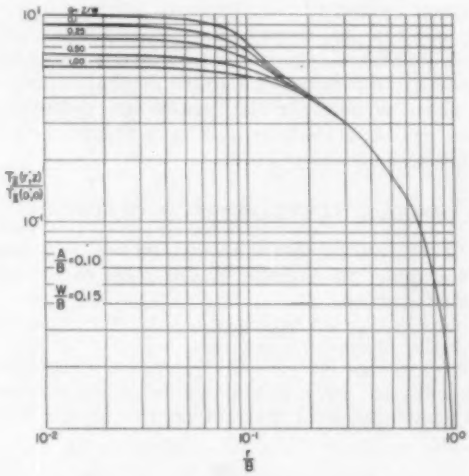

FIG. 7. Temperature distribution—case II—when $(0.10 = A/B;\ 0.15 = W/B)$.

Spreading Resistance. Case I

Many problems encountered in the design of semiconductor devices are approximated by this particular boundary value problem. A constant heat flux, f, is assumed to enter the cylindrical conductor, Fig. 3, throughout a circular region located symmetrically at one end $(0<r<A;\ z=0)$. Further, an isothermal surface, of zero temperature, is assumed at the other end of this cylinder $(0<r<B;\ z=W)$, thereby providing a heat sink; the remaining surfaces $(A<r<B;\ z=0)$ and $(r=B;\ 0<z<W)$ are assumed insulated.

The base of a high-current diode, Fig. 1(a), is an example of the type structure approximated by these boundary conditions. The circular semiconductor heat source is represented, Fig. 3, by a region of constant flux density at the surface of the cylindrical conductor. The assumed isothermal boundary—although a theo-

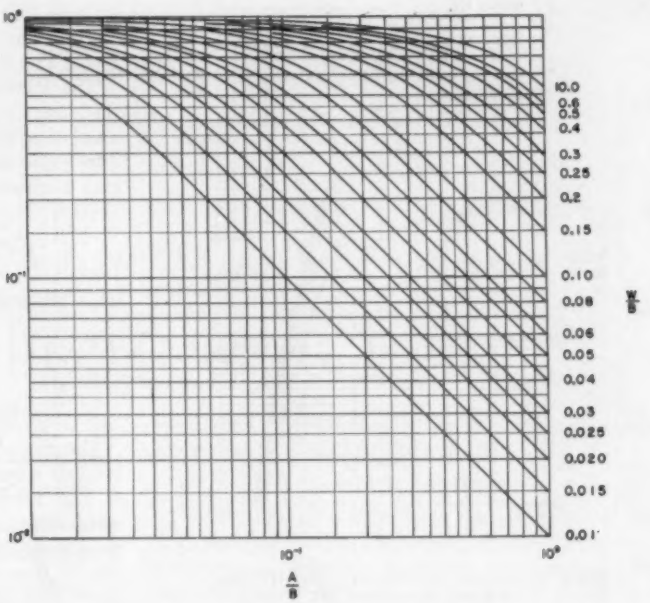

FIG. 8. Maximum cylinder temperature—case III.

retical idealization—is often approximated by mounting the diode upon a liquid-cooled heat sink. A further application of this analysis is found in the electrical and thermal properties of a mesa-type semiconductor device, Fig. 2. A region of constant flux density is assumed at the *p-n* junction while the ohmic contact approximates a constant potential surface.

When computing the spreading resistance in a semiconductor device, consideration must be given to its mechanisms of operation. The mesa transistor, for example, has a radius of constant flux density—either thermal or electrical—approximately equal the emitter radius; this results from a negligible minority carrier spreading within the base region.[3] If, on the other hand, this solution is used to determine the magnitude of spreading resistance in series with the collector junction capacity, the radius of constant flux density is equal to the collector junction radius.

From Appendix I the temperature distribution throughout this solid cylinder (case I) is given by

$$T_I(r;z)=\frac{f}{k}(W-z)\left\{\frac{A^2}{B^2}+\frac{2A}{W-z}\sum_{l=1}^{\infty}\left[\sinh\left(\frac{\alpha_l}{B}(W-z)\right)\Big/\cosh\left(\alpha_l\frac{W}{B}\right)\right]\left[J_1\left(\alpha_l\frac{A}{B}\right)J_0\left(\alpha_l\frac{r}{B}\right)\Big/\alpha_l^2J_0^2(\alpha_l)\right]\right\}. \quad (6)$$

The maximum cylinder temperature appears at $(r=0;z=0)$ and has a magnitude of

$$T_I(0;0)=\frac{fW}{k}\left\{\frac{A^2}{B^2}+\frac{2A}{W}\sum_{l=1}^{\infty}\left[J_1\left(\alpha_l\frac{A}{B}\right)\Big/\alpha_l^2J_0^2(\alpha_l)\right]\tanh\left(\frac{\alpha_lW}{B}\right)\right\}. \quad (7)$$

From Eq. (6) and Eq. (7) we can describe a normalized temperature distribution throughout this cylinder by the expression

$$\frac{T_I(r;z)}{T_I(0;0)}=\frac{\dfrac{A^2}{B^2}\left(1-\dfrac{z}{W}\right)+\dfrac{2A}{W}\displaystyle\sum_{l=1}^{\infty}\left[\sinh\left(\frac{\alpha_l}{B}(W-z)\right)\Big/\cosh\left(\frac{\alpha_lW}{B}\right)\right]\left[J_1\left(\alpha_l\frac{A}{B}\right)J_0\left(\alpha_l\frac{r}{B}\right)\Big/\alpha_l^2J_0^2(\alpha_l)\right]}{\dfrac{A^2}{B^2}+\dfrac{2A}{W}\displaystyle\sum_{l=1}^{\infty}\left[J_1\left(\alpha_l\frac{A}{B}\right)\Big/\alpha_l^2J_0^2(\alpha_l)\right]\tanh\left(\frac{\alpha_lW}{B}\right)}. \quad (8)$$

Equation (7) has been numerically evaluated, Fig. 4, for a range of geometrical parameters applicable to a large number of practical situations. This graph permits the computation of thermal—or electrical—spreading resistance within a cylindrical conductor satisfying the previously stated boundary conditions. The limited

[3] D. P. Kennedy, "Minority carrier recombination in a cylindrical transistor base region (to be published).

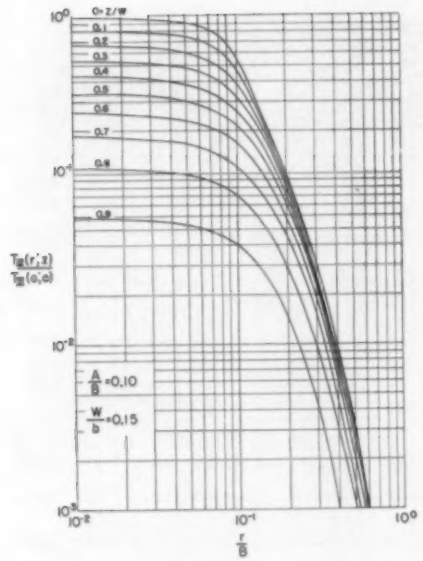

FIG. 9. Temperature distribution—case III—when $(0.10=A/B; 0.15=W/B)$.

number of independent variables associated with Eq. (7) permits a general representation of this expression; this is not so for Eq. (8). The multitude of parameters associated with the normalized temperature distribution does not permit a single, graphical representation of this characteristic. To illustrate the temperature distribution within this heat conductor an example is given, Fig. 5, where $(0.10=A/B; 1.00=W/B)$.

The thermal—or electrical—spreading resistance of this structure is determined from Fig. 4 with a minimum of additional computation. Assuming the cylinder dimensions are measured in inches, the thermal resistance is given by

$$R_t=\frac{H}{10.6\pi kA}\left(\frac{^\circ\text{C}}{\text{watt}}\right) \quad H=\frac{T(0;0)k}{fA}, \tag{9}$$

while the electrical spreading resistance is

$$R_e=\frac{H}{2.54\pi\sigma A}(\text{ohms}). \tag{10}$$

Spreading Resistance. Case II

The next boundary value problem establishes the thermal spreading resistance within the solid cylinder of Fig. 3 when its outer surface $(r=B; 0<z<W)$ is maintained at a constant temperature. The boundary conditions established at the upper end of this cylinder $(0<r<B; z=0)$ are identical to case I while at the lower end $(0<r<B; z=W)$ we have an insulated surface. This problem approximates the conditions encountered in the base of a transistor package, Fig. 2(b), when its outer edge is in thermal contact with an external heat sink.

From Appendix II the temperature distribution throughout this solid cylinder is given by

$$T_{II}(r;z)=\frac{2fA}{k}\sum_{n=1}^{\infty}\left[\cosh\left(\frac{\alpha_n}{B}(W-z)\right)\Big/\sinh\left(\frac{\alpha_n W}{B}\right)\right]\left[J_1\left(\alpha_n\frac{A}{B}\right)J_0\left(\alpha_n\frac{r}{B}\right)\Big/\alpha_n^2J_1^2(\alpha_n)\right], \tag{11}$$

while the maximum temperature occurs at $(r=0; z=0)$ and has a magnitude of

$$T_{II}(0;0)=\frac{2fA}{k}\sum_{n=1}^{\infty}\left[J_1\left(\alpha_n\frac{A}{B}\right)\Big/\alpha_n^2J_1^2(\alpha_n)\right]\text{ctnh}\left(\frac{\alpha_n W}{B}\right). \tag{12}$$

From Eq. (11) and Eq. (12) we can now characterize the normalized temperature distribution within this cylinder by

$$\frac{T_{II}(r;z)}{T_{II}(0;0)}=\frac{\sum_{n=1}^{\infty}\left[\cosh\left(\frac{\alpha_n}{B}(W-z)\right)\Big/\sinh\left(\frac{\alpha_n W}{B}\right)\right]\left[J_1\left(\alpha_n\frac{A}{B}\right)J_0\left(\alpha_n\frac{r}{B}\right)\Big/\alpha_n^2J_1^2(\alpha_n)\right]}{\sum_{n=1}^{\infty}\left[J_1\left(\alpha_n\frac{A}{B}\right)\Big/\alpha_n^2J_1^2(\alpha_n)\right]\text{ctnh}(\alpha_n W/B)}. \tag{13}$$

Equation (12) establishes the maximum temperature within this cylindrical conductor; numerical evaluation of Eq. (12) has been conducted for a wide range of geometrical parameters, Fig. 6. In a manner identical to case I the thermal spreading resistance is established by Eq. (9) while the electrical spreading resistance is obtained from Eq. (10). An illustrative example is given, Fig. 7, for the normalized temperature distribution within this structure, Eq. (13), with the assumed geometrical parameters $(0.10=A/B; 0.15=W/B)$.

Spreading Resistance. Case III

To complete this analysis the thermal resistance has been established for a solid cylinder when an isotherm is assumed at both surfaces $(r=B; 0<z<W)$ and $(0<r<B; z=W)$. The upper end of this heat conductor $(0<r<B; z=0)$, Fig. 3, is assumed to have the same boundary conditions as the previous cases.

From Appendix III the temperature distribution within this structure is given by

$$T_{III}(r;z)=\frac{2fA}{k}\sum_{n=1}^{\infty}\left[\sinh\left(\frac{\alpha_n}{B}(W-z)\right)\Big/\cosh\left(\alpha_n\frac{W}{B}\right)\right]\left[J_1\left(\alpha_n\frac{A}{B}\right)J_0\left(\alpha_n\frac{r}{B}\right)\Big/\alpha_n^2J_1^2(\alpha_n)\right]. \tag{14}$$

As in the other cases a temperature maximum occurs at $(r=0;z=0)$ with a magnitude of

$$T_{III}(0;0)=\frac{2fA}{k}\sum_{n=1}^{\infty}\left[J_1\left(\alpha_n\frac{A}{B}\right)\Big/\alpha_n^2J_1^2(\alpha_n)\right]\tanh\left(\alpha_n\frac{W}{B}\right). \tag{15}$$

From Eq. (14) and Eq. (15) the normalized temperature distribution within this solid cylinder is given by

$$\frac{T_{III}(r;z)}{T_{III}(0;0)}=\frac{\sum_{n=1}^{\infty}\left[\sinh\left(\frac{\alpha_n}{B}(W-z)\right)\Big/\cosh\left(\frac{\alpha_nW}{B}\right)\right]\left[J_1\left(\alpha_n\frac{A}{B}\right)J_0\left(\alpha_n\frac{r}{B}\right)\Big/\alpha_n^2J_1^2(\alpha_n)\right]}{\sum_{n=1}^{\infty}\left[J_1\left(\alpha_n\frac{A}{B}\right)\Big/\alpha_n^2J_1^2(\alpha_n)\right]\tanh\left(\frac{\alpha_nW}{B}\right)}. \tag{16}$$

Figure 8 characterizes the maximum cylinder temperature, Eq. (14), throughout a range of geometrical parameters applicable to a large number of design problems. From this graph the thermal—or electrical—spreading resistance can be established with a minimum of additional computation. Further, an example is given, Fig. 9, for the normalized temperature distribution, Eq. (16), with the assumed geometrical parameters $(0.10=A/B;0.15=W/B)$.

ACKNOWLEDGMENT

I would like to acknowledge the assistance of Mr. F. J. Goth of the Data Systems Division Laboratory, International Business Machines Corporation. Mr. Goth developed the computer programs which have been used extensively throughout this analysis.

APPENDIX I

Temperature Distribution. Case I

The general solution of Laplace's equation which is applicable to this problem has the form

$$T_I(r;z)=\psi_0+\psi_1z+\psi_2[c_1\sinh(\lambda z)+c_2\cosh(\lambda z)]J_0(\lambda r). \tag{I-1}$$

The constants of Eq. (I-1) must be adjusted to satisfy the boundary equations

$$\partial T/\partial r=0 \qquad r=B;\quad 0<z<W \tag{I-2a}$$

$$T(r;z)=0 \qquad 0<r<B;\quad z=W \tag{I-2b}$$

$$\partial T/\partial z=\begin{cases}-f/k & 0<r<A;\quad z=0\\ 0 & A<r<B;\quad z=0.\end{cases} \tag{I-2c}$$

Substituting Eq. (I-1) into Eq. (I-2a) yields the relation

$$T_I(r;z)=\psi_0+\psi_1z+\sum_{l=1}^{\infty}\psi_l\left[c_1\sinh\left(\frac{\alpha_lz}{B}\right)+c_2\cosh\left(\frac{\alpha_lz}{B}\right)\right]J_0\left(\frac{\alpha_lr}{B}\right), \tag{I-3}$$

where α_l is the root of the first-order Bessel function, $J_1(x)$; the summation is conducted over ascending values of α_l. Upon substituting Eq. (I-3) into Eq. (I-2b) and Eq. (I-2c) we obtain

$$T_I(r;z)=\psi_0(W-z)+\sum_{l=1}^{\infty}\left[\psi_l\sinh\left(\frac{\alpha_l}{B}(W-z)\right)\Big/\alpha_l\cosh\left(\frac{\alpha_lW}{B}\right)\right]J_0\left(\alpha_l\frac{r}{B}\right), \tag{I-4}$$

where

$$\psi_0+\sum_{l=1}^{\infty}\psi_lJ_0\left(\alpha_l\frac{r}{B}\right)=\begin{cases}f/k & 0<r<A\\ 0 & A<r<B.\end{cases} \tag{I-5}$$

Equation (I-5) is a Dini series type of approximation[4] for the boundary conditions specified by Eq. (I-2c). The constants ψ_0 and ψ_l within Eq. (I-5) are given by

$$\psi_0 = 2f/kB^2 \int_0^A r dr = fA^2/kB^2 \tag{I-6a}$$

$$\psi_l = \frac{2f}{kB^2 J_0^2(\alpha_l)} \int_0^A r J_0\left(\alpha_l \frac{r}{B}\right) dr = 2fAJ_1\left(\alpha_l \frac{A}{B}\right) \Big/ kB J_1^2(\alpha_l). \tag{I-6b}$$

Substituting Eqs. (I-6) into Eq. (I-4) we obtain the temperature distribution throughout this solid cylinder

$$T_I(r;z) = \frac{f(W-z)}{k}\left\{\frac{A^2}{B^2} + \frac{2A}{W-z}\sum_{l=1}^{\infty}\left[\sinh\left(\frac{\alpha_l}{B}(W-z)\right) \Big/ \cosh\left(\frac{\alpha_l W}{B}\right)\right]\left[J_0\left(\alpha_l \frac{A}{B}\right) J_1\left(\alpha_l \frac{r}{B}\right) \Big/ \alpha_l J_0^2(\alpha_l)\right]\right. \tag{I-7}$$

APPENDIX II

Temperature Distribution. Case II

The same general temperature distribution equation is used in the solution of this boundary value problem as in case I, Eq. (I-1). The constants of Eq. (I-1) must be adjusted to satisfy the boundary equations

$$T(r;z) = 0 \qquad r = B; \quad 0 < z < W \tag{II-1a}$$

$$\partial T/\partial z = 0 \qquad 0 < r < B; \quad z = W \tag{II-1b}$$

$$\partial T/\partial z = \begin{cases} -f/k & 0 < r < A; \quad z = 0 \\ 0 & A < r < B; \quad z = 0 \end{cases} \tag{II-1c}$$

Substituting Eq. (I-1) into Eq. (II-1a) yields the relation

$$T_{II}(r;z) = \sum_{n=1}^{\infty} \psi_n \left[c_1 \sinh\left(\frac{\alpha_n z}{B}\right) + c_2 \cosh\left(\frac{\alpha_n z}{B}\right)\right] J_0\left(\alpha_n \frac{r}{B}\right), \tag{II-2}$$

where the term α_n represents the roots of the zero-order Bessel function, $J_0(x)$; the summation is conducted over ascending values of α_n. Further, upon substituting Eq. (II-2) into the boundary equations, Eq. (II-1b) and Eq. (II-1c), we obtain

$$T_{II}(r;z) = \sum_{n=1}^{\infty} \frac{\psi_n B}{\alpha_n}\left[\cosh\left(\frac{\alpha_n}{B}(W-z)\right) \Big/ \sinh\left(\frac{\alpha_n W}{B}\right)\right]\left(J_0\right)\left(\alpha_n \frac{r}{B}\right), \tag{II-3}$$

where

$$\sum_{n=1}^{\infty} \psi_n J_0\left(\alpha_n \frac{r}{B}\right) = \begin{cases} f/k & 0 < r < A \\ 0 & A < r < B. \end{cases} \tag{II-4}$$

Equation (II-4) is a Fourier-Bessel series type of approximation[4,5] for the boundary conditions specified by Eq. (II-1c). The constant ψ_n is given by

$$\psi_n = \frac{2f}{kB^2 J_1^2(\alpha_n)} \int_0^A r J_0\left(\alpha_n \frac{r}{B}\right) dr = 2Af J_1\left(\alpha_n \frac{A}{B}\right) \Big/ kB\alpha_n J_1^2(\alpha_n) \tag{II-5}$$

From Eq. (II-3) and Eq. (II-5) the desired temperature distribution equation is

$$T_{II}(r;z) = \frac{2fA}{k}\sum_{n=1}^{\infty}\left[\cosh\left(\frac{\alpha_n}{B}(W-z)\right) \Big/ \sinh\left(\frac{\alpha_n W}{B}\right)\right]\left[J_1\left(\alpha_n \frac{A}{B}\right) J_0\left(\alpha_n \frac{r}{B}\right) \Big/ \alpha_n^2 J_1^2(\alpha_n)\right]. \tag{II-6}$$

[4] G. N. Watson, *A Treatise on the Theory of Bessel Functions* (Cambridge University Press, London, 1945).
[5] E. T. Whittaker and G. N. Watson, *A Course of Modern Analysis* (Cambridge University Press, London, 1945), 4th ed.
[6] H. S. Carslaw and J. C. Jaeger, *Conduction of Heat in Solids* (Oxford University Press, New York, 1947).

APPENDIX III

Temperature Distribution. Case III

Using the general temperature distribution equation of case I, Eq. (I-1), the constants must be adjusted to satisfy the boundary equations

$$T(r;z)=0 \qquad r=B;\quad 0<z<W \tag{III-1a}$$

$$T(r;z)=0 \qquad 0<r<B;\quad z=W \tag{III-1b}$$

$$\partial T/\partial z=\begin{cases}-f/k & 0<r<A;\quad z=0\\ 0 & A<r<B;\quad z=0.\end{cases} \tag{III-1c}$$

Substituting Eq. (I-1) into Eq. (III-1a) yields the relation

$$T_{III}(r;z)=\sum_{n=1}^{\infty}\psi_n\left[c_1\sinh\left(\alpha_n\frac{z}{B}\right)+c_2\cosh\left(\alpha_n\frac{z}{B}\right)\right]J_0\left(\alpha_n\frac{r}{B}\right), \tag{III-2}$$

where α_n are the roots of the zero-order Bessel function, $J_0(x)$; the summation is conducted over ascending values of α_n. Further, upon substituting Eq. Eq. (III-2) into the boundary relations Eq. (III-2c) we have

$$T_{III}(r;z)=\sum_{n=1}^{\infty}\frac{\psi_n B}{\alpha_n}\left(\sinh\left[\frac{\alpha_n}{B}(W-z)\right]\Big/\cosh\left(\frac{\alpha_n W}{B}\right)\right)J_0\left(\alpha_n\frac{r}{B}\right), \tag{III-3}$$

where

$$\sum_{n=1}^{\infty}\psi_n J_0\left(\alpha_n\frac{r}{B}\right)=\begin{cases}f/k & 0<r<A\\ 0 & A<r<0.\end{cases} \tag{III-4}$$

Equation (III-4) is identical to Eq. (II-4); hence the temperature distribution equation applicable to this situation is obtained from Eq. (III-3) and Eq. (II-5),

$$T_{III}(r;z)=\frac{2Af}{k}\sum_{n=1}^{\infty}\left[\sinh\left(\frac{\alpha_n}{B}(W-z)\right)\Big/\cosh\left(\frac{\alpha_n W}{B}\right)\right]\left[J_1\left(\alpha_n\frac{A}{B}\right)J_0\left(\alpha_n\frac{r}{B}\right)\Big/\alpha_n^2 J_1^2(\alpha_n)\right]. \tag{III-5}$$

SYMBOLS

A = Geometrical parameter of cylinder (see Fig. 3)
B = Geometrical parameter of cylinder (see Fig. 3)
f = Heat flux density (cal/sec-cm²)
k = Heat conductivity of cylinder (cal/sec-cm-°C)
r = Radial coordinate of cylinder
$T(r;z)$ = Temperature distribution
W = Geometrical parameter of cylinder (see Fig. 3)
z = Axial coordinate of cylinder
α_l = Roots of zero-order Bessel function, $J_0(x)$
α_n = Roots of first-order Bessel function, $J_1(x)$
σ = Electrical conductivity of cylinder (ohm-cm)$^{-1}$

Letters to the Editor

Inversion by Fast Passage in a Multilevel Spin System*

P. E. WAGNER,† J. G. CASTLE, JR., AND P. F. CHESTER
Westinghouse Research Laboratories, Pittsburgh 35, Pennsylvania
(Received April 14, 1960)

THIS letter describes some measurements of adiabatic fast passage in a multilevel-electron spin system, with particular reference to a recent proposal by Siegman and Morris[1] for a "staircase" maser.

Consider a spin system in thermal equilibrium, having three nearly equidistant energy levels. We shall number the states in order of increasing energy and denote the populations by N_1, N_2, and N_3. The original proposal was to obtain $N_3 > N_1$ by successive fast passages through the (1–2) and (2–3) transitions.

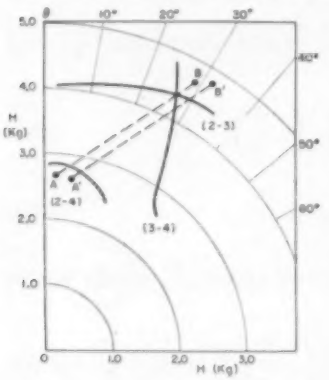

FIG. 1. Magnetic field for resonance at 9.05 kMc/sec as a function of the angle between the field and the crystalline c axis. The dashed lines represent two different pulsed field sweeps. Field pulsed either $B \rightarrow A \rightarrow B$ or $B' \rightarrow A' \rightarrow B'$.

Since fast passage may not result in perfect inversion, we introduce a turnover efficiency α_{ij} = (population difference after passage)/(population difference before). We assume for simplicity that $\alpha_{12} = \alpha_{23} = \alpha$. It can easily be shown that N_3 will be greater than N_1 only if $\alpha > 0.47$, a value we have often found difficult to achieve. In the case of four nearly equidistant levels and three successive passages, the efficiency must exceed 0.7 to obtain $N_4 > N_1$.

Now consider passage through the (1–2) and (2–3) lines when they are exactly coincident in frequency. If spin-spin coupling between the superposed lines holds them at the same spin temperature throughout passage,[2] then any turnover efficiency greater than zero will result in $N_2 > N_1$. Simultaneous inversion offers another advantage when cross relaxation[3] between the (1–2) and (2–3) lines is important. In the sequential case, the (1–2) transition is much hotter than the (2–3) transition during the interval between passages. If appreciable cross relaxation occurs during this interval, the degree of inversion ultimately produced in the (1–3) line is seriously reduced; with complete cross relaxation, the (1–3) transition remains absorptive. In the case of simultaneous inversion, the question of cross relaxation will not arise if the (1-2) and (2–3) lines always have a common spin temperature.

Experiments were carried out on Cr^{3+} in pink ruby at 9.05 kMc/sec; the apparatus is described elsewhere.[4] Figure 1 shows the magnetic field required for observation of the (2–3), (3–4), and (2–4) lines, as a function of orientation. The field could be swept from B to A and back by means of a condensor discharge through coils mounted on the cavity.[5] The duration of the sweep was much less than the spin lattice relaxation time at the temperature of measurement, 2.16°K. Fast passage was brought about by increasing the microwave power from 1 μw to 12 w for the duration of the first passage through the single (2–3, 3–4) line. Results are shown in Fig. 2(a) and (b). In Fig. 2(a), the lines appear in normal absorption in the order: (2–3, 3–4), (2–4), (2–4), (2–3, 3–4). The step in the baseline indicates where the inverting power will be applied. In Fig. 2(b), the full inverting power is switched on and both the (2–4) and the coincident (2–3, 3–4) lines invert.

Conditions were then changed to obtain sequential passage by altering the sweep path of Fig. 1 to B′-A′-B′. The sequence is now (2–3), (3–4), (2–4), (2–4), (3–4), and (2–3) as shown in Fig. 2(c). Figure 2(d) shows the result of full microwave power. The (3–4) line inverts and the (2–3) line becomes slightly less absorptive. It should be noted that (2–4) line does not invert. Inversion of the (2–4) line was never obtained with sequential passage.

In principle the method of simultaneous inversion can be used to generate pulses of millimeter radiation. It has the advantage over other methods[6,7] of requiring only a small field sweep. The extension to more than three levels is obvious if a working substance can be found which satisfies the requirements of equally spaced levels and allowed transitions between adjacent levels and between the outside pair.

We are indebted to B. R. McAvoy for valuable assistance in the instrumentation.

* Based on research work supported by the Electronics Directorate of U. S. Air Force-Cambridge Research Center under contract.
† Present address: Department of Electrical Engineering, The Johns Hopkins University, Baltimore 18, Maryland.
[1] A. E. Siegman and R. J. Morris, Phys. Rev. Letters **2**, 302 (1959).
[2] A. G. Redfield, Phys. Rev. **98**, 1787 (1955).
[3] N. Bloembergen, S. Shapiro, P. S. Pershan, and J. O. Artman, Phys. Rev. **114**, 445 (1959).
[4] J. G. Castle, Jr., P. F. Chester, and P. E. Wagner, Phys. Rev. (to be published).
[5] P. F. Chester, P. E. Wagner, J. G. Castle, Jr., and G. Conn, Rev. Sci. Instr. **30**, 1127 (1959).
[6] R. H. Hoskins, Phys. Rev. Letters **3**, 174 (1959).
[7] S. Foner, L. R. Momo, and A. Mayer, Phys. Rev. Letters **3**, 36 (1959).

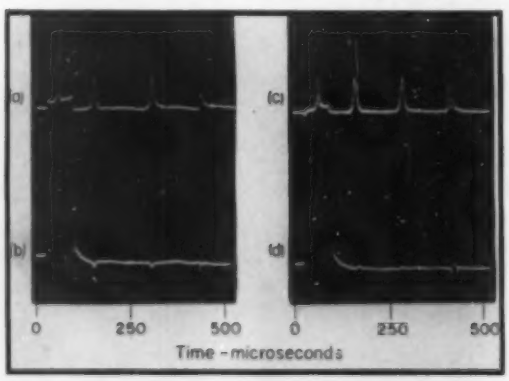

FIG. 2. Appearance of lines during pulsed field sweep. (a) and (b) (2–3) and (3–4) lines coincident. (b) shows result of rapid passage. (c) and (d) (2–3) and (3–4) lines separate. (a) shows result of rapid passage.

Detection of Growth Striations in Germanium Crystals

ALBERT C. ENGLISH
University of California, Berkeley, California
(Received April 15, 1960)

IT is well known that fluctuations in impurity concentration and imperfections in a single crystal may be detected by a variety of techniques. The observation of growth striations in germanium was reported by Camp[1] using a pulse-plating method on the germanium surface. This paper is a report of two experimental situations in which such striations are strongly delineated.[2]

Cylindrical germanium single crystals were grown in the 111 direction by the Czochralski method[3] under conditions of the one rotation of the seed per minute and a growth rate of 7.5 cm/hr.

Wafers were cut parallel to the axis of the cylindrical crystal, so as to intersect the growth face, and etched glossy.

The first method of showing growth-dependent inhomogeneity consists in heating a wafer in contact with a sheet of iron, nickel, or copper (or other metals) to a temperature of about 700°C in hydrogen for a few minutes. The result of two such experiments is shown in Fig. 1 where sample A is a germanium wafer, soldered to a backing plate, showing an iron film on its surface, and sample B is a sheet of iron showing a film of germanium (from another experiment) on its surface.[4] Microscopically, the film on the germanium surface has a very fine structure, barely resolvable at 1000× magnification and having the appearance of minute reflection scales. The darkest areas have the original glossy finish of the etched germanium. The iron sheet has the appearance of the negative of the matching germanium wafer, that is, the pale curved lines of the film correspond with the dark lines on the germanium.

It is occasionally observed after such treatment of a germanium wafer that, starting at the edge of the wafer, a curved uniform groove extends about one-third of the width of the wafer along some of the dark curved lines of the film pattern. Under 1000× magnification these grooves appear to be no more than one μ wide

FIG. 1. A. Germanium wafer, on backing plate, showing film of iron on surface. B. Iron plate showing film of germanium on surface. (Sample B is from a different experiment than sample A.) 2.2×.

yet they reflect oblique light clearly from both sides of the mark as though from a V-shaped valley. On stressing a crystal close to a groove, the fracture does not follow the curved line but is straight and in the (111) plane. A wafer annealed for 7 hr at 900°C shows no diminution of the periodic film effect. No film appears when the germanium is heated in contact with glass. The periodicity of the film deposit matches the pitch of the elevating screw on the crystal-growing equipment.

The second method consists in melting a layer of indium on the germanium wafer at about 550°C in hydrogen or an inert gas with a cover plate of iron to spread the layer of indium, and after cooling, dissolving off the indium in hydrochloric acid so that the structure of the germanium surface may be examined. Figure 2 is an example of a wafer treated under helium. The central area has been quite deeply attacked by the indium melt and then the whole surface covered with oriented germanium crystals during cooling.[5] It will be observed that seven parallel curved lines of uniform spacing extend over the central area in a manner similar to the film deposit discussed above. A line is found to be a wall of crystals jutting out from the surrounding crystals although still correctly oriented with the base germanium. There is no detectable variation in crystal plane orientation over the whole surface of the wafer.

Figure 3 is a photograph of the central part of a wafer treated under argon. In this case part of the germanium surface, although attacked by the melt, has not been subsequently covered by regrown crystals. The lines on the germanium prove to be unsymmetrical grooves, having a steep slope for the side nearer the

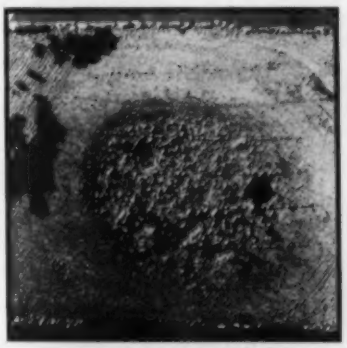

FIG. 2. Germanium surface after indium alloy attack. 4.5×.

bottom of the original crystal and a shallow slope for the upper side (seed end). On this sample, secondary lines can be observed between the main lines, some curved, some straight; all less distinct than the main lines.

The general aspects of the experimental results are clear. Both methods demonstrate the presence in the crystal of periodic regions of high activity, with a periodicity matching the distance of elevation per rotation during crystal growing. In the case of the film-depositing method, iron and germanium vapors deposit on the opposite material under conditions of close contact. It appears that in the region of the curved lines seen in both methods the germanium evaporates much faster than from the remaining surface, since the deposit on the iron plate is heaviest opposite these regions and since the germanium surface is kept relatively free of iron deposit in these regions. Also the presence of the fine curved grooves implies extraordinarily rapid evaporation from the position of the groove.

In the indium alloying method there is a clear demonstration of highly localized germanium activity in the consistent production of regular grooves. The crystal-growing furnace is designed with

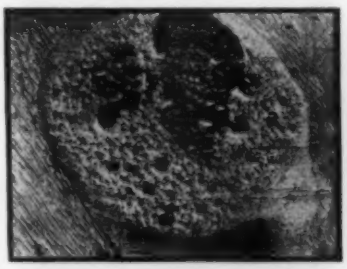

FIG. 3. Germanium surface after indium alloy attack. ~6×.

one principal "cold-spot" so that the rate of growth of the crystal is controlled in strongly periodic fashion. The position of the groove in the germanium probably marks the limit of a period of fast growth ending in slow and zero or even negative growth as the crystal passes the cold-spot and turns toward the hotter regions. The solid surface is then essentially stagnant and held at the melting temperature for a sensible fraction of a minute, during which time diffusion and annealing processes can make significant

changes. On reapproaching the cold-spot, rapid growth should then add new material with properties sufficiently different to cause the observed effects. The wall of crystals seen in Fig. 2 can be explained on a simple geometric basis derived from a careful microscopic examination. The groove cut by the indium is unsymmetrical, with one side much closer in shape to a rectangular cliff than the other, which has a smoother more gradual curve from the bottom of the groove. The rectangular cliff is a more favorable site for the rapid growth of crystals from the indium solution.[6] The shape of the groove etched by the indium is probably determined by the orientation of "simple" planes, such as the (111), as recently discussed by Moore[7] for the case of thermal etching of silver. As yet there is no clear evidence on the structure of the crystal in the region of the groove.[8]

R. N. Hall and others[9] have shown the effect of growth rate on the impurity segregation coefficient and Camp's results show such effects in germanium crystals grown as reported here. However, it does not appear that all of the phenomena noted in the present study can be readily explained solely on the basis of impurity distribution.

The experiments were performed at the General Electric Company in Lynn, Massachusetts with the help of J. B. Seabrook and others.

[1] P. R. Camp, J. Appl. Phys. **25**, 459 (1954).
[2] A part of this material was reported orally. A. C. English, I.R.E.-A.I.E.E. Conference, Durham, New Hampshire, June, 1951.
[3] See for example, H. F. Priest, in *Handbook of Semiconductor Electronics*, edited by L. P. Hunter (McGraw-Hill Book Publishing Company, New York, 1956), Sect. 6.
[4] The two nonmatching samples are shown since the best contrast for photography is obtained on the two materials at different times.
[5] J. I. Pankove, R C A Rev. **15**, 75 (1954).
[6] J. I. Pankove, J. Appl. Phys. **28**, 1054 (1957). In this paper, insufficient recognition is given to the influence of geometry on the delivery of germanium from an indium melt to the growing crystals.
[7] A. J. W. Moore, Acta Met. **6**, 293 (1958). (See particularly his Fig. 13.)
[8] A reviewer of this paper comments that he is almost convinced that there are narrow bands of high defect concentration created by the variation of growth rate.
[9] R. N. Hall, Phys. Rev. **88**, 139 (1952); J. A. Burton, R. C. Prim, and W. P. Slichter, J. Chem. Phys. **21**, 1987–1996 (1953).

Metastable Solid Solutions in the Gallium Antimonide-Germanium Pseudobinary System*

POL DUWEZ, R. H. WILLENS, AND W. KLEMENT, JR.
Division of Engineering, California Institute of Technology, Pasadena, California
(Received April 14, 1960)

THERE seems to be a dearth of published work on the Ga-Sb-Ge ternary system despite the great interest in the semiconductors GaSb and Ge. However, unpublished work[1] indicates that gallium antimonide and germanium may be regarded as the components of a simple eutectic pseudobinary system. The eutectic is estimated to occur at 35±10 at. % germanium at a temperature of 648±4°C. The maximum solubility of germanium in gallium antimonide is probably less than 2 at. % under equilibrium conditions.

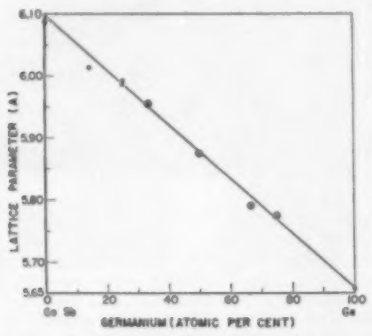

FIG. 1. Lattice parameter vs composition in the germanium-gallium antimonide psuedobinary system.

The procedure by which small amounts of liquid alloys can be quenched rapidly enough to forestall the normal nucleation and growth processes has been previously reported.[2] A series of alloys was prepared from stoichiometric gallium antimonide ($a=6.097$ A) and zone refined germanium ($a=5.658$ A). The alloys were cooled rapidly and their resultant structures studied by means of x-ray diffraction. A single phase—with the disordered zincblende structure—was observed in all of the alloys investigated. The plot of lattice parameter vs composition (Fig. 1)[3] does not indicate significant or systematic deviation from Vegard's law.

These results were not unexpected. The zincblende structure of gallium antimonide and the diamond structure of germanium are both based upon the necessity of each atom having four nearest neighbors which, in turn, is demanded by the covalent bonding. If the conventional valancies are assigned to the elements, the number of valence electrons/atom remains four throughout the pseudobinary system. Furthermore, the germanium atoms seem to be of such a size as to fit substitutionally into the lattice without causing undue distortion. From a qualitative study of the intensities of the diffraction lines on the Debye-Scherrer films and the absence of any detectable splitting of these lines, it is hypothesized that germanium substitutes randomly in the lattice, and does not destroy the cubic symmetry.

Acknowledgments are made to J. O. McCaldin for providing the alloys and for his continuing interest in this investigation.

* This work was jointly sponsored by the U. S. Office of Naval Research and the U. S. Atomic Energy Commission.
[1] J. O. McCaldin (private communication).
[2] Pol Duwez, R. H. Willens, and W. Klement, Jr., J. Appl. Phys. **31**, 1136 (1960).
[3] The graph of Fig. 1 is based on the nominal composition of the alloys before melting. It has not been possible to obtain reliable chemical analyses thus far. Maximum deviation between nominal and actual compositions might be as large as 5 at.% germanium.

Anomalous Thermionic Emission from UC and $(ZrC)_{0.8}(UC)_{0.2}$*

G. C. KUCZYNSKI
Department of Metallurgical Engineering, University of Notre Dame, Notre Dame, Indiana
(Received March 18, 1960)

THE thermionic emission from UC and $(ZrC)_{0.8}(UC)_{0.2}$ solid solution is anomalous in the sense that the parameter A obtained by best fitting the emission data into the Richardson-Dushman equation

$$I=AT^2\exp(-\varphi/kT)$$

is very much larger than A_0, the theoretical maximum of 120 amp/cm²(°K)² (work function φ is assumed constant). Indeed Pidd *et al.*[1] report its value as 7.3×10^5 amp/cm²(°K)² for UC and 6.6×10^4 amp/cm²(°K)² for the $(ZrC)_{0.8}(UC)_{0.2}$ solid solution, when for pure ZrC it is only 134 amp/cm²(°K)². It should be added that previous measurements of the thermionic characteristics of ZrC by Goldwater and Haddad[2] yielded the value of only 0.3 amp/cm²(°K)² for the coefficient A. The latter authors also reported $A=3\times10^4$ amp/cm²(°K) for ZrB and 550 amp/cm²(°K)² for ThC; however, they point out that in the latter cases the thermionic emission current never reached steady state. Recently Kmetko[3] suggested that such anomalously large emission constants, as well as some anomalously small ones, are due to the relatively large distances between metal atoms in the carbide or boride lattices, as a result of which the energy bands originating from the incomplete atomic f and/or d sublevels are narrow

enough for nondegeneracy to occur in the experimental temperature range.

The purpose of this note is to indicate that the results of Pidd *et al.* also allow another interpretation. Figure 1 represents the

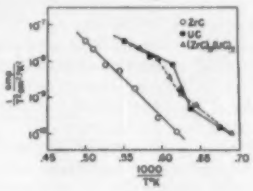

FIG. 1. A representation of the conventional plot of $\ln(I/T^2)$ vs $1/T$ of results obtained by Pidd *et al.*

conventional plot of $\ln(I/T^2)$ vs $1/T$ of the results obtained by them. (In the original paper, $\ln I$ is plotted against T°K.) Whereas the points representing emission current density I from ZrC can be reasonably approximated by one straight line, the ones obtained for UC and $(ZrC)_{0.8}(UC)_{0.2}$ would best be fitted by two straight lines separated by an interval of temperatures [1590°–1610°K for UC and 1610°–1650°K for $(ZrC)_{0.8}(UC)_{0.2}$] in which rather a sharp increase in current density takes place. It should be emphasized that the above interpretation of these plots may be offered as only a suggestion because of the paucity of data available. The emission data obtained from the plots in Fig. 1 are summarized in Table I.

TABLE I.

Material	Temp. Range	φ v	A amp/cm^2(°K)^2
UC	$T<1590$°K	3.62	90.0
	$T>1610$°K	2.67	3.5
$(ZrC)_{0.8}(UC)_{0.2}$	$T<1610$°K	3.53	55.0
	$T>1650$°K	2.53	0.3

In this interpretation the anomaly in A completely disappears. At this point it should be noted that an extremely sharp increase in current density was observed by Pidd *et al.*[4] when the thermionic current was drawn from a ZrC cathode at Cs vapor pressure of about 2 mm Hg.

The data plotted in Fig. 1 may suggest that the jump in current density in the regions of temperature previously specified is due to some transformation in the cathode materials. As there is no report that the compounds in question undergo any bulk allotropic transformation the only alternative is that the transformation involves the surface atoms.

* This work was performed at the Lockheed Aircraft Corporation Laboratory at Palo Alto, California, to which the author is a consultant.

[1] R. W. Pidd, G. M. Grover, D. J. Roehling, E. W. Salmi, J. D. Farr, N. H. Krikorian, and W. G. Witteman, J. Appl. Phys. **30**, 1575 (1959).
[2] D. C. Goldwater and R. E. Haddad, J. Appl. Phys. **22**, 70 (1951).
[3] E. A. Kmetko, Phys. Rev. **116**, 895 (1959).
[4] R. W. Pidd, G. M. Grover, E. W. Salmi, D. J. Roehling, and G. F. Erickson, J. Appl. Phys. **30**, 1861 (1959).

Dislocation Networks in a Low-Alloy Steel

A. S. KEH
Edgar C. Bain Laboratory for Fundamental Research, United States Steel Corporation Research Center, Monroeville, Pennsylvania
(Received April 14, 1960)

PREVIOUSLY, dislocation networks have been observed and studied in some detail in ionic crystals[1,2] by a decoration technique, and in some fcc metals[3,4] by the thin-film transmission technique. There is little published information on similar studies in bcc materials. Hirsch,[5] in a recent review article, showed one picture of such networks due to Venables in strained alpha-iron, whereas Allen[6] showed one due to McLean in annealed alpha-iron. It is the purpose of this note to report some recent observations of dislocation networks in a low-alloy steel.

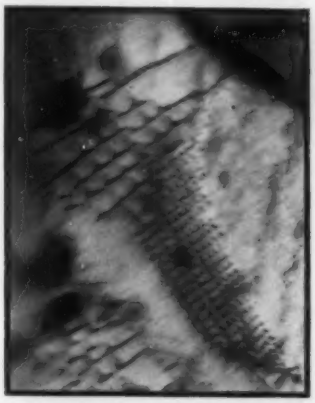

FIG. 1. Square dislocation network. ~80 000 ×.

The steel used had a nominal composition of 1% Cr, 1% Mn, and 0.4% C. It was first hot rolled to 0.030 in. thick. Subsequent heat treatment consisted of quenching from the austenite region and then tempering at 1250°F (667°C) for 24 hr or at 1325°F (718°C) for 72 hr. To obtain thin sections for electron transmission, the steel was first thinned in orthophosphoric acid to about 0.004 in., then electrolytically polished in a solution of chromic and acetic acid to a thickness of 1000–2000 A. Observations of the undeformed films were made in a Siemens electron microscope at 100 kv.

The microstructure of the steel (by light micrography) consists of small ferrite grains, either equiaxed or elongated, and carbide particles at the grain boundaries and within the grains. When thin films were examined in the electron microscope, dislocation networks were observed within ferrite grains. Figures 1 and 2 show some typical networks. In Fig. 1 the dark band at the upper right corner is a grain boundary and the black spherical particles are carbides. Several dislocation networks in the form of square grids can be seen. Hexagonal networks were also observed, as shown in Fig. 2. These networks are actually subboundaries which divide

FIG. 2. Hexagonal dislocation network. ~40 000 ×.

each grain into several subgrains. Frequently they were observed between carbide particles or completely surrounding them. Figures 3 and 4 illustrate these two cases.

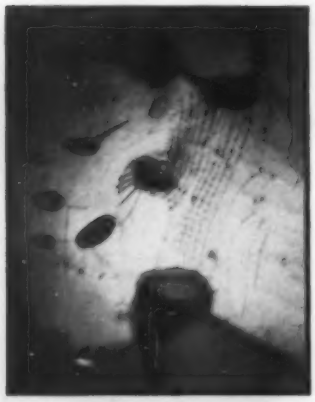

FIG. 3. Dislocation network between carbide particles. 33 333×.

FIG. 4. Dislocations surrounding a carbide particle. 33 333×.

The origin of these networks is unknown. Presumably, dislocations were introduced into the material either during transformation to martensite, or more likely, during the first stage of tempering. At a later stage of tempering, they probably rearranged themselves into stable networks of lower energy of the type shown in Figs. 1 and 2. According to Amelinckx and Dekeyser[7] both square and hexagonal networks are stable in bcc material. The dislocation reactions involved in their formation are being analyzed.

The author is grateful to A. Szirmae for his assistance in making the electron micrographs.

[1] J. M. Hedges and J. W. Mitchell, Phil. Mag. **44**, 223 (1953).
[2] S. Amelinckx, *Dislocations and Mechanical Properties of Crystals* (John Wiley & Sons, Inc., New York, 1957), p. 3.
[3] P. B. Hirsch, R. N. Horne, and M. J. Whelan, Phil. Mag. **1**, 677 (1956).
[4] M. J. Whelan, Proc. Royal Soc. (London) **A249**, 114 (1958).
[5] P. B. Hirsch, J. Inst. Metals **87**, 414 (1959).
[6] N. P. Allen, J. Iron Steel Inst. (London) **191**, 1 (1959).
[7] S. Amelinckx and W. Dekeyser, *Solid State Physics* (Academic Press, Inc., New York, 1959), Vol. 8, p. 325.

Probes at High Pressure

JOHN E. WHITE
General Electric Lamp Research Laboratory, Cleveland, Ohio
(Received May 2, 1960)

AS is well known, the Langmuir technique of probe measurements in gas discharges is not applicable at high pressures. Consequently, probes have been generally avoided above pressures of a few millimeters of mercury except for determinations of gradient in a uniform positive column. It now appears that there is a property of fine probes which has been overlooked, and which may add a useful technique for the study of high-pressure discharges.

In our laboratory, it was necessary to determine the cathode fall of potential in a xenon arc, operating in the thermionic mode at currents of 50–100 amp rms.[1] For this purpose, short probes of 5-mil diam tungsten wire were placed close above the emitting surface of a thin-film-activated tungsten coil which served as cathode. Contact potential errors were minimized by using a probe of the same material as the cathode, and subjecting it to the same flux of evaporant.

When a positive pulse of potential was applied to the probe, the voltage rose at essentially zero current up to a certain value of potential, at which the current rose abruptly. This is shown in a typical volt-ampere characteristic reproduced in Fig. 1. In this oscillogram, positive voltage increases to the right, and electron collection is in the upward direction. It is seen that as voltage rises above the current-zero point, a maximum voltage is dictated by ionization produced by the probe until the probe becomes an anode at the vertical line which terminates the oscillogram. The voltage at this last "anode potential" must be positive with respect to the potential of space around the probe. Since the "anode potential" is less than 0.2 v positive with respect to the current-zero point, current-zero must occur very close to space potential.

This is consistent with Schottky's unipolar diffusion theory. If we start with a probe at very slightly negative potential with respect to a surrounding plasma, under conditions of thermal equilibrium such that Boltzmann's equation is valid and transport is by mobility and diffusion, the electron density is given by

$$n=n_0\exp(Ve/kT), \tag{1}$$

in which n is the density of electrons in a region of potential V with respect to the undisturbed plasma, and where the density is n_0. T is the electron temperature. If, under our conditions of measurement, the ion current is so small as to register zero on our instrument, it may be neglected. The electron current flowing toward the probe has a mobility component i_v, and a diffusion component i_d

$$\begin{aligned} i&=i_v+i_d \\ &=\mu ne\,\mathrm{grad}V-eD\,\mathrm{grad}n, \end{aligned} \tag{2}$$

where μ is the electron mobility and D the diffusion coefficient. The Einstein equation relates μ and D,

$$D/\mu=kT/e. \tag{3}$$

On differentiating (1),

$$\mathrm{grad}n=ne/kT\,\mathrm{grad}V. \tag{4}$$

On substituting (4) and (3) into (2), Eq. (5) is obtained,

$$i=0. \tag{5}$$

One concludes from (5) that if ion current to the probe is really negligible and diffusion conditions prevail, zero current will flow to the probe until the voltage applied begins to be more positive than space potential, at which the electron current will rapidly rise under the influence of high mobility and an accelerating field. The Boltzmann condition for electrons breaks down at this point because electrons are free to enter and leave the plasma-to-probe "sheath" as soon as the probe becomes positive. The zero-current point should be a good approximation of space potential.

Under the conditions of Fig. 1, the pressure was 1.4 atm and the electron mobility more than 1000 times that of the ions; ion current to, plus electron current from, a negative probe were about 2 ma. So on the scale of the oscillogram, ion current to the probe was in effect zero.

What criterion may be employed for the applicability of this simple technique? M. A. Weinstein[2] has proposed that the basic relations used above, Eqs. (1) and (2), are applicable if the negative voltage region surrounding the probe extends into the plasma for many free paths. For the conditions of Fig. 1, it is easy to show

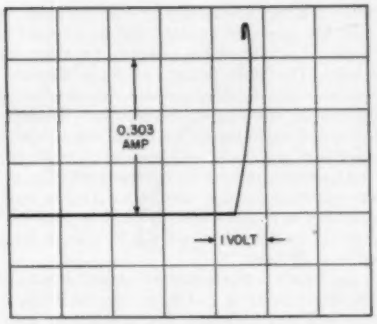

FIG. 1. Oscillogram of probe volt-ampere characteristic, obtained from a 10^{-4} sec pulse.

that the field from a negative voltage of 0.1 v applied to a 5-mil probe, extends for approximately 100 classical electronic free paths from the probe before falling to the gradient of the positive column. Even allowing for a considerable Ramsauer reduction in collision cross section, diffusion conditions prevail here. The zero-current of the probe characteristic appears to give the value of space potential within about 0.1 v.

The problem of local cooling of the plasma by a probe, discussed by R. C. Mason[3] for an arc in a molecular gas, is not so serious in a gas of poor heat conductivity such as xenon.

Constructive discussions with M. A. Weinstein are sincerely appreciated.

[1] To be published.
[2] Private discussion.
[3] R. C. Mason, Phys. Rev. 51, 28 (1937).

Cleavage Whiskers

JOHN D. VENABLES
Union Carbide Corporation, Parma Research Laboratory, Cleveland 1, Ohio
(Received May 2, 1960)

GILMAN and Johnston[1] have observed that elongated fragments are formed at cleavage steps when LiF is cleaved. The fragments can be several millimeters long, with the other two dimensions rarely exceeding 2 μ. Work performed in these laboratories has shown that "cleavage whiskers" can be produced in a wide variety of materials, with the list to date including: Si, Ge, InSb, HgSe, Mg_2Ge, MgO, Sb, and rubber erasers. The whiskers are observed on a freshly cleaved surface with the optical microscope, using either dark field illumination or reflected-polarized light. They may also be stripped from the surface with transparent Scotch tape and viewed with transmitted polarized light. In the case of Si, which has a relatively low optical absorption coefficient[2] in the visible region, the whiskers are transparent and vividly colored, showing variations in color with strain and thickness. The conditions which lead to these effects are undoubtedly related to the high index of refraction of Si, the photoelastic effect, and the variation of absorption coefficient with wavelength, but as yet no quantitative work has been done in this regard.

For observation in the electron microscope, the stripping may be done with either Formvar or Parlodion films using standard techniques. In this manner, using an EMU-3B microscope and an EMD-2 diffraction unit, it has been established for Si and InSb that the whiskers are single crystals, range in size from 5000 to <500 A, are the same composition as the parent material, i.e., are not oxides, etc., and are quite uniform in cross section from end to end.

With both the optical and electron microscopes, it is observed that many of the whiskers lie completely in cleavage steps while others have a free end running out of the step. Still others lie, debris-like, loose on the surface, having presumably been torn from a step during cleavage. Figure 1 shows an electron micrograph of two Si whiskers, one of which has partially separated from a step before the replica was made. Shown here is only one of several types of fine structure patterns which have been observed in the whiskers. Some of the patterns appear to arise due to strain and can be made to move with stresses caused by beam heating. Many of the lines are probably "bend contours" similar to those observed by Bendler.[2]

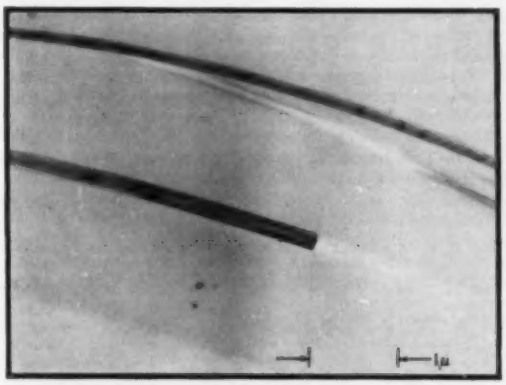

FIG. 1. Electron micrograph of Si "cleavage whiskers." The cleavage steps at which they were formed are visible.

The formation of the whiskers does not appear to be critically dependent upon the method of cleaving. Three-point loading of a rectangular beam or just hand breaking leads to a profusion of whiskers, as long as there are cleavage steps at which they may be formed. The origin of the steps has been considered by others,[4,5] and Gilman[6] has shown that the steps run perpendicular to the cleavage front as shown in Fig. 2. That whiskers should be formed at these steps is not obvious, and it is of interest to consider a

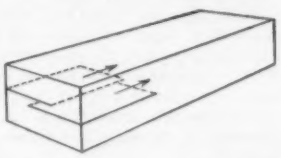

FIG. 2. Cleavage front with step advancing through crystal. Arrows show propagation direction of crack.

model derived in part from Orowan[7] and in part from Gilman[8] which might lead to such an unusual formation.

Consider Fig. 2 which shows a cleavage front broken by a step. Each segment of the front propagates in the cleavage direction, as shown by the arrows, but, in addition, must undergo lateral propagation as well. In fact, each segment would move completely across the crystal laterally if it were not held up by the canceling stress (see Orowan[7]) of the other cleavage crack. The end

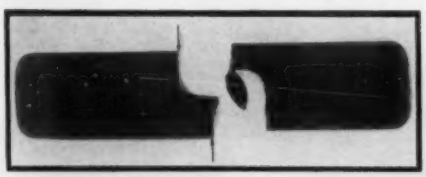

FIG. 3. "Cleavage rod" formation in rubber eraser. Small notches were cut at positions indicated by arrows. Tensile stress applied parallel to long direction forced planar "cleavage" and subsequent formation of rod upon separation.

view of the sample shows the two cracks in their "arrested" position. (See also Gilman.[4]) The upper half of the crystal is connected to the lower half via a small filament sandwiched between the two cleavage planes and when the final separation of the two halves is made, the filament is either torn loose to become a whisker or remains on one of the steps as a filament having three free sides. The filament would be visible in the optical microscope due to the air space between it and the parent material.

If a rubber eraser is notched with a razor blade in the special manner indicated in Fig. 3 and then pulled apart with a tensile stress applied parallel to the long axis, it is observed that a rubber "cleavage rod" is invariably formed upon separation. The rod is shown in section in the photograph. It will be noted that this geometry is not exactly analogous to the real cleavage case, but nevertheless this demonstration does tend to substantiate the above model.

The author is indebted to Professor C. S. Smith, G. Wagoner, R. Broudy, R. Bacon, R. Cummerow, and other members of the Parma Research Center for suggestions and criticisms. C. R. Whitsett provided the HgSe and Mg_2Ge. Special thanks are due R. Sprague who did the electron microscope and diffraction work.

[1] See F. R. N. Nabarro and P. J. Jackson in, *Growth and Perfection of Crystals* (John Wiley & Sons, Inc., New York, 1958), p. 84.
[2] W. C. Dash and R. Newman, Phys. Rev. **99**, 1151 (1955).
[3] H. M. Bendler, *Internal Stresses and Fatigue in Metals* (Elsevier, Amsterdam, 1959), p. 120.
[4] J. J. Gilman, J. Metals, **303**, 1252 (1955).
[5] T. L. Johnston, R. J. Stokes, and C. H. Li, Acta. Met. **6**, 713 (1958).
[6] J. J. Gilman, J. Metals **209**, 449 (1957).
[7] E. Orowan, *Dislocations in Metals* (AIME, New York, 1954), p. 144.
[8] J. J. Gilman, J. Appl. Phys. **27**, 1262 (1956).

Device for Measurement of the Electrical Properties of Bi_2Se_3 at Elevated Temperatures*

MAC J. SMITH, E. S. KIRK, AND C. W. SPENCER
Cornell University, Ithaca, New York
(Received June 3, 1960)

WHEN heated under air, nitrogen, or argon, crystals of Bi_2Se_3 begin to undergo rapid decomposition before reaching 250°C, well below the melting point at 706°C. Presumably selenium is lost from the structure since a red vapor is observed to form over specimens when heated in sealed quartz capsules and since the principle constituent in the vapor over liquid of stoichiometric composition is Se_2.[1] The purpose of this letter is to report a device which permits resistivity and Hall measurements to temperatures exceeding 600°C while the partial pressures of the constituent elements are maintained over the specimen.

The device is constructed by enclosing a specimen-mount assembly and associated electrical leads in a vacuum-tight glass container (Fig. 1.) A specimen of Bi_2Se_3, approximately 0.80 cm long, 0.15 cm wide, and 0.01 cm thick, is mounted on baked Lava stone. The mount is cut to the desired dimensions and drilled. It is then baked for 12 hr at 1000°C in air,[2] then placed in an evacuated capsule and baked for 12 hr at 600°C while in the presence of a mixture of Bi_2Se_3 and selenium. Current leads, which also serve to hold the specimen in place, are constructed of 0.03-cm thick Nichrome sheet. These are bolted to the stone, using stainless steel bolts. The Hall contact, an arrow-shaped section of Nichrome sheet, bolted to the stone base, can be adjusted to make point contact with the edge of the specimen. Resistivity leads, constructed from B and S Gauge No. 28 Nichrome wire, are bolted to the underside of the mount and inserted through drilled holes in the mount to make contact with the specimen edge on the upper surface. The specimen position may be adjusted to maintain contact through tension in these wires. If desired, each contact may be welded to the specimen by applying 10 v along the lead until it is heated to a red heat.

FIG. 1. Photograph of device used to maintain partial pressures of constituent elements over a specimen of Bi_2Se_3 during the course of measurement of resistivity and Hall coefficient at elevated temperatures. ~0.62 ×.

In order to provide a supplementary source of selenium to the vapor phase, either about 10 g of finely devided Bi_2Se_3 is included or a mixture of Bi_2Se_3 and about 1 g of selenium is included. A small perforated Vycor tube, attached to the specimen mount, is used as a container.

In principle, inclusion of only Bi_2Se_3 solid in the container would permit the solid phase to come into equilibrium with the vapor phase at compositions throughout the solid solution range. An approximate calculation shows that the electrical behavior of the solid will not be significantly affected by selenium lost to the vapor phase if approximately 10 g of Bi_2Se_3 is incorporated into the system. In this calculation, it is assumed that the vapor pressure of selenium over Bi_2Se_3 is not more that one-tenth of that for pure selenium at any particular temperature. It is also assumed that the molecular species in the vapor is Se_2, and that each selenium atom lost to the vapor phase is associated with one current carrier. As an example, a vapor volume of $10^6/cm^3$ then corresponds to not more than 10^{17} current carriers/cm^3 at 350°C. This is an order of magnitude less than the number actually present at this temperature.

Inclusion of a mixture of Bi_2Se_3 and selenium permits equilibrium only at the selenium-rich side of the solid solution phase field. Experimentally, little difference is observed between the behavior of specimens heated in the presence of the mixture and in the presence of only Bi_2Se_3 up to the vicinity of the intrinsic temperature range. The mixture is preferred in the intrinsic range since at these relatively high temperatures there is a tendency for the metal parts of the system to take up the selenium.

The specimen-mount assembly is spot-welded to a 5-lead flare stem of Nonex glass. A Nonex glass bulb, which has a glass tube attached to permit evacuation, is then placed over the specimen-mount assembly and sealed to the stem. The device is evacuated to 10^{-6} mm Hg, baked for 1 hr at 100°C, and sealed off. Lead wires are spot-welded to the stem leads and the device is inserted into a resistance furnace or into a low-temperature bath for temperature variation. The circuit used during measurement of the electrical properties is described by Dauphimee and Mooser.[3]

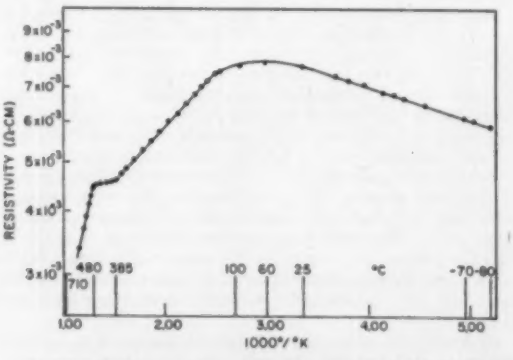

FIG. 2. Resistivity vs reciprocal of temperature for a Bi_2Se_3 single crystal. Current flow in cleavage plane.

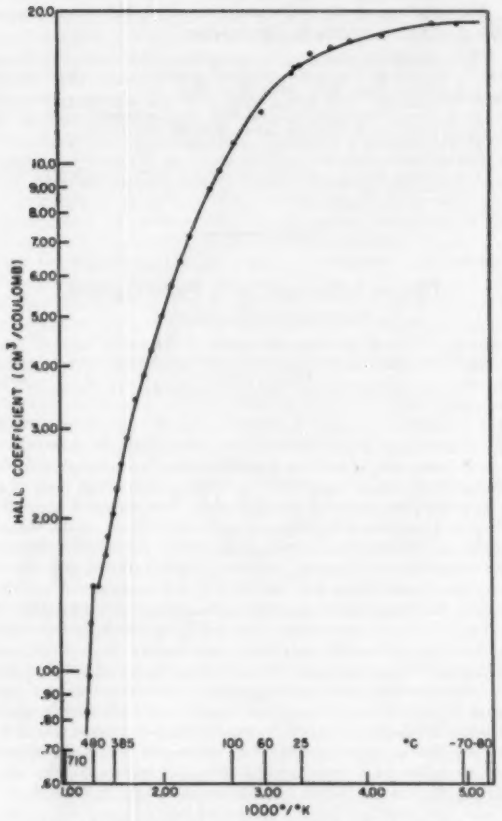

FIG. 3. Hall coefficient vs reciprocal of temperature for the Bi_2Se_3 single crystal, parallel to cleavage plane.

Plots of typical resistivity and Hall-coefficient data obtained on Bi_2Se_3 single crystals in a direction parallel to the cleavage plane are shown in Figs. 2 and 3, respectively. The slope of the linear portion of the resistivity curve in the temperature range above 480°C corresponds to an energy gap of 0.36 ev. This agrees closely with the optical value 0.35 ev reported by Black *et al.*,[4] but is somewhat higher than the optical value 0.275 ev reported by Austin and Sheard.[5] The slope of the linear portion of the curve in the temperature range 125° to 350°C corresponds to an energy of 0.09 ev. Presumably this energy is associated with donor levels below the conduction band, since the specimen shows *n*-type behavior over the entire temperature range studied, and since the two curves tend to indicate an exhaustion range for these levels.

Assuming a single-valley semiconductor model and neglecting details of scattering processes, these data yield 4×10^{17} and 5×10^{17} electrons/cm³ at −80° and 25°C, respectively. The corresponding mobility values are 2600 and 1600 cm²/v-sec, respectively. This is to be compared to a mobility of 600 cm²/v-sec reported earlier for a specimen at 25°C containing 2×10^{19} electrons/cm².[4]

* This research was supported by the U. S. Air Force under a contract monitored by the AF Office of Scientific Research at the Air Research and Development Command.

[1] R. F. Porter and C. W. Spencer, J. Chem. Phys. **32**, 943 (1960).
[2] A. U. Seybolt and J. E. Burke, *Experimental Metallurgy* (John Wiley & Sons, Inc., New York, 1953), p. 77.
[3] T. M. Dauphimee and E. Mooser, Rev. Sci. Instr. **26**, 660 (1955).
[4] J. Black, E. M. Conwell, L. Seigle, and C. W. Spencer, J. Phys. Chem. Solids **2**, 240 (1957).
[5] I. G. Austin and A. Sheard, J. Electronics and Control **3**, 236 (1957).

Field Induced Photoemission and Hot-Electron Emission from Germanium*

R. E. SIMON AND W. E. SPICER
RCA Laboratories, Princeton, New Jersey
(Received May 9, 1960)

HOT-ELECTRON emission and photoemission induced by an internal field have been observed from a germanium *p-n* junction. The surface of the germanium had been treated with cesium to reduce the electron affinity. These effects are similar to those previously reported for silicon.[1-3]

The experimental details including crystal geometry, the experimental tube, cesium treatment, and measuring techniques were similar to those used in the previous work on silicon.[2,3] The hot-electron emission was produced by applying a reverse bias to the *p-n* junction. Above 10 v, 20-μsec voltage pulses were used. The spectral distribution of field-induced photoemission was taken using chopped radiation from a monochromator with a band pass of 0.03 ev or less and with a reverse bias of 6 v applied to the crystal. The data from the better of two germanium crystals which we have studied will be presented here. This crystal had a grown *p-n* junction perpendicular to the emitting surface with a 0.01 ohm-cm *n*-type region and a 1 ohm-cm *p*-type region.

The spectral distributions of the photoelectric yield both with and without an internal electric field applied across the *p-n* junction are shown in Fig. 1. With no field applied, the threshold for photoemission from cesium-treated germanium (1.5 ev) is approximately the same as that previously reported for cesium-treated silicon.[3] This suggests that the surface barrier of the germanium is equal to or larger than that of cesium-treated silicon. The actual magnitude of the surface barrier cannot be determined until the energy levels from which the photoelectrons are excited are identified; however, it is possible to put limits on the surface barrier height. If the photoelectrons at the threshold of response originate from the bottom of the conduction band or from near the Fermi level of a metallic cesium surface layer, the barrier height would be about 1.5 ev; if they originate from the top of the valence band, the barrier height would be about 0.8 ev. These two values probably represent the upper and lower limits of barrier height.

Upon the application of a voltage across the *p-n* junction, field-induced photoemission appears. The threshold of this emission,

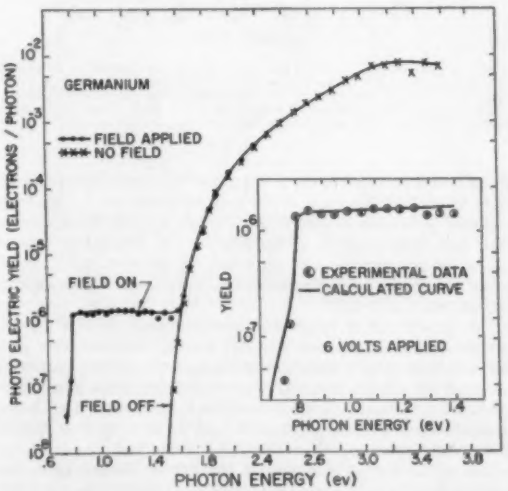

FIG. 1. The spectral response of the photoelectric yield from cesium-treated germanium with and without a reverse bias of 6 v applied across the *p-n* junction. The inset shows the fit between the experimental results and the calculated curve.

about 0.7 ev, corresponds to the band gap of germanium in agreement with the model previously proposed for field-induced photoemission.[3] In this model it is assumed that electrons which are generated by the light in the p-type material diffuse to the p-n junction where they are accelerated through the internal field and thus receive sufficient energy to escape from the crystal. A simple theory based on this model has previously been described.[3] The inset on Fig. 1 shows the fit obtained between this theory and experiment using the absorption data of Dash and Newman[4] and assuming a diffusion length of 10^{-3} cm.

Figure 2 shows the hot-electron emission and field-induced photoemission currents as a function of the voltage between two probes on opposite sides of the junction. The magnitude of the field-induced photoemission is, of course, arbitrary since it is proportional to the light intensity. For voltages below 3 v, the hot-electron and field-induced photoemission have almost the same voltage dependence. This indicates that in this low-voltage range the hot-electron emission is proportional to the rate of thermal

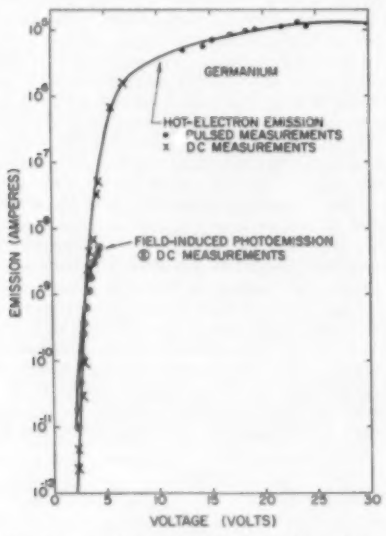

FIG. 2. Hot-electron emission and field-induced photoemission as a function of voltage applied in the reverse direction across the p-n junction. Since chopped light was not used in this experiment, the field-induced photoemission current was obtained by taking the difference between the emission currents observed with and without light incident on the sample.

generation of electrons in the p-type material. As would be expected because of the difference in their band gaps, the hot-electron emission from germanium in this voltage range is much greater than that from similarly doped silicon.[5] The decreasing rate of rise of the photoemissive yield, which can be seen in Fig. 2, at higher voltages probably indicates the onset of avalanche breakdown.

The appearance of appreciable photoemission induced by an internal field and prebreakdown hot-electron emission from germanium treated with cesium suggests that the surface barrier is less than the minimum energy that an electron needs to produce a hole-electron pair[6,7] (1.5–1.9 ev). This is in agreement with the range of values which we estimated from the spectral distribution of the photoemission with no internal field applied.

It is interesting to note that in the sample studied here, the junction-depletion layer is determined by the p-type material since it has the higher resistivity. Thus, the surface breakdown mechanism of Garrett and Brattain[8] is probably not applicable here as Burton thought was the case for his silicon sample.[1]

The assistance of Glenn O. Fowler in making the measurements described here is gratefully acknowledged.

* The research reported in this paper has been supported in whole or in part by U. S. Signal Corps, Fort Monmouth, New Jersey, under contract.

[1] J. A. Burton, Phys. Rev. **108**, 1342 (1957).
[2] R. E. Simon and W. E. Spicer, Phys. Rev. (to be published).
[3] W. E. Spicer, Bull. Am. Phys. Soc. Ser. II, **5**, 69 (1960).
[4] W. C. Dash and R. Newman, Phys. Rev. **99**, 1151 (1955).
[5] W. E. Spicer and R. E. Simon (unpublished data).
[6] S. Koc, Czech. J. Phys. **7**, 91 (1957).
[7] V. S. Vavilov and K. I. Britsin, Zh. Eksp. i Teoret. Fiz. **34**, 521 (1958).
[8] G. B. Garrett and W. H. Brattain, J. Appl. Phys. **27**, 299 (1956).

Charred Dextrose as a Paramagnetic Resonance Standard*

R. H. HOSKINS AND R. C. PASTOR
Hughes Research Laboratories, A Division of Hughes Aircraft Company, Malibu, California

(Received February 25, 1960; and in final form May 2, 1960)

IT is common practice in several types of magnetic resonance experiments (e.g., susceptibility measurements, saturation experiments, magnetic field determination) to compare the behavior of the spin system under investigation with that of a standard whose behavior is predictable. The standard generally used is 1,1-diphenyl-2-picrylhydrazyl (DPPH). Certain inconveniences, chiefly temperature dependence of the properties of the resonance, can arise in the case of DPPH. We should like to propose dextrose charred at 560°C (CD)[1,2] as an alternative substance. We have made spin-resonance measurements on CD at X band over a temperature range 1.4°K to 500°K and find no variation in line width, g value, or spin density. In addition, cw saturation measurements at 300°, 77°, and 4.2°K indicate that the thermal relaxation time is independent of temperature over this range: $T_1=T_2\approx 2\times10^{-7}$ sec; thus no saturation effects will occur at power levels used in many types of resonance experiments. The temperature independence of these resonance properties makes CD attractive as a paramagnetic resonance standard. The pertinent properties of DPPH and CD are compared in Table I.

TABLE I. Comparison of properties of DPPH and CD.

	DPPH	CD
Availability	Commercially available as single crystal or powder.	Easily prepared as powder sealed in vacuum.
Stability	Fairly good storage properties when kept from heat and light. Decomposes markedly above 75°C.	Excellent when properly sealed.[a] May be heated to 560°C.
Spin density	1.5×10^{21} cm^{-3}	5×10^{20} cm^{-3}
Line width (3-db points)	2.8 oe (may vary according to sample preparation; single crystals anisotropic).	0.6 oe
g value	2.0037 ± 0.0002[b]	2.0023 ± 0.0003[c]
Temperature dependence of resonance properties	Line width starts to increase below 77°K, evidence of antiferromagnetic transition.[d]	No change in line width, g value, or spin density from 500°–1.4°K, cw-saturation experiments at 300°, 77°, and 4.2°K show $T_1=T_2\approx2\times10^{-7}$ sec at all temperatures.[e]

[a] In the event the seal is broken, the sample may be rejuvenated by repumping; or in the case of a small leak, it may be restored by resealing and heating at 400°C for 1 hr as the substance acts as its own "getter." See footnote reference 2.
[b] A. N. Holden, C. Kittel, F. R. Merritt, and W. A. Yager, Phys. Rev. **77**, 147 (1950); C. H. Townes and J. Turkevich, Phys. Rev. **77**, 148 (1950).
[c] Our value is in substantial agreement with that (2.0025) reported by Singer, Spry, and Smith, *Proceedings of the Third Conference on Carbon* (Pergamon Press, New York, 1959), p. 125.
[d] L. S. Singer and E. G. Spencer, J. Chem. Phys. **21**, 939 (1953); Gerven, Van Itterbeek, and Wolf, J. phys. radium, **18**, 417 (1957).
[e] All values measured at X band. The line width has been measured at 50 Mc at room temperature and found to be 0.7 ± 0.1 oe (T. H. Maiman, unpublished). The range of the temperature independence of the properties of the resonance probably extends from 800°–1.4°K.

The effect of exchange in this material is strong enough to produce a conveniently narrow line for field calibration purposes and provide a sink for rapid thermal relaxation,[3] but not strong enough to cause a ferromagnetic or antiferromagnetic transition to occur in the temperature region of general interest in magnetic resonance experiments. We can estimate, from the exchange narrowing of the resonance following Anderson and Weiss,[4] that any transition should take place below 1°K. Therefore, CD makes a standard with a conveniently narrow line and a conveniently short relaxation time with both properties independent of temperature over a very wide range. It may also be noted that since the high-spin density and narrow line width of CD allow observation of the resonance without cavity at liquid-helium temperatures, a signal may be observed by placing a sample at the end of an untuned waveguide and sweeping frequency. This makes possible the precise measurement of magnetic fields (in the range of thousands of oersteds) which may be confined in low-temperature apparatus and thus not accessible to the usual room-temperature field measuring devices. No sample shape demagnetizing effects are observed if the samples are tightly packed spheres; however, some broadening and asymmetry may be noted in samples of other shapes at 1.4°K.

The char sample (CD) was prepared from anhydrous dextrose (Mallinckrodt, Analytical Grade). The material was heated gradually in an atmosphere of nitrogen. A period of about two days was required to reach 200°C in order to avoid excessive frothing. The latter effect subsides considerably when the temperature of the char reaches about 300°C. At this point the material was cooled while still under an atmosphere of nitrogen. The sample was then ground in air to a fine powder and introduced again into the furnace after the container was thoroughly flushed with nitrogen. The temperature was gradually raised to 560°C and maintained at this value for at least 12 hr. The char was cooled to room temperature under an atmosphere of nitrogen, ground in air to a fine powder, and introduced in a glass bulb formed at one end of a sample tube. The sample tube was connected to a vacuum manifold, the bulb kept under liquid nitrogen, and its contents gradually outgassed. A two-day period of slow pumping, combined with the gradual recession of the coolant level, made it possible to obtain a pressure of 10^{-4} mm without causing any violent agitation of the fine powder. This procedure left the capillary stem free of char particles, a condition necessary to ensure a vacuum-tight seal when the sample was sealed off the line. About a week of outgassing was needed before the pressure was less than or equal to 10^{-7} mm with the sample either hot (450°C) or cold (25°C). This condition was taken to be the point of minimum outgassing and the sample was sealed off the line.

It should be noted that any sealed sample that is immersed in liquid helium should be treated with some caution on warmup. The danger is that a helium leak may develop which is undetectable until the sample is warmed; then makes itself evident in an explosive manner.

* This work was supported in part by the U. S. Army Signal Corps.

[1] R. C. Pastor, J. A. Weil, T. H. Brown, and J. Turkevich, Phys. Rev. 102, 918 (1956).
[3] R. C. Pastor and R. H. Hoskins, J. Chem. Phys. 32, 264 (1960).
[2] J. P. Goldsborough, M. Mandel, and G. E. Pake, Phys. Rev. Letters 4, 13 (1960).
[4] P. W. Anderson and P. R. Weiss, Revs. Modern Phys. 25, 269 (1953).

Precipitation of Copper in Gallium Arsenide

J. M. Whelan and C. S. Fuller
Bell Telephone Laboratories, Inc., Murray Hill, New Jersey
(Received May 2, 1960)

COPPER is known to be an acceptor impurity in GaAs which diffuses rapidly in the temperature range 650–1200°C.[1] The diffusion is consistent with the mechanism of interstitial-substitutional equilibrium diffusion. At 480°C the rate of precipitation is slow in floating-zone GaAs crystals supersaturated with Cu. We have followed the changes in the electrical properties associated with the precipitation of Cu from samples containing 10^{17} Cu atoms cm^{-3}, the solubility in intrinsic GaAs at 725°C. Precipitation was caused by annealing over the temperature range 500–600°C. The results for one sample annealed at 550°C are described here. These are typical of the behavior of others amples annealed at 500 and 600°C.

Copper introduced at 1000–1200°C has a single acceptor level in GaAs. This has been established by diffusing limited amounts of Cu^{64} into samples containing S or Se and then treating them at 1000–1200°C. In all cases, the Cu concentrations[2] were insufficient to convert the samples from n to p type. The decrease in electron concentrations equaled the Cu concentrations within the experimental error, $\pm 10\%$. The acceptor ionization energies of Cu-doped p-type samples varied from 0.14 to 0.16 ev depending on the Cu concentration and the degree of compensation. The upper limit was observed for closely compensated samples and the lower value in essentially uncompensated samples containing 10^{17} Cu atoms cm^{-3}. This variation may be due to the effects of excited states. On the basis of previous arguments, we believe the acceptor center is a Cu atom substituted on the Ga sublattice.[1]

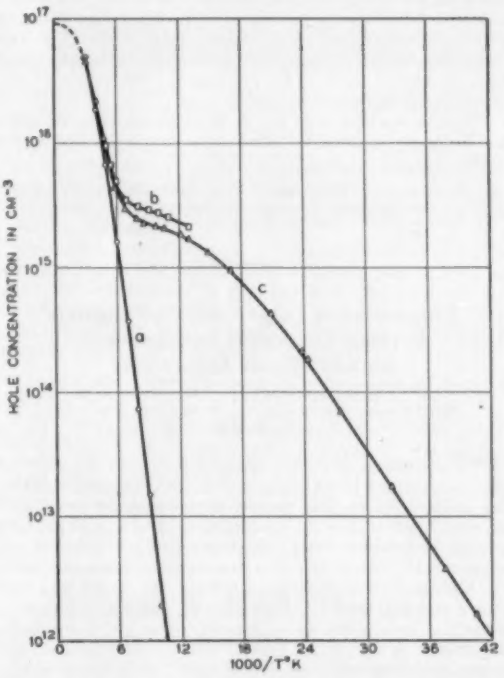

FIG. 1. (a) Variations in hole concentration with temperature for GaAs saturated with Cu at 725°C, heated to 1000°C, and quenched; (b) sample after additional anneal at 550°C for 2 min; (c) sample after anneal at 550°C for a total of 6 min.

Curve a in Fig. 1 shows the variation in hole concentration, $1/Re$, with temperature for a sample containing 1×10^{17} Cu atoms cm^{-3} and 5×10^{15} unidentified donors cm^{-3}. The acceptor ionization energy is 0.14 ev. This sample was prepared by saturating a n-type sample with Cu at 725°, removing the excess surface Cu, heating to 1000°C for 10 min, and quenching. It was then heated for 2 min at 550°C and quenched. The formation of an additional acceptor with a low-ionization energy is evident from curve b. Associated with this is a slight decrease in concentration of the

0.14 ev Cu level. Further annealing at 550°C for 4 min reduced the concentration of the shallow acceptor and, to a smaller degree, the concentration of the substitutional Cu. The ionization energy of the shallow acceptor is 0.021 ev. This behavior was observed in other samples originally containing 10^{17} Cu atoms cm^{-3} and annealed at 500–600°C. At 500°C, the rate of formation of the shallow acceptor was lower, also much longer annealing times were required for the removal of substitutional Cu and the shallow acceptor. At 600°C the rates of formation and disappearance of the shallow acceptor as well as the Cu level were considerably faster.

The previous results closely parallel the effects observed by Penning in his study of the precipitation of Ni in Ge.[3] He observed the rapid formation of an acceptor whose ionization energy was 0.02 ev. On further annealing the rate of removal of this defect paralleled the Ni precipitation. Ni in Ge also diffuses by an interstitial-substitutional mechanism. Penning assumed the 0.02 ev acceptor was associated with vacancies left behind in the lattice when substitutional Ni atoms move to interstitial sites. The interstitial Ni atoms diffuse rapidly to precipitation nuclei. Thus, the rate of precipitation is ultimately limited by the rate of removal of vacancies at dislocations or at the surfaces.

From the similarity of the precipitation of Cu in GaAs and Ni in Ge, we tentatively conclude that the 0.021 ev acceptor in GaAs is associated with a Ga vacancy or a Ga vacancy-impurity complex. If this is correct, the precipitation of impurities in *III-V* compounds which diffuse via an interstitial-substitutional mechnism provides a method for investigating the effects of nonstoichiometry in these compounds.

The authors are indebted to J. A. Ditzenberger, G. H. Wheatley, and Katherine Wolfstirn for their assistance with the experimental work.

[1] C. S. Fuller and J. M. Whelan, J. Phys. Chem. Solids **6**, 173 (1958).
[2] These were determined by use of tracer techniques.
[3] P. Penning, Philips Research Repts. **13**, 17 (1958).

Preparation of Large Calcium-Tungstate Crystals Containing Paramagnetic Ions for Maser Applications

K. Nassau and L. G. Van Uitert
Bell Telephone Laboratories, Inc., Murray Hill, New Jersey
(Received April 25, 1960)

THE technique of pulling single crystals from the melt[1] has been applied to calcium tungstate, both pure and containing rare earth additions. This appears to represent the first clearly successful application of the Czochralski method to multiple oxide systems. This method seems to have been used in the case of pure oxides only for V_2O_5 by Boros,[2] who gives no experimental details. The Kyropoulos technique (growth below the surface of a melt from a rotating seed) has been used for potassium niobate by Miller[3] and barium titanate by Linares,[4] using K_2CO_3 and BaF_2, respectively, as flux. In the present work no flux was used, and continuous pulling produced crystals up to 7 in. in length and up to ½ in. in diam, essentially free from visible defects.

Calcium-tungstate crystals containing rare earth ions are of interest for maser applications.[5,6] Masers employing traveling wave structures in particular require long rods of these materials.

Previous methods used to obtain crystals of calcium tungstate have included growth from the flux[6,7,8] and applications of the Bridgman-Stockbarger[9] and the Verneuil (flame fusion) processes.[9,10] Hydrothermal growth has also been used.[11] Large single crystals have proven to be difficult to obtain by these methods, while the pulling technique employed below appears to impose no limitation as to size, even when appreciable rare earth additions are present.

In the present work, a rhodium crucible was heated directly by rf induction. Crystals were rotated during growth at 12 rpm and pulled at rates of up to 3 in./hr. Seed crystals were not essential, as growth initiated readily on a platinum wire. Small pieces so obtained are then tied to a platinum rod to grow larger crystals. Calcium tungstate grown from the flux as well as commercial luminescent grade material were used, both pure and in combination with flux-grown[8] $Na_{0.5}re_{0.5}WO_4$, where re has included elements such as cerium, europium, gadolinium, terbium, dysprosium, and erbium. Rare earth concentrations as high as 4 formula % are readily incorporated. Other alkali rare earth tungstates, or pure rare earth tungstates, undoubtedly will incorporate readily. It seems likely that at least in the case of low concentrations some sodium is lost.

In the experimental apparatus used, single crystals were readily grown at temperatures near 1600°C. Some annealing was helpful both to prevent cracking of the thicker crystals and to remove the slight discoloration sometimes observed. The latter is believed to originate from slight reduction due to limited access of atmospheric oxygen during growth. The crystals obtained are usually perfectly transparent and fluoresce brightly under ultraviolet illumination. Figure 1 shows a calcium-tungstate crystal containing

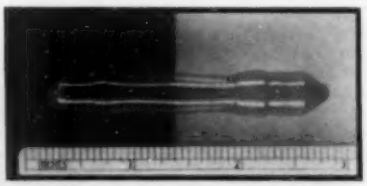

FIG. 1. Calcium-tungstate single crystal containing 0.3% dysprosium pulled from the melt.

0.3% dysprosium and grown as described above. The diameter is nonuniform, due to lack of temperature control during growth. Preliminary results indicate the feasibility of growth in several crystallographic directions. It appears that the maximum dimensions that can be attained are limited only by the sizes of the crucible and pulling mechanism.

The authors wish to acknowledge the assistance of K. E. Benson and F. W. Swanekamp of these Laboratories in the early phases of this work. The flux-grown material was prepared by R. R. Soden and the photograph taken by S. Preziosi.

[1] W. D. Lawson and S. Nielsen, *Preparation of Single Crystals* (Academic Press, Inc., New York, 1958), p. 10 ff.
[2] J. Boros, Z. Physik **126**, 721 (1949).
[3] C. E. Miller, J. Appl. Phys. **29**, 233 (1958).
[4] R. C. Linares, J. Phys. Chem. (to be published).
[5] L. G. Van Uitert and R. R. Soden, J. Appl. Phys. **31**, 328 (1960).
[6] C. F. Hempstead and K. D. Bowers, Phys. Rev. **118**, 131 (1960).
[7] L. G. Sillen and A. L. Nylander, Arkiv. Kemi, Mineral. Geol. **17A**, No. 4 (1943).
[8] I. N. Anikin, Doklady Akad. Nauk. S.S.S.R. **110**, 645 (1956).
[9] S. Zerfoss, L. R. Johnson, and O. Imber, Phys. Rev. **75**, 320 (1949).
[10] R. K. Verma, G. N. Sirkar, and S. Chaterjee, J. Sci. Ind. Research (India) **13A**, 516 (1954).
[11] R. A. Laudise (to be published).

Generation of Alternating Current in the Cesium Cell*

H. L. Garvin, W. B. Teutsch, and R. W. Pidd
John Jay Hopkins Laboratory for Pure and Applied Science, General Atomic Division of General Dynamics Corporation, San Diego, California
(Received April 26, 1960)

THE use of a cesium cell as a heat-to-electric-energy converter has been described extensively in the literature of the past two years.[1–5] The cell is a vacuum diode which is modified by introducing the vapor of cesium metal, at pressures from 10^{-6} to 1 mm Hg, into the vacuum envelope. Some of the vapor is ionized through an interaction with the hot cathode, usually to such an

extent that the electronic space charge in the diode is completely suppressed by the presence of positive ions. In this condition the diode has demonstrated an electric power output as high as 30 w for each square centimeter of cathode surface area; this output is dc, of about 30 amp/cm² at 1-v terminal potential. The purpose of this Letter is to report that under certain conditions the cell also produces ac in significant amounts. This ac appears to be related to intrinsic phenomena occurring within the cell, and it is only slightly affected by the nature of the external circuit.

A graph, such as the one shown in Fig. 1, of the cell current vs terminal potential difference displays the essential features of the operation of the cell in producing dc power. As the load resistance is increased from zero, the cell current at first is nearly constant at a value corresponding to the emission limit of the cathode. A breaking point is reached, usually at about 2 v, where the terminal potential has a retarding effect on the cell current. A further increase in the load resistance sharply reduces the current until the open-circuit voltage is reached.

We have found that over a substantial range of this power curve an ac signal is also being produced. Between points 2 and 1 in Fig. 1, where the current is changing sharply with voltage, there is no alternating signal. Near point 2 there is an onset of current and voltage variation in the form of sharp pulses superimposed on the steady output. The pulses represent a turning off of the current, that is, a reduction below the dc level. It appears that the cell current is being interrupted at regular time intervals. At a lower voltage (point 3), the repetition rate increases to a frequency of 10^8 cps, which is about a factor of two times the rate at onset. At point 4, a fully developed alternating signal is found. Oscillogram records of the wave shapes are shown in Fig. 2.

The cell is in the form of plane-parallel geometry, as described previously, in which a cathode emitter of 2-cm² area is opposed by an oil-cooled collector 4 mm away. The cathode is made of tantalum, the anode of copper. The data presented were obtained at a cathode temperature of 2000°C, an anode temperature of 150°C, and a cell envelope temperature of 60°C. The cathode temperature is measured by use of an optical pyrometer, whereas the collector and envelope temperatures were monitored by use of thermocouples. The vapor pressure of cesium in the cell is adjusted by immersion of the envelope into a thermostatically controlled oil bath.

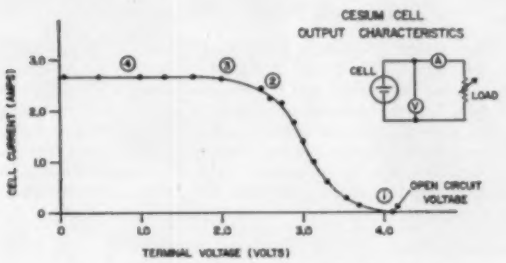

FIG. 1. Output characteristics of the cesium cell.

The ac phenomena occur over a wide range of variables. The appearance of the waveforms depends systematically on the dc terminal potential difference. For example, if the emitter is reduced by 200 C°, the cell current is lowered by a large factor, and the matched-load resistance is correspondingly increased. However, the voltages at which the various waveforms appear change very little, if at all. In all cases, some dc must be drawn from the cell before the alternating signal appears.

The experimental evidence obtained so far does not justify a positive identification of a mechanism of ac production. On the basis of what is known, it appears that an intrinsic instability exists, in the plasma region between the cell electrodes, such that the electronic current is automatically interrupted. It may be noted that the period of oscillation corresponds roughly with the transit time in the cell of ions (or neutrals) of thermal energy. Experiments now under way should yield a more decisive picture of this new phenomenon.

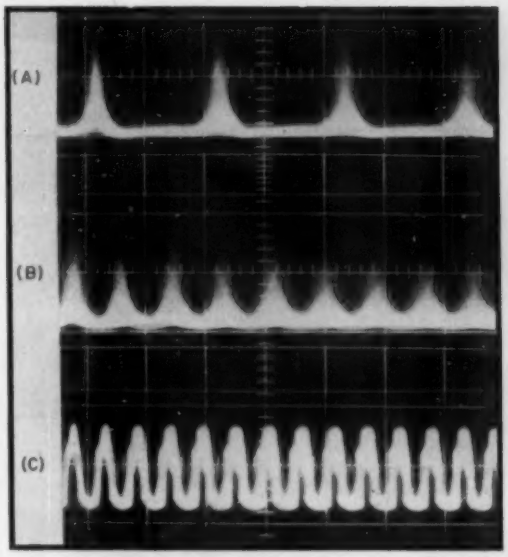

FIG. 2. Oscilloscope traces of output waveforms at 2.5 v (A), 2.0 v (B), and 1.0 v (C) terminal voltage. Voltage scale is 1 v/division; sweep time is 10 μsec/division.

Subsequent to the preparation of this Letter it has come to the author's attention that similar oscillations have been observed in cesium cells which differ in geometry from the one described herein.[4]

The authors wish to acknowledge the invaluable assistance of R. Hamerdinger in performing the experiments.

* This work was supported in part by the eight companies comprising the Rocky Mountain-Pacific Nuclear Research Group and by the San Diego Gas & Electric Company.

[1] G. M. Grover, D. J. Roehling, E. W. Salmi, and R. W. Pidd, J. Appl. Phys. **29**, 1611 (1958).
[2] K. G. Hernqvist, M. Kanefsky, and F. H. Norman, R C A Rev. **19**, 244 (1958).
[3] V. C. Wilson, J. Appl. Phys. **30**, 475 (1959).
[4] R. Fox and W. Gust, Bull. Am. Phys. Soc. Ser. II, **5**, 80 (1960). Similar observations made in several other laboratories have also been reported to us.

Books Reviewed

Prompt, noncritical reviews appear in this column. Critical reviews of many of the books described here will appear in Physics Today, The Review of Scientific Instruments, *or* American Journal of Physics.

International Directory of Radioisotopes. Vol. I. Pp. 264. International Atomic Energy Agency, Vienna, 1959.

This directory lists radioisotopes commercially available from 44 suppliers (28 American, 2 Canadian, 11 European, plus 1 Indian and 2 Japanese). One supplier is the Russian State Union Trust, SOYUZREAKTIV. The compilation resembles closely in form that used by the Oak Ridge and other catalogs, by providing data on chemical form, specific and total activity, price, purity, etc. Volume I lists radioactive isotopes and sealed or plated sources only; tagged compounds will be

compiled in volume II, which is due to appear shortly. Two omissions should be pointed out: The dates of the information from the suppliers are not given, and information on stable isotopes is neither provided nor planned. The directory will be very useful for those purchasing isotopes. For example, some isotopes listed are not available in the Oak Ridge catalog. In addition, the directory provides amusing browsing. Why is the world's only supplier of Kr^{79} and Pb^{209} the Soviet Trust? Would the Soviets really sell the U^{235} and Pu^{239} listed? How does the Radiochemical Center, Buckinghamshire, England, hope to compete in sales of 100 Mc RaD-Be neutron sources at $28,000 apiece, when the Canadian AECL offers them for $3,750?

Electron Physics. O. KLEMPERER. Pp. 248+xi. Academic Press, Inc., New York, 1959. Price $7.00.

This small volume is devoted to a survey and summary of the properties of the electron in the "quasi-free" state. The topics included are: electron ballistics (including electron optics), electron space charge, measurement of electronic charge and electronic charge to mass ratio, wave properties of electrons, and electron spin. Each topic is treated quite briefly, but important references to more extensive treatments are given. A few problems appear at the end of each chapter.

Books Received

Electricity and Magnetism. HENRY E. DUCKWORTH. Pp. 409. Holt, Rinehart, and Winston, Inc., New York, 1960. Price $8.00.

Thermochemistry for Steelmaking. JOHN F. ELLIOTT AND MOLLY GLEISER. Sponsored by the American Iron and Steel Institute. Pp. 294. Addision-Wesley Publishing Company, Inc., Reading, Massachusetts, 1960. Price $10.50.

Foundations of Electromagnetic Theory. JOHN R. REITZ AND FREDERICK J. MILFORD. Pp. 362+xii. Addison-Wesley Publishing Company, Inc., Reading, Massachusetts, 1960. Price $8.75.

Principles of Electricity and Magnetism. E. M. PUGH AND E. W. PUGH. Pp. 414. Addison-Wesley Publishing Company, Inc., 1960. Price $0.00.

Atomic Energy in the Soviet Union. ARNOLD KRAMISH. Pp. 210 +xiv. Stanford University Press, Stanford, California, 1959. Price $4.75.

Magnesium and its Alloys. C. SHELDON ROBERTS. Pp. 224. John Wiley & Sons, Inc., New York, 1960. Price $9.00.

Elementary Statistics. SIDNEY F. MACK. Pp. 170+xxiii. Henry Holt and Company, Inc., New York, 1960. Price $4.50.

Electrical Noise, Fundamentals and Physical Mechanism. D. A. BELL. Pp. 336. D. Van Nostrand Company, Inc., New York, 1960. Price $9.75.

Physics for Students of Science and Engineering. Part II. (Continued from Part I). D. HALLIDAY AND R. RESNICK. Pp. 1024. John Wiley & Sons, Inc., New York, 1960.

Introduction a L'Etude De La Rheologie. B. PERSOZ. Pp. 242. Dunod Press, Paris, 1960. Price 44NF.

Announcements

Engineering Applications Symposium

A two-day Symposium on Engineering Applications of Probability and Random Function Theory sponsored by Purdue University will be held November 15–16, 1960, at Lafayette, Indiana. The symposium will stress applications of probability and random function theory to problems associated with factors of safety in structures, reliability of structures and systems, optimization of systems of all types which are subject to random disturbances, jet and rocket engine noise fields, and traffic control. Requests for further information should be addressed to either J. L. Bogdanoff or F. Kozin, Co-chairmen of the Symposium, Division of Engineering Science, Purdue University, Lafayette, Indiana.

Pittsburgh Diffraction Conference

The annual Pittsburgh Diffraction Conference will be held November 9–11, 1960, at Mellon Institute, Pittsburgh, Pennsylvania. Sessions will be devoted to metals and alloys, instrumentation, structures, polymers and fibers, refractories, electron probe, and electron diffraction. The evening meeting will be addressed by Professor I. Fankuchen of the Polytechnic Institute of Brooklyn. Further information can be obtained from L. F. Vassamillet, Mellon Institute, 4400 Fifth Avenue, Pittsburgh 13, Pennsylvania.

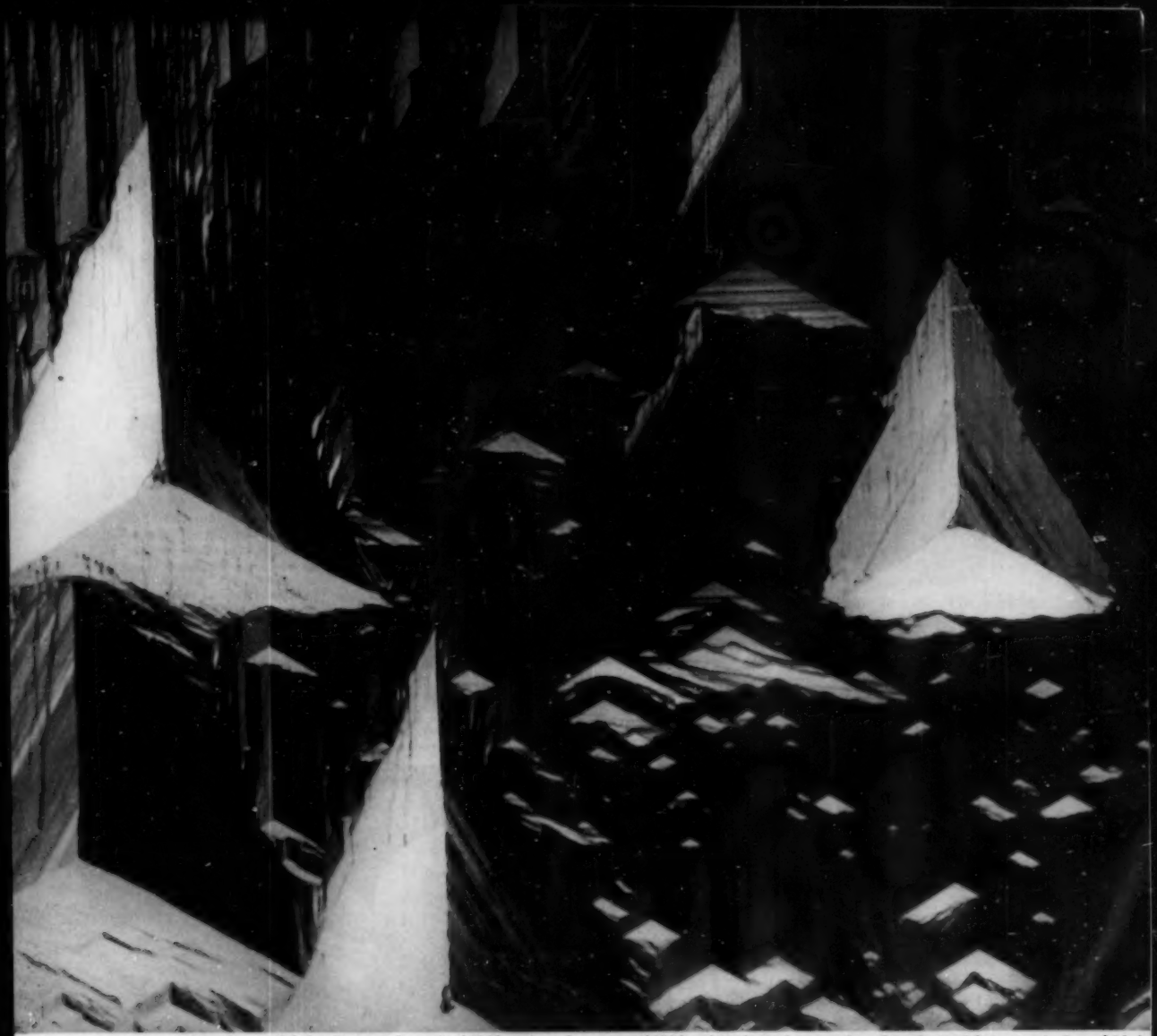

Vapor-grown germanium has well-defined pyramids on the {111} surface, but not on {110} or {211} which are preferred for device fabrication (enlarged 11x).

Growing junctions from the vapor state

Scientists at IBM Research are developing a process by which semiconductors can be grown from the vapor state to almost any desired purity or configuration—a process that will simplify fabrication of such devices as Esaki diodes and high-speed transistors.

A typical process involves a reaction in which two germanium iodide molecules react on the surface of a seed crystal to form one molecule of germanium tetraiodide and a germanium atom:

$$2GeI_2 \leftrightharpoons GeI_4 + Ge$$

Early work showed that the semiconductor deposits epitaxially; that is, takes on the crystal structure of the seed material.

Later, it was found that certain desirable impurities can be transferred to produce either n- or p-type semiconductors, and that by proper reactant arrangement and temperature control, alternating n- and p-type layers can be deposited without interruption. Crystal growing from the vapor differs in several important ways from crystal growing from the melt.

By this process, scientists at IBM Research have fabricated germanium-gallium arsenide heterojunctions (junctions between two different semiconductors of the same crystal structure). Study revealed certain unexpected properties of these junctions. For example, n-n and p-p abrupt junctions do not obey Ohm's law. This unusual phenomenon may lead to the development of a very high-speed diode. It also opens an unexplored field of semiconductor study.

IBM.RESEARCH

Investigate the many career opportunities available in exciting new fields at IBM
International Business Machines Corporation, Dept. 579T, 590 Madison Avenue, New York 22, New York

WHAT
do
you need to know
about...

PURE
FERRIC OXIDES

MAGNETIC
IRON OXIDES

MAGNETIC
IRON POWDERS

?

Since final quality of your production of ferrites, electronic cores, and magnetic recording media depends on proper use of 3 specialized groups of magnetic materials . . . you'll find it mighty helpful to have all the latest, authoritative technical data describing the physical and chemical characteristics of each. This information is available to you just for the asking. Meanwhile, here are highlights of each product group.

PURE FERRIC OXIDES—For the production of ferrite bodies, we manufacture a complete range of high purity ferric oxide powders. These are available in both the spheroidal and acicular shapes, with average particle diameters from 0.2 to 0.8 microns. Impurities such as soluble salts, silica, alumina and calcium are at a minimum.

MAGNETIC IRON OXIDES—For magnetic recording—audio, video, instrumentation etc.—we produce a group of special magnetic oxides with a range of controlled magnetic properties. Both the black ferroso-ferric and brown gamma ferric oxides are available.

MAGNETIC IRON POWDERS—For the fabrication of magnetic cores in high-frequency, tele-communication, and other magnetic applications, we make a series of high purity iron powders.

If you have problems involving any of these materials, please let us go to work for you. We maintain fully equipped laboratories for the development of new and better inorganic materials. Write . . . stating your problem . . . to C. K. Williams & Co., Dept. 38, 640 N. 13th St., Easton, Penna.

WILLIAMS
COLORS & PIGMENTS
C. K. WILLIAMS & CO.
E. ST. LOUIS, ILL. • EASTON, PA. • EMERYVILLE, CAL.

LONG RANGE VISIBILITY

The NEW
CENCO
Lecture
Room
Meter

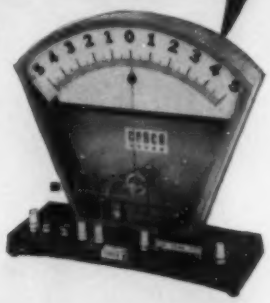

Now—a combination galvanometer, four-range voltmeter and four-range ammeter with figures and graduations on a large 17" scale that is plainly seen from both sides over any distance in the classroom. An accurate, versatile lecture meter with a modern, shielded movement. All parts and circuits clearly visible.

Cenco No. 82140
complete with shunts and multipliers $260.00

cenco
Serving education since 1889.

CENTRAL SCIENTIFIC CO.
A Subsidiary of Cenco Instruments Corporation
1718-A Irving Park Road • Chicago 13, Illinois
Branches and Warehouses—Mountainside, N. J. Boston • Birmingham • Santa Clara • Los Angeles • Tulsa Houston • Toronto • Montreal • Vancouver • Ottawa

FOR PRECISE CONTROL OF GAS FLOW

Granville-Phillips
SERIES 9100
VARIABLE LEAK

Pressure control in a baked out N_2 trapped system pumped by a Veeco EP2AB Diffusion Pump. The leak inlet tubulation was open to the atmosphere during the test.

- Seals mass spectrometer leak tight at 10 in. oz. even at inlet pressures of 500 PSI
- Conductance variable from 10 cc/sec to less than 10^{-11} cc/sec
- Bakeable to 450°C
- Controls all non-corrosive gases
- Useful in ambients up to 400 PSI

Write for complete specifications

Granville-Phillips Co.
P. O. Box J-193 Pullman, Washington

to simplify vacuum control . . .

NEW CENCO DISCHARGE GAGE AND CONTROLLER

A gage and automatic controller that continuously reads from 0.001 to 20 microns total pressure of all condensable vapors and gases in your system. Starts instantly at any pressure. Controller provides automatic on-off switching at pre-set pressures—transistorized amplifier opens or closes contacts of relay to control up to 1 amp.

No. 94183 $249.50

cenco®

CENTRAL SCIENTIFIC CO.
A Subsidiary of Cenco Instruments Corporation
1718-A Irving Park Road • Chicago 13, Illinois
Branches and Warehouses—Mountainside, N. J. Boston • Birmingham • Santa Clara • Los Angeles • Tulsa Houston • Toronto • Montreal • Vancouver • Ottawa

High Performance ELECTROMAGNETS and Power Supplies

RUGGEDNESS

4" Electromagnet Type A
(4" pole diameter)
Fields up to 25,000 gauss.
Homogeneity of at least 1 part in 10^5 in ½ cc.

ROTATION

Rotating Base Type AE
360° scale.
Positive friction lock.

STABILITY

Current-Stabilized Power Supply Unit Type B.

Also available:—
1½" Electromagnet Type C—for Teaching purposes.
7" Electromagnet Type E—for Electron Resonance Work.
8" Electromagnet Type D—for Electron Resonance and Nuclear Magnetic Resonance work.
Direct Reading Magnetometer Type G.
Proton Resonance Magnetometer Type P.

NEWPORT INSTRUMENTS
(Scientific & Mobile) Ltd.
NEWPORT PAGNELL, BUCKS, ENGLAND
Telephone: NEWPORT PAGNELL 401/2

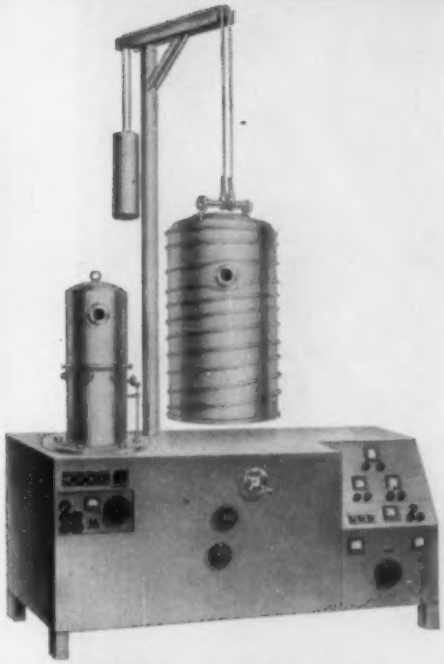

WHAT HAPPENS AT 1,200,000 FEET UP?

You can have the answer NOW . . . and leave theory and the educated guess to others. KINNEY offers fully developed working tools which provide pressures of better than 1×10^{-9} mm Hg . . . ready to work in areas heretofore closed to physicist and researcher.

Kinney®

TWO NEW DEVELOPMENTS IN ULTRA HIGH VACUUM

The KINNEY UH-9A Ultra High Vacuum System, (illustrated above) employing the principle of differential pumping, consistently produces Vacuum in the order of 1×10^{-9} mm Hg in the work chamber. KINNEY also offers a new Ionic High Vacuum System which develops pressures even lower than the $^{-9}$ scale. This system features the Ultek® Ion Pump for which KINNEY is exclusive distributor.

The facts about these significant developments in Vacuum technology are yours for the asking. **Write for KINNEY bulletins 4150, 4160 and 4450 today!**

KINNEY VACUUM DIVISION
THE NEW YORK AIR BRAKE COMPANY
3556H WASHINGTON STREET • BOSTON 30 • MASS.

Please send me copies of Bulletins 4150, 4160 and 4450 describing KINNEY Ultra High Vacuum Systems.

Name_____

Company_____

Address_____

City_____ Zone____ State_____

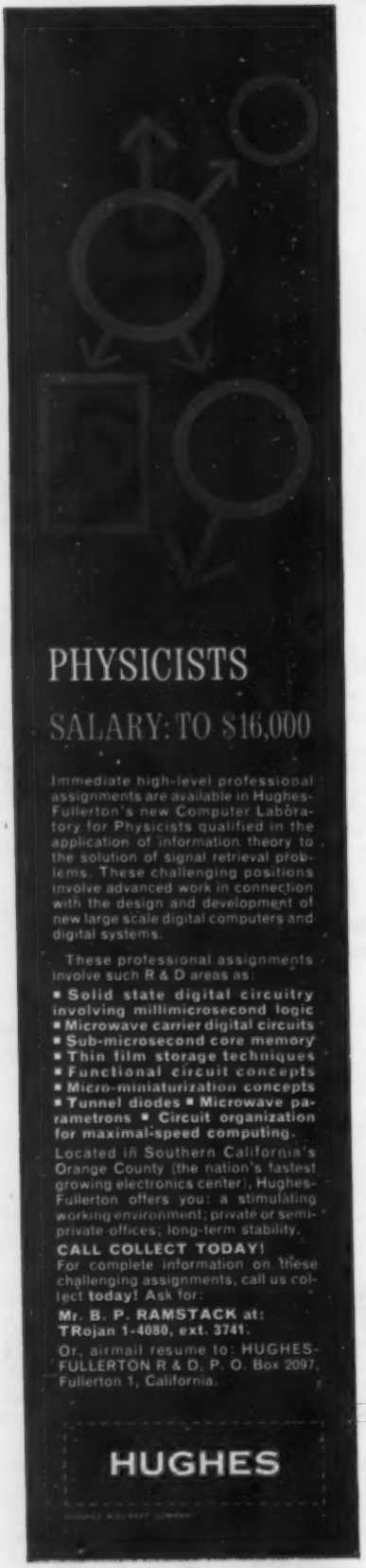

PHYSICISTS

SALARY: TO $16,000

Immediate high-level professional assignments are available in Hughes-Fullerton's new Computer Laboratory for Physicists qualified in the application of information theory to the solution of signal retrieval problems. These challenging positions involve advanced work in connection with the design and development of new large scale digital computers and digital systems.

These professional assignments involve such R & D areas as:

- **Solid state digital circuitry involving millimicrosecond logic**
- **Microwave carrier digital circuits**
- **Sub-microsecond core memory**
- **Thin film storage techniques**
- **Functional circuit concepts**
- **Micro-miniaturization concepts**
- **Tunnel diodes ■ Microwave parametrons ■ Circuit organization for maximal-speed computing.**

Located in Southern California's Orange County (the nation's fastest growing electronics center), Hughes-Fullerton offers you: a stimulating working environment; private or semi-private offices; long-term stability.

CALL COLLECT TODAY!
For complete information on these challenging assignments, call us collect **today!** Ask for:

Mr. B. P. RAMSTACK at: TRojan 1-4080, ext. 3741.

Or, airmail resume to: HUGHES-FULLERTON R & D, P. O. Box 2097, Fullerton 1, California.

HUGHES

Under the direction of The American Ceramic Society . . . a major source of scientific communication—

GLASS AND CERAMICS

Translated from Russian into English

This Soviet monthly, published for glass and ceramic researchers, technologists and production workers, provides Western scientists with reports on the latest technical advances from the laboratories and plants of the USSR.

Translation of GLASS AND CERAMICS, prompted by the recognition given to Soviet work in the field, permits you to take advantage of their intensified research program. Using these accurate translations by a staff of bilingual scientists can eliminate costly duplication of research. Scientists in this country can learn the specifics about how their Soviet counterparts upgrade products and improve processes; design unique, improved equipment; break production records and reduce costs.

GLASS AND CERAMICS will be published in the most effective manner possible to bridge the gap since this journal was last available in complete translation.

1956 and 1957 have been published. 1958 and 1959 will be brought out in four-issue volumes on a bimonthly basis until they are completed.

Subscription prices: $80.00 per year.
Foreign: $85.00 per year.

Also available in English:

1. **1st Conference on the Structure of Glass** (held in Leningrad), 296 pp., profusely illustrated . . . $20.00.

2. **Proceedings of 2nd Conference on Structure of Glass,** to be published soon . . . $20.00.

Detailed tables of contents will be sent upon request.

Order on approval from:

CONSULTANTS BUREAU ENTERPRISES, INC.

227 W. 17th St., New York 11, N.Y.

IONOSPHERIC PROPAGATION AND HF COMMUNICATIONS

If you have the background, the imagination and the desire to contribute to important projects in these fields, you are invited to join a carefully selected team of outstanding scientists and engineers now conducting research programs furthering the state-of-the-art.

Our present needs are for:

SENIOR IONOSPHERIC PHYSICISTS

Ph.D. preferred, with several years' experience in the study of ionospheric phenomena. Should be familiar with present knowledge of upper atmosphere physics and possess an understanding of current programs using rockets and satellites for studies in F-region and beyond. Qualified individuals with supervisory abilities will have an exceptional opportunity to assume project leadership duties on HF projects already under way involving F-layer propagation studies backed by a substantial experimental program.

SENIOR DEVELOPMENT ENGINEERS

Advanced degree in E.E. or Physics preferred. Must be familiar with present state-of-the-art in the design of advanced HF receivers and transmitters and possess working knowledge of modern HF networks employing ferrites and metallic tape cores. Strong theoretical background in modern linear circuit theory desired. Will carry out laboratory development and implementation of new HF communications systems.

SENIOR ELECTRONIC ENGINEERS

Advanced degree in E.E. preferred. Must be familiar with conventional pulse circuit designs and applications. Technical background should include substantial experience in data process and data recovery systems using both analog and digital techniques. Knowledge of principles and application of modern information theory including correlation techniques helpful. Will be responsible for the design of sub-systems.

Our location in the suburban Washington D.C. area is ideal from the viewpoint of advanced study which may be conducted at one of several nearby universities, for readily available housing in pleasant residential neighborhoods, and for the general amenities of living offered by this important Metropolitan center.

For a prompt reply to your inquiry, please forward resume in confidence to:

Mr. William T. Whelan
Director, Research & Development

ACF ELECTRONICS DIVISION
ACF INDUSTRIES
RIVERDALE, MARYLAND

a vacuum pump as quiet as a . . .

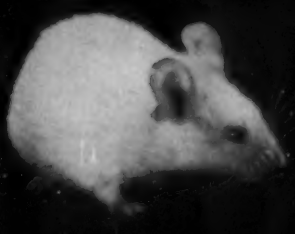

Steady and silent. That's the new Stokes Series H Microvac pump. Unique dynamic balancing provides hushed operation. And the compact Stokes pump saves up to 50% in valuable floor space.

Find out all the reasons why you get *more pumping performance per dollar* with Stokes Microvac pumps. Just write: Vacuum Equipment Division, F. J. STOKES CORPORATION, 5500 TABOR RD., PHILA. 20, PA.

STOKES

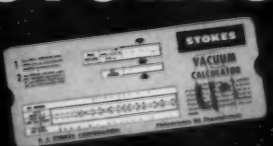

SEND TODAY
for your free
Vacuum Slide Calculator

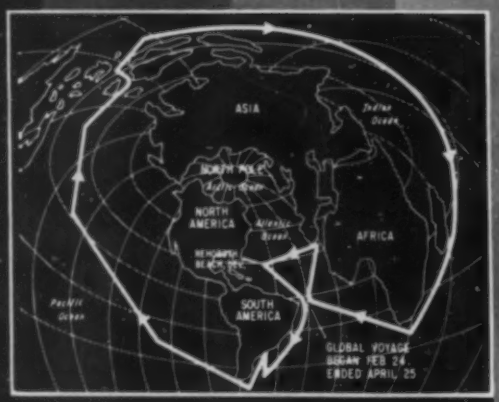

*USS TRITON'S HISTORIC VOYAGE

Nuclear Engineers and Scientists

When the Navy's first nuclear radar picket submarine surfaced after its pioneering underwater trip around the world, its engineroom log showed 41,500 trouble-free miles traversed in 84 days.

For KAPL engineers and scientists who designed and developed Triton's unique twin reactor propulsion system, this invisible voyage was a new triumph in nuclear engineering. The world's largest submarine is powered by a KAPL pressurized water cooled system fueled by enriched uranium. It features compact reactor cores and low weight-per-shaft horsepower.

NEW REACTOR MILESTONE LOGGED

BY THE KNOLLS ATOMIC POWER LABORATORY

Explorations currently underway at KAPL are aimed at achieving a new regime of simplification in reactor technology. Qualified Nuclear Engineers and Physicists are invited to inquire about current openings.

Appropriate scientific or engineering degree and U.S. citizenship required.

Address: Mr. A. J. Scipione, Dept. 37-MH

Knolls Atomic Power Laboratory

OPERATED FOR A E C BY

GENERAL ELECTRIC

Schenectady, New York

Gaertner Precision Optical Bench Assembly

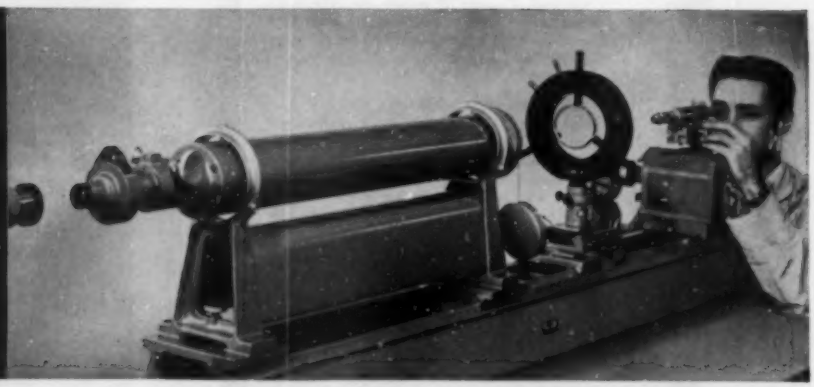

Useful in checking optics and for experimental instrumentation setups

The Precision Optical Bench is a versatile measuring instrument consisting of a lathe-bed-type base, light source, collimator with interchangeable filters and targets, nodal slide and microscope with three-dimensional adjustment. Focal lengths, resolving power and the various aberrations of optical parts and systems can be measured.

The several components can be used independently for special test setups, mock-ups and experimental instrumentation—providing linear and angular motions and measurements, alignment and stable support.

Double and single rod benches and a large selection of carriages, holders and supports provide a complete selection from which to choose.

Gaertner offers a wide range of optical and measuring instruments, including special modifications, design and manufacture of special instruments and optical systems, and manufacture of subassemblies and instruments from customer sketches and drawings.

Send for bulletin 156-59

Designed and manufactured in the U.S.A. by

Gaertner

SCIENTIFIC CORPORATION

1246 Wrightwood Ave., Chicago 14, Illinois • BU 1-5335

NEWS from the NRC Vacuum MICRONICLE*

ULTRA HIGH VACUUM GAGE AIDS STUDIES

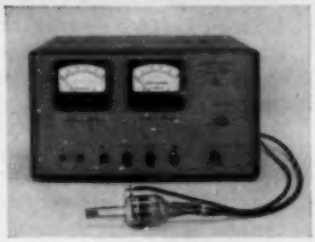

It has been hard to measure the pressures in ultra high vacuum systems used for space chamber testing, thermonuclear power research, micromolecular circuit development and solid state studies. The new Nottingham Ionization Gage gives direct measurements of 10^{-10} mm mercury and indirect estimates of pressures to 10^{-12}. The Gage is linear, stable and repetitive.

***FREE NRC Vacuum Micronicle**

A periodical containing news about improving products with NRC high vacuum equipment. Write on your firm letterhead.

NRC EQUIPMENT CORPORATION

A Subsidiary of National Research Corporation

DEPT. P-8, 160 Charlemont St., Newton 61, Mass.

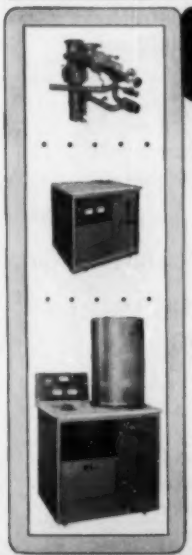

You're guaranteed 10^{-6} mm Hg *fast* with . . .

THE MODULAR "400" SERIES 4" VACUUM SYSTEMS & EVAPORATORS

GUARANTEED PERFORMANCE:

5×10^{-4} in 45 sec. Less than 5×10^{-7} ultimate (blanked port)

5×10^{-4} in 4 min. Less than 10^{-6} ultimate (18" x 30" Bell Jar)

MODULAR CONSTRUCTION:

Buy exactly what you need, from basic plumbing to complete Evaporators and Bakeout Systems. Incorporate additional equipment as your requirements grow.

TROUBLE-FREE PERFORMANCE:

Each VE-400 System undergoes a full week (168 hrs.) of test run and inspection before shipment.

FREE "400" SERIES BROCHURE contains complete performance data and design specifications on the 4" building block components and modular systems. Write Department A-1436.

Veeco

VEECO VACUUM CORP.

86 Denton Avenue, New Hyde Park
Long Island, New York

HIGH VACUUM & LEAK DETECTION EQUIPMENT

NOW— 15,000°F. PLASMA FLAME SPRAY IN YOUR OWN PLANT

Apply coatings of high melting point materials such as tungsten, tungsten carbide, molybdenum, chromium carbide, titanium oxides, calcium zirconate, rare earth oxides. Operates at 10,000°-15,000°F.

Plasma flame spraying hi-temperature crucible

Now any material that can be melted without decomposing can be sprayed. Despite high melting temperature, object sprayed stays cool.

High fluidity of particles and high velocity of impingement bond the particles together to produce high density coatings semi-fused to work. Absence of air eliminates oxidation.

The METCO Plasma Flame Spray Gun is a valuable new tool for the metalworking research department or production line. Operates on inexpensive inert gases with high electrical power conversion efficiency, long component life. Continuous gas streams, as high as 30,000°F., with accurate control of temperature, generated at costs of ⅛ to ½ those of oxygen-fuel gas equipment for equivalent heat output. No combustion—uses inert gases. No flashback or explosion hazards—push-button operation.

Write today for free bulletin describing the METCO Plasma Flame Gun.

METCO

Metallizing Engineering Co., Inc.

Flame Spray Equipment and Supplies

1143 Prospect Avenue, Westbury, Long Island, N. Y.

In Great Britain METALLIZING EQUIPMENT CO., Ltd. Chobham-near-Woking, England

Please send me free bulletin on the Metco Plasma Flame Spray Gun.

Name _____ Title _____

Company _____

Address _____

City _____ Zone _____ State _____

INDEX TO ADVERTISERS

Name	*Page*
A.C.F. INDUSTRIES, INC.	xxi
AMERICAN CERAMIC SOCIETY	xx
AUTONETICS Div. of North American Avia.	viii
BECKMAN & WHITLEY, INC. Manufacturers of high-speed research cameras—both framing and sweeping-image type; specialized meteorological instruments; heat-flow transducers; and explosive-actuated mechanisms.	Cover 2
BELL TELEPHONE LABORATORIES	iii
CENTRAL SCIENTIFIC CO. Manufacturers of Cenco physical apparatus and instruments to meet all requirements of University, College and High School Physics Laboratories. Specializing in high vacuum pumps and development of instruments and apparatus for various sciences.	xviii, xix
CONVAIR/FORT WORTH Div. of General Dynamics	xxvi
CORNELL-DUBILIER ELECTRIC CORP. Primarily interested in the design and manufacture of special type capacitors for thermonuclear work along the lines of the enclosed illustrations. These special fast discharge low inductance capacitors, operating in voltages up to 160 KV, have extensive use in the advanced study of high temperature and high current fields.	xiv
GAERTNER SCIENTIFIC CORP. Spectroscopes, spectrometers, spectrographs, spectrophotometers, heliostats, measuring microscopes, comparators, cathetometers, reading telescopes, interferometers, chronographs, dividing machines, etc.	xxii
GENERAL ELECTRIC Knolls Atomic Power Lab.	xxii
GENERAL MOTORS Delco Radio Div.	iv
GENERAL RADIO CO. Manufacturers of electronic measuring instruments; vacuum-tube voltmeters, amplifiers, and oscillators; wave analyzers, noise meters and analyzers, stroboscopes, laboratory standards of capacitance; inductance and frequency; impedance bridges, decade resistors and condensers, air condensers and variable inductors; rheostats, variacs, transformers; other laboratory accessories.	Cover 3
GRANVILLE-PHILLIPS CO.	xviii
HUGHES AIRCRAFT CO.	xv, xx
I.B.M. CORPORATION	xvii, xxvi
KEITHLEY INSTRUMENTS, INC. Vacuum tube electrometers, microammeters, kilovoltmeters, static detectors, meg-megohm-meters, high gain dc amplifiers, dc vacuum tube voltmeters, high input impedance ac isolation amplifiers.	vii
KINNEY VACUUM DIVISION, N. Y. AIR BRAKE CO.	xix
LOCKHEED MISSILES & SPACE DIV.	xi
LOS ALAMOS SCIENTIFIC LAB.	xiii
McGRAW-HILL BOOK CO., INC.	xii
METALLIZING ENGINEERING CO., INC.	xxiii
NRC EQUIPMENT CORP. Manufacturers of standard and special high vacuum components, equipment, and systems including mechanical booster, and diffusion pumps; gauges; valves; seals; connectors; melting and heat-treating furnaces; coaters; impregnators; gas in metal analyzers; driers and freeze driers; altitude chambers; and leak detectors.	xxiii

INDEX—*Continued*

Name	*Page*
NEWPORT INSTRUMENTS LTD. ...	xix
PACIFIC SEMICONDUCTORS, INC. .	x
RAMO-WOOLDRIDGE LABS. .... Research, development, and manufacture in the field of electronic systems for commercial and military applications, and in the field of guided missiles.	Cover 4
STOKES CORP., F. J. ..... Mechanical and oil vapor pumps; vacuum valves, gauges and other components; vacuum furnaces, metalizers, processing systems and other special high vacuum equipment.	xxi
SYLVANIA ELECTRIC PRODUCTS, INC.	vi
TEXAS INSTRUMENTS, INC.	ix
VARIAN ASSOCIATES	v
VEECO VACUUM CORP.	xxiii
WELCH SCIENTIFIC CO., W. M. .... Manufacturers of high-vacuum pumps, both mechanical and diffusion; vacuum gauges; electrical measuring instruments; physics equipment; and other items for the physical and chemical laboratories.	xvi
WILLIAMS & CO., C. K.	xviii

SEVENTH MIDWESTERN CONFERENCE FLUID MECHANICS AND SOLID MECHANICS

An attractive and broad program is being prepared for the Seventh Midwestern Conference on Fluid Mechanics and Solid Mechanics. Authors wishing to present papers should send in their abstracts by January 1, 1961. For further information, address inquiries to: Professor J. E. Lay, Mechanical Engineering Department, Michigan State University, East Lansing, Michigan.

Michigan State University
East Lansing, Michigan
September 6, 7, 8, 1961

TRANSLATIONS OF . . . .
SOVIET JOURNALS

Published by the American Institute of Physics with the cooperation of the National Science Foundation.

SOVIET PHYSICS—JETP

Monthly. Translation of *Zhurnal Eksperimental'noi I Teoreticheskoi Fiziki* of Academy of Sciences, USSR.

SOVIET PHYSICS—SOLID STATE

Monthly. Translation of *Fizika Tverdogo Tela* of Academy of Sciences, USSR.

SOVIET PHYSICS—TECHNICAL PHYSICS

Monthly. Translation of *Zhurnal Tekhnicheskoi Fiziki* of Academy of Sciences, USSR.

SOVIET PHYSICS—DOKLADY

Bimonthly. Translation of the Physics Section of Proceedings of Academy of Sciences, USSR.

SOVIET PHYSICS—ACOUSTICS

Quarterly. Translation of *Akusticheskii Zhurnal* of Academy of Sciences, USSR.

SOVIET PHYSICS—CRYSTALLOGRAPHY

Bimonthly. Translation of *Kristallografiya* of Academy of Sciences, USSR.

SOVIET PHYSICS—USPEKHI

Bimonthly. Translation of *Uspekhi Fizicheskikh Nauk* of Academy of Sciences, USSR.

SOVIET ASTRONOMY—AJ

Bimonthly. Translation of *Astronomicheskii Zhurnal* of Academy of Sciences, USSR.

Send orders and inquiries to:

American Institute of Physics
335 East 45 Street, New York 17, N. Y.

THE 1960's WILL BE A DECADE OF TIME COMPRESSION . . .

More people will travel further in a shorter time—men will move in geocentric orbits at 18,000 mph—space probes will shrink our celestial environment. To accomplish these things, the time between research and application engineering will shrink dramatically.

Convair believes that the full potential of Technology in the Sixties will be realized through ideas originating in the minds of creative scientists and engineers. To implement this conviction, Convair-Fort Worth is pursuing an active research program in the engineering and physical sciences.

A position on the staff of the newly formed Applied Research Section offers opportunity rarely found for physicists and engineers at the doctorate level. Research programs in the fields of astrophysics, relativity, gravitation, physics of materials, and geophysics are in the formative stages of planning and activation. Active and mature programs in electronics, space mechanics, and thermodynamics are underway.

If you can qualify, a position within this section will offer unlimited growth potential. For further information, forward your personal resume to Dr. E. L. Secrest, Chief of Applied Research, Convair-Fort Worth, P. O. Box 748 J, Fort Worth, Texas.

CONVAIR/FORT WORTH
CONVAIR DIVISION OF
GENERAL DYNAMICS

IBM has career opportunities for Physicists in basic studies in properties of materials

IMAGE STORAGE AND DISPLAY

IBM's Advanced Systems Development Division has immediate openings for Physicists to conduct basic studies in the properties of materials. The output of these studies will be applied by our Engineers to develop systems components for the storage and display of graphic information.

Qualifications include an advanced degree in Physics with experience in the study of material properties such as magnetic, photoconductive, optical, phosphorescent and fluorescent.

The Advanced Systems Development Laboratories are located in Westchester County, just north of New York City. Excellent schools and housing. At ASDD you will be offered all the opportunities of a new company combined with the stability and enterprise of IBM.

For further information, please write, outlining briefly your background and experience, to:

Mr. H. J. Cooke, Dept. 579T1
IBM Advanced Systems Development Division
2651 Strang Boulevard
Yorktown Heights, New York

IBM®

INTERNATIONAL BUSINESS MACHINES CORPORATION

Sound and Vibration Analysis with One Versatile Instrument

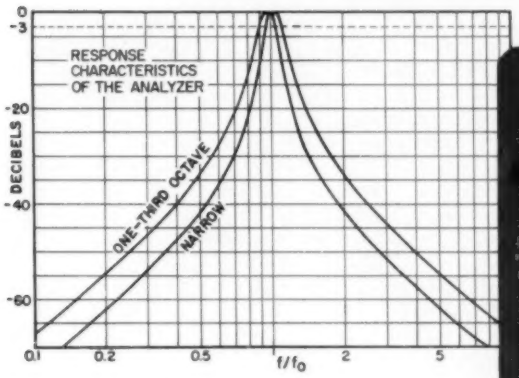

THREE BANDWIDTHS:

"NARROW" — for measurement of single-frequency components of spectrum — bandwidth is 8% of center frequency at 3-db points.

"ONE-THIRD OCTAVE" for analysis of noise — bandwidth is 1.26 times center frequency.

"ALL-PASS" for convenient adjustment of overall level — flat from 2.5 to 25,000 cps ±2 db.

Both Analyzer characteristics fall off at 12-db per octave far from center frequency.

Type 1564-A
Sound and Vibration Analyzer . . . $1,060.

Designed for use with a Sound-Level or Vibration Meter — where levels exceed 50 db, the Analyzer may be used directly with an accessory microphone.

Wide Range: continuously tunable from 2.5 to 25,000 cps

Convenient, adjustable decibel dial makes Analyzer direct reading in sound pressure level, one-third octave-band level, or any other desired level — can be calibrated against 115v line to make Analyzer direct reading in input volts.

Portable and battery-operated for field use.

AUTOMATIC LEVEL RECORDING:

The Sound and Vibration Analyzer may be conveniently coupled by means of a link unit, to the TYPE 1521-A Graphic Level Recorder (frequency range, 20 cps to 200kc) for automatic analysis of sounds, vibrations, or electrical signals. Special chart paper for the Recorder has a frequency scale which matches the dial of the Analyzer.

Write For Complete Information

GENERAL RADIO COMPANY

WEST CONCORD, MASSACHUSETTS

our 45th year in Electronics

NEW YORK, WOrth 4-2722	CHICAGO	PHILADELPHIA	WASHINGTON, D.C.	SAN FRANCISCO	LOS ANGELES	IN CANADA
District Office in Ridgefield, N. J. WHitney 3-3140	Oak Park Village 8-9400	Abington HAncock 4-7419	Silver Spring JUniper 5-1088	Los Altos WHitecliff 8-8233	Los Angeles HOllywood 9-6201	Toronto CHerry 6-2171

At The Ramo-Wooldridge Laboratories... integrated programs of research & development of electronic systems and components.

The new Ramo-Wooldridge Laboratories in Canoga Park provide an environment for creative work in an academic setting. Here, scientists and engineers seek solutions to the technological problems of today. The Ramo-Wooldridge research and development philosophy places major emphasis on the imaginative contributions of the members of the technical staff. ■ There are outstanding opportunities for scientists and engineers. *Write* Dr. Richard C. Potter, Head, Technical Staff Development, Department 16-G.

THE RAMO-WOOLDRIDGE LABORATORIES

A DIVISION OF THOMPSON RAMO WOOLDRIDGE INC.

8433 FALLBROOK AVENUE, CANOGA PARK, CALIFORNIA

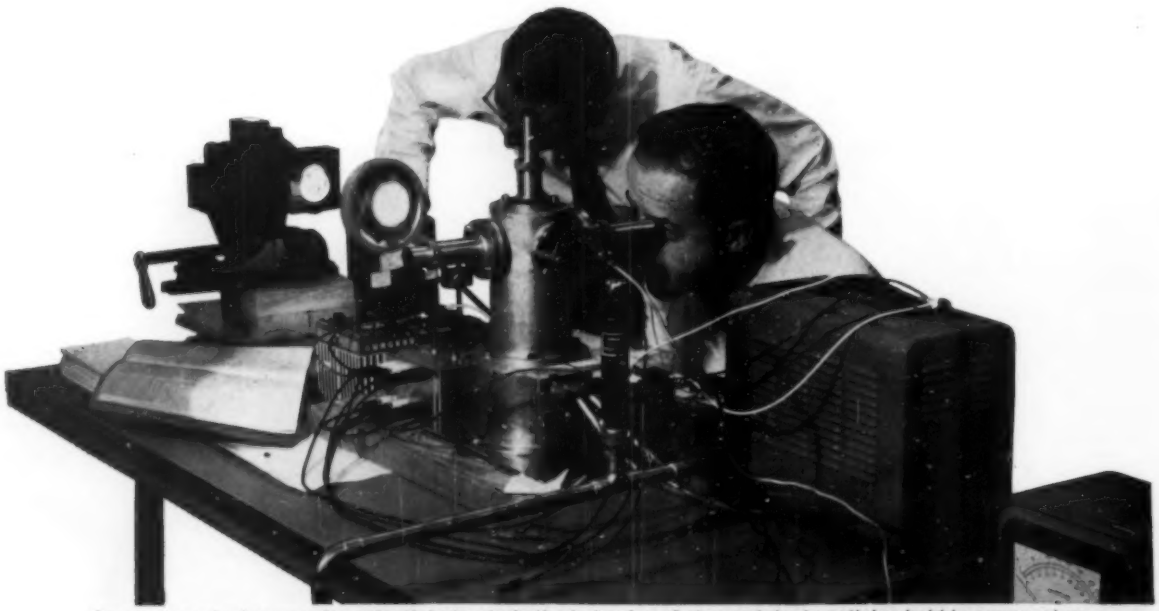

An electron device permits scientists to study the behavior of charged dust particles held in suspension.